

# Numerical Modeling and Neural Networks to Identify Constitutive Parameters from In Situ Tests

THÈSE N° 4457 (2009)

PRÉSENTÉE LE 24 JUILLET 2009

À LA FACULTÉ ENVIRONNEMENT NATUREL, ARCHITECTURAL ET CONSTRUIT  
LABORATOIRE DE MÉCANIQUE DES SOLS  
PROGRAMME DOCTORAL EN MÉCANIQUE

ÉCOLE POLYTECHNIQUE FÉDÉRALE DE LAUSANNE

POUR L'OBTENTION DU GRADE DE DOCTEUR ÈS SCIENCES

PAR

Rafal Filip OBRZUD

acceptée sur proposition du jury:

Prof. J.-F. Molinari, président du jury  
Prof. L. Vulliet, Prof. A. Truty, directeurs de thèse  
Prof. M. Boulon, rapporteur  
Prof. J. Zhao, rapporteur  
Prof. T. Zimmermann, rapporteur



ÉCOLE POLYTECHNIQUE  
FÉDÉRALE DE LAUSANNE

Suisse  
2009



*To my late father*



# Contents

<b>Table of Contents</b>	<b>i</b>
<b>Abstract</b>	<b>v</b>
<b>Résumé</b>	<b>vii</b>
<b>Acknowledgments</b>	<b>ix</b>
<b>List of Symbols</b>	<b>xi</b>
<b>1 Introduction</b>	<b>1</b>
1.1 Evaluation of engineering properties of soils . . . . .	1
1.2 Objectives of the thesis . . . . .	2
1.3 Outline of the thesis . . . . .	4
<b>2 Fundamentals of Parameter Identification</b>	<b>7</b>
2.1 Testing as a tool for parameter identification . . . . .	10
2.2 Reliability of experimental measurements . . . . .	14
2.3 Classical approaches to the inverse problem . . . . .	15
2.3.1 Constitutive equations and direct approach . . . . .	16
2.3.2 Objective function and its minimization . . . . .	17
2.3.3 Gradient-based search algorithm . . . . .	18
2.3.4 Limitations of gradient-based optimization . . . . .	21
2.4 Enhanced approach to parameter identification . . . . .	22
2.5 Summary and anticipated contribution . . . . .	25
<b>3 Neural Networks as Identification Method</b>	<b>27</b>
3.1 Introduction . . . . .	27
3.2 Identification based on neural networks . . . . .	30
3.2.1 Numerical approach for database generation . . . . .	31
3.2.2 Preparation of training patterns . . . . .	32
3.3 Theory of feed-forward neural networks . . . . .	32
3.3.1 Model of a neuron . . . . .	33
3.3.2 Network architecture and feed-forward procedure . . . . .	34
3.3.3 Neural network training . . . . .	35
3.3.3.1 Selection of training database . . . . .	36
3.3.3.2 Data pre-processing . . . . .	36

3.3.3.3	Determination of network topology . . . . .	38
3.3.3.4	Back-propagation algorithm . . . . .	38
3.3.3.5	Network performance monitoring . . . . .	40
3.3.4	Post-training network analysis . . . . .	41
3.4	Remarks on NN's shortcomings . . . . .	42
3.5	Summary . . . . .	43
<b>4</b>	<b>Mathematical Model of Soil</b>	<b>45</b>
4.1	Constitutive equations of the Modified Cam Clay model . . . . .	46
4.2	Hydro-mechanical solid-fluid interaction . . . . .	47
4.3	Remarks on model shortcomings . . . . .	49
<b>5</b>	<b>Enhanced Identification Verification</b>	<b>51</b>
5.1	Numerical implementation for drained triaxial compression test	51
5.1.1	Space of parameters . . . . .	53
5.1.2	Parameter identification for isotropic consolidation test .	54
5.1.3	Parameter identification for the drained compression test	54
5.2	Parameter identification for real experimental data . . . . .	58
5.2.1	Material and test procedure . . . . .	58
5.2.2	Example of parameter identification for the isotropic con- solidation test . . . . .	58
5.2.3	Example of parameter identification for the drained com- pression test . . . . .	59
5.2.4	Efficiency test . . . . .	63
5.3	Summary . . . . .	64
<b>6</b>	<b>BVPs of Selected <i>In Situ</i> Tests</b>	<b>67</b>
6.1	Overview of <i>in situ</i> tests . . . . .	67
6.1.1	Self-boring pressuremeter test . . . . .	68
6.1.2	Piezocone penetration test . . . . .	69
6.2	Analytical analysis of self-boring pressuremeter test . . . . .	71
6.2.1	<i>In situ</i> state of soil . . . . .	71
6.2.2	Cavity expansion test . . . . .	72
6.2.3	Analysis of dissipation test . . . . .	80
6.2.4	Overestimation of determined parameters . . . . .	83
6.2.5	Hydro-mechanical coupling of pressuremeter tests . . . . .	85
6.3	Analysis of the piezocone penetration test . . . . .	86
6.3.1	Theoretical analysis of cone resistance . . . . .	88
6.3.2	Interpretation of CPTU measurements . . . . .	92
6.3.2.1	Normalization of CPTU data . . . . .	93
6.3.2.2	Undrained shear strength . . . . .	93
6.3.2.3	Effective stress strength . . . . .	96
6.3.2.4	Stress history . . . . .	97
6.3.2.5	Horizontal stress . . . . .	99
6.3.2.6	Stiffness characteristics . . . . .	100
6.3.2.7	Rigidity index and consolidations characteristics	101
6.3.3	Effect of drainage conditions on penetration results . . . . .	103

6.3.4	Remarks . . . . .	104
<b>7</b>	<b>Numerical Modeling of Selected Field Tests</b>	<b>107</b>
7.1	Numerical model of pressuremeter test . . . . .	108
7.1.1	Finite element model . . . . .	108
7.1.2	Effect of soil permeability . . . . .	109
7.1.3	Non-uniqueness and sensitivity of strength parameters . . . . .	111
7.1.4	Effect of stress anisotropy . . . . .	111
7.1.5	Sensitivity analysis of pressure holding test . . . . .	113
7.2	Numerical model of piezocone test . . . . .	114
7.2.1	Finite element model . . . . .	115
7.2.1.1	Cone-soil interface modeling . . . . .	116
7.2.1.2	Experimental evidence of the steel-soil interface . . . . .	118
7.2.1.3	Strength anisotropy . . . . .	119
7.2.1.4	Finite element discretization . . . . .	120
7.2.2	Analysis of finite element model . . . . .	124
7.2.2.1	Analysis of cone factors . . . . .	127
7.2.2.2	Analysis of drainage conditions . . . . .	134
7.2.2.3	Friction effects on piezocone measurements . . . . .	136
7.2.3	Semi-numerical model for the NN pattern generation . . . . .	145
7.3	Summary and remarks . . . . .	145
<b>8</b>	<b>Parameter Identification for <i>In Situ</i> Tests</b>	<b>147</b>
8.1	Hybrid neural network/gradient-based model calibration based on pressuremeter tests . . . . .	148
8.1.1	Strategy of parameter identification . . . . .	148
8.1.2	Numerical generation of training patterns . . . . .	152
8.1.3	Definition of network input . . . . .	155
8.1.4	Training and post-training analysis . . . . .	157
8.1.5	Efficiency and convergence analysis . . . . .	160
8.1.6	Effect of initial state variables . . . . .	162
8.1.7	Summary . . . . .	163
8.2	Neural networks for parameter estimation based on piezocone data	164
8.2.1	Strategy of parameter estimation . . . . .	164
8.2.2	Numerical generation of training patterns . . . . .	170
8.2.3	Verification of numerical database . . . . .	170
8.2.4	Definition and notation of network inputs and outputs . . . . .	175
8.2.5	Training and post-training analysis . . . . .	176
8.2.5.1	Undrained shear strength . . . . .	176
8.2.5.2	Effective stress strength . . . . .	179
8.2.5.3	Stress history . . . . .	181
8.2.5.4	Horizontal stress . . . . .	188
8.2.5.5	Deformation characteristics . . . . .	190
8.2.6	Knowledge extraction . . . . .	192
8.2.7	Summary . . . . .	194
<b>9</b>	<b>Validation of Enhanced Parameter Identification</b>	<b>197</b>

9.1	Model calibration using pressuremeter test . . . . .	198
9.1.1	Experimental data . . . . .	198
9.1.2	Parameter identification . . . . .	201
9.1.3	Analysis of obtained results . . . . .	202
9.1.4	Summary . . . . .	204
9.2	Parameter estimation using piezocone test . . . . .	205
9.2.1	Estimation of OCR for a worldwide database . . . . .	205
9.2.2	Parameter estimation for Bäckebol site, Sweden . . . . .	206
9.2.3	Parameter estimation for Skå-Edeby site, Sweden . . . . .	213
9.2.4	Parameter estimation for Port Huron site, USA . . . . .	215
9.2.5	Parameter estimation for Amherst site, USA . . . . .	218
9.2.6	Parameter estimation for Bothkennar site, UK . . . . .	222
9.2.7	Conclusions . . . . .	227
<b>10</b>	<b>Final Conclusions and Recommendations</b>	<b>229</b>
10.1	Conclusions . . . . .	229
10.1.1	Enhanced parameter identification . . . . .	230
10.1.2	Model calibration with SBPT . . . . .	231
10.1.3	Soil profiling with CPTU . . . . .	233
10.1.4	Summary of original contributions . . . . .	236
10.2	Outlook for future research . . . . .	237
<b>A</b>	<b>Modified Gauss-Newton Algorithm</b>	<b>257</b>
	<b>References</b>	<b>257</b>
<b>B</b>	<b>Material Data for Numerical Simulations</b>	<b>265</b>
<b>C</b>	<b><math>R_p</math> versus OCR in the MCC</b>	<b>267</b>
<b>D</b>	<b>Pattern Generation for CPTU</b>	<b>269</b>
<b>E</b>	<b>GUI for CPTU Data</b>	<b>271</b>
<b>F</b>	<b>NN Training for CPTU Data</b>	<b>273</b>
<b>G</b>	<b>Material Data</b>	<b>281</b>
G.1	Database of discrete piezocone results from clay sites . . . . .	281
G.2	Database of continuous CPTU results from clay sites . . . . .	284
	<b>Curriculum Vitae</b>	<b>287</b>



# Abstract

This study proposes a new advanced algorithm for determining material parameters based on *in situ* tests.

*In situ* testing gives an opportunity to perform soil characterization in natural stress conditions on a representative soil mass. Most field techniques reduce soil disturbances to minimum, allowing investigating the response of virgin soil. Self-boring pressuremeter tests (SBPT) and standard piezocone tests (CPTU) are widely used to deduce properties of clayey soils through analytical and empirical correlations between soil properties and experimental measurements. Empirical correlations usually require some tuning based on reference laboratory data because first-order estimates for typical correlation coefficients may give unreliable evaluation of soil properties. Analytical correlations are mostly based on cavity expansion methods which are restricted to either fully drained or perfectly undrained problems, so that inverse closed-form solutions for relatively simple constitutive models can be derived. In practice, however, depending on physical and consolidation properties of the soil, partially drained conditions may occur during field testing, leading to an erroneous estimation of clay characteristics. Therefore, elaborating a generic parameter identification framework, which is based on the artificial neural network (NN) technique and which may improve the reliability of soil properties derived from *in situ* testing, is the main goal of this research.

This study explores the possibility of using NNs to solve complex inverse problems including partially drained conditions. In other words, NNs are used to map experimental measurements onto set of soil properties. The development of NN-based inverse models is based on a training data sets which consists of pseudo-experimental measurements derived from numerical simulations of both the SBPT and the CPTU test in normally- and lightly overconsolidated clay type material.

The study presents a generic two-level procedure designed for the calibration of constitutive models of soils. It is demonstrated that NN inverse models can be easily integrated into the classical back-analysis. At the first level, the NN approach is applied to achieve the first approximation of parameters. This technique is used to avoid potential pitfalls related to the conventional gradient-based optimization (GBO) technique, considered here as a corrector that improves predicted parameters. Trained NNs as parallel operating systems can provide output variables instantly and without a costly GBO iterative scheme. The proposed framework is verified for the elasto-plastic Modified Cam Clay (MCC) model that can be calibrated based on standard triaxial laboratory tests, i.e. the isotropic consolidation test and the consolidated isotropic drained compression test. The study presents formulations of the input data for the NN predictors, enhanced by a dimensional reduction of experimental data using principal component analysis (PCA). The determination of model characteristics is demonstrated, first on numerical pseudo-experiments and then on the experimental data. Furthermore, the efficiency of the proposed approach in terms of accuracy and computational effort is also discussed.

The verified two-level strategy is applied to a numerical procedure of parameter identification for the boundary value problem (BVP) of the SBPT. The coupled hydro-mechanical finite element (FE) formulation allows the generated excess pore water pressure to be dissipated during simulations of the expansion test, followed then by a holding test. Numerical simulations demonstrate that volume changes that may occur in clay during the expansion test due to partial drainage, can cause local soil hardening near the cavity wall and affect parameter interpretation for pressuremeter

tests. Therefore, the NN technique is applied to obtain an initial guess for model parameters, taking into account the possible partially drained conditions during the expansion test. Parameter identification based on measurements obtained through the pressuremeter expansion test and two types of holding tests is illustrated on the MCC model. NNs are trained using a set of synthetic test samples, which are generated by means of FE simulations based on constrained random permutations of input model parameters. The measurements obtained through expansion and consolidation tests are normalized by the proposed normalizing formulas so that NN predictors operate independently of the testing depth. Examples of parameter determination are demonstrated on both numerical data and field measurements from the Fucino clay deposit. The efficiency of the combined parameter identification in terms of accuracy, effectiveness and computational effort is also discussed.

Finally, an application of NN predictors as a stand-alone support for soil profiling is presented for the piezocone test. By similarity to the SBPT problem, a number of NN inverse models are developed based on the results derived from rigorous FE analyzes. The FE model of piezocone penetration involves numerical formulation for the two-phase material obeying the MCC law and including the large strain theory, as well as the large deformation formulation for contact interface. It is demonstrated that a considerable computational effort related to the generation of the training database can be reduced by optimizing the mesh size and "steady-state" depth in function of soil rigidity index. Due to a severe loss of measurement accuracy observed in the finite elements adhered to the "rough" interface, an equivalent semi-numerical approach is proposed to account for frictional effects in different drainage conditions which are delineated from a number of numerical simulations. The validity of the developed penetration model is verified in detail by means of comparisons with other theoretical solutions and parametric studies synthesized from literature, as well as experimental evidence for both undrained and partially drained scenarios. An extended parametric study including influence analyzes of strength and stress anisotropy, rigidity index and cone roughness on two cone factors provides new insight into the analysis of cone penetration. The shortcomings of the FE model due to the limitations of the applied constitutive model are also discussed. As regards NN models, different configurations of input variables, including standard normalized piezocone metrics and other available soil characteristics are investigated in terms of feasibility of effective NN training. The post-training regression analyzes are performed for numerical data allowing the assessment of the influence of specific input variables on accuracy of parameters predictions. Finally, the developed NN models are applied to predict parameters based on field measurements for a number of characterization sites. Provided examples demonstrate that NN inverse models may constitute an effective complementary support during the first-order quantification of the MCC parameters from piezocone measurements.

**Keywords:** back analysis, parameter identification, elasto-plastic model calibration, optimization, neural networks, principal component analysis, Modified Cam Clay model, finite element modeling, hydro-mechanical coupling, soft clay deposits, self-boring pressuremeter testing, piezocone testing, soil profiling

# Résumé

Cette étude propose un nouvel algorithme avancé pour la détermination des paramètres des matériaux à partir de tests *in situ*.

Les tests *in situ* permettent de caractériser un échantillon de sol représentatif dans des conditions de contraintes naturelles, tout en réduisant l'altération des échantillons au minimum et en favorisant l'analyse du comportement d'un sol intact. Les essais pressiométriques auto-foreur (SBPT) et les essais de pénétration de cône (CPTU) sont couramment utilisés pour la détermination des propriétés des sols argileux ; ils utilisent des corrélations analytiques et empiriques entre les propriétés du sol et les mesures expérimentales. Les corrélations empiriques exigent habituellement un ajustement sur la base d'essais de laboratoire de référence, afin d'améliorer les estimations de premier ordre pour les coefficients de corrélation typiques. Les corrélations analytiques sont pour la plupart basées sur les méthodes d'expansion d'une cavité. Ces méthodes sont limitées aux problèmes entièrement drainés ou parfaitement non drainés, de sorte que des solutions inverses en forme fermée peuvent être obtenues pour des modèles constitutifs relativement simples. Or, les tests *in situ* peuvent présenter des conditions partiellement drainées, lesquelles dépendent des propriétés physiques et de consolidation du sol et peuvent induire des estimations erronées des caractéristiques de l'argile. Le but de cette recherche est ainsi d'élaborer un système générique d'identification des paramètres basé sur la technique des réseaux de neurones artificiels (artificial neuronal network NN) et permettant d'améliorer la fiabilité des caractéristiques du sol déterminées à partir de tests *in situ*.

On explore la possibilité d'utiliser les NN pour résoudre des problèmes inverses complexes, notamment en conditions partiellement drainées. En d'autres termes, les NN sont utilisés pour transformer des mesures expérimentales en un ensemble de propriétés du sol. Le développement de modèles inverses basés sur des NN s'appuie sur des données issues de mesures pseudo expérimentales dérivées d'une simulation numérique des deux tests - SBPT et CPTU - exécutés dans de l'argile normale et légèrement surconsolidée.

On présente une procédure générique à deux niveaux conçue pour la calibration des modèles constitutifs de sols. On démontre que les modèles inverses NN peuvent facilement être intégrés dans des rétro-analyses classiques. D'abord, l'approche NN est appliquée afin d'obtenir une première approximation des paramètres, ce qui permet d'éviter les pièges potentiels liés aux techniques conventionnelles d'optimisation par gradient (gradient-based optimisation GBO), considéré ici comme un correcteur qui améliore les paramètres prédits. Le système d'exploitation parallèle des réseaux de neurones, fournit instantanément les variables de sortie sans passer par un système itératif coûteux tel que le GBO. Le système proposé a été vérifié pour le modèle elasto-plastique Modified Cam Clay (MCC), qui peut être calibré par le biais de tests triaxiaux standards en laboratoire, c'est-à-dire la consolidation isotrope et l'essai drainé de compression triaxiale conventionnelle. L'étude formule les données d'entrée pour les prédicteurs du NN, enrichies par une réduction dimensionnelle des données expérimentales par analyse des composantes principales (principal component analysis, PCA). Les caractéristiques du modèle sont déterminées d'abord sur les pseudo-expériences numériques puis sur les données expérimentales. De plus, l'efficacité de l'approche proposée est discutée en termes de précision et de coût de calcul.

La stratégie à deux niveaux validée est appliquée à une procédure numérique d'identification de paramètres pour le problème aux limites (boundary value problem, BVP) de la SBPT. La formulation couplée hydromécanique aux éléments finis (EF) inclut la dissipation de l'excès de pression interstitielle pendant la simulation des essais d'expansion suivis d'un essai de holding. Les simulations numériques démontrent

que les changements de volume survenant dans l'argile pendant les essais d'expansion en raison d'un drainage partiel, peuvent causer un écoulement local du sol proche des parois de la cavité et donc affecter l'interprétation des paramètres pour les essais de pressiomètre. C'est pourquoi on applique la technique des réseaux de neurones afin d'obtenir une première estimation des paramètres du modèle, tout en tenant compte des conditions partiellement drainées durant les essais d'expansion. L'identification des paramètres basée sur les mesures obtenues grâce aux essais d'expansion de pressiomètre et aux deux types d'essais de holding est appliquée au modèle MCC. Les NN sont développés en utilisant un ensemble d'échantillons de tests numériques générés au moyen de simulations EF basées sur une permutation aléatoire contrainte des paramètres d'entrée du modèle. Les mesures obtenues par les essais d'expansion et de consolidation sont normalisées afin que les prédicteurs NN fonctionnent indépendamment de la profondeur d'essai. On présente des exemples d'identification de paramètres pour des données numériques ainsi que pour des mesures sur le terrain d'un dépôt d'argile Fucino. De plus, l'identification combinée des paramètres est discutée en termes de précision, d'efficacité et de coût de calcul.

Enfin, on présente l'application des prédicteurs de réseaux de neurones en tant que support autonome pour effectuer le profil du sol pour l'essai de pénétration du cône. Comme pour le problème SBPT, des modèles inverses NN sont développés sur la base de résultats provenant d'analyses EF rigoureuses. Le modèle EF de la pénétration du cône implique une formulation numérique pour le matériau biphasique qui obéit à la loi MCC et contenant la théorie des grandes déformations ainsi qu'une formulation de grands déplacements pour l'interface. Il a pu être démontré que l'important effort de calcul lié à la génération de la base de données peut être réduit en optimisant la taille du maillage et la profondeur "d'état stationnaire" en fonction de l'indice de rigidité du sol. Afin de solutionner l'imprécision des mesures prises dans les éléments finis adhérant à la surface rugueuse, on propose une approche semi-numérique équivalente qui explique les effets de friction dans les différentes conditions de drainage déterminées sur la base de nombreuses simulations numériques. Le modèle de pénétration proposé est validé par comparaison avec d'autres solutions théoriques et études paramétriques issues de la littérature, ainsi que des données expérimentales de scénarios drainé et partiellement drainé. Une étude paramétrique plus étendue et comprenant l'analyse de l'influence de l'anisotropie de la résistance et de la contrainte, de l'indice de rigidité et de la rugosité du cône, offre un nouveau regard sur l'analyse des essais de pénétration de cône. Les défauts du modèle EF dus aux limitations du modèle constitutif appliqué sont également discutés. Quant aux modèles NN, différentes configurations des variables d'entrées, y compris les mesures des cônes normalisés ou autres caractéristiques du sol, sont examinées en termes de faisabilité d'apprentissage effectif des NN. Une analyse post-apprentissage est réalisée sur les données numériques afin d'évaluer l'influence de variables d'entrée spécifiques sur la précision des paramètres de prédiction. Enfin, les modèles NN développés sont appliqués aux paramètres de prédiction basés sur les mesures du terrain pour un certain nombre de sites caractéristiques. Les exemples présentés démontrent que les modèles NN inverses constituent un support complémentaire et efficace lors de la quantification de premier ordre des paramètres MCC des mesures de pénétration du cône.

**Mots-clefs:** rétro-analyse, identification de paramètres, calibration de modèle elasto-plastique, optimisation, réseaux de neurones, analyse de composantes principales, Modified Cam Clay, modélisation aux éléments finis, couplage hydromécanique, dépôts d'argile molle, pressiomètre autoforeur, pénétration d'un cône, profil géotechnique

## Acknowledgments

This study is the fruit of almost four years of research and it could not have been accomplished without the assistance of many wonderful people. Therefore, I would like to express my infinite gratitude to those who influenced and stimulated my work and supported me during this time.

First of all, I would like to thank my two PhD supervisors, Prof. Laurent Vulliet and Prof. Andrzej Truty, whose support and professional management have resulted in the accomplishment of this multi-disciplinary study. I want to express my deep appreciation to them for their confidence in my skills, for systematizing my knowledge, providing me with useful hints and creative comments, and more generally, for exploring with me the boundaries of professional friendship. I would like to address my special gratitude to Prof. Vulliet for his open-minded attitude which allowed me to conduct my research at the prestigious Laboratoire de Mécanique de Sols (LMS) and to execute my projects and ideas. I am infinitely indebted to Prof. Truty for providing me with constant encouragement, invaluable guidance and for revealing to me the secrets of computational mechanics. Thank you, Professors, for this wonderful school of life!

Financial support for this research was provided by the Laboratoire de Mécanique de Sols (LMS) and, partially, by the Federal Commission for Scholarships for Foreign Students (FCS). I am grateful for the efforts of those LMS members who contributed to this project. I would like to thank Prof. Lyesse Laloui who contributed to arranging my internship in the LMS and made it possible for me to complete my PhD research.

I am also very grateful to Patrick Dubey, Gilbert Gruaz and Gilbert Stainmann for their active help in performing some laboratory experiments.

I would also like to thank Dr Łukasz Kaczmarczyk for his precious hints and inspiration regarding artificial neural network techniques.

I would like to address my special thanks to Prof. Thomas Zimmermann and the Zace Services' team for providing me with their support and various versions of Z\_SOIL.

I would like to thank Dr Joël Cugnoni (EPFL-LMAF) and the Laboratoire de la Construction Métallique (ICOM) for providing me with various versions of Abaqus, and Tomasz Jodłowski and Dr Piotr Krawczyk for their assistance in my first steps with this code, as well as for their friendship.

I am also grateful to Prof. Vincenzo Fioravante for providing experimental data from the Fucino clay characterization site.

I want to express my sincere gratitude to the members of the examination committee, Prof. Marc Boulon, Prof. Jian Zhao, and Prof. Thomas Zimmermann for accepting my invitation to review and evaluate this dissertation, and to Prof. Jean-François Molinari who has agreed to be in the chair of the PhD thesis committee.

Many thanks to the computer scientists Stefano Nepa and Nicolas Dubois for their invaluable help and for numerous "golden" discussions, not forgetting Laurent Jäggi and Thierry Schepmans who helped me in solving numerous

computer problems.

I would like to express my deepest gratitude to all the members - past and present - of the LMS and the twin LMR, for their friendship, support, helping me on countless occasions and taking care of my French. I am particularly grateful to Suzanne Fauriel, Irene Manzella, Marta Rizzi, Federica Sandrone, Jean-Paul Dudit, Alessio Ferrari, Bertrand François, Laurent Gastaldo, Jean-François Mathier, Thibaud Meynet, Rafael Rojas, Simon Salager and Jean-Marc Terraz. Sincere thanks to Carlos Carranza-Torres, Pierre Christe, John Eichenberger, Azad Koliji and Hervé Peron for enriching multi-topic discussions and sharing their opinions. I want to address my special thanks to Emilie Rascol and Mathieu Nuth for their readiness to help me on many occasions.

I also convey much appreciation to Karine Barone, Anh Le, RosaAna Menendez, Antonella Simone who also helped me with many administrative issues.

Many thanks to my great office mates Clément Laurent, Hongsu Ma and Jean-François St-Laurent for their friendship and creating an excellent atmosphere in our working office.

I want to address my very special thanks to Valérie Herzig and Claire Silvani for their encouragement in difficult moments of my work.

I would like to thank my family and friends for their constant support during the last four years. I wish to express my deepest gratefulness to my father, Kazimierz, who shaped my education, and who sadly did not live to see this moment.

Last but not least, I would like to thank Ewa for her affection and support over these four years, as well as the effort that she made to ensure a high linguistic quality of this thesis.

Rafał Obrzud

9 May 2009, Lausanne

# List of Symbols

## Stress and Strain Notation

$\gamma$	shear strain
$\sigma$	stress
$\tau$	shear stress
$\varepsilon$	strain
$E$	Green-Lagrange strain
$p$	total mean stress $= \frac{1}{3}(\sigma_1 + \sigma_2 + \sigma_3)$
$q$	deviatoric stress $= \frac{1}{\sqrt{2}}[(\sigma_1 - \sigma_2)^2 + (\sigma_2 + \sigma_3)^2 + (\sigma_3 - \sigma_1)^2]^{1/2}$
$S$	2 <sup>nd</sup> Piola-Kirchhoff stress

## Subscripts and Superscripts

'	effective
.	rate
a	axial
c	cavity
m	maximum (peak)
p	at boundary surface
ref	reference
u	ultimate/critical state
v	volumetric
$\theta$	circumferential
e	elastic
h	horizontal
$N$	normalized
$n$	normal
$nc$	normally consolidated
$o$	initial
$p$	plastic
$p$	preconsolidated
$r$	radial
$v$	vertical

$z$  vertical

## Neural Network Notation

$\Delta\omega$	network weight increment
$\mathcal{D}$	neural network training data base
$\omega_{ij}$	network weight of $i$ -th connection of $j$ -th unit
$\mathbf{o}$	output vector produced by neural network with respect to $\mathbf{p}$
$\mathbf{p}$	input vector activating neural network
$\mathbf{t}$	target vector corresponding to input vector $\mathbf{p}$
$\theta_j$	bias of $j$ -th unit
$\xi_j$	internal state parameter of $j$ -th unit
$a_j$	activation level of $j$ -th unit (neuron)
$f(\xi)$	nonlinear transfer function
$F^{(g)}$	global error function
$F_t$	error function for a single training pattern
$F_v$	error function for a single validation pattern
$N^{(h)}$	number of units in input hidden layer
$N^{(o)}$	dimension of output vector
$N^{(p)}$	dimension of input vector
$NS^{(s)}$	number of testing data sets
$NS^{(t)}$	number of training data sets
$NS^{(v)}$	number of validation data sets

## Roman Symbols

$\Delta u$  excess pore water pressure =  $u - u_o$

$\Delta u_c$	excess pore water pressure at cavity wall	$B_q$	pore pressure parameter
$\mathcal{R}_b$	admissible parameter domain	$c$	specific storage coefficient
$\bar{p}'_n$	effective normal component of contact pressure measured for frictionless interface	$c'$	effective cohesion intercept
$\bar{q}_t$	theoretical cone resistance obtained for frictionless interface	$c_u$	undrained shear strength
$\bar{u}_2$	theoretical pore pressure measured for frictionless interface	$C_c$	slope of the normal compression line in $\log_{10}$ scale
<b>B</b>	geometry matrix relating strains and nodal displacements	$C_h$	horizontal coefficient of consolidation
<b>C</b>	4 <sup>th</sup> order constitutive tensor	$C_r$	slope of unload-reload consolidation line in $\log_{10}$ scale
<b>D<sup>e</sup></b>	elastic stiffness tensor	$D$	probe diameter
<b>f</b>	vector of nodal forces	$d_c$	cone diameter
<b>I</b>	unity tensor	$E$	Young's modulus
<b>k</b>	permeability tensor of fully saturated medium	$e$	voids ratio
<b>k*</b>	permeability tensor of unsaturated medium	$e_o$	initial void ratio
<b>N</b>	shape function matrix	$E_r$	reconstruction error
<b>n</b>	normal vector	$F$	state boundary surface
<b>q</b>	relative fluid velocity vector	$F_c$	total cone resistance
<b>R</b>	empirical correlation matrix	$F_r$	normalized friction ratio
<b>u</b>	vector of displacements	$F_s$	total shaft friction resistance
<b>V</b>	matrix of eigenvalues	$f_s$	unit sleeve friction resistance
<b>W</b>	matrix of eigenvectors	$F_t$	total cone tip resistance
$\hat{\mathbf{y}}'$	vector of discrete model measurements normalized with respect to the initial stress state	$G$	shear modulus
$\tilde{\mathbf{y}}'$	vector of discrete model measurements with random noise	$g$	gravity vector
$a$	current cavity radius	$G_{ur}$	unload-reload shear modulus
$a'$	attraction ( $= c' \cot \phi'$ )	$g_n$	distance between master surface and slave node
$A'_c$	tip area	$G_o$	(or $G_{\max}$ ) initial small-strain shear modulus
$A_c$	projected cone area	$H$	height of mesh domain
$a_n$	net area ratio of the cone ( $= q_c + (1 - a_n)u_2$ )	$I_r$	rigidity index ( $= G/c_u$ )
$a_o$	initial cavity radius	$I_P$	plasticity index ( $= w_L - w_P$ )
$A_r$	strength anisotropy ratio ( $= c_{ue}/c_{uc}$ )	$K$	soil bulk modulus
$b$	body forces	$k_a$	coefficient of strength anisotropy ( $= M_e/M_c$ )
$b_j$	vector of $j$ number of identified parameters	$K_D$	horizontal stress index for DMT
		$K_f$	fluid bulk modulus
		$k_h$	coefficient of permeability in horizontal direction
		$k_K$	correlation coefficient for $K_o$
		$K_o$	coefficient of <i>in situ</i> earth pressure at rest
		$k_v$	coefficient of permeability in vertical direction



$k_{\sigma e}$	correlation coefficient for OCR	$s$	random noise
$k_{\sigma t}$	correlation coefficient for OCR	$S(\mathbf{b})$	weighted least-squared objective function in function of $\mathbf{b}$
$K_{onc}$	coefficient of earth pressure at rest of normally-consolidated soil	$S_{res}$	degree of residual saturation
$L$	probe length	$S_r$	degree of saturation
$M$	(or $M_c$ ) slope of critical state line ( $= 6 \sin \phi'_c / (3 - \sin \phi'_c)$ )	$T$	dimensionless time factor
$M_D$	one-dimensional constrained modulus	$t$	time
$M_e$	slope of critical state line ( $= 6 \sin \phi'_c / (3 + \sin \phi'_c)$ )	$T_{50}$	dimensionless time factor corresponding to 50% consolidation
$m_v$	coefficient of soil compressibility	$t_{50}$	time for 50% dissipation of excess pore water pressure
$n$	porosity	$U$	normalized excess pore water pressure
$N_c$	cone factor	$u$	pore pressure
$N_q$	bearing capacity factor	$u_1$	pore pressure on the cone tip
$N_u$	bearing capacity factor	$u_2$	pore pressure behind cone base
$N_{\Delta u}$	cone factor with respect to $\Delta u$	$u_c$	cavity wall displacement
$N_{kt}$	cone factor with respect to $q_t$	$u_r$	radial displacement
$p'_n$	effective normal component of contact pressure	$u_{rp}$	radial displacement corresponding to stresses at plastic surface
$p_c$	effective preconsolidation pressure	$V$	normalized velocity of penetration ( $= vd/c_v$ )
$p_f$	hydrostatic pressure of fluid	$V$	volume of cavity at any stage of test
$p_{co}$	initial effective preconsolidation pressure	$v$	eigenvalue
$q_c$	cone resistance	$v$	velocity
$q_e$	effective cone resistance ( $= q_t - u_2$ )	$V_o$	initial volume of cavity
$q_n$	net cone resistance ( $= q_t - \sigma_{vo}$ )	$w_L$	liquid limit
$Q_t$	normalized cone resistance	$w_P$	plastic limit
$q_t$	corrected cone resistance	$X$	vector of initial configuration coordinates
$R$	coefficient of correlation	$x$	vector of current configuration coordinates
$R$	radius of mesh domain	$y'_i(b_j)$	vector of $i$ number of discrete model measurements depending on $j$ parameters $b$
$r$	current radius of element		
$r_c$	cone radius	$y_i$	vector of $i$ number of discrete experimental measurements
$R_f$	friction ratio		
$r_o$	initial radius of element		
$R_p$	overconsolidation ratio in terms of mean stress ( $= p_{co}/p'_o$ )	$z$	depth
$r_p$	radius of plastic region	$z_s$	steady-state depth for cone penetration model

ARE	absolute relative error	$\phi'_e$	effective friction angle from extension test
$ARE_m$	mean absolute relative error		
$ARE_{sd}$	standard deviation of the absolute relative error	$\phi'_{tc}$	effective friction angle determined from triaxial compression test
COV	coefficient of variation		
MSE	mean square error	$\phi_i$	friction angle of an interface
ND	number of discrete measurements	$\psi$	inflating pressure, pressure at the cavity wall
NP	number of parameters	$\psi_u$	limit pressure at the cavity wall
NS	number of analyzes		
OCR	overconsolidation ratio ( $= \sigma'_p / \sigma'_{vo}$ )	$\rho$	soil density or density of the total composite
PI	plasticity index	$\rho_f$	density of fluid
RE	relative error	$\rho_s$	density of skeleton particles
		$\theta_w$	volumetric water content

## Greek Symbols

$\alpha$	apex angle of cone	$v$	specific volume ( $= 1 + e$ )
$\alpha_f$	cone roughness ( $= \tan \phi_i / \tan \phi'$ )	$\vartheta_t$	correction coefficient for tip friction factor $\eta_t$
$\beta$	rebound parameter ( $= \sin \phi'$ )	$\vartheta_u$	correction coefficient for pore pressure friction factor $\eta_u$
$\beta_1$	random dispersal for rebound parameter $\beta$		
$\beta_2$	random dispersal for $K_{onc}$		
$\omega$	diagonal weighting matrix		
$\Delta$	stress anisotropy parameter ( $= (\sigma_{vo} - \sigma_{ho}) / c_u$ )		
$\delta$	Kronecker's symbol		
$\dot{\lambda}$	plastic multiplier		
$\eta$	$= q / p'$		
$\eta_s$	shaft friction factor		
$\eta_t$	tip friction factor		
$\eta_u$	pore pressure friction factor		
$\gamma$	shear strain		
$\gamma_f$	unit weight of fluid		
$\gamma_w$	unit weight of water		
$\kappa$	slope of unload-reload consolidation line in ln scale		
$\Lambda$	plastic volumetric strain ratio ( $= 1 - \kappa / \lambda$ )		
$\lambda$	slope of primary consolidation line in ln scale		
$\mu$	friction coefficient ( $= \tan \phi$ )		
$\nu$	Poisson's coefficient		
$\phi'_c$	effective friction angle from compression test		

## Abbreviations

BPNN	back-propagation neural network
BVP	boundary value problem
CK <sub>o</sub> UC	$K_o$ consolidated undrained compression
CK <sub>o</sub> UE	$K_o$ consolidated undrained extension
CIDC	consolidated isotropic drained compression
CIUC	consolidated isotropic undrained compression
CIUE	consolidated isotropic undrained extension
CPTU	cone penetration test with pore pressure measurements (electric piezocone)
CRS	constant rate of strain
CSL	critical state line
DEM	discrete element method
DMT	Marchetti dilatometer test
DSS	direct simple shear
FEM	finite element method
FFNN	feed-forward neural network

FVT	field vane test
GA	genetic algorithm
GBO	gradient based optimization
IL	incremental load
ISSMFE	International Society of Soil Mechanics and Foundation Engineering
MCC	Modified Cam clay model
MGN	modified Gauss-Newton algorithm
NCL	normally consolidation line
NN	artificial neural network
NTNU	Norwegian University of Science and Technology
OED	oedometric test
PCA	principal component analysis
pdf	probability density function
PET	pressuremeter expansion test
PHT	pressuremeter pressure holding test
PMT	pressuremeter test
PSC	plain strain compression
RF	restricted flow
SBP(T)	self-boring pressuremeter (test)
SBT	soil behavior type
SCPTU	electric piezocone test with seismic sensor
SGI	Swedish Geotechnical Institute
SHT	pressuremeter strain holding test
TC	triaxial compression
UU	unconfined undrained compression

**Sign convention:** Throughout this dissertation, with exception for Chapter 5, the sign convention is the standard convention of soil mechanics, i.e. compression is assigned as positive.



# Chapter 1

## Introduction

*Reading maketh a full man,  
conference; a ready man,  
and writing; an exact man.*

Francis Bacon

### 1.1 Evaluation of engineering properties of soils

Over the last few decades, the developments in the fields of constitutive modeling and numerical methods have given engineers a robust tool which allows analyzing soil behavior by means of computer simulations. Complex soil behavior can be represented by mathematical models which are governed by a set of material properties. However, *"with exceptions, there seems to be less confidence in assessing material properties effectively"* (Graham, 2006) due to the rising complexity of constitutive soil models and the increasing number of parameters. Obviously, some parameters can be estimated directly through closed-form solutions; others can be found only through time-consuming trial-and-error and curve-fitting procedures. Hence, the identification of reliable design properties to be used in numerical modeling is often a challenging task.

In geotechnical practice, engineers face the problem of interpreting experimental data acquired by means of a variety of laboratory and field testing techniques. While parameter identification based on laboratory tests can be, in general, performed directly, the interpretation of field tests requires solving complex boundary value problems involving theoretical assumptions and simplifications of soil behavior, geometry and water drainage conditions (Yu, 2006). On the other hand, *in situ* testing provides a good opportunity for soil characterization in natural stress conditions on a representative soil mass. Most field techniques reduce soil disturbances to minimum, capturing the response of

virgin soil. However, the interpretation of field tests often involves a large dose of empiricism since the inverse solutions are too complex to conceive or their oversimplification can lead to unreliable parameter estimation. Effective parameter identification is thus of great importance in numerical modeling since the interpretation of test measurements may significantly affect a project's serviceability or its economical aspects. Hence, there is an understandable demand for efficient parameter identification systems which - integrated with commercial applications - may encourage practical engineers to use more advanced models and run numerical simulations with a higher level of confidence.

Over the last two decades, biologically inspired soft computing methods such as neural networks (NNs) or genetic algorithms, have been exploited in many domains of engineering. NNs, with their ability to learn from examples, were soon applied in a broad range of geo-engineering tasks where traditional methods prove to be inefficient or there is a need for alternative complementing solutions. The universality of NNs allows engineers to tackle problems which require approximating highly non-linear functional relationships or performing multi-dimensional regression analyzes. In the light of the NN features, the application of NNs to parameter identification may improve its efficiency or provide complementary solutions for inverse problems.

The goal of the following research is to elaborate a parameter identification framework which is based on the neural network technique and which may raise reliability of soil properties derived from experimental *in situ* testing. In the context of parameter identification, NN inverse models can be integrated into the classical back-analysis scheme or they can provide a complementary stand-alone support for existing parameter identification systems.

## 1.2 Objectives of the thesis

The present study explores the applicability of NN models in a reliable prediction of constitutive parameters based on experimental evidence derived from field tests. In the context of such a defined task, NN inverse models are developed based on a large number of reference measurements which are derived from numerical simulations representing boundary conditions of selected laboratory and field tests, and which are in the form of standardized test results. Numerical measurements are obtained for corresponding constrained permutations of material parameters for an applied deterministic constitutive model. Parameter permutations are constrained in the sense that random parameter values are drawn from admissible parameter sets which are defined with intervals and statistical intercorrelations observed in geotechnical evidence, and which are of practical interest. Since a numerical model idealizes real soil behavior, an artificial "noise" is introduced into numerical measurements in order to account for geometrical and material variability. Hence, NNs are trained by providing their input with test results which correspond to the specific parameter values which are expected in the NN output. Thus, NNs gain knowledge about model behavior under selected boundary conditions and for a broad class of soils. Once NNs are trained, no further computational cost is borne and they can be applied to

parameter prediction from a wide spectrum of real test results.

In addition, a parametric study which accompanies the numerical generation of training database makes it possible to evaluate whether a given model is able to qualitatively and quantitatively describe soil behavior under specific boundary conditions.

The research focuses on parameter identification for normally- to lightly overconsolidated clayey soils which can be modeled with the Modified Cam Clay model (MCC). However, the proposed strategy can also be adapted to other constitutive relationships. Firstly, the triaxial compression test is used to verify the proposed strategy and then, the identification procedure is developed for two commonly applied field testing probes, i.e. the self-boring pressuremeter and the piezocone. For these selected field tests, the effect of partial drainage which may occur during testing is studied with particular attention.

Since NNs may inherit their imprecisions from, among other reasons, training data sets, they produce results which, although meaningful, can be considered as approximative in the light of mathematical precision. However, considering that solutions provided by NNs are close to the global minimum in the context of a given objective function, the results can be quickly corrected using the gradient-based optimization.

Although the main objective of the thesis is to develop NN-based inverse models through supervised NN training, the research also involves a deductive process related to numerical generation of the training database, as well as an abductive part associated with the validation of developed NN models with the aid of experimental evidence. The main goals of the present study are as follows:

- elaborating finite element models which reliably reflect the boundary value problems of selected field tests including complex drainage condition,
- working out a generic framework for developing inverse NN models for *in situ* tests based on pseudo-experimental measurements derived from numerical simulations,
- developing inverse NN models which, based on field measurements, provide meaningful first-order estimates of soil parameters taking into account a possible occurrence of partial drainage during testing,
- enhancing a conventional curve-fitting scheme with neural network prediction of the initial vector of parameters for a coupled hydro-mechanical problem of the pressuremeter expansion and holding tests,
- performing a validation of developed inverse NN models using experimental evidence from a number of well-documented characterization sites.

Finally, it should be emphasized that the presented parameter characterization deals with individual soil tests and the analysis of spatial parameter variability in subsoil is beyond the scope of this study.

This research can be applied in a broad range of civil and environmental geoenvironmental projects, where reliable quantifying of parameters plays an essential role in the designing process. The proposed reasoning can be employed in expert systems supporting parameter interpretation for advanced soil constitutive models from laboratory or *in situ* tests. Using a well-designed interface, the proposed generic scheme for the development of NN inverse models can be adapted to any constitutive model or boundary value problem with only few modifications. The developed methodology can constitute a part of automated identification toolboxes combined with, for instance, FE packages.

### 1.3 Outline of the thesis

The dissertation presents a development of a parameter identification framework which includes numerical modeling of two field tests, the generation of training patterns and the development of NN-based inverse models. The study is organized as follows:

**Chapter 2** introduces fundamentals of parameter identification in geotechnical engineering including brief reviews of existing back-calculation methods and soil testing techniques. The concept of an enhanced approach to parameter calibration is then introduced based on the recognized shortcomings of the gradient-based optimization approach. Finally, the anticipated contribution of the study is presented.

**Chapter 3** covers the state-of-the-art for neural networks in geomechanics, and focuses on theoretical aspects of this technique in the context of parameter estimation from experimental measurements. The main concepts of the feed-forward neural network and the supervised network training are demonstrated. The strategy of numerical generation of the training database is introduced and compared with other approaches. Remarks on NN shortcomings are also outlined.

**Chapter 4** presents the main aspects of the Modified Cam Clay (MCC) constitutive model used throughout the study in numerical simulations. The governing equations for the hydro-mechanical analysis are recalled. Some shortcomings of the MCC constitutive model are also acknowledged.

**Chapter 5** demonstrates the initial validation of the proposed hybrid parameter identification framework on experimental measurements derived from triaxial compression tests.

**Chapter 6** focuses on two *in situ* tests, i.e. the self-boring pressuremeter and the piezocone test. In the context of interpreting these tests, the concept of the cavity expansion theory with an extension to the critical state mechanics model is recalled. As regards the pressuremeter test, the interpretation of the expansion test and the holding tests is reviewed revealing the directions of improvements to be explored. The part related to the piezocone test includes a condensed review of the existing methods for analyzing cone resistance, as



well as a presentation of the most commonly applied interpretation formulas. Finally, an unfavorable effect of partial drainage considered, among others, as a source of parameter overestimation, is analyzed and discussed.

**Chapter 7** is organized into two main sections dealing separately with finite element modeling of the pressuremeter and the piezocone tests. Each section contains a detailed description of the developed numerical model considered as pattern generator for the supervised NN training. Additional investigations presented in the chapter concern parametric studies, analysis of the partial drainage effect. As regards the piezocone model, comparative analyzes with existing models and experimental evidence are also presented.

**Chapter 8** describes in detail the development of NN inverse models, from FE-based generation of the synthetic training dataset and specific configurations of input vectors to post-training performance analyzes. The synthetic database of piezocone measurement is verified with trends observed for real experimental data. In the case of pressuremeter tests, the efficiency of the enhanced two-level parameter identification is demonstrated on numerical simulations.

**Chapter 9** presents an application of developed NN inverse models to parameter assessment from real testing measurements derived from both, the pressuremeter and the piezocone tests. In the the case of SBPT, an application of the hybrid strategy for parameter identification is also presented. Efficiency of NN predictors is verified by performing comparative analyzes for obtained NN predictions and experimental evidence collected for various characterization sites.

Finally, **Chapter 10** presents the main achievements of this study and suggests areas for further research.



## Chapter 2

# Fundamentals of Parameter Identification

*A proper characterization of natural geomaterials  
is paramount in all site investigations  
because the results will impact the solution  
with respect to safety, performance, and economy.*

Paul W. Mayne

Identification of soil parameters is an inseparable part of site characterization and designing process in geotechnics. The knowledge of soil design properties is necessary when using theoretical models which allow practitioners to solve problems such as the estimation of foundation settlements, stability of slopes and embankments, bearing capacity and many others. These theoretical descriptions include constitutive equations which require certain material properties to be set. These properties can be used to establish and analyze the stress-strain state of the solid/soil system.

In geotechnical engineering, parameter identification mostly deals with assessing three general groups of parameters which define stiffness, strength and seepage properties of soil. Soil characteristics are commonly assessed through soil testing which provides experimental measurements. The measured soil response can be then analyzed using a suitable deterministic solution which corresponds to the considered phenomena, the particular soil type and the relevant test geometry. Deterministic algorithms are often developed under rigorous theoretical assumptions and simplifications which may, unfortunately, neglect important factors affecting the studied problem.

Sometimes, the complexity of the inverse problem to be solved leads to applying simplified empirical formulas which rely on regression analyzes performed for a large number of collected experimental data. This can be the

Table 2.1: Categories of back-calculation methods in geomechanics (modified after Hight and Leroueil, 2003).

CATEGORY	DESCRIPTION
<i>Empirical</i>	Direct use of test results based on correlations obtained through regression analyzes.
<i>Analytical</i>	Theoretical models based on elasticity and plasticity theories.
<i>Semi-numerical</i>	Numerical integration of equations obtained for analytical models.
<i>Numerical</i>	Complex soil models partly or completely based on real soil behavior, combined with numerical post-processing of measurements.
<i>Soft-computing</i>	Direct mapping experimental results for complex phenomena by computational methods including artificial intelligence techniques.

case with electric piezocone test, for which the complex penetration mechanism makes it difficult to unambiguously interpret probe measurements (e.g. Sully and Campanella, 1991; Demers and Leroueil, 2002). In other cases, when e.g. an advanced effective stress model and undrained conditions, are considered, a closed-form solution needs to be achieved by means of numerical methods (cf. Table 2.1). The solution of the cavity expansion problem for the Modified Cam Clay model can serve as an example (Collins and Yu, 1996; Cao et al., 2001). It may also happen that some theoretical assumptions which are assumed in closed-form solutions are not fulfilled. In such a case, in order to rationally calibrate a model, a complex inverse problem needs to be solved by an indirect technique using fitting procedures and numerical methods, such as finite difference (FDM), discrete element (DEM) or finite element method (FEM), etc. This may be the case with hydro-mechanical coupling for the pressuremeter boundary value problem, where the assumption of undrained expansion is sometimes violated (Fioravante et al., 1994; Rangeard et al., 2003; Obrzud et al., 2009a). Such a numerical approach typically involves complex soil models partly or completely based on real soil behavior and realistic modeling of relevant boundary and drainage conditions, initial stress state and stress history. If all these requirements are fulfilled in the case of field tests, such a back analysis provides the most reliable assessment of geotechnical design parameters (Jamiolkowski et al., 1985; Graham, 2006). Numerical methods may be also advantageous for calibrating models complex multi-parameter constitutive models (e.g. Anandarajah and Dafalias, 1986; Whittle and Kavvas, 1994; Benz, 2007), and they can be indispensable for multi-mechanism models including parameters with no physical meaning (e.g. Hujeux, 1985) or micro-parameters for DEM models (Yoon, 2007). Such a calibration usually requires an automatic procedure which combines a numerical solver with a gradient-based optimization technique (Anandarajah and Agarwal, 1991). However, indirect techniques are

computationally expensive in the sense that the amount of time required to calibrate the model increases with the number of independent variables (Flood and Kartam, 1994b). Another inconvenience is that the final solution provided by a gradient-based algorithm depends on an initial trial guess which initiates a local search in the space of solutions. *Soft-computing* techniques can serve us an alternative to the indirect methods.

In the last two decades, soft-computing methods such as genetic algorithms, neural networks (NN) or fuzzy logic systems, have attracted researchers' attention because of their ability to solve inverse problems which are poorly-understood or for which deterministic algorithms are not feasible, not complete or give unreliable results (Shahin et al., 2008)<sup>1</sup>. This class of methods has been inspired by the biological strategies for solving problems. With the feature of inherited imprecision tolerance (Ghaboussi, 2001), the bio-inspired algorithms provide approximated solutions which, nevertheless, can be very close to exact solution. Another common feature of these techniques is that they can be applied to inverse problems to approximate optimal solution from the space of admissible parameter ranges. Unlike to the indirect method, the solution can be provided instantly without the iterative procedures. On the other hand, unlike deterministic methods which describe precisely how the output is obtained from the input, soft-computing methods determine the solution in the implicit manner. The advantage of these methods is that they can be regarded as the main source of parameter identification or they can be incorporated to the standard optimization schemes providing first estimations which may accelerate the indirect searching process (Flood and Kartam, 1994b; Obrzud et al., 2009a).

A reliable parameter identification may combine several identification meth-

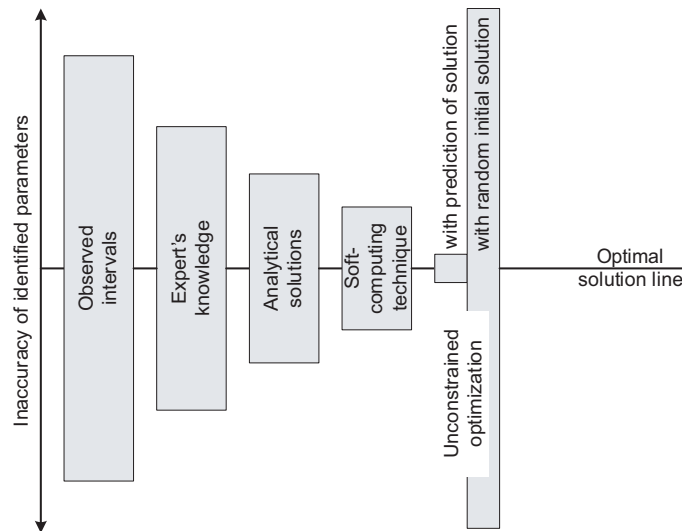


Figure 2.1: A schematic representation of possible inaccuracy extents for the parameter identification based on various methods of estimations.

<sup>1</sup>A review of a number of neural network applications for complex geomechanical problems is provided in Chapter 3.

ods to reduce uncertainty in determined parameters. A search for the best solution can rely on expert knowledge, available existing methods or self-developed identification solutions, etc. However, uncertainty of identified parameters can vary depending on the applied approach (Figure 2.1). Obviously, an expert can provide precise solutions but he or she may also suggest highly inaccurate estimations. Analytical methods may also be accurate but since they are constrained by several simplifications and assumptions, they may also be imprecise. A correctly developed bio-inspired inverse model may reduce the inaccuracy range which may stem from theoretical constraints and provide meaningful solutions. Such inverse models can provide solutions which can be then refined by the gradient-based methods. In such a case, a local search algorithm avoids being attracted by another possible, although seemingly-correct solutions. Clearly, the use of many possible identification approaches may amplify the reliability of parameter assessment for geomaterials which are inherently subject to high uncertainty and variability.

The subject of interest in this study will be the application of the multi-layer perceptron, feed forward neural networks for prediction of geomechanical parameters. Their ability to generalize, which is the derivative of the imprecision tolerance (Ghaboussi, 2001), seems to be a very suitable solution for the problems subject to measurement uncertainties and material variability. It will be demonstrated that the NNs can be easily combined with the standard direct local searching scheme to improve reliability of results and speed up the calibration process. The NNs will be applied to solve the inverse problems of pressuremeter and piezocone tests. For these tests, the complexity of the boundary value problem (BVP) with possible partial drainage and the non-linear constitutive model pose difficulties in finding a deterministic algorithm which would take into account many factors affecting the test results.

## 2.1 Testing as a tool for parameter identification

Parameter identification inseparably accompanies material testing which is usually performed by standardized mechanical devices. The testing methods can be classified into two main groups according to the actual soil localization with regards to the virgin deposition, i.e. laboratory and *in situ* tests. The number of testing devices used to determine specific soil properties is very large. The most commonly used ones are the triaxial cell, the oedometer or the direct simple shear apparatus as regards laboratory tests, and the field investigation tools such as standard penetrometers, electric piezocone penetrometers, pressuremeters, flat dilatometers, vanes, T-bars, etc. (Jamiolkowski et al., 1985; Mayne, 2006). Depending on the budget and the project's complexity, different laboratory and *in situ* tests can be employed and combined to amplify reliability of soil investigations. Combining laboratory and field tests lies in the economical issue. Laboratory tests are relatively expensive and time-consuming, while field probes can provide, in general, a continuous or quasi-continuous soil profile in a

considerably short period of time. Collecting undisturbed samples and laboratory testing is often required to reliably calibrate interpretation formula for field tests, e.g. piezocone records (Mayne, 2006). It is common practice to carry out more than one different field tests side-by-side, confirming reliability of measured and interpreted results or providing complementary data (e.g. DeGroot and Lutenecker, 2003; Hight et al., 2003).

Engineers face the problem of interpreting experimental measurements to determine material properties. Parameter identification based on laboratory tests is usually relatively straightforward since constitutive models are typically developed on the basis of well-defined and fully-controlled boundary conditions. Assuming that a soil sample represents a material point subject to a homogeneous state of stress and strain, the majority of parameters can be derived directly from experimental curves. The interpretation of field tests may be inconvenient because it requires solving complex inverse BVPs, involving theoretical assumptions and simplifications of soil behavior, geometry and drainage conditions (Jamiolkowski et al., 1985; Yu, 2006). Hence, the use of neural networks that account for the factors which are neglected in theoretical considerations, is encouraged here.

It has been widely recognized that the *in situ* behavior of soils may be significantly different from that of laboratory samples. This can be mainly attributed to the quality of the intact specimens which may depend on drilling and sampling methods and sample geometry (DeGroot and Sandven, 2004).

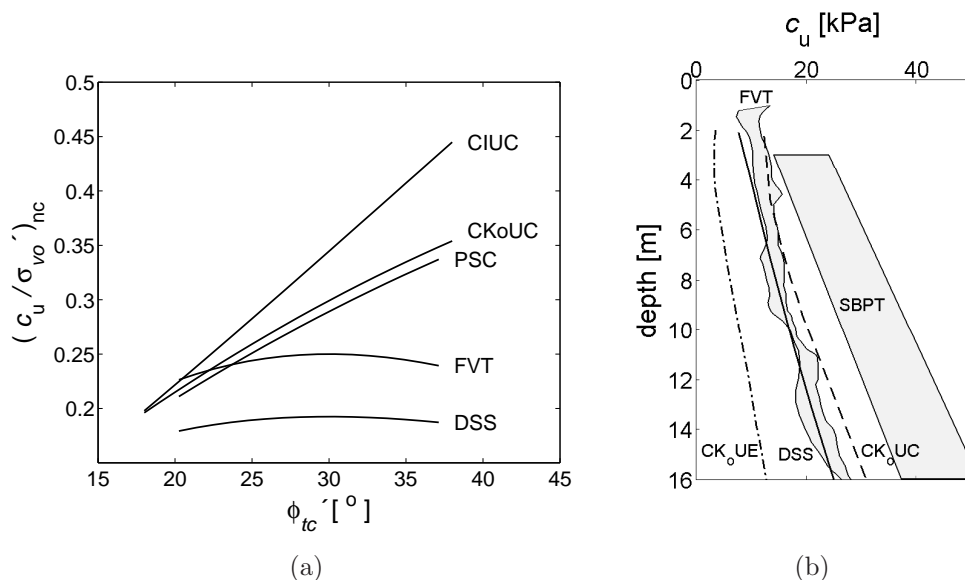


Figure 2.2: Undrained shear strength in normally consolidated soil (a) as a function of shear modes for various tests: triaxial undrained compression tests (CIUC and CK<sub>o</sub>UC), plain strain compression test (PSC), direct simple shear test (DSS) and field vane test (FVT) (after Wroth, 1984), (b) profiles for field and laboratory tests on Onsøy clay (from Lacasse et al., 1981).

The disturbance of samples may increase during their insertion into a sampling tube, transportation, relaxation of stresses, drying, temperature changes, trimming and, finally, their installation in the testing cells, etc. (Hight et al., 1992a). Different sampling devices such as piston samplers, thin walled tubes or down-hole block samplers can provide specimens for which different magnitudes of preconsolidation pressure or undrained shear strength are measured (e.g. Hight et al., 1992a; Tanaka and Tanaka, 1999). Experience shows that sample disturbance may lead to underestimation of the apparent preconsolidation pressure, softer soil response, and consequently, to the over-dimensioning of foundation structures and costly project design (Karlsrud, 1999; Fioravante, 2004). Most field techniques reduce the effect of soil disturbances to minimum by capturing the response of the virgin soil in natural stress conditions and preserving the original fabric structure of soil. Moreover, *in situ* testing provides a good opportunity for soil characterization on a representative soil mass (Jamiolkowski et al., 1985; Graham, 2006). Contrary to discontinuous sampling for laboratory tests, continuous or semi-continuous field profiles allow investigating the inherent natural spatial variability of soil properties.

It also has to be mentioned that the inconsistencies in parameter values measured by laboratory and field tests may also stem from the non-uniqueness of some properties. For example, it is commonly known that the undrained shear strength  $c_u$  is not a unique soil parameter (Wroth, 1984; Jamiolkowski et al., 1985), as it depends on the type of test, which involves particular strain paths (Figure 2.2).

The differences in interpreted results also stems from the time-dependent

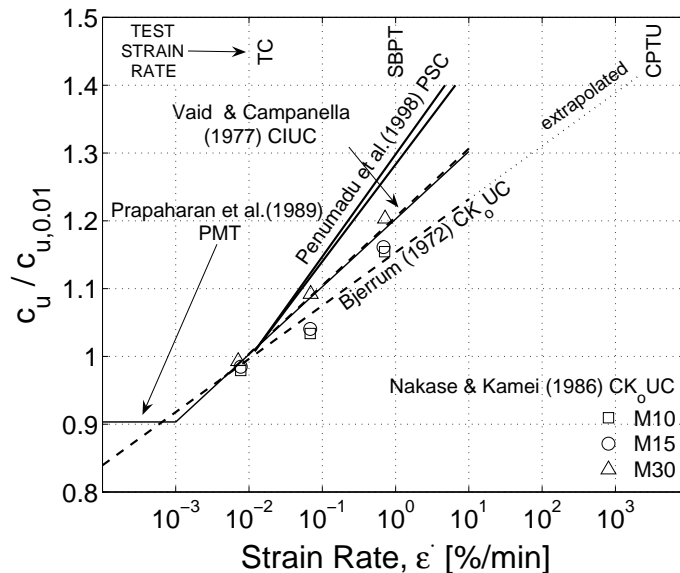


Figure 2.3: The strain rate effect on undrained shear strength  $c_u$  for different shear modes and a schematic comparison of test strain rates for triaxial compression (TC), self-boring pressuremeter (SBPT) and piezocone (CPTU).



behavior of soils (e.g. Vaid and Campanella, 1977; Leroueil, 1988; Sheahan et al., 1996; Penumadu et al., 1998). The undrained shear strength increases linearly with the logarithm of the shear strain (Bjerrum, 1972; Nakase and Kamei, 1986). For instance, the testing speed for SBPT or CPTU can be one or more orders of magnitude greater than that used in the triaxial compression test TC ( $\dot{\epsilon} = 0.01\%/min$ ), see Figure 2.3. Laboratory tests with the use of a model pressuremeter in clays have revealed an increase of  $c_u$  of about 10% for every tenfold increase of strain rate (Prapaharan et al., 1989). While the overestimation of  $c_u$  derived from pressuremeter test due to the strain rate effect can be reasonably small, in the order of 10-20%, the differences for CPTU can be much larger. The extrapolated results of Bjerrum (1972) (Figure 2.3) can indicate that neglecting the strain effect in the analysis of penetration may lead to the considerable overestimation of  $c_u$  of about 40% with respect to the value obtained for the conventional triaxial compression. Since the undrained shear strength is a function of the stress history, the similar effects can be observed for the derived values of preconsolidation pressure  $\sigma'_p$ . The study carried out by Leroueil et al. (1983b) revealed the increase of about 10-14% for  $\sigma'_p$  per log cycle of volumetric strain rate  $\dot{\epsilon}_v$  in the constant rate of strain oedometer test (CRS).

A number of studies also link the misinterpreting of strength parameters in clays with partial consolidation, which may occur in the case of field testing. Laboratory studies in a calibration chamber have revealed that partial drainage increases soil strength around the pressuremeter probe (Anderson et al., 1987). The occurrence of partial drainage may be attributed to soil permeability and drainage path. A numerical study of the cylindrical expansion test with the standard strain rate of 1%/min has revealed a possible pore pressure dissipation for soil with the coefficient of permeability  $k$  greater than  $10^{-10}$  m/s (Fioravante et al., 1994). As the undrained shear strength is a function of soil critical state and stress history, the local increase of the preconsolidation stress may strongly affect the expansion stress relief, which may clearly have a significant influence on subsequently evaluated consolidation parameters (Fukagawa et al., 1990; Rangeard et al., 2003). Numerical studies of the piezocone test have shown that the partial dissipation of excess pore water pressure behind the cone tip ( $u_2$  configuration) for 2cm/s penetration rate may occur for  $k > 10^{-10}$ m/s (Voyiadjis and Kim, 2003; Markauskas et al., 2005). In consequence, partial dissipation may increase soil resistance during penetration.

A summarized comparison of advantages and disadvantages of laboratory and *in situ* testing is provided in Table 2.2.

The following sections will introduce the reliability of experimental measurements in geotechnics and show how experimental data can be included into the framework of numerical parameter identification, aiming to account for the complexity of constitutive models and boundary value problems.

## 2.2 Reliability of experimental measurements

Material testing is usually performed with the aid of mechanical devices. Testing provides a physical response of a material specimen subject to an imposed action, e.g. applied load - deformation. The material response which is transformed onto experimental data may be, however, a burden with uncertainties related to the quality of device readings, homogeneity or inherent properties of a material, etc. Generally, the uncertainties in experimental data include (i) incompleteness, (ii) data noise and (iii) data scatter, which are briefly explained below.

*Incompleteness* is epistemic uncertainty and can be associated with the frequency of sampling or intentions of testing (cf. Lunne et al., 1997). The first may affect the continuity of data due to a discrete character of measurements, but this can be usually overcome by frequent sampling or interpolating missing data. However, incompleteness cannot be avoided if a testing program does not provide a sufficient number of measured quantities (in order to avoid the non-uniqueness of solution) or the program is not adequate to a studied phenomena

Table 2.2: A comparison of laboratory and *in situ* testing (after Jamiolkowski et al., 1985; Hight and Leroueil, 2003).

LABORATORY TESTING	IN SITU TESTING
<p><i>Advantages</i></p> <ul style="list-style-type: none"> <li>• Well-defined boundary conditions.</li> <li>• Strictly controlled drainage conditions.</li> <li>• Stress (or strain) fields reasonably uniform.</li> <li>• Well-defined stress (or strain) paths imposed and response observed. Interpretation possible as element test.</li> <li>• With increasing sophistication, stress paths can match some field paths.</li> <li>• Strain rates can be controlled.</li> <li>• Soil and physical features positively identified.</li> <li>• Level of disturbance can be assessed approximately.</li> </ul> <p><i>Disadvantages</i></p> <ul style="list-style-type: none"> <li>• Cumulative effects of sampling, storage and specimen preparation.</li> <li>• Changes in temperature.</li> <li>• Discontinuous information from small volume of soil.</li> <li>• Time-consuming and relatively expensive testing.</li> </ul>	<p><i>Disadvantages</i></p> <ul style="list-style-type: none"> <li>• Boundary conditions often poorly defined.</li> <li>• Drainage conditions often poorly defined and not controlled.</li> <li>• Stress and stress fields non-uniform.</li> <li>• Stress (or strain) paths vary. Interpretation only possible if the whole boundary value problem considered.</li> <li>• Modes of deformation and failure often different from civil engineering structures.</li> <li>• Strain rates often higher than in laboratory or field.</li> <li>• Nature of tested soil frequently not identified.</li> <li>• Degree of disturbance often unknown.</li> </ul> <p><i>Advantages</i></p> <ul style="list-style-type: none"> <li>• Can be carried out in some soils that cannot be sampled without considerable disturbance.</li> <li>• Tests carried out in natural environment.</li> <li>• Semi- or continuous readings record of soil response for some penetration devices. Larger volume of soil tested than in laboratory.</li> <li>• Reduced time and economical aspects in terms of the size of investigated area.</li> </ul>

so that model parameters are insensitive to measured variables. For example, parameter identification of consolidation characteristics will fail if the testing device is not instrumented with pore pressure sensors and the testing program does not ensure seepage in a sample.

*Data noise* arises from measuring errors or non-homogeneity of a single sample. The former may be the result of inertia of the testing apparatus, its precision or simply of the preparation mode, i.e. undisturbed installation of probe or sample. Non-homogeneity of a single sample is highly connected with random nature of soil genesis. The variability may rise with an increasing representative volume. Generally, data noise has a smaller influence than data scatter, which concerns results for a set of samples.

*Data scatter* is an inherent (aleatory) uncertainty and represents the natural randomness of the material. Unlike to manufactured materials like concrete or steel, natural soils reveal a considerable spatial variability. In the case of testing of an extensive volume of soils, data scatter cannot be avoided since soil properties fluctuate over space and time (Lunne et al., 1997). The data scatter can be reduced by probing in a "statistically homogeneous" soil layers, which ensure representativeness of data samples. However, in natural soils, the variation of soil property values even in statistically homogeneous layer may be quite wide. For natural clays, the measured properties are fairly uniform with depth but the reported coefficients of variation for mechanical properties reach on average 20-50% depending on parameter whereas for hydraulic conductivity the variation can be observed as high as 200-300% (Baecher and Christian, 2003). Prediction of representative design parameters for more and more sophisticated soil models is thus a challenging task for practicing engineers.

Throughout this dissertation, it is assumed that the presented experimental data does not include errors stemming from installation disturbances or specimen sampling, and data noise is eliminated using interpolation and smoothing techniques.

## 2.3 Classical approaches to the inverse problem

Generally, the problem of parameter identification lies in proposing a set of characteristics which would minimize the difference between the quantities obtained from the stress-strain analysis and experimental measurements. A problem of the back-analysis can be solved using two different approaches called *inverse* and *direct* strategy (Gioda and Sakurai, 1987).

The *inverse approach* is simply the reverse process of the standard stress analysis with geometrical constraints. In the case of a simple geometry of a system, the solution can be found in a closed form while complex boundary conditions need a support of a numerical "engine" such as FEM (Sakurai and Takeuchi, 1983).

The *direct approach* consists of solving a non-linear problem using the iterative

technique. It consists of correcting an *ad hoc* assumed set of parameters in order to minimize an error function which is formally defined as follows:

$$S(\mathbf{b}) = \frac{1}{t_1 - t_0} \int_{t_0}^{t_1} \|y(t) - y'(\mathbf{b}, t)\| dt \quad \text{where } \mathbf{b} \in \mathcal{R}_b \quad (2.1)$$

where  $t_1 - t_0$  is the length of the observation time,  $y(t) - y'(\mathbf{b}, t)$  denotes the difference between experimental data and calculated quantities, and  $\mathbf{b}$  is the vector of model parameters adhered to the physical parameter space  $\mathcal{R}_b$ .

In geomechanics, complexity of both constitutive model and the boundary value problem, often enforces the use of the direct approach and numerical methods to solve the inverse problem. The numerical optimization of model parameters consists of the following steps:

1. Test the soil and provide comprehensive experimental data.
2. Provide an initial guess of material parameters.
3. Carry out a numerical simulation of the BVP that represents the experiment.
4. Evaluate the magnitude of the objective function that is a measure of discrepancy between the numerical response and experimental data.
5. Update the initial guess of parameters by means of a gradient-based minimization technique if the objective function exceeds a user-specified tolerance.
6. Return to step 3 unless the convergence of optimization is achieved.

Although the set of parameters obtained in the last iteration is considered as the optimal one, the final solution may not be the best one since it strongly depends on the initial guess given by the user (see Section 2.3.4).

### 2.3.1 Constitutive equations and direct approach

A general mathematical solution of the direct problem can be formulated for the FE analysis as:

$$\mathbf{F}_{\text{ext}}(t) - \mathbf{F}_{\text{int}}(\mathbf{u}, \mathbf{b}, t) = 0 \quad , \text{ s.t. boundary condition and } \mathbf{b} \in \mathcal{R}_b \quad (2.2)$$

where  $\mathbf{F}_{\text{int}}(\mathbf{u}, \mathbf{b}, t)$  is the internal force vector which evolves in time  $t$  and depends on model variables  $\mathbf{b}$ ,  $\mathbf{u}$  is the displacement vector, and  $\mathbf{F}_{\text{ext}}(t)$  denotes the vector of external forces. The vector of internal forces in the domain  $\Omega$  is computed using the following formula:

$$\mathbf{F}_{\text{int}} = \int_{\Omega} \mathbf{B}^T \sigma d\Omega \quad (2.3)$$

Linearization of Equation (2.2) yields an iterative scheme:

$$\mathbf{K}_{t+1}^{(i)} \partial \mathbf{u}^{(i+1)} = \mathbf{F}_{t+1}^{\text{ext}} - \mathbf{F}_{t+1}^{\text{int}(i)} \quad (2.4)$$

where  $\mathbf{K}$  is a global stiffness matrix is defined as:

$$\mathbf{K} = \int_{\Omega} \mathbf{B}^T \mathbf{D}_t \mathbf{B} d\Omega \quad (2.5)$$

In the above expressions strain-displacement matrix is denoted by  $\mathbf{B}$  and the tangent stress-strain operator by  $\mathbf{D}_t$ .

Hence, the parameter identification is the inverse procedure which enables an unknown vector  $\mathbf{b}$  to be established if  $\mathbf{u}$ ,  $\mathbf{F}_{\text{ext}}$  are measured, and constitutive equations and boundary conditions are known.

### 2.3.2 Objective function and its minimization

Various definitions of the objective function  $S$  can be adopted to measure discrepancies between experimentally measured data and a model response (cf. Sakurai and Takeuchi, 1983; Gioda and Sakurai, 1987; Cailletaud and Pilvin, 1994; Ledesma et al., 1996a; Poeter and Hill, 1998). Apart from conventionally taken measurements, any prior information such as measurement reliability of estimated parameters or measurement errors can also be introduced into the back-analysis to improve parameter identification. In geotechnical practice, the following approaches have been proposed: the *least-squares* function (e.g. Gioda and Sakurai, 1987; Anandarajah and Agarwal, 1991), the *weighted least-squares* function (e.g. Finno and Calvello, 2005; Lefasseur et al., 2008), the *maximum likelihood* approach (e.g. Ledesma et al., 1996b), the *Bayesian approach* (e.g. Cividini et al., 1983). The *Kalman filter* method (Murakami and Hasegawa, 1988) can be also adopted if, for instance, the whole construction process with varying influence of measurements at different stages is taken into account. Refer to Xiang et al. (2003) for other examples.

In the least-squares approach, the error function depends on the squared differences between measured data and model response without any prior information. The information about error measurements can be incorporated into the weighted least-squares function which introduces the weighting of observational data. Each measurement can be weighted separately so that data with a greater weight contribute more to the fit. Usually, weights are taken as an inverse of the measurement error variance. Hereafter, in the regression analysis, the weighted least-squares approach is used and is given as:

$$S(\mathbf{b}) = [\mathbf{y} - \mathbf{y}'(\mathbf{x}|\mathbf{b})]^T \cdot \boldsymbol{\omega} \cdot [\mathbf{y} - \mathbf{y}'(\mathbf{x}|\mathbf{b})] \quad (2.6)$$

where  $\mathbf{y}$  is a vector of empirical data,  $\mathbf{y}'(\mathbf{x}|\mathbf{b})$  is a vector containing the model response at discrete points  $x_j$ ,  $j = 1, \text{ND}$  for a set of parameters  $\mathbf{b}$ ; a diagonal weighting matrix,  $\boldsymbol{\omega}$  is introduced in order to transform the observable variables into dimensionless quantities, wherein the weight of every observation can be taken as the inverse of its error variance  $\omega_{kk} = 1/\sigma^2$ .

In the context of linear regression the function  $\mathbf{y}'$  can be approximated as (Bates and Watts, 1988):

$$\mathbf{y}' = \mathbf{x}^T \mathbf{b} \quad (2.7)$$

Hence, the solution of the parameter identification consists of minimizing the error function, which can be formulated as:

$$\min [\mathbf{y} - \mathbf{x}^T \mathbf{b}] \cdot \boldsymbol{\omega} \cdot [\mathbf{y} - \mathbf{x}^T \mathbf{b}] \quad (2.8)$$

and can be achieved using one of the known optimization methods.

### 2.3.3 Gradient-based search algorithm

The minimization of the objective function is typically performed by means of a suitable gradient-based optimization (GBO) algorithm. Among many optimization algorithms used in geotechnics, the most popular are the conjugate gradient algorithms (e.g. Ou and Tang, 1994), the Newton's methods with the Gauss-Newton algorithm (e.g. Zentar et al., 2001; Finno and Calvello, 2005; Levasseur et al., 2008) and the quasi-Newton algorithm (e.g. Anandarajah and Agarwal, 1991). These gradient-based algorithms allow the objective function to be effectively minimized during the process of parameter determination. As reported by several researchers, the Gauss-Newton is a suitable and efficient algorithm when the weighted least-squares objective function is adopted (e.g. Gioda and Sakurai, 1987; Ledesma et al., 1996b). This method can also be extended with the Levenberg-Marquardt algorithm, what can result in an improved convergence rate (Marquardt, 1963). Therefore, the Modified Gauss-Newton algorithm reported in Hill (1998) is adopted in the present study.

When dealing with elastic-plastic problems the objective function is a highly non-linear function of unknown variables. Typically, the objective function can be minimized by means of an unconstrained optimization. The Newtonian algorithms search for the function gradient in the entire solution domain solving linear equations. It consists of linear direct searching along directions which reduce the objective function in an NP-dimensional space. At each iteration  $r$ , an update of a NP-dimensional vector of parameters  $\mathbf{b}^r$  is evaluated as:

$$\mathbf{b}^{r+1} = \mathbf{b}^r + \mathbf{d}^r \quad (2.9)$$

where  $\mathbf{b}^{r+1}$  denotes updated vector of parameters in  $r$ -th iteration,  $\mathbf{d}^r$  is the updating vector which represents a search direction. To determine  $\mathbf{d}^r$ , one may linearize the function  $f$ :

$$f(\mathbf{b}^r + \mathbf{d}^r) \approx f(\mathbf{b}^r) + \nabla f(\mathbf{b}^r) \mathbf{d}^r \quad (2.10)$$

where  $\nabla f(\mathbf{b}^r)$  is the first derivative of  $f$  with respect to  $\mathbf{b}_r$ . In Equation (2.10), an expansion into quadratic form is omitted to avoid an expensive direct calculating of the Hessian. Typically, information about function curvature can be evaluated using quasi-Newton methods which approximate the second derivative relying on the observed trend of the objective function and its gradient (Anandarajah and Agarwal, 1991).

The direct searching achieves its goal if a strong local minimum is met. Mathematically, it can be expressed as:

$$\mathbf{X}_r = 0 \quad (2.11)$$

that is the necessary and sufficient condition of the existence of a local minimum for a continuous and differentiable function at point  $\mathbf{b}^r$ . Differentiating Equation (2.10) with the function defined in Equation (2.8) and setting to zero leads to the following expression:

$$(\mathbf{X}_r^T \boldsymbol{\omega} \mathbf{X}_r) \hat{\mathbf{b}} = \mathbf{X}_r^T \boldsymbol{\omega} \mathbf{y} \quad (2.12)$$

where  $\hat{\mathbf{b}}$  is the weighted least-squares estimator. Finally, the linear equation of the Modified Gauss-Newton algorithm is obtained by introducing the Levenberg-Marquardt term  $m_r \mathbf{I}$  and a diagonal scaling matrix  $\mathbf{C} = (\mathbf{X}^T \boldsymbol{\omega} \mathbf{X})_{kk}^{-1/2}$  (Hill, 1998). Thus, Equation (2.12) can be rearranged into:

$$(\mathbf{C}^T \mathbf{X}_r^T \boldsymbol{\omega} \mathbf{X}_r \mathbf{C} + m_r \mathbf{I}) \mathbf{C}^{-1} \cdot \mathbf{d}^r = \mathbf{C}^T \mathbf{X}_r^T \boldsymbol{\omega} (\mathbf{y} - \mathbf{y}'(\mathbf{b}^r)) \quad (2.13)$$

where  $m_r$  is the Marquardt parameter and  $\mathbf{I}$  is the identity matrix. The Marquardt parameter is introduced to improve the convergence for ill-posed problems. At the beginning, this parameter is equal to zero and can be adjusted at consecutive iterations using the formula  $m_{r+1} = 1.5m_r + 0.001$  (Hill, 1998). In the case of a complex non-linear function, the sensitivity matrix  $\mathbf{X} = \partial \mathbf{y}' / \partial \mathbf{b}$  can be evaluated directly by the FEM subroutine using central or forward differences. Hereafter, the latter is adopted in order to reduce a computational cost.

The updating vector  $\mathbf{d}^r$  (Equation (2.9)) can be controlled by introducing a scaling parameter  $\rho_r$ :

$$\mathbf{b}^{r+1} = \rho_r \cdot \mathbf{d}^r + \mathbf{b}^r \quad (2.14)$$

The scaling parameter controls the length of  $\mathbf{d}^r$  so that the maximal absolute value of fractional parameter value  $(b_j^{r+1} - b_j^r) / |b_j^r|$  changes less than user-specified tolerance  $d_{\max}$ . The parameter can be calculated as:

$$\rho_r = \frac{d_{\max}}{|d_i^r| / |b_i^r|} \quad (2.15)$$

where the superscript  $i$  is attributed to the maximal absolute change of NP parameters. The scaling parameter is a scalar  $\rho_r \in (0, 1)$  so the search direction  $\mathbf{d}^r$  is preserved.

The performance of an iterative search procedure is accomplished if one of the two convergence conditions is achieved:

1. The error function  $S(\mathbf{b})$  changes in three sequential iterations less than the user-defined amount. In this case, for ill-conditioned problems the search process risks getting stuck in a narrow valley associated with a weak minimum if the tolerance is set too high.

$$|S(\mathbf{b}^r) - S(\mathbf{b}^{r-1})| \leq \varepsilon_I \quad \text{and} \quad |S(\mathbf{b}^r) - S(\mathbf{b}^{r-2})| \leq \varepsilon_I \quad (2.16)$$

2. The largest and absolute change of each optimized parameter in  $r$ -th iteration is smaller than user-specified tolerance.

$$\left| \frac{d_k^r}{b_k^r} \right| \leq \varepsilon_{II} \quad \forall k \quad (2.17)$$

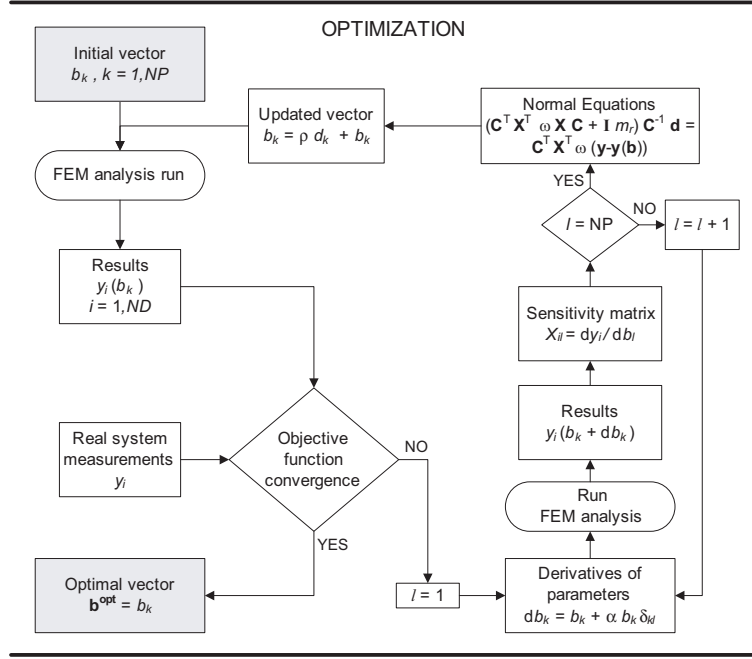


Figure 2.4: Scheme of optimization algorithm coupled with FE analysis.

The main steps of the direct search strategy coupled with FEM solver (refer to Figure 2.4) can be summarized as follows<sup>2</sup>:

1. Assign tolerances of convergence conditions and maximal parameter changes. Deliver prior information about measurement errors to calculate the diagonal weighting matrix  $\omega_{jj}$ .
2. Assign the components of the initial vector of NP-number of parameters,  $b_k^r$ ,  $k = 1, NP$ . The parameter  $m_r$  is initially set equal to zero.
3. For a specified boundary problem, compute the vector  $\mathbf{y}'(\mathbf{b}^r)$  through the FEM analysis with respect to the current vector of parameters  $\mathbf{b}^r$ .
4. Compute the current sensitivity matrix  $X_{ik} = \partial y'_i / \partial b_k^r$ ; the procedure requires  $l = NP$  runs of the FEM model with a small perturbation of  $k$ -th parameter  $\Delta b_k^r = \alpha b_k^r \delta_{kl}$  ( $\delta_{kl}$  is the Kronecker's symbol). Assign the difference between data for perturbed parameters and the vector  $y'_i(b_k^r)$  as  $\Delta y'_i$ , so that the sensitivity matrix becomes  $X_{ik} \cong \Delta y'_i / \Delta b_k$ .
5. Assign the search direction  $\mathbf{d}^r$  by solving Equation (2.13). Then, calculate the scaling parameter  $\rho_r$  using Equation (2.15) with a temporary assigned value  $\rho_r = 1$  in Equation (2.14).
6. Update the vector  $\mathbf{b}^{r+1}$  using Equation (2.14). Set  $r = r + 1$  and return to the step 3 until one of the convergence criteria is satisfied.

<sup>2</sup>For details of the Modified Gauss-Newton algorithm also refer to Appendix A.



### 2.3.4 Limitations of gradient-based optimization

The GBO techniques search for the minimum of  $S(\mathbf{b})$  using its value and derivatives with respect to each parameter  $X_{ij} = \partial y'_i / \partial b_j$ . In the case of a nonlinear problem, the gradient of  $S(\mathbf{b})$  may be computed using, for instance, the FE analysis. As regards multiple FE analysis runs providing the current response of the BVP, a trial-and-error search for a neighborhood of the global minimum may prove to be very time-consuming due to the iterative manner of minimization and the number of parameters that describe constitutive relations. Moreover, the number of FE analyses can be multiplied by the number of structural tests (or processes) considered in the calibration procedure. Typically, the minimization is terminated if a strong minimum is met. Hence, the final solution strongly depends on accuracy of the user-specified initial vector of parameters  $\mathbf{b}^0$ . Starting from different initial vectors, the inverse problem may exhibit the *non-uniqueness* of the solution because the algorithm may yield different local minima (Xiang et al., 2003; Finno and Calvello, 2005; Levasseur et al., 2008). The non-uniqueness may stem from a complex nonlinear system involving multi-variable model, Figure 2.5(a), but it can also be a result of the insensitivity of model parameters with respect to the provided input information, Figure 2.5(b)). Assuming that the alleged global minimum is found, verification of the solution is usually required. Starting from different initial points in the parameter space, the minimization should converge to the unique optimal solution, i.e. global minimum.

In certain cases, the ill-posed initial vector may lead to *instability* of the FE analysis because the algorithm searches for the solution in an inadmissible space of parameters. Consequently, the function  $S$ , losing its continuity, is no longer differentiable. Sometimes, the problem of instability can be avoided by means of the constrained optimization, i.e. by imposing parameter bounds (e.g. Anandarajah and Agarwal, 1991). Nevertheless, the identification procedure involves several time-consuming trial-and-error runs using various random starting points in order to find the global minimum (Raphael and Smith, 2003).

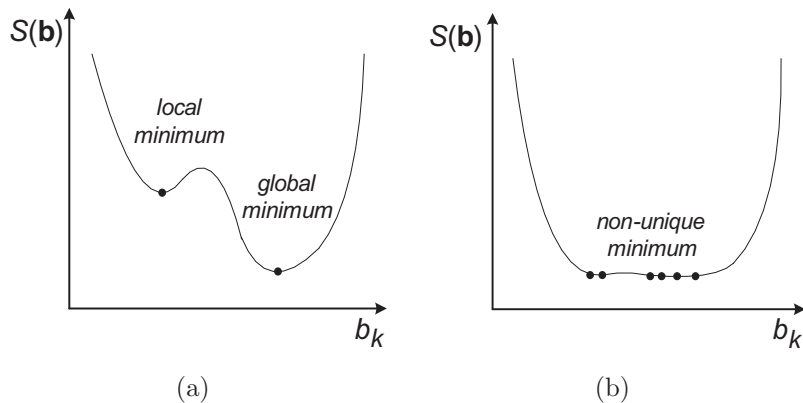


Figure 2.5: Non-uniqueness of the objective function: (a) existence of local minima, (b) insensitivity of model parameters to provided input information.

Table 2.3: Main difficulties related to the gradient-based optimization.

PROBLEM	CAUSE	CONSEQUENCES
<i>Non-existence</i>	Model cannot describe modeled problem or measurements provide incomplete data	Impossible to determine reliable model parameters
<i>Non-uniqueness</i>	Complex non-linear problem including multi-variable material model and complex BVP	Existence of many local minima providing many equivalent solutions
	Parameters insensitive to measurements (not enough information provided)	Existence of a flat local minimum satisfying infinite number of parameter pairs
<i>Instability</i>	Non-linear problem and unconstrained model parameters	Loss of objective function continuity due to instability of the model

## 2.4 Enhanced approach to parameter identification

In order to avoid potential pitfalls related to GBO, there is a need for using methods which directly approximate the final solution, i.e. that find the vicinity of the global minimum by means of an *implicit inverse strategy*. Typically, statistical methods can be used to solve an identification problem. A mixed formulation of genetic algorithms (GA) and neural networks (NN) (Pichler et al., 2003) or the stochastic binary search approach (Cekerevac et al., 2006) can be found in literature. Recently, the GA have also been adapted to solve some model calibration problems (Pal et al., 1996; Samarajiva et al., 2005; Levasseur et al., 2008). However, the efficient and stable application of genetic algorithms to inverse problems may prove to be computationally expensive, as it requires generating a large number of individuals in each optimization run (Levasseur et al., 2008, 2009).

In this study, the NN approach is proposed to search the entire multi-dimensional space of parameters and to approximate soil model characteristics (Obrzud et al., 2009b). The approach will be applied to parameter identification based on two commonly recognized field tests, i.e. SBPT and CPTU. By mapping experimental measurements, an approximated solution will be generated by the NN. The prediction provided by the NN can be accepted as the final estimate or it can be used as a prediction of the initial vector which is then refined through the gradient-based optimization. The first-order estimation will be demonstrated on piezocone results, while the coupled identification NN-GBO will be applied first to the triaxial compression test to validate the hybrid strategy, and then to the pressuremeter results.

The *Feed-Forward Neural Network* (FFNN) approach (see Chapter 3) is

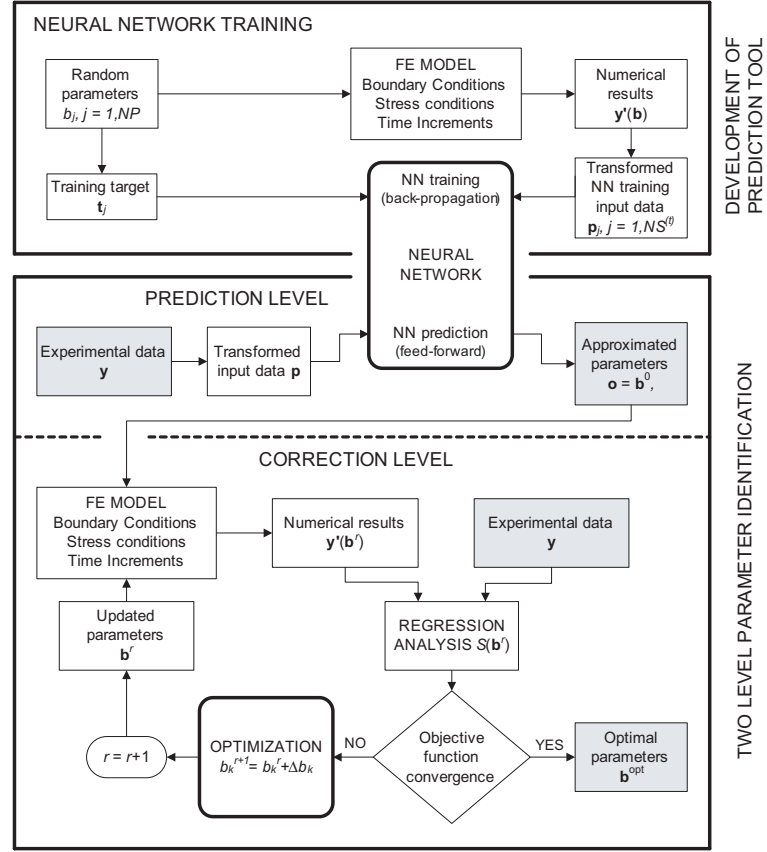


Figure 2.6: Scheme of the two-level parameter identification with the development of prediction tool.

proposed to be the first step of the calibration of the applied elasto-plastic constitutive model. The FFNN algorithm can be used as a predictor which instantly maps the experimental data of a given test onto model parameters. Such prediction may constitute the initial vector of parameters used later on by the GBO, regarded as the correction step. Such a prediction can be regarded as an *inverse* solution of the identification problem while the optimization involves the *direct* approach. The strategy of the two-level parameter identification is schematically presented in Figure 2.6.

The self-organizing ability of NNs is used to prepare the prediction tool. The supervised NN training (see Section 3.3.3) is performed only once based on the results from numerical pseudo-experiments. The numerical model which is used to generate numerical measurements, should reflect the boundary value problem (BVP) of the real system. The sufficient number of training patterns allows the NN to gain enough knowledge in order to be able to generalize further new inputs. Numerical simulations are carried out for random variations of model parameters,  $b_j$ ,  $j = 1, \dots, NP$  and  $\mathbf{b} \in \mathcal{R}_b$ . Vectors of parameters constitute the NN training target sets  $\mathbf{t} = \{\mathbf{b}_k^T\}$ , i.e. the values of parameters expected for the corresponding results of previously computed  $NS^{(t)}$ -number of pseudo-experiments, where  $k = 1, \dots, NS^{(t)}$ . Correspondingly, the numerical results are collected in the training input set  $\mathbf{p} = \{\mathbf{y}_k^T\}$ , where each vector

$\mathbf{y}'_k(\mathbf{b}_k)$  contains ND-number of discrete measurements.

As constitutive models only approximate real soil behavior, the numerical simulations tend to idealize the test response. Hence, the numerical response may never be fitted ideally to the real curve. This suggests that numerical data would lead to the overfitting of the NN and, consequently, to improper prediction. Hence, the NN can be correctly trained by means of two discretization approaches. The first approach assumes that only gradient-delivering discrete points are chosen and provided as the training input; an example will be presented in Chapter 5. The second method consists of introducing noise into the smooth computed equilibrium paths using, for instance, the Gaussian *probability density function* (pdf) and presenting to the network all observational measurements. In this case, the mean value of the noise is prescribed as equal to zero in each equilibrium point while the standard deviation can be derived from a variability of the data dispersion observed for experimental curves. The noise simultaneously introduces material and geometrical imperfections regarded, among others, as sources of geotechnical uncertainty (Goh and Kulhawy, 2005). Since the whole range of measurements of an experiment is considered, a dimensional reduction of data is desired. This can be easily carried out by applying the *principal component analysis* (PCA) which maps data into a new coordinate system (Haykin, 1999).

The choice of the method may depend on the possible level of data fitting which is influenced by smoothness of the response of a model subject to given boundary conditions.

For a considered constitutive model, the NN training can be regarded as the one-time process, only if the broad spans of parameter values are covered, for the generation of training patterns. Obviously, a further development of an NN inverse model is not precluded, and any expected parameter extensions can be reconsidered to retrain the existing NN. Hence, with the single computational effort related to the NN model generation, the efficiently trained NN becomes a robust prediction tool ready to solve any inverse problem for a variety of soil stress-strain responses for a given BVP. The activated trained NN with experimental data will respond generating the vector of material properties  $b_j^0$ . Then, the quality of predicted parameters can easily be controlled by performing the regression analysis of experimental data  $\mathbf{y}$  and numerical results  $\mathbf{y}'(\mathbf{b}^0)$ . Since the NN is created to seek the vicinity of the global minimum, the identified parameters may need only slight corrections using the GBO technique. The relatively poorly-recognized parameters  $b_k$  can be quickly updated within  $r$ -iterations with a substantially reduced computational effort.

Considering the high complexity of non-linear soil constitutive models and the number of parameters included, the performance of a traditional trial-and-error calibration with a large number of tests is often computationally expensive and does not always lead to satisfactory results. These problems related to the GBO can be clearly illustrated using an example of parameter identification for the cavity expansion BVP. Figure 2.7 presents a highly nonlinear character of the error function with respect to consolidation characteristics (permeability coefficient  $k$  and slope of the normal consolidation line  $\lambda$ ). The presented error

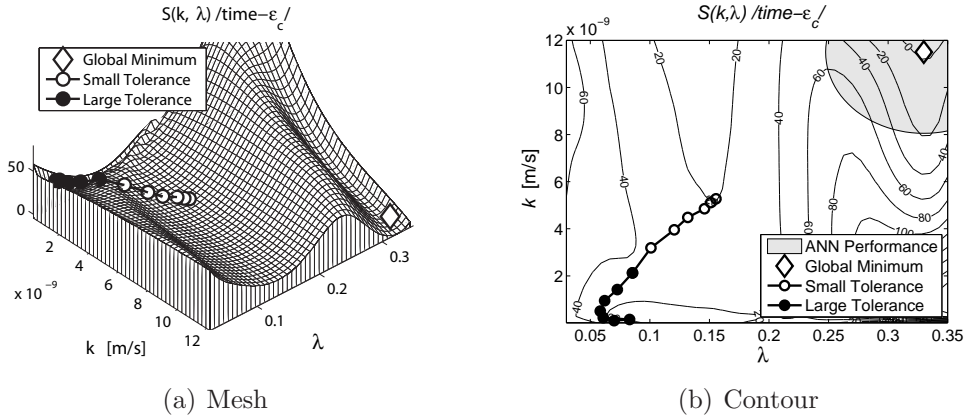


Figure 2.7: Example of computationally expensive optimization and its trapping before reaching the global minimum, and the possible space of prediction with neural networks

function is associated with the variation of cavity strain in time, for a simulation of the pressuremeter *pressure holding test* (PHT, see Section 6.2.3). In order to transparently illustrate the problem, the error function was extracted from the total error function, including the error function related to the second curve provided by the test, i.e. pore pressure dissipation in time. It is shown that starting from a remote point, the calibration can be prematurely finished if the small tolerance for one of the convergence criteria is set. Despite the raising of the tolerance threshold, the procedure can be terminated if the broad valley in the functional is met. On the other hand, Figure 2.7(b) shows that the possible region of network prediction is close to global minimum. A potential prediction area can easily be deduced from the post-training analysis of NN performance.

## 2.5 Summary and anticipated contribution

In this study, a development of the neural network (NN) approach for parameter prediction with special reference to two complex boundary value problems (BVP) of pressuremeter and piezocone tests will be investigated. NNs will be used to map experimental data of field tests onto estimates of characteristics of the Modified Cam Clay (MCC) model taking into account the complexity of BVPs. NNs are known as information-processing systems that can generalize even highly non-linear functions and can be used to solve inverse problems in computational mechanics. Another main feature of NNs is that a parallel operating system instantly transforms input variables onto output parameters. These two features may considerably accelerate the parameter identification procedure and improve the accuracy of the identified parameters.

In the proposed approach, NNs are to predict the vector of model parameters in order to avoid potential shortcomings and pitfalls, such as non-uniqueness, solution instability or computational effort, which are related to the gradient-based minimization technique. It will be demonstrated that NNs

can be trained based on measurements obtained through a number of numerical pseudo-experiments representing BVPs of *in situ* tests. Moreover, in numerical simulations, different drainage conditions will be imposed in order to raise NN awareness of possible occurrence of partial dissipation during the test.

As regards the BVP of the pressuremeter test, a hybrid parameter identification combining neural networks and gradient-based optimization (GBO) will be proposed to ensure accuracy of the identified parameters. The effectiveness of such a two-level parameter identification will be first investigated and demonstrated on the well-defined boundary value problem of the drained triaxial test. Then the strategy will be adopted to SBPT.

As regards the piezocone test, it is expected that the NNs will be able to provide first estimates of some model parameters without the necessity of test calibration based on a reference benchmark value obtained through laboratory tests (e.g. undrained shear strength). A well-designed interface should provide not only the facility to train NN for standard piezocone measurements but also the possibility of including in the training additionally acquired information about other soil properties.

In the context of NN training, a set of training patterns will be generated numerically by means of FE simulations of field tests applying the MCC constitutive law. It is intended that the identification framework will operate regardless of the testing depth. Thus, non-dimensionality, regarded as normalization with respect to the initial effective stress conditions will be introduced to input and output vectors containing test measurements.

Finally, results of the computational parameter identification applied to experimental data will be compared with the results obtained through various laboratory and field tests for several characterization sites.

# Chapter 3

## Neural Networks as Identification Method

*When the only tool you have is a hammer,  
every problem you encounter tends to resemble a nail.*

Abraham H. Maslow

### 3.1 Introduction

In recent decades, neural networks (NN) have gained current acceptance in many domains of science and engineering where straightforward modeling is unfeasible or the existing problem solutions need to be improved. With reference to the quote opening this chapter, the feed-forward neural networks (FFNN) are considered as a universal approximation tool for any continuous function (Hornik et al., 1989). The concept of an artificial neural network was inspired by the complex architecture of the human brain, regarded as a complex, highly non-linear, parallel operating system (Haykin, 1999). NNs are known as information-processing systems that can generalize even highly non-linear functions providing meaningful solutions for input data which includes error or presents incompleteness. They can be applied to problems which are not well-understood or for which deterministic models involve many assumptions or simplifications. In computational mechanics, they can deal with problems which involve time-dependent multi-phase processes including inverse problems (Flood and Kartam, 1994a). One of their main features is that a parallel operating system instantly transforms input variables onto sought outputs. The main features of NNs are the ability to learn and generalize solutions from a set of examples, and to provide meaningful results for input data which includes

error or presents incompleteness.

One of the first papers concerning constitutive modeling by means of neural networks by Ghaboussi et al. (1991) encouraged geotechnical researchers to begin exploring the potential of artificial intelligence, adopting the NNs to solve various mechanical problems. Ghaboussi and his colleagues originally proposed an NN-based framework for constitutive modeling in geomechanics (Ghaboussi and Sidarta, 1998; Sidarta and Ghaboussi, 1998). They introduced a concept of nested adaptive neural networks which consider the nested structure of the material test data, e.g. dimensionality, stress path dependency or drainage conditions. By means of the FE method and the auto-progressive training algorithm proposed in Ghaboussi et al. (1998), they trained neural networks with experimental non-uniform triaxial test data, in order to capture and reproduce the non-linear response of soil without using the conventional concepts of the theory of plasticity. Further research proved that NN constitutive models can be successfully embedded within the FE codes to compute the consistent tangent stiffness matrix (Shin and Pande, 2000; Lefik and Schrefler, 2003; Hashash et al., 2004). Hashash et al. (2004) demonstrated that a tangent stiffness matrix can be derived from NN-based material models, using the explicit formulation represented by network parameters. However, the main drawback of NN constitutive models is that it is valid only for a specific material for which a new NN has to be adopted each time. Moreover a material model loses its "flexibility" which is inherent in the case of conventional models and which is controlled by parameters explicitly describing concepts of plasticity such as yield surface, flow rule and hardening law. Other examples of constitutive modeling without standard mechanical concepts present the prediction of nonlinear stress-strain behavior using the *recurrent neural networks* (RNN). In this approach, apart from physical or mechanical properties, the actual stress-strain state which is provided by previous network activation complements the input vector in order to iteratively reproduce and predict complex soil behavior. Based on grain size distribution, stress history or initial voids ratio, such modeling was proposed for cohesionless soils (Ellis et al., 1995; Penumadu and Zhao, 1999) and for fine-grained soils (Zhu et al., 1998; Najjar and Huang, 2007). The RNN potential was also used to model hysteric soil behavior for cyclic loadings (Basheer, 2000, 2002).

Since the NNs are able to generalize a multi-variable complex relationships, they can assist in solving typical geotechnical problems like forecasting of slope movements or vertical ground movements based on rainfall history (Mayoraz and Vulliet, 2002; Neaupane and Achet, 2004; Doris et al., 2008), prediction of deflections of diaphragm walls and earth retaining structures (Goh et al., 1995; Jan et al., 2002; Hashash et al., 2003; Kung et al., 2007) and their reliability assessment (Goh and Kulhawy, 2005), assessment of shallow foundation settlements (Shahin et al., 2005). Further studies present successful applications of NNs for pile designing. Chan et al. (1995); Goh (1996b); Lee and Lee (1996); Abu-Kiefa (1998) compared the conventional methods for estimating load capacity of driven piles with NN models. Hanna et al. (2004) compared an effective NN model with existing empirical approaches for assessing the group efficiency



of axially loaded piles installed in cohesionless soil. In other studies, Nawari et al. (1999); Goh et al. (2005) proposed various approaches of NN modeling to analyze, respectively, the deflection and undrained shear resistance of drilled shafts.

Another category of NN applications deals with liquefaction phenomenon. Although the phenomenon is well known, the assessment of liquefaction susceptibility is not easy and is mostly based on empirical methods due to the complexity and uncertainty of the mechanism (Agrawal et al., 1997). The liquefaction potential was initially investigated with the aid of NN by Goh (1994, 1996a) based on SPT records and CPT cone resistance data, respectively. In his further study, Goh (2002) showed the application of the *probabilistic neural network* model in order to assess the liquefaction potential based on CPT and shear wave velocity data. Recently, Baziar and Ghorbani (2005) proposed the NN model to predict the lateral ground displacement induced by the liquefaction.

The NN strategy has been also successfully applied to three-dimensional site characterization. Typically, such investigations involve assessing the spatial variability of soil properties or field measurements based on reanalyzed discrete soil profiles or sections. Published examples demonstrate the feasibility of estimating the spatial distribution of the rockhead elevation based on seismic refraction survey data (Zhou and Wu, 1994), capturing the spatial variability of soil permeability (Basheer et al., 1996), and a three-dimensional variability analysis of the cone resistance records using CPT data in discrete test locations (Juang et al., 2001).

A development of the multi-regression analysis using NN technique has been found highly suitable for parameter identification in geotechnical engineering. The deterministic inverse solutions may rely on theoretical assumptions or simplifications, often justifiable, although occasionally neglecting important factors which are involved in some processes. The complexity of geomaterials with their inherent variability makes the identification challenging as many properties can be intercorrelated (Yang and Rosenbaum, 2002). This fact may be a significant difficulty when performing a traditional statistical regression analysis. In consequence, many researchers have leaned towards the NN methods to estimate geotechnical properties based on physical soil characteristics, e.g. hydraulic conductivity of compacted clay liners (Agrawal et al., 1994; Goh, 1995; Najjar and Basheer, 1996), compaction characteristics (Najjar et al., 1996), ultimate shear strength for unsaturated soil (Lee et al., 2003), or effective stress parameter  $\chi$  (Kayadelen, 2007). The NNs can be also used to map experimental test measurements onto geotechnical properties such as undrained shear strength (Kim, 2004), stress history (Kurup and Dudani, 2002) from CPT data, preconsolidation pressure from laboratory tests (Celk and Tan, 2005) or water content, degree of saturation and dry soil density based on measurements of the complex permittivity of a soil-water electrolyte system (Ding and Shang, 2004). NNs have been used to identify various mechanical properties from structural tests (Waszczyszyn, 1998; Shin and Pande, 2003; Nardin et al., 2003; Obrzud et al., 2009b) or some geotechnical properties from *in situ* experimental data

(Pichler et al., 2003; Obrzud et al., 2009a). Shin and Pande (2003) proposed an identification of the orthotropic elastic constants by forming a set of equations representing components of the computed tangent non-symmetric stiffness matrix for the NN-based constitutive model with the unknown elements of the conventional orthotropic stiffness matrix. Nardin et al. (2003) performed an identification of macro- and micro-parameters for a discrete element model.

For further reading, please refer to Toll (1996); Shahin et al. (2001, 2008) who provide a comprehensive review of a large number of complex geomechanical tasks which have been solved by means of neural networks.

Inverse modeling is one of the major issue in geomechanics. The inverse problems are often characterized by non-unique solutions which is derivative of the highly non-linear functional relationships between measured dependent and identified independent variables. In fact, many solutions may satisfy a formulated inverse problem. One of the reasons that the NNs are suitable to assist in solving the inverse problems is that they are able to map an admissible space of solution domain providing close approximates of the optimal solution. In connection with the supervised training algorithm, the NNs can serve as a powerful tool for solving inverse problems. Among variety of neural network algorithms, the multi-layer, feed-forward neural networks are most commonly used in engineering (Ghaboussi, 2001). The following sections present a brief overview on development and applicability of NN-based models.

## 3.2 Identification based on neural networks

Generally, development of an NN-based model consists of *(i)* assembling sufficiently large training database, *(ii)* selecting correlated input/output pairs and *(iii)* performing an efficient model calibration, i.e. the supervised NN training. Clearly, the efficiency of the NN model depends on the coherency of a collected database and the amount of information which is provided. Then, with the inherent imprecision tolerance feature, the NN models are able to find a general solution even for experimental data containing erroneous measurements. Typically, assembling of training patterns can be carried out by means of *(i)* synthesis of published historic data (e.g. Abu-Kiefa, 1998; Hanna et al., 2007), *(ii)* direct experimental observations of modeled problem (e.g. Ellis et al., 1995), *(iii)* acquiring experimental results through an alternative model (e.g. Basheer, 2000), *(iv)* performing inverse analysis to the problem under consideration using relevant numerical modeling (e.g. Goh et al., 1995; Hashash et al., 2003; Lefik and Schrefler, 2003). The first two approaches enable to develop phenomenological NN models as soon as results include no theoretical assumptions and simplifications, whereas other methods provide results which highly depend on the adequacy of an applied model. On the other hand, the first two approaches do not ensure a full control over pattern distribution in the problem domain (Flood and Kartam, 1994a).

### 3.2.1 Numerical approach for database generation

In this study, neural networks will be trained based on a set of synthetic curves which are produced by numerical simulations. This approach to training pattern generation has the following advantages:

- The approach provides full control across the space of constitutive model parameters. The parameters can be regularly distributed in the training set using relevant probability density functions (pdf). The constraints for parameter relationships stemming from model mechanics or observed relationships can be imposed. Thus, the non-physical or unlike combination of parameters are skipped reducing dimensions of parameter space and improving the accuracy for densely clustered regions.
- Contrary to the synthesis of available experimental or historical data which may prove to be time-consuming and expensive, the number of training patterns is defined by the user and depends only on storage capacities or computational time restrictions. The numerical database can be enlarged at any moment if an improved accuracy of problem solution is required in some problem domains.
- The quality of numerical measurements rigorously depends on the developed numerical model which depends on the capacities of constitutive law, the adequacy of BVP modeling and the robustness of numerical procedures. If two latter issues are met, the measurements are directly proportional to the initial model variables and do not include disturbance effects, as is the case with the conventional testing procedures.
- Contrary to the synthesis of historical data, the measurements can be provided by one probing unit driven by one operator. Then, the numerical pseudo-experiments reveal numerical accuracy and coherency of results.

Hence, NN training in such a case can be regarded as an organization of "knowledge" about constitutive relations of a selected model, subject to selected boundary conditions. On the other hand, the generation of numerical patterns may bear some shortcomings. It can be questionable to what extent the constitutive model represents real soil behavior for the imposed boundary conditions and how it affects the quality of measurements (cf. the discussion in Section 4.3). Another limitation of this approach is that the modeling of the boundary value problem for a selected constitutive model is sometimes unfeasible or limited due to insufficient capabilities of numerical procedures (e.g. see Section 7.2.2.3). In certain cases, the numerical generation of training patterns can prove to be time-consuming since it depends on the robustness of numerical procedures and the number of samples in the experimental database.

In this study, the development of neural network models in the context of parameter prediction consists of two main tasks which comprise of: (1) generation of NS number of training samples using the numerical model of the selected

BVP so that the database comprises of input-target pairs  $\mathcal{D} = \{\mathbf{p}_m, \mathbf{t}_m\}$ , with  $m = 1, \dots, NS$ ; (2) performance of the NN training until the neural network is able to reproduce target parameters and to generalize the problem for new numerical data. This part may be regarded as a one-time process if the sufficiently large space of parameters,  $\mathcal{R}_b$ , is covered.

In the identification mode, the developed prediction tool is used to map real experimental data onto output vector,  $\mathbf{o}$ , regarded as a set of mechanical soil characteristics.

### 3.2.2 Preparation of training patterns

The supervised training is based on a sufficiently rich set of representative numerical samples,  $\mathcal{D} = \{\hat{\mathbf{y}}'(\mathbf{b})_m, \mathbf{b}_m\}$  which ensures an effective training so that the properly trained network gives acceptable accuracy of predicted variables. These samples comprise of input vectors corresponding to the normalized numerical measurements  $\hat{\mathbf{y}}'(\mathbf{b})$  and expected outputs representing target model parameters  $\mathbf{b} \in \mathcal{R}_b$ . In the context of field tests, non-dimensionality, regarded as normalization with respect to the initial effective mean stress  $p'_o$ , is introduced to reduce this variable in random generation of samples. Since field measurements exhibit a non-smooth stress-strain relief, artificial noise can be introduced to the smooth numerical data. This helps to avoid an over-fitting of the trained network and to improve the ability of generalization. Generation of  $\mathcal{D}$  consists of the following steps:

1. Generating random permutations of  $b_n$ , within  $\mathcal{R}_b$  observable in geotechnical practice and preserving statistical correlations between model parameters (where  $n = 1, \dots, NC$ , and  $NC$  is the overall number of variables defining numerical model),
2. Computing numerical model responses  $\mathbf{y}'(\mathbf{b})$  by means of FE simulations,
3. Introducing random noise  $s$  to numerical results  $\tilde{\mathbf{y}}'(\mathbf{b}) = \mathbf{y}'(\mathbf{b}, \mathbf{s})$ ,
4. Introducing non-dimensionality of measured variables with respect to the initial stress state  $\hat{\mathbf{y}}'(\mathbf{b}) = \tilde{\mathbf{y}}'(\mathbf{b}, p'_o)$ .

The above approach will be presented on examples in Sections 5.1 and 8.

## 3.3 Theory of feed-forward neural networks

This section introduces the main issues as regards the *feed-forward neural networks*. The description includes the basics of neural network topography as well as the concept of the *back-propagation* training algorithm. A reduction of multidimensional data set by means of the *principal component analysis* (PCA) will also be described.

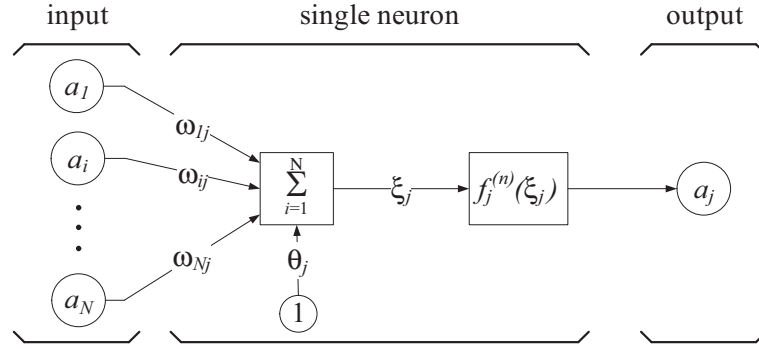


Figure 3.1: Scheme of single neuron.

### 3.3.1 Model of a neuron

Each neural network is composed of an assembly of single interconnected processing units which represent neurons of human brain. The terms unit and neuron will be used alternately in the later part of this study. The concept of a simple mathematical model of a neuron was conceived of by McCulloch and Pitts (1943) and still remains the basic unit used in neural processing. An elementary neuron with  $N$  number of activating inputs is shown in Figure 3.1. A single unit consists of weights storing knowledge gained during the training, computing an activation level, and a differentiable transfer function transmitting processed inputs to other units as outputs. The basic activities performed by a single neuron in the so-called feed-forward procedure can be summarized as follows:

1. Processing unit  $j$  receives signals coming from incoming inputs,  $a_i$ . These signals, however, are modified by the strengths called network weights,  $\omega_{ij}$ . The weights are network parameters which interconnect input elements with an internal state parameter,  $\xi_j$ , also called the excitation of the neuron. The modified signals are summed up as shown below:

$$\xi_j^{(n)} = \omega_{1j}^{(n)} a_1 + \omega_{2j}^{(n)} a_2 + \dots + \omega_{Nj}^{(n)} a_N + \theta_j^{(n)} = \sum_{i=1}^N \omega_{ij}^{(n)} a_i + \theta_j^{(n)}, \quad (3.1)$$

$j = 1, M$

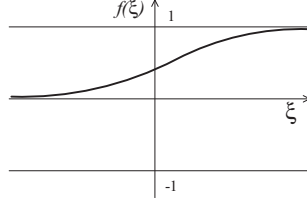
where  $n$  is an identity of the layer,  $N$  is the number of elements in the input vector and  $M$  is the number of neurons in  $n$ -th layer. Moreover, neurons can also contain an additional input node, so-called bias,  $\theta_j$ , acting as a form of threshold. Its value is equal to 1.

2. The activation level,  $a_j$ , which is an output of the processing unit, is computed through a non-linear transfer function,  $f_j$ , which is a threshold function of the value  $a_j$ . In addition, the unity output may be affected by the bias  $\theta_j$ . The outgoing unity value is given by:

$$a_j = f_j(\xi_j) \quad (3.2)$$

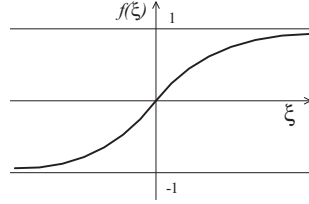
The output signal  $a_j$  is restricted by the upper and lower thresholds depending on the form of the differentiable transfer function. Generally, the log-sigmoid and tan-sigmoid functions are used generating output values between 0 to 1, and -1 to 1, respectively:

a) log-sigmoid function



$$f(\xi) = \frac{1}{1 + e^{-\xi}} \quad (3.3)$$

b) tan-sigmoid function



$$f(\xi) = \frac{2}{1 + e^{-2\xi}} - 1 \quad (3.4)$$

For the output layers, the linear transfer function is often used to calculate a layer's output from its net input. This function is represented in a simple form:

$$f(\xi) = \xi \quad (3.5)$$

Since  $N$  single units can be interconnected through so-called hidden layers, they create a collective network which is able to solve even highly non-linear problems. Nowadays, the most popular neural network applied in civil engineering is a multi-layered, feed-forward network.

### 3.3.2 Network architecture and feed-forward procedure

The multi-layered network is designed hierarchically and consists of hidden layers. Each layer comprises of processing units which are fully interconnected with units in the next layer. A typical architecture of the multi-layered network with input, output and one hidden layer is presented in Figure 3.2. The input layer consisting of  $N^{(p)}$  input units activates a hidden layer containing  $N^{(h)}$  neurons. Then, the signal is transmitted across outgoing connections to the  $N^{(o)}$ -dimensional output layer. In other words, the feed-forward algorithm maps the dimensionless values of the input vector  $p_i$ ,  $i = 1, \dots, N^{(p)}$  into the output vector  $o_k$ ,  $k = 1, \dots, N^{(o)}$ . The output vector for a network with one hidden layer can be thus expressed using Equation (3.2):

$$o_k = f_k^{(o)} \left( \sum_{j=1}^{N^{(h)}} \omega_{jk}^{(o)} f_j^{(h)} \left( \sum_{i=1}^{N^{(p)}} \omega_{ij}^{(h)} p_i + \theta_j^{(h)} \right) + \theta_k^{(o)} \right) \quad (3.6)$$

This formula can be regarded as the closed-form solution to a given problem if network weights are correctly adjusted. Such designed NN has the ability to generalize a specified problem for which the solution can be represented by an unknown non-linear function.

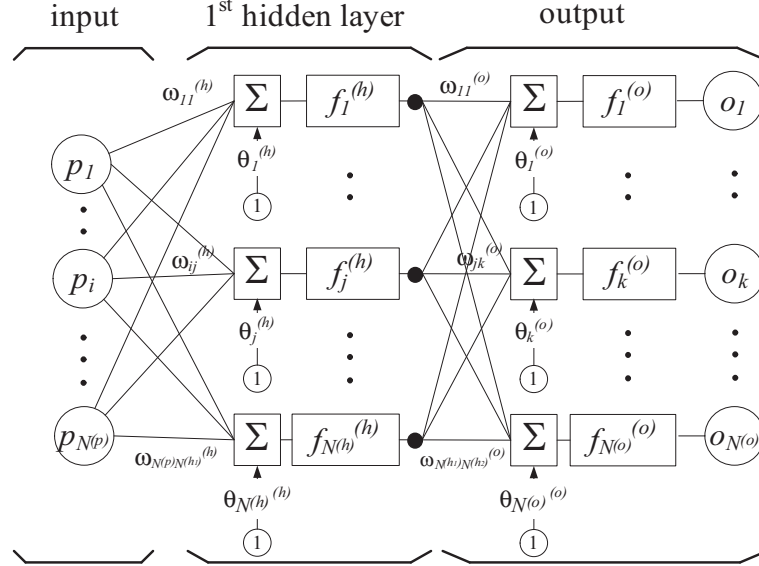


Figure 3.2: Example of the NN topology with one hidden layer.

### 3.3.3 Neural network training

Apart from the ability to generalize, a neural network possesses the important feature of self-organizing in the light of a specified problem. The self-organization requires adjusting network weights by means of performing supervised training. The NN training is equivalent to the minimization of discrepancies between output values produced by the untrained NN and target solutions considered as the part of a training set. Supposing that the important input factors affecting further output products are recognized, then NN modeling algorithm comprises of the following subroutines:

1. Division of experimental database into training, validation and testing subsets.
2. Data pre-processing.
3. Specification of network topology.
4. NN training with network performance monitoring.
5. Post-training performance analysis.

The following subsections are addressed to these issues.

### 3.3.3.1 Selection of training database

Similarly to conventional statistical inverse models, the calibration of NN parameters requires a set of experimental results  $\mathcal{D}$  which comprises of representative input/output pairs. Usually, the training set is divided into three subsets: *training*, *validating* and *testing*.

The first set is used to adjust network weights to feed trained network during the back-propagation procedure (Section 3.3.3.4). This set should be large enough and well-specified so that the trained NN is able to generalize within the range of variables used for NN learning. It is well recognized that NNs optimally perform for the range of data which is included in the training set and their abilities of extrapolation are limited (Flood and Kartam, 1994a; Shahin et al., 2008). Therefore, the extreme data points for all dimensions of the database should be included in the training subset.

The validation set is used to perform the *cross-validation* of the trained network (Section 3.3.3.5). This procedure is used to avoid network overfitting when performing training cycles. In other words, this subset controls whether network performance maintains the general trend for the solution. The overfitting may lead to the memorization of single data points losing the ability to generalize a problem.

The last testing subset is used after the training to independently assess network performance using the new data points that have not been presented to the network before (see Section 3.3.4). Clearly, the best network performance can be achieved for the data points within the space of data points included in the training set. If this is the case, a reasonable performance analysis of NN model can be carried out. Masters (1993) suggested that the statistical properties, i.e. mean and standard deviation for each subset should be similar so that they represent the same statistical population.

Generally, no unified guidelines exist for the determination of proportions for training subsets. Apart from random or statistically consistent data division, some systematic approaches for data division, such as the self-organizing map or the fuzzy clustering technique have been proposed in literature. Shahin et al. (2004) compared these various data division approaches in a case study for settlement prediction of shallow foundations in granular soils. They found optimal proportions of 20% of the dataset for the validation test whereas the remaining part was divided into 70% for training and 30% for testing. Typically, the 60-70% of the dataset can be used as the training set, whereas the other sets can contain 15-20% each.

### 3.3.3.2 Data pre-processing

It may occur that input and output vectors contain data comprising of physical values often varying in order of magnitude. This may result in large amplitudes of the target solution surfaces and attract the training attention to the regions with the highest amplitudes (Flood and Kartam, 1994a). In such cases, it may be useful to transform the input and output vectors so that all variables would receive similar attention during training. All variables can be scaled into



dimensionless values falling into an interval  $\langle -1, 1 \rangle$ . Thus, the elements of the column vectors  $\mathbf{x}_1, \mathbf{x}_2, \dots, \mathbf{x}_n$  are scaled to values  $\hat{x}$  according:

$$\hat{x} = \frac{2(x - x_{min})}{x_{max} - x_{min}} - 1 \quad (3.7)$$

Another approach to scale network input/output pairs is normalization with respect to the mean and standard deviation of the training set (Equation (3.8)).

In the present study, training data samples are generated by means of FE analyzes. For some analyzes the final results can be provided in rows of many discrete measurements. Many of these measurements, provided also with artificial noise imitating a natural scatter, can be correlated and, in the context of parameter identification, may be redundant. Hence, it is useful to compute the most meaningful basis to filter out the noise from numerical and further experimental measurements and to extract the most meaningful information from a large data set. The principal component analysis (PCA) is a statistical method which reduces multidimensional data sets to lower dimensions (Haykin, 1999). Reducing a large data set, PCA reveals a simplified hidden structure that can be nested in the test measurements. PCA is an orthogonal linear transformation that transforms the data to a new coordinate system so that the greatest variance of the projected data lies on the first principal axis, the second greatest variance on the second axis etc. Ignoring the higher-order principal components, the most affecting data in the analysis are retained by lower-order ones.

Supposing that column vectors  $\hat{\mathbf{x}}_1, \hat{\mathbf{x}}_2, \dots, \hat{\mathbf{x}}_n$  contain scaled observations of  $m = ND$  variables of  $n = NS$  stress-strain analyses, means and deviations along each dimension  $m$  are mapped respectively onto 0 and 1 according to the following equation:

$$\hat{\mathbf{x}}_j = \frac{(\mathbf{x}_j - E[\mathbf{x}_j])}{\sqrt{E[\mathbf{x}_j^2] - (E[\mathbf{x}_j])^2}} \quad \text{and} \quad j = 1, \dots, m \quad (3.8)$$

The empirical correlation matrix ( $m \times m$ ) can be estimated as (Diamantaras and Kung, 1996):

$$\mathbf{R} \cong \frac{1}{n} \sum_{i=1}^n \hat{\mathbf{x}}_i \hat{\mathbf{x}}_i^T = \frac{1}{n} \mathbf{X} \mathbf{X}^T \quad (3.9)$$

where  $\mathbf{X} = [\hat{\mathbf{x}}_1, \dots, \hat{\mathbf{x}}_i, \dots, \hat{\mathbf{x}}_n]$ . Then, using the orthogonal similarity of transformation

$$\mathbf{W}^T \mathbf{R} \mathbf{W} = \mathbf{V} \quad (3.10)$$

the matrix of eigenvectors  $\mathbf{W} = [\mathbf{w}_1, \dots, \mathbf{w}_j, \dots, \mathbf{w}_m]$  and the diagonal matrix of eigenvalues  $\mathbf{V} = \text{diag}[v_1, \dots, v_j, \dots, v_m]$  can be computed and arranged according to a descending order. The principal component vectors can be thus computed as:

$$\mathbf{y}_j = \mathbf{w}_j^T \hat{\mathbf{x}}, \quad j = 1, \dots, l \quad (3.11)$$

where  $l$  denotes the reduced number of observations  $1 \leq l < m$  under the condition that  $v_l \gg v_{l+1}$ . This operation transforms the  $\mathcal{R}_m$  space into the reduced dimension  $\mathcal{R}_l$  retaining those variables which contribute most to the variance.

### 3.3.3.3 Determination of network topology

Network topology should be selected prior to NN training. It requires assigning a number of neurons which are distributed in a number of hidden layers. The choice of the optimal network configuration is not straightforward since it may be influenced by the number of elements in the input and output vectors, as well as by a dimension of a training set or complexity of the problem. Flood and Kartam (1994a) stated that *"two hidden layers provide the greater flexibility necessary to model complex-shaped solution surfaces, and are thus recommended as a starting point when developing a layered feed-forward network of sigmoidal neurons"*. On the other hand, more than one hidden layer may increase the risk of getting trapped in local minima (Shahin et al., 2008). Usually, the number of hidden layers is selected arbitrarily and a trial-and-error procedure is performed to find an optimal number of processing units. It is well known that a large number of neurons increases the risk of over-fitting. Thus, it is recommended to keep the number of neurons as small as possible which (i) ensures a reduced computational cost of the training, (ii) improves generalization performance by avoiding network overfitting, (iii) makes the trained network easier to be analyzed (Shahin et al., 2008).

Usually, the trial-and-error procedure is initiated with a small number of neurons. This number remains constant for a given training trial and is modified as necessary if the performance of the network is not satisfactory.

Ghaboussi and Sidarta (1998) proposed an adaptive method of network topology determination which consists of starting the training with a small number of neurons which is dynamically updated during the training cycles. The discussion on the other approaches to the determination of the optimal network architecture is provided by Shahin et al. (2008).

In this study, optimal network topologies will be found with a few trial-and-error training runs.

### 3.3.3.4 Back-propagation algorithm

In the supervised training,  $NS^{(t)}$ -number of representative patterns comprising of input vectors and corresponding targets is used to adjust network weights until the NN satisfactorily approximates a function. This is usually performed by using one of gradient-based optimization techniques. The quality of network performance can be validated by means of  $NS^{(s)}$ -number of testing patterns which have not been presented to the network before. As mentioned above, each training pattern comprises the input vector  $p_i$  within  $N^{(p)}$ -number of elements ( $i = 1, \dots, N^{(p)}$ ) and the corresponding output vector  $o_k$  of  $N^{(o)}$  elements ( $k = 1, \dots, N^{(o)}$ ). During the first activation of the untrained network, the network weights are chosen randomly, and therefore, discrepancies between each output vector  $o_k$  and target vector  $t_k$  are expected. Hence, the global error function to be minimized,  $F^{(g)}$ , for the total number of training sets,  $NS^{(t)}$ , can be calculated

as follows:

$$\begin{aligned}
F^{(g)} &= \frac{1}{NS^{(t)}} \sum_{t=1}^{NS^{(t)}} F_t = \\
&= \frac{1}{NS^{(t)}} \sum_{t=1}^{NS^{(t)}} \frac{1}{N^{(o)}} \sum_{k=1}^{N^{(o)}} \left( t_k(\mathbf{p}) - o_k(\mathbf{p}) \right)^2 \rightarrow \text{minimize}
\end{aligned} \tag{3.12}$$

where  $t$  denotes the index of the training pattern ( $t = 1, \dots, NS^{(t)}$ ).

NN training aims at minimizing the global error by an iterative adjustment of the network weights according to the *generalized delta rule* (Rumelhart et al., 1986). The global error is gradually reduced in each network activation, using one of gradient-based optimization algorithms, such as conjugate gradient, Newtonian or quasi-Newtonian algorithms, etc. Partial derivatives of the global error with respect to the weights,  $\omega_{jk}^{(o)}$  and  $\omega_{ij}^{(h)}$ , determine the gradient of weights increments,  $\Delta\omega_{jk}^{(o)}$  and  $\Delta\omega_{ij}^{(h)}$ , by means of the generalized delta rule. Hence, the learning process is referred to the back-propagation term, as the derivative of the global error is back-calculated contrary to the direction of activated network calculations. The increments of weights are functions of partial derivatives of the global error with respect to weights:

$$\Delta\omega_{jk}^{(o)} = \Delta\omega_{jk}^{(o)} \left( -\eta \frac{\partial F^{(g)}}{\partial \omega_{jk}^{(o)}} \right) \quad \text{and} \quad \Delta\omega_{ij}^{(h)} = \Delta\omega_{ij}^{(h)} \left( -\eta \frac{\partial F^{(g)}}{\partial \omega_{ij}^{(h)}} \right) \tag{3.13}$$

where  $\eta$  denotes the learning-rate parameter, superscripts  $(o)$  and  $(h)$  concern respectively the output and the hidden layer while  $i, j, k$  denote the number of elements of a relevant layer presented in Figure 3.2,  $i = 1, \dots, N^{(p)}$ ,  $j = 1, \dots, N^{(h)}$ ,  $k = 1, \dots, N^{(o)}$ .

The direction of weight changes is directly calculated as:

$$\frac{\partial F^{(g)}}{\partial \omega_{jk}^{(o)}} = \sum_{t=1}^{NS^{(t)}} \frac{\partial F^{(g)}}{\partial F_t} \frac{\partial F_t}{\omega_{jk}^{(o)}} \tag{3.14a}$$

$$\frac{\partial F^{(g)}}{\partial \omega_{ij}^{(h)}} = \sum_{t=1}^{NS^{(t)}} \frac{\partial F^{(g)}}{\partial F_t} \frac{\partial F_t}{\omega_{ij}^{(h)}} \tag{3.14b}$$

where partial derivatives for the error function  $F_t$ , for pairs input/output  $\mathbf{o}(\mathbf{p})$  and input/target  $\mathbf{t}(\mathbf{p})$  are calculated as:

$$\frac{\partial F_t}{\partial \omega_{jk}^{(o)}} = \frac{\partial F_t}{\partial o_k} \frac{\partial o_k}{\partial \xi_k^{(o)}} \frac{\partial \xi_k^{(o)}}{\partial \omega_{jk}^{(o)}} = \frac{2}{N^{(o)}} \left( t_k(\mathbf{p}) - o_k(\mathbf{p}) \right) \frac{\partial f(\xi_k^{(o)})}{\partial \xi_k^{(o)}} f(\xi_j^{(h)}) \tag{3.15a}$$

$$\begin{aligned}
\frac{\partial F_t}{\partial \omega_{ij}^{(h)}} &= \sum_{k=1}^{N^{(o)}} \left[ \frac{\partial F_t}{\partial o_k} \frac{\partial o_k}{\partial \xi_k^{(o)}} \frac{\partial \xi_k^{(o)}}{\partial f(\xi_j^{(h)})} \right] \frac{\partial f(\xi_j^{(h)})}{\partial \xi_j^{(h)}} \frac{\partial \xi_j^{(h)}}{\partial \omega_{ij}^{(h)}} = \\
&= \frac{2}{N^{(o)}} \sum_{k=1}^{N^{(o)}} \left[ \left( t_k(\mathbf{p}) - o_k(\mathbf{p}) \right) \frac{\partial f(\xi_k^{(o)})}{\partial \xi_k^{(o)}} \omega_{jk}^{(o)} \right] \frac{\partial f(\xi_j^{(h)})}{\partial \xi_j^{(h)}} p_j
\end{aligned} \tag{3.15b}$$

In Equation 3.15 the derivative of the linear transfer function in the output layer is trivial and derivatives for the log-sigmoid or tan-sigmoid functions (Equation 3.3 and 3.4) which may be used alternately in hidden layers are calculated respectively as:

$$\frac{\partial f(\xi_j^{(h)})}{\partial \xi_j^{(h)}} = f(\xi_j^{(h)}) \left( f(\xi_j^{(h)}) - 1 \right) \quad (3.16a)$$

or

$$\frac{\partial f(\xi_j^{(h)})}{\partial \xi_j^{(h)}} = 4f(\xi_j^{(h)}) \left( f(\xi_j^{(h)}) - 1 \right) \quad (3.16b)$$

For further details, please refer to literature of the topic (Rumelhart et al., 1986; Haykin, 1999).

Sometimes the gradient descent algorithm may be prone to get stuck in local minima if the network weights are selected randomly at the beginning of the training. In such cases, the learning process needs to be repeated or the global search techniques such as genetic algorithms can be used to find the values of weights that are close to the optimal ones (e.g. Pichler et al., 2003).

Depending on the problem, the complexity of solution surfaces, extension of the training patterns and network topology, different optimization techniques can be employed during the process of training. In this study, the Levenberg-Marquardt algorithm (Marquardt, 1963) will be used for all training sessions since it delivers the fastest training for a moderate-sized network topology (Hagan et al., 1996).

### 3.3.3.5 Network performance monitoring

The optimal calibration of network parameters requires the monitoring the network performance during the learning process. The training can be stopped if the global error  $F^{(g)}$  achieves the user-specified threshold. However, this criterion may lead to network over-fitting or premature stopping the calibration of under-optimized weights (Shahin et al., 2008). Such pitfalls can be avoided using the *cross-validation* technique (Figure 3.3). Before the training, a representative set of patterns is divided into three parts: training, validation and testing subsets comprising, respectively,  $NS^{(t)}$ ,  $NS^{(v)}$  and  $NS^{(s)}$  numbers of patterns. As shown before, the determination of the global error  $F^{(g)}$  in order to modify network weights is computed as the sum of errors  $F_t$  obtained for each pair of network output-target belonging to the training set. By analogy, the global error for the validation set can be established as a sum of errors  $F_v$  corresponding to  $NS^{(v)}$ - validation patterns:

$$F_v^{(g)} = \frac{1}{NS^{(v)}} \sum_{v=1}^{NS^{(v)}} F_v \quad (3.17)$$

An accurate ability to generalize is achieved by the trained network if the global errors  $F^{(g)}$  and  $F_v^{(g)}$  decrease with the similar rate until the user-specified tolerance is met or if the further cycles deliver no downward trend for both training

and validation patterns (Figure 3.3). On the other hand, a limited ability of the network is recognized if the global error  $F_v^{(g)}$  displays no further improvements or the increasing trend as the training progresses.

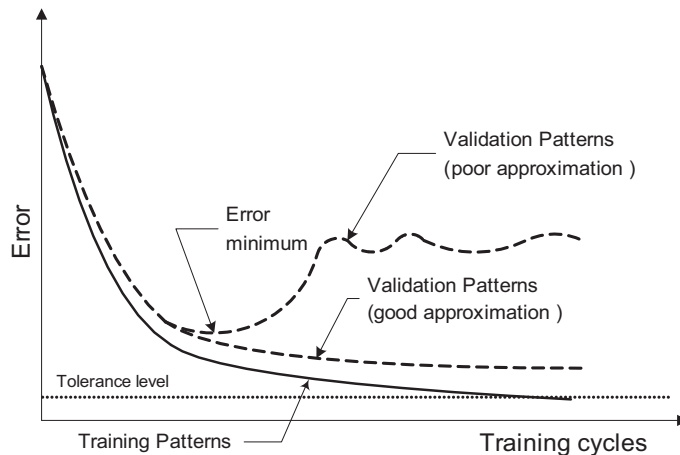


Figure 3.3: Network performance monitoring during training.

### 3.3.4 Post-training network analysis

Before applying the network to a case study, the degree of confidence has to be established (Flood and Kartam, 1994a). The applicability of the trained network can be assessed by performing the post-training analysis. It requires providing the trained network with the testing set containing  $NS^{(s)}$  representative solutions which are not presented to the network during training. The accuracy of fit can be then evaluated by comparing the network output products with the benchmark targets. For this purpose, a qualitative evaluation of plotted data points and a quantitative statistical analysis by means of a coefficient of correlation  $R$  and mean squared error MSE are typically carried out (Figure 3.4). A good approximation is thus characterized by MSE which tends to reach 0. For this measure, large errors receive greater attention than small errors (Shahin et al., 2008). As regards the quality of correlation measured by  $R$ , according to Smith (1986) (after Shahin et al., 2008), this measure can be tentatively classified as follows:

$$\begin{aligned}
 |R| \geq 0.8 & \quad \text{strong correlation exists} \\
 0.2 < |R| < 0.8 & \quad \text{medium correlation exists} \\
 |R| \leq 0.2 & \quad \text{weak correlation exists}
 \end{aligned} \tag{3.18}$$

Since the training patterns in this study are generated with the aid of FE simulations, it is strongly recommended to check the applicability of the NN inverse models for real case studies. Such a validation is necessary because NN models will be developed based on the results provided by the simplified constitutive relations of the soil model subject to idealized boundary conditions.

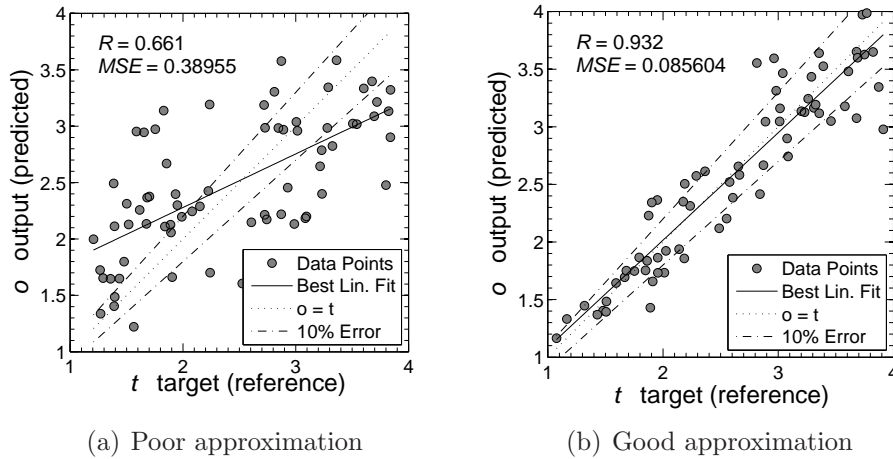


Figure 3.4: Post-training analysis of network performance for patterns never presented to the network.

Examples of the validations with the real experimental measurements will be presented in Sections 5.2, 9.1 and 9.2.

### 3.4 Remarks on NN’s shortcomings

There are four main issues which may discourage engineers from using NNs, i.e. (i) the lack of transparency of NN models, (ii) the lack of precision, (iii) the uncertainty related to knowledge extraction, and (iv) reduced ability of extrapolation. The latter is clearly a derivative of the strictly-defined space of training dataset. The application of developed NN models is thus restricted to the range of data points that are included in the training database (Flood and Kartam, 1994a). Since the value of extrapolated solutions can sometimes be doubtful, the acquisition of training patterns well representing the modeled task plays an important role in the development of the NN models.

*Lack of precision* is related to the non-uniqueness of network topology. Different configurations may give different results, and yet they are reasonable and close to the exact solution. The imprecision may sometimes stem from the random assignment of network weights at the beginning of the training or the random character of pattern sampling within the entire training dataset. In the context of inverse modeling, the mathematical precision is typically not required since this kind of problems are characterized by the inherent non-uniqueness of solutions. Hence, the NN ability to find the vicinity of the most optimal solution is appreciated in most practical problems.

*Lack of transparency* is related to network parameters which store the knowledge gained by neural networks. Since network weights have no physical meaning, as is the case of conventional mechanical characteristics, NN are often considered as "black boxes" (Shahin et al., 2008). *Knowledge extraction* has been the subject of many studies (e.g. Garson, 1991; Yang and Zhang, 1997; Gevrey et al., 2003; Olden et al., 2004). Generally, it consists of carrying out

a hierarchical analysis which specifies input variables which mostly affect the corresponding outputs. In other words, such an analysis allows the user to detect the factors which have the most influence on the problem under consideration. Typically, the existing methods of knowledge extraction are based on an examination of network weights (e.g. Goh, 1994) or on carrying out the sensitivity analysis (e.g. Yang and Zhang, 1997). Among the proposed methods, the most popular ones are weight partitioning algorithm (Garson, 1991), the connection weights algorithm (Olden and Jackson, 2002) and the input perturbation approach (e.g. Yao et al., 1998; Scardi and Harding, 1999; Sudheer, 2005), partial derivatives approach (e.g. Yang and Zhang, 1997), etc.<sup>1</sup> In this study, the first three approaches will be used in an example of finding factors which have the largest impact on the predicted parameter (see Section 8.2.6). Although the Garson's algorithm is proved to provide sometimes unreasonable results (cf. Olden et al., 2004), the approach will also be considered in further analyzes. This algorithm involves partitioning of the absolute values of connection weights to calculate variable contributions (for details see Goh, 1994; Olden et al., 2004). The "connection weights" approach calculates the product of the raw input-hidden and hidden-output connection weights between each input and output unit and sums the products across all hidden neurons (for details see Olden et al., 2004). In the input perturbation approach, a selected variable is perturbed with artificial noise while the other variables remain unchanged. The mean square error MSE can be a measure of the input contribution. Hence, the input variable which produces the largest error has the most relative influence. The input values can be perturbed in 5% increments varying from 75 to 125% of the reference values.

### 3.5 Summary

Over the last two decades, the feed-forward neural networks have drawn a lot of attention from geotechnical engineers. It has been proved in many studies that, as universal and rapid function approximators, they are suitable to assist in solving inherently complex geotechnical problems. They can also be complementary to the mathematical models which often suffer from theoretical assumptions and simplifications. The NN ability to learn with a set of examples, problem generalization and imprecision tolerance make them a powerful tool for modeling the inverse problems. As a parallel operating system, they provide solutions rapidly, without iterative procedures characteristic to direct search approaches. Despite their advantages, NNs possess some shortcomings such as lack of "mathematical" precision or limited possibility of knowledge extraction and rationalizing provided solutions. However, these shortcomings do not diminish the value of NNs in the context of inverse modeling.

In this chapter, the main concepts of feed-forward networks and the effective supervised training have been briefly introduced and analyzed. The strategy

---

<sup>1</sup>Refer to Gevrey et al. (2003); Olden et al. (2004) for comprehensive reviews of the knowledge extraction approaches.

of numerical pattern generation has been presented and compared with other approaches. Such a strategy provides a full control over the parameter space and ensures coherency of measurements corresponding to model characteristics.



# Chapter 4

## Mathematical Model of Soil

*Entia non sunt multiplicanda praeter necessitatem*<sup>1</sup>

William of Ockham

In this study, the application of neural networks for parameter prediction will be applied for the isotropic elasto-plastic Modified Cam-Clay (MCC) model (Roscoe and Burland, 1968). This model is often the kernel of more complex models such as multi-mechanism model by Hujieux (1985). Despite certain limitations, this strain-hardening model describes the behavior of normally- and lightly overconsolidated cohesive soil incorporating the effect of stress path history fairly well. In natural clays, overconsolidation may stem from mechanical unloading such as erosion, excavations, changes in ground water level, or due to other phenomena such as dessication, melting of ice cover, secondary compression, and cementation (Whittle and Kavvas, 1994).

In Chapter 5 the MCC model will be used to illustrate the application of the hybrid parameter identification on a simple example of the drained triaxial compression test. Although the feasibility of the identification technique is investigated with the MCC model, it can be adopted for much more complex constitutive models. Such a simple model was selected to reliably verify the proposed parameter identification strategy. Although most of model parameters have a clear physical meaning and can be directly estimated for the considered BVPs, in the case of numerical parameter identification, they can be artificially perceived as "non-physical" properties. This is so because all these parameters may control and affect the stress-strain response of the model. This assumption is introduced only for the purpose of demonstration because it is obvious that the MCC parameter estimates can be directly assessed from the conventional triaxial test curves.

---

<sup>1</sup>"Entities should not be multiplied beyond necessity", also paraphrased as "All other things being equal, the simplest solution is the best".

The proposed parameter prediction and identification strategy for the MCC will be investigated for field tests in Chapters 8 and 9. Two of the most common standardized tests, i.e. pressuremeter and piezocone test, will be investigated with the special reference to complexity of their BVPs, as well as possible occurrence of partial drainage. However, in order to avoid further complexity associated with the increasing number of parameters, the strain-rate effects will be neglected in this study.

## 4.1 Constitutive equations of the Modified Cam Clay model

The yield and plastic potential surface of the model are defined in terms of effective stress invariants  $p' = -I_1/3$  and  $q = \sqrt{3J_2}$  and the preconsolidation pressure  $p_{co}$  which defines the overconsolidation ratio  $R_p = p_{co}/p'$ <sup>2</sup>. The equation for the state boundary surface for MCC (cf. Figure 5.1b) is defined as follows:

$$F(\sigma', p_{co}) = q^2 + M^2 \cdot p'(p' - p_{co}) = 0 \quad (4.1)$$

The constitutive model is characterized by five model parameters  $M$ ,  $\lambda$ ,  $\kappa$ ,  $p_{co}$  and  $\nu$ . The  $M$  parameter is the slope of the critical state line (CSL) in the  $p' - q$  plane (Figure 5.1(b)) and can be expressed as  $M = 6 \sin \phi'_c / (3 - \sin \phi'_c)$ , where  $\phi'_c$  is the effective friction angle determined from the triaxial compression test;  $\nu$  is the Poisson's ratio,  $\lambda$  and  $\kappa$  denote respectively the slope of normal consolidation (NCL) and unload-reload compression lines in isotropic compression tests (Figure 5.1(a)). In the model, lines of virgin loading and swelling are approximated linearly in the  $e - \ln p'$  axes, which consequently implies a linear relationship between bulk modulus,  $K$ , and the effective mean stress,  $p'$ .

$$K = K(p') = \frac{1 + e_o}{\kappa} p' \quad (4.2)$$

where  $e_o$  denotes the initial voids ratio. In that case,  $G/K = \text{const}$  and is expressed by the formula:

$$\frac{G}{K} = \frac{3}{2} \frac{1 - 2\nu}{1 + \nu} \quad (4.3)$$

Hence, the current shear modulus is computed through:

$$G = \frac{3(1 - 2\nu)(1 + e_o)p'}{2(1 + \nu)\kappa} \quad (4.4)$$

The total strain increment (rate) is decomposed into elastic,  $\dot{\epsilon}^e$ , and plastic parts,  $\dot{\epsilon}^p$ :

$$\dot{\epsilon} = \dot{\epsilon}^e + \dot{\epsilon}^p \quad (4.5)$$

---

<sup>2</sup>Note that the overconsolidation ratio in the MCC is defined in terms of effective mean stress unlike to traditionally expressed overconsolidation ratio  $\text{OCR} = \sigma'_p / \sigma'_{vo}$  where  $\sigma'_p$  is the preconsolidation pressure with respect to the uni-axial compression conditions. For further discussion see Section 8.1.

where the effective stress rate is computed with the aid of the elastic stiffness matrix  $\mathbf{D}^e$ :

$$\dot{\boldsymbol{\sigma}}' = \mathbf{D}^e \cdot \dot{\boldsymbol{\varepsilon}}^e \quad (4.6)$$

$$\mathbf{D}^e = \left(K - \frac{2}{3}G\right)\mathbf{I} + G2\mathbf{I}^s \quad (4.7)$$

The  $\mathbf{I}$  symbol represents the unity tensor ( $I_{ijkl} = \delta_{ik}\delta_{jl}$ ) and  $\mathbf{I}^s$  is the symmetrized unity tensor ( $I_{ijkl}^s = (\delta_{ik}\delta_{jl} + \delta_{il}\delta_{jk})/2$ ). Plastic strains occur when the stress state reaches the state boundary surface given by Equations (4.1) and the flow rule is assumed to be associated:

$$\dot{\boldsymbol{\varepsilon}}^p = \dot{\lambda} \frac{\partial F}{\partial \boldsymbol{\sigma}} \quad (4.8)$$

where  $\dot{\lambda}$  is a plastic multiplier.

The hardening parameter modifies the state boundary surface and its evolution connected to the irreversible (plastic) strains,  $\varepsilon_v^p$ , is given by:

$$\dot{p}_c = -\frac{1 + e_o}{\lambda - \kappa} p_c \dot{\varepsilon}_{kk}^p \quad (4.9)$$

## 4.2 Hydro-mechanical solid-fluid interaction

Numerical simulations of *in situ* tests require taking into account hydro-mechanical behavior of a three-phase medium, i.e. solid, water and air. In this study, the numerical simulations have been carried out using two commercial implicit finite-element codes, i.e. Z.Soil (ZACE, 2003) and ABAQUS/Standard (ABAQUS, 2007). The mathematical formulation implemented in these codes approximates the soil "mixture" as an equivalent two-phase medium with compressible fluid, i.e. air bubbles are trapped in the liquid phase and there is no transition of the air bubbles relatively to the liquid. The time-dependent soil behavior is described by means of consolidation and transient flow formulations, in which the conservation of mass and momentum balance of two phases are considered.

Considering soil as a two-phase medium, the total stress tensor is decomposed into the effective stress tensor,  $\sigma'_{ij}$ , and the fluid pressure,  $p_f$ .

$$\sigma_{ij} = \sigma'_{ij} + \chi p_f \delta_{ij} \quad (4.10)$$

where  $\chi$  factor depending on saturation is assumed to be the degree of saturation  $S_r$ . In this work, attention is limited to the behavior of saturated clays so the soil can be represented by the solid-water system, i.e. the degree of saturation is equal to 1.0.

With the assumption of small strains, an increment of the stress is expressed in terms of an increment of the total strain tensor  $\Delta\varepsilon_{ij}$  and the constitutive tensor  $C_{ijkl}$  as follows:

$$\Delta\sigma'_{ij} = C_{ijkl}\Delta\varepsilon_{kl} \quad (4.11)$$

If the assumption of small strains is accepted, the strain increment is computed as follows:

$$\Delta\varepsilon_{ij} = \frac{1}{2} \left( \frac{\partial \Delta u_i}{\partial X_j} + \frac{\partial \Delta u_j}{\partial X_i} \right) \quad (4.12)$$

and rotations increments,  $\Delta\varepsilon_{ij}$ , are determined in terms of displacement increments.

For simulations of cone penetration test, the large strain theory was assumed for which the Green-Lagrange strain increment is calculated as (cf. Belytschko et al., 2000):

$$\Delta E_{ij} = \frac{1}{2} \left( \frac{\partial \Delta u_i}{\partial X_j} + \frac{\partial \Delta u_j}{\partial X_i} + \frac{\partial \Delta u_k}{\partial X_i} \frac{\partial \Delta u_k}{\partial X_j} \right) \quad (4.13)$$

The stress-strain relation links  $\Delta E_{ij}$  and the second Piola-Kirchhoff stress  $S_{ij}$  through the formula:

$$\Delta S'_{ij} = C_{ijkl} \Delta E_{kl} \quad (4.14)$$

and the second Piola-Kirchhoff stress tensor is related to the Cauchy stress tensor by:

$$\sigma'_{ij} = \frac{1}{J} F_{ik} S'_{kl} F_{jl} \quad (4.15)$$

where  $J$  is the determinant of the deformation gradient  $F$  which is defined by  $F_{ij} = \partial x_i / \partial X_i$ . The initial configuration specified by coordinates  $X_i$  and the current configuration coordinates  $x_i$  are related by the displacement vector  $u_i$  by  $x_i = X_i + u_i$ .

In numerical simulations, the Updated Lagrangian formulation was considered, which means that all current variables at time  $t + \Delta t$  are referred to the last equilibrium configuration at time  $t$ .

The hydraulic conductivity of partially saturated medium is governed by the Darcy's seepage law, and therefore, the fluid velocity relative to the solid phase,  $q_i$ , is obtained from the flow equations:

$$q_i = k_{ij}^* \left( -\frac{p_f}{\gamma_f} + z \right)_{,j} \quad (4.16)$$

in which, the permeability tensor for the porous medium,  $k_{ij}^*$ , is computed by scaling the tensor of fully saturated medium by a scalar function,  $k_r(S)$ , dependent on the degree of saturation (in the case of full saturation  $k_r(1.0) = 1.0$ ).

$$k_{ij}^* = k_r(S_r) k_{ij} \quad (4.17a)$$

and

$$k_r = \left( \frac{S_r - S_{res}}{1 - S_{res}} \right)^3 \quad (4.17b)$$

with  $S_{res}$  denoting a residual degree of saturation. The principle of mass conservation is introduced in order to control the fluid flow. Thus, mass conservation is obeyed with the continuity equation:

$$S_r \dot{\varepsilon}_{kk} + q_{k,k} = c \dot{p}_f \quad (4.18)$$

where  $c$ , is the specific storage coefficient dependent on the total pore pressure:

$$c = c(p_f) = n \left( \frac{S_r}{K_f} + \frac{dS_r}{dp_f} \right) \quad (4.19)$$

where porosity,  $n$  denotes porosity and  $K_f$  is the bulk modulus of fluid. The validity of the continuity equation, requires that the density of the fluid is constant, so that conservation of mass means conservation of volume. Finally, the overall solid-fluid equilibrium equation is expressed by momentum balance given by:

$$\frac{\partial \sigma_{ij}}{\partial x_j} + b_i = 0 \quad (4.20)$$

where  $\sigma_{ij}$  is the total stress tensor and  $b_i$  denotes body forces. The body force per volume is expressed by gravity vector,  $g_i$ , and the density of the solid-fluid composite,  $\rho$ :

$$b_i = \rho g_i \quad (4.21)$$

and for two-phase partially saturated medium, we have:

$$\rho = n S_r \rho_f + (1 - n) \rho_s \quad (4.22)$$

where  $\rho_f$ , is the density of the fluid and  $\rho_s$  is the density of the skeleton particles.

### 4.3 Remarks on model shortcomings

The MCC represents the simplest among the critical state concept models. This fact imposes certain shortcomings which are briefly recalled here.

In the model, stress paths within the yield surface are fully reversible which means that no plastic strains are generated inside the bounding surface. Hence, there is no coupling between volumetric and shear response until yield limit occurs (Whittle and Kavvadas, 1994). The yield surface defines the sharp transition between elastic and plastic deformations. In consequence, the model generates no shear-induced pore pressure excess in undrained shearing. In effect, the accuracy of results for highly overconsolidated clays would be doubtful for modeled field tests.

Furthermore, the assumption of linearity within yield surface neglects small strain stiffness behavior which is observed in laboratory tests (Jardine et al., 1984). Neglecting small strains may clearly affect the results of modeled BVPs. Since the MCC is the isotropic strain-hardening model, it contains no anisotropic properties which would describe behavior of  $K_o$ -normally consolidated clays in subsequent hardening (e.g. Whittle and Kavvadas, 1994). In effect, modeling of highly overconsolidated clays, with  $K_o$  values far from 1, would be doubtful. Consequently, the anisotropy effect will be taken into account by means of imposing the initial stress anisotropy.

Considering the model limitations, the use of MCC in this study will be restricted to modeling normally- and lightly overconsolidated clays.



# Chapter 5

## Enhanced Identification Verification

In order to investigate the robustness of the proposed identification scheme on a well-defined boundary conditions, routinely performed triaxial tests, i.e. (i) isotropic consolidation test (CI), (ii) isotropically consolidated drained compression test (CIDC), were adopted to compare the quality of analytically and numerically evaluated/predicted characteristics of the MCC model. These two examples were also chosen to illustrate the adoption of two approaches for the training input discretization that have been presented in Section 2.4.

### 5.1 Numerical implementation for drained triaxial compression test

Performing the CI test for the preconsolidated material, consolidation characteristics  $\kappa$ ,  $\lambda$ ,  $p_{co}$  can be obtained if the test is run through the elastic and plastic domains. The simulation of CI does not require running FE analyses due to the linear solution in  $\ln p' - e$  space (Figure 5.1(a)). To obtain a numerical response of the model, each simulation contains five isotropic equilibrium paths (points O, Y, A, B, C, see Figure 5.1(a)) corresponding to two measured vari-

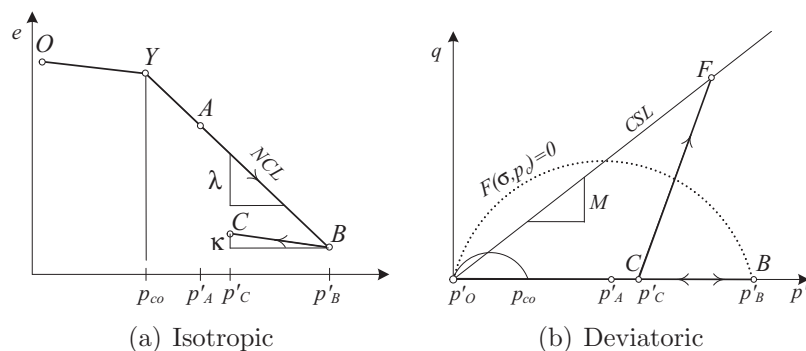


Figure 5.1: Scheme of test stress paths in (a) isotropic and (b) deviatoric plane.

ables, i.e. the mean pressure at points,  $p'_O, p_{co}, p'_A, p'_B, p'_C$ , and the volumetric strain,  $\varepsilon_O^v, \varepsilon_Y^v, \varepsilon_A^v, \varepsilon_B^v, \varepsilon_C^v$ . Assuming that the slopes of consolidation lines can be evaluated using the gradients of A-B and B-C paths, the pressure  $p'_A$  is kept constant for each numerical simulation while the ratios  $p'_B/p'_A$  and  $p'_C/p'_B$  are randomly imposed within the interval presented in Table 5.1. Introducing a random variable of  $p_{co}/p'_A$  that imposes an occurrence of plastic straining, various degrees of preconsolidation are taken into account. Furthermore, to allow the identification to be executable regardless of the applied stress increments, a normalization of mean stresses  $p'_i$  with respect to the maximal mean stress  $p'_{max}$  was introduced applying dimensionless variables  $p'_i/p'_{max}$ . A discussion on the choice of space of parameters as well as details concerning the NN training will be presented in the following subsections.

The axisymmetrical simulations of the drained compression test were performed with the use a FE model. Simulations of the compression under triaxial conditions were carried out using the MCC driver within the Z\_Soil v.6 code (ZACE, 2003). In each computation, a strain-controlled compression test was performed on the isotropically preconsolidated material subject to the stress path C-F (Figure 5.1(b)). The degree of preconsolidation was imposed through initial stress conditions  $\sigma_3 = p'_C$  and the random values of  $R_p = p'_B/p'_C$  within the interval depicted in Table 5.1. This interval ensures the occurrence of yielding on the "wet" side of boundary surface. For each simulation, three variables, i.e. axial strain  $\varepsilon_1$ , volumetric strain  $\varepsilon_v$  and deviatoric stress  $q$  were computed in 31 increments until  $\varepsilon_1 = 20\%$ . Small increments were imposed at the beginning of the test and then were gradually extended toward the end of the test in order to capture the elastic gradient regardless of the chosen set of parameters as well as to ensure the accurate convergence of the FE analysis. For practical reasons, the normalization of the measured  $q$  was applied so that the identification could be executed regardless of the magnitude of the initial confining pressure  $p'_C$ :

$$\mathbf{q}^N = \mathbf{q}/p'_C \quad (5.1)$$

Table 5.1: Intervals of variables considered in the NN training.

Variable	Interval	
	CI test	CIDC test
$e_o$	$\langle 0.10; 1.20 \rangle$	
$\nu$	–	$\langle 0.25; 0.40 \rangle$
$M$	–	$\langle 0.50; 1.50 \rangle$
$\lambda$	cf. Figure 5.2	
$\Lambda$	$\langle 0.50; 0.95 \rangle$	
$p_{co}/p'_A$	$\langle 0.2; 0.8 \rangle$	–
$p'_B/p'_A$	$\langle 1.5; 2.1 \rangle$	–
$p'_B/p'_C$	$\langle 1.1; 16.0 \rangle$	$\langle 1.1; 2.2 \rangle$



### 5.1.1 Space of parameters

The choice of the admissible space of parameters  $\mathcal{B}_b$  plays an important role in NN training. Parameters should be chosen from ranges which are observable in geotechnical practice in order to (i) reduce parameter domain, (ii) regularize distribution in this domain, (iii) avoid non-physical vector of variables. The reduction of the multi-dimensional space of parameters may lead to a significant decrease of the number of generated patterns with a simultaneous improvement of accuracy. This may be of utmost importance if the large-scale FE models are considered in patterns generation.

The intervals adopted in the generation of training patterns are presented in Table 5.1. Typical correlations between  $e_o$  and  $\lambda$  for clayey soils reported in Dascal and Laroque (1973); Dzwilewski and Richards (1974); Rendon-Herrero (1980); Krizek et al. (1977); Leroueil et al. (1983a) can be taken between the upper and lower bounds, cf. Figure 5.2. Observable relationship between  $\lambda$  and  $\kappa$  represented through the plastic volumetric strain ratio  $\Lambda = 1 - \kappa/\lambda$  may typically fall into an interval  $\Lambda \in \langle 0.5; 0.95 \rangle$  (Mayne, 1980). The intervals for the remaining model characteristics,  $M$  and  $\nu$  were set according to commonly observable values for clays.

Generally, a regular distribution of training data points in the parameter space improves further network predictions. In the case of using a numerical solver as the pattern generator, the parameter combinations which are used to generate experimental measurements can be chosen through the sample selection method. The methods such as *orthogonal array*, *full factorial*, *hypercube*<sup>1</sup>, aim to reduce the size of training dataset by a regular sampling which preserves efficiency of NN training for a small number of patterns (Chang et al., 2002). In this study, the random method of selecting training patterns was adopted to avoid introducing unnecessary degree of complexity which would arise from parameter intercorrelations. Typically, the random selection method gives satisfactory results, however, it may be computationally expensive.

Parameter and stress state distributions within the intervals were assumed uni-

<sup>1</sup>For details refer to Chang et al. (2002).

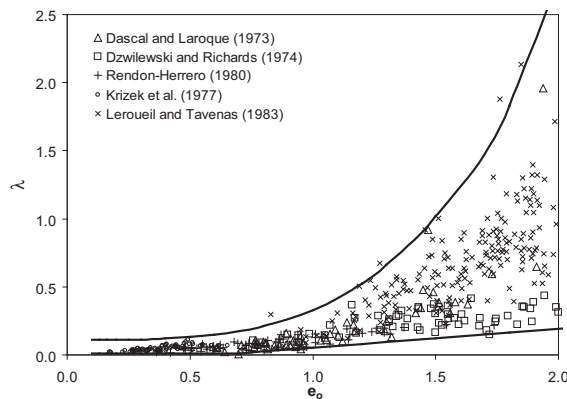


Figure 5.2: Typical observable relationship between  $e_o$  and  $\lambda$ .

form except for the voids ratio  $e_o$ , for which the exponential probability density function (pdf) was adopted to generate random numbers due to the logarithmic approximation of the upper bound of  $\lambda$  (Figure 5.2). The exponential distribution is given by:

$$P(x|\mu) = \int_0^x \frac{1}{\mu} e^{-\frac{t}{\mu}} dt = 1 - e^{-\frac{x}{\mu}} \quad (5.2)$$

where  $\mu$  is the mean value and  $\sigma$  is the standard deviation while  $x$  denotes the random value from uniform distribution. The log-normal distribution of  $e_o$  is to ensure a uniform distribution in the  $\lambda$  interval.

### 5.1.2 Parameter identification for isotropic consolidation test

For the purpose of the identification of soil properties from the CI test, a two-hidden layer FFNN was optimally designed for the 5-component input as NN(5|7-7|3), i.e. 7 neurons in each hidden layer for 3-output parameters. The optimal number of neurons was reduced to a minimum to avoid an over-fitting tendency of the network (Flood and Kartam, 1994a). Apart from the training set containing  $NS^{(t)} = 130$  numerical patterns, a set of 70 pseudo-experiments was prepared additionally to illustrate the efficiency of the approximation. For each numerical experiment  $p'_A, p'_B, p'_C$  and the corresponding  $\varepsilon_v$  were measured. Thus, the dimensionless input vectors corresponding to measured variables and the outputs regarded as unknown parameters are respectively given as:

$$\mathbf{p}_t = [\varepsilon_A^v, \varepsilon_B^v, \varepsilon_C^v, p'_A/p'_B, p'_C/p'_B]^T \mapsto \mathbf{NN} \mapsto \mathbf{o}_t = [\kappa, \lambda, p_{co}/p'_B]^T \quad (5.3)$$

where  $t = 1, \dots, NS^{(t)}$ . Note, that the proper value of  $p_{co}$  is obtained by multiplying the dimensionless component by the maximum applied mean pressure  $p'_B$ . To improve the performance of the NN training, the input and output vectors were scaled so that their components fall into  $\langle -1, 1 \rangle$  interval.

The quality of the approximation performance was assessed by presenting unknown measurements to the trained network (Figure 5.3). The linear regression analysis performed after 70 activations of the NN exhibited a satisfactory agreement between accurate and NN-predicted values of  $p_{co}, \lambda, \kappa$ , with the correlation coefficient  $R$  equal 0.99 for each parameter and small values of mean squared error MSE (cf. Equation (3.12)). Moreover, the NN inverse models exhibit the best linear fits which overlap the perfect linear fits  $o = t$ . A visual inspection of post-training analysis shown in Figure 5.3 confirms the acceptable degree of approximation, generally falling in 10% bounds of the relative error for target values. An example of the parameter identification for real experimental measurements is presented in Section 5.2.2.

### 5.1.3 Parameter identification for the drained compression test

For each numerical simulation, three groups of variables were incrementally computed, i.e. axial strain  $\varepsilon_a$ , deviatoric stress  $q$ , and volumetric strain  $\varepsilon_v$ .

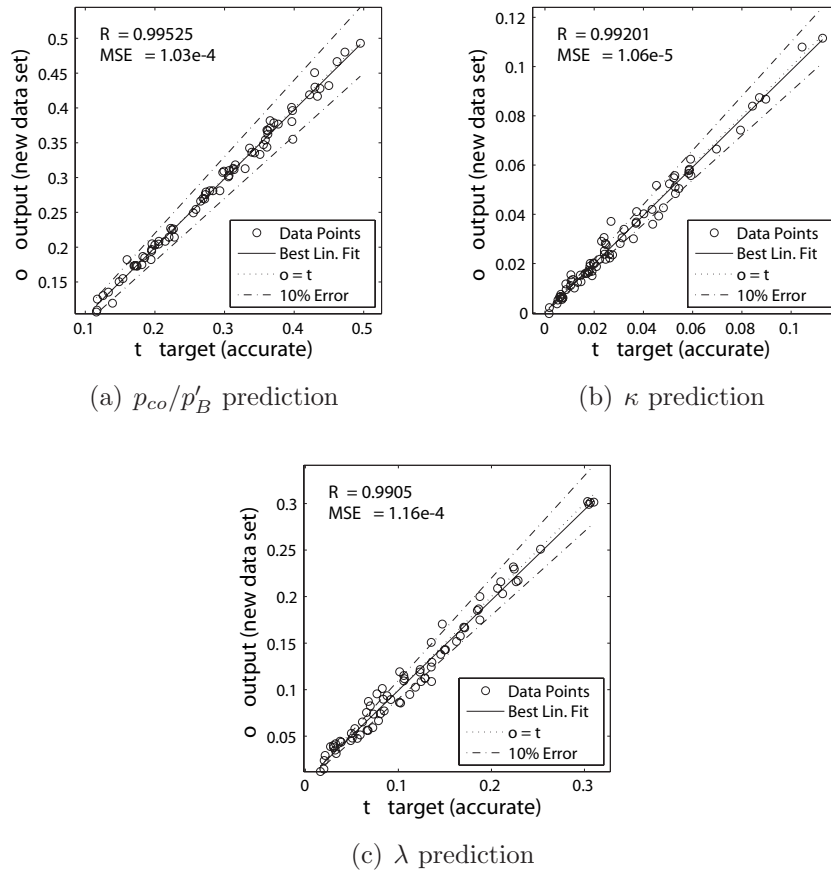


Figure 5.3: Isotropic consolidation problem: post-training regression analysis for the data set never presented to the trained network.

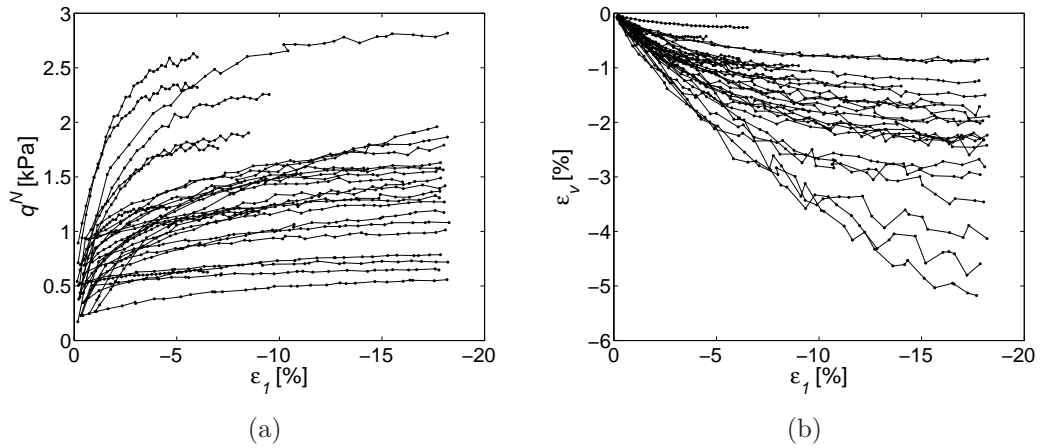


Figure 5.4: Example of 30 normalized numerical simulations of CIDC including artificial noise.

From among 32 equilibrium paths for  $\varepsilon_a \in \langle -0.2, 0 \rangle$ , the post-failure results were skipped, i.e.  $\varepsilon_a \in \langle 0, \varepsilon_f^a \rangle$  where  $\varepsilon_f^a$  corresponds to  $q_f = q_{\max}$ . Then, 31 discrete observational points  $\tilde{\varepsilon}_a$  were randomly chosen with corresponding interpolated variables  $\tilde{q}$ ,  $\tilde{\varepsilon}_v$ . Moreover,  $\tilde{q}$  was normalized into dimensionless variable  $\tilde{q}^N$  (Equation (5.1)). In order to avoid the overfitted solutions and improve generalization, the artificial noise was introduced into "smooth" numerical results for each discrete observation of  $\tilde{q}$ ,  $\tilde{\varepsilon}_v$  (see Figure 5.4). The random noise was introduced using Gaussian pdf, with the coefficient of variation  $\text{COV} = \sigma/\mu$  equal to 3% for any numerical measurement. This artificially burdens the numerical results with testing uncertainties i.e. device measurement errors, geometrical imperfections and natural variability of an individual specimen. Each training pattern consisted of 3-element target vector representing the identified parameters  $M, \lambda, \kappa$  and the dimensionless input vector that comprised of the normalized variables (cf. Equation (3.8)), i.e. Poisson's ratio  $\nu$ , initial voids ratio  $e_o$  and overconsolidation ratio  $R_p$ , and the noisy measurements of 3 state variables:

$$\hat{\mathbf{p}}_t = [\hat{\nu}, \hat{e}_o, \hat{R}_p, \hat{\varepsilon}_1^a, \dots, \hat{\varepsilon}_{\text{ND}}^a, \hat{\varepsilon}_1^v, \dots, \hat{\varepsilon}_{\text{ND}}^v, \hat{q}_1^N, \dots, \hat{q}_{\text{ND}}^N]^T \quad (5.4)$$

where  $\text{ND}=31$  discrete measurements. Therefore, the extensive dimension of the 96-component input vectors for  $\text{NS}=175$  training patterns was reduced by invoking the PCA before NN training. The empirical correlation matrix (Equation (3.9)) and the transformation matrix were calculated (Equation (3.10)). The input vector was thus reduced from 96 to  $\text{NR}=15$  components. The calculated eigenvalues of the corresponding 15 dominant principal components for the training set under study were 90.510, 71.287,  $\dots$ , 4.128 for which the total variability explained by dominant principal components was 82.76% (Figure 5.5). The reconstruction error  $E_r$  (Haykin, 1999) corresponding to the variance of 16th principal component is thus:

$$E_r = E [\|\mathbf{X} - \mathbf{W}^T \mathbf{Y}\|] = 3.262 \quad (5.5)$$

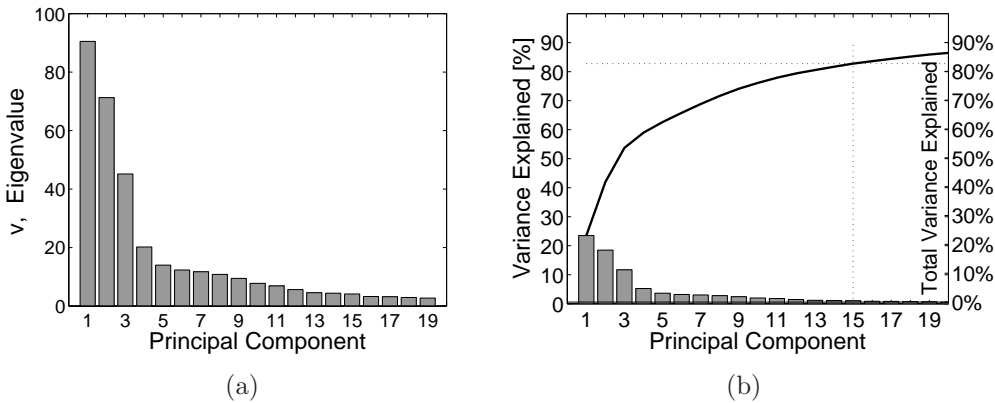


Figure 5.5: Summary of the input data reduction using the PCA: (a) principal components and corresponding eigenvalues  $v$ , (b) variances explained by dominant principal components and the cumulative percentage of the total variability.

where the matrix  $\mathbf{X} = [\hat{\mathbf{x}}_1, \hat{\mathbf{x}}_2, \dots, \hat{\mathbf{x}}_{NS}]$  contains all data with  $m = 96$  scaled observations in each vector, while the matrix  $\mathbf{Y} = [\mathbf{y}_1, \mathbf{y}_2, \dots, \mathbf{y}_{NS}]$  contains NS dimensionally reduced vectors where each NR-component vector is the projection of the corresponding data vector from matrix  $\mathbf{X}$  onto the basis vectors contained in the columns of matrix  $\mathbf{W} = [\mathbf{w}_1, \mathbf{w}_2, \dots, \mathbf{w}_{NR}]$ . Thus, taking into account only 15 principal components the extensive 96 data input is significantly reduced preserving a small reconstruction error.

Then, a two-hidden layer neural network with the input vectors projected on the principal axes was optimally designed with 6 neurons in each hidden layer and the training set comprised of 175 training sets. The identification can thus be expressed as:

$$\hat{\mathbf{p}}_t \mapsto (\text{PCA})\mathbf{p}_t \mapsto \text{NN}(15|6 - 6|3) \mapsto \mathbf{o}_t = [M, \kappa, \lambda]^T \quad (5.6)$$

The quality of the network performance was assessed with a set of 75 results of the random pseudo-experiments comprising of noisy measurements never presented to the network. The results of the performed regression analysis presented in Figure 5.6, indicate the fair correctness of the parameters prediction

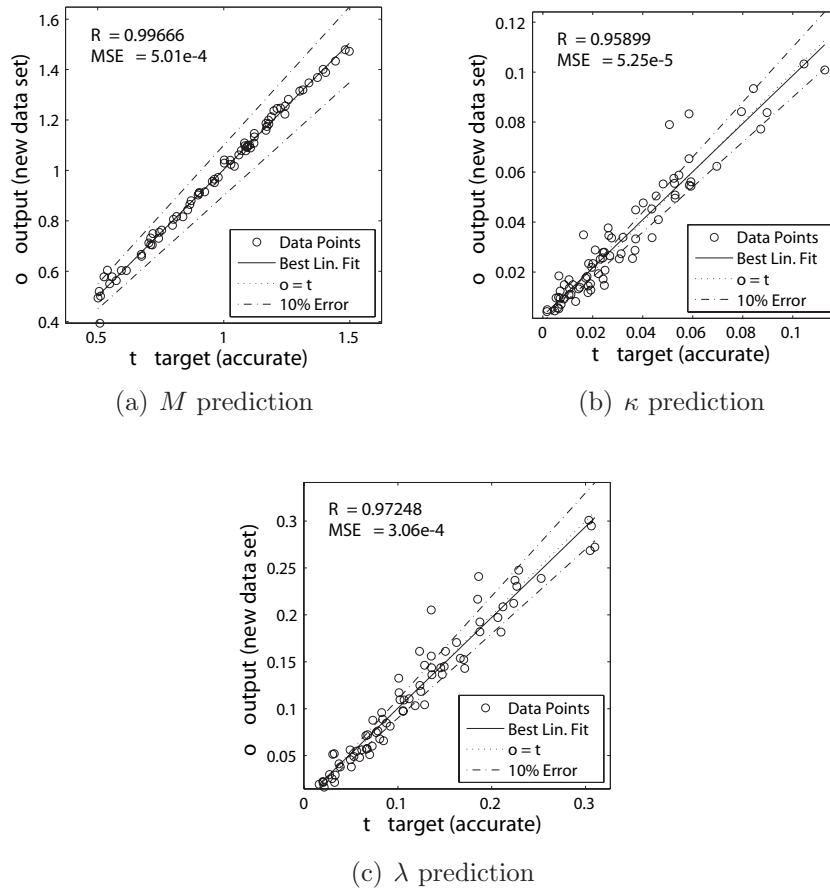


Figure 5.6: Drained compression test: post-training regression analysis for the data set never presented to the trained network.

in terms of the correlation coefficient  $R$  and the mean squared error MSE. It is also indicated that the best linear fits and the perfect models  $o = t$  exhibit conformity. A visual inspection of  $M$  predictions shows an excellent performance of the estimator while the predictions of remaining parameters reveal a slight scatter outside of 10% of relative error of target values. This can be explained by the fact that the measurements comprised artificial noise. However, such accuracy is absolutely sufficient to find a neighborhood of the global solution. An example of parameter identification for real experimental measurements is presented in the following section.

## 5.2 Parameter identification for real experimental data

The following section demonstrates an application of the identification strategy for real experimental data. Model parameters are conventionally evaluated based on measurements coming from laboratory tests carried out by the authors of this paper, using a triaxial chamber. The compressed specimens were subject to boundary conditions as described above in Section 5.1.

### 5.2.1 Material and test procedure

A series of isotropic consolidation and drained triaxial compression tests was performed on the Bioley clayey silt samples (liquid limit  $w_L = 31.8\%$ ; plastic limit  $w_P = 16.9\%$ ; unit weight of solid particles  $\gamma_s = 27.1 \text{ kN/m}^3$ ; clay fraction 27%). The remoulded and homogenized specimens were initially formed in a 80 mm-diameter tube. The 120mm high specimens were first isotropically consolidated with the pressure of  $p_c = 100 \text{ kPa}$  and then unloaded and carefully trimmed into the standard dimensions of 38x76 mm. The experiment comprised of: (i) one triaxial CI test with the following sequence of isotropic loads  $p' = 15, 30, 60, 120, 240, 480 \text{ kPa}$  and unloading to  $p' = 280 \text{ kPa}$  and (ii) three triaxial drained shear tests preceded by the isotropic consolidation of specimens to  $p'_B = 150, 210, 180 \text{ kPa}$  and unloading with the same overconsolidation ratio  $p'_B/p'_C = 1.25$ . In the case of CIDC, the standard shear paths  $dq/dp' = 3$  were applied (Figure 5.1(b)). The initial value of voids ratio for CI test was  $e_o = 0.535$ , while for CIDC tests  $e_o$  at the beginning of shearing paths was respectively equal to 0.478, 0.488 and 0.482. Based on the measured variation of  $\varepsilon_3$  against  $\varepsilon_1$ , the calculated mean value of the Poisson's ratio was equal  $\nu = 0.368$ .

### 5.2.2 Example of parameter identification for the isotropic consolidation test

An identification of three variables  $\kappa$ ,  $\lambda$  and  $p_{co}$  was carried out by presenting to the trained network the variations of the volumetric strain  $\varepsilon_v$  of last three measurements and corresponding mean pressures  $p'$  normalized with respect to the maximal one. An illustrative comparison of the test measurements and

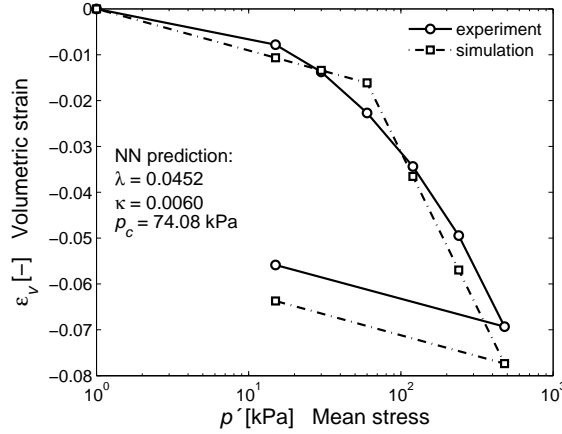


Figure 5.7: Comparison between experimental data and the model response using NN-predicted parameters  $\lambda$ ,  $\kappa$ ,  $p_{co}$  for the isotropic consolidation test.

the model response using the NN-predicted parameters is shown in Figure 5.7. Values of NN-identified parameters are also compared with the values which were back-calculated using the conventional method, i.e. the linear regression of loading curves.

The results presented in Table 5.2 show a good approximation of the identified parameters with the maximal relative error of 3.79% corresponding to  $p_{co}$ . Note that the identified  $p_{co}$  is smaller than the real consolidation pressure ( $p_{co} = 100$  kPa) due to the earlier mobilization of plastic strains and possibly the trimming effect.

Table 5.2: Identified parameters for isotropic consolidation test.

Variable	Analytical back-calculation	NN prediction	
	Value	Value	Error (%)
$\kappa$	0.0060	0.0060	0.00
$\lambda$	0.0440	0.0452	0.27
$p_{co}^*$	77.00 kPa	74.08 kPa	3.79

\*The specimen preconsolidated with real pressure  $p_c = 100$  kPa.

### 5.2.3 Example of parameter identification for the drained compression test

A numerical identification of three variables  $\kappa$ ,  $\lambda$  and  $M$  was carried out separately for each test by presenting to the trained network variations of three measured variables, i.e. axial strain  $\varepsilon_a = \varepsilon_1$  and corresponding volumetric strain  $\varepsilon_v$  and normalized deviatoric stress  $q^N$  taken within  $\varepsilon_a \in \langle -0.12, 0 \rangle$ . 31 measurements of each variable completed with the values of the Poisson's ratio, voids ratio and preconsolidation ratio were collected in the input vector  $\mathbf{p}$ .

Then, using the transformation matrix  $\mathbf{W}_i^T$  the normalized input  $\hat{\mathbf{p}}_t^T$  (Equation (5.4)) was projected onto the subspace spanned by the eigenvectors and presented to the network. The NN determined parameters, their mean values and relative errors with reference to optimal values are presented in Table 5.4.

The identified parameters of the second test were taken to illustrate the quality of the prediction in comparison to the values obtained through the optimization. This analysis shows the effect of the measured data discretization on the evaluated parameters. Two optimization runs were invoked, i.e. (i) for all 31 discrete points along the whole interval of  $\varepsilon_1$ , and (ii) for the chosen points within elastic and failure domain (the points in between were skipped). Equal importance of  $q$  and  $\varepsilon_v$  measurements was assumed by introducing weights as the inverse of error variance where the errors were adopted as equal to  $e_q = 0.5$  kPa and  $e_\varepsilon = 0.0001$  (cf. Calvello and Finno, 2002). During iterations, only identified parameters were updated.

The results presented in Figure 5.8 show that the fitting of all discrete points leads to the underestimating of  $M$  with reference to the maximal value of  $q/p'$ . The relative error that appeared reaches 4.5%, see Table 5.3. On the other hand, the fitting of arbitrarily chosen fitting zones leads to the value of  $M$  for the maximal  $q/p'$  with a loss of the degree of the fitting in the middle of  $\varepsilon_1 - q$  curve.

Clearly, the choice of the discretization approach will depend on the assumed criterion imposed by a further geotechnical problem. It is worthy noting that the model response with the NN gives a very close prediction especially for  $\varepsilon_1 - q$  variation (the error of the identified parameter  $M$  is equal 0.16%). This demonstrates that an NN additionally preceded by the PCA is able to extract itself the most important information from the whole family of measurements. It also means that the network weights provide the sensitivity of model parameters. Moreover, the NN considers the overall material behavior, and not only its specific state, which can be illustrated by the sensitivity of the NN to the dilatant behavior of the soil at the final part of  $\varepsilon_1 - \varepsilon_v$  curve. The NN considers the overall variation of  $\varepsilon_v$ , providing an averaged value of  $\lambda$ , which is smaller than the value identified for the maximal volume change (cf. Table 5.4).

Table 5.3: Comparison of the identified parameter  $M$  by means of the analytical back-calculation, NN prediction and optimization with important discrete points and an entire vector of measurements.

Variable	Maximal $q/p'$ value	NN prediction		Optimal: chosen discrete measurements		Optimal: all discrete measurements	
		Value	Error (%)	Value	Error (%)	Value	Error (%)
M	1.223	1.221	0.16	1.218	0.41	1.168	4.50



Table 5.4: Comparison of variables evaluated by means of analytical back-calculation, NN prediction and optimization for three drained compression tests, 1.  $p'_o = 120$  kPa, 2.  $p'_o = 168$  kPa, 3.  $p'_o = 144$  kPa, respectively.

Variable	Analytical back-calculation			NN prediction			Optimization		
	Value	Mean	Errors (%)	Value	Mean	Errors (%)	Single run	Three curves	Three curves
$\kappa$	0.0013		85.7	0.0019		171.4	0.0007		
	0.0013	0.0012	67.5	0.0030	0.0028	25.0	57.4	0.0040	0.0018
	0.0019		18.8	0.0036		125.0	0.0016		
$\lambda$	0.0010		92.8	0.0137		4.9	0.0144		
	0.0011	0.0104	93.5	0.0156	0.0147	6.6	2.0	0.0167	0.0150
	0.0112		22.2	0.0148		2.8	0.0144		
$M$	1.223		0.4	1.221		0.2	1.218		
	1.240	1.227	0.1	1.209	1.203	2.4	1.5	1.239	1.222
	1.217		0.5	1.180		2.6	1.211		

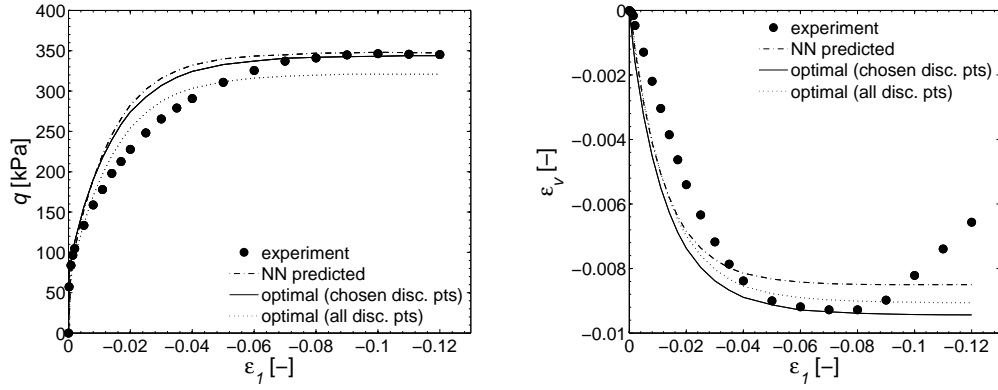


Figure 5.8: Optimization with the NN-predicted initial vector of parameters for the drained compression test ( $p'_o = 120\text{kPa}$ ). A comparison of fitting for the discrete points of the arbitrarily significant importance and for all the discrete measurements.

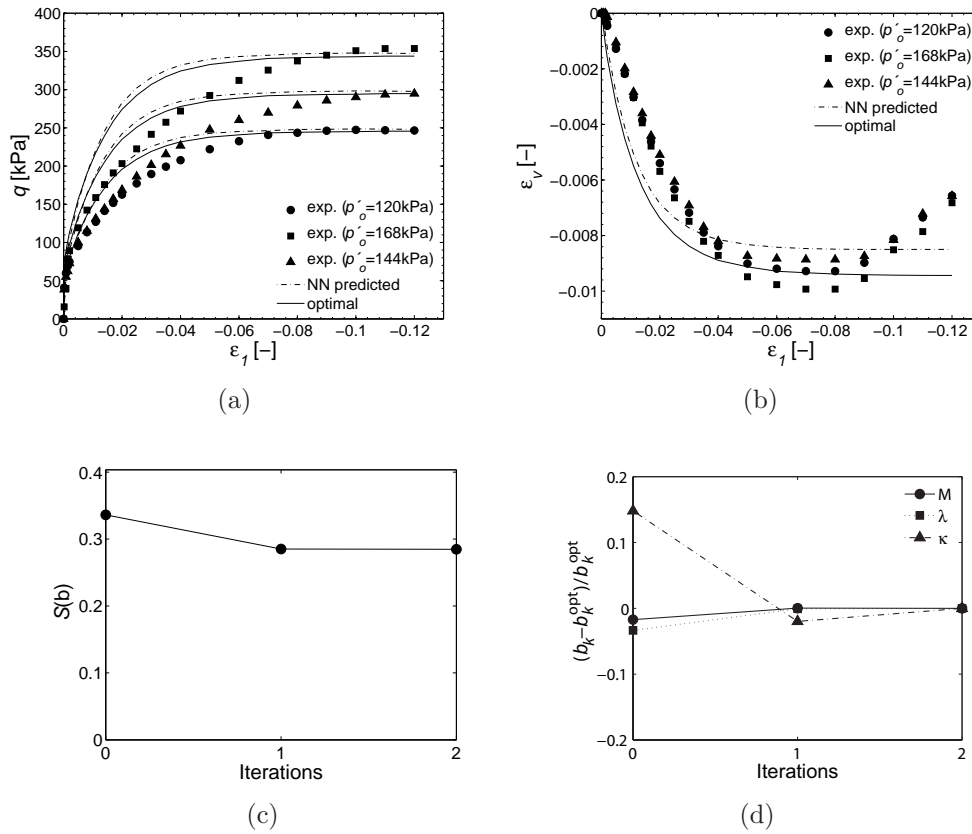


Figure 5.9: Optimization with the NN-predicted initial vector of parameters: (a-b) model calibration with experimental data for 3 drained compression tests, (c) convergence rate of the GBO, (d) convergence rate of NN-assigned parameters.

Hereafter, the fitting procedures are carried out merely for chosen discrete points in the elastic and failure regions. The results of three separate parameter identification runs and one mutual optimization containing data of three tests are presented in Table 5.4. In the table, the relative errors of the identified parameters for the NN predictions and analytical calculations are calculated with respect to the values obtained through the subsequent GBO runs. A surprisingly large error of the evaluated value of  $\kappa$  can be explained by the high order of the identified parameter and this is not significantly reflected in the model response presented in Figure 5.9. The NN-recognized parameters are quickly updated with the minimum computational cost within 2 iterations. Figure 5.9 reveals limitations of the MCC model which make it impossible to obtain a perfect agreement between experimental and numerical data. For example, the MCC is not able to reflect the shear strain induced dilatancy observed in the tested material.

It can be noted that the optimal values of  $\kappa$  and  $\lambda$  obtained from consolidation and compression tests are inconsistent. This is due to prescribing the value of  $R_p = 1.25$  with the measured confining pressures  $p'_B$  and  $p'_C$ . This state parameter could be incorporated into the optimized vector under condition that additional results of isotropic consolidation are included.

## 5.2.4 Efficiency test

The quantitative test of efficiency of the proposed two-level scheme was performed on one of the compression tests starting from different remote points chosen arbitrarily. Since a large change of parameters may lead to an instability of optimization, convergence was controlled by the scaling parameter prescribed in each run equal  $\rho_r = 0.5$ . The rate of the convergence was measured for the optimization with the NN-assigned and 3 testing the user-specified initial vectors. Testing patterns comprised the values of  $M$ ,  $\lambda$ ,  $\kappa$  given respectively as  $\mathbf{b}_1 = [0.8, 0.1, 0.01]$ ,  $\mathbf{b}_2 = [1.6, 0.1, 0.01]$ ,  $\mathbf{b}_3 = [0.8, 1.0, 0.1]$ . Each minimization converged to the same optimal solution. Note that starting from remote initial points, instabilities of the solution may often occur, for instance, in the case of calibration of hydro-mechanical problems (cf. Figure 2.7).

Figure 5.10(a) clearly shows the fast convergence of the optimization with the NN-assigned parameters. Automated minimization is accomplished within 2 iterations while optimizations regarded as trial-and-error examples with user-assigned parameters require at least 4 iterations. Note that in each iteration, beside the error function computation, the number of FE runs is expanded by the number of optimized parameters if the forward finite difference method is used to evaluate of the sensitivity matrix. This number can be multiplied if the model calibration is carried out for several experimental tests simultaneously<sup>2</sup>. Consequently, the increasing number of iterations results in the increase of computational cost which was augmented for the considered testing sets about  $2 \div 4$  times (Figure 5.10(b) presents CPU time which is normalized with respect to the CPU time measured for the NN-enhanced optimization).

---

<sup>2</sup>Each test requires running an individual model due to different initial stress conditions.

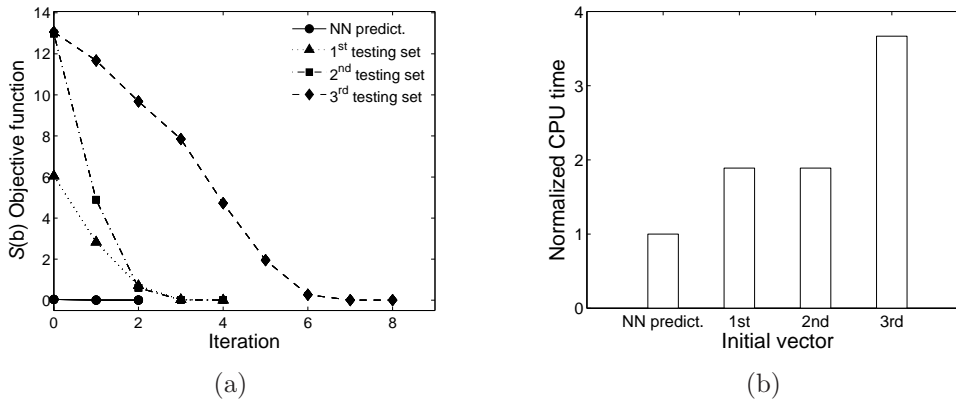


Figure 5.10: Efficiency test of the optimization preceded by the NN prediction in comparison with 3 optimization runs with the user-specified initial vector: (a) rate of convergence, (b) computational effort.

Clearly, the number of iteration may also increase with the enhancement of the constitutive model resulting in an increase of the number of parameters and experimental curves.

### 5.3 Summary

This chapter demonstrated the efficient generic scheme of the automated calibration procedure for multi-parameter constitutive models. The potential of the hybrid parameter identification method combining the GBO technique supported by the feed-forward neural network FFNN algorithm is presented in detail. The efficiency of the presented strategy has been proved by means of a test calibration of the Modified Cam clay model using experimental measurements from the benchmark triaxial drained compression test. Some general conclusions can thus be drawn:

- The application of the NN technique to solve an inverse problem provides an efficient and accurate search of the vicinity of a global solution skipping local minima. The close approximation of parameters preserves the minimal computational expense during the subsequent optimization (here two iterations) and helps the user to avoid performing time consuming trial-and-error runs. This is a crucial feature, if the complex multi-variable models are considered to be calibrated with the subsequent direct line search.
- The choice of an admissible space of parameters plays an important role in NN training leading to the reduction of the multi-dimensional space of parameters and a significant decrease of the number of generated pattern population with a simultaneous improvement of the accuracy of predictions.
- Incorporating the PCA into NN training results in significant reduction

of large-dimensional data with no significant loss of accuracy of evaluated parameters.

- The choice of discrete points during curve fitting has a significant importance on calibrated parameters unless the constitutive model is able to precisely reproduce experimental curves. The examples presented in this chapter demonstrate that the NNs possess the ability to extract meaningful information about the parameters' sensitivity from the numerical training dataset. The model responses with the input parameters provided by an NN, revealed that the NN mapping atypical experimental measurements is able properly extract soil properties for the considered constitutive law.
- A potential application of the NN-based technique for the parameter identification of enhanced constitutive models basically involves delivering relevant data which illustrates the physical phenomena that are considered in the model. Obviously, in the case of a calibration of more complex soil models, the parameters which can be directly estimated with the high degree of confidence, can constitute a part of the NN input vector (e.g. the Poisson's coefficient or the friction angle), while the characteristics of no physical meaning for a given BVP become the objects of optimization.

Using a well-designed interface, the proposed parameter identification can be adapted to any constitutive model or BVP with only few modifications. Different models or structural tests can be attached as modules to the fully-automated pattern generator. The numerical results are used once to properly adjust network weights which are stored with negligible storage cost. Since NNs are trained with broad intervals of parameters, they are able to correctly map any experimental set of measurements. Thus, the trained NNs can be part of the automated optimization module incorporated into numerical solution applications like FE packages. This can show to be of particular value for multi-parameter models characterized by the nontrivial parameter assessment.

Further chapter is devoted to adopting the method for complex BVPs where the efficiency of the existing closed-form solution is restricted by imposed theoretical assumptions.



# Chapter 6

## BVPs of Selected *In Situ* Tests

*The ability to treat the results of cone penetration and pressuremeter tests in sand and clay on a realistic theoretical basis enhances their value for site characterization and determination of relevant soil mechanical properties.*

James K. Mitchell

### 6.1 Overview of *in situ* tests

Field testing provides a great opportunity to investigate soil in natural stress conditions with minor soil disturbances. Generally, field tests are well suited for site classification, soil profiling and evaluating spatial variability of soil properties (Jamiolkowski et al., 1985; DeGroot and Sandven, 2004). As an economical means for large scale soil investigations, field tests are often used to estimate specific soil properties. Field tests can be divided into three general categories (Mayne, 2006), i.e. (i) geophysical tests for mapping relative variances across a site, (ii) tests allowing vertical subsoil profiling and parameter estimation, and (iii) drilling and sampling techniques which provide site-representative specimens for laboratory tests. The second category of tests includes a variety of mechanical device tests and the standard penetration test (SPT), the piezocone test (CPTU) also with seismic sensor (SCPTU), the flat dilatometers test (DMT), the self-boring pressuremeter test (SBPT), the field vane test (FVT) are the most popular. Extensive reviews of the most common standardized field tests are published by Wroth (1984); Jamiolkowski et al. (1985); Lunne et al. (1989). Generally, interpretation of field measurements involves a distinct interpretation method with respect to both the type of test and the specific soil property. Recently, Schnaid (2005); Yu (2006) provided an extensive review of theoretical analyzes for interpretation of test measurements for SBPT, CPTU

and DMT. Other summary studies also provide the reviews of generalized interpretation techniques, which additionally include empirical formulas for CPTU data (Lunne et al., 1997; Mayne, 2006, 2007).

This chapter is divided into two main sections related to the SBPT and the CPTU test respectively. In these parts, the main concepts of self-boring pressuremeter and piezocone testing are recalled. As regards the pressuremeter test, a concept of the *undrained cavity expansion* is presented in detail including an extension to the MCC model. The section also contains a review of interpretation methods for both the expansion and the holding tests. Finally, possible sources of inaccuracy of parameters derived from the pressuremeter test are discussed. The part related to the piezocone test includes a compact review which investigates the existing approaches and the interpretation formulas for this boundary value problem. An effect of partial drainage during penetration is finally discussed.

### 6.1.1 Self-boring pressuremeter test

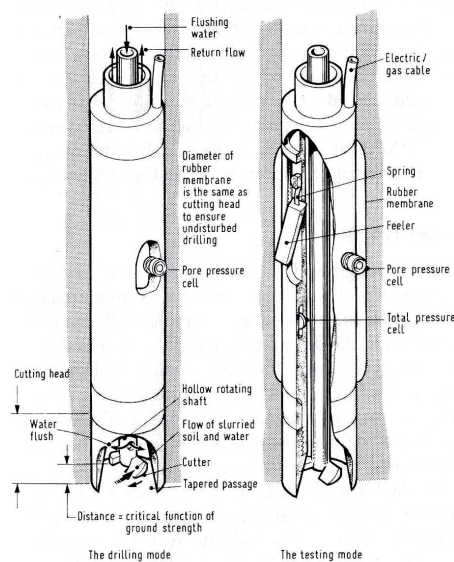


Figure 6.1: A detailed construction of the Camkometer (after Mair and Wood, 1987).

The concept of the self-boring probe and its first prototypes were developed and introduced into geotechnical practice independently by the Cambridge University in the early 1970's by Wroth and Hughes (1973, Camkometer, see Figure 6.1) and by a group of French researchers led by Baguelin and Jézéquel (1973). The main objective of this system is to install the probe with a minimum level of disturbance of the adjacent soil. Among the available mechanical field devices used today, the self-boring pressuremeter (SBP) is considered to cause minor disturbances of adjacent soil during installation (Wood and Wroth, 1977; Baguelin et al., 1978; Jamiolkowski et al., 1985; Mair and Wood, 1987; Mayne, 2006). The cylindrical instrument is introduced into the ground by simulta-



neously cutting and flushing up the underlying soil layers by a cutting shoe. Then, with an inflating membrane under constant rate of strain or pressure, the continuous readings of applied pressure and radial displacements are monitored producing the strain-stress response of investigated soil. With the measurements of elastically and plastically deformed soil during the *pressuremeter expansion test* (PET), the stiffness and strength soil characteristics can be evaluated. Furthermore, the in situ total horizontal stress  $\sigma'_{ho}$  can be directly estimated from the so-called lift-off pressure.

As the expansion test results in an increase of excess pore water pressure at the cavity wall, subsequent strain or pressure holding tests can be performed to evaluate consolidation characteristics of soil. While in the *strain holding test* (SHT), the decay of excess pore water pressure is measured with no further expansion of the membrane (Clarke et al., 1979), the *pressure holding test* (PHT) results in a further expansion due to the compensation of the applied pressure, which remains constant during the test (Fahey and Carter, 1986). Typical results of the PHT test in clay are presented in Figure 6.2.

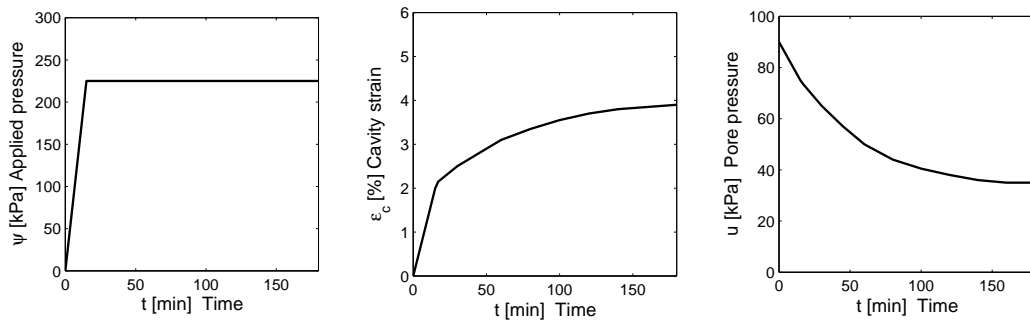


Figure 6.2: Typical results of PHT in clays: expansion under constant pressure, cavity strain variation and excess pore water pressure in time (after Fioravante et al., 1994).

### 6.1.2 Piezocone penetration test

The cone penetrometer test with pore pressure sensors (CPTU) was introduced into geotechnical site investigations in the late 1970's. Initially used as a research device, the CPTU gained a common acceptance in commercial engineering and its potential was firstly applied to soil investigations for offshore structures (Karlsrud et al., 2005). The CPTU is an economical tool which provides continuous and repeatable data records along the soil profile within a short-time period. The continues piezocone measurements can be used for soil profiling and estimation of a number of soil parameters related to shear strength, stress history or soil stiffness. In clays, consolidation characteristics can also be derived by performing the dissipation tests at discrete depths. In the CPTU, the electronic cone is pushed into the ground with a series of rods and, typically, measurements of cone resistance  $q_c$ , sleeve friction  $f_s$  and pore pressure  $u_2$

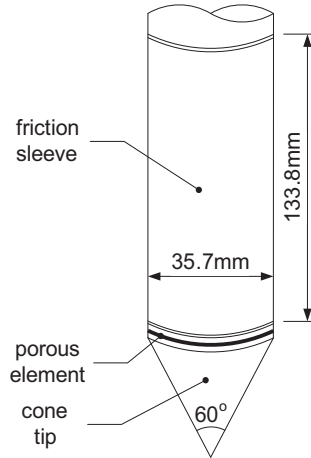


Figure 6.3: Standardized electric piezocone penetrometer.

(including  $t_{50}$  for dissipation test) are recorded. In the case of seismic piezocone (SCPTU), a set of measurements can also be extended with shear wave velocity measurements  $V_s$  (Campanella et al., 1986). In this study, the analysis is restricted to the standardized cone with the 60 degree apex angle, the diameter of 35.7mm (10cm<sup>2</sup> cross-sectional area), the friction sleeve area 150cm<sup>2</sup>, and the constant rate of penetration of 2cm/s (see Figure 6.3, ISSMGE, 1999).

The CPTU is mostly used to (i) determine soil stratigraphy, ground water conditions and to identify deposited materials, (ii) evaluate geotechnical properties, (iii) provide results for direct geotechnical design (Jamiolkowski et al., 1985; Lunne et al., 1997). The CPTU can provide guidance on critical weak zones and mechanical behavior of particular substrata. Since the advent of the electric cone (CPT) and CPTU, many classification charts have been proposed to identify soil behavior type along a subsoil profile (e.g. Schmertmann, 1978; Douglas and Olsen, 1981; Robertson et al., 1986; Robertson, 1990; Eslami and Fellenius, 1997; Zhang and Tumay, 1999). These charts help to determine the degree of subsoil heterogeneity and to precisely establish investigation programme which may include other field tests or sampling for laboratory tests. The piezocone results are often accompanied by laboratory tests since the derivation of parameters is typically based on semi-empirical correlations against parameters evaluated through conventional tests such as triaxial apparatus, oedometer or direct simple shear box (Karlsrud et al., 2005; Mayne, 2006). The laboratory tests may provide verification for local correlations or enable the calibration of the CPT results accounting for partial drainage conditions (Lunne et al., 1997).

In clayey soils, the application of CPTU for the identification of geotechnical parameters mainly deals with the estimation of preconsolidation pressure, undrained shear strength, constrained modulus and consolidation characteristics. However, the complexity of piezocone BVP makes the theoretical analysis demanding and uncertain. A brief review of existing interpretation methodologies is provided in Section 6.3.

## 6.2 Analytical analysis of self-boring pressuremeter test

In general, theoretical interpretations of the expansion test in saturated clay are based on the cavity expansion theory, which assumes that an expansion of an infinite cylindrical cavity takes place under perfectly undrained conditions, in homogeneous soil. In the case of a less complex model, the well-defined boundary conditions allow an analytical interpretation of the experimental data. The load-deformation relief and the time-dependent (clay) response provide the results, which once interpreted may result in an assessment of in situ stress state, stiffness, strength and consolidation characteristics (Baguelin et al., 1978; Clarke et al., 1979). Examples of theoretical interpretations based on the total stress analysis include a solution for elastic/perfectly plastic soil (Gibson and Anderson, 1961), hyperbolic equations for the stress-strain behavior (Prevost and Hoeg, 1975; Denby and Clough, 1980), non-linear elastic/perfectly plastic soil (Bolton and Whittle, 1999), the sub-tangent method that allows the deduction of a complete shear stress-strain curve (Palmer, 1972; Ladanyi, 1972; Baguelin et al., 1972), etc. Finally, using the effective stress analysis, analytical solutions for elastic/plastic critical state models have been proposed by Collins and Yu (1996); Cao et al. (2001).

The following sections will recall analytical solutions used to interpret pressuremeter test results. Although in this study a numerical identification of model parameters is presented, understanding of these formulas is of great importance for selecting appropriate input variables for the development of effectively operating NN-based inverse models. Some fundamental analytical solutions can be adopted in order to transform test measurements onto a relevant network input. Hence, the following brief review of theoretical analyzes mainly deals with solutions for the elastic/plastic soil with special reference to the Modified Cam clay (MCC) model.

### 6.2.1 *In situ* state of soil

The initial *in situ* stress state is indispensable in the designing process as the non-linear constitutive behavior highly depends on the stress anisotropy related to the stress history (Sivakumar et al., 2001). While the vertical effective stress  $\sigma'_{vo}$  can be derived based on depth, unit weight and groundwater information, the estimation of the horizontal effective stress  $\sigma'_{ho}$  requires the use of some empirical correlations for the coefficient of earth pressure "at rest"  $K_o$ . In the case of SBPT, the in situ total horizontal stress can be directly estimated from the "lift-off" pressure (Jamiolkowski et al., 1985; Clough et al., 1990; Amar et al., 1991). The "lift-off" pressure corresponds to the internal cavity pressure  $\psi_o$  when the membrane starts to deform the wall of a borehole, therefore  $\psi_o \cong \sigma'_{ho}$  (Figure 6.4). The "lift-off" is typically estimated based on the averaging procedure including the measurements of three feeler arms spaced at  $120^\circ$  around the instrument (Dalton and Hawkins, 1982; Mair and Wood, 1987). The reliability of the derived horizontal stress highly depends on the undisturbed probe

installation. The incorrect installation or device imperfections may lead to erroneous results. Benoit and Clough (1986) showed a 20% underestimation of the lateral pressure for SBP tests conducted with 1.1% oversized cutting shoe. In general, the lateral stress measurements can be considered as fairly accurate in clays, particularly in soft deposits (Jamiolkowski et al., 1985). The increasing soil stiffness may procure large differences between feeler arm measurements (Dalton and Hawkins, 1982).

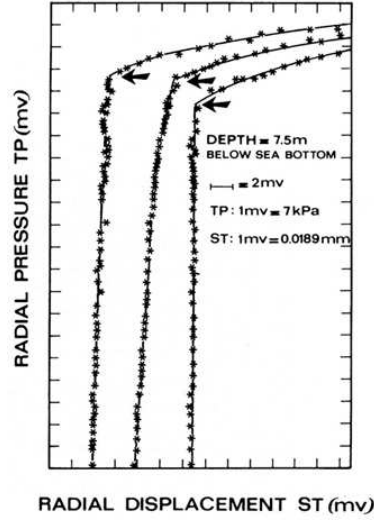


Figure 6.4: Example of the total horizontal stress estimation from the lift-off pressure in soft clay at Panigaglia site (after Jamiolkowski et al., 1985).

## 6.2.2 Cavity expansion test

The cavity expansion theory for cohesive soils assumes that an expansion of an infinite cylindrical cavity takes place under perfectly undrained conditions, in homogeneous and saturated soil. The first assumption allows us to adopt plain strain conditions ( $\varepsilon_z = 0$ ) and therefore, the cylindrical coordinates imply the principal stresses: radial  $\sigma_r$ , circumferential  $\sigma_\theta$  and vertical  $\sigma_z$  (Figure 6.5(a)). The initial equilibrium state is defined by the initial radius of cavity,  $a_o$ , and internal pressure,  $\psi_o$ , which compensates the total horizontal stress,  $\sigma_{ho}$ , acting on the cavity wall (Figure 6.5(b)). The pressure increment from  $\psi_o$  to  $\psi$  induces cavity deformation from radius configuration  $a_o$  to  $a$ . At the same time, the element at the initial radius,  $r_o$ , moves to a new position  $r = r_o + u_r$ , where  $u_r$  denotes the radial displacement. The plastic zone with radius  $r_p$  arises with soil yielding. The elements beyond this zone remains in elastic state. The second assumption implies no volume changes in adjacent soil during expansion, i.e.  $\varepsilon_v = \varepsilon_r + \varepsilon_\theta + \varepsilon_z = 0$  with  $\varepsilon_\theta = u_r/r$  and  $\varepsilon_r = du_r/dr$  or in other words, no seepage of the fluid may occur.

Due to  $\varepsilon_z = 0$  and axial symmetry conditions:

$$\varepsilon_r + \varepsilon_\theta = \frac{du_r}{dr} - \frac{u_r}{r} \quad (6.1)$$

and the equation of equilibrium can be written as follows:

$$\frac{d\sigma_r}{dr} + \frac{\sigma_r - \sigma_\theta}{r} = 0 \quad (6.2)$$

Replacing  $\sigma_r - \sigma_\theta$  by the shear stress  $\tau$  which corresponds to the shear strain,  $\gamma = \varepsilon_r - \varepsilon_\theta = du_r/dr + u_r/r = 2u_r/r$ , Equation (6.2) yields:

$$r \frac{d\sigma_r}{dr} + 2\tau = 0 \quad (6.3)$$

According to the Tresca's failure criterion, the plastic yielding occurs when:

$$\sigma_r - \sigma_\theta = 2c_u \quad (6.4)$$

where undrained shear strength is denoted by  $c_u$ .

### *Stiffness in linear elasticity*

Assuming linear elasticity, the soil obeys the Hooke's law at the beginning of expansion. The radial displacement is thus inversely proportional to the radius:

$$u_r = u_c \frac{a}{r} = \varepsilon_c \frac{a_o a}{r} \quad (6.5)$$

where  $u_c$  denotes the cavity wall displacement and  $\varepsilon_c$  is the cavity strain:

$$\varepsilon_c = \frac{a - a_o}{a_o} = \frac{u_c}{a_o} \quad (6.6)$$

As the deformation takes place with no volume changes, the radial and circumferential strains are equal and have opposite signs, Equation (6.1), and they vary inversely with the square of the radius:

$$\varepsilon_\theta = u_c \frac{a}{r^2} = -\varepsilon_r \quad (6.7)$$

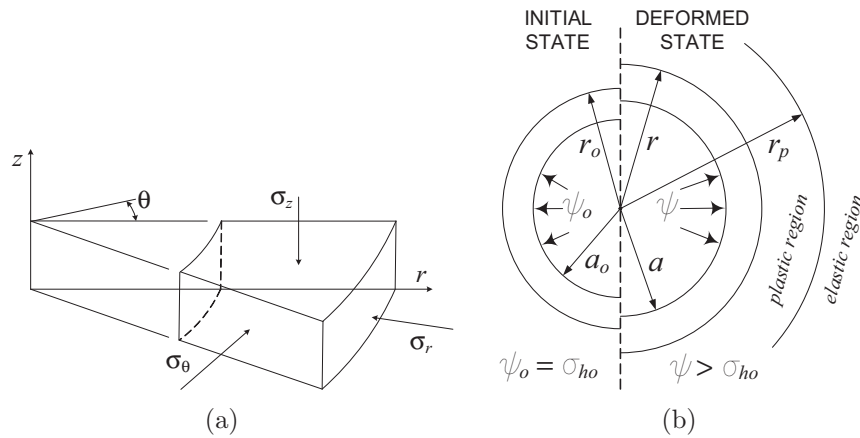


Figure 6.5: Scheme of cylindrical cavity expansion: (a) stress components in cylindrical coordinates and (b) boundary conditions of cavity.

In the elastic material principal strains are related to the changes of principal stresses. Hence in the cylindrical coordinate system:

$$E\Delta\varepsilon_z = \Delta\sigma_z - \nu(\Delta\sigma_\theta + \Delta\sigma_r) \quad (6.8a)$$

$$E\Delta\varepsilon_r = \Delta\sigma_r - \nu(\Delta\sigma_z + \Delta\sigma_\theta) \quad (6.8b)$$

$$E\Delta\varepsilon_\theta = \Delta\sigma_\theta - \nu(\Delta\sigma_z + \Delta\sigma_r) \quad (6.8c)$$

where  $E$ , is the Young's modulus and  $\nu$  denotes Poisson's coefficient under drained conditions. Due to  $\Delta\varepsilon_z = 0$  and  $\Delta\varepsilon_v = 0$  conditions:

$$\Delta\sigma_z = 0 \quad (6.9a)$$

$$\Delta\sigma_r = \sigma_r - \sigma_{ho} = 2G\varepsilon_c \frac{a_o a}{r^2} \quad (6.9b)$$

$$\Delta\sigma_\theta = \sigma_\theta - \sigma_{ho} = -2G\varepsilon_c \frac{a_o a}{r^2} \quad (6.9c)$$

where the shear modulus is defined as  $G = E/2(1 + \nu)$ . Hence, the radial and circumferential stresses change by equal and opposite values from the *in situ* horizontal stress and in the elastic phase:

$$\Delta\sigma_r + \Delta\sigma_\theta + \Delta\sigma_z = 0 \quad (6.10)$$

This implies that no excess of pore water pressure occurs during the expansion in the elastic material and, in consequence, material stiffness is independent of drainage conditions. At the cavity wall,  $r = a$ , and total radial stress is equal to the applied pressure,  $\sigma_r = \psi$ , so Equation (6.9b) can be written as follows:

$$\psi - \sigma_{ho} = 2G\varepsilon_c \frac{a_o}{a} \quad (6.11)$$

The shear modulus can be derived directly from the initial response of the cavity wall on the applied pressure under condition that the probe is installed without severe disturbances (Figure 6.6). At the beginning of the test,  $a = a_o$ , so the initial tangent stiffness parameter is:

$$G_t = \frac{1}{2} \frac{d\psi}{d\varepsilon_c} = V_o \frac{d\psi}{dV} \quad (6.12)$$

Sometimes, in the case where disturbance effects occur during the installation of the SBP probe, the shear modulus may be more representative when derived from a slope of the hysteresis for an unloading/reloading cycle (Jamiolkowski et al., 1985). Assuming that soil responds elastically during the unloading/reloading cycle, the shear modulus is evaluated from Equation (6.11):

$$G_{ur} = \frac{1}{2} \frac{a}{a_o} \frac{d\psi}{d\varepsilon_c} = V \frac{d\psi}{dV} \quad (6.13)$$

where the change of cavity volume is  $\Delta V = V - V_o$  with  $V_o$  corresponding to  $a_o$ .

However, observations show that the shear modulus tends to be smaller than

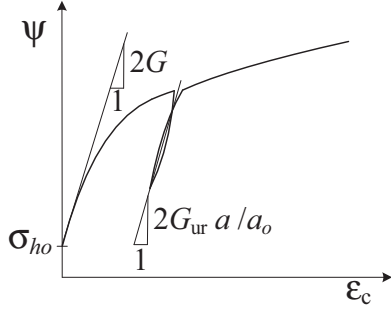


Figure 6.6: Derivation of initial tangent shear modulus,  $G$  and unload-reload shear modulus,  $G_{ur}$  from the pressuremeter expansion curve.

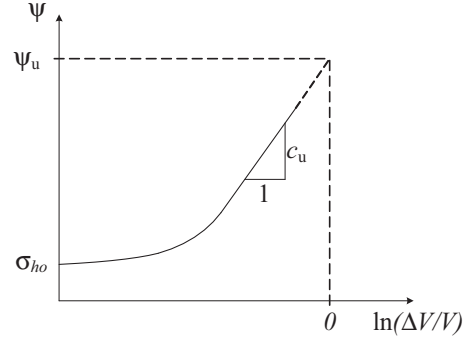


Figure 6.7: Derivation of limit pressure  $\psi_u$  and undrained shear strength  $c_u$  by extrapolating the pressuremeter data.

the initial value since cyclic loadings gradually decrease a tangent modulus until its stabilization after a few cycles (Benoit and Clough, 1986). It can be explained by the well-known decrease of stiffness with the amplitude of the shear strain (non-linear relationship  $G/p' - \ln \gamma$ ). Taking into account the fact that the soil elements undergo different strain amplitudes at different distances from the pressuremeter, Houlsby (1998) demonstrated that the measured  $G_{ur}$  is dominated by the stiffness of the soil in the close vicinity of the cavity wall. Since in the MCC model, an isotropic material obeys the Hooke's law until reaching yield locus, Equation (6.11) can be rewritten for the cylindrical and spherical cases as (Yu et al., 2000; Cao et al., 2001):

$$\psi - p_o = 2mG \left( 1 - \frac{a_o}{a} \right) \quad (6.14)$$

with  $m = 1$  and  $m = 2$  respectively, and  $p_o$  denotes the initial total mean stress and  $G$  is expressed as the function of the voids ratio, Poisson's coefficient and effective mean stress (see Equation (4.4)).

#### *Shear strength in elastic/perfectly plastic material*

The methods commonly used to date to estimate the soil shear strength  $c_u$ , under perfectly undrained conditions, are based on solutions proposed by Gibson and Anderson (1961) and Baguelin et al. (1972), Ladanyi (1972), Palmer (1972). The first solution allows  $c_u$  to be determined in the elastic/perfectly plastic cohesive soil using the expression for the total pressure acting at the cavity wall:

$$\psi = \sigma_{ho} + c_u \left[ 1 + \ln \left( \frac{G}{c_u} \right) + \ln \left( \frac{\Delta V}{V} \right) \right] \quad (6.15)$$

and the corresponding maximum excess pore water pressure is expressed as:

$$\Delta u_{\max} = c_u \ln \left( \frac{G \Delta V}{c_u V} \right) \quad (6.16)$$

where  $\Delta V/V$ , is the volumetric strain expressed by the cavity strain:

$$\frac{\Delta V}{V} = \frac{a^2 - a_o^2}{a^2} = 1 - (1 + \varepsilon_c)^{-2} \quad (6.17)$$

The meaning of Equation (6.15) is that clay which is deforming plastically has no shear stiffness, and it may deform infinitely (Figure 6.7). Theoretically, the pressuremeter expansion reaches the so-called limit pressure (ultimate cavity pressure)  $\psi_u$  at the limiting condition of  $\Delta V/V = 1$  (cf. Clarke, 1995; Mair and Wood, 1987):

$$\psi_u = \sigma_{ho} + c_u \left[ 1 + \ln \left( \frac{G}{c_u} \right) \right] \quad (6.18)$$

Equation (6.18) is graphically presented in Figure 6.7.

Baguelin et al. (1972); Ladanyi (1972); Palmer (1972) independently proposed the *sub-tangent method* which allows the reproduction of the relation between deviatoric stress ( $\sigma_r - \sigma_\theta = 2\tau$ ) and cavity strain  $\varepsilon_c$  (Figure 6.8(a)). Based on the expansion curve, the method produces a complete stress-strain soil response at the cavity wall with the assumptions of fully undrained conditions through the following expression:

$$\tau = \frac{1}{2} \varepsilon_c (1 + \varepsilon_c) (2 + \varepsilon_c) \frac{d\psi}{d\varepsilon_c} \quad (6.19)$$

For small strains the above equation can be rewritten as:

$$\tau = \varepsilon_c \frac{d\psi}{d\varepsilon_c} \quad (6.20)$$

For large deformations, the above equation becomes:

$$\tau = \frac{d\psi}{d(\ln(\Delta V/V))} \quad (6.21)$$

An example of the stress-strain curve for an ideally smooth relationship  $\psi - \varepsilon_c$  is presented in Figure 6.8(b).

Silvestri (1998) proposed a similar approach, i.e. the sub-tangent method for the hollow cylinder expansion. The method gives essentially the same results as the previously presented approach.

The sub-tangent method depends notably on the smoothness of measurements causing some curve oscillations and irregularities. The data obtained from SBPT can be smoothed, however, it should be considered that small changes of the gradient on loading path do not have to be random. Therefore, the curve fitting is not recommended in this case. Moreover, the method is highly sensitive to the disturbance effect. It can appear in apparent peaks in the beginning of the stress/strain relationship. Therefore, the sub-tangent method can only be useful in understanding soil behavior, but cannot be used directly to provide information for the NN training.



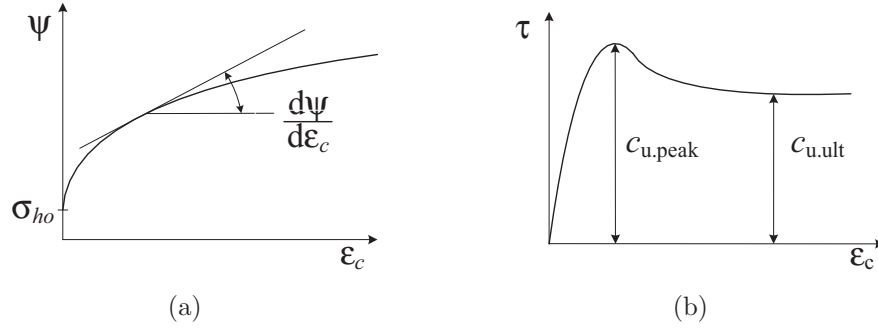


Figure 6.8: Derivation of the undrained shear strength  $c_u$  using the sub-tangent method: (a) undrained expansion curve, (b) derived deviatoric curve.

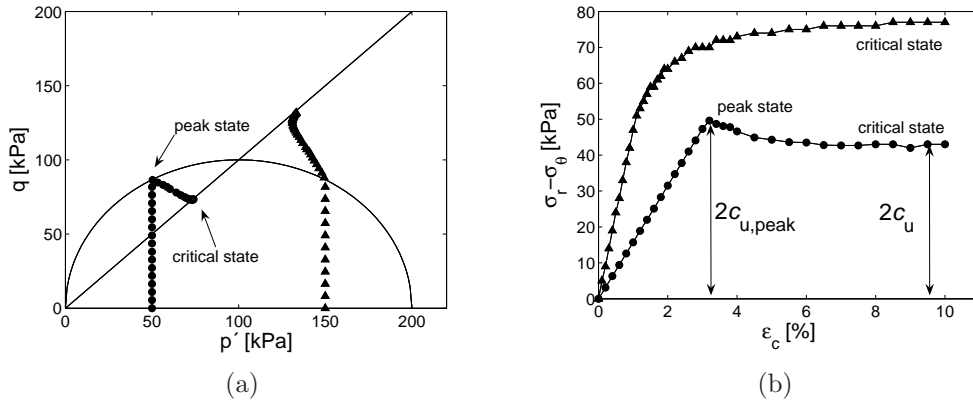


Figure 6.9: Numerical simulations of the strain controlled undrained pressuremeter test with the MCC model: (a) effective stress paths in the  $p' - q$  plane, (b) deviatoric stress-cavity strain plane.

### Shear strength in the critical state model

In the MCC, the undrained shear strength  $c_u$  depends on the shape of the yield surface which is defined by two independent variables  $M$  and  $R_p$  (Figure 6.9). For the overconsolidated soil, the shear strength reaches its maximum ( $c_{u,peak}$ ) at the yield point and if the expansion continues, the soil undergoes softening and reaches the ultimate state ( $c_u$ ). Hence,  $c_u$  which corresponds to the ultimate deviatoric stress  $q_u$ , can be obtained for plain strain expansion and initially isotropic stress state as (cf. Cao et al., 2001):

$$c_u = \frac{q_u}{\sqrt{3}} = \frac{Mp'_o}{\sqrt{3}} \left( \frac{R_p}{2} \right)^\Lambda \quad (6.22)$$

where  $\Lambda$  is the plastic volumetric strain ratio which describes the ratio between the slopes of the normal consolidation line  $\lambda$ , and unloading-reloading line  $\kappa$ :

$$\Lambda = 1 - \frac{\kappa}{\lambda} \quad (6.23)$$

The previous consideration for elastic/perfectly plastic material showed that the undrained expansion problem deals with total stresses. In the MCC, the

function describing the yield locus is given in terms of effective stresses (cf. Equation (4.1)). It means that total stress analysis does not take into account an effect of the stress history. The analysis of the cavity expansion in the MMC requires considering four equations: the equilibrium (Equation (6.2)), the plastic potential (Equation (4.1)), the flow rule (Equation (4.8)), and the equation of mass conservation (Equation (4.18)). The latter is satisfied if the expansion takes place in undrained conditions. The effective stresses can be determined by integrating Equation (4.1) and Equation (4.8) and the excess pore water pressure is then computed by means of equilibrium equation (Collins and Yu, 1996; Cao et al., 2001). An increase of the internal pressure has consequences in a yielding and increasing range of a plastic region of surrounding material. When the boundary surface is reached obeying Equation (4.1), increasing pressure extends the plastic zone described by a radial distance  $r_p$ , Figure 6.5(b).

Rearranging Equation (4.1) and introducing the mean effective stress at the yield surface as  $p'_p = p'_o$  the corresponding deviatoric stress at the cavity wall is equal to:

$$q_p = Mp'_o \sqrt{R_p - 1} \quad (6.24)$$

In every case, the infinite expansion in undrained conditions leads to reaching the critical state of soil for ultimate stresses  $p'_u$  and  $q_u$  (see Figure 6.10). With the assumption of no volume change  $q_u$  can be calculated as (Cao et al., 2001):

$$p'_u = p'_o \left( \frac{R_p}{2} \right)^\Lambda \quad (6.25a)$$

$$q_u = Mp'_u = Mp'_o \left( \frac{R_p}{2} \right)^\Lambda \quad (6.25b)$$

Finally, the maximum deviatoric stress  $q_m$  corresponding to the effective mean stress  $p'_m$  can be obtained from (Cao et al., 2001):

$$p'_m = p'_o \left[ \frac{(2\Lambda - 1)R_p}{2\Lambda} \right]^\Lambda = p'_u \left( 2 - \frac{1}{\Lambda} \right)^\Lambda \quad (6.26a)$$

$$q_m = Mp'_o (2\Lambda - 1)^{-1/2} \left[ \frac{(2\Lambda - 1)R_p}{2\Lambda} \right]^\Lambda \quad (6.26b)$$

Cao et al. (2001) demonstrated that integrating the total deviatoric strain composed of reversible and irreversible parts, the relationship between effective stresses and the radial distance from the center of cavity can be expressed as:

$$\ln \left( 1 - \frac{a^{m+1} - a_o^{m+1}}{r^{m+1}} \right) = - \frac{q}{G\sqrt{m+2}} - \frac{2\sqrt{3}^m}{m} \frac{\kappa\Lambda}{\nu M} \left[ \beta - \tan^{-1} \left( \frac{\eta}{M} \right) \tan^{-1} \sqrt{R_p - 1} \right] \quad (6.27a)$$

where:

$$\beta = \frac{1}{2} \ln \left[ \frac{(\eta + M)(\sqrt{R_p - 1} - 1)}{(\eta - M)(\sqrt{R_p - 1} + 1)} \right] \quad \text{and} \quad \eta = q/p' \quad (6.27b)$$

with  $m$  assigned for the cylindrical and the spherical case equal to 1 and 2 respectively. The graphical interpretation of Equation (6.27) is presented in Figure 6.11. In order to estimate the total stress in the plastic region, Equation (6.27) has to be integrated with Equation (6.2). Since the direct integration in case of the MCC is not possible, Cao et al. (2001) proposed to calculate the radial stress with the radial distance from the center of cavity by a numerical integration of the following expression:

$$\sigma_r = \sigma_{rp} - \frac{2}{\sqrt{m+2}} \int_{r_p}^r \frac{q}{r} dr \quad (6.28)$$

Since the deviatoric stress,  $q$ , calculated from Equation (6.27), is dependent on the radius distance from the center of cavity  $r$ , the total radial stress in the

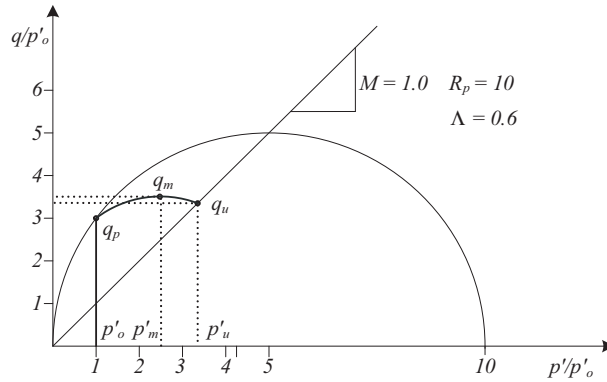


Figure 6.10: Effective stress path for the cavity expansion in overconsolidated soil.

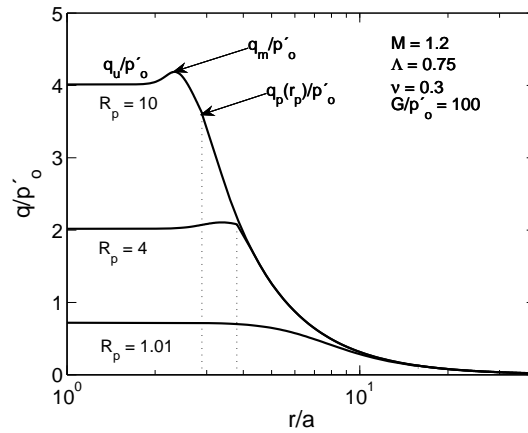


Figure 6.11: Variation of the deviatoric stress with the radial distance around the cylindrical cavity.

plastic region  $\sigma_r$  can be obtained through the numerical integration of Equation (6.28). Having determined the mean effective stress,  $p'$  and the total mean stress,  $p = (\sigma_r + \sigma_\theta)/2$ , the excess pore water pressure can be established from:

$$\Delta u = u - u_o = (p - p_o) - (p' - p'_o) \quad (6.29)$$

Examples of numerical integration of Equation (6.28) are presented in Figure 6.12 for various overconsolidation ratios,  $R_p$ . The results show that the heavily overconsolidated soil exhibits suction during yielding, i.e. negative value of excess pore water pressure  $\Delta u$ . The figures clearly demonstrate a large influence of the overconsolidation ratio. The increase of  $R_p$  leads to reduction of both the radius of plastic region and the pore pressure at the yield locus.

Cao et al. (2001) introduced a simplification of the above solution by assuming that the deviatoric stress  $q$  in the plastic zone is equal to the ultimate deviatoric stress  $q_u$  as the differences between  $q_p$ ,  $q_m$  and  $q_u$  are relatively small. Hence, in the plastic zone, the radial total stress at the cavity wall  $\sigma_r$  corresponding to the applied pressure  $\psi$  may be evaluated as:

$$\psi = p_o + \frac{m}{\sqrt{3}^m} q_u \left\{ 1 + \ln \left[ \frac{G\sqrt{m+2}}{q_u} \left( \frac{a^{m+1} - a_o^{m+1}}{a^{m+1}} \right) \right] \right\} \quad (6.30)$$

while the excess pore water pressure corresponding to the approximated total stress at the cavity wall may be obtained from:

$$\Delta u = \frac{m}{\sqrt{3}^m} q_u \ln \left[ \frac{G\sqrt{m+2}}{q_u} \left( \frac{a^{m+1} - a_o^{m+1}}{a^{m+1}} \right) \right] + p'_o \left[ 1 - \left( \frac{R_p}{2} \right)^\Lambda \right] \quad (6.31)$$

Note that for  $R_p = 2$ , Equation (6.30) and (6.31) reduce to the expressions for elastic/perfectly plastic soil obtained by Gibson and Anderson (1961, Equations (6.15) and (6.16)).

### 6.2.3 Analysis of dissipation test

Consolidation characteristics can be derived based on SHT measurements, using a closed-form solution proposed by Randolph and Wroth (1979) for the consolidation around driven piles. This solution was adopted for SHT because of the similarity to the pressuremeter boundary problem (Clarke et al., 1979).

#### *Stress Holding Test*

Assuming that the relaxation of the adjacent soil takes place in the elastic homogeneous medium in plain strain horizontal conditions, the coefficient of consolidation can be calculated using a non-dimensional time factor  $T_{50}$ :

$$T_{50} = \frac{c_h t_{50}}{a_o^2} \quad \text{where} \quad c_h = \frac{k}{\gamma_w} 2G \frac{1 - \nu}{1 - 2\nu} \quad (6.32)$$

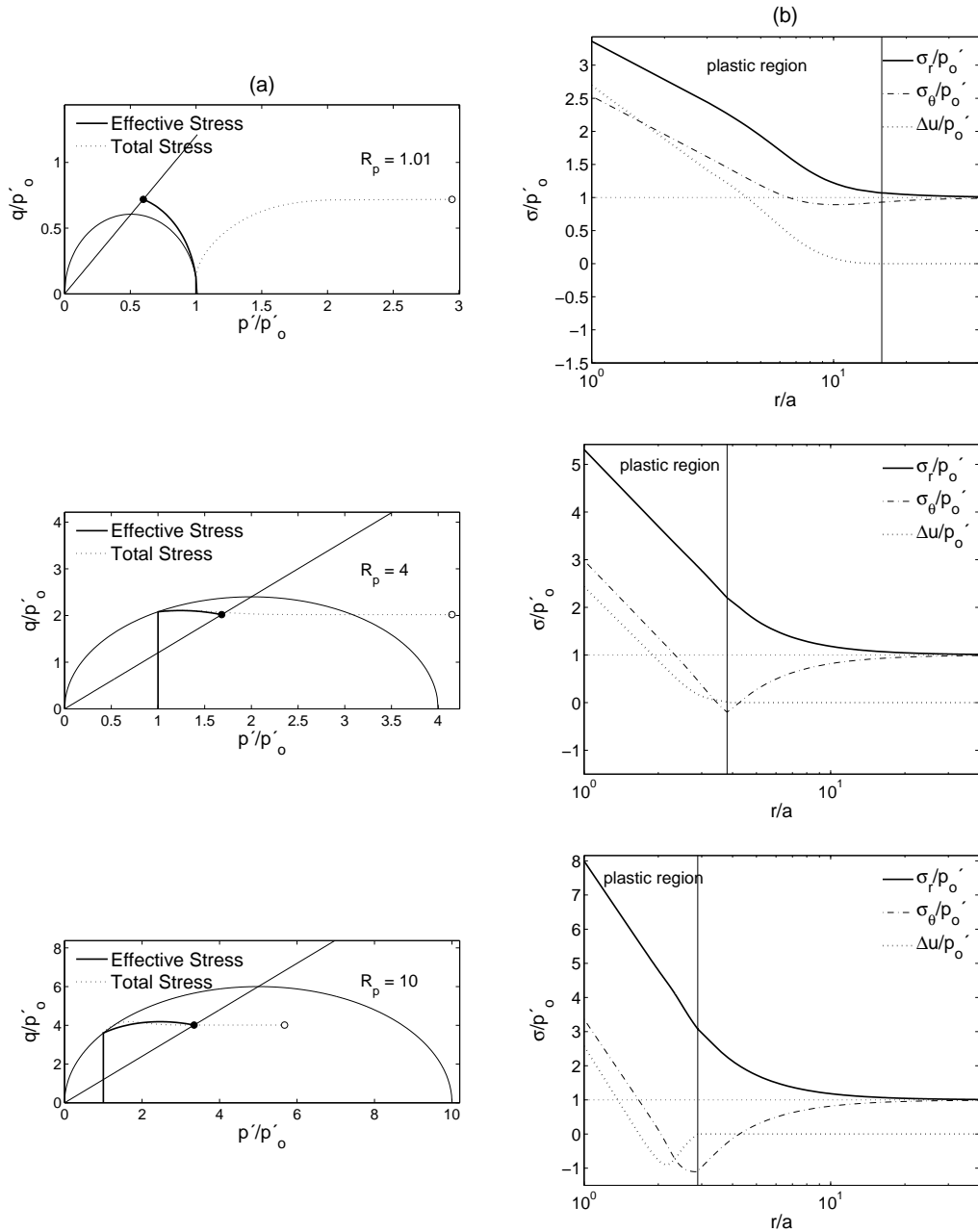


Figure 6.12: Analytical solution of the cylindrical cavity expansion problem for the Modified Cam clay for different overconsolidation ratio  $R_p = 1.01, 4.0, 10.0$ , (a) effective and total stress paths, (b) stress and pore pressure distribution around the cavity for the cavity strain  $\epsilon_c = 10\%$ .

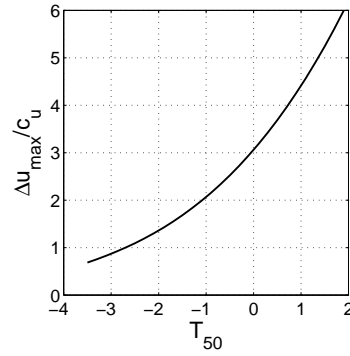


Figure 6.13: Dependence of time factor for 50% consolidation,  $T_{50}$  on the maximum excess pore water pressure at the cavity wall (after Clarke et al., 1979).

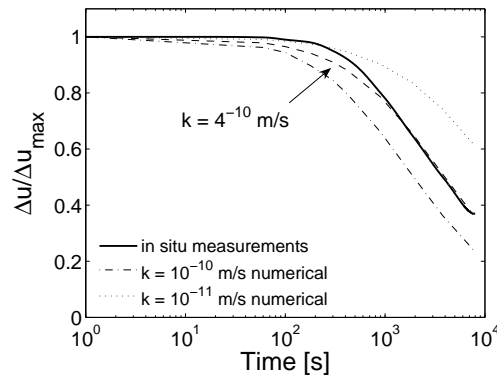


Figure 6.14: Prediction of permeability coefficient from pressure holding test by means of numerical simulations (from Fioravante et al., 1994).

where  $t_{50}$  is the time of 50% excess pore water pressure decay,  $a_o$  is the cavity radius at the beginning of the dissipation,  $\gamma_w$  is the unit weight of water,  $\nu'$  denotes Poisson's coefficient under drained conditions. The time factor  $T_{50}$  can be obtained using the ratio  $\Delta u_{\max}/c_u$  (Equation (6.16)) and the graphical solution presented in Figure 6.13.

### Pressure Holding Test

To the author's knowledge, a closed-form solution does not exist for PHT. This can be explained by the complexity of the problem which includes the plastic soil flow during the test. Thus, the test can only be interpreted through numerical methods and curve-fitting procedures (Carter et al., 1979; Fioravante et al., 1994).

Surprisingly, there is no evidence in the literature, of any attempt to determine the characteristics of virgin compressibility through PHT measurements. In this study, it is suggested to evaluate the slope of normal consolidation line,  $\lambda$ , using the variation of cavity strain radius which occurs due to increasing effective radial stress accompanying the pore pressure decay in the adjacent soil. Assuming that soil responds plastically at the end of the expansion test,

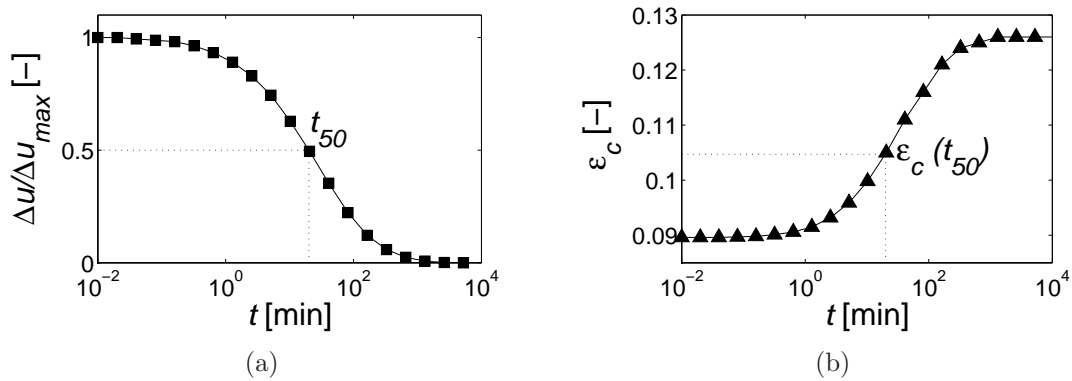


Figure 6.15: Example of a numerical simulation of the pressure holding test: (a) dissipation of the normalized excess pore water pressure in time, (b) variation of the cavity strain in time.

maintained constant pressure during the holding test may result in soil hardening along the normal consolidation line. Thus, the difference between the initial and the actual cavity radius corresponds to the difference between the minimal effective stress at the beginning of consolidation and the current state. In the context of numerical assessment of  $\lambda$ , the variation of cavity strain  $\Delta\varepsilon_c$  in the dissipation time (Figure 6.15) may be fit to experimental measurements. As this may seem impractical in the case of a less permeable soil to entirely complete the long dissipation test, it is suggested to fit the cavity strain which corresponds to the time of 50% excess pore water pressure decay, i.e.  $\varepsilon_c(t_{50})$ . Examples of the numerical determination of  $\lambda$  through PHT will be presented in Sections 8.1.5 and 9.1.2.

#### 6.2.4 Overestimation of determined parameters

It is commonly known that some soil characteristics such as  $c_u$  can be overestimated compared to other reference test results, e.g. to triaxial test (Eden and Law, 1980; Penumadu and Chameau, 1997). The derived parameters can be affected by many factors such as partial drainage, strain rate, soil disturbance during pressuremeter installation, material and stress anisotropy, uniqueness of stress-strain relationship, radial cracking (Baguelin et al., 1972; Benoit and Clough, 1986; Wroth, 1984; Penumadu et al., 1998). Several researchers investigated potential factors having the greatest impact on the overestimation of characteristics derived from SBPT. It is believed that soil disturbance during probe installation and partial drainage during expansion are the most important factors affecting soil properties derived from the SBPT (Benoit and Clough, 1986; Wood and Wroth, 1977). Benoit and Clough (1986) reported that a slight oversizing of a cutting shoe (around 1.1%) can lead to a significant overestimation of the derived shear strength in order of magnitude of 60-100%.

The analyzes presented in Section 6.2.2 are developed with the assumption that the expansion test is carried out in undrained conditions implying no vol-

ume changes. In practice, the expansion test in clays should thus be performed fast enough to avoid the possible partial drainage. On the other hand, the high expansion rate may affect stress paths due to rheological effects (e.g. Figure 6.16). It has been reported that  $c_u$  increases linearly with the logarithm of the shear strain rate (Bjerrum, 1972; Nakase and Kamei, 1986; Penumadu et al., 1998, cf. Figure 2.3). Consequently, a similar effect can be observed for the derived values of preconsolidation pressure  $\sigma'_p$ . The study carried out by Leroueil et al. (1983b) revealed the increase of about 10-14% for  $\sigma'_p$  per log cycle of volumetric strain rate  $\dot{\epsilon}_v$  in the constant rate of strain oedometer test (CRS). The strain rate effect on  $c_u$  can be taken into account using a general expression (e.g. Prapaharan et al., 1989; Chang et al., 2001; Schnaid, 2005):

$$\frac{c_u}{c_u^{\text{ref}}} = 1 + \beta_\epsilon \log \left( \frac{\dot{\epsilon}}{\dot{\epsilon}^{\text{ref}}} \right) \quad (6.33)$$

where  $\beta_\epsilon$  is the strain rate coefficient (typically ranging between 0.08 and 0.15 and the mean value of about 0.10),  $c_u$  and  $c_u^{\text{ref}}$  are the values of the undrained shear strength that correspond to the strain rate for a given test  $\dot{\epsilon}$  and the strain rate  $\dot{\epsilon}^{\text{ref}}$  for a reference test respectively.

On the other hand, the strain rate does not affect derived values of  $M$  (Penumadu et al., 1998, see Figure 6.16). The strain rate effect can also be observed for the initial part of pressuremeter stress-strain curves (Penumadu and Chameau, 1997). In consequence, the shear modulus  $G$  can increase with rising strain rate. This effect is more pronounced in the normally consolidated clay than in overconsolidated deposits. Vinale et al. (2001) showed the increase of  $G$  around 6% for each log cycle increase of the shear strain rate in resonant column and torsional shear tests.

Prapaharan et al. (1989) pointed out, however, that the strain-rate effect is not as significant as the disturbance effect. They reported that the pressuremeter tests at 1%/min of strain rate increased the undrained shear strength of about 8-13% with regards to the reference rate of 0.1%/min.

In practice, a decrease of the rate of cavity strain would increase the probability of partial drainage occurrence during the expansion. Wood and Wroth (1977) strongly affirmed that even for quick expansion, some drainage is in-

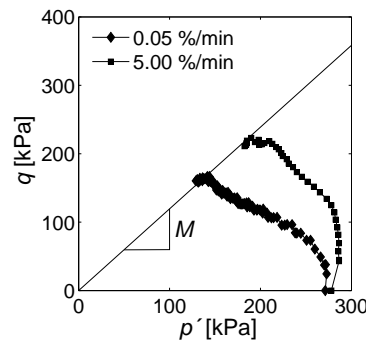


Figure 6.16: Effect of strain rate  $\dot{\epsilon}$  on stress paths (from Penumadu et al., 1998); no influence on the slope of critical state line  $M$ .



evitable. Clearly, the occurrence of partial drainage affects the stress-strain relationship and, in effect, the derived parameters. The further discussion on the effect of partial drainage is provided in Section 6.2.5.

### 6.2.5 Hydro-mechanical coupling of pressuremeter tests

The analytical solutions for the expansion test are developed with the assumption that the expansion test is carried out in undrained conditions. Numerical simulations of the expansion at the standardized rate of  $\dot{\epsilon}_c = 1\%/min$  reveal that the assumed undrained conditions may be violated if the coefficient of permeability is larger than  $10^{-10}m/s$  (cf. Fioravante et al., 1994)<sup>1</sup>. This means that partially drained conditions may occur even for clays, cf. Figure 6.17. In effect, the partial drainage may affect the stress paths (Figure 6.18(a)) and, as proved experimentally, the shape stress-strain curve (Fukagawa et al., 1990). Consequently, instead of tending to the ultimate value of the undrained shear strength  $c_u$  (Figure 6.18(b)), the soil may locally harden at the cavity wall, due to volume changes that may occur with the partial consolidation. The occurrence of hydro-mechanical coupling may lead to an overestimation of  $c_u$  which may thus result in a feedback affecting an assessment of consolidation characteristics (Rangeard et al., 2003). For example, the determination of the coefficient of permeability  $k$  using Equation (6.32) requires an estimation of  $T_{50}$  which, in turn, depends on  $c_u$ . The laboratory small-scale, triaxial cell simulations of pressuremeter testing carried out by Ali (1989) confirmed that consolidation which occurs during the expansion, leads to erroneous results if the analytical methods assume deformations under undrained conditions. For further discussion on the influence of partial drainage on parameter identification refer to Section 7.1.2.

In conclusion, the occurrence of partial drainage requires a coupled hydro-mechanical analysis, which makes the problem too complicated to be solved analytically. Hence, it seems that parameter identification for the pressuremeter BVP requires the use of a numerical modeling. Furthermore, the calibration of model characteristics should be considered as a parallel fitting of all the available experimental measurements as the parameter feedback exists. The use of

<sup>1</sup>Numerical simulations performed in the present study leads to the same conclusion, please refer to Section 7.1.2.

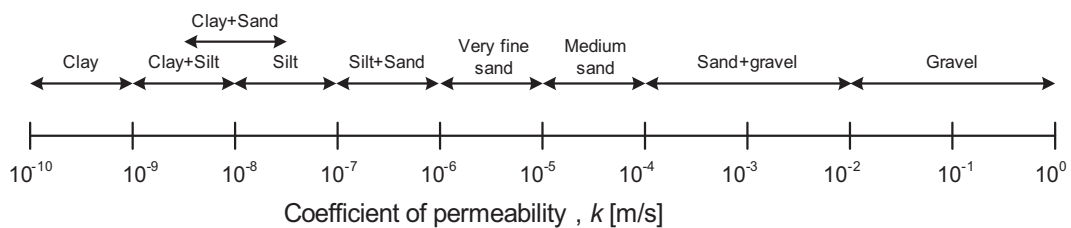


Figure 6.17: Approximate soil permeability for variety of soils (after Hight and Leroeuil, 2003).

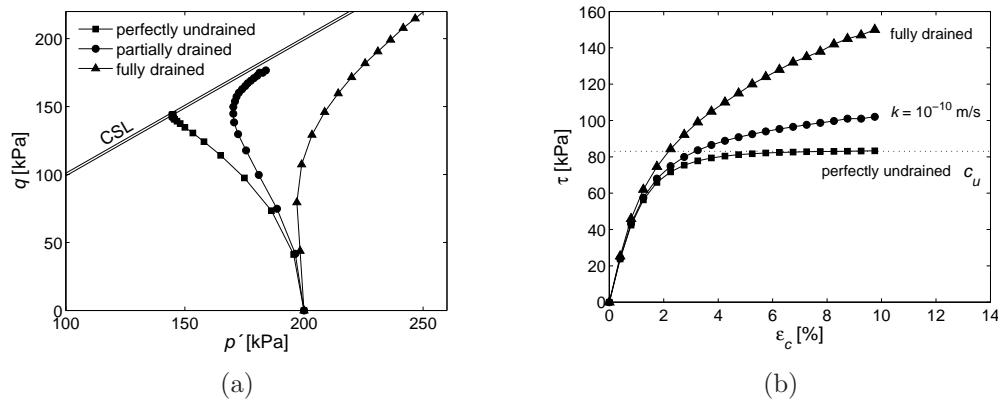


Figure 6.18: Influence of soil permeability on shear strength for a normally-consolidated soil: (a) effective stress paths, (b) evolution of shear stress during expansion (the results obtained from numerical simulations presented in Section 7.1).

numerical simulation of SBPT will be thus enforced in the further part of this study (see Section 7.1).

### 6.3 Analysis of the piezocone penetration test

The application of CPTU to evaluate geotechnical parameters in clayey soils is focused mainly on the determination of stress history (OCR), undrained shear strength ( $c_u$ ), constrained modulus ( $M_D$ ) or consolidation characteristics ( $k$  and  $c_h$ ), etc. Different levels of confidence for derived parameters can be expected when interpreting CPT data. Lunne et al. (1997) provided a summary of perceived applicability of CPT for the determination of typical soil properties with a qualitative evaluation of the level of confidence for estimated characteristics. A modified summary is presented in Table 6.1.

In general, interpretation approaches can be divided into three general categories including: (i) empirical and statistical methods, (ii) analytical or semi-analytical inverse solutions, and (iii) numerical simulations. The first approach

Table 6.1: Perceived applicability of CPT for estimation typical soil parameters in clays (based on Lunne et al., 1997).

Initial state parameters			Strength parameters		Deformation characteristics			Flow charact.	
$\gamma$	$K_o$	OCR	$c_u$	$\phi'$	$E, G$	$M_D$	$G_o$	$k$	$c_h$
3-4	4-5	2-3	1-2	3-4	4-5	4-5	4-5	2-4	2-3

Reliability rating: 1 High; 2 High to moderate; 3 Moderate; 4 Moderate to low; 5 Low.

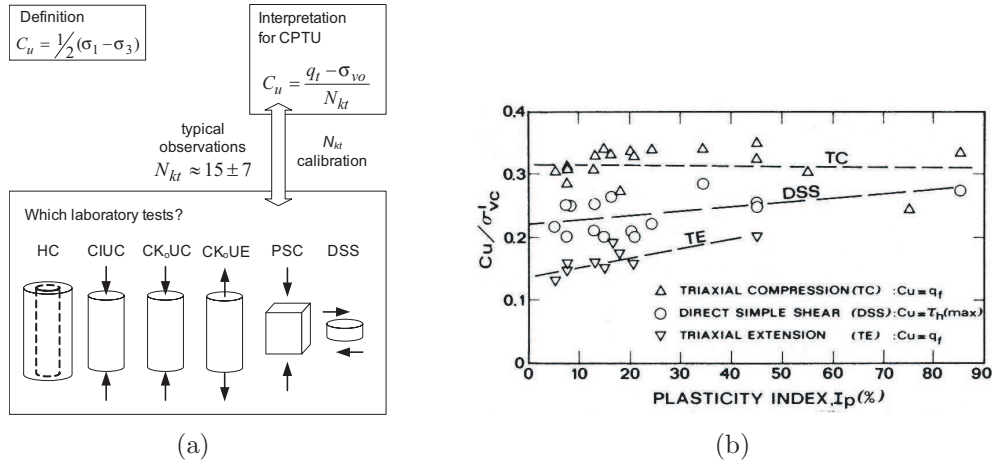


Figure 6.19: Dilemma in calibrating *in situ* tests based on laboratory benchmark shear tests: (a) calibration of  $N_{kt}$  (based on Mayne, 2006), (b) various  $c_u$  from different CK<sub>o</sub>U tests (from Jamiolkowski et al., 1985).

allows a generalized empirical formula to be developed based on a regression analysis involving a large number of results from various characterization sites (e.g. Chen and Mayne, 1994; Mayne and Rix, 1995; Mayne, 2007). However, the site-specific calibration of generalized correlations is necessary when dealing with non-textbook geomaterials (e.g. loess, silts or sensitive structured clays, etc.) and it is recommended to assure satisfying accuracy of estimations for particular geological deposits. In such a case, the reference benchmark value of parameter is required to calibrate the particular empirical formula. Such an approach can be advantageous because it may take into account the factors which can be neglected in the solutions developed based on theoretical considerations (e.g. rate, boundary or drainage effects, etc.). On the other hand, the determination of the reference parameter can be proved to be time-consuming as it requires sampling, transportation and laboratory procedures. The reference parameters can also be underestimated due to the effect of disturbances. Sometimes, engineers have to tackle the problem of selecting the benchmark test for which the reference value of parameter is established (Mayne, 2006). For example, the calibration of the benchmark value  $c_u$  requires prior knowledge of an appropriate shear mode which is expected for a particular designing problem (see Figure 6.19). Sometimes, the average value of parameter can be assigned if many reference tests are involved.

The theoretical analysis of piezocone penetration is rigorous and uncertain owing to material, boundary and geometrical nonlinearities. The penetration mechanisms is extremely complex as it involves a continuous rotation of principal stresses, including many shear modes which are relevant to various tests such as triaxial compression, direct simple shear and pressuremeter (cf. Figure 6.20). Baligh (1985) affirmed that "*realistic closed-form solutions to installation problems are not conceivable*". Due to complexity of piezocone BVP, the analytical analyzes such as the cavity expansion method, are usually limited to rather simple linear-elastic/perfectly-plastic or plastic models which do not

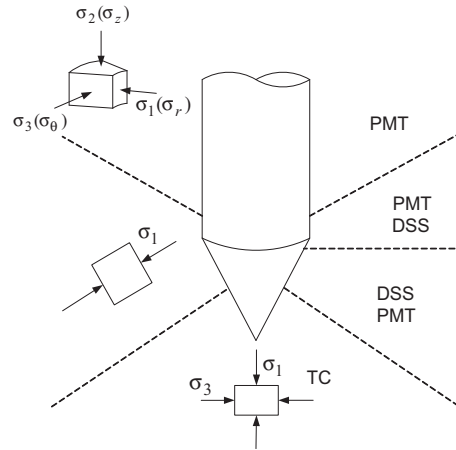


Figure 6.20: Predominant failure modes during cone penetration in clays (after Keaveny and Mitchell, 1986).

reflect the observed non-linear elasticity of natural soils. Uncertainty may also be associated with lack of the full stress-strain relief of the penetrated material or data normalization in terms of the vertical stress rather than the mean or horizontal stress. Such a normalization form follows the practical reasons since there is much of uncertainty and difficulty in the precise estimation of the horizontal stress. This approach may lead to inaccuracies as the cone resistance is much more related to the horizontal stress than the vertical stress (Lunne et al., 1997; Houlsby, 1998).

In the following subsections, the existing methods for interpretation of CPTU data will be briefly reviewed. Section 6.3.1 presents a brief review of theoretical approaches for the analysis of cone resistance, whereas Section 6.3.2 provides selected solutions from theoretical and empirical analyzes for interpretation of CPTU data in clays with reference to the commonly used geotechnical parameters. For a broad spectrum of interpretation guidelines, refer to the general reports on CPTU investigations provided by Lunne et al. (1997); Mayne et al. (2001); Mayne (2007).

### 6.3.1 Theoretical analysis of cone resistance

The theoretical analysis of cone resistance is demanding and difficult. As regards only pure mechanical aspects of the penetration, the cone resistance depends on many factors such as soil rigidity, shear strength, stress history, initial stress anisotropy, shear strength anisotropy, friction at the cone-soil interface, etc. A realistic interpretation of the penetration mechanism thus requires taking into account both the geometry of the cone with its frictional nature and material non-linearities. Mayne (2007) affirmed that *"no uniform and consistent methodology currently exists to interpret all necessary soil engineering parameters within a common framework"*. The existing theoretical approaches that are used to analyze the penetration test can be divided into four main categories: (i) bearing capacity methods, (ii) cavity methods, (iii) strain path methods,

and (iv) numerical modeling that includes the finite element method. The interpretation procedures rely either on the solutions which are based on individual theories or on their combinations.

The following section briefly reviews these approaches. For additional details, refer also to the review provided by Yu and Mitchell (1998).

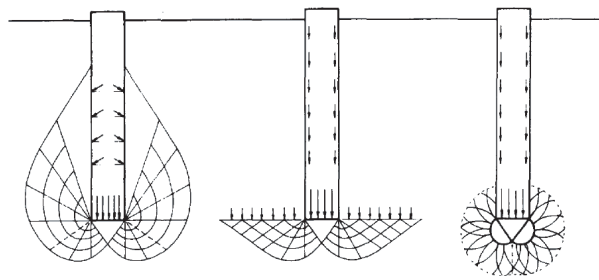


Figure 6.21: Examples of assumed failure mechanism under deep foundations (after Vesić, 1967).

**Bearing capacity method (BCM).** In this analysis, the cone resistance is regarded as the ultimate bearing capacity of a deep circular foundation in rigid plastic material. The analysis is performed for an assumed incipient failure mechanism (e.g. Figure 6.21) and the system equilibrium associated with the failure load is determined. Some solutions for the axis-symmetric foundation were provided by (Meyerhof, 1961). Durgunoglu and Mitchell (1975) adopted a number of other failure patterns to investigate deep penetration problems. Despite its simplicity, the method presents, however, some shortcomings. The influence of soil stiffness and compressibility on cone resistance is ignored. In consequence, the horizontal stress which depends on soil deformations and increases with cone penetration, is not taken into account. Moreover, the derived solutions for cone factors are represented by constant values.

**Cavity expansion method (CEM).** The cone penetration can be considered as an expanding *spherical cavity* in an infinite soil mass. Unlike the BCM, the cavity expansion method accounts for material compressibility (cf. Section 6.2.2). Hence, in the case of elastic-plastic material, the cone resistance is the function of soil compressibility and shear resistance. Determination of cone resistance thus requires developing a theoretical limit pressure solution which is related to the pressure around the cone tip. As regards the spherical cavity expansion problem in cohesive soils, some solutions for different types of materials have been proposed. Vesić (1972) provided a generalized analytical solution for the Mohr-Coulomb material obeying associated flow rule. Carter et al. (1986) provided the analytical solution for the non-associated M-C, extended by Yu and Houlsby (1991) with large strains in the plastic region. The semi-analytical solutions for the critical state material with large strains have been provided by Collins and Yu (1996) and Cao et al. (2001). Some practical examples of using the spherical cavity expansion approach concerns the evaluation of soil stress history (Mayne, 1991; Chang et al., 2001), or recovering soil permeability

profiles from standardly normalized CPTU records (Elsworth and Lee, 2007).

Cone penetration can also be modeled by means of the *cylindrical cavity* approach. In such case, the cavity is radially expanded to a radius which correspond to the cone radius dimension. An example of such an approach combined with the FE analysis can be found in Silva et al. (2006). Combining the cylindrical expansion approach and anisotropic undrained shear strength models, Su and Liao (2002) obtained a set of cone factors that account for material anisotropy.

The main disadvantages of CEM is that the proper geometry of cone cannot be modeled. The spherical expansion only approximates the shape of cone and the deformation patterns are different from real displacement fields. In consequence, correct strain paths corresponding to different shear modes cannot be obtained.

**Strain path method (SPM).** In order to account for the shape of the penetration flow, Baligh (1985) proposed a steady state approach. In the strain path method, the penetration process is considered as a steady state flow of soil passing around a stationary cone. In the first step, approximate velocity fields are evaluated and differentiated with respect to spatial coordinates in order to obtain strain rates. Then, integration of the strain rates along the streamlines defines strain paths for individual soil elements around the cone (Van der Berg, 1994). The final step includes introducing a relevant constitutive model, finding equilibrium and calculating stress field around the cone. Yu and Mitchell (1998) concluded that "*although promising in theory, the application of the steady state approach to the analysis of cone penetration in soils has not been entirely satisfactory*"; the method is limited to undrained penetration.

**Finite-element method (FEM).** The developments of robust numerical procedures allow researchers to model the penetration process with a greater dose of realism. In order to simulate the penetration mechanism, the incremental displacement FE analysis is mostly used<sup>2</sup>. Some first attempts to modeling penetration in soil type material by means of FEM were provided by de Borst and Vermeer (1982, 1984); Griffiths (1982). These studies present the analysis of cone indentation (not penetration) in purely cohesive material with the *small strain* formulation. In these analyzes the cone is introduced into a "pre-bored" hole and the surrounding initial stress state is taken as the homogeneous *in situ* stress. Cone resistance was interpreted as the ultimate indentation pressure. Such solution can be considered as a rough approximation because a correct analysis requires a *large deformation* approach for the penetrating cone, i.e. a distance of penetration should be several times greater than the cone diameter in order to establish a realistic stress field which is built up around the advancing cone (Van der Berg, 1994). While the solution of the small strain analysis can be acceptable for a purely cohesive model, the frictional, stress-dependent materials require modeling in the *large strain* regime. The penetration process indeed involves large deformations and large strains exceeding 100%. The large

---

<sup>2</sup>Details of FEM modeling of penetration test are provided in Section 7.2.

strain formulation is necessary to obtain a reliable stress field in the plastic region around the advancing cone.

One of the first examples of penetration modeling with the large strain approach in conjunction with *Updated Lagrangian* (UL) formulation (Bathe et al., 1975) were proposed by Cividini and Gioda (1988) for the Drucker-Prager material and frictional interface, and by Kioussis et al. (1988) for the frictional cap model and the perfectly smooth cone. Van der Berg (1994) concluded that the disadvantage of these models is that after each calculation step, a new location of the boundary nodes needed to be determined (cf. also Abu-Farsakh et al., 1998). The degree of complexity arises if the frictional interface is taken into account. Examples of cone penetration modeling in the UL description are also provided by Huang et al. (2004) for cohesive soil obeying non-associated Mohr-Coulomb criterion, Sheng et al. (1997); Abu-Farsakh et al. (1998) for MCC model, Wei et al. (2005) for the anisotropic MCC model. Voyiadjis and Kim (2003) also used the UL formulation to demonstrate penetration in the anisotropic elastoplastic-viscoplastic bounding surface model which is able to take into account strain rate effects. Using the finite sliding scheme for frictional interface, Huang et al. (2004) modeled the penetration process from the top surface of mesh so that a heterogeneous stress field around the cone shaft was built up in the expanding soil. The so-called *steady state*<sup>3</sup> was obtained in a penetration depth of several diameters of the cone.

The use of large deformation and finite sliding frictional elements has to be treated carefully. In the case of penetration problems, the UL formulation may suffer from severe loss of accuracy with the occurrence of highly distorted elements induced by local, very large deformations (e.g. Susila and Hryciw, 2003)<sup>4</sup>. Large element distortions occur even for relatively small values of friction coefficient, i.e. around  $\mu = 0.1$  (e.g. Sheng et al., 2006).

Van der Berg (1994) proposed a large deformation analysis using *Eulerian* formulation as an alternative approach to UL. Unlike the Lagrangian approach where the material points are coupled with the nodal points of the finite element mesh, in the Eulerian the material flows through the finite element mesh and the geometry is fixed (i.e. material and nodal points are uncoupled). In this approach, however, the treatment of moving boundaries, constitutive equations and time derivatives may prove to be complicated (Belytschko et al., 2000, Chapter 7).

In order to maintain a high-quality mesh throughout the analysis, Van der Berg (1994) proposed a large strain analysis using the *Arbitrarily Lagrangian-Eulerian* formulation which combines the pure Lagrangian and pure Eulerian analyzes. The ALE adaptive meshing maintains the topologically similar mesh thanks to introducing additional continuous state variable fields (e.g. stress, strain, hardening parameter) by interpolation of nodal stresses and strains. Distorted regions are then remeshed and the interpolated state variable fields

---

<sup>3</sup>The steady state is defined by a constant cone resistance vs. increasing penetration depth for the smooth soil-cone interface.

<sup>4</sup>The problem of mesh distortion under large deformations and its effect on accuracy of results is further discussed in Section 7.2.2.3.

are remapped to the new mesh. The features of the remeshing approach were also presented using the explicit iteration technique to simulate the cone penetration in sand obeying Drucker-Pruger criterion (Susila and Hryciw, 2003) and in a purely cohesive material (Walker and Yu, 2006). Although the ALE method seems to be suitable for large deformation problems with highly distorted meshes, its application to the coupled hydro-mechanical analysis of the penetration problem is extremely difficult and still limited due to the necessity of handling both deformations and fluid flow (Nazem et al., 2008). An effective coupled analysis of cone penetration thus requires a robust remeshing procedure which satisfies stability of calculations for each time increment. Lu et al. (2004) used the remeshing and interpolation with small strain technique (RITSS, Hu and Randolph, 1998) to tackle the large deformation problem of penetration in Tresca material. In this approach, small strain analysis increments are followed by remeshing and interpolation of state variables. Markauskas et al. (2005) presented a combined FE remeshing technique for the coupled penetration analysis in Drucker-Pruger/Cap model. The remeshing method involves superconvergent patch recovery technique for Gauss point state variables and polynomial interpolation for pore pressure nodes.

Despite many advancements in the existing numerical procedures, the realistic coupled analysis of the penetration problem in cohesive soil still remains challenging. To recapitulate, an effective FE model should simultaneously involve large strain and deformation analysis using the frictional cone-soil interface, the efficient remeshing technique and, finally, a realistic soil model which would account for factors such as stress history, anisotropy and even soil sensitivity.

**Combined analyzes.** Since the individual interpretation theories may include particular assumptions and limitations, the combination of two approaches may lead to more realistic solutions. Some examples can be found in the literature such as combinations of SPM-FEM (Teh and Houlsby, 1991), SPM-CEM (Yu and Whittle, 1999) or CEM-FEM (Abu-Farsakh et al., 2003).

### 6.3.2 Interpretation of CPTU measurements

The following section mainly reviews the most standardized and common approaches to the interpretation of soil characteristics from CPT data in fine-grained materials. The review is also limited to the solutions that are used in this study to compare results obtained using the existing methods and NN-based predictions (see Sections 8.2 and 9.2). For extended reviews of interpretation approaches for CPT and further comprehensive discussions on the existing methods, please refer to general reports on the topic (Jamiolkowski et al., 1985; Lunne et al., 1997; Schnaid, 2005; Mayne, 2006, 2007).

The evaluation of geotechnical properties based on the standard cone measurements is based on three independent measurements of cone resistance  $q_c$ , sleeve friction  $f_s$  and pore pressure  $u_2$ . In practice,  $q_c$  is corrected in order to



account for "the unequal area effect". The corrected cone tip resistance  $q_t$  is calculated as:

$$q_t = q_c + (1 - a_n)u_2 \quad (6.34)$$

where  $a_n$  is the net area ratio of the cone (see Lunne et al., 1997). While the values of  $q_t$  and  $u_2$  are typically used to evaluate mechanical or consolidation characteristics, the  $f_s$  records are mainly used for soil type classification and assessment of the unit weight  $\gamma$  (Lunne et al., 1997; Mayne, 2007).

### 6.3.2.1 Normalization of CPTU data

Conceptually, normalization of data in terms of initial stress conditions removes the effect of depth. Although the mechanism of penetration is mainly influenced by the effective horizontal stress, the normalization of cone resistance is commonly carried out in terms of vertical effective stress  $\sigma'_{vo}$ , since there is often little information about  $\sigma'_{ho}$  (Robertson, 1990). The following is the standard calculation of the normalized cone resistance:

$$Q_t = \frac{q_t - \sigma_{vo}}{\sigma'_{vo}} \quad (6.35)$$

The friction resistance is normalized using the net cone resistance  $q_n = q_t - \sigma_{vo}$ :

$$F_r = \frac{f_s}{q_t - \sigma_{vo}} \quad (6.36)$$

where  $F_r$  denotes the normalized friction ratio.

As recommended by Wroth (1984), the remaining measured variable  $u_2$  can be normalized using the pore pressure ratio:

$$B_q = \frac{u_2 - u_o}{q_t - \sigma_{vo}} \quad (6.37)$$

where  $u_o$  is the *in situ* pore pressure.

$B_q$  is analogous to the Skempton's pore pressure parameter ( $A_f$ ) referred to the triaxial shear test (Mayne and Bachus, 1988).

### 6.3.2.2 Undrained shear strength

As already discussed in Section 2.1, no unique undrained shear strength exists. The value of  $c_u$  depends on many factors such as soil history, material and stress anisotropy, strain rate, and shear failure mode, etc. As presented in the theoretical background the analytical solutions for cone resistance are based on the bearing capacity method, cavity expansion method, strain path method, numerical methods such as finite element method or finite difference method. The common relation which links the cone resistance  $q_c$  and  $c_u$  for all these approaches is related to the bearing capacity theory and can be written as:

$$q_c = N_c c_u + \sigma_o \Rightarrow c_u = \frac{q_c - \sigma_o}{N_c} \quad (6.38)$$

where  $\sigma_o$ , depending on the theory, can be  $\sigma_{vo}$ ,  $\sigma_{ho}$  or  $p_o$ , and  $N_c$  denotes a cone factor.

As pointed out by Lunne et al. (1997) and Houlsby (1998), the *in situ* horizontal effective stress  $\sigma'_{ho}$  has the dominant effect on the cone tip and friction sleeve resistance. In practice, however, normalization in terms of  $\sigma_{vo}$  is preferable because a reliable evaluation of  $\sigma_{ho}$  is often not available. Using  $\sigma_{vo}$ , the cone factor can be defined in terms of the cone tip resistance  $q_t$  and  $c_u$  as:

$$N_{kt} = \frac{q_t - \sigma_{vo}}{c_u} \quad (6.39)$$

As recognized in previous studies (e.g. Teh and Houlsby, 1991; Van der Berg, 1994; Yu et al., 2000; Su and Liao, 2002; Lu et al., 2004),  $N_{kt}$  depends on relative soil rigidity, stress anisotropy, strength anisotropy, cone roughness, cone geometry and other factors:

$$N_{kt} = N_{kt}(I_r, \Delta, A_r, \alpha_f, \Omega, \dots) \quad (6.40)$$

where  $I_r = G/c_u$  denotes the rigidity index,  $\Delta$  is the initial stress anisotropy parameter,  $\Delta = (\sigma_{vo} - \sigma_{ho})/2c_u$  (Teh and Houlsby, 1991),  $A_r$  is the strength anisotropy ratio,  $\alpha_f$  is the cone roughness and  $\Omega$  represents the geometry.

Since the cone factor is calibrated for a specific site using the benchmark values of  $c_u$ , the value of  $N_{kt}$  is also affected by the shear mode of a particular test. Using FVT as a reference test for the normally consolidated marine clays, Lunne and Kleven (1981) obtained the values falling between 11 and 19 with the average value of 15. Rad and Lunne (1988), for variously overconsolidated marine clays obtained the values of  $N_{kt}$  between 8 to 29 referencing to  $c_u$  from the triaxial test. It must also be noted that an underestimated  $c_u$  due to, for example, disturbance effects may lead to an overestimation of  $N_{kt}$ .

Over the years, many theoretical interpretations of  $N_{kt}$  have been proposed in the literature. Some solutions, collected in Table 6.2, clearly present the dependence of stress anisotropy ( $\Delta$ ), soil strength and stiffness ( $I_r$ ), and the cone roughness ( $\alpha_f$ ) on  $N_{kt}$ . The values of  $N_{kt}$  for  $I_r = 25 \div 1000$  vary from 6 to 21.

Table 6.2: Comparison of cone factors derived in various studies.

Cone factor $N_{kt}$	Method	Remarks	Reference
$1.33 + 1.33 \ln I_r$	CEM	spherical cavity	Vesic (1972)
$1.25 + 1.84 \ln I_r + 2\alpha_f - 2\Delta$	SPM	von Mises	Teh and Houlsby (1991)
$(1.67 + I_r/1500) \cdot (1 + \ln I_r) + 2.4\alpha_f$	SPM+FEM	von Mises	Teh and Houlsby (1991)
$1.51 + 2.00 \ln I_r$	SPM	based on Baligh (1985)	Van der Berg (1994)
$1.93 + 2.00 \ln I_r$	SPM+CEM		Yu and Whittle (1999)
$0.33 + 2.00 \ln I_r + 2.37\phi_i/\phi'_c - 1.83\Delta$	FEM	MCC model	Yu et al. (2000)
$\frac{1+A_r}{\sqrt{1+2A_r}} \ln I_r + \frac{1-A_r}{3} + R_r \left[ 1 + \frac{1+A_r}{\sqrt{1+2A_r}} + 0.52A_r^{1/8}(1+A_r) \right] - 2\Delta$	CET	anisotropic $c_u$ model	Su and Liao (2002)
$2.45 + 1.80 \ln I_r - 2.1\Delta$	FEM	MCC model	Abu-Farsakh et al. (2003)
$3.40 + 1.60 \ln I_r + 1.3\alpha_f - 1.9\Delta$	FEM	Tresca	Lu et al. (2004)
$0.20 + 2.02 \ln I_r - 1.95\Delta$	FEM explicit	von Mises	Walker and Yu (2006)

$\alpha_f$  - cone roughness factor ( $0 \leq \alpha_f \leq 1$ ) and  $\alpha_f = 1$  corresponds to fully rough cone.

$\phi_i$  - interface friction angle.

$A_r$  - strength anisotropy ratio ( $= c_{ue}/c_{uc}$ ).

$R_r$  - roughness factor equal to 3.13 and 1.39 for rough and smooth cone, respectively.

Another relationship that can be established for  $c_u$  is based on the cavity expansion theory and includes excess pore water pressure:

$$N_{\Delta u} = \frac{\Delta u}{c_u} \quad (\Delta u = u_2 - u_o) \quad (6.41)$$

The results for the cavity expansion solution give the values of  $N_{\Delta u}$  from 2 to 20. The experimental evidence based on triaxial tests provides values of  $N_{\Delta u}$  between 4 and 10 and shows its dependence on the overconsolidation ratio and soil sensitivity (Lunne et al., 1997; Karlsrud et al., 2005). By analogy to  $N_{kt}$ , a higher level of confidence for  $c_u$  values is obtained by a specific-site calibration of  $N_{\Delta u}$ .

The undrained shear strength can also be estimated using the cone factor  $N_{ke}$  which corresponds to the "effective" cone resistance  $q_e$ :

$$N_{ke} = \frac{q_e}{c_u} = \frac{q_t - u_2}{c_u} \quad (6.42)$$

According to experimental evidence, the value of  $N_{ke}$  may vary between 1 and 13. In practice, this approach shows much uncertainty in soft normally consolidated clays as the measured  $u_2$  is often 90% or more of the measured cone resistance leading to small numbers of  $q_e$  (Lunne et al., 1997). In effect, the interpretation is sensitive to small errors in  $q_c$ .

### 6.3.2.3 Effective stress strength

The estimation of effective stress parameters from the total stress analysis of undrained penetration is difficult. The solution needs to account for excess pore water pressure for which the distribution around the cone is highly complex and difficult to model analytically. Interpretation methods can be thus viewed as rather approximative.

The effective friction angle  $\phi'$  can be estimated using the solution which is based on the bearing capacity theory (Sandven et al., 1988)<sup>5</sup>:

$$q_t - \sigma_{vo} = N_m(\sigma'_{vo} + a) \quad \text{with} \quad N_m = \frac{N_q - 1}{1 + N_u B_q} \quad (6.43)$$

where  $a'$  denotes the attraction ( $a' = c' \cot \phi'$ ),  $\beta$  is the angle of plastification,  $N_q$  and  $N_u$  are the bearing capacity factors ( $N_q = N_q(\phi', \beta)$  and  $N_u \cong N_u(\phi)$ ). Mayne (2005, 2007) proposed a simplified expression applying to the ranges of  $20^\circ \leq \phi' \leq 45^\circ$  and  $0.1 \leq B_q \leq 1.0$ . By setting for the above method the effective cohesion intercept  $c' = 0$  and plastification angle  $\beta = 0$ , the values of  $\phi'$  were evaluated line-by-line and the following approximate expression was obtained:

$$\phi' \approx 29.5^\circ B_q^{0.121} (0.256 + 0.336 B_q + \log Q_t) \quad (6.44)$$

<sup>5</sup>The approach proposed by researchers from the Norwegian University of Science and Technology (NTNU) is referred to NTNU method in Section 8.2.5.2.

### 6.3.2.4 Stress history

Over the years, many different approaches have been proposed for interpreting the stress history (see e.g. Mayne, 1991; Lunne et al., 1997; Mayne et al., 2001; Demers and Leroueil, 2002). The stress history is typically represented by the overconsolidation ratio OCR which is defined as the ratio of the gross effective yield stress and the actual effective overburden stress ( $\text{OCR} = \sigma'_p / \sigma'_{vo}$ ).

One of the best working approaches relates the preconsolidation pressure to the net cone resistance:

$$\text{OCR} = k_{\sigma t} \frac{q_t - \sigma_{vo}}{\sigma'_{vo}} = k_{\sigma t} Q_t \quad (6.45)$$

where  $k_{\sigma t}$  is an empirical coefficient which falls in the interval from 0.1 to 0.5 for non-fissured clays (Larsson and Mulabdić, 1991; Hight and Leroueil, 2003). The higher values are suggested for cemented, aged and heavily consolidated soils (between 0.9 and 2.2). Clearly, this coefficient needs to be calibrated for specific site conditions. However, the first-order approximates of OCR can be obtained using the values of  $k_{\sigma t}$  from multiple regression analyzes which are based on historical syntheses from many characterization sites (see Table 6.3). Mayne (2006) suggests assuming  $k_{\sigma t} = 0.30$  for first-order estimates. However, even well correlated data in terms of the coefficient  $R^2$  may present large scatter and should also be evaluated in terms of the mean squared error MSE.

Table 6.3: Comparison of the empirical coefficients obtained from multiple regression analyzes for non-fissured clays.

Ref.	Geographical region	Results of regression analysis					
		Number of sites/points	$k_{\sigma t}$	$R^2$	Number of sites/points	$k_{\sigma e}$	$R^2$
[1]	Sweden	9/110	0.292	-	9/110	0.50	-
[2]	Canada	31/153	0.294	0.90	31/153	0.546	0.96
[3]	Worldwide	123/1121	0.305	0.84	84/811	0.50	0.75

[1] Larsson and Mulabdić (1991); [2] Demers and Leroueil (2002);  
 [3] Chen and Mayne (1994, 1996)

Another approach combines measurements of cone resistance and pore pressure by means of the effective cone resistance:

$$\text{OCR} = k_{\sigma e} \left( \frac{q_t - u_2}{\sigma'_{vo}} \right) = k_{\sigma e} \frac{q_e}{\sigma'_{vo}} \quad (6.46)$$

with  $k_{\sigma e}$  being obtained through site-specific correlations. By analogy to the previous approach, the first-order approximates of OCR can be obtained using the values of  $k_{\sigma e}$  through regression analyzes (see Table 6.3). Mayne (2006, 2007) suggested assuming  $k_{\sigma e} = 0.60$  for the first-order estimates. This approach is often used as a comparative to the previous one and local correlations

are strongly recommended. The formula is also viewed as less reliable in soft, lightly overconsolidated clays the  $q_t$  results accompanied by large values of  $u_2$  yield in a small number for  $q_t - u_2$  (Houlsby, 1988; Lunne et al., 1997).

A method combining the solution for the spherical cavity expansion with the undrained shear strength related to the critical state concept of the MCC was proposed by Mayne (1991). Adopting the undrained shear strength for the spherical expansion case as (Wroth, 1984; Cao et al., 2001):

$$c_u = \frac{Mp'_o}{2} \left( \frac{R_p}{2} \right)^\Lambda \quad (6.47)$$

and introducing some simplifications, Mayne (1991) obtained the following expression to interpret the overconsolidation ratio:

$$\text{OCR} = 2 \left[ \frac{1}{1 + 1.95M} \left( \frac{q_t - u_2}{\sigma'_{vo}} \right) \right]^{\frac{1}{\Lambda}} \quad (6.48)$$

where the mean value for  $\Lambda$  can be assumed for the first-order estimates as around  $0.75 \div 0.80$  (Wroth and Houlsby, 1985; Mayne, 1991).

Fairly recently, a similar expression was proposed by Chang et al. (2001) based on a rigorous closed-form analysis of the undrained cavity expansion in the MCC (Cao et al., 2001, see Section 6.2.2). For pore pressure measurements behind the cone tip, Chang et al. (2001) proposed using the solution based on the cylindrical expansion for most clays:

$$\text{OCR} = 2 \left[ \frac{1}{1 + 0.67M} \left( \frac{0.866q_t + 0.134\sigma_{vo} - u_2}{\alpha_\varepsilon \sigma'_{vo}} \right) \right]^{\frac{1}{\Lambda}} \quad (6.49)$$

while for the sensitive and special clays, they suggested using the solution for the spherical expansion:

$$\text{OCR} = 2 \left[ \frac{1}{\alpha_\varepsilon(1 + 0.67M)} \left( \frac{q_t - u_2}{\sigma'_{vo}} \right) \right]^{\frac{1}{\Lambda}} \quad (6.50)$$

Such an approach was explained by the fact that the spherical expression gives values of  $B_q$  larger than 0.75 which are observed in the sensitive clays<sup>6</sup>. A coefficient  $\alpha_\varepsilon$  which appears in both expressions is introduced to account for the strain rate effect and is expressed as:

$$\alpha_\varepsilon = \frac{c_u^{\text{CPT}}}{c_u^{\text{ref}}} \quad (6.51)$$

In the above expression  $c_u^{\text{CPT}}$  is the value of the undrained shear strength that corresponds to the strain rate related to the advancing cone ( $\dot{\varepsilon}^{\text{CPT}}$ ), whereas  $c_u^{\text{ref}}$  is the undrained shear strength obtained for a reference test. The question arises how the true strain rate for the penetration test can be calculated. The

---

<sup>6</sup> $B_q = 0.75$  is the upper bound of the cylindrical solution for  $I_r = 300$ .

CPT pseudo-strain rate for a standard  $10\text{cm}^2$  cone ( $D = 35.7\text{cm}$ ) with the advancing rate of  $v = 2\text{cm/s}$  can be estimated as  $v/D$  (Mayne, 2006), providing the value of  $\dot{\varepsilon}^{\text{CPT}}$  is equal to  $2 \cdot 10^5\%/h$ . By assigning the reference strain rate as for a typical triaxial compression test rate of  $\dot{\varepsilon}^{\text{TC}} = 1\%/h$  and using Equation 6.33, the coefficient  $\alpha_\varepsilon$  is equal to 1.53 (i.e. 53%-overstimation of  $c_u$  for the five orders of magnitude a large strain rate). The CPT strain rate can also be calculated using the radial strain rate for the spherical cavity expansion as (Chang et al., 2001):

$$\dot{\varepsilon}_c = \frac{d\varepsilon_c}{dt} = \frac{2}{a} \frac{da}{dt} \quad (6.52)$$

For the standard cone, the above expression leads to the strain rate  $\dot{\varepsilon}^{\text{CPT}}$  equal to  $8 \cdot 10^5\%/h$  which gives the coefficient  $\alpha_\varepsilon$  equal to 1.59.

Assuming that the strain rate factor  $\alpha_\varepsilon$  for  $c_u$  is equal to 1.53, the strain

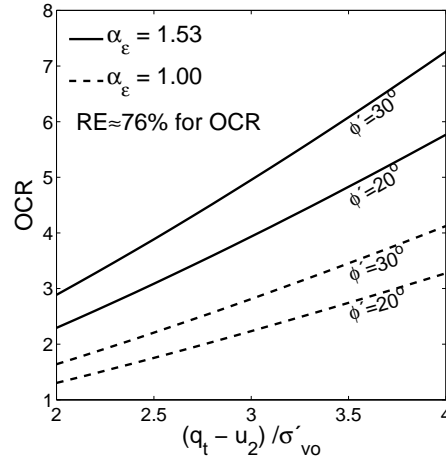


Figure 6.22: Theoretical assessment of strain rate effect on OCR from CPTU.

factor for overconsolidation ratio ( $\text{OCR}^{\text{CPT}} / \text{OCR}^{\text{TC}}$ ) can be theoretically evaluated from Equation (6.50) ( $\Lambda = 0.75$ ) to be equal around 1.76 (see Figure 6.22).

### 6.3.2.5 Horizontal stress

The horizontal *in situ* stress can be represented by the coefficient of earth pressure at rest  $K_o = \sigma'_{ho} / \sigma'_{vo}$ . At present, no reliable method exists for the CPT data. Rough evaluations related directly to CPTU measurements can be made using various approximative methods.

Observing that the pore pressure distribution around the cone is a function of  $\sigma'_{ho}$ , Sully and Campanella (1991) proposed to approximate  $K_o$  based on a linear regression analysis using the normalized difference between pore pressure measured behind the cone tip and sleeve shoulder ( $\text{PPSV} = (u_1 - u_2) / \sigma'_{vo}$ ).

Masood and Mitchell (1993) proposed the estimation of  $K_o$  based on  $f_s$  measurements. In this method,  $K_o$  is a function of the normalized sleeve friction

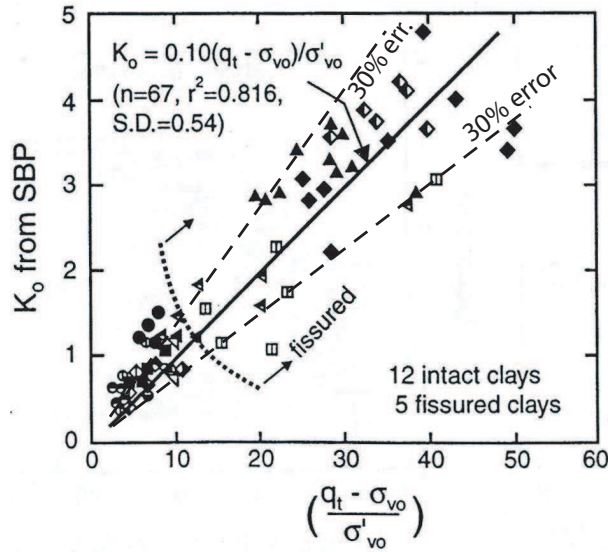


Figure 6.23: General  $K_o$  correlation for CPTU data proposed by Kulhawy and Mayne (1990) (from Lunne et al. (1997)).

$f_s/\sigma'_{vo}$  and the overconsolidation ratio OCR. Thus the approach requires prior evaluation of OCR and reliable measurements of  $f_s$ .

The most popular technique for estimating  $K_o$  employs an empirical formula which is based on the normalized cone resistance:

$$K_o = k_K \left( \frac{q_t - \sigma_{vo}}{\sigma'_{vo}} \right) \quad (6.53)$$

where  $k_K$  is an empirical parameter. Using the regression analysis, Kulhawy and Mayne (1990) obtained the value of  $k_K = 0.1$  for several  $K_o$  values estimated from SBPT (Figure 6.23). However, a considerable scatter for this correlation is observed and  $k_K$  should be calibrated for a specific site.

### 6.3.2.6 Stiffness characteristics

The group of deformation characteristics for clays includes one dimensional constrained modulus  $M_D$ , the Young's modulus for undrained compression  $E_u$ , the secant shear modulus  $G$ , the small-strain shear modulus  $G_o$  (or  $G_{max}$ ), etc. The identification of the latter applies strictly to nondestructive geophysical methods which are associated with measurements of the shear wave velocity ( $V_s$ ). As regards penetration testing, the measurements of  $V_s$  are typically made using the seismic cone (SCPT, Campanella et al., 1986) and the small-strain shear modulus is obtained through  $G_o = \rho V_s^2$ .

The one-dimensional constrained modulus is obtained for steady state measurements based on the oedometer test through the expression:

$$M_D = \frac{\Delta \sigma'_v}{\Delta \varepsilon_v} \quad (6.54)$$



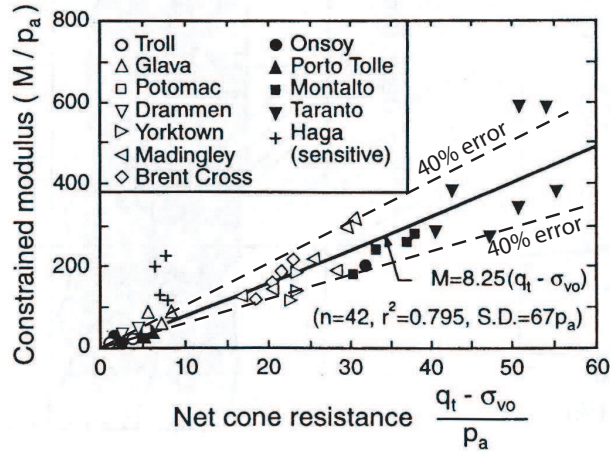


Figure 6.24: General  $M_D$  correlation for CPTU data proposed by Kulhawy and Mayne (1990) (from Lunne et al., 1997).

which can also be expressed as:

$$M_D = \frac{2.3(1+e)\sigma'_v}{C_c} = \frac{(1+e)\sigma'_v}{\lambda} \quad (6.55)$$

where  $C_c$  is the compression index ( $C_c = 2.3\lambda$ ).

The constrained modulus can be interpreted from the CPTU using the net cone resistance:

$$M_D = \alpha_n(q_t - \sigma_{vo}) \quad (6.56)$$

where  $\alpha_n$  is observed for most clays between 5 and 15 while for normally consolidated clays, it is between 4 to 8 (Sandven et al., 1988; Senneset et al., 1989). A more general correlation was suggested by Kulhawy and Mayne (1990) (cf. Figure 6.24):

$$M_D = 8.25(q_t - \sigma_{vo}) \quad (6.57)$$

As discussed by Lunne et al. (1997), the estimation of "drained" parameter  $M_D$  from an undrained penetration test using general empirical correlations may suffer from errors as large as  $\pm 100\%$ . An individual site-specific calibration is thus recommended for  $\alpha_n$ . They also concluded that it is difficult to correlate "drained" parameters without accounting for the pore pressure measurements as the cone resistance is measured in total stress.

### 6.3.2.7 Rigidity index and consolidations characteristics

In general, the consolidation characteristics of clays are usually represented by the consolidation coefficient  $c$  or the permeability coefficient  $k$  which can be related through:

$$c = k \frac{M_D}{\gamma_w} \quad (6.58)$$

where  $\gamma_w$  is the unit weight of water and  $M_D$  is the constrained modulus relevant to the modeled problem.

The consolidation characteristics which can be interpreted from the CPTU dissipation test are usually predominately associated with the direction that is perpendicular to the cone axis, typically horizontal:  $c_h$  and  $k_h$ . Typically, in natural soft homogeneous clays ratio  $k_h/k_v$  is smaller than 1.5 while larger values are expected in sedimentary and varved clays<sup>7</sup>.

Over the years, several analytical and numerical solutions have been proposed to estimate  $c_h$  from the monitored decay of excess pore water pressure in time (after the penetration has been paused). These methods are based on the solutions for the one-dimensional cavity expansion (Torstensson, 1977; Randolph and Wroth, 1979, see Equation (6.32)) or the two dimensional strain path analysis (Levadoux and Baligh, 1986; Baligh and Levadoux, 1986; Teh and Houlsby, 1991; Burns and Mayne, 1998). Based on the solution for an elastoplastic soil model for which the soil stiffness can be expressed by the rigidity index  $I_r$ , Teh and Houlsby (1991) suggested a modified dimensionless time factor  $T^*$  for the consolidation process:

$$T^* = \frac{c_h t}{a^2 \sqrt{I_r}} \quad (6.59)$$

where  $a$  is the probe radius and  $t$  denotes the dissipation time. The above solution was graphically interpreted by Robertson et al. (1992) to estimate  $c_h$  from the measured time  $t_{50}$  required for 50% of consolidation.

The soil permeability, if not predicted approximatively based on the soil behavior type (see Lunne et al., 1997), can be back-calculated using Equation 6.58. This approach requires the estimation of  $I_r$  to determine  $c_h$  and evaluated  $M_D$ . Alternative approaches for interpreting  $k$  from CPTU concern on-the-fly measurements (e.g. Song et al., 1999; Voyiadjis and Song, 2003; Elsworth and Lee, 2007).

The knowledge about the value of rigidity index  $I_r$  is generally required to predict  $c_u$ ,  $c_h$  or  $k$  from piezocone data. Formally, the rigidity index is defined as the ratio of shear modulus and undrained shear strength  $I_r = G/c_u$ . If any other approach to evaluate rigidity index is not available (e.g. laboratory compression test or pressuremeter test),  $I_r$  can be approximated through the expression derived from a combination of the solution for the spherical cavity expansion,  $c_u$  for the MCC concept and Equation (6.48) (Mayne et al., 2001):

$$I_r = \exp \left[ \left( \frac{1.5}{M} + 2.925 \right) \left( \frac{q_t - \sigma_{vo}}{q_t - u_2} \right) - 2.925 \right] \quad (6.60)$$

An empirical formula obtained for series of triaxial CK<sub>o</sub>UC tests (Keaveny and Mitchell, 1986) can also be used as the first-order approximation (Mayne et al.,

---

<sup>7</sup>Refer to Lunne et al. (1997); Leroueil and Hight (2003) for the discussion on anisotropy of consolidation and flow characteristics.

2001):

$$I_r = \frac{\exp\left(\frac{137-PI}{23}\right)}{\left\{1 + \ln\left[1 + \frac{(OCR-1)^{3.2}}{26}\right]\right\}^{0.8}} \quad (6.61)$$

where PI is the plasticity index (here in %).

### 6.3.3 Effect of drainage conditions on penetration results

It is commonly recognized that in the case of *in situ* tests, the drainage conditions cannot be precisely controlled as in the case of laboratory tests. The interpretation methods for clays or sands can be unreliable when interpreting silty soils for which partial drainage may occur during penetration (Lunne et al., 1995; Schnaid, 2005). According to the experimental field evidence provided by McNeilan and Bugno (1984, see Figure 6.25), the effect of partial drainage is believed to occur at the standard penetration rate (20mm/s) in materials with the permeability coefficient between  $10^{-9}$  to  $10^{-5}$  m/s. Such range of permeability coefficients is observed for silty clays to clayey sands (cf. Figure 6.17).

Since drainage conditions also depend on other consolidation characteristics, Finnie and Randolph (1994) suggested a non-dimensional analysis of the partial drainage effects on penetration resistance using normalized velocity which is defined as:

$$V = \frac{v \cdot d}{c_v} \quad (6.62)$$

where  $v$  denotes penetration velocity and  $d$  is the probe diameter. Based on Equation (6.58), the vertical coefficient for normally consolidated soil  $c_v$  can be expressed as:

$$c_v = \frac{k(1+e)}{\lambda} \frac{\sigma'_{vo}}{\gamma_w} \quad (6.63)$$

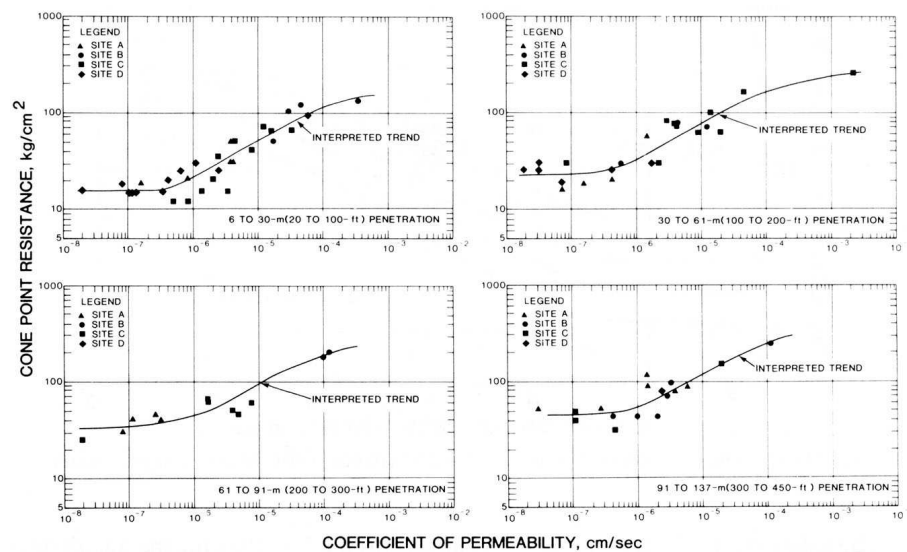


Figure 6.25: Effect of permeability on measured values of cone resistance in clayey silts to sandy silts (after McNeilan and Bugno, 1984).

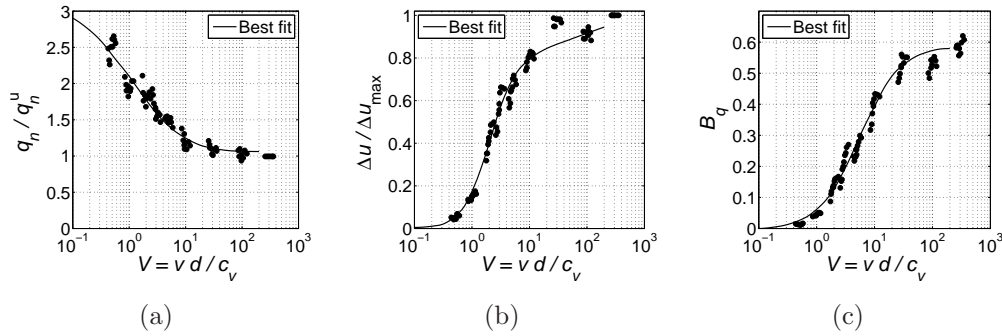


Figure 6.26: Effect of penetration rate on piezocone measurements, (a) net cone resistance, (b) excess pore water pressure, (c) pore pressure parameter (after Randolph and Hope, 2004).

Normalization introduced by means of  $V$  is thus relevant in laboratory tests because experiments can be performed in different drainage conditions by varying the penetration rate in the same type of soil instead of preparing different soil permeability mixtures (Randolph and Hope, 2004).

A number of laboratory studies has been carried out to examine the partial drainage effect on piezocone measurements (Randolph and Hope, 2004; Chung et al., 2006; Schneider et al., 2007). These studies confirm a gain in cone resistance with an occurrence of drainage, while measured pore pressures can undergo partial dissipation decreasing values of  $B_q$  as demonstrated in Figure 6.26. In their study, Randolph and Hope (2004) noted undrained conditions in normally consolidated kaolin for normalized velocity  $V$  larger than  $30 \div 100$ , while Schneider et al. (2007) obtained undrained penetration for  $V$  larger than 100 for kaolin and highly overconsolidated mixture of silica flour and bentonite slurry. Fully drained conditions can be expected when  $V$  is less than 0.01 (Hight and Leroueil, 2003).

### 6.3.4 Remarks

The interpretation of field tests requires a rigorous analysis which involves both deep bases of mechanics and practical geotechnical knowledge. The existing interpretation methods encompass simple, basic empirical formulas, as well as demanding numerical solutions including complex constitutive laws. Rational theoretical solutions can only be obtained through rigorous analyzes which should take into account many factors that may appear in the analyzed process. However the number of factors is often reduced due to mathematical restrictions and capabilities of the interpreting approach. The interpretation of field tests is thus subject to a large dose of uncertainty. The inaccuracies and uncertainty for interpreted parameters may stem from many reasons such as:

- negligence of partial drainage effects resulting in the mutual feedback for interpreted parameters;
- negligence of strain rate effects resulting in the increase of parameter val-

ues with respect to those obtained through laboratory tests;

- existence of various shear modes corresponding to different tests resulting in the non-uniqueness of parameters;
- negligence anisotropy of stress or measured parameters;
- representative selection of the relevant mathematical approach, constitutive model and boundary conditions adopted in the analysis of a specific test;
- existence of intercorrelations between parameters in both empirical, analytical or numerical solutions.

Although much effort was made to propose the closed-form solutions for the SBPT, the use of numerical simulations that would account for complex constitutive laws and a possible occurrence of partial drainage is necessary.

As regards the CPTU testing, the first-order assessment of geotechnical parameters is mostly based on general empirical or semi-empirical correlations which provide approximative estimations. A higher degree of accuracy requires correlating empirical coefficients with the results obtained for high-quality, intact samples from time-consuming laboratory testing. The use of analytical or numerical solutions is rather restricted to the materials for which observed behavior is closely related to the constitutive model considered in the inverse solution. However, the numerical models should include many factors affecting cone penetration such as material and geometrical non-linearities, stress and strength anisotropy, partial drainage and friction effects.



## Chapter 7

# Numerical Modeling of Selected Field Tests

*The progression of a painter's work  
as it travels in time from point to point,  
will be toward clarity ...  
toward the elimination of all obstacles  
between the painter and the idea ...  
and the idea and the observer ...  
To achieve this clarity is inevitably to be understood.*

Mark Rothko

As previously discussed in Sections 2.4 and 3.2, for the purpose of this study, neural network-based identification models are developed based on numerical pseudo-experiments representing a boundary value problem of a specific field test. The generation of NN training database thus relies on solving a number of example tests by means of a numerical model. In this study, an incremental finite element technique has been adopted to model and solve the boundary value problems of two commonly applied *in situ* tests, i.e. the self-boring pressuremeter and the piezocone.

The chapter is divided into two main sections related to the SBPT and the CPTU test respectively. Each section contains a detailed description of the developed numerical model as well as additional investigations including sensitivity analyzes of a specific model. For each model, the partial drainage effect on field measurements is also investigated. As regards the piezocone model, comparative analyzes with existing numerical models and experimental evidence are also presented. Finally, an equivalent semi-numerical model for the piezocone test is proposed, owing to the loss of accuracy observed when applying a "rough" frictional interface.

## 7.1 Numerical model of pressuremeter test

The main advantage of FE modeling of the pressuremeter test is that a BVP model is able to combine both a complex constitutive model and a time-dependent, hydro-mechanical coupling. The following section presents a simplified pressuremeter test model that accounts for possible partial drainage during cavity expansion.

### 7.1.1 Finite element model

Numerical parameter identification based on SBPT measurements was worked out for the elastic/plastic MCC model. The set of parameters to be identified by means of coupled hydro-mechanical analysis can be collected in vector  $\mathbf{b} = [\nu, M, R_p, \kappa, \lambda, k, e_o]$ . Since the elastic part of the pressuremeter expansion curve is affected by two independent variables, namely  $\nu$  and  $\kappa$ , both appearing in Equation (4.4), the solution of parameter identification can be non-unique. However, for clayey soils, the parameter  $\kappa$  exhibits a larger range of values than  $\nu$ , and thus, in the present parameter identification, Poisson's coefficient is assumed to be constant and equal to  $\nu = 0.32$ . This value was chosen as the designing average for clayey soils.

In order to analyze the coupled hydro-mechanical problem of the pressuremeter test, a finite element code Z\_Soil v.6 has been adopted as a numerical solver (ZACE, 2003). The finite element mesh of the pressuremeter test, shown in Figure 7.1, was discretized with the aid of 4-node axisymmetric quadrilateral finite elements. Thus, it was assumed that the model reflects soil behavior in the centered unit of the pressuremeter membrane. The finite element mesh was built with the full awareness of the existing analyzes of the  $L/D$  geometry effect (e.g. Yu et al., 2005). It was also assumed that the expansion takes place in a fully saturated medium. The radius of the outer boundary ( $30a_o$ ) is far enough from the inner radius,  $a_o$ , so that it does not affect numerical results at the cavity wall.

On the top and bottom boundaries of the FE model, vertical displacements and fluid flux in the vertical direction are precluded. At the external edge boundary condition, equivalent to the initial total radial stress  $\sigma_{ho}$ , and pore pressure boundary condition, equivalent to the initial pore pressure  $u_o$ , are enforced during the simulation. At the cavity wall, the hydraulic boundary conditions enable

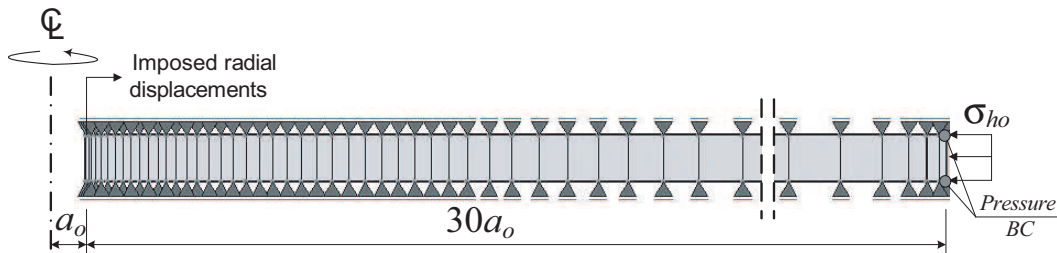


Figure 7.1: FE mesh of simplified axis-symmetrical model of the pressuremeter test.



the unconstrained development of excess pore water pressure so that the fluid flow, both in a normal and tangential direction, is precluded. The initial conditions consist of the initial effective stress state, which takes into account the effect of stress anisotropy, and the initial pore pressure. In the case of SBPT, we assume that disturbances due to probe installation can be neglected.

The loading programme is assumed to be displacement-controlled with resulting cavity strain rate of  $\dot{\varepsilon}_c = 1\%/min$ , following suggestions by Baguelin et al. (1978); Clarke et al. (1979). As typically for the expansion test, the cavity strain was increased up to  $\varepsilon_c = 8 \div 10\%$  (Benoit and Clough, 1986).

Simulations of the holding test were modeled by fixing displacements at the inner radius for SHT or, in the case of PHT, by holding the maximum cavity pressure constant. The latter is the maximal pressure obtained at the end of the expansion.

### 7.1.2 Effect of soil permeability

An analysis of the permeability influence on the PET was performed by means of a parametric study for the pressuremeter model developed in Section 7.1.1. Simulations were carried out for various values of permeability coefficient  $k = k_h$  in range  $10^{-12} \div 10^{-8} m/s$ , while the remaining model parameters were kept constant. The numerical results shown in Figure 7.2 reveal partial dissipation of excess pore water pressure during expansion for  $k$  larger than  $10^{-11} m/s$ . A similar effect was observed by (Fioravante et al., 1994). This indicates that the partial drainage may practically occur even for low-permeable clays (cf. Figure 6.17) as the undrained conditions are satisfied for  $k$  less than  $10^{-11} m/s$ .

As previously demonstrated in Figure 6.18, the drainage affects the shape of the effective stress paths. Partial consolidation leads to a local hardening in the soil elements adjacent to cavity wall and, in effect, may increase an apparent

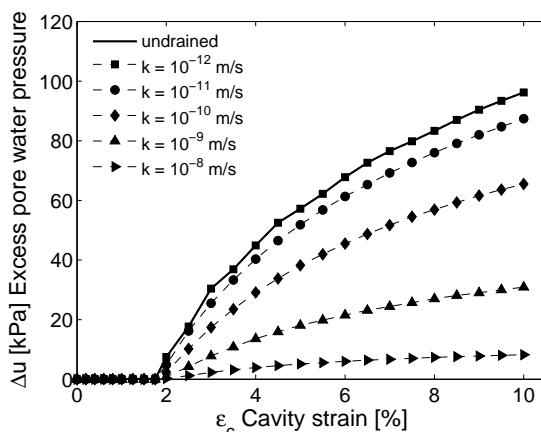


Figure 7.2: Effect of permeability on excess pore water pressure in the PET with the cavity strain rate of 1.0%/min.

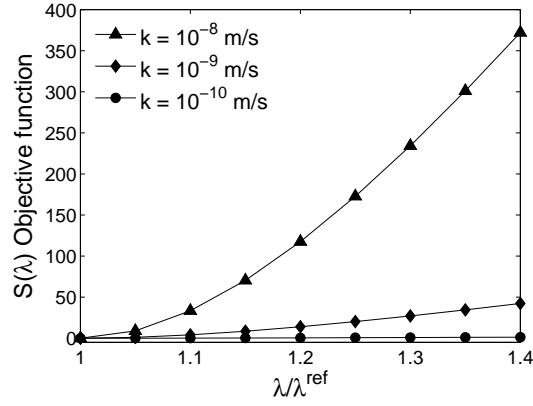


Figure 7.3: Sensitivity of the pressuremeter expansion curve shape to changes of the slope of a normal consolidation line  $\lambda$  in different drainage conditions.

undrained shear strength. Since the undrained shear strength  $c_u$  is a function of the preconsolidation pressure  $p_{co}$  and the slope of critical state line  $M$ , the identification of strength parameters may result in their overestimation. Thus the use of numerical simulations is recommended instead of relying on analytical solutions that are based on assumptions of an undrained expansion.

In the following analysis, the influence of the consolidation parameter  $\lambda$  on the shape of the pressuremeter expansion curve  $\varepsilon_c - \psi$  was investigated with respect to partial drainage conditions. The reference value  $\lambda^{ref}$  (see Table B.1) was perturbed from 0 to 40% for three different drainage conditions defined by  $k$ . The influence of  $\lambda$  was measured in terms of the least-squared objective function (Equation (2.6),  $\omega = \mathbf{I}$ ) which was computed in each case for all discrete measurements and with respect to the measurements corresponding to the undrained case. The analysis is graphically presented in Figure 7.3, wherein the vertical axis represents the magnitude of the objective function,  $S(\lambda)$ , and the horizontal axis is plotted as the normalized slope of the normal consolidation line,  $\lambda/\lambda^{ref}$ . It can be concluded that  $\lambda$  has negligible influence, or no influence at all, on the pressuremeter expansion curve if  $k$  is less than  $k = 10^{-9}$  m/s. In such a case the identification of other parameters can be performed even for an imprecisely estimated value of  $\lambda$  because it does not change the shape of the stress-strain curve ( $\varepsilon_c - \psi$ ). On the other hand, in the case of  $k > 10^{-9}$  m/s, the identification of  $\kappa$ ,  $M$ ,  $p_{co}$  should be preceded by the precise evaluating the parameter  $\lambda$  or include the results from the PHT (see Section 6.2.5). The presented results indicate growing sensitivity of the expansion curve to both increasing soil permeability and inaccurately evaluated  $\lambda$ .

### 7.1.3 Non-uniqueness and sensitivity of strength parameters

Non-uniqueness of model parameters in the identification process is often observed in the case of non-linear problems. Non-uniqueness may lead to several combinations of values of parameters providing the same response of a system (e.g. Hicher and Michali, 1996; Ledesma et al., 1996a; Gens et al., 1996; Zentar et al., 2001; Calvello and Finno, 2002). The non-uniqueness of the strength parameters in the MCC is the result of model properties. The elliptical yield surface, described in Equation (4.1), combines two parameters  $M$  and  $p_{co}$ . Since both parameters define the undrained shear strength of the MCC (see Equation (6.22)), their identification from a single  $\varepsilon_c - \phi$  curve may lead to the same solution for different parameter combinations (see Figure 7.4(a)). In the context of parameter identification, this problem can be viewed as an existence of equivalent minima in the space of parameters (see Figure 7.4(b)). On the other hand, two pairs of parameters produce different effective stress paths. Hence, the simultaneous identification of both parameters by means of NN or GBO requires accounting for data measured by the SBP pore pressure sensors.

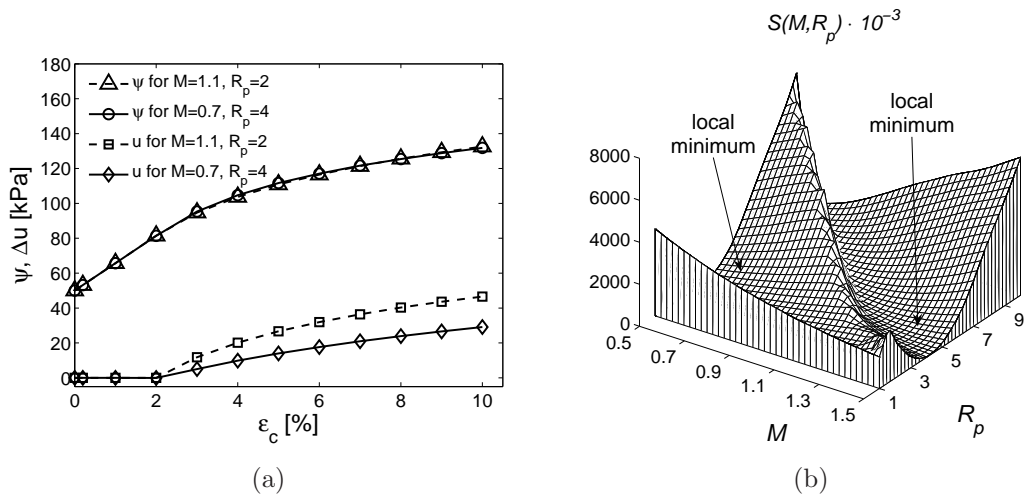


Figure 7.4: Non-uniqueness of strength parameters  $M$  and  $p_{co}$  (a) with respect to the total stress expansion curve  $\varepsilon_c - \psi$ , (b) in terms of the least square objective function  $S(M, R_p)$ .

### 7.1.4 Effect of stress anisotropy

The initial *in situ* stress is another factor that affects pressuremeter results. The stress anisotropy can be expressed by the coefficient of earth pressure 'at rest'  $K_o = \sigma'_{ho}/\sigma'_{vo}$ . The analysis of the stress anisotropy effect was performed using "undrained" simulations for various  $K_o$  values perturbed with respect to  $K_o^{ref}$ . In the analysis, preserving the reference values<sup>1</sup> of  $R_p$  and  $p_{co}$  described in terms of the mean stress, required different combinations of  $\sigma'_{ho}$  and  $\sigma'_{vo}$  to

<sup>1</sup>The reference parameters values are provided in Table B.1.

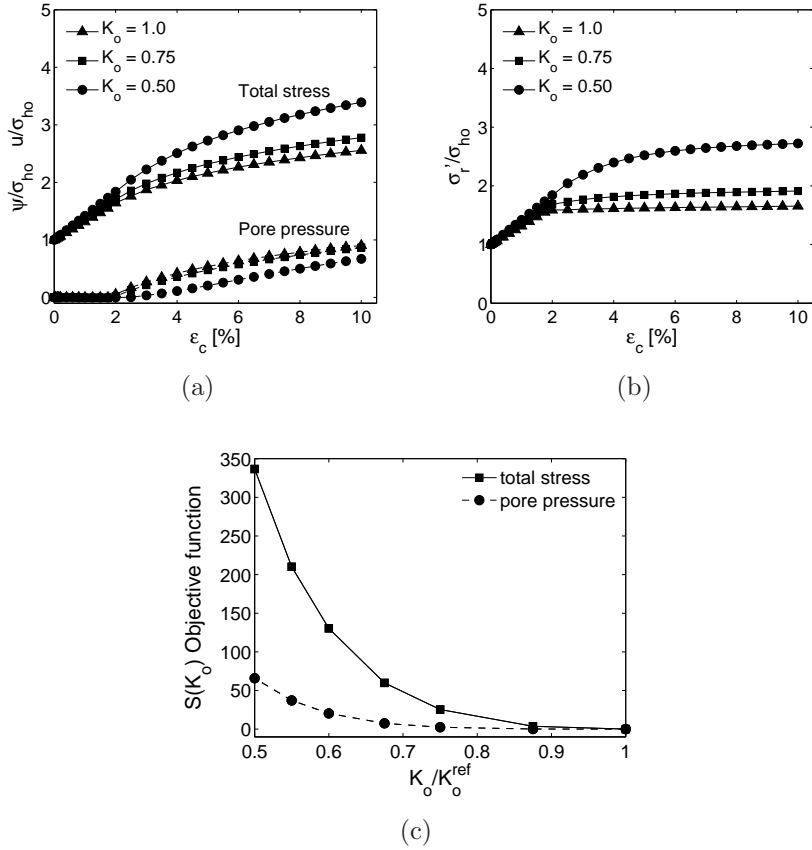


Figure 7.5: Effect of *in situ* stress anisotropy on the expansion curve presented in terms of  $K_o$ : (a) evolution of the total radial stress and excess pore water pressure, (b) evolution of the effective radial stress, (c) variation of the least-squared error function with respect to perturbed  $K_o^{ref}$  value.

obtain various  $K_o$  values. Consequently, in order to present quantitative results on the same chart, the total stress and pore pressure curves were normalized by the initial horizontal stress  $\sigma'_{ho}$ . The results of the evolution of the total stress acting on the cavity wall and excess pore water pressure with respect to the cavity strain are shown in Figure 7.5(a) while Figure 7.5(b) presents changes in the effective stress. It can be noticed that with a linear decrease of  $K_o$ , an exponential increase of the ultimate effective stress can be observed.

The influence of stress anisotropy was also measured in terms of the least-squared objective function computed with respect to the results from the reference simulation for  $K_o^{ref}$ . Simulations were computed for perturbed values of  $K_o^{ref}$  from 0 to 50%. The variation of the error function  $S(K_o)$ , with respect to the ratio  $K_o/K_o^{ref}$  is shown in Figure 7.5(c). The chart shows that a small error for  $K_o$  up to about 10% may not significantly affect the pressuremeter curves. It means that in this range an imprecise identification of  $K_o$  has a negligible influence on other parameters to be identified. On the other hand, a strong, exponentially increasing influence on the pressuremeter expansion curves is observed for the  $K_o$ -identification error larger than 10%.

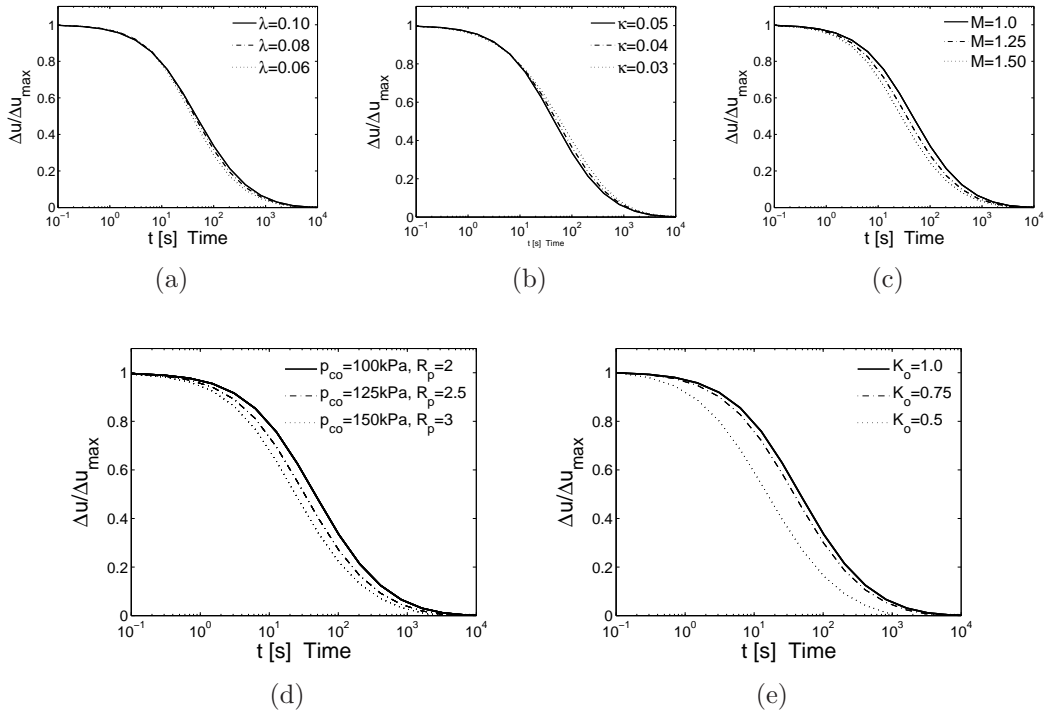


Figure 7.6: Sensitivity of the dissipation test to mechanical properties and initial stress anisotropy.

### 7.1.5 Sensitivity analysis of pressure holding test

As already shown in Section 7.1.2, soil permeability considerably affects the pressuremeter expansion curve. What has also been presented in Section 6.2.3 is that the horizontal permeability coefficient can be evaluated from the PHT by means of numerical simulations. Unless a coupled hydro-mechanical parameter identification is considered, running numerical simulations of the PHT requires arbitrarily assigned values of mechanical properties at the beginning of the analysis. Therefore, it is interesting to investigate the influence of MCC properties on the PHT. The sensitivity analysis was carried out based on simulations of the dissipation test under constant applied pressure and preceded by 10%-cavity strain expansion test.

The first analysis concerns a qualitative evaluation of the dissipation curve sensitivity for the model parameters perturbed by 25 and 50% with respect to the reference values. The results presented in Figure 7.6 show that initial state variables  $K_o$  and  $p_{co}$  have a strong influence on the dissipation curve whereas a moderate on  $M$  and a small influence on the deformation characteristics  $\kappa$  and  $\lambda$  are observed.

Thus, in the following analysis, the attention is drawn to those parameters which have the strongest influence on the dissipation curve, i.e.  $R_p(p_{co})$  and  $K_o$ . The weighted<sup>2</sup> least-squared objective function was used to qualitatively

<sup>2</sup>In order to make the results comparable with the previous analyzes, the elements in the weighting matrix  $\omega$  were adjusted by equalizing the magnitude of the error function  $S(K_o)$

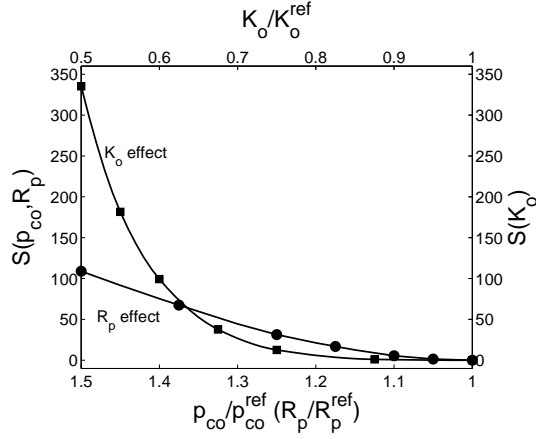


Figure 7.7: Sensitivity of the dissipation test to the stress state parameters presented measured in terms of the least-squared objective function.

analyze the magnitude of the error between measured variables obtained for parameters perturbed up to 50% and results for the reference dissipation curve. Figure 7.7 shows a strong exponential effect of  $K_o$  on the dissipation curve with the error for  $K_o$  beyond 25%. In the case of  $R_p$ , the influence is not as strong as for the erroneous  $K_o$  values, however a considerable magnitude of error can be observed for the  $R_p$  values perturbed more than 15%.

## 7.2 Numerical model of piezocone test

As already discussed in Section 6.3.1, a reliable numerical modeling of cone penetration in soil is still challenging. A successful modeling of the problem involves an efficient framework of many coupled numerical procedures which should deal with material and geometrical non-linearities including non-smooth frictional law. This chapter presents the finite element model of the piezocone penetration test in the elastic-plastic soil model. The validity of the developed CPTU model is investigated in detail. Such verification is necessary as the model will be used to generate a number of cone readings being used as NN training patterns. The verification of the developed model is demonstrated through a comparison with other solutions synthesized from literature. An analysis of penetration in various drainage conditions will be carried out in order to investigate soil behavior under partial drainage conditions which may occur in intermediate soils. An analysis of limitations of adopted numerical procedures and their effect on accuracy of numerical predictions is also presented. As the model imperfections may also stem from shortcomings of the adopted material model, its applicability to the NN training is also discussed.

---

obtained for  $K_o = 0.5K_o^{ref}$  in this analysis with the corresponding error presented in Figure 7.5(c).

### 7.2.1 Finite element model

As discussed in the introductory sections, in this study, a generation of the NN training database relies on the collection of synthetic test results produced by numerical simulations. Development of a reliable numerical simulation for the penetration problem can be formulated as:

*Find a numerical, coupled hydro-mechanical model that describes penetration of a saturated elasto-plastic medium by a frictional cone, obeying Darcy's law for fluid flow and generating excess pore pressure and stress fields with a reasonable accuracy.*

For the sake of availability, the environment of the commercial code ABAQUS has been used to simulate the cone penetration problem as the application offers many advanced built-in algorithms that can be used in the advanced FE element modeling (ABAQUS, 2007). The code has already been found to be suitable (with some limitations) to model penetration problems as it offers a description of constitutive soil behavior in the regime of large strains and large deformation contact formulation. The complex quasi-static non-linear analysis can be solved by means of two iterative techniques, as presented in Figure 7.8. One-phase material problems can be solved using the explicit time integration scheme which is proved to be stable for adequate small time increments and very well suited to complex contact problems involving frictional sliding (Prior, 1994). The explicit technique in conjunction with the efficient ALE adaptive meshing algorithm allows the accuracy of results to be improved. Since the adaptive meshing maintains a high quality mesh throughout the analysis involving severe mesh distortions, the use of small size mesh elements around the cone with maintained numerical stability is possible (e.g. Susila and Hryciw, 2003; Walker and Yu, 2006).

A cone insertion into a coupled hydro-mechanical system requires the use of the implicit time integration scheme which is available in ABAQUS/Standard (e.g. Sheng et al., 1997; Huang et al., 2004; Wei et al., 2005; Markauskas et al., 2005; Sheng et al., 2005). However, the implicit algorithm is not well suited to non-linear problems which include frequent changes of contact configuration including contact opening. While the problem of contact opening in the case of penetration problem can be avoided by smoothing the sharp cone transitions, the convergence problems may arise with severe element mesh distortions. As experienced by the author in preliminary tests, the use of ALE algorithm in conjunction with both complex frictional sliding, the coupled material behavior and the implicit technique, led to global numerical instabilities in the initial phase of penetration. Although various mesh topologies and frequent mesh sweeps were tested, the force and contact equilibrium was not achieved. According to the author's knowledge, a successful implementation of the adaptive meshing for the penetration problem has been proposed by Markauskas et al. (2005); however, the whole procedure does not seem to be well documented. Recently, Nazem et al. (2008) presented the ALE technique for large deformation consolidation

problems which has not been tested for insertion problems yet.

The inability of applying the mesh adaptivity enforces the use of the pure Updated Lagrangian description, as well as large size mesh elements around the cone tip in order to avoid negative Jacobians occurring for large mesh distortions (see e.g. Huang et al., 2004). Severe mesh distortions may also occur with increasing cone roughness resulting in considerable loss of solution accuracy. Considering the unfavorable distortion effect, a semi-analytical solution that accounts for the cone friction effect will be proposed in Section 7.2.2.3. The solution is calibrated for relatively small numbers of friction coefficient for which a good mesh quality is conserved providing acceptably consistent results.

In the proposed finite element model, the rheological effects were not considered in order to avoid an additional degree of complexity related to supplementary material constants.

### 7.2.1.1 Cone-soil interface modeling

Modeling of the contact between the penetrating cone and the soil involves large frictional sliding including a non-smooth frictional law. In the present model, the widely used node-to-surface algorithm has been adopted (ABAQUS, 2007; Fischer et al., 2007). Using this concept, the master surface is defined by the cone geometry while the slave nodes belong to the deformable soil mesh.

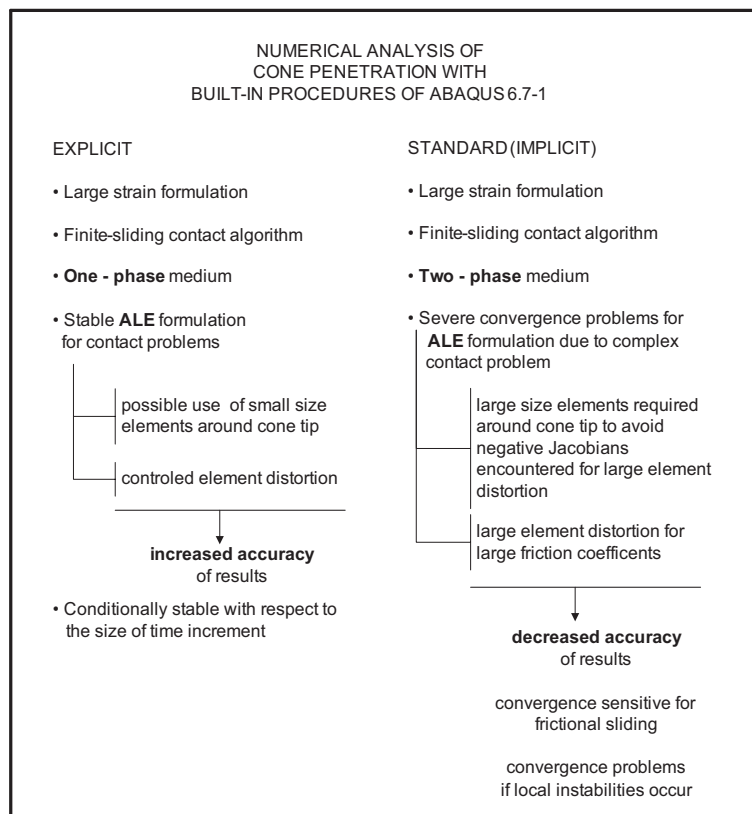


Figure 7.8: Numerical modeling of cone penetration using ABAQUS environment.



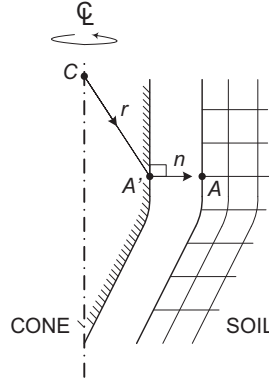


Figure 7.9: Scheme of cone-soil interface.

### *Kinematics at the interface*

Let us define a point  $A$  on the deforming mesh, with current coordinates  $\mathbf{x}_A$  and the closest point  $A'$  on the rigid body surface at which the normal vector to the surface  $\mathbf{n}$  passes through  $A$  (Figure 7.9). Then, the overclosure distance (or normal gap) between two bodies is calculated as:

$$g_n = \mathbf{n}^T(-\mathbf{x}_A + \mathbf{x}_C + \mathbf{r}) \quad (7.1)$$

where  $g_n$  is the gap between two bodies,  $\mathbf{x}_C$  are the current coordinates of the reference rigid body node and  $\mathbf{r}$  denotes the vector  $\overline{CA}$ . Contact conditions between two surfaces are governed by kinematic constraints in the normal and tangential directions (Figure 7.10). In the normal direction, the assumed non-adhesional interface is governed by the hard contact formulation which is given for every possible contact pair as:

$$g_n \geq 0, \quad p'_n \geq 0, \quad g_n p'_n = 0 \quad (7.2)$$

where  $p'_n$  denotes the normal effective pressure at contact and is taken as positive for compression. The contact between two bodies is detected when  $g_n = 0$  and  $p'_n > 0$ . Once the slave nodes are in contact with the master surface the sliding may occur.

### *Frictional interface constitutive law*

The frictional sliding is governed by the Coulomb's friction contact law. A critical shear contact stress is proportional to the normal stress at the interface based on  $\tau_f = p'_n \tan \phi_i$ , where  $\phi_i$  represents the friction angle of the cone-soil interface. Unless the value of the shear stress is smaller than the critical value, two surfaces remain in a sticking mode and no relative displacement takes place. Otherwise, perfectly-plastic sliding occurs in the direction of the shear stress, thus:

$$\begin{aligned} \text{if } |\tau/\mu p'_n| < 1 & \text{ then } u_t = 0 \text{ (sticking mode)} \\ \text{if } |\tau/\mu p'_n| = 1 & \text{ then } u_t > 0 \text{ (sliding)} \end{aligned} \quad (7.3)$$

where  $\mu$  is the coefficient of friction and is equal to  $\tan \phi_i$ . It is also assumed

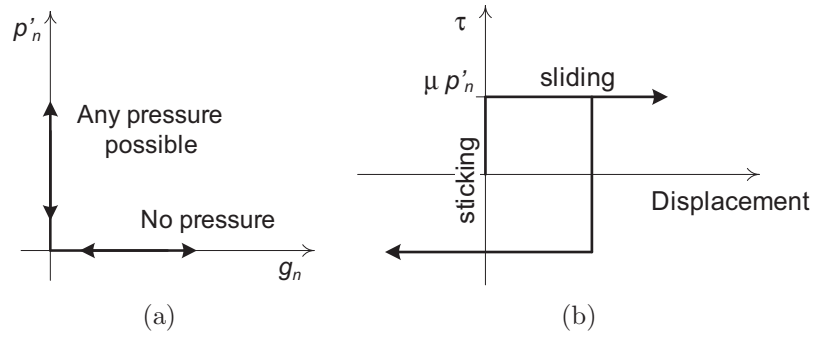


Figure 7.10: Constitutive behavior of the non-adhesive frictional contact (a) in the normal direction, (b) in the tangential direction.

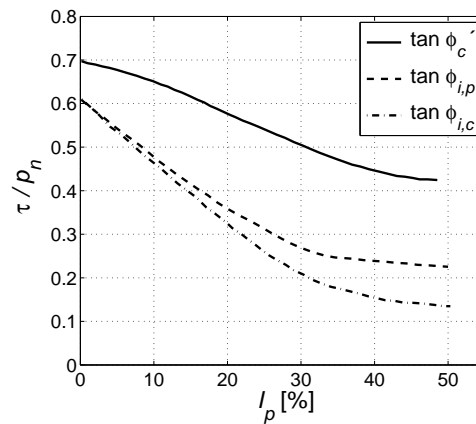


Figure 7.11: Relationship between the friction coefficient and the plasticity index: proposed values of design  $\phi_i$  values for steel piles after (Jardine and Chow, 1996).

that in the contact, there is no tangential fluid flow.

In the model, the Lagrange multipliers method is used to enforce the contact constraints. Although the algorithm adds additional degrees of freedom increasing the size of the problem, it satisfies the contact constraints exactly (Sheng et al., 2007). Further details on finite element algorithms for the frictional contact can be found in (Wriggers, 2002).

### 7.2.1.2 Experimental evidence of the steel-soil interface

Typically, the friction angle  $\phi_i$  for the steel-clay interface is smaller than the soil residual effective friction angle  $\phi'_c$  (Lehane et al., 2000). For the friction angle at the interface, the peak  $\phi_{i,p}$  and residual (critical)  $\phi_{i,c}$  may also be distinguished depending on the relative displacement between the shaft and the soil during penetration. Based on an extended research program including results from the field tests and "Bishop ring"-shear tests, the approximate design values for  $\phi_i$  were proposed for steel piles in Jardine and Chow (1996). As shown in Figure 7.11, in clays, the ratio  $\tan \phi_{i,c} / \tan \phi'_c$  can be observed approximately between

0.25 ÷ 0.5 and the dependency on the plasticity index  $I_P$  is also recognized. Koumoto (1988) reported the results of constant volume friction tests in Toyoura sand for which the ratio  $\tan \phi_i / \tan \phi'_c$  was observed between 0.22 ÷ 0.26. Since the observed variations of  $\phi_i$  may be large, as discussed by Ramsey et al. (1998), the dependency on the  $I_P$  will be omitted further in this study.

For the purpose of training pattern generation, the contact parameter  $\phi_i$  will be assigned using a randomly drawn value of cone roughness  $\alpha_f = \tan \phi_i / \tan \phi'_c$  within an interval from 0.25 to 0.35. The assumed interval will be further justified based on  $F_r - Q_t$  classification chart in Section 8.2.3.

### 7.2.1.3 Strength anisotropy

Natural clays usually exhibit the strength anisotropy which is the result of the deposition process. This anisotropy may thus affect cone resistance, as the rotation of principal stresses can be expected due to different shear modes involved during penetration (see Figure 6.20). The effect is not of great importance however, it can be taken into account in the numerical model. Based on the results for the strength anisotropic criterion and the cavity expansion method, Su and Liao (2002) affirmed that the anisotropy effect becomes significant for clays which exhibit a strong anisotropy, i.e. the strength anisotropy ratio  $A_r$ , less than 0.6.

In the finite element model, in order to account for the strength anisotropy, Equation (4.1) which defines the plastic surface can be rewritten as:

$$F(p', q, r, p_{co}) = q^2 + M^2 r^2(\theta) \cdot p'(p' - p_{co}) = 0 \quad (7.4)$$

where  $\theta$  denotes Lode angle and  $r(\theta)$  describes the shape of the yield surface in the octahedral plane and is defined in ABAQUS through the expression proposed by Argyris et al. (1974):

$$r(\theta) = \frac{2k_a}{1 + k_a + (1 - k_a) \sin(3\theta)} \quad (7.5)$$

where the coefficient of strength anisotropy  $k_a$  ( $= M_e/M_c$ ) can be typically related to the friction angle through the Mohr-Coulomb criterion as:

$$k_a = \frac{3 - \sin \phi}{3 + \sin \phi} \quad (7.6)$$

In the MCC, the coefficient  $k_a$  is equivalent to the undrained shear strength ratio  $A_r$  ( $= c_{uc}/c_{uc}$ ) as its magnitude is controlled by the ratio  $M_e/M_c$  (cf. Equation (6.47)).

Contrary to the formula proposed by van Eekelen (1980) which can be applied for the friction angle up to  $\phi = 46.55^\circ$  (see Figure 7.12(a)), Equation (7.5) preserves the convexity of the yield surface if  $0.778 \leq k_a \leq 1.0$ , and thus becomes non-convex for  $\phi > 22.1^\circ$  as shown in Figure 7.12(b). In the presented model, the strength anisotropy is thus assumed as a constant equal to  $k_a = 0.78$  for each considered simulation or training pattern.

### 7.2.1.4 Finite element discretization

An FE model of the standard cone with tip angle  $\alpha = 60^\circ$  and diameter  $d_c = 35.7\text{mm}$  was designed to study a displacement-controlled test with a standardized rate of penetration equal to  $20\text{mm/s}$ . The cone is modeled as an axis-symmetric rigid body which penetrates the underlying deformable soil from its top surface. The penetration takes place in a pre-existing cavity with the initial radius equal to  $0.1\text{mm}$  which is introduced to allow penetration. The finite-sliding formulation with the Coulomb's frictional law is used for modeling the interface between cone and soil. The FE mesh representing a fully saturated soil is discretized using 8-node axis-symmetric quadrilateral isoparametric elements with the reduced integration scheme, i.e. four Gauss points and is presented in Figure 7.13(a). Higher order shape function elements are used to improve accuracy and avoid locking effects. The soil elements near the rigid cone are intentionally skewed at the beginning of the analysis in order to avoid severe distortions during a subsequent deep penetration. The element distortions may cause a loss of accuracy, especially, if the analysis is performed with a "rough" interface, i.e.  $\mu > 0$ . The size of elements in the horizontal direction is biased toward the outer radius of the domain, while in the vertical direction, the elements have a constant height until they reach a level slightly below the depth of penetration.

In the FE model bottom boundaries are fixed in the vertical direction while the top surface is loaded with the equivalent of total *in situ* vertical stress  $\sigma_{vo}$ . At the external edge, traction boundary condition, equivalent to the initial total horizontal stress  $\sigma_{ho}$ , and pore pressure boundary condition, equivalent to the initial hydrostatic pore pressure  $u_o$ , are enforced. Moreover, the initial state of the effective stress is assumed to be homogeneous through the overall height of

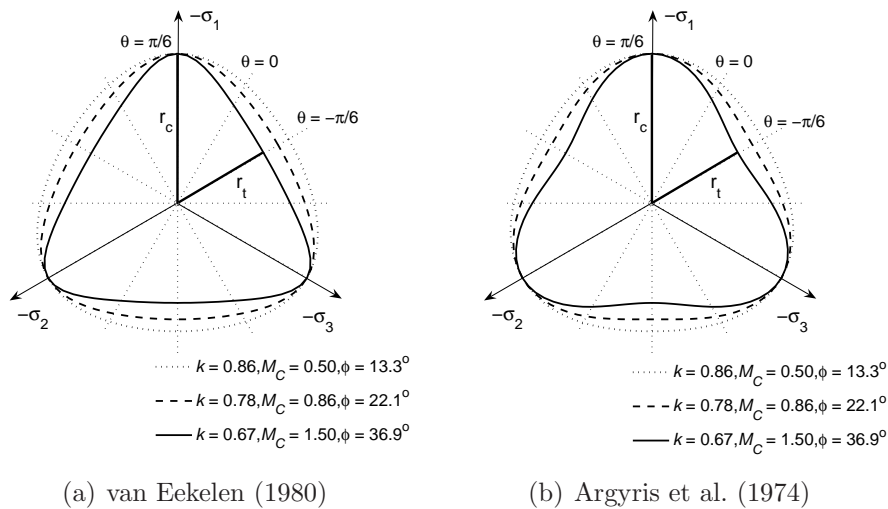


Figure 7.12: Failure surface of the MCC in octahedral plane.

the mesh at the beginning of the analysis. In the analysis, soil can be considered as weightless since it does not affect the penetration mechanism and simplifies capturing the so-called "steady-state" which is characterized by a linear increase of the cone resistance force  $F_c$  (e.g. Figure 7.15). The homogeneous geostatic conditions, i.e. the initial vertical and horizontal effective stresses,  $\sigma'_{vo}$  and  $\sigma'_{ho}$  respectively, are imposed over the mesh domain.

### Mesh size optimization

The size of the mesh domain is designed to satisfy two requirements, i.e. that the radius of external boundaries ( $R$ ) be large enough compared to the plastic radius and that the height of mesh  $H$  allow an unaffected steady-state to be reached. Hence, the size of the soil domain can be specified according to the cavity expansion theory (Vesić, 1972) which says that the range of plastic radius  $r_p$  depends on the rigidity index  $I_r$ . A solution for  $r_p$  based on the cavity expansion from zero initial radius to the cone radius  $r_c$  can be calculated for cylindrical cavity as  $\sqrt{I_r}r_c$  (cf. Lu et al., 2004)). For the sake of the accuracy of results, the radial extent was taken as  $R \approx 2.8\sqrt{I_r}r_c$  and the mesh height as twice of the external radius  $R$ . Three meshes were designed to deal with

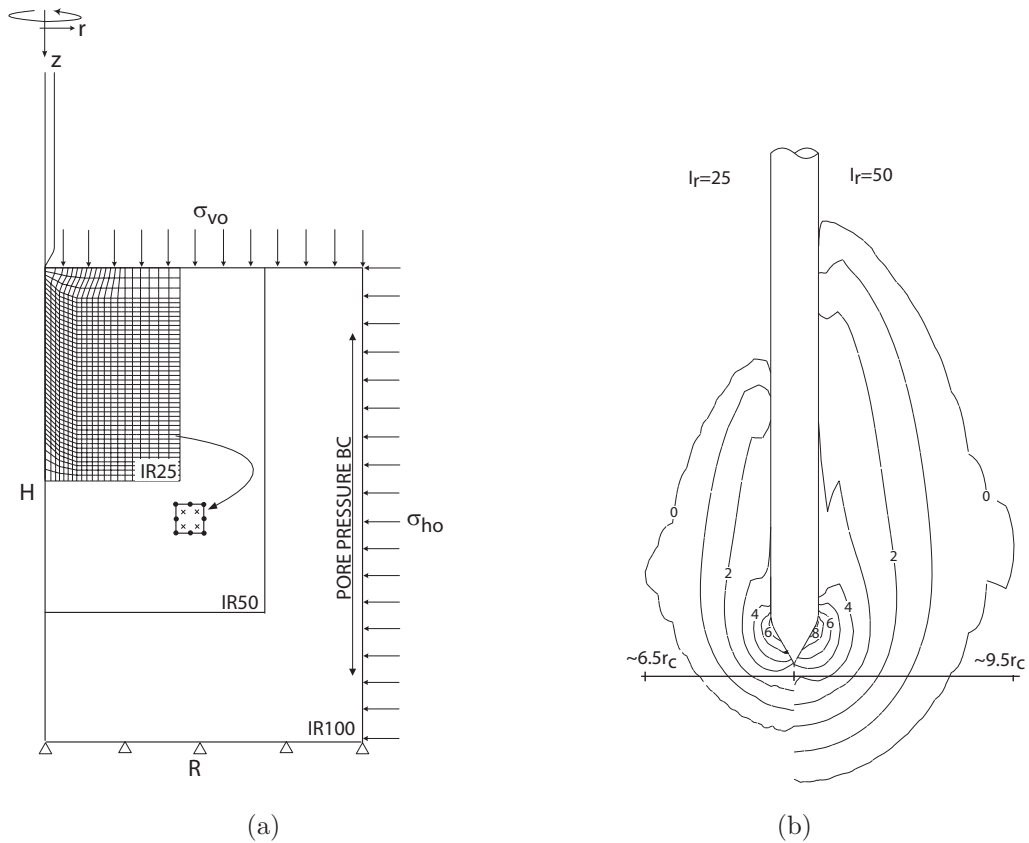


Figure 7.13: Mesh size optimization in function of  $I_r$ : (a) schematic layout of the FE meshes for CPTU, (b) contour plots of  $\Delta u/c_u$ .

various  $I_r$ , namely IR25, IR50 and IR100, and their dimensions are summarized in Table 7.1 and illustrated in Figure 7.13(a). The optimization of the mesh dimensions is proposed to control the total number of equations to be solved, as well as to reduce an extended CPU time which is expected during the data base generation of numerical samples for NN training. Figure 7.13(b) presents exemplary simulations in two materials defined by  $I_r$  equal to 25 and 50. Taking into account properties of the MCC during the undrained compression, the non-zero pore pressures around the penetrated zone can be identified with the region of plastic deformations. The presented results show that in both cases, the outer vertical boundary conditions  $R$  are far enough from the plastic radius.

Table 7.1: Summary of the finite element mesh sizes.

Mesh name	Rigidity Index Range $I_r$	Radius $R$ (m)	Height $H$ (m)	Radius/Cone radius $R/r_c$
IR25	10 ÷ 25	0.25	0.4	14.0
IR50	25 ÷ 50	0.35	0.6	19.6
IR100	50 ÷ 110	0.50	0.8	28.0

#### *Optimization of penetration depth*

Representative variables for a modeled penetration test can be acquired as soon as the steady-state condition is achieved for both cone tip resistance  $q_t$ , sleeve friction  $f_s$  and pore pressure  $u_2$  readings. As demonstrated in earlier studies (e.g. Huang et al., 2004; Walker and Yu, 2006), the steady-state depth  $z_s$  is related to  $I_r$ . A number of test runs was carried out to capture  $z_s$  and the results of this analysis are presented in Figure 7.14. For example, starting from the soil surface, the steady-state is achieved at  $z_s \cong 0.23\text{m}$  with  $I_r = 25$  corresponding to about 6 times of  $d_c$  while for  $I_r = 100$ ,  $z_s \cong 0.41\text{m}$  which corresponds to about 11 times of  $d_c$ . Note that the steady-state condition is achieved earlier for the cone resistance than for shaft resistance readings (compare, for example, Figure 7.19(a) with Figure 7.22(a)). The latter determines the occurrence of the steady-state. By taking only the cone resistance at the steady-state from Figure 7.19(a) for  $I_r = 100$  which corresponds to  $z_s$  equal to 8 times of  $d_c$ , the result corresponds well with  $z_s$  obtained with an explicit FE model presented by Walker and Yu (2006).

Hence, in order to ensure the minimal CPU time of the cone penetration simulation, a dependence between  $I_r$  and  $z_s$  should be introduced. This is essential to perform an "economical" generation of NN training patterns.

#### *Smoothing numerical measurements*

In practice, continuous data readings reveal fluctuations of different magnitudes. Clearly, the first group of oscillations stems from the local variability of

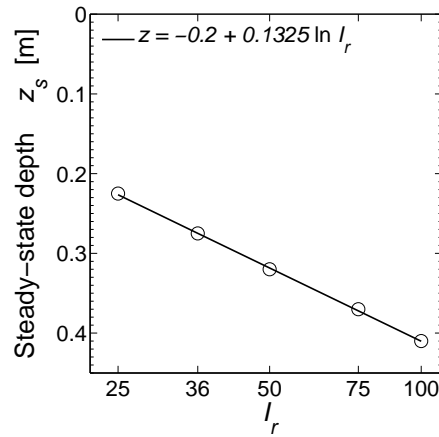


Figure 7.14: Optimization of the computational effort for cone penetration runs by evaluation of the steady-state depth  $z_s$ .

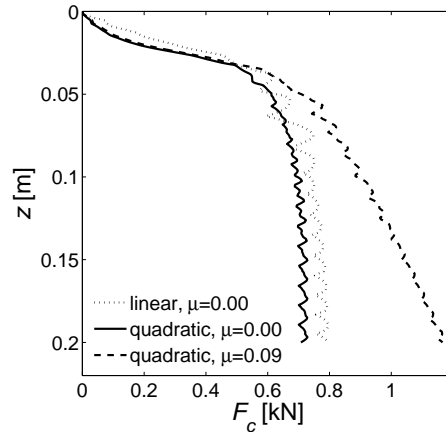


Figure 7.15: Non-smoothed measurements of total cone resistance  $F_c$  for linear and quadratic elements with the height of 10mm.

soil. However, in a "statistically homogeneous" soil layer, oscillations may be caused by randomly encountered larger grains or soil fracturing. In the finite element model, oscillations stem from the node-to-surface contact discretization. The sudden drops of cone resistance, e.g. Figure 7.15, take place when soil elements pass the transition point between the cone tip and the cone shaft. The transition mode may also be the source of numerical instabilities due to highly distorted elements around the transition point and sudden changes of contact stress directions (Fischer et al., 2007). In order to ensure the solution stability and to improve smoothness of readings, the transition between the cone tip and the cone shaft is slightly rounded.

Thus the magnitude of oscillations depends on the size of elements; Figure 7.15 presents results for the model with the element height of 10mm. In this case, the linear elements present a more "resistant" response to the quadratic

elements, which can be explained by the topology of linear elements. The amplitude of oscillations may be reduced by decreasing the height of elements (Figure 7.30(a) shows numerical results for the element height 7.5mm). In the present study, smooth numerical results are obtained through the moving average filtering, i.e. each  $i$ th data point is replaced with the average of the neighboring data points through:

$$\tilde{y}_i = \frac{1}{2N+1}(y_{i+N} + y_{i+N-1} + \dots + y_{i-N}) \quad (7.7)$$

where  $\tilde{y}_i$  denotes the smoothed value,  $N$  is the number of neighboring data points and  $2N+1$  represents the smoothing span.

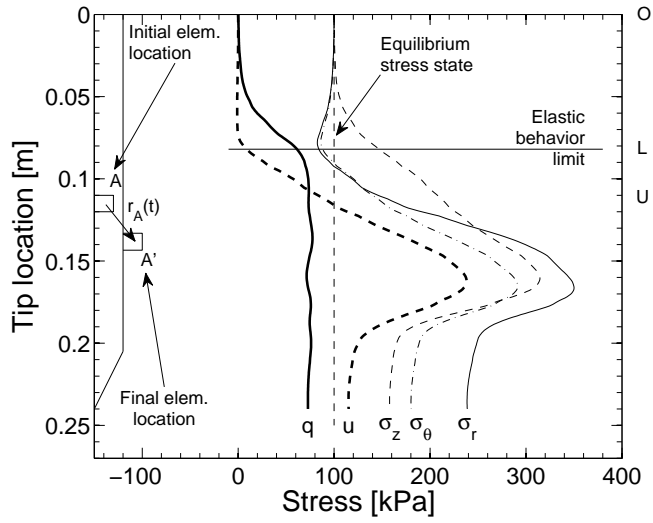
## 7.2.2 Analysis of finite element model

As discussed in Section 6.3.1, the finite element modeling seems to be the most appropriate to theoretically analyze cone penetration in clays since many factors such as cone geometry, frictional sliding or advanced constitutive law, can be taken into account. The soil elements adjacent to the cone experience complex stress paths as a consequence of different shearing modes that are involved in the test. Figure 7.16 presents the results of the "undrained" cone penetration in an isotropically consolidated material. During penetration, the cone moves the point  $A$  to the new position  $A'$  of a vector  $r_A(t)$  disturbing the isotropic initial stress state  $O$  (see Figure 7.16(a) and 7.16(b)). The soil element remains in the elastic equilibrium until reaching the yielding point  $L$  which corresponds to the location of the soil element in the zone beneath the cone tip. With the soil yielding, a strong gradient of pore pressure  $u$  is built-up and subsequently the deviatoric stress  $q$  accompanied by the rotation of principal stresses achieves its ultimate magnitude (point  $U$ ). This moment is also marked by the maximum excess pore water pressure which subsequently decays as soon as the cone base passes by the soil element. A similar pattern for pore pressure variations was observed by Whittle and Aubeny (1991) for the MCC using the strain path method.

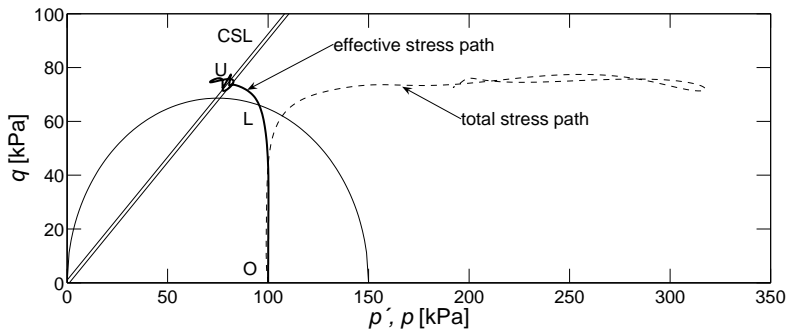
Figures 7.16(c) and 7.16(d) confirm that the strength anisotropy affects effective stress paths in the penetration process. However, a larger influence can be expected for pore pressure readings behind the cone base  $u_2$  than for cone resistance  $q_t$ . This is due to the fact that the former is measured at cone shaft in soil being subject to the full rotation of principal stresses, i.e.  $\sigma_1$  initially corresponding to the vertical stress becomes the radial stress direction as shown in Figure 7.17(a). The record of cone resistance  $q_t$  includes a mixture of resistance forces related to both vertical and transitional compression. The parametric study for three different values of anisotropy coefficient  $k_a$  confirms the above hypothesis, as shown in Figure 7.17(b). The measurement of  $q_t$  for fully isotropic strength is 0.6% higher with respect to the reference  $q_t^{\text{ref}}$  corresponding to  $k_a = 0.78$ , whereas neglecting the strength anisotropy leads to underestimation of pore pressure  $u_2$  of about 5% with respect to  $u_2^{\text{ref}}$ .

Figure 7.18 illustrates pore pressure distributions along the cone in normally-

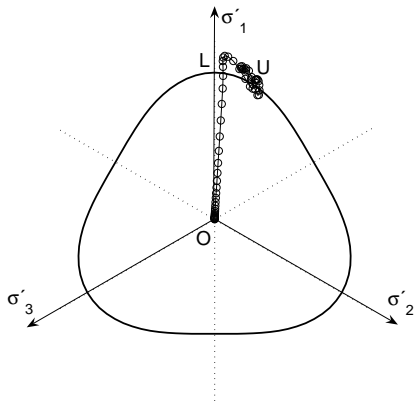




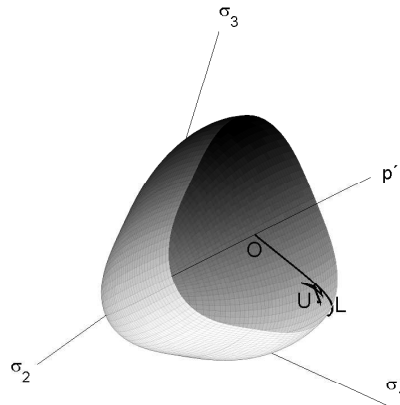
(a) variation of stress components for the soil element located next to the axis of symmetry



(b) total and effective stress paths



(c) anisotropic failure surface of MCC and the effective stress path in octahedral plane



(d)  $p'$ - $q$  section through the anisotropic yield surface with the effective stress path

Figure 7.16: A numerical simulation of the "undrained" cone penetration in an isotropically consolidated material.

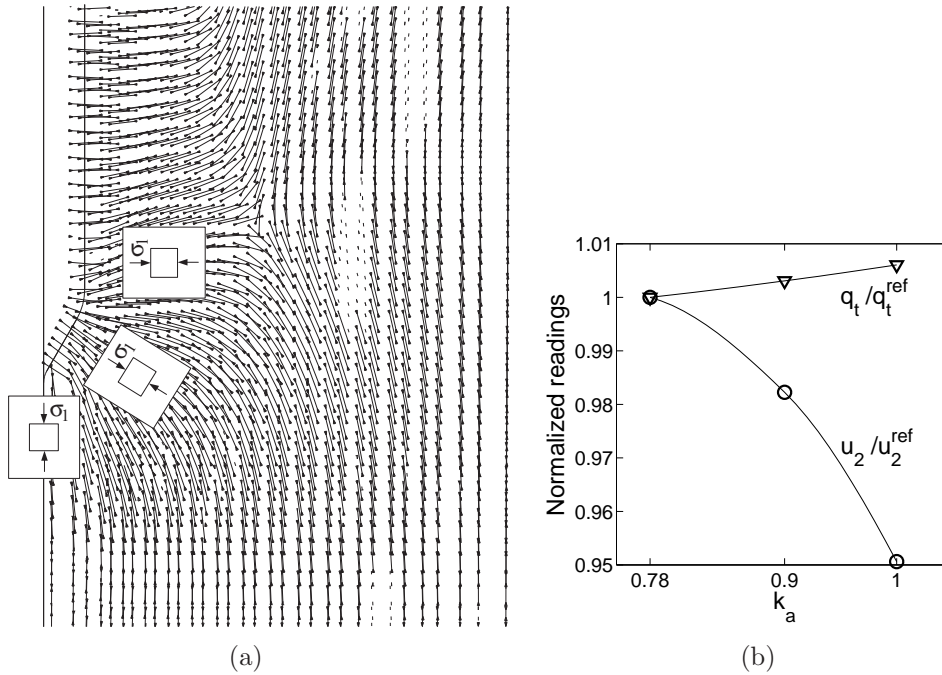


Figure 7.17: Rotation of the principal stresses during cone penetration: (a) rotation of  $\sigma_1$  directions (b) influence of the strength anisotropy on cone readings.

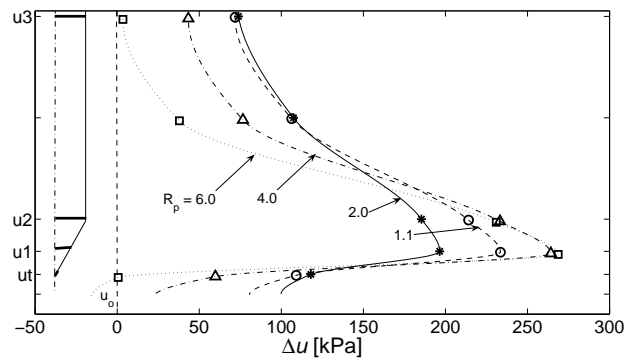


Figure 7.18: Pore pressure distributions generated by the numerical model for various overconsolidation ratios.

and lightly overconsolidated materials. The numerical patterns are, generally, in agreement with the field test results summarized by Robertson et al. (1986); Lunne et al. (1997). The largest positive pore pressures are developed at the cone tip surface where the maximum compressive stresses are observed. Behind the cone base, the positive pore pressures decrease along the shaft with a stronger gradient marked for dilative materials. The chart shows, however, that the pore pressure  $u_t$  measured at the cone tip apex may be underestimated. This fact can be considered as a shortcoming of the MCC model which generates no excess pore water pressure within the elastic region and, in consequence, the pore pressure gradient at  $u_t$  location can be delayed.

### 7.2.2.1 Analysis of cone factors

As already discussed in 2.1, no unique undrained shear strength exists. The value of  $c_u$  depends on soil history, soil anisotropy, strain rate, interface friction and finally on the failure mode (Wroth, 1984; Teh and Houlsby, 1991; Mayne, 2006). The common relation that links the tip cone resistance  $q_t$  and  $c_u$  is expressed applying the cone factor  $N_{kt}$ :

$$q_t = N_{kt}c_u + \sigma_{vo} \quad (7.8)$$

The model developed in the present study, can be thus verified by carrying out a comparison with results from other studies in terms of  $N_{kt}$ . Another model evaluation can also be made in terms of factor  $N_{\Delta u}$  (Equation (6.41)). However, only a few studies have been made to analyze the hydro-mechanical mechanism of penetration and no comparative solutions for  $N_{\Delta u}$  have been found in literature.

All the calculations presented throughout this section were carried out for the saturated two-phase material with the Modified Cam clay criterion and the compressible fluid phase. Parameters used for calculations are summarized in Table B.2. As regards the analysis of the soil rigidity effect, the rigidity index  $I_r$  was adjusted by changing the value of either  $\kappa$ , which controls the soil stiffness<sup>3</sup>, or  $R_p$  which defines  $c_u$ . Since the undrained shear strength is non-unique, two approaches were applied to compare obtained results using Equation (6.47) and (6.22) which refer to the three-dimensional case and the plane strain expansion respectively. In the analysis of the initial stress anisotropy effect, the parameter  $\Delta$  was adjusted by changing  $\sigma'_{vo}$  and  $\sigma'_{ho}$ , and keeping  $p'_o$  constant.

#### *Effect of soil stiffness on cone factors*

The effect of soil stiffness was analyzed for frictionless penetration in undrained conditions and isotropic initial stress state. Values of  $q_t$  were computed for various rigidity indexes  $I_r$  corresponding to three optimal size meshes, i.e. IR25, IR50 and IR100. In order to examine the consistency of the meshes, additional calculations were carried out for the same  $I_r$  using different meshes. The results of this analysis, presented in Figures 7.19(a) and 7.19(c), show that the test points calculated for various meshes and  $I_r$  varying from 10 to 110 lie exactly on the linear correlation, affirming the consistency of the meshes. The following correlations were obtained for different  $I_r$  values:

$$N_{kt}^s = -0.55 + 2.37 \ln I_r \quad (7.9a)$$

for  $I_r$  obtained through variations of  $\kappa$  and  $c_u$  calculated for a spherical expansion, and:

$$N_{kt}^c = -0.18 + 2.05 \ln I_r \quad (7.9b)$$

for  $c_u$  calculated for a cylindrical expansion.

Additional computations were carried out using the model IR25 for which

---

<sup>3</sup>See Equation (4.4).

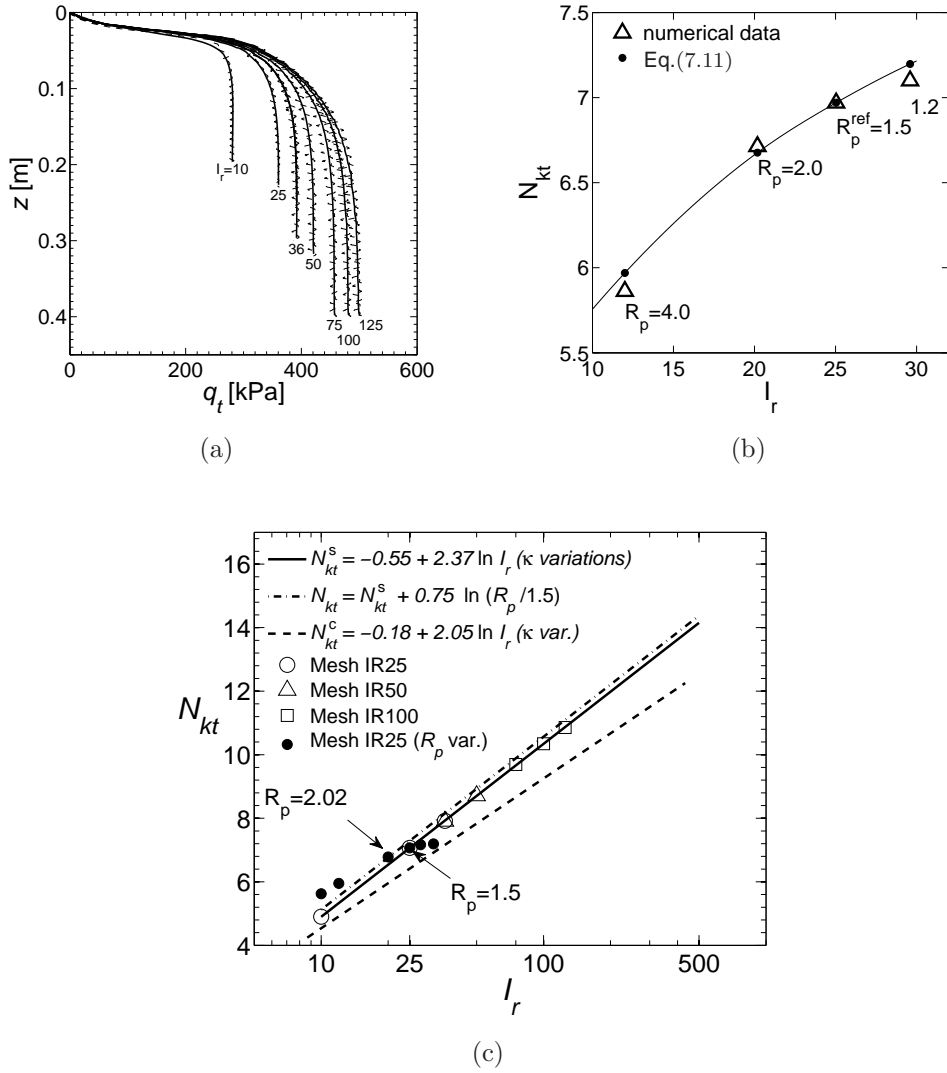


Figure 7.19: Effect of soil rigidity on the cone factor  $N_{kt}$ , (a) evolution of the cone resistance with depth (raw and smoothed measurements), (b)  $N_{kt}$  in function of  $R_p$ , (c)  $N_{kt}$  in function of rigidity index in various mesh designs.

$I_r$  values were modified through  $R_p$  varying from 1.08 and 5.1, and  $c_u$  was calculated using the equation for the spherical case. Owing to different definitions of  $c_u$ , the values of  $N_{kt}$  for the cylindrical  $c_u$  definition are smaller than for the spherical case. Interestingly, despite using the same expression for calculating  $c_u$ , the numerical results for  $\kappa$  and  $R_p$  variations present different solutions. Simulations run with the same  $G$  modulus but the variable  $R_p$  give experimental points lying along an ellipsoid-shape trend (Figure 7.19(c)). Assuming that the change of the reference value  $I_r^{\text{ref}}$  is inversely proportional to the change of the reference overconsolidation ratio  $R_p^{\text{ref}}$  (cf. Equation (6.47)):

$$\ln \left( \frac{I_r^{\text{ref}}}{I_r} \right) = \ln \left( \frac{R_p}{R_p^{\text{ref}}} \right)^\Lambda \quad (7.10)$$

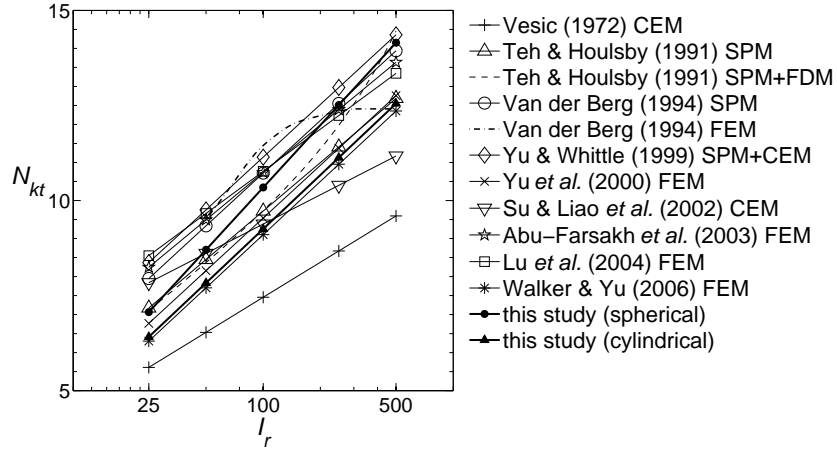


Figure 7.20: Comparison of the rigidity index effect on the cone factor  $N_{kt}$  obtained in different studies.

the following expression can be proposed to adjust the solution presented in Equation (7.9a) to any value of  $R_p$ :

$$N_{kt}(R_p) = N_{kt}^{\text{ref}} + 0.75 \ln \frac{R_p}{R_p^{\text{ref}}} \quad (7.11)$$

Figure 7.19(b) shows that the above equation fairly approximates data points obtained in numerical simulations. Figure 7.19(c) demonstrates that the solution obtained using Equation (7.9a) for  $R_p^{\text{ref}} = 1.5$  and shifted up applying  $R_p = 2.02$ , passes the corresponding experimental point indicated in the diagram.

Figure 7.20 shows that the general trends proposed in Equations (7.9) are similar to solutions obtained in other studies which are summarized in Table 6.2<sup>4</sup>. The slope gradient in Equation (7.9a) resembles the initial gradient of FEM solution obtained by Van der Berg (1994). However, this solution exhibits a strong non-linearity when  $I_r$  is larger than 100. It is supposed that this inconsistency can be attributed to inefficiency of numerical procedures for penetration in stiffer materials. Severe convergence problems and numerical inefficiency were also experienced in the present study for  $I_r$  values larger than 110.

As regards the solution expressed by Equation (7.9b), the slope gradient is similar to those obtained for SPM by Teh and Houlsby (1991); Van der Berg (1994); Yu and Whittle (1999) and for FEM by Yu et al. (2000); Abu-Farsakh et al. (2003); Walker and Yu (2006).

A similar analysis of the stiffness effect was carried out for the cone factor  $N_{\Delta u}$  derived for pore pressure measurements taken behind the cone tip. Figure 7.21(a) presents the results of  $u_2$  evolution with penetration depth for

<sup>4</sup>The graphical interpretation for expression proposed by Su and Liao (2002) was obtained with  $A_r = 0.78$ .

different  $I_r$  levels. Note that numerical raw readings of  $u_2$  are characterized by larger amplitudes of oscillations than those observed for  $q_t$  readings (cf. Figure 7.19(a)). The intensity of amplitudes rises with increasing  $I_r$  and the highest amplitudes were observed in the initial phase of penetration. Figure 7.21(c) presents the cone factors  $N_{\Delta u}$  calculated from smoothed measurements corresponding to steady-state penetration and plotted against  $I_r$ . Based on these data points, the following expressions have been proposed to fit the data:

$$N_{\Delta u}^s = 1.12 + 1.34 \ln I_r \quad (7.12a)$$

for  $I_r$  obtained through variations of  $\kappa$  and  $c_u$  calculated for spherical expansion, and:

$$N_{\Delta u}^c = 1.14 + 1.16 \ln I_r \quad (7.12b)$$

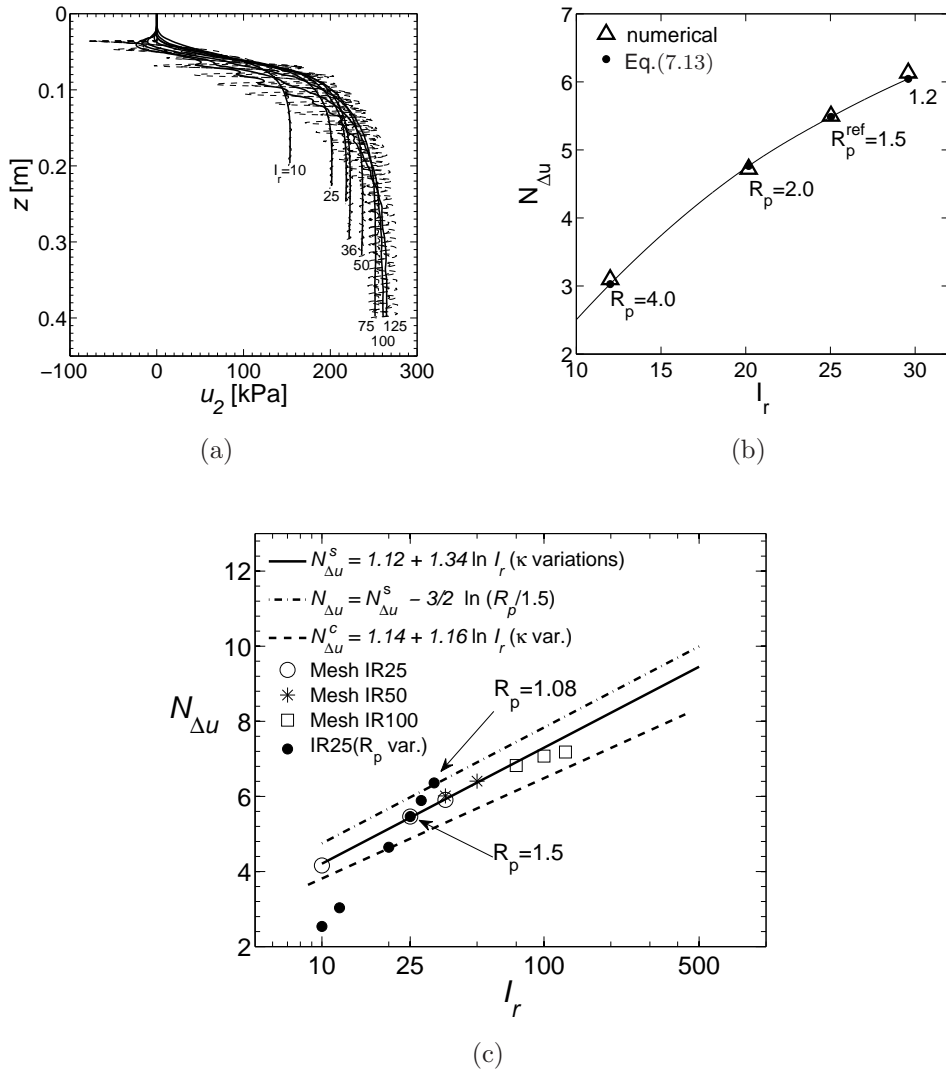


Figure 7.21: Effect of soil rigidity on the cone factor  $N_{\Delta u}$ , (a) evolution of excess pore water pressure with depth (raw and smoothed measurements), (b)  $N_{\Delta u}$  in function of  $R_p$ , (c)  $N_{\Delta u}$  in function of rigidity index in various mesh designs.

for  $c_u$  derived from cylindrical expansion case.

Owing to the occurrence of large measurement oscillations, the data points exhibit a slight scatter with respect to the solution proposed in Equation (7.12a). Slightly scattered data can be, however, advantageous for NN training since it may accelerate training and also improve their ability to generalize. It is also remarkable that data points above  $I_r = 75$  slightly deviate from the linear trend which can be also associated with numerical oscillations which rise with increasing soil rigidity. This remark may partially explain severe convergence problems encountered during numerical simulations for materials with  $I_r$  larger than 125. It was next observed that severe numerical problems begin to occur if the ratio  $G/p'_o$  exceeds the value of about 50 with  $I_r$  larger than 110 at the same time. Assigning the values of  $\nu = 0.3$  and  $e_o = 0.1$ , the ratio  $G/p'_o = 50$  corresponds to  $\kappa = 0.01$  and further decreasing this value may lead to divergence in the numerical model before achieving the steady state. Severe problems with convergence due to pore pressure oscillations were observed at the critical depth of  $0.08 \div 0.09\text{m}$  from the top surface. Unfortunately, the use of the developed model for the generation of NN training patterns has been restricted to the values of  $G/p'_o < 70$ , in conjunction with  $I_r$  smaller than 110.

By analogy to  $N_{kt}$ , the solution for  $N_{\Delta u}$  proposed in Equation (7.12a) is non-unique and depends on the overconsolidation ratio as demonstrated in Figure 7.21(c). In order to account for this factor, the following expression has been proposed:

$$N_{\Delta u}(R_p) = N_{\Delta u}^{\text{ref}} - \frac{3}{2} \ln \frac{R_p}{R_p^{\text{ref}}} \quad (7.13)$$

Figure 7.21(b) shows that the above expression fairly approximates data points obtained in numerical simulations using different values of  $R_p$ . Figure 7.21(c) illustrates that the solution obtained using Equation (7.12a) for  $R_p^{\text{ref}} = 1.5$  and shifted up for  $R_p = 1.08$ , passes the corresponding data point as indicated in the chart.

The effect of soil rigidity was also investigated in terms of the normal effective pressure  $p'_n$  acting on the cone shaft. The values of  $p'_n$  at the steady state were taken as a sum of the normal effective pressures integrated over the cone friction sleeve area of  $150\text{cm}^2$  above the cone tip. Figure 7.22(a) shows that  $I_r$  has no significant influence on the results as the penetration has reached the steady-state. A sudden drop of effective pressures for rigid materials in the initial phase of penetration can be explained by high amplitudes of pore pressures as previously shown in Figure 7.21(a). The effect of material rigidity can be quantified by plotting the ratio  $p'_n/c_u$  (which is similar to the cone factor  $N_{\Delta u}$ ) against  $I_r$  as shown in Figure 7.22(b). In this diagram the effect of pore pressure oscillations is notably manifested for the data point corresponding to  $I_r = 125$  which deviates from the general trend expressed by:

$$\frac{p'_n}{c_u} = 3.73 - 0.11 \ln I_r \quad (7.14)$$

It can be concluded that the soil rigidity marginally affects the effective pres-

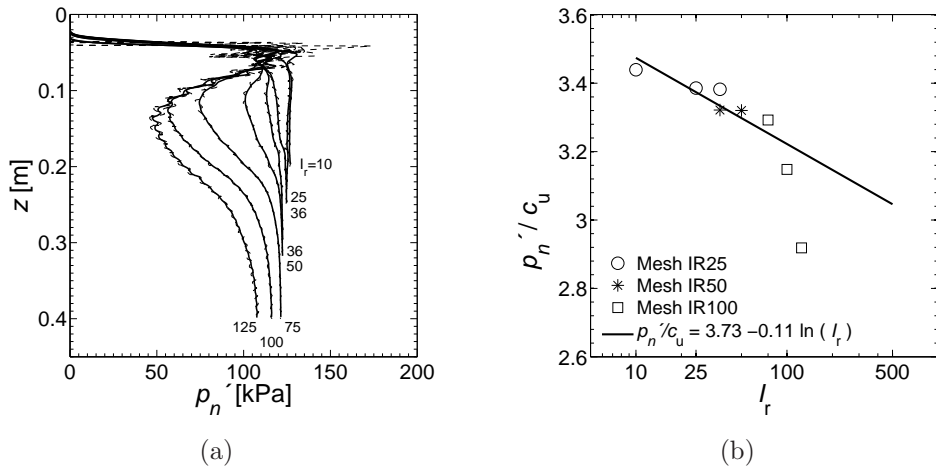


Figure 7.22: Effect of soil rigidity on the normal effective pressure acting on the cone shaft, (a) evolution of the normal effective pressure with depth and (b) variation of the effective pressure ratio for various  $I_r$  and mesh designs.

sure acting on the cone shaft since the observed trend gradient is significantly smaller compared to gradients observed for other cone factors.

#### Effect of strength anisotropy on cone factors

Su and Liao (2002) demonstrated that the strength anisotropy included in the material model affects the penetration process. As illustrated in Figure 7.17(b), the cone resistance derived for isotropic strength criterion is higher than for anisotropic criterion and inversely, lower pore pressure records  $u_2$  can be expected towards to strength isotropy state.

A series of numerical simulations for adopted strength criterion was carried out for various anisotropy ratios  $k_a$  and overconsolidation ratios  $R_p$ . The ob-

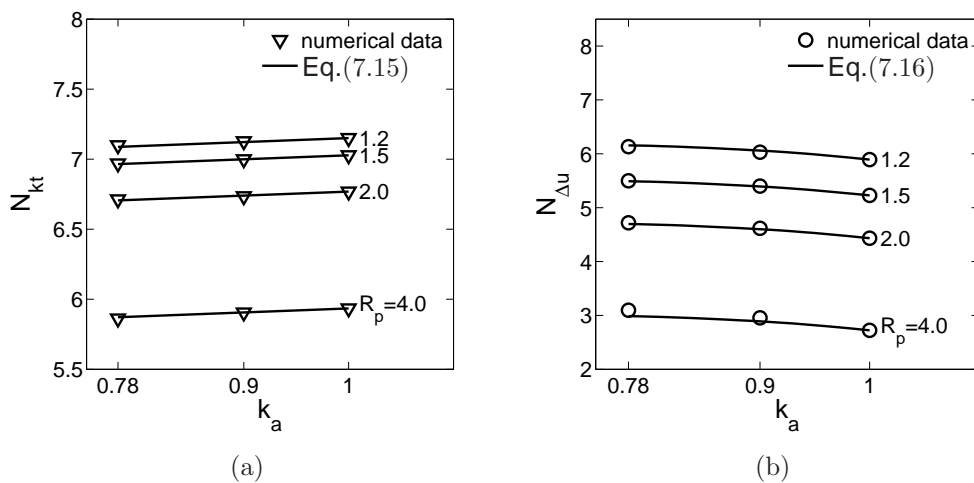


Figure 7.23: Effect of strength anisotropy on the cone factors.



tained results which are shown in Figure 7.23 reveal that the adopted strength criterion marginally affects the cone factors<sup>5</sup>. In the presented model, the strength anisotropy effect on the cone factors can thus be taken into account using the following proposed correlations:

$$N_{kt}(k_a) = N_{kt}^{k,iso} + \frac{k_a - 1}{3.5} \quad (7.15)$$

and

$$N_{\Delta u}(k_a) = N_{\Delta u}^{k,iso} + \frac{\sqrt{k_a - 1}}{1 + k_a} \quad (7.16)$$

where  $N_{kt}^{k,iso}$  and  $N_{\Delta u}^{k,iso}$  denote the cone factors corresponding to the isotropic strength envelope, i.e.  $k_a = 1$ .

#### *Effect of initial stress anisotropy on cone factors*

The effect of initial stress anisotropy was investigated by fixing  $I_r$  equal to 25, and changing values of parameter  $\Delta$  between -0.5 and 0.5. In each simulation the strength anisotropy was enforced by setting  $k_a = 0.78$ . By maintaining the initial effective mean pressure  $p'_o$  constant, the same value of  $c_u$  was obtained for each test, whereas various  $\Delta$  was obtained by changing the ratio between horizontal and vertical stresses. The effect of stress anisotropy was analyzed in terms of both cone factors and effective pressure ratio ( $p'_n/c_u$ ) and the results are plotted in Figure 7.24. As expected, the relationship between  $\Delta u$  and  $N_{kt}$  is basically linear and the cone factor which accounts for the stress anisotropy  $N_{kt}(\Delta)$  can be calculated through:

$$N_{kt}(\Delta) = N_{kt}^{\Delta,iso} - 2.21\Delta \quad (7.17)$$

where  $N_{kt}^{\Delta,iso}$  corresponds to isotropic stress conditions and can be derived using Equation (7.9).

The gradient of  $\Delta$  obtained for the present model exhibits consistency with the

---

<sup>5</sup>In the analysis, the cone factors were derived taking the values of  $c_u$  obtained for the spherical expansion criterion and the compression meridian, i.e.  $r(\theta) = 1$ .

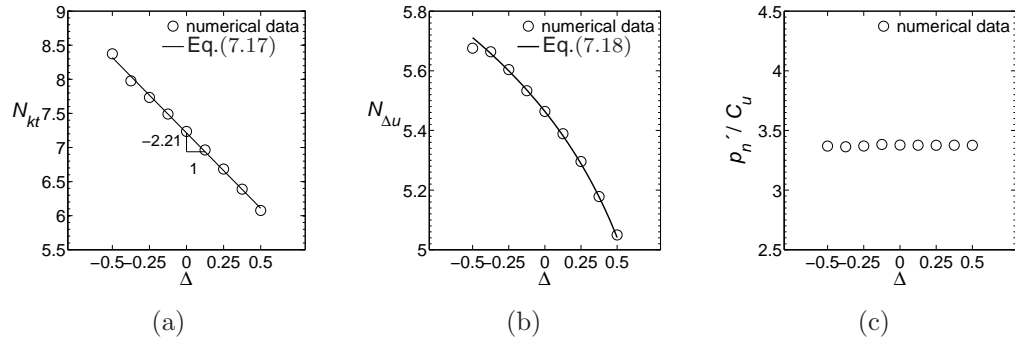


Figure 7.24: Effect of the initial stress anisotropy on the cone factors.

results derived from other studies which suggest the values of  $\Delta$  between -2.1 and -1.83 (refer to Table 6.2).

A non-linear relationship can, however, be observed for the factor  $N_{\Delta u}$ , as shown in Figure 7.24(b)). This observation can be explained by the fact that  $u_2$  measurements are sensitive to the rotation of the principal stresses. Hence, a stronger effect is observed for positive values of  $\Delta$  (i.e.  $\sigma_{vo}$  larger than  $\sigma_{ho}$ ) due to rotation of the maximal principal stress  $\sigma_1$  initially associated with  $\sigma_{vo}$  to horizontal stress components. The following non-linear expression has been proposed to consider stress anisotropy in the present model:

$$N_{\Delta u}(\Delta) = N_{\Delta u}^{\Delta, \text{iso}} + 0.61 \ln(1 - \Delta) \quad (7.18)$$

where  $N_{\Delta u}^{\Delta, \text{iso}}$  corresponds to isotropic stress conditions and can be derived using Equation (7.12).

On the other hand, as illustrated in Figure 7.24(c), the stress anisotropy has no influence on the effective pressure acting on the cone shaft and, in consequence, does not affect sleeve friction measurements  $f_s$ .

### 7.2.2.2 Analysis of drainage conditions

The case of the pressuremeter test (Section 6.2.5) shows that the effect of partial drainage may result in hydro-mechanical coupling of material properties. This fact is clearly associated with plastic straining of the material during partial consolidation. As discussed in Section 6.3.3, in the case of the penetration test, a gain of cone resistance can be expected if partial drainage occurs. The following analysis shows the evolution of cone resistance  $q_t$  computed for various permeability coefficients  $k$  varying from  $10^{-10}$  to  $10^{-3}$  m/s.

In order to qualitatively compare the obtained results with other numerical studies, the values of cone resistance were normalized using the minimal and maximal values of  $q_t$  corresponding to perfectly undrained  $q_t^u$  and fully drained penetration  $q_t^d$  respectively. The results presented in Figure 7.25(a) are compared with other studies of the penetration model. In the first study reported by

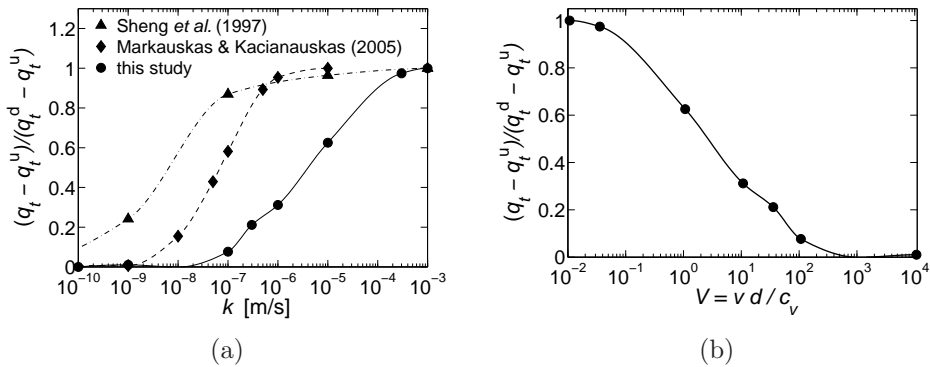


Figure 7.25: Effect of partial drainage on cone resistance in the numerical model. Evolution of  $q_t$  normalized by the measurements corresponding to the fully drained  $q_t^d$  and the perfectly undrained  $q_t^u$  penetration, (a) versus coefficient of permeability, (b) versus normalized velocity of penetration.

Sheng et al. (1997), the penetration is simulated using the MCC model ( $I_r = 32$ ). A relatively coarse mesh in this model could have, however, an influence on the precision of results. The second group of results obtained by Markauskas et al. (2005) was obtained for the Drucker-Prager/Cap model with ( $I_r = 43$ ). For the present model, transient drainage conditions may occur for  $k$  from  $10^{-8}$  to  $10^{-3}$  m/s. Note that the undrained threshold is similar to the field data presented in Figure 6.25. However, various thresholds for drained and undrained penetration can be observed for different models, which can be explained by employing different consolidation characteristics (i.e.  $c_v$ ). Therefore, the present model is further evaluated by means of normalized velocity of penetration  $V$  (Equation (6.62)). The results presented in 7.25(b) exhibit considerable consistency with the experimental measurements derived from laboratory centrifuge tests, i.e. undrained conditions are met for normalized velocities larger than approximately 100 (Randolph and Hope, 2004; Schneider et al., 2007, see Figure 6.26(a)). This number corresponds to the coefficients of compressibility  $c_v$  larger than  $7.14 \cdot 10^{-5} \text{m}^2/\text{s}$ , assuming both standard velocity of penetration and the standard cone diameter (ISSMGE, 1999).

These results clearly show that for intermediate soils like silts ( $k \cong 10^{-8} \div 10^{-6} \text{m/s}$ ), cone resistance may increase up to approximately 30% with respect to "undrained" resistance. The simulations of penetration in less permeable materials corresponding to silty clays ( $k \cong 10^{-9} \div 10^{-8} \text{m/s}$ ), show that the undrained regime is preserved.

A gain in cone resistance has its source in the partial dissipation of pore pressure during penetration. Figure 7.26 demonstrates that in the case of undrained

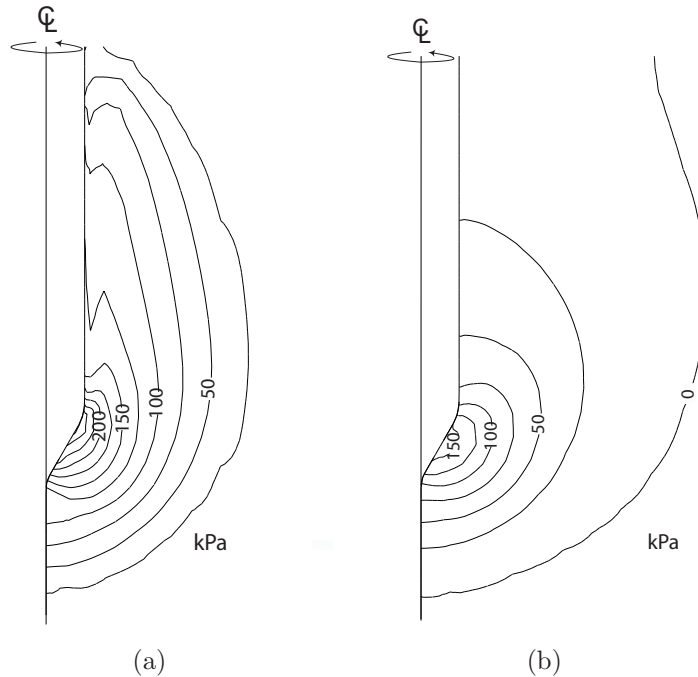


Figure 7.26: Excess pore water pressure (kPa) around the cone at steady state: (a) undrained  $k = 10^{-10} \text{m/s}$ , (b) partially drained  $k = 10^{-6} \text{m/s}$ .

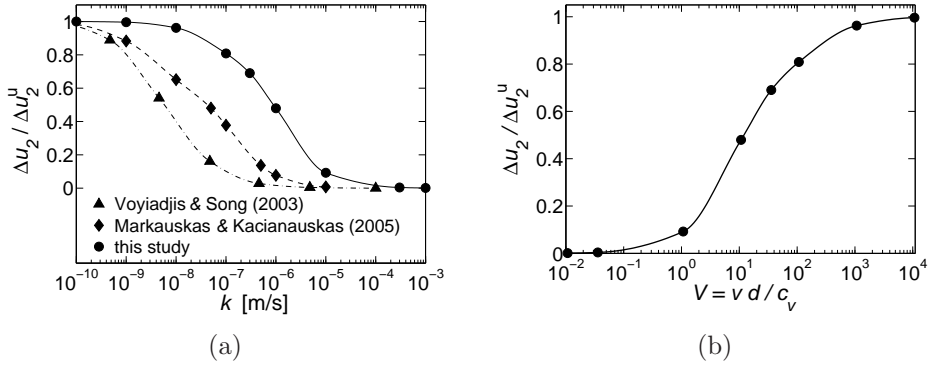


Figure 7.27: Effect of partial drainage on pore pressure in numerical models. Evolution of  $\Delta u_2$  normalized by  $\Delta u_2^u$  corresponding to undrained penetration, (a) versus coefficient of permeability, and (b) versus normalized velocity of penetration.

penetration, soil permeability does not allow the excess pore pressure to quickly dissipate right behind the cone and the pore pressure distribution is stretched along the shaft. On the other hand, the dissipation which occurs in conditions privileging partially drained conditions, reduces the zone of high pressure iso-lines which are formed, in this case, as a round bulb.

In the further analysis, thresholds for fully drained and perfectly undrained penetration were investigated in terms of  $u_2$  measurements. For each test, the pore pressure record was taken as the maximal pore pressure  $\Delta u_2$  built-up with achieving the steady state. The obtained results were then normalized by the value  $\Delta u_2^u$  corresponding to the undrained penetration 7.27. Similarly to the analysis of cone resistance, the results derived from the present model vary in comparison to other numerical models which, again, may be attributed to various consolidation characteristics assigned in the analyzes. For assumed material properties in the present study, the undrained and drained thresholds are observed as around  $k = 10^{-9}$ m/s and  $10^{-4}$ m/s respectively. On the other hand, an analysis in terms of the normalized velocity  $V$  reveals a high level of coherency of the developed model with laboratory results presented in Figure 6.26(b), i.e. transient drainage conditions can be expected for normalized velocities between 0.01 and 1000. This observation is also confirmed by the evolution of the pore pressure parameter  $B_q$  presented which is shown in Figure 7.28.

### 7.2.2.3 Friction effects on piezocone measurements

During penetration, three variables can be independently measured, namely cone resistance, shaft resistance and excess pore water pressure. In a numerical analysis, total cone resistance  $q_c$  can be calculated by dividing the total cone pushing force  $F_c$  by the projected cone area  $A_c$  (Figure 7.29):

$$q_c = F_c / A_c = 4F_c / \pi d_c^2 \quad (7.19)$$

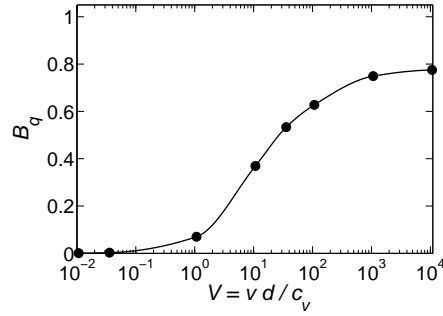


Figure 7.28: Effect of partial drainage on pore pressure parameter plotted against normalized velocity of penetration.

*Contribution of the frictional interface to the total cone resistance*

The total cone pushing force can be decomposed into the resistance force at the tip  $F_t$  and friction force on the cone shaft  $F_s$ :

$$F_c = F_t + F_s \quad (7.20)$$

Figure 7.30 shows the evolution of the total cone pushing force with the cone advancing downward. As the steady-state is achieved at the depth of about 5 cone diameters, no further increase of  $F_c$  is observed in the case of perfectly smooth interface (i.e.  $\mu = 0$ ). An introduction of non-smooth interface leads to a further linear increase of  $F_c$  which is associated to an increasing total resistance of the interface. Clearly, the slope of  $F_c$  is proportional to the friction coefficient  $\mu$ . Note that for the smooth interface, total cone resistance is equal to the tip force, i.e.  $F_c|_{\phi_i=0} = F_t|_{\phi_i=0}$  and the latter is directly the resistance force corresponding to the actual tip resistance  $q_t$  which should also include tip frictional resistance. The actual tip resistance  $q_t$  can be obtained for the frictionless interface model by multiplying the nominal cone resistance corresponding

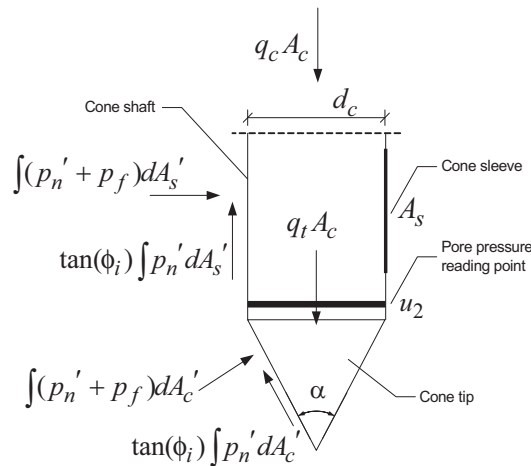


Figure 7.29: Scheme of contribution of the interface friction to the total cone resistance and regions of measurements.

to the smooth interface  $\bar{q}_t = q_c|_{\phi_i=0}$  by a tip friction factor  $\eta_t$ :

$$q_t = \eta_t \bar{q}_t \quad (7.21)$$

The tip friction factor  $\eta_t$  can be derived from the cone tip equilibrium presented in Figure 7.29:

$$q_t A_c = \sin(\alpha/2) \int_{A'_c} (p'_n + p_f) dA'_c + \cos(\alpha/2) \tan \phi_i \int_{A'_c} p'_n dA'_c \quad (7.22)$$

where  $A'_c$  denotes a tip area,  $\alpha$  is the angle of the cone tip,  $p'_n$  is the effective pressure normal to the cone surface and  $p_f$  is the fluid pressure. Hence, the cone tip factor can be derived from the ratio  $q_t A_c / \bar{q}_t A_c$  which leads to:

$$\eta_t = 1 + \cot(\alpha/2) \tan \phi_i \frac{\int_{A'_c} p'_n dA'_c}{\int_{A'_c} (p'_n + p_f) dA'_c} \quad (7.23)$$

Hence,  $\eta_t$  may depend on cone roughness and the degree of fluid pressure dissipation during penetration. Replacing the last component with coefficient  $\vartheta_t$ , the above equation can be written as:

$$\eta_t = 1 + \vartheta_t \cot(\alpha/2) \tan \phi_i \quad (7.24)$$

In order to deduce an actual  $\eta_t$  which accounts for different drainage conditions, numerical tests with different friction coefficients need to be performed. As the steady-state is reached, the tip friction factor can be obtained from numerical results (cf. Huang et al., 2004):

$$\eta_t = \frac{F_c - F_s}{\bar{F}_c} \quad (7.25)$$

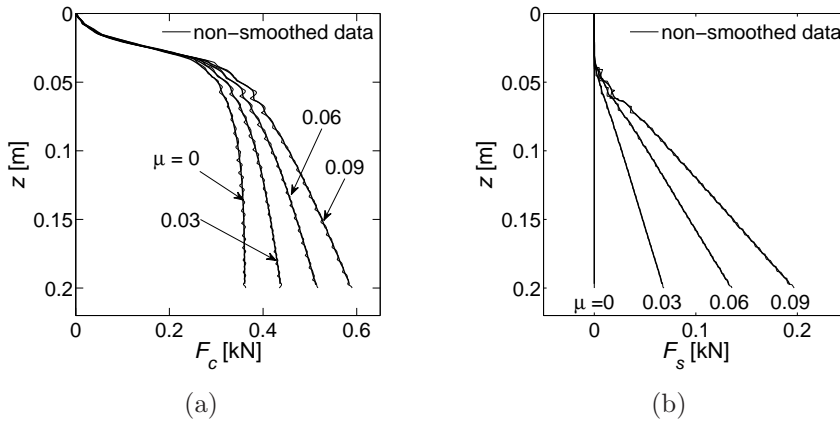


Figure 7.30: Evolution of (a) the total pushing force, and (b) the total shaft force with penetration depth for various interface friction.

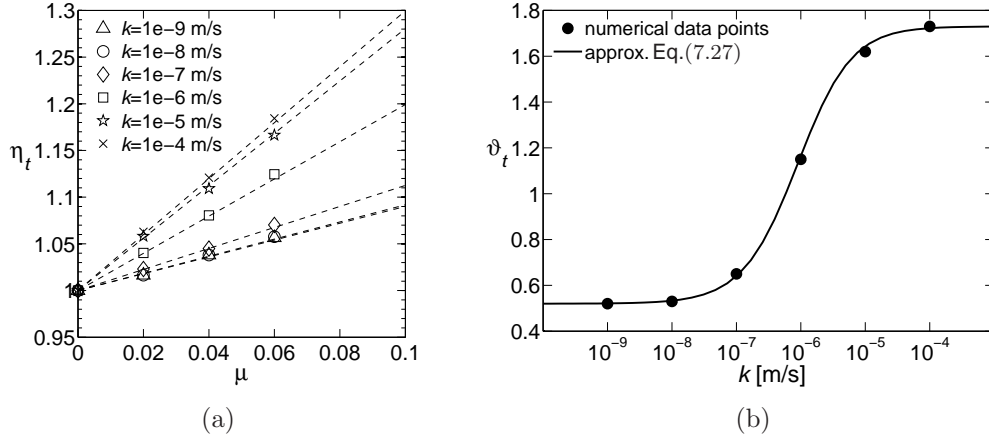


Figure 7.31: Calibration of the cone tip friction factor  $\eta_t$ , (a)  $\eta_t$  derived from numerical simulations, (b) approximation of the correction coefficient  $\vartheta_t$  as a function of soil permeability.

where  $\bar{F}_c$  denotes cone resistance for perfectly smooth interface, i.e.  $\bar{F}_c = F_c|_{\phi_i=0}$ , and  $F_s$  is computed by integrating the shear stress along the interface surface:

$$F_s = \int_{A'_s} p'_n \tan \phi_i dA'_s \quad (7.26)$$

where  $A'_s$  is the total shaft area.

Performed numerical simulations demonstrate that  $\vartheta_t$  indeed depends on drainage conditions, as shown in Figure 7.31(a). While for perfectly undrained and perfectly drained conditions  $\vartheta_t$  remains constant, the occurrence of partial drainage introduces variability of this coefficient from 0.52 to 1.73. The approximation of the correction coefficient  $\vartheta_t = \vartheta_t(k)$ , which is presented in Figure 7.31(b), can be derived from:

$$\vartheta_t(k) = \vartheta_t^d + \frac{\vartheta_t^u - \vartheta_t^d}{(1 + \alpha_i k)^n} \quad (7.27)$$

where  $\vartheta_t^d$  and  $\vartheta_t^u$  correspond to the results obtained for perfectly drained and perfectly undrained conditions respectively, and the other fitted parameters are  $\alpha_i = 10^6$  and  $n = 0.75$ . Note that  $\alpha_i$  corresponds to the inverse of the mean value of the limit permeability coefficients, which ensure the penetration under undrained and drained conditions, i.e.  $k = 10^{-9}$  and  $k = 10^{-3}$  respectively (see Section 7.2.2.2).

Since the partial drainage is also related to other characteristics such as  $e$  or  $\lambda$ , it is thus more appropriate to make  $\vartheta_t$  the function of normalized penetration velocity  $V$ . The approximation of the correction coefficient  $\vartheta_t = \vartheta_t(V)$  becomes then:

$$\vartheta_t(V) = \vartheta_t^u - \frac{\vartheta_t^u - \vartheta_t^d}{(1 + \alpha_i V)^n} \quad (7.28)$$

where  $\alpha_i$  is calibrated equal to 0.07 and  $n = 1.1$  for the standardized rate of penetration  $v = 2$  cm/s and the cone diameter  $d = 35.7$  mm. A graphical interpretation of the above equation is shown in Figure 7.32.

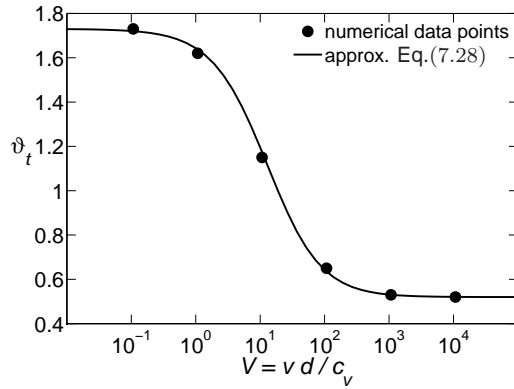


Figure 7.32: Approximation of the correction coefficient  $\vartheta_t$  as a function of normalized penetration velocity.

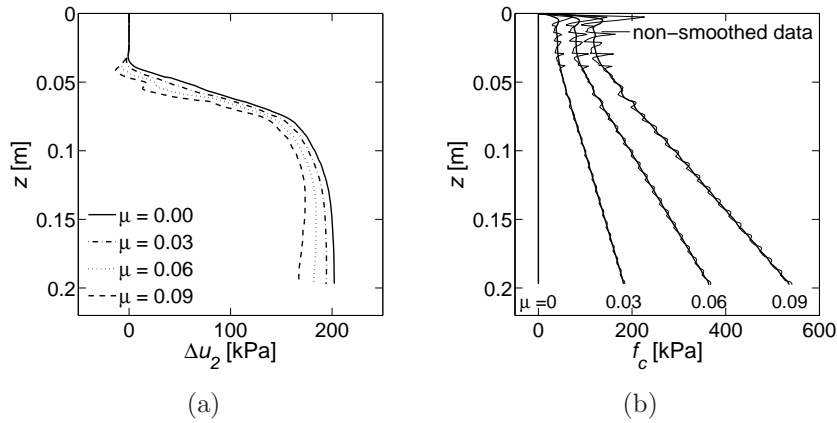


Figure 7.33: Evolution of (a) excess pore water pressure, (b) the total shaft resistance with the penetration depth for various interface friction.

### *Contribution of the frictional interface to excess pore water pressure*

The frictional interface may also affect the magnitude of pore pressure measurements. Performing two numerical simulations for perfectly "smooth" and "rough" cones, Sheng et al. (1997) revealed some differences in pore pressure distribution around the cone. Hereafter, the friction effect on pore pressure readings will be investigated using the developed model of penetration. Figure 7.33(a) shows the evolution of excess pore pressure during undrained penetration for various friction coefficients.

Although accounting for cone geometry is not necessary when analyzing the effect of friction on pore pressure measurements, the pore pressure factor can be defined similarly to  $\eta_t$  in order to compare magnitude of the friction effect:

$$\eta_u = \frac{\Delta \bar{u}_2}{\Delta u_2} \quad (7.29)$$

where  $\Delta \bar{u}_2$  denotes the excess pore water pressure at the steady-state for a



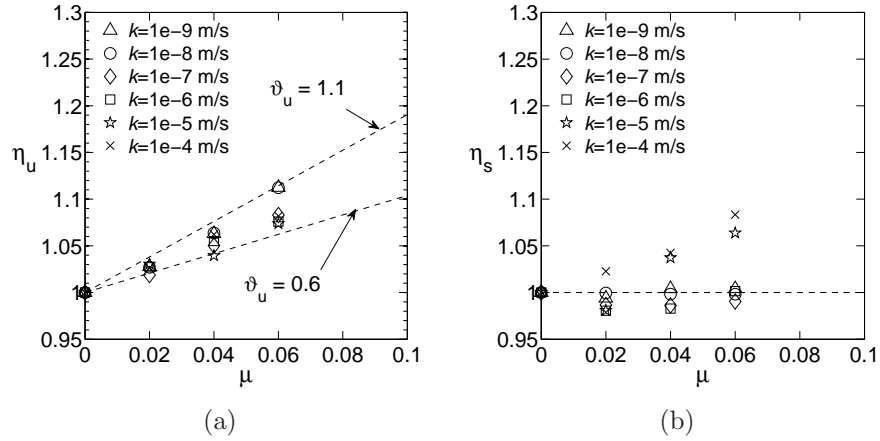


Figure 7.34: Calibration of the friction factors (a)  $\eta_u$ , and (b)  $\eta_s$ .

perfectly smooth shaft, i.e.  $\Delta \bar{u}_2 = \Delta u_2|_{\phi_i=0}$ .

Similarly to Equation (7.24), the pore pressure friction factor can be calculated accordingly:

$$\eta_u = 1 + \vartheta_u \cot(\alpha/2) \tan \phi_i \quad (7.30)$$

where  $\vartheta_u$  is the correction coefficient varying between 0.6 and 1.1 as derived from numerical results, as presented in Figure 7.34(a). Note that the increasing friction reduces  $u_2$ . Since no regular trend of drainage effect is observed for the excess pore water pressure, a constant value for  $\vartheta_u$  can be assumed. A further analysis presented in Section 8.2 revealed that the value for  $\vartheta_u$  equal to 0.60 is more appropriate for a numerically generated database of piezocone measurements.

#### Contribution of friction to the cone factors

Considering the results derived from two previous analyzes, the magnitude of the friction effect on the tip cone factor  $N_{kt}$  and the pore pressure factor  $N_{\Delta u}$  can be evaluated. Figure 7.35 shows quantitatively a contribution of friction to these factors for various cone roughness  $\alpha_f$ . Based on these results, the cone factor  $N_{kt}$  developed in Equation (7.9a) for undrained conditions becomes:

$$N_{kt}^s = -0.55 + 2.37 \ln I_r + 3.81\alpha_f \quad (7.31)$$

and correspondingly, the cone factor  $N_{\Delta u}$  proposed in Equation (7.12a) is obtained as:

$$N_{\Delta u}^s = 1.12 + 1.34 \ln I_r - 2.00\alpha_f \quad (7.32)$$

It has to be noticed that the gradient of  $\alpha_f$  in Equation (7.31) is surprisingly high in comparison with other studies as presented in Table 6.2. However, the final solution for the cone factor  $N_{kt}$  derived from the present model applying  $\alpha_f$  equal to 0.3, reveals consistency with the typical  $N_{kt}$  values quoted by Lunne et al. (1997), as shown in Figure 7.36.

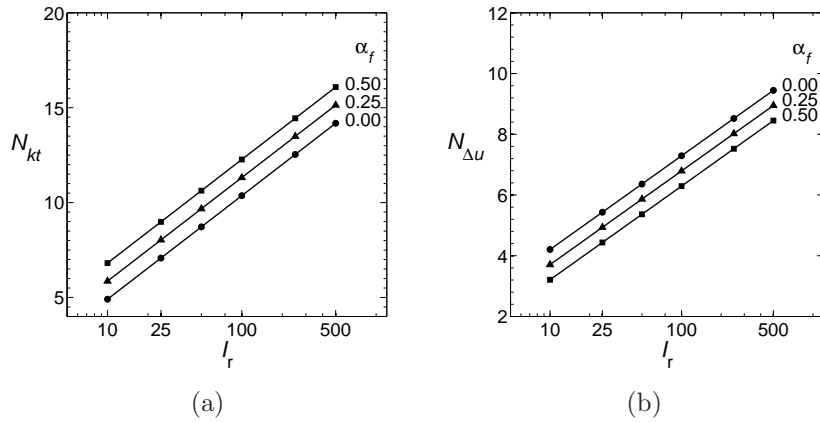


Figure 7.35: Friction contribution to cone factors in undrained conditions, (a)  $N_{kt}$ , and (b)  $N_{\Delta u}$ .

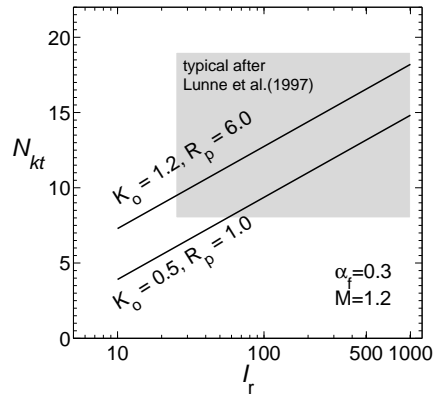


Figure 7.36: Theoretical solution of the cone factor  $N_{kt}$  derived from the developed model and a typically observed range quoted by Lunne et al. (1997).

### *Contribution of the frictional interface to the normal effective contact force at the cone shaft*

Assuming that the friction force on the shaft  $F_s$  can be evaluated from Equation (7.26) for a numerical analysis with the zero-friction interface, it is necessary to investigate the influence of interface friction on the effective normal contact force  $P'_n$ . The latter can be determined from numerical results by integrating the effective normal contact pressure  $p'_n$  along the cone shaft  $A'_s$ . The friction effect was analyzed for different drainage conditions for which  $P'_n$  values were computed. Figure 7.33(b) shows examples of the evolution of total shaft resistance during undrained penetration in various friction conditions.

The friction effect on the shaft resistance was measured through the shaft fric-

tion ratio  $\eta_s$  defined as:

$$\eta_s = \frac{\bar{P}'_n}{P'_n} \quad (7.33)$$

where  $\bar{P}'_n$  denotes the cone resistance for a perfectly smooth interface, i.e.  $\bar{P}'_n = P'_n|_{\phi_i=0}$ .

Figure 7.34(b) shows that the interface friction on the normal effective contact pressure can be considered as negligible for analyzes with  $k = 10^{-9} \div 10^{-6}$  m/s. Some influence can be observed for quasi-drained analyzes ( $k = 10^{-5} \div 10^{-4}$  m/s). It can be explained by an increase of effective stresses in soil, and consequently, of the normal effective contact pressure behind the cone tip due to quick pore pressure dissipation in this region. An example of the reduced 'pore pressure bulb' which stems from the quick dissipation has already been presented in Figure 7.26(b). However, the order of magnitude  $k = 10^{-5} \div 10^{-4}$  m/s will not be taken into consideration during NN pattern generation because such coefficients are observed for sands.

Since the interface friction has a negligible influence on the normal effective contact pressure, during the generation of NN training patterns, cone readings will be computed for zero-friction interface models and the contribution to the sleeve resistance  $f_s$  will be calculated by multiplying the integrated normal effective contact pressure  $\bar{p}'_n$  over the cone sleeve  $A_s$  (refer to Figure 7.29) by a randomly assigned friction coefficient  $\mu^6$ :

$$f_s = \mu \int_{A_s} \bar{p}'_n dA_s \quad \text{where} \quad \bar{p}'_n = p'_n|_{\phi_i=0} \quad (7.34)$$

#### *Friction-induced effect of element distortion*

Since the Arbitrary Lagrangian-Eulerian formulation has not been successfully applied in the presented FE model of cone penetration, the use of a frictional interface may create some limitations. These are mainly related to the distorted mesh quality which may affect either the stability of the solution or the quality and accuracy of the obtained numerical results<sup>7</sup>.

A number of tests for various friction coefficients was performed in order to investigate a range of applications of a "rough" interface in the developed model. The results derived from undrained penetrations for  $\mu = 0 \div 0.12$  corresponding to  $\phi_i = 0^\circ \div 6.84^\circ$  are presented in Figure 7.37. The figure demonstrates that the linear influence of the increasing cone roughness on cone resistance, excess pore water pressure and shaft resistance is observed up to certain thresholds. The results presented in Figure 7.37(a) show that cone resistance exhibits pure linear increase up to  $\mu$  approximately equal to 0.10. The results above this point start to deviate slightly from the linear trend. The effect of element distortion

<sup>6</sup>An interval of considered friction coefficients is assumed according to analysis presented in Section 7.2.1.2.

<sup>7</sup>Isoparametric elements should not be distorted less than  $45^\circ$  or more than  $135^\circ$ , cf. ABAQUS (2007).

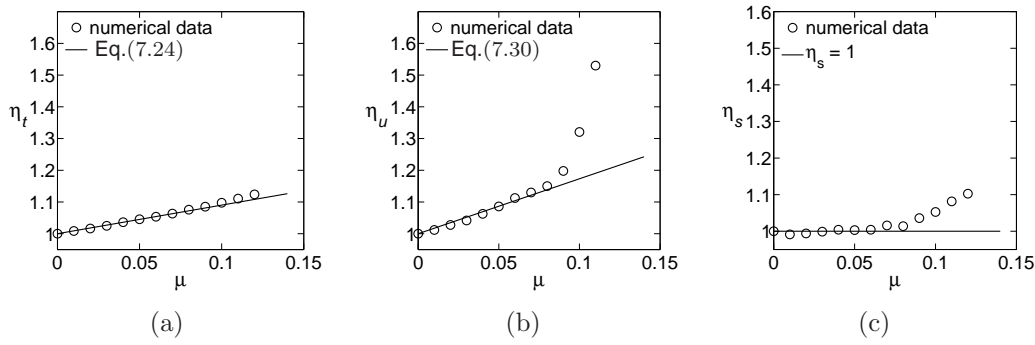


Figure 7.37: Friction effect on numerical measurements derived from distorted elements. Evolution of friction factors in the function of the friction coefficient  $\mu$ : (a) cone tip friction factor  $\eta_t$ , (b) pore pressure friction factor  $\eta_u$ , (c) shaft friction factor  $\eta_s$ .

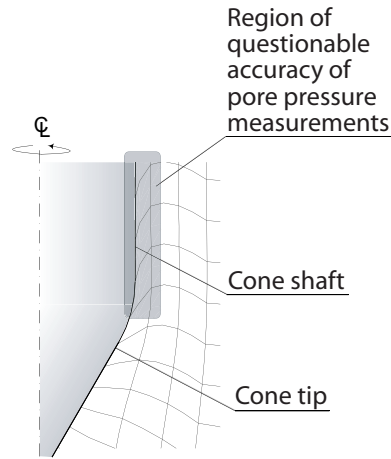


Figure 7.38: Effect of mesh distortion after cone penetration for friction coefficient  $\mu$  equal to 0.12.

for a "rough" interface is shown in Figure 7.38. The effect of element distortion on cone resistance is not very severe as the response of the material below the cone tip belongs, to a large degree to undistorted elements. The noticeable influence is thus related to the element distortions that can be observed in the transition region including the part of the cone tip next to the cone base. On the other hand, the diagram demonstrates high mesh distortions along the cone shaft. High element distortions strongly affect pore pressure and shaft friction results, as shown in Figure 7.37(b) and 7.37(c). These results reveal a linear trend until the friction coefficient threshold of around 0.08. In particular, it can be noticed that pore pressure results are very sensitive to element distortion. This loss of accuracy due to high element distortion may also be attributed to possible element locking effects.

### 7.2.3 Semi-numerical model for the NN pattern generation

The above analyzes demonstrate that the rigorous FE simulation of cone penetration in a two-phase soil must be carefully analyzed if "rough" interface is considered. An effective analysis of "rough" interface penetration requires the use of a robust ALE formulation which would be able to maintain a high quality mesh throughout the whole penetration. Due to limitations of the pure UL formulation used in the presented FE model, the NN training patterns will be computed for perfectly "smooth" interface. In this case, the final measurements of tip cone resistance  $q_t$  and pore pressure  $u_2$  will be evaluated using Equation (7.21) and Equation (7.29) using relevantly derived friction factors,  $\eta_t$  and  $\eta_u$  from Equation (7.24) and Equation (7.30) respectively. Taking into account a number of NN training patterns to be generated, such an approach can be considered as advantageous for the CPU time which is substantially reduced for a "smooth" contact problem.

## 7.3 Summary and remarks

This chapter demonstrates that numerical modeling is suitable to solve complex hydro-mechanical systems representing the boundary value problems of both the pressuremeter and the piezocone tests.

The numerical model of a pressuremeter shows that a partial drainage may occur during an expansion test even in clay, which is characterized by the coefficient of permeability  $k$  larger than around  $10^{-11}$ m/s. In effect, partial consolidation that occurs may strongly affect the shape of pressuremeter curves. It has been illustrated that, owing to the non-uniqueness of strength parameters in the case of the MCC model, a simultaneous identification of  $M$  and  $R_p$  requires the use of both PET records, i.e. applied pressure and pore pressure. Furthermore, the performed sensitivity analysis confirms coupling of deformation, strength and consolidation characteristics. The feedback between model parameters may be strongly pronounced in the event of partial drainage occurrence suggesting a mutual fitting of all available pressuremeter curves in the same optimization run.

As regards the piezocone test, the development of a rigorous FE model of cone penetration has been presented. The model involves numerical formulation for two-phase non-linear material including the large strain theory as well as the finite contact formulation allowing large displacements to be applied. Despite of the failure in incorporating the ALE technique into the model framework, the model reliably represents the behavior of a normally- and lightly consolidated soil revealing considerable consistency in terms of the measured cone factors with the experimental data and numerical predictions derived from other studies. An equivalent semi-numerical approach has been proposed to account for a frictional interface due to a severe loss of results accuracy observed in the fi-

nite elements adhered to the "rough" interface described by friction coefficients  $\mu$  larger than 0.08. In accordance with centrifuge laboratory tests, numerical simulations revealed the occurrence of a partial drainage effect during penetration for soils which exhibits values of consolidation coefficient  $c_v$  larger than  $7.14 \cdot 10^{-5} \text{m}^2/\text{s}$  roughly corresponding to the permeability coefficients larger than about  $10^{-8} \text{m}/\text{s}$ .

The numerical models of the pressuremeter and piezocone will be used for generating a synthetic database of field measurements being employed in the NN training, according to the strategy presented in the following Section 8. In the case of the piezocone test, a considerable computational effort is reduced by optimizing the mesh size and steady-state depth, which both depend on the rigidity of the material. The different mesh sizes revealed consistency in computed measurements. Unfortunately, some shortcomings of the model have been recognized due to the inefficiency of numerical procedures. The use of the numerical model to generate synthetic database is thus limited to representing rather soft soil which exhibits the rigidity index  $I_r$  less than 110 and  $G/p'_o$  less than 70. However, an extension of model applicability for  $I_r$  larger than 110 can be carried out using the proposed theoretical solutions derived from the presented numerical simulations of the undrained penetration.

## Chapter 8

# Parameter Identification for *In Situ* Tests

*Statistics are like bikinis.  
What they reveal is suggestive,  
but what they conceal is vital.*

Aaron Levenstein

In this chapter, an application of the parameter identification strategy which has been proposed in Section 2.4 is presented for the SBPT. Moreover, an application of NNs to predict model parameters from the CPTU is demonstrated. The FE models developed for these two field tests are used to generate a numerical database of pseudo-experiments. A synthetic database can be generated based on a large number of permutations which widely cluster the multidimensional space of constitutive parameters and state variables. Test measurements which correspond to particular parameter permutations can be then used to perform the NN training with the aid of the back-propagation algorithm. The trained NNs can be then used to predict model parameters from experimental data.

The chapter is divided into two main sections related to the SBPT and the CPTU test respectively. Each section describes in detail a numerical generation of databases which contain synthetic measurements derived from FE models. In the case of the piezocone test, the generated database is verified with trends observed for real experimental data. For each considered BVP, specific definitions of the NN input vectors are proposed and NN training is performed. In the post-training analysis, regression analyzes are carried out to investigate accuracy of NN predictions. Moreover, in the case of SBPT, the efficiency of the two-level parameter identification is analyzed through numerical simulations of the test.

## 8.1 Hybrid neural network/gradient-based model calibration based on pressuremeter tests

In the following section, an enhanced back-analysis scheme proposed in Section 2.4 is adopted for the SBPT problem in order to identify the MCC model parameters.

### 8.1.1 Strategy of parameter identification

The main goal of the hybrid approach is to map field measurements, through the neural network, onto model parameters with a decreased computational time. Thanks to parallel processing of input data, model parameters are predicted instantly without the necessity of running FE analyzes. Such a quickly and well-approximated vector of parameters, if needed, may then be optimized within very few iterations using the gradient-based local update procedure in which FE simulations of SBPT have to be carried out. The flow chart of the proposed methodology is shown in Figure 8.1.

The numerical minimization of SBPT data requires mutual fitting of all possible measurements due to the hydro-mechanical parameter feedback. Such a gradient-based optimization of pressuremeter data was presented by Rangeard et al. (2003). They suggest to prescribe a fixed value of the coefficient of permeability and to optimize strength and stiffness properties based on expansion curves. Then, inversely, those optimized parameters are fixed in order to update the coefficient of permeability by fitting the dissipation curve. The procedure is repeated until convergence is achieved. However, as experienced by the author, this approach may sometimes sustain oscillations at the final stage of optimization leading to long-term global iterations or causing a divergence of the algorithm. The latter may also lead to the instability of the FE analysis if the unconstrained optimization is considered. Divergence can be caused by movable local minima which are a side effect of parameter fixing.

Hence, it is suggested here that all available curves from both the PET and

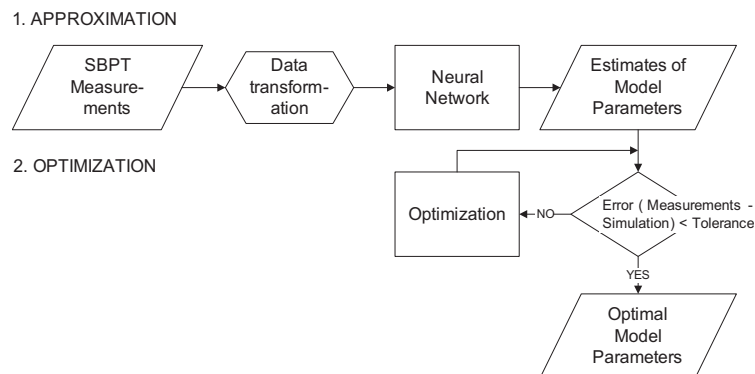


Figure 8.1: Flow chart of numerical processing of SBPT measurements in the two-level parameter identification.



Table 8.1: Summary of parameters intervals considered in the NN training for SBPT problem.

Parameter	Unit	Value or Interval	Pdf or intercorrelation $f(b_j)$
<i>Constants</i>			
$\nu$		0.32	
$p'_o$	[kPa]	200.0	
<i>Variables</i>			
$\varepsilon_c^{\max}$ (for PET)	[%]	$\langle 8.5; 10.5 \rangle$	Uniform
$e_o$		$\langle 0.10; 3.00 \rangle$	Exponential
$\Lambda = 1 - \kappa/\lambda$		$\langle 0.50; 0.95 \rangle$	Normal
$OCR$		$\langle 1.00; 2.00 \rangle$	Uniform
$\beta_1$		$\langle -0.18; 0.18 \rangle$	Uniform
$\beta_2$		$\langle -0.15; 0.15 \rangle$	Uniform
$K_o$		$\langle 0.35; 1.00 \rangle$	$f(OCR, M, \beta)^*$
<i>Parameters to be identified</i>			
$k$	[m/s]	$\langle 10^{-8}; 10^{-12} \rangle$	Uniform of $\ln(k)$
$\lambda$		$\langle 0.0102; 0.499 \rangle$	Uniform, $f(e_o)$
$\kappa$		$\langle 0.0012; 0.226 \rangle$	$f(\Lambda, \lambda)$
$M$		$\langle 0.70; 1.40 \rangle$	Normal
$R_p$		$\langle 1.14; 3.15 \rangle$	$f(M, OCR, K_o, K_{onc})$

\*Mayne and Kulhawy (1982)

the PHT test should be fitted simultaneously. The problem which may appear during mutual fitting is that parameters with values of lower order of magnitude (like the coefficient of permeability  $k$ ) may have a stronger influence on the computed scaling parameter  $\rho_r$  which controls the magnitude of the change of native parameters (see Appendix A). However, this can be avoided by introducing a log-transformation of the native values of this kind of parameters (Poeter and Hill, 1998).

Numerous sets of representative training patterns have to be prepared to adjust network weights. Since these patterns are generated numerically, it is highly desired to reduce the computational effort by a careful selection of the parameter permutations for which the FE solver generates the measurements. The number of training patterns can be decreased once reasonable constraints are put on multi-dimensional space of variables  $\mathcal{R}_b$ . Hence, parameter intervals and correlations observed in geotechnical practice can be introduced to skip non-physical or unlikely vectors of parameters. Furthermore, through preserving parameter constraints, the stability of an FE computation for each pattern is assured, so that computational cost is respected. It is also desired to uniformly cover  $\mathcal{R}_b$ , using relevant probability distribution functions (pdf) in order to improve the accuracy of further NN predictions.

The selected intervals, correlations and statistics of the particular variables are described below and are summarized in Table 8.1.

**Slope of normal consolidation line vs. void ratio.** Typical correla-

tions between  $e_o$  and  $\lambda$  are shown in Figure 5.2. In order to cover the presented parameter space, permutations of  $\lambda$  were randomly drawn from the uniform pdf with the variable constrains defined by the upper and lower observable bounds. A random value of  $e_o$  was previously drawn using the exponential pdf. Since  $\lambda$  depends on  $e_o$ , the distribution of  $\lambda$  results in exponential-like pdf which is shown in Figure 8.2(a).

**Slope of the unloading-reloading line.** The observable relationship between  $\lambda$  and  $\kappa$  represented through the plastic volumetric strain ratio  $\Lambda = 1 - \kappa/\lambda$  may fall into an interval  $\Lambda \in \langle 0.50; 0.95 \rangle$  (Mayne, 1980, 2007). For this variable, the normal distribution was assumed to reduce number of patterns with higher values of  $\kappa$  which would be after-effect of high values of  $\lambda$ . A combination of low value of  $\kappa$  and high values of  $M$  and  $R_p$  may result in no excess pore pressure for the MCC model within a considered range of the cavity strain. In the case of undrained or quasi undrained conditions, no excess pore pressure would be generated as no volume change is possible in the elastic domain (cf. Cao et al., 2001). Hence patterns which comprise zero pore pressure measurements are useless by means of parameter identification based on the dissipation test. The distribution of  $\kappa$  in the training pattern set is shown in Figure 8.2(b).

**Slope of the critical state line.** For the aforementioned reason, the distribution of  $M$  was assumed arbitrarily as the normal within intervals which are generally observed in geotechnical practice Figure 8.2(d).

**Coefficient of earth pressure 'at rest'.** Natural soil, in its history, was subject to loading during deposition and then unloading causing change of stress state. Hence, natural deposits, in general, remain in the anisotropic *in situ* stress state which can be characterized by the coefficient of earth pressure at rest  $K_o = \sigma'_{ho}/\sigma'_{vo}$ . The coefficient  $K_o$  for unloaded deposit can be approximated through the empirical correlation which takes into account stress history and value of the coefficient  $K_{onc}$  for normally consolidated soil:

$$K_o = K_{onc}(\text{OCR})^\beta \quad (8.1)$$

where the overconsolidation ratio is defined as  $\text{OCR} = \sigma'_p/\sigma'_{vo}$  with the maximal vertical effective stress denoted as  $\sigma'_p$ ; and the rebound parameter,  $\beta$ , as proposed by Mayne and Kulhawy (1982), can be estimated as  $\beta = \sin \phi'$ , where  $\phi'$  is the effective friction angle. In order to account for an observable divergence for  $\beta$  (Figure 8.3(b)) random dispersals  $\beta_1$  were drawn using the uniform pdf within the interval  $\langle -0.18; 0.18 \rangle$ , so that:

$$\beta = \sin(\phi') + \beta_1 \quad (8.2)$$

Furthermore, the stress path for normally consolidated material can be approximated through the well-known formula  $K_{onc} = 1 - \sin \phi'$  (e.g. Sivakumar et al., 2001). Similarly to  $K_o$ , the scatter for  $K_{onc}$  (Figure 8.3(a)) was drawn from the uniform pdf within the range  $\beta_2 \in \langle 0.15; 0.15 \rangle$ :

$$K_{onc} = (1 - \sin \phi') + \beta_2 \quad (8.3)$$

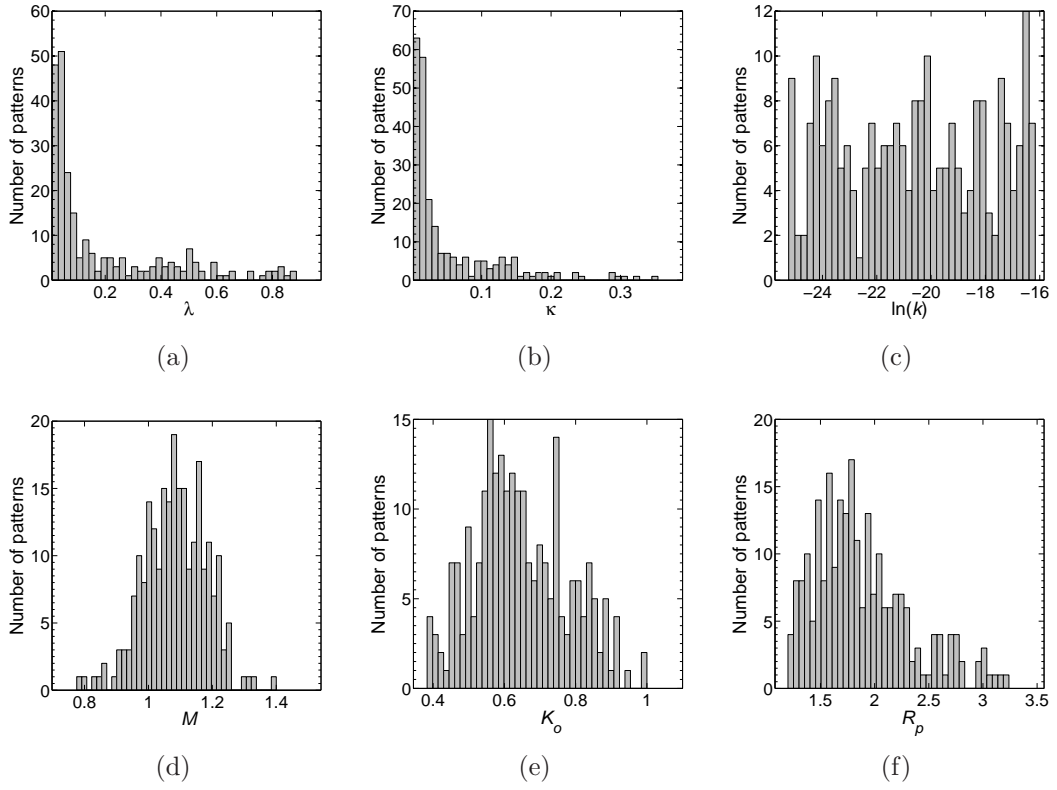


Figure 8.2: Histograms of parameter distributions used to generate the NN training patterns.

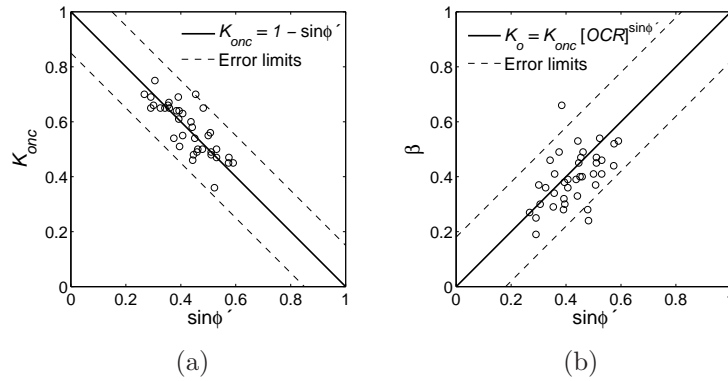


Figure 8.3: Results reported Mayne and Kulhawy (1982) for clays: (a) observed relationship between  $K_{onc}$  and  $\sin \phi'$  with the error limits used in the NN training patterns, (b) observed relationship between 'at rest' rebound parameter  $\beta$  and  $\sin \phi'$  with the error limits used in the NN training patterns.

With the assumption of the uniform pdf for OCR, the distribution of  $K_o$  as the function of OCR,  $M$  and  $\beta$  results in normal-like pdf which is presented in Figure 8.2(e).

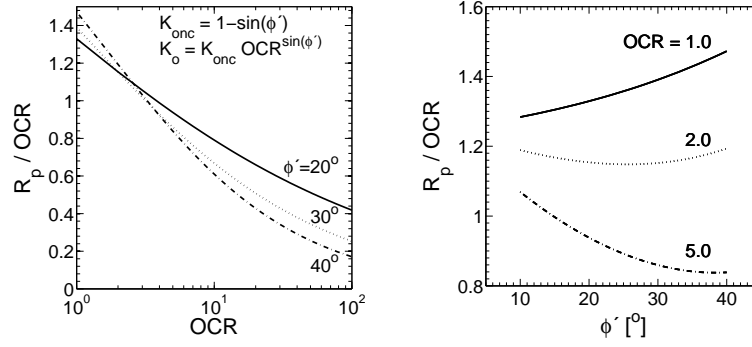


Figure 8.4: Relationship between  $R_p$  and OCR in the Modified Cam clay model.

**Overconsolidation ratio.** The assumption that  $R_p$  is equal to OCR may lead to significant errors as the relationship between  $R_p$  and OCR is expressed as (see Appendix C):

$$R_p = \text{OCR} \frac{9(1 - K_{onc})^2 + M^2(1 + 2K_{onc})^2}{M^2(1 + 2K_o)(1 + 2K_{onc})} \quad (8.4)$$

The graphical interpretation of the above equation is presented Figure 8.4. The distribution of  $R_p$  in training patterns is thus a function of  $M$ , OCR,  $K_o$  and  $K_{onc}$ . The obtained log-normal-like pdf is presented in Figure 8.2(f).

**Coefficient of permeability.** The assumed values of  $k$  for clayey soils are in the range  $k < 10^{-8}$  m/s. Since the upper and lower bounds of the interval vary in four orders of magnitude, the distribution of  $k$  was assumed uniform for the log-transformed parameter, in order to cover wide spectrum of possible drainage conditions (Figure 8.2(c)).

## 8.1.2 Numerical generation of training patterns

In the context of the SBPT, the numerical generation of training patterns was performed according to the approach proposed in Section 3.2.2. The numerical test curves are obtained with the aid of FE simulations using generated combinations of parameters. Figure 8.5 presents 35 exemplary training samples which consist of computed hypothetical curves for PET and PHT. It can be noticed that curves broadly cover the space of possible measurements. Numerical simulations of the holding tests provide experimental curves of excess pore water pressure decay  $\Delta u$  in time  $t$ . Additionally, PHT also provides variation of the cavity strain  $\varepsilon_c$  with respect to time. These measurements combined with variation of the applied pressure  $\psi$  during expansion test enable to train neural networks which will be attributed to the identification of consolidation parameters (see Table 8.2). Apart from provided measurements, additional initial state variables, i.e.  $e_o$  and  $K_o$ , should be defined and evaluated.

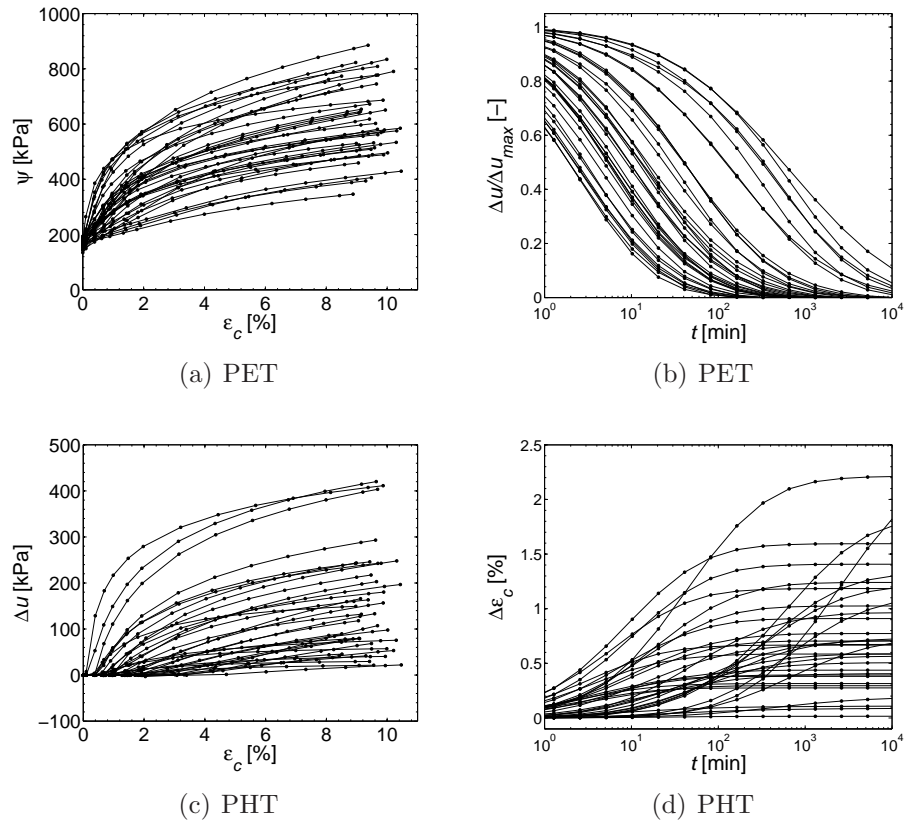


Figure 8.5: Example of 35 training samples comprising of numerical raw measurements.

Other mechanical parameters, i.e.  $M$ ,  $R_p$  and  $\kappa$ , can be identified based on provided measurements of applied pressure  $\psi$  and excess pore water pressure  $\Delta u$ , with respect to the increasing cavity strain  $\epsilon_c$ . Due to the coupled BVP, the input data should additionally be complemented with the NN-identified consolidation parameters and defined initial state parameters. In case of unreliable or inaccessible pore pressure data, it is recommended to set up slope of the CSL line,  $M$ , first; as it is the parameter insensitive to soil sampling (a unique void ratio at failure for a given soil) or the strain rate effect. It is commonly known that the soil preconsolidation pressure is very sensitive to disturbances related to soil sampling or to the strain rate. A mutual identification of  $M$  and  $R_p$  without total and effective stress-strain relief is unreliable due to the non-uniqueness of the solution (see Section 7.1.3).

Table 8.2: Summary of pressuremeter test measurements used for parameter identification by means of suitably generated neural networks.

Parameters to be identified	Test type			Network input data				NN name	
	PET	SHT	PHT	Evaluated parameters	Measurement				
$\kappa, R_p$	•			$M, \lambda, k, e_o, K_o$	$\varepsilon_c - \psi$	$\varepsilon_c - \Delta u$	$t - \Delta u$	$t - \varepsilon_c$	NN12
$\kappa, M, R_p$	•			$\lambda, k, e_o, K_o$		+			NN13
$k$		•		$e_o, \lambda, K_o$			+		NN31
$k, \lambda$			•	$e_o, K_o$				+	NN22

Table 8.3: Summary of input and output vectors used in the neural networks training and prediction.

Input vector $\hat{\mathbf{y}}'(\mathbf{b})$	Neural network name (network architecture*)	Output vector $\mathbf{b}$
$[e_o, K_o, \lambda, k, \varepsilon_1^c, \dots, \varepsilon_{ND}^c, \psi_1^N, \dots, \psi_{ND}^N, M]^T$	$\mapsto$ NN12 (31 6 - 6 2)	$\mapsto$ $[\kappa, R_p]^T$
$[e_o, K_o, \lambda, k, \varepsilon_1^c, \dots, \varepsilon_{ND}^c, \psi_1^N, \dots, \psi_{ND}^N, \Delta u_{ND}^N]^T$	$\mapsto$ NN13 (32 5 - 5 3)	$\mapsto$ $[\kappa, R_p, M]^T$
$[e_o, K_o, \lambda, T_{50}(t_{50}), G/p'_o, c_u^*/p'_o]^T$	$\mapsto$ NN31 (7 3 - 3 1)	$\mapsto$ $[\ln k]$
$[e_o, K_o, T_{50}(t_{50}), \varepsilon_c^N(t_{50}), G/p'_o, c_u^*/p'_o]^T$	$\mapsto$ NN22 (7 6 - 6 2)	$\mapsto$ $[\ln k, \lambda]^T$

\*Number of components in layers: (input | 1<sup>st</sup> layer - 2<sup>nd</sup> layer | output)

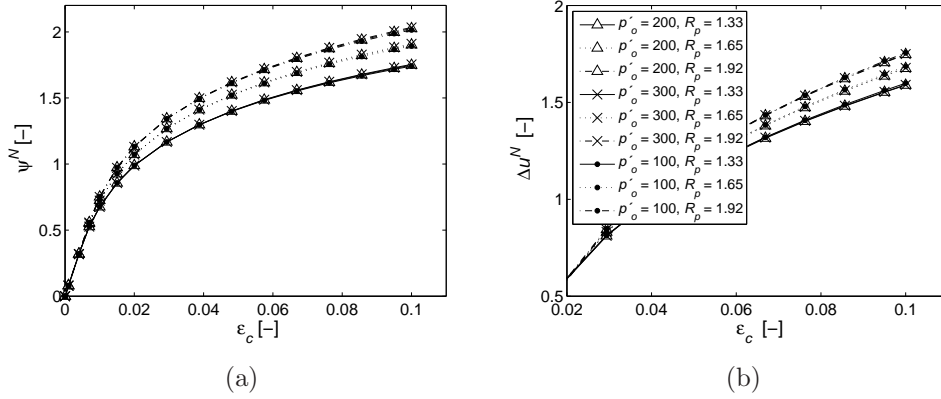


Figure 8.6: Normalization of numerical data of the pressuremeter expansion test for different preconsolidation ratio  $R_p$  with respect to initial stress conditions  $p'_o$ : (a) applied pressure  $\psi$ , (b) excess pore water pressure  $\Delta u$  (the common legend applied).

### 8.1.3 Definition of network input

For practical reasons, it is desired to exclude (but not ignore) the initial stress conditions, i.e. initial effective mean stress  $p'_o$ , from the vector of input variables. It can be achieved by normalizing the experimental measurements with respect to the  $p'_o$ . It means that identification can be carried out regardless of the testing depth. Hence, all the simulations can be run for an arbitrarily assumed value of  $p'_o$ , here  $p'_o = 200\text{kPa}$ , considering the initial stress anisotropy. Such condition implies the necessity of pre-processing measurements contributing to the network input.

A detailed review of analytical closed-form solutions of the cavity expansion problem has led the author to suggest the following normalizing expressions. Total stress/applied pressure measurements can be normalized through:

$$\psi^N = \frac{\psi - \psi_o}{p'_o} \quad (8.5)$$

Based on Equation (6.16), the normalized excess pore water pressure can be calculated as:

$$\Delta u^N = \frac{\Delta u \frac{\Delta V}{V} + c_u^* \ln \left( \frac{G \Delta V}{c_u^* V} \right)}{p'_o} \quad (8.6)$$

where  $G$  can be derived from initial slope of the expansion curve (Equation (6.12)) and  $c_u^*$  denotes the slope of the total stress curve at the final stage of the expansion plotted in the logarithmic scale:

$$c_u^* = \frac{d\psi}{d(\ln \Delta V/V)} \quad (8.7)$$

Note that  $c_u^*$  has no longer meaning of the undrained shear strength  $c_u$ , since the total stress curve can sustain a possible partial drainage effect.

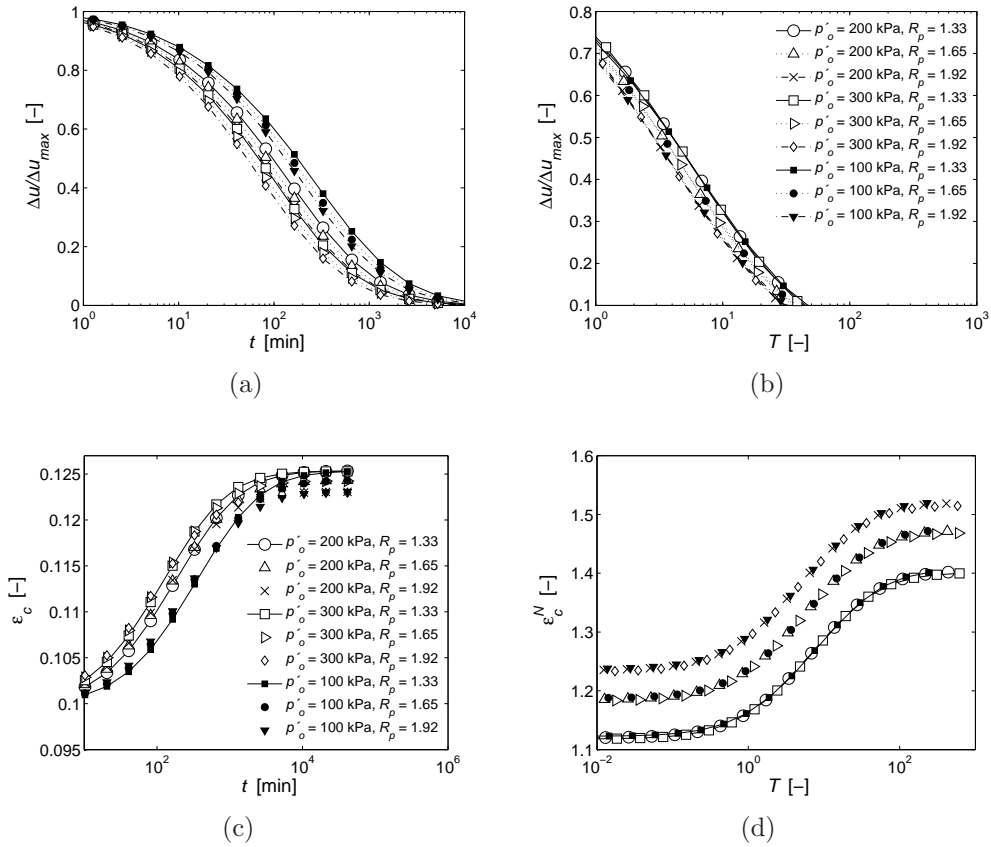


Figure 8.7: Normalization of numerical data of the pressure holding test by means of the time factor  $T$  with respect to the initial stress conditions  $p'_o$  for different overconsolidation ratios  $R_p$ : (a), (b) pore water pressure decay before and after normalization respectively (the common legend applied); (c), (d) consolidation test before and after normalization respectively (the common legend applied).

Examples which justify normalization with respect to  $p'_o$  for different overconsolidation ratios are shown in Figure 8.6.

Since the coefficient of soil permeability  $k$  is unknown during the parameter identification, normalization of the decay of pore water pressure with respect to initial stress conditions can be proceeded similarly to Equation (6.32) as:

$$T = \frac{t}{a_o^2} \frac{k_{\text{ref}}}{\gamma_w} p'_o \frac{\Delta u_{\text{max}}}{\psi_{\text{max}}} \quad (8.8)$$

where the reference coefficient of permeability  $k_{\text{ref}}$  preserves the non-dimensionality of  $T$  and can be assigned arbitrarily as a constant for all the normalized patterns. Note that the unprocessed measurements of  $\Delta u_{\text{max}}$  and  $\psi_{\text{max}}$  provide information concerning soil compressibility. The normalization expression is valid for both the SHT and the PHT. An example of normalization of numerical data of PHT with respect to different initial stress conditions for the different pre-consolidation ratios using Equation (8.8) is shown in Figure 8.7(a) and 8.7(b). These plots justify the proposed normalization.



Similarly, the cavity strain variation for the PHT can be normalized with respect to the initial stress conditions as:

$$\varepsilon_c^N = \varepsilon_c \ln \left( \frac{G}{c_u^*} \right) \frac{\psi_{\max} - u_o}{p'_o} \quad (8.9)$$

where  $\varepsilon_c^N$  is the normalized cavity strain corresponding to the PHT. To justify the above formula, the results of the normalization with respect to the initial stress conditions are presented in Figure 8.7(c) and 8.7(d) for the different over-consolidation ratios.

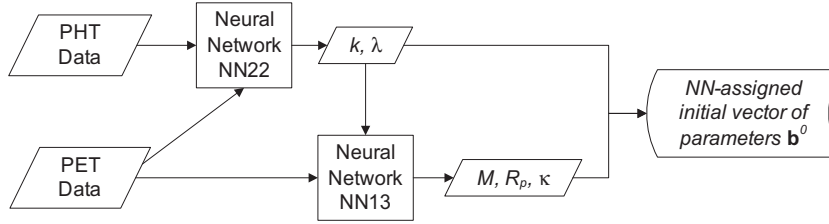
### 8.1.4 Training and post-training analysis

In this study, 240 patterns were used in NN training. This number was based on the experience but it could be further optimized by means of a sensitivity analysis. The patterns included computed simulations of both holding tests which were preceded by the expansion test. Within this set of patterns, 48 samples were randomly designated to be a validation subset which is used to avoid network overfitting during training. Additionally, 161 pseudo-experiments were computed in order to test the post-training performance of neural networks. The testing patterns were not presented to the NNs during the training. The number of the testing samples was intentionally increased for demonstrative purpose. We wanted to demonstrate the performance of NNs which are able to capture a neighborhood of the global solution for many randomly generated tasks.

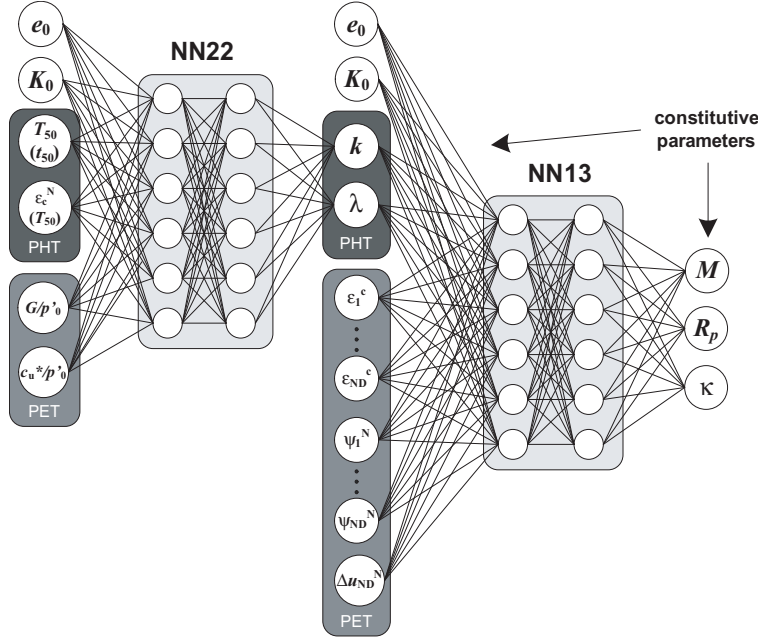
For each expansion test, discrete incremental measurements of the cavity strain  $\varepsilon_i^c$ , applied pressure  $\psi_i$  were drawn ( $i = 1, \dots, \text{ND}$ ). In case of the pore pressure-based identification, the last measurements of  $\Delta u_{\text{ND}}$  were additionally captured. In order to improve generalization, the artificial noise was introduced into smooth numerical results for each discrete observation of  $\psi_i$ . Random noise was introduced using normal pdf, with the coefficient of variation  $\text{COV} = 0.2\%$  for any numerical measurement.

Simulations of both holding tests provided the discrete measurements of  $t_{50}$  corresponding to the time of 50% of excess pore water pressure decay ( $0.5\Delta u_{\max}$ ). Additionally, discrete observations of the cavity strain  $\varepsilon_c(t_{50})$  corresponding to  $t_{50}$  were captured for PHT simulations.

A couple of two-hidden layer network architectures was designed to identify individual parameters based on the results of expansion tests and holding tests, preserving their mutual interaction. For the hidden layers, the log-sigmoid transfer functions were adopted. The normalized components of the input and output vectors, as well as, network characteristics are summarized in Table 8.3. Network NN31 is designed to predict  $k$  based on SHT and PET data while NN22 maps the results of PHT and PET onto  $k$  and  $\lambda$ . Two other networks, namely NN12 and NN13, are attributed to the PET problem without and with pore pressure data respectively. In this case, predicted or prescribed values of  $k$  and  $\lambda$  are also part of the input incorporating the hydro-mechanical feedback. Hence, an exemplary identification of all the parameters based on all possible



(a) flow chart for parameter prediction from pressuremeter data



(b) scheme for coupled neural networks: NN22 and NN13

Figure 8.8: Neural network parameter prediction from coupled PET and PHT data.

SBPT measurements can be proceeded as shown in Figure 8.8.

At the end of NN training, the quality of network performance was assessed by presenting to the trained networks with a set of 161 numerical pseudo-experiments, comprising of noisy measurements previously unknown to the trained neural network. The results of the performed regression analyses for four trained networks are graphically presented in Figure 8.9, 8.10 and 8.11. These results reveal a fair correctness of the parameter prediction in terms of the coefficient of correlation  $R$  and the mean squared error MSE. In general, a visual inspection of the parameter predictions show, a good performance of the NN-based parameter identification. The predictions of strength parameters mostly fall into 10% bounds of relative error of target values. Less accuracy is observed for the parameter  $\lambda$ ; however, it is sufficient to assess the order of magnitude and to capture a neighborhood of the optimal solution. The predictions of  $k$  plotted in log-scales prove that networks correctly capture the order of magnitude of the permeability coefficient. A visible scatter can also be observed in the case of predictions of  $M$  based on applied pressure and pore pressure measurements; however further tests did not reveal that such an error

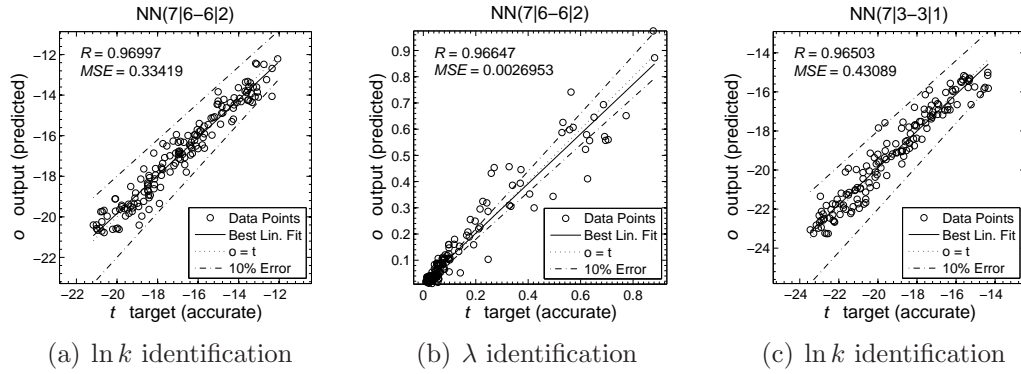


Figure 8.9: Prediction of consolidation parameters based on (a), (b) PET and PHT, (c) PET and SHT measurements by means of the network NN22 and NN31 respectively. Post-training regression analysis for 161 data sets previously unknown to the trained neural network.

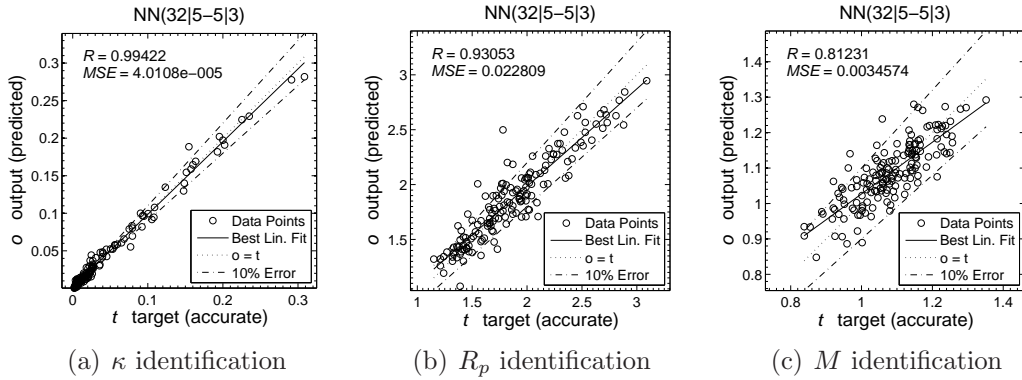


Figure 8.10: Prediction of strength and stiffness parameters based on PET measurements by means of network NN13: post-training regression analysis for 161 data sets previously unknown to the trained neural network.

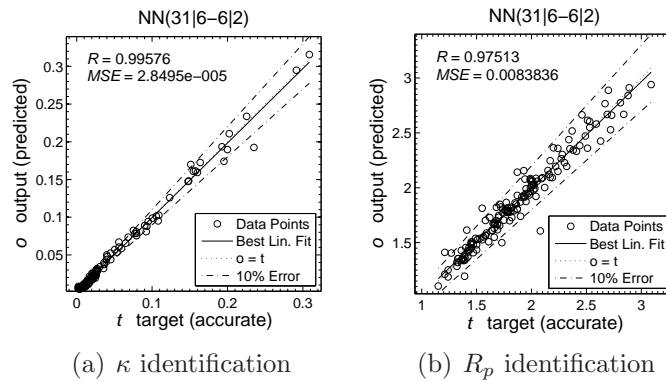


Figure 8.11: Prediction of strength and stiffness parameters based on PET measurements by means of NN12: post-training regression analysis for 161 data sets previously unknown to the trained neural network.

affects capturing vicinities of the global minima.

### 8.1.5 Efficiency and convergence analysis

A quantitative test of effectiveness of the proposed two-level identification scheme was performed on the numerically computed measurements for a pseudo - experiment of PET and PHT. The normalized measurements were presented to the relevant neural networks which predicted the vector of model parameters. The quality of the predicted parameters can be then evaluated by comparing the model response with the measurements corresponding to the optimal properties according to the scheme presented in Figure 8.1. A relatively small error is supposed to be minimized within very few iterations by an invoked gradient-based algorithm.

The main objectives of the performance analysis were to check the convergence rate of the minimization procedure, as well as to check the quality of optimized parameters.

The numerical experimental data for test PMTNV9 was obtained for the following set of parameters regarded as reference optimal values:  $M^{\text{opt}} = 0.98$ ,  $R_p^{\text{opt}} = 1.915$ ,  $\kappa^{\text{opt}} = 0.02$ ,  $\lambda^{\text{opt}} = 0.08$ ,  $k^{\text{opt}} = 2.5 \cdot 10^{-10} \text{m/s}$ . Other parameters characterizing the initial state of the test were assigned as  $p'_o = 100 \text{kPa}$ ,  $u_o = 20 \text{kPa}$ ,  $K_o = 0.90$ ,  $e_o = 1.0$ .

Next, numerical measurements were back-analyzed by networks NN22 and NN13 which instantly produced parameter estimations according to the scheme shown in Figure 8.8. The vector of predicted parameters was then iteratively updated using four PET and PHT curves. Using the MGN algorithm, the NN-identified parameters quickly converged to the expected values within 2 iterations as shown in Figure 8.12. It means that neural networks closely determined the vicinity of the global minimum.

The next comparative test was performed to check the convergence rate and the stability of the gradient-based identification without using the NN-based prediction. Since the MGN algorithm was initialized with arbitrarily chosen vectors of parameters, the existence of local minima was also investigated. Four testing initial vectors of parameters were prepared by perturbing their reference values with the error calculated based on the coefficients of variance COV observable in geotechnical practice. These observable values of COV for particular properties make the test more realistic and can be found in Baecher and Christian (2003). The optimal and corresponding perturbed values of parameters taken to generate the testing sets are summarized in Table 8.4. The testing sets 1 and 2 were created by respectively rising and reducing all the native values of parameters. In two other tests, parameter values were picked alternately. For all testing sets parameters were supposed to converge in the optimal values under equally conditioned parameters of MGN.

The analysis presented in Figure 8.13 shows much quicker convergence of NN-assigned parameters (2 iterations) in comparison to arbitrarily specified pa-

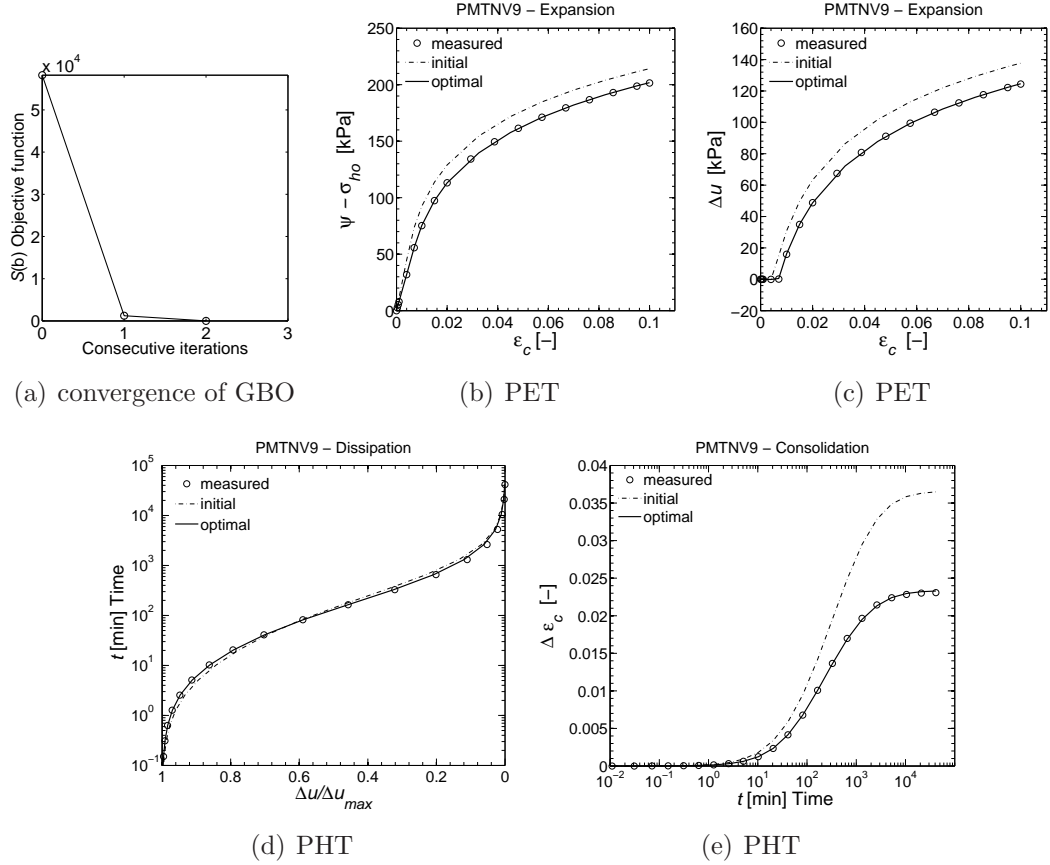


Figure 8.12: Parameter calibration for numerical simulation of PET and PHT tests with the initial vector of model characteristics predicted by neural networks.

rameters. It is worth noting that runs no. 2 and 4 are attracted by other local minima which caused divergence and finally instabilities of FE computing at 5-th iteration due to the ill-conditioning of other parameters. In both cases, this can mainly be attributed to the small value of  $k = 10^{-12}$  m/s selected for the initial vector which drive the algorithm into a local minimum. Two remain-

Table 8.4: Summary of perturbed parameters considered in efficiency and convergence analysis.

Parameter	Coefficient of variation COV (%)	Optimal value	Perturbed value	
			+	-
$M$	20	0.98	1.13	0.84
$R_p$	20	1.915	2.20	1.63
$\kappa$	30	0.02	0.026	0.014
$\lambda$	30	0.08	0.104	0.026
$k$ [m/s]	300	$2.5 \cdot 10^{-10}$	$7.5 \cdot 10^{-10}$	$10^{-12}$

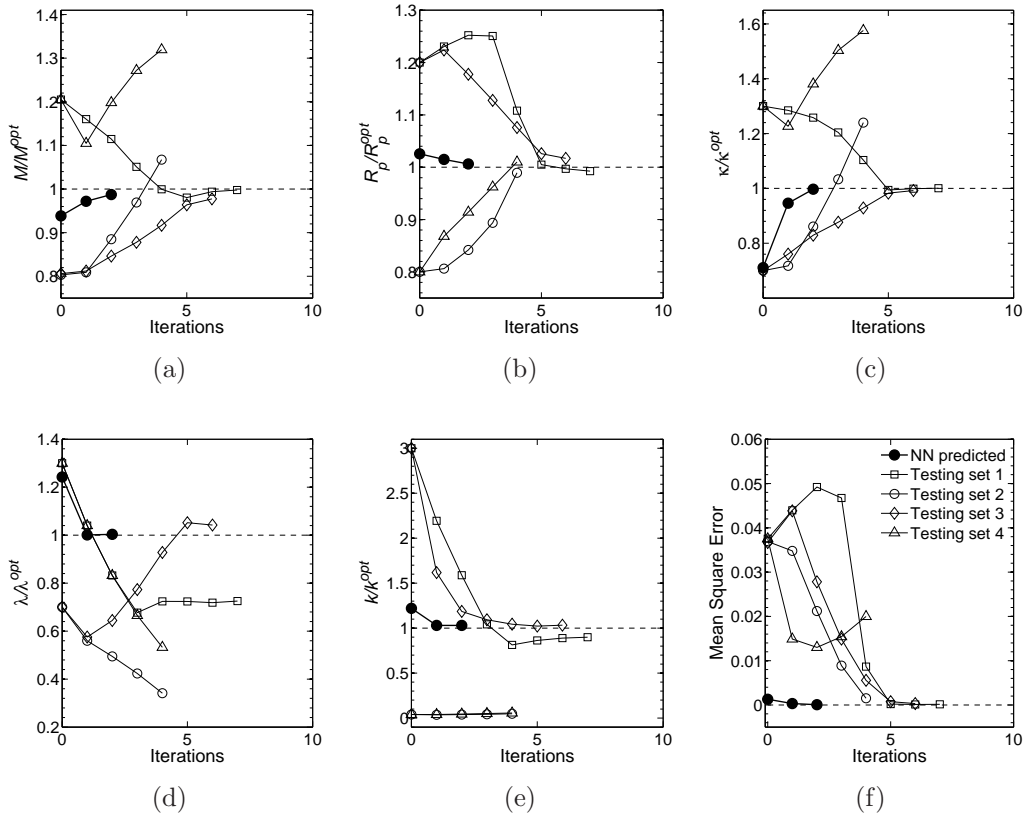


Figure 8.13: Convergence test for 5 optimization runs including NN-predicted initial vector and 4 arbitrarily specified permutations of initial parameters: (a-e) convergence of parameters, (f) convergence of the mean squared error for all parameters.

ing testing sets, i.e. no. 1 and 3, revealed a convergence after an elongated minimization within  $6 \div 7$  iterations. It means that the optimization required  $30 \div 35$  FE runs to fit 4 curves. However, some of parameters did not converge at their reference values revealing an error of up to 30%.

The analysis revealed the effectiveness of NN parameter identification with regard to the rate of model calibration and accuracy of optimized parameter values.

### 8.1.6 Effect of initial state variables

Since the numerical model, prior to identification of parameters, requires the initial state constants, i.e.  $e_o$  and  $\sigma'_{vo}$  to be specified, it is interesting to check the effect of these variables on the identified parameters. Clearly, the initially estimated  $\sigma'_{vo}$  which defines  $p'_o$ , may strongly affect the identified  $R_p$ . Two separate analyzes were carried out for the test PMTNV9 (Section 8.1.5) by perturbing the reference values of  $e_o^{\text{opt}} = 1.0$  and  $K_o^{\text{opt}} = 0.9$  regarded as the optimal ones.

Results of these analyzes are presented in Figure 8.14. As it was expected,  $e_o$  mainly affects parameters  $\kappa$  and  $\lambda$ , while the influence on the other parameters

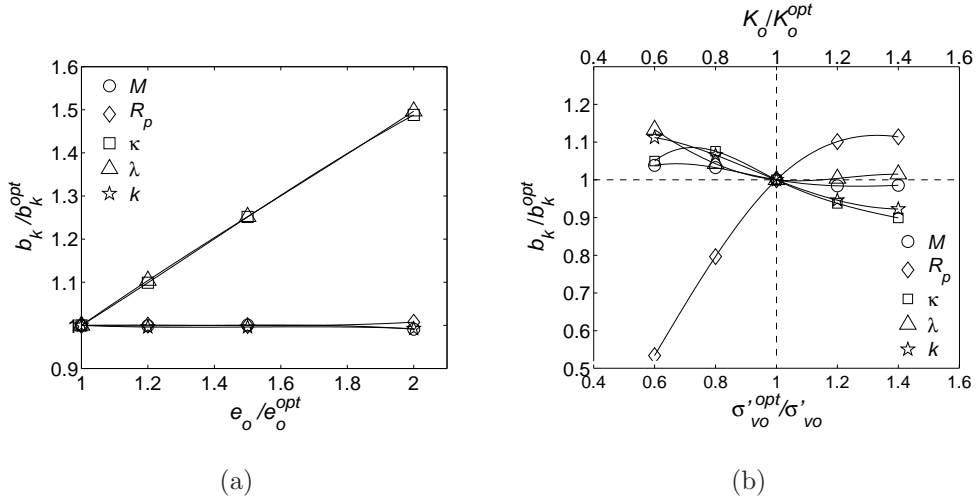


Figure 8.14: Effect of the initially specified state variables: (a) voids ratio, (b)  $K_o$  (or vertical effective stress), on the finally identified parameters.

is negligible. Assuming a natural variation of  $e_o$  in natural deposits, the variation of identified values of  $\kappa$  and  $\lambda$  may be assumed to be inversely proportional to the variation of  $e_o$ , since the variation of the error is linear.

The results of the second analysis show (see Figure 8.14(b)) a strong influence of  $K_o$  on  $R_p$ . The latter significantly decreases with an underestimation of  $K_o$ , whereas other identified parameters differ from the reference values by up to 10% ÷ 15% correspondingly to  $\pm 40\%$ -error of  $K_o$ . Hence, the overestimation of  $K_o$  may less affect the estimated  $R_p$ .

### 8.1.7 Summary

The above section concerning the pressuremeter test demonstrates the effectiveness of the combined computational parameter identification for the coupled hydro-mechanical BVP of the SBPT. It has been illustrated that the characteristics of the MCC model can be estimated fairly accurately by means of NNs and then corrected with the minimum computational cost related to the iterative parameter correction. The effectiveness of the method has been confirmed for numerical measurements and will be further verified for real experimental measurements in Section 9.1. The example of parameter identification based on numerical SBP measurements reveals that, starting from a remote initial vector of parameters, the gradient-based algorithm risks either an increased computational cost or getting trapped by a local minimum. In certain cases, the latter can also lead to instabilities of a FE solver if a wrong search direction is chosen. This analysis shows that the neural network-assigned parameters facilitate parameter identification by substantially reducing the computational effort, as well as by ensuring a quick convergence of the Modified Gauss-Newton algorithm at the expected optimal vector of parameters.

## 8.2 Neural networks for parameter estimation based on piezocone data

The following section presents in detail the development of a numerical tool for the evaluation of MCC parameters from CPTU data. In the context of this particular test, the methodology of the data mining and the NN training is demonstrated.

### 8.2.1 Strategy of parameter estimation

In the context of the CPTU test, a simplified approach is proposed to determine model parameters. The identification scheme is thus reduced to the prediction step involving solely NN prediction (i.e. the optimization step is skipped). It is expected that properly trained networks will be able to evaluate soil characteristics with acceptable accuracy related to NN training feasibility, as well as with possible accuracy with regards to limitations of the MCC model. It is also expected that NNs will provide meaningful solutions regardless of drainage conditions in which the penetration takes place. By analogy to the algorithm presented for pressuremeter tests in Section 8.1, the training database  $\mathcal{D}$  is generated by means of numerical simulations. Numerical results are obtained based on the developed FE model presented in Section 7.2. The results include measurements of  $q_t$ ,  $u_2$  and  $f_s$  which, when normalized, can constitute the network input (Figure 8.15). Accuracy of NN model predictions both for synthetic

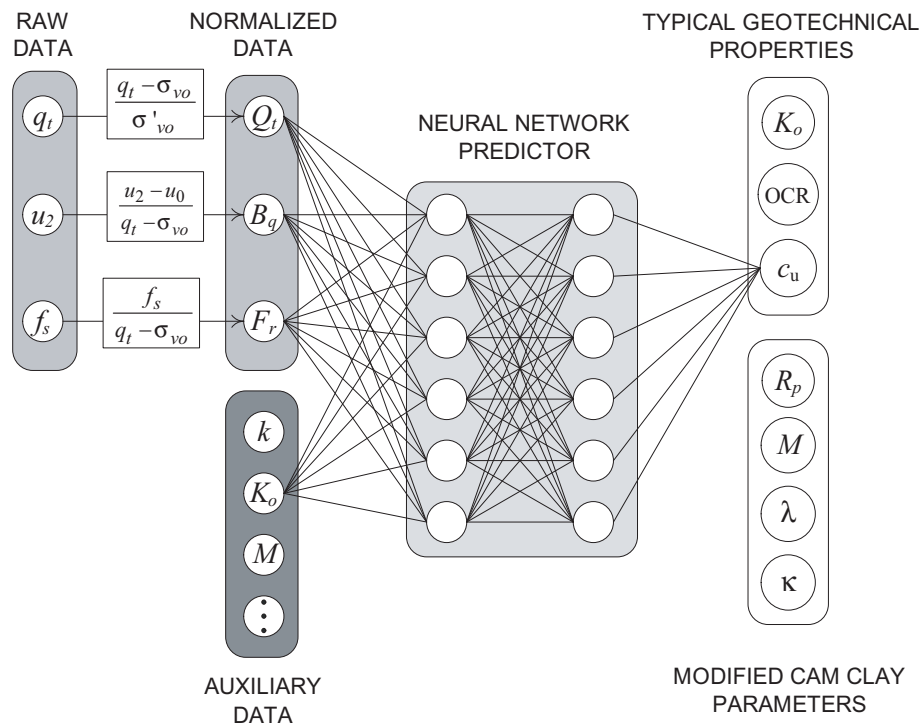


Figure 8.15: A concept of neural network parameter prediction based on piezocone measurements and auxiliary data.



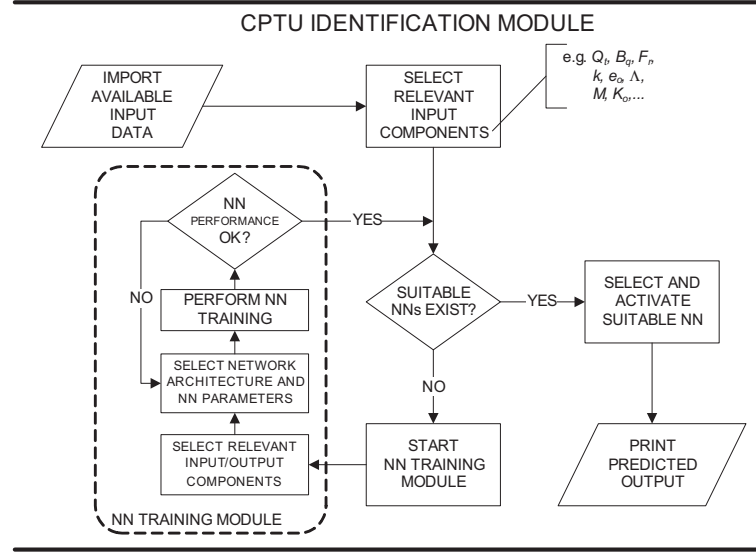


Figure 8.16: Flowchart of NN-based parameter prediction from piezocone data.

data during NN training and for real experimental data, can be improved by complementing the input vector with other auxiliary information which can be acquired for specific soil and which is compatible with a property defining the FE model. An interface of the identification module for the CPTU test has been designed in a way that it enables a dynamic upgrade of the existing database of neural networks according to the flowchart presented in Figure 8.16. It means that the training module can be invoked if the database of trained neural networks does not contain a network which is suitable for available or selected input data. The graphical user interface (GUI) of the identification module and the training module are presented in Appendix E.

Numerous sets of representative training patterns can be generated respecting the computational effort by a careful selection of parameter permutations for which the FE solver produces synthetic measurements (cf. Section 8.1.2). Parameter intervals and correlations observed in geotechnical practice can be introduced to skip non-physical or unlikely vectors of parameters. A multi-dimensional space of model variables  $\mathcal{R}_b$  can be uniformly clustered using relevant probability distribution functions (pdf) in order to improve the accuracy of further NN predictions. The selected intervals, correlations and statistics of the particular variables are described below and are summarized in Table 8.5. Moreover, a flowchart presented in Appendix D demonstrates a sequence for the generation of parameter permutations.

**Constants.** In the context of numerical simulations, the parameters of negligible influence and identifiable uniquely by means of specific laboratory procedures, are assumed as constants. It particularly applies to the Poisson's coefficient  $\nu$  and the strength anisotropy parameter  $A_r$ . The first variable is assumed to equal 0.3 as an average designing value for clays and silts. The use of various  $\nu$  coefficients between 0.1 and 0.4, Sheng et al. (2005) demon-

Table 8.5: Summary of parameters intervals considered in generation NN training patterns for CPT problem.

Parameter	Unit	Value or Interval	Pdf or intercorrelation $f(b_j)$
<i>Constants</i>			
$\nu$		0.3	
$p'_o$	(kPa)	100.0	
$A_r$		0.78	
<i>Variables</i>			
$e_o$		$\langle 0.1; 3 \rangle$	uniform
$\Lambda$		$\langle 0.60; 0.95 \rangle$	uniform
$\beta_1$		$\langle -0.18; 0.18 \rangle$	normal
$\beta_2$		$\langle -0.15; 0.15 \rangle$	normal
$k$	(m/s)	$\langle 10^{-10}; 3 \cdot 10^{-6} \rangle$	uniform $\ln k$
$\alpha_f^\dagger$		$\langle 0.25; 0.35 \rangle$	uniform
$I_r$		$\langle 10; 110 \rangle$	$f(G, c_u)$
<i>Parameters to be identified</i>			
$\lambda$		$\langle 0.025; 1.2 \rangle$	$f(\kappa, \Lambda)$
$\kappa$		$\langle 0.01; 0.2 \rangle$	exponential
$M$		$\langle 0.7; 1.7 \rangle$	uniform
$R_p$		$\langle 1.2; 5.0 \rangle$	$f(M, \text{OCR}, K_o, K_{onc})$
OCR		$\langle 1.05; 4.0 \rangle$	uniform
$K_o$		$\langle 0.32; 1.35 \rangle$	$f(\text{OCR}, M, \beta)^*$
$c_u/\sigma'_{vo}$		$\langle 0.21; 1.31 \rangle$	$f(R_p, M, \Lambda)$

\* Mayne and Kulhawy (1982).

†  $\tan \phi_i = \alpha_f \tan \phi'_c$  introduced to numerical measurements derived from simulations of "smooth" penetration.

strated that the parameter does not significantly affect total shaft resistance. As regards parameter  $A_r$ , the assumed value of 0.78 is considered the average value for clays and enforces convexity of the yielding surface (cf. Section 7.2.1.3).

**Cone roughness.** Since numerical simulations are performed for "smooth" interface conditions, the contribution of cone friction to measured data can be introduced after numerical computations (cf. Section 7.2.3). Friction coefficient of interface  $\tan \phi_i$  can be obtained by drawing a random value of cone roughness from the uniform pdf within the interval  $\alpha_f \in \langle 0.25; 0.35 \rangle$ . This interval was calibrated assuming that the penetration takes place in normally- to lightly overconsolidated clay-type material and the modeling of penetration in structured, sensitive clay with the pure Modified Cam clay is not relevant. The latter assumption means that the effect of reduced effective pressure acting on the cone shaft due to soil destructuration can not be reliably modeled and measured with the applied constitutive law. In this way, the interval can be calibrated based on soil type classification charts, i.e.  $F_r - Q_t$  (Robertson, 1990), for which generated numerical points should occupy the regions above the normally consolidated zone and in accordance with the increasing OCR, as shown in Figures 8.21(a). The assumed interval is also consistent with the experimental data obtained from laboratory tests (cf. Section 7.2.1.2).

**Slope of the unloading-reloading line and the normal consolidation line.** An exponential distribution function was chosen for parameter  $\kappa$ . Unfortunately, due to severe convergence problems (see discussion in 7.2.2.1), the interval for  $\kappa$  was limited to  $\langle 0.01; 0.2 \rangle$ . Such a range corresponds to the ratios of  $G/p'_o < 70$  which are observed more frequently in the case of soft soils. As regards the slope of the normal consolidation line  $\lambda$ , random values were computed through the plastic volumetric ratio  $\Lambda$  which was drawn from the uniformly distributed interval  $\langle 0.6; 0.95 \rangle$ <sup>1</sup>. The distribution of  $\kappa$  and  $\lambda$  in the training patterns is shown in Figures 8.17(b) and 8.17(c) respectively.

**Slope of the critical state line.** Random values of  $M$  were drawn from the uniformly clustered interval  $\langle 0.7; 1.7 \rangle$  (Figure 8.17(d)). This corresponds to the interval of the friction angle which is observable for a variety of clayey soils (cf. Mayne, 1991, 2007), i.e.  $\phi'_c \in \langle 18.3^\circ; 41.5^\circ \rangle$  (Figure 8.17(e)).

**Coefficient of earth pressure 'at rest'.** Random values of  $K_o$  and  $K_{onc}$  was obtained likewise for the pressuremeter test (see Section 8.1.1), with the exception of normal pdf assumed for random dispersals  $\beta_1$  and  $\beta_2$  and a uniformly sampled interval for  $OCR \in \langle 1; 4 \rangle$  owing to the applicability of MMC to lightly consolidated clays (Figure 8.17(f)). The distribution of  $K_{onc}$  as the function of  $M$  and  $\beta_1$  results in normal-like pdf (Figure 8.17(g)), whereas the values of  $K_o$  as the function of  $OCR$ ,  $K_{onc}$  and  $\beta_2$  form log-normal-like pdf (Figure 8.17(h)).

**Overconsolidation ratio.** The values of  $R_p$  were obtained using Equation (8.4) resulting in normal-like pdf between 1 and 4.6 (Figure 8.17(i)).

**Coefficient of permeability.** The assumed values of  $k$  for clays and silts are in the range of  $k < 3 \cdot 10^{-6}$  m/s. Since the upper and lower bounds of the interval vary in four orders of magnitude, the distribution of  $k$  was assumed uniform for the log-transformed parameter, in order to cover a wide spectrum of possible drainage conditions (Figure 8.17(j)).

**Undrained shear strength.** Having drawn parameters which define the strength of the MCC, the distribution in the training pool for normalized  $c_u$  can be plotted. Note that  $c_u$  values were obtained using the definition in Equation (6.47). The distribution of  $c_u/\sigma'_{vo}$  reveals a log-normal pdf shape (Figure 8.17(k)). Further verification of permuted values obtained for  $c_u/\sigma'_{vo}$  can be carried out based on the experimental data of CAUC strengths. For natural clays, Mayne (1988) observed the following limit trends:

$$c_u/\sigma'_{vo} = 0.20 \cdot OCR^{0.78} \quad (8.10a)$$

and

$$c_u/\sigma'_{vo} = 0.45 \cdot OCR^{0.78} \quad (8.10b)$$

---

<sup>1</sup>Divergence of the numerical procedure was observed for most of the patterns including  $\Lambda < 0.6$ .

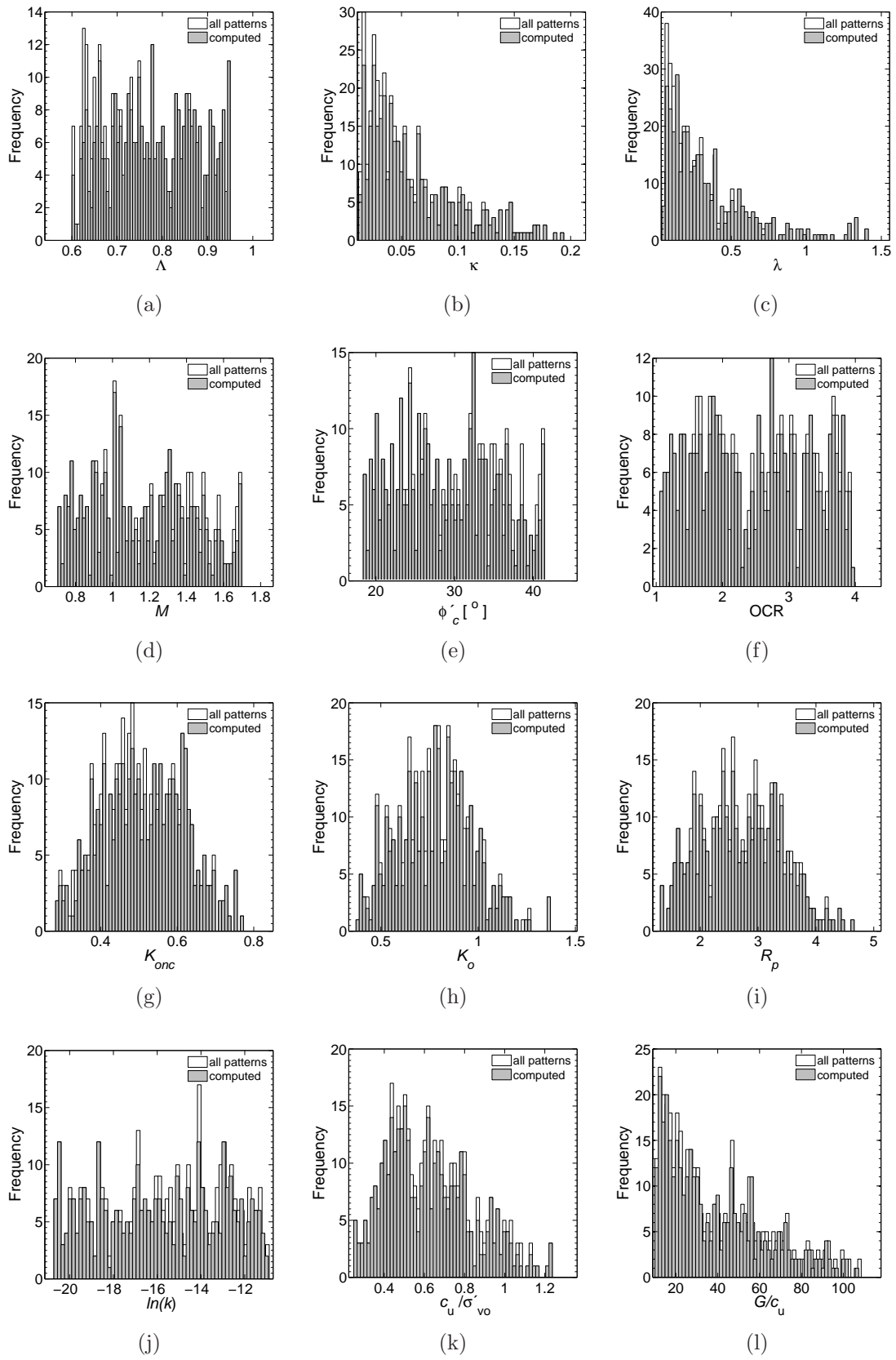


Figure 8.17: Histograms of parameter distributions used to generate the NN training patterns.

Figure 8.18(a) and 8.18(b) show that the synthetically obtained  $c_u$  are uniformly sampled within the natural limits. The artificial  $c_u$  samples normalized in terms of the mean stress and plotted against  $R_p$  (Figure 8.18(c) and 8.18(d)) give the following estimate for the upper limit:

$$c_u/p'_o = 0.52R_p^{0.78} \quad (8.11)$$

whereas the lower limit remains similar to Equation (8.10a).

**Rigidity index.** Since the developed numerical model revealed frequent numerical instabilities for the cases characterized by the ratio  $G/p'_o > 70$ , randomly drawn vectors of parameters which led to such values were rejected and redrawn according to the scheme presented in Figure D.1. The permutations were also constrained by the interval for the rigidity index  $I_r \in \langle 10; 110 \rangle$ . Finally, an exponential pdf for  $I_r$  values was obtained, as shown in Figure 8.17(l).

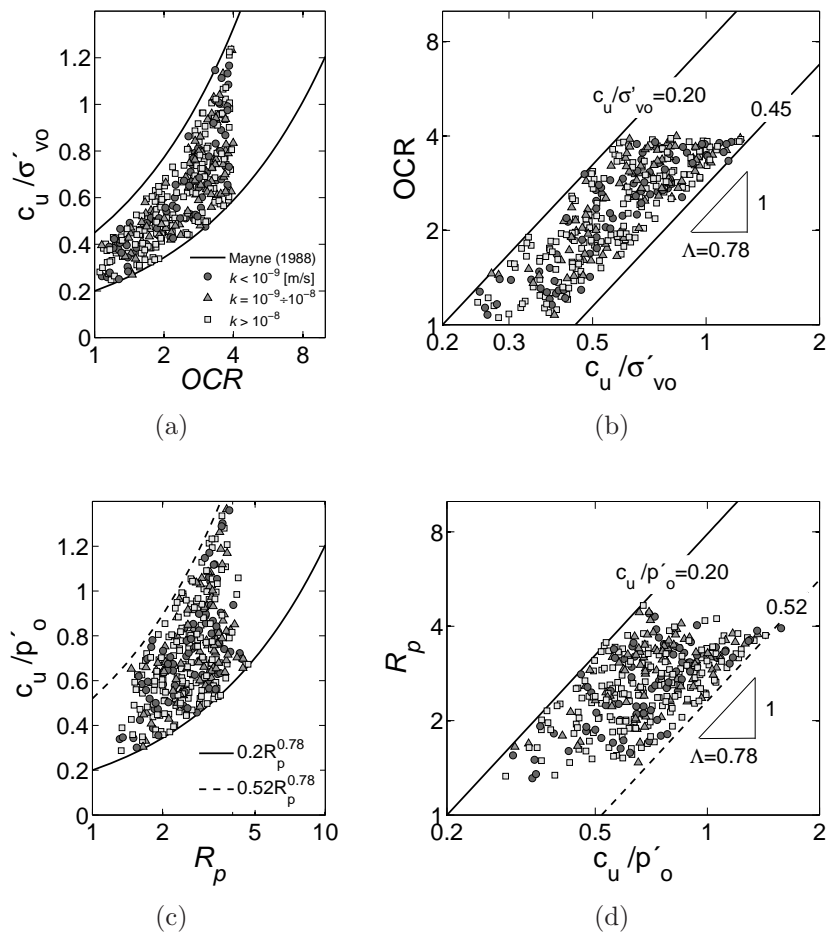


Figure 8.18: Generated permutations of normalized undrained shear strength against overconsolidation ratio: (a-b) comparison with the observed limits for CAUC strength in natural clays by Mayne (1988), and (c-d) proposed relationship between  $R_p$  and  $c_u$  normalized in terms of  $p'_o$ .

## 8.2.2 Numerical generation of training patterns

Having permuted vectors of model parameters, and enforcing optimal mesh sizes and penetration depths (see Section 7.2.1.4), a number of FE simulations were carried out in a batch mode. The simulations with any occurrence of numerical instability were rejected from the training set. From among 400 FE runs, 355 simulations effectively converged at the steady-state. No general reason for non-converged FE patterns has been found using the adopted parameter permutations (cf. Figure 8.17). A relatively large number of non-computed patterns can be observed for low values of  $\Lambda$  which are smaller than 0.7 (see Figure 8.17(a)).

Three variables corresponding to frictionless penetration,  $\bar{q}_t$ ,  $\bar{u}_2$  and  $\bar{p}'_n$ , were derived from each computed simulation. Since field measurements may exhibit a random experimental error, artificial "noise" can be introduced into numerical data to improve the ability of network to generalize. It was, however, assumed that a part of "noise" can be attributed to numerical inaccuracies and raw data smoothing. A higher degree of experiment uncertainty was obtained by introducing random numbers for cone roughness  $\alpha_f$  when calculating the final values of  $q_t$ ,  $u_2$  and  $f_s$  which include rough cone effects. A certain degree of uncertainty can be also related to the fact that friction effects under partial drainage conditions are introduced using the criterion proposed in Equation (7.28) which is developed for isotropic stress and permeability conditions. The use of this criterion to find the correction coefficient  $\vartheta_t$  as a function of  $V$  enforced consistent calculations of the operational coefficient of consolidation  $c_{vh}$  by introducing  $p'_o$  into Equation (6.63).

In the last step of data post-processing, three variables were standardly normalized in terms of  $\sigma'_{vo}$  in order to remove depth effects (cf. Section 6.3.2.1).

In order to gain insight into the shortage of stiff soils in the FE-generated database, additional numerical database was computed based on the proposed theoretical solution developed in Section 7.2.2.1. The database contains "undrained" patterns for the rigidity index from 10 to 750<sup>2</sup>. The following section presents in detail a comparative analysis of two databases.

## 8.2.3 Verification of numerical database

The computed synthetic data points can be compared with geotechnical evidence which was acquired for natural clays by Lunne et al. (1989); Robertson et al. (1986). Figure 8.19 presents the normalized synthetic data derived from numerical simulations ( $I_r = 10 \div 110$ ), whereas Figure 8.20 shows data points obtained using the theoretical solution for undrained penetration extended to the material cases defined with large rigidity indexes ( $I_r = 10 \div 750$ ). In accordance with experimentally observed trends, the synthetic points reveal

---

<sup>2</sup>The expanded range of  $I_r$  was obtained by decreasing the lower bound for parameter  $\kappa$ , while the interval for OCR remained unchanged.

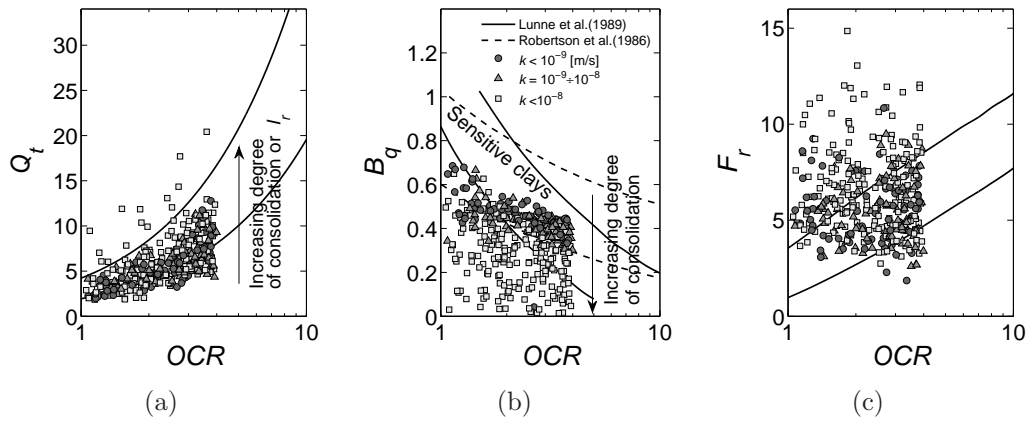


Figure 8.19: Normalized numerical data ( $I_r = 10 \div 110$ ) vs OCR compared with empirical bounds suggested by Lunne et al. (1989) and Robertson et al. (1986).

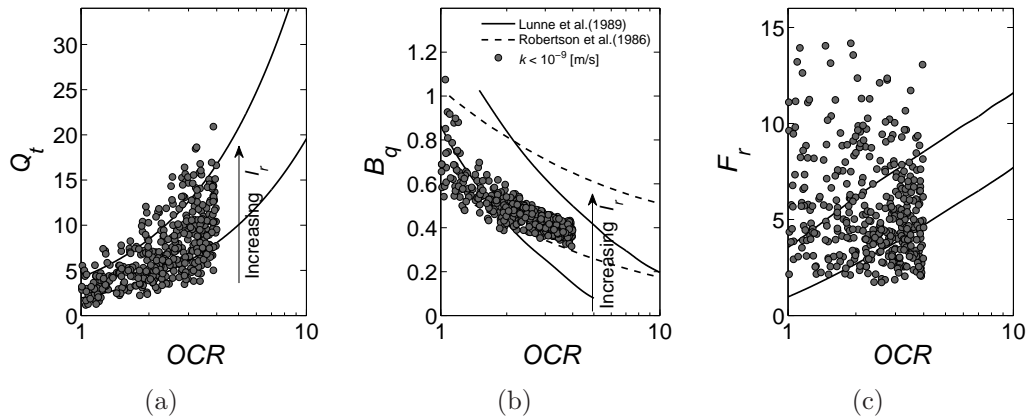


Figure 8.20: Normalized theoretical data ( $I_r = 10 \div 750$ , undrained) vs OCR compared with empirical bounds suggested by Lunne et al. (1989) and Robertson et al. (1986).

a general increase of  $Q_t$  with a corresponding decrease of  $B_q$  for the increasing overconsolidation ratio.

As regards  $Q_t$ , the numerical patterns corresponding to undrained conditions ( $k < 10^{-9}$  m/s) fall between the lower and the middle observed bounds due to the assumed low values of  $I_r$  which correspond to soft clays (Figure 8.19(a)). However, the increasing degree of consolidation for transitional drainage conditions can significantly raise  $Q_t$ . On the other hand, theoretical undrained patterns for the expanded range of  $I_r$  will correlate with the observed trends and clearly show the effect of increasing  $I_r$  (Figure 8.20(a)).

An opposite effect of partial consolidation can be observed for  $B_q$  which is reduced with the increasing degree of consolidation (Figure 8.19(b)). The undrained patterns of both numerical and theoretical data points (Figure 8.20(b)) are located above the lower limit suggested by Robertson et al. (1986) and ap-

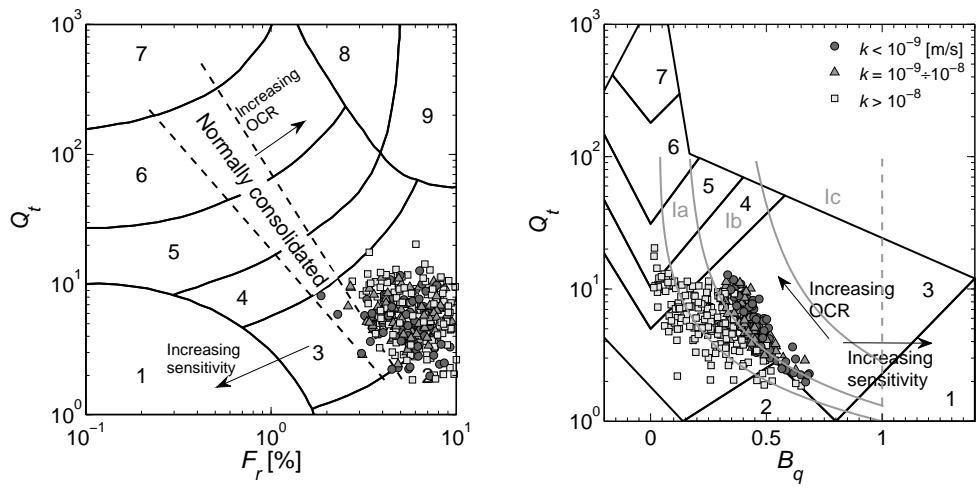
proximately cluster the lower middle part of the experimentally observed zone. The upper part of this area cannot be covered using the simple MCC model as its formulation does not allow soil sensitivity to be taken into account. In the case of sensitive, normally consolidated clays, high shear-induced pore pressures can be expected due to soil softening (Schneider et al., 2008).

In the case of  $F_r$ , the synthetic data does not reflect the trend suggested by Lunne et al. (1989). It is likely because the proposed experimental bounds were developed partially based on the results for sensitive, normally- and lightly marine clays for which a decrease of effective stresses acting at the cone shaft can be typically expected. It can also be noticed that in the case of data points corresponding to soft clays (Figure 8.19(c)), the data points above the upper limit observed by Lunne et al. (1989) generally represent the patterns subject to partial drainage conditions. On the other hand, many data points from the "undrained" population including stiffer patterns ( $I_r = 10 \div 750$ ) also fill the region above the experimentally observed bound (Figure 8.19(c)). However, these results have to be carefully analyzed since the data points were extrapolated through Equation (7.14) which is proposed based on numerical results subject to a considerable dose of numerical uncertainty (see Figure 7.22(b)).

The generated numerical database can also be verified using soil classification charts. Many classifications for soil profiling based on CPT data have been proposed in the past. Many researchers have made the effort to use an extensive geotechnical evidence to provide a guide which classifies soils in terms of the so-called soil behavior type (SBT). Using raw, corrected or transformed records of cone and sleeve resistances, and incorporating pore pressure measurements in further analyzes a number of empirical classification charts have been developed, e.g. Schmertmann (1978); Douglas and Olsen (1981); Olsen and Farr (1986); Robertson et al. (1986); Robertson (1990); Jefferies and Davis (1991); Eslami and Fellenius (1997); Fellenius and Eslami (2000). Alternative classification methods like combined statistical and fuzzy logic have also been proposed (Zhang and Tumay, 1999). Recently, Schneider et al. (2008) presented a novel classifying framework which combines theoretical considerations including an analysis of soil parameters affecting cone penetration and observations of drainage conditions during penetration.

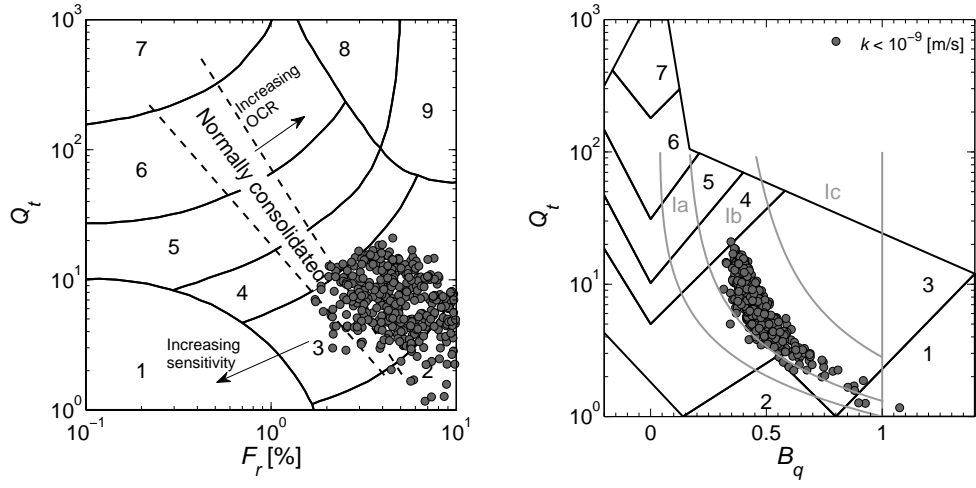
It should be recalled that the post-processed numerical data was obtained using smooth cone measurements ( $\bar{q}_t$ ,  $\bar{u}_2$  and  $\bar{p}'_n$ ) for which random values of cone roughness  $\alpha_f$  were attributed (cf. Table 8.5). The calibration of the interval for  $\alpha_f$  was partially based on the commonly applied classification chart  $Q_t - F_r$  proposed by Robertson (1990). It was assumed that due to constitutive model formulation referred to non-sensitive clays, the data points should be located above the delineated region of normally consolidated soils, as shown in Figure 8.21(a). Consequently, the post-processed numerical data widely covers the region delineated as non-sensitive clays and silty clays (3) and partially the zone of soft organic clays (2). Although the numerical database contains patterns characterized by permeability coefficients which correspond to clayey silt





(a) Robertson (1990)

(b) Robertson (1990) and Schneider et al. (2008) - gray lines



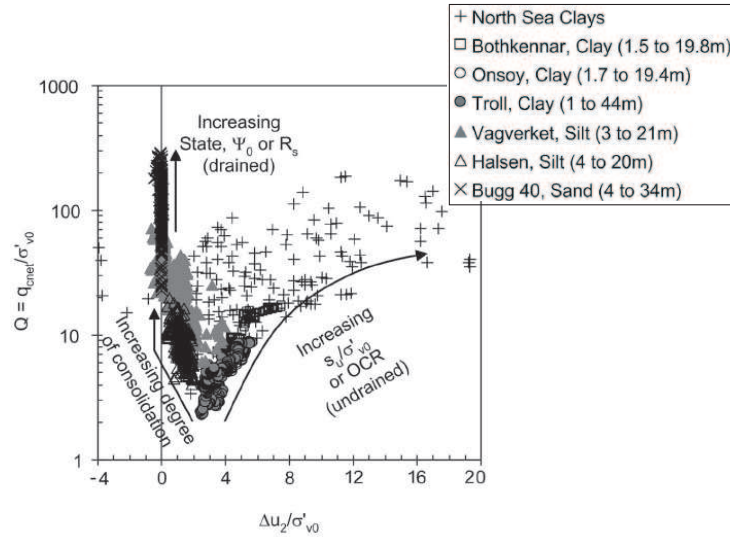
(c) Robertson (1990)

(d) Robertson (1990) and Schneider et al. (2008) - gray lines

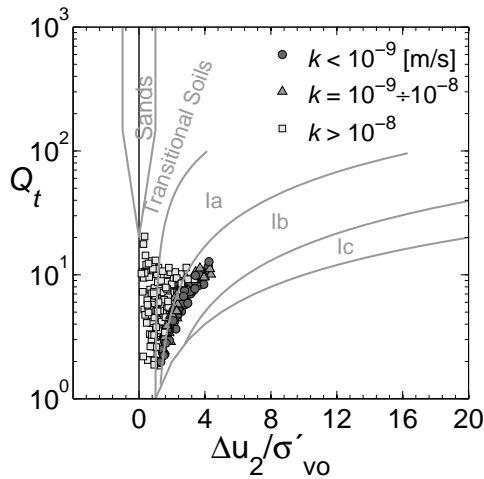
Zone	Soil Behavior Type	Zone	Soil Behavior Type	Zone	Soil Behavior Type
1	Sensitive, fine grained	4	Clayey silt to silty clay	7	Gravelly sand to sand
2	Organic soils-peat	5	Silty sand to sandy silt	8	Very stiff sand to clayey sand
3	Clays, clays to silty clay	6	Clean sand to silty sand	9	Very stiff, fine grained
Ia	Silts and Low $I_r$ clays	Ib	Clays	Ic	Sensitive clays

Figure 8.21: Representation of (a-b) numerical ( $I_r = 10 \div 110$ ) and (c-d) theoretical data points ( $I_r = 10 \div 750$ , undrained) projected on various soil classification charts.

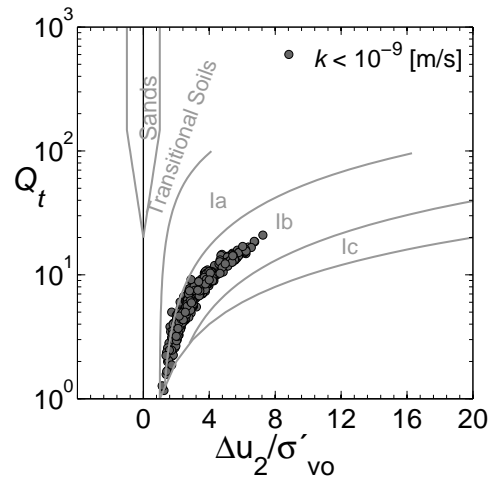
or silt-like soils, the corresponding regions are not represented, as the numerical model was limited to low  $I_r$ . On the other hand, some "stiff" patterns can be classified as silty clay using the  $Q_t - B_q$  chart, as shown in Figure 8.21(b). It can, however, be noticed that many "partially drained" patterns are erroneously classified as clays. A correct membership of "partially drained" patterns in the silt SBT can be recognized using the novel classification method proposed by



(a) experimental



(b) numerical



(c) theoretical undrained

Figure 8.22: Trends of increasing  $c_u/\sigma'_{v0}$  and the degree of consolidation for (a) different characterization sites (from Schneider et al., 2008), (b) numerical patterns also subject to partial consolidation, and (c) theoretical, undrained patterns plotted in  $Q_t - \Delta u_2/\sigma'_{v0}$  space (gray lines represent the soil classification system by Schneider et al., 2008).

Schneider et al. (2008). The method effectively separates the undrained and transitional penetration conditions, taking into account the reduction of  $B_q$  due to partial consolidation.

In the case of "undrained" database derived from theoretical solution, the patterns obtained for a wide range of parameters observed for clays widely cover the region of non-sensitive clays on the  $Q_t - F_r$  chart (Figure 8.21(c)). Moreover, both classification systems consistently classify the theoretical data points as clay-like soil, as shown in Figure 8.21(d).

Numerical and theoretical data points can also be plotted in  $\Delta u_2/\sigma'_{v0}$  space which readily separates the influence of both soil overconsolidation and the degree of consolidation (Figure 8.22). Synthetic data shows considerable con-

Table 8.6: Notation adopted for specific parameters defining neural network input-output pairs in parameter prediction from the CPTU data.

	Basic input parameters			Additional input or output parameters								
Parameter symbol	$Q_t$	$B_q$	$F_r$	$e_o$	$\ln k$	$\Lambda$	$\lambda$	OCR	$R_p$	$M$	$c_u/\sigma'_{vo}$	$K_o$
Acronym in NN notation	Q	B	F	V	K	L	P	O	R	M	U	H

sistency with the trends observed for non-sensitive natural clays in terms of both factors affecting cone penetration; the "undrained" patterns are clustered in the zone Ib referred to clays, whereas partially drained cases cover the region Ia (silts) and transitional soils.

It can be concluded that synthetic data points obtained for the MCC model mostly represent soil behavior of "well-behaved" fine grained soils while the surrounding regions which can be the case of sensitive soils and highly over-consolidated, remain uncovered. This is clearly a derivative of the MCC model limitations and the specified interval of OCR, respectively. The analysis of the numerically clustered data space may also serve as a guideline for a reasonable application of the MCC model in terms of parameter prediction using NNs which are prepared with synthetic database.

#### 8.2.4 Definition and notation of network inputs and outputs

In the context of parameter prediction from CPTU data, network input consist of test measurements, i.e.  $Q_t$ ,  $B_q$  and  $F_r$  which can also be expanded with corresponding available information about other soil properties. Such an additional information may improve accuracy of NN predictions. Clearly, the complementing data needs to be compatible with properties defining the FE model. Hence, the input vector may consist of selected discrete piezocone measurements and additional dimensionless parameters with the exception of the permeability coefficient  $k$  provided in m/s.

The following presents the general form of NN topology notation adopted in this study:

$$\text{NN name notation: NN( input |1}^{st} \text{ layer} - 2^{nd} \text{ layer | output )} \quad (8.12)$$

which provides information about the number of neurons in each hidden layer and the type of components in the input and output vectors according to the notation provided in Table 8.6.

During the training, a general strategy of one-component output parameter has been chosen in order to readily separate factors improving the accuracy

of predictions for a particular parameter. An alternative approach of multi-component input and output network can also effectively be used to reduce the number of trained NNs. From a practical point of view, the use of such an approach requires detailed knowledge about input data affecting the accuracy of particular output parameters or performing regression analysis with respect to each output parameter for the selected NN.

## 8.2.5 Training and post-training analysis

In this section, a development of NN predictors for material properties will be presented in detail. In this context, the factors influencing the accuracy of NN predictions for specific parameters will be analyzed. The post-training analysis will be presented based on the regression analysis using predictions provided by trained NNs and empirical approaches presented in Section 6.3.2. Throughout this section, all the regression analyzes are performed using testing sets which contain results derived from numerical simulations.

355 synthetic patterns obtained through FE simulations were used in NN training. Within this set of patterns, 80% pseudo-experiments were randomly designated to be a training subset in each training run, while the remaining 20% ( $NS^{(s)} = 71$ ) was used to test developed NNs in the post-training analysis. Additionally, 20% of the overall number of patterns was selected from the training set in order to control network overfitting.

### 8.2.5.1 Undrained shear strength

A number of two-hidden layer network architectures were designed to predict the normalized undrained shear strength  $c_u/\sigma'_{vo}$ . At the beginning of analysis, the simplest network containing only  $Q_t$  in the input vector was compared with the related empirical method given in Equation (6.39); Figure 8.23(a) presents the results obtained in the post-training analysis. As regards the empirical formula,  $c_u/\sigma'_{vo}$  values were obtained for the mean value of  $N_{kt} = 8.60$  which was calculated through the theoretical solution:

$$N_{kt}^{\text{mean}} = \sum_{i=1}^{NS^{(s)}} (-0.55 + 2.37 \ln I_{r_i} - 2.21 \Delta_i + 3.81 \alpha_f) / NS^{(s)} \quad (8.13)$$

with  $\alpha_f$  assumed equal to 0.3.

The regression analysis reveals that both approaches present a similar correlation measured in terms of the coefficient of correlation  $R$  around 0.74. On the other hand, NN predictions in comparison with the empirical method present about 50% improvement in the MSE. Both methods present sensitivity to partially drained conditions and it is manifested by the increasing ARE for the increasing soil permeability, as shown in Figure 8.23(b). In the case of undrained results, both methods present the upper error bound for ARE around 35%. The mean absolute relative error  $ARE_m$  computed for all considered patterns is about 20% and 26.5% for NNs and empirical method respectively (see Appendix

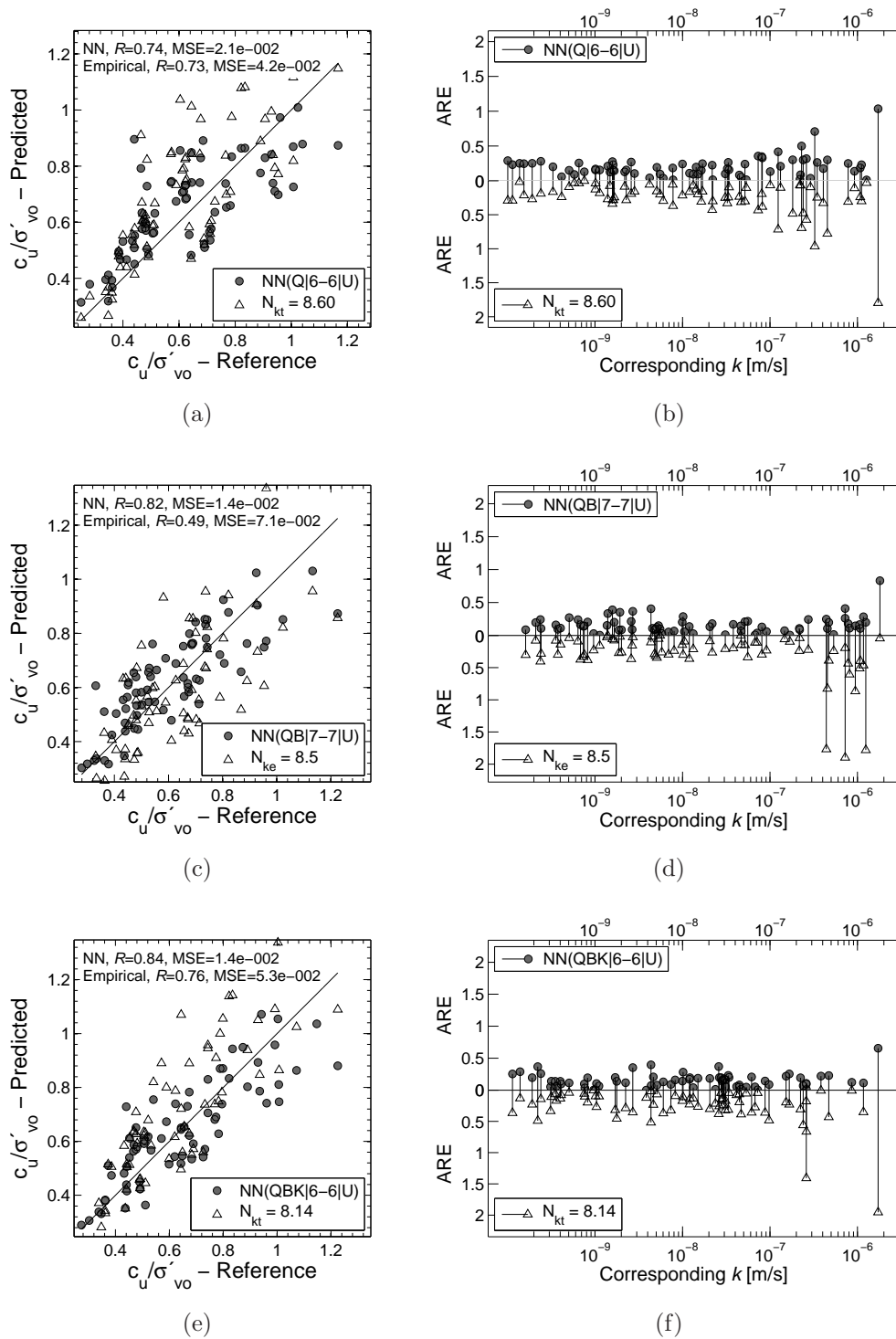


Figure 8.23: Partial drainage effect on predictions of  $c_{u1}$  using empirical methods (empty triangles) and neural networks (solid circles). Post-training analysis for 71 numerical patterns previously unknown to the trained neural network.

F, Figure F.1).

Clearly, an improvement of NN predictions can be expected with additionally provided information about pore pressure measurements (parameter  $B_q$ ) or soil permeability. Figure 8.23(c) presents the regression analysis performed for the network containing  $Q_t$  and  $B_q$  in the input, whereas the results for network complemented by the permeability coefficient  $k$  are shown in Figure 8.23(e). In the first case, NN predictions are compared with the "input-related" empirical approach provided in Equation (6.42) for which the operational value of  $N_{ke}$  was assumed equal to 8.5. Both trained NNs exhibit superior correlations in comparison with the previously developed NN(Q|6 – 6|U) and two empirical methods. The networks present improved correlations measured in terms of  $R$  (about 0.83) and MSE, with the mean ARE of about 15% (Figure F.1). Furthermore, both NNs dump the effect of partial drainage which affects predictions of  $c_u$  when using empirical methods, as shown in Figure 8.23(d) and 8.23(f). Although NN(QB|6 – 6|U) is not provided with  $k$  supplement, in the case of drained patterns, the network exhibits sensitivity to the increasing  $Q_t$  and the correspondingly decreasing  $B_q$  and provides a meaningful accuracy of predictions.

A similarly good correlation performance is exhibited by two networks where the basic inputs,  $Q_t$  and  $B_q$  are complemented with information on  $K_o$  (Figure 8.24(a) and 8.24(b)). However, it emerges that the network with no  $k$  supplement achieves worse performance than NN(QBKH|6 – 6|U) due to increasing error in the predictions for the drained patterns (Figure F.2). It explained by the fact that when predicting  $c_u$ , NN(QBH|6 – 6|U) exhibits a superior sensitivity to  $K_o$  than to parameter  $B_q$ .

Improved quality of predictions can also be achieved by providing the input vector with information on  $M$  or  $F_r$  (cf. Table 8.7). Figure 8.24(c) and 8.24(d) show respectively the regression analyzes carried out for NN(QBM|7 – 7|U) and NN(QBF|6 – 6|U). For the synthetic database, the networks provide the predictions characterized by  $ARE_m$  around  $10 \div 14\%$  (Figure F.2). However, a practical application of NN(QBF|6 – 6|U) for the real experimental data has to be restricted to non-sensitive soils due to the formulation of the MCC model.

Table 8.7: Performance of the trained neural networks designed to predict  $c_u$  (statistical features obtained for testing sets containing 71 random synthetic patterns).

Network name	$R$ (-)	MSE (-)	$ARE_m$ (%)	$ARE_{sd}$ (%)
NN(Q 6 – 6 U)	0.74	$2.1e - 02$	20.2	16.0
NN(QB 7 – 7 U)	0.82	$1.4e - 02$	16.2	13.0
NN(QBK 6 – 6 U)	0.84	$1.4e - 02$	15.0	11.0
NN(QBH 6 – 6 U)	0.81	$1.6e - 02$	19.1	13.0
NN(QBKH 6 – 6 U)	0.85	$1.3e - 02$	14.0	11.0
NN(QBM 7 – 7 U)	0.90	$8.6e - 03$	13.4	11.0
NN(QBF 6 – 6 U)	0.91	$7.0e - 03$	10.1	9.7

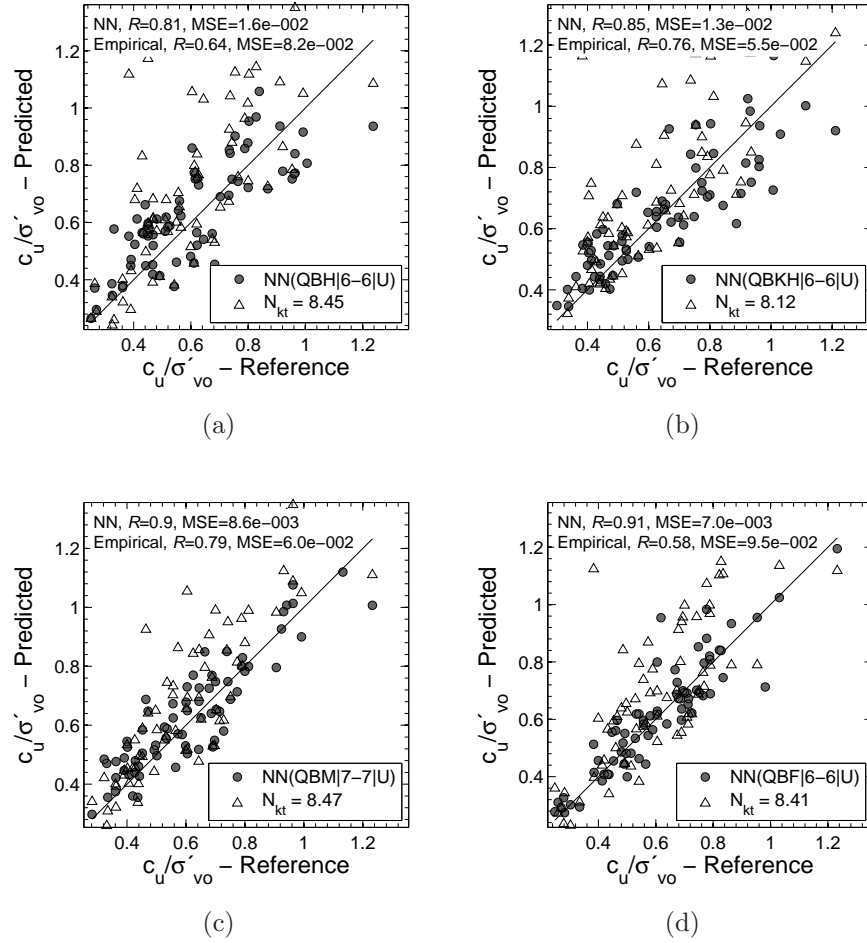


Figure 8.24: Predictions of  $c_u$  using the empirical method (Equation (6.39), empty triangles) and neural networks (solid circles).

The  $F_r$ -based predictions could be reliable for the NN predictor developed using a constitutive model accounting for bounding and destructuration effects. On the other hand, incorporating sensitivity effects which moves the results along the  $F_r$  axis could result in the increased uncertainty of predictions due to the non-uniqueness of the solution. In such a case, a satisfactory accuracy of NN predictions could be obtained using a complementary input parameter describing soil sensitivity.

### 8.2.5.2 Effective stress strength

In the context of parameter prediction of  $M$ , which maps two basic variables  $Q_t$  and  $B_q$  was first designed by analogy with the input components of the simplified NTNU method (Equation 6.44). The regression analysis performed for numerical patterns shows that both the NN predictor and the empirical method provide poor, highly approximate estimates (Figure 8.25(a)). This example shows that the problem cannot be accurately modeled based merely on two basic input variables. A quantitative analysis carried out for two methods

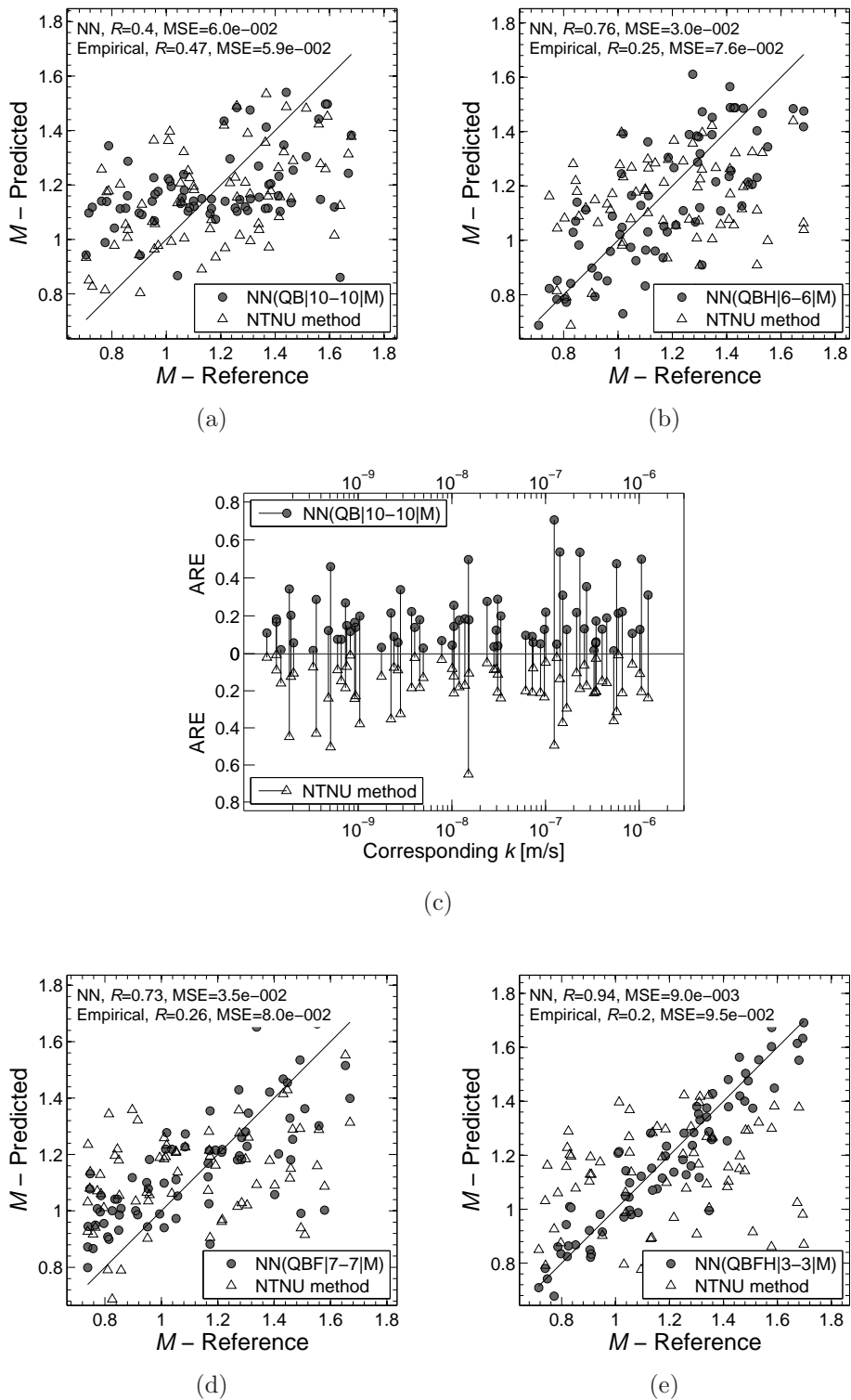


Figure 8.25: Prediction of parameter  $M$  using the NTNU method (Equation (6.44), empty triangles) and neural networks (solid circles).



reveals low values of  $R$  and high relative errors up to about 50-60% with the mean value  $ARE_m$  of approximately 18% (see Figure F.3(a)). The analysis also shows that drainage conditions do not visibly affect predictions as the error distribution remains uniform along the axis of permeability coefficient (Figure 8.25(c)). This observation was also confirmed in the case of subsequently trained NNs.

Another three NN architectures were designed by including either  $K_o$  or  $F_r$  data, and finally both information in the input vector. While the second variable delivers information related to frictional resistance at the cone shaft, the combination of the first variable with  $Q_t$  and  $B_q$  resembles Equation (8.1) used in random pattern generation. The results of post-training analysis for NN(QBH|6 – 6|M), Figure 8.25(b), and NN(QBF|7 – 7|M), Figure 8.25(d), exhibit noticeable improvements of predictions which are measured in terms of  $R$  (about 0.75), MSE (decreased of about 50%) and  $ARE_m$  (about  $12 \div 14\%$ ), as shown in Figure F.3. Incorporating  $k$  in the input vector results in a minor improvement of NN(QBKH|6 – 6|M) performance (see Table 8.8).

Finally, a contribution of both variables in the NN input results in a significant improvement of the correlation (Figure 8.25(e)). The network NN(QBFH|3 – 3|M) produces predictions of  $M$  with AREs up to 20%, and the mean value  $ARE_m$  about 6.5% (Figure F.3).

### 8.2.5.3 Stress history

The modeling of the inverse problem for interpretation of stress history for piezocone data is divided into two parts. The first part deals with prediction of standardly defined overconsolidation ratio OCR, whereas the second part extends the analysis to prediction of the constitutive overconsolidation ratio for the MCC, i.e.  $R_p$ . Finally, a summary of both analyzes is provided in Table 8.9.

The first trained network which is designed to predict OCR contains  $Q_t$  and  $k$  as the input components. Such an entry is similar to the formula given in Equation (6.45) for which the empirical coefficient  $k_{\sigma t} = 0.3$  has been adopted as typical value assumed for the first-order estimations. A comparison of the predictions derived from NN(QK|6 – 6|O) and the empirical method is illustrated

Table 8.8: Performance of the trained neural networks and the empirical approach designed to predict  $M$  (statistical features obtained for testing sets containing 71 random synthetic patterns).

Method Network name	Neural network				Equation (6.44)			
	$R$ (-)	MSE (-)	$ARE_m$ (%)	$ARE_{sd}$ (%)	$R$ (-)	MSE (-)	$ARE_m$ (%)	$ARE_{sd}$ (%)
NN(QB 10 – 10 M)	0.40	$6.0e - 02$	18.6	15.0	0.47	$5.9e - 02$	17.8	13.0
NN(QBH 6 – 6 M)	0.76	$3.0e - 02$	12.1	8.6	0.25	$7.6e - 02$	19.3	13.0
NN(QBKH 6 – 6 M)	0.81	$2.2e - 02$	11.1	8.4	0.54	$4.9e - 02$	15.2	10.0
NN(QBF 7 – 7 M)	0.73	$3.5e - 02$	14.1	11.0	0.26	$8.0e - 02$	22.5	16.0
NN(QBFH 3 – 3 M)	0.94	$9.0e - 03$	6.5	5.7	0.20	$9.5e - 02$	22.2	14.0
Mean					0.34	$7.2e - 01$	19.4	13.2

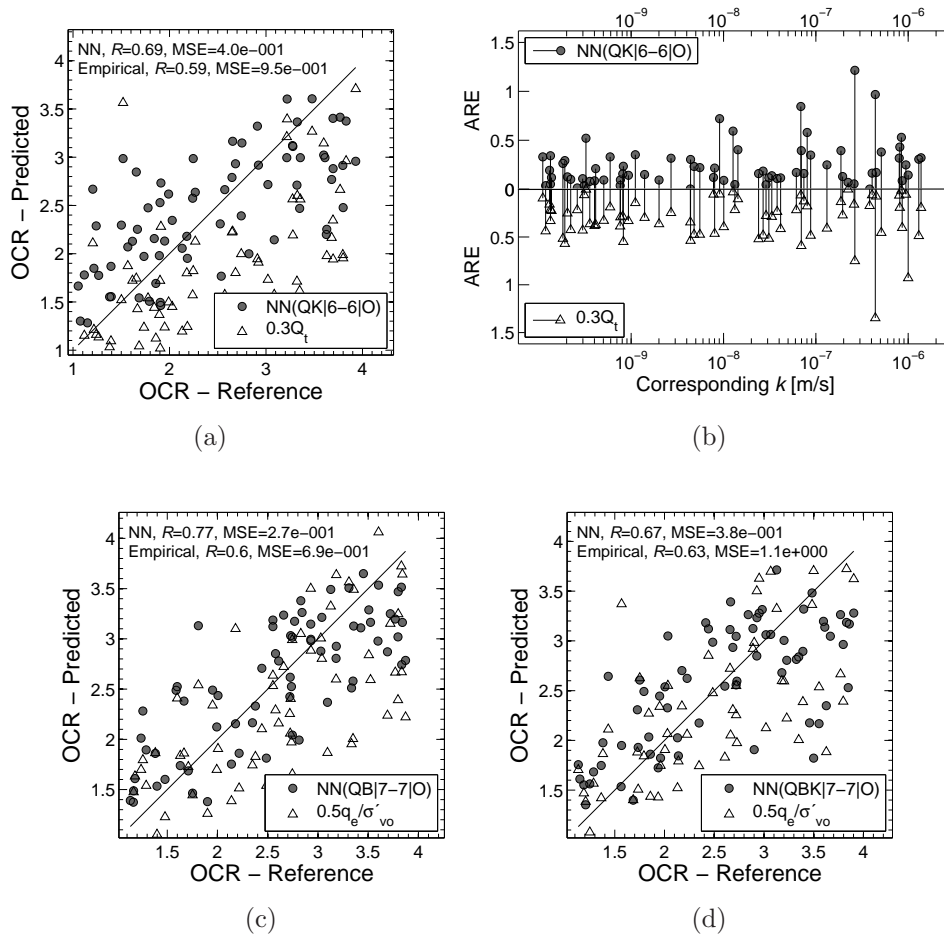


Figure 8.26: Partial drainage effect on predictions of OCR using empirical methods (empty triangles) and neural networks (solid circles).

in Figure 8.26(a). Although the NN exhibits a slightly better performance, it does not dump efficiently the influence of partial drainage for the patterns in which the phenomena may occur (Figure 8.26(b)). The chart also shows that the effect of partial drainage does not affect the empirical solution<sup>3</sup> as significantly as in the case of other methods (e.g. Figure 8.27(d) and 8.28(b)). In general, misinterpretation of patterns subject to partial consolidation is stronger pronounced for low values of OCR when looking at the corresponding Figure F.4(a).

In order to improve the accuracy of predictions,  $B_q$  was added to the input vector in the first order. In this case, the corresponding empirical method given in Equation (6.46) was chosen as a comparative method assuming the typically assigned empirical coefficient  $k_{\sigma e}$  equal to 0.5. As shown in Figure 8.26(c) and 8.26(d), both developed NNs, NN(QB|7-7|O) and NN(QBK|7-7|O), achieve reasonable performances which are slightly better than the one observed for the empirical method. The mean AREs computed for the considered NNs oscillate around 20%, whereas the empirical method is characterized by ARE<sub>m</sub> about

<sup>3</sup>The observation was confirmed using different testing sets.

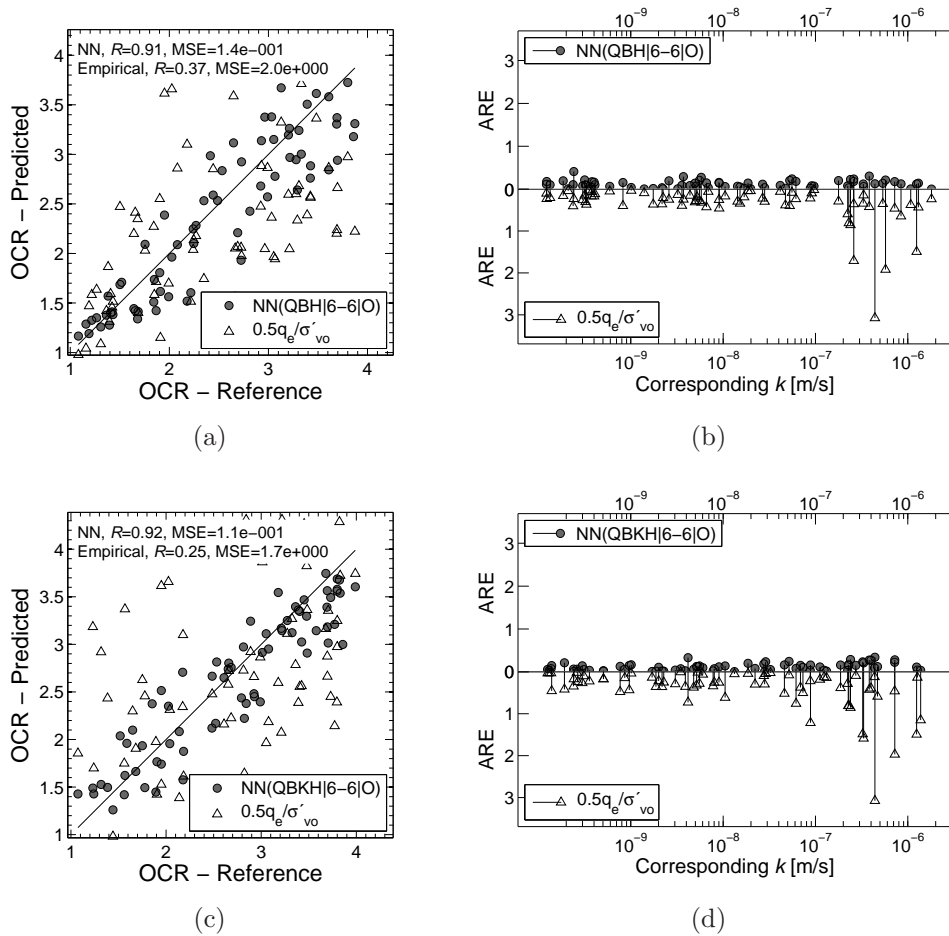


Figure 8.27: Partial drainage effect on predictions of OCR using the empirical method (empty triangles) and neural networks (solid circles).

26 ÷ 28% (Figure F.4).

Further improvement of accuracy can be expected using  $K_o$  as a supplementary component of the input vector since the parameter is somehow correlated with OCR (cf. Section 8.2.1). Post-training analysis performed for two developed NNs, NN(QBH|6 – 6|O) and NN(QBKH|6 – 6|O), present a very good performance characterized by a high value of correlation coefficient  $R$  equal to 0.91 and 0.92, respectively (Figure 8.27). The NN predictions well track the target OCRs and reveal moderate dispersal of the data points even for "drained" patterns. It can be noticed that the empirical method is very sensitive to an occurrence of partial drainage. Moreover, the empirical method exhibits high randomness of target prediction for pseudo-experimental data as high amplitudes of the computed  $R$  values are noticed for different testing sets, i.e. from 0.25 to 0.63 (cf. Table 8.9). In the case of both considered NNs, the mean ARE for OCR predictions was reduced to around 11% (Figure F.4). This analysis shows that  $K_o$  plays a key role in improving correlation of OCR with piezocone data.

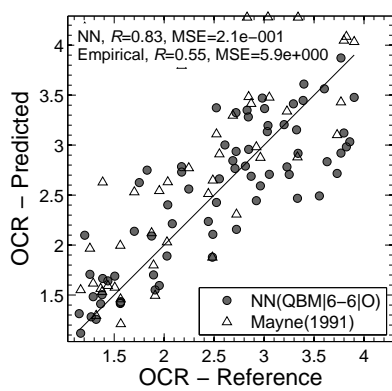
Another group of NNs was created including parameter  $M$  by similarity

to the input components in the formula presented in Equation (6.48). In the post-training analysis, NN(QBM|6 – 6|O) and NN(QBKM|5 – 5|O) demonstrate similar statistical features, as shown in Figure 8.28(a) and 8.28(c), respectively. Although information about soil permeability is not included, the first network recognizes "drained" patterns well, as illustrated in Figure 8.28(b). The chart also indicates that the formula proposed by Mayne (1991) can be strongly sensitive to drainage effects exhibiting even 100-300% errors for silt-like coefficients of permeability. The recognition of "drained" patterns by the NNs lead to reasonably small values of the mean ARE of around 15% (Figure F.5).

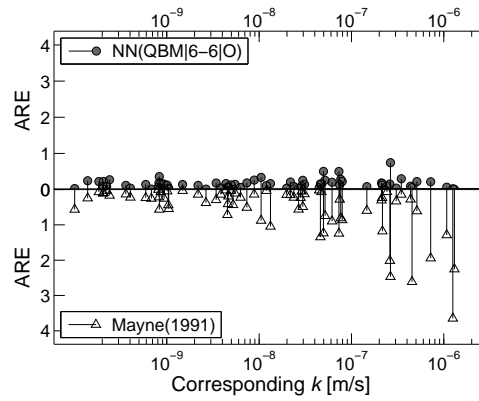
A replacement of the parameter  $M$  by the measured variable  $F_r$  in the input vector results in the reduction of network performance, as demonstrated in Figure 8.28(d). In effect, the data dispersal rises and an increase of the mean ARE to 20% is observed (Figure F.5).

The above analyzes have shown that the NN, which includes the basic piezocone data complemented with  $K_o$  parameter, achieves the best correlation performance. The following analysis investigates whether further supplementing of the input vector may increase the statistical performance of correlations for OCR. Figure 8.29 and F.5 presents the post-training analysis for two trained networks: NN(QBMH|5 – 5|O) and NN(QBFKH|7 – 7|O). It appears that the computed statistical features do not gain significant improvement in comparison with the features obtained for NN(QBH|6 – 6|O) (cf. Table 8.9).

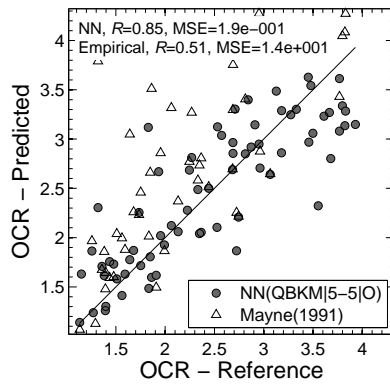
Correlating the constitutive overconsolidation ratio  $R_p$  with CPTU data is more demanding than OCR by virtue of its definition in terms of the effective mean stress and the fact that the piezocone measurements are normalized in terms of the effective vertical stress. Hence, such a conclusion would suggest a need of complementing the piezocone measurements with  $K_o$  in the input vector. In order to verify this need, two networks were created, i.e. NN(QB|7 – 7|OR) and NN(QBH|6 – 6|OR). Figure 8.30(a)-8.30(d) present a comparative analysis with both networks and two empirical methods. In the context of  $R_p$  prediction using the empirical Equation (6.46), the synthetic data points better correlate when assuming the empirical coefficient  $k_{\sigma e}$  equal to 0.55. As regards the second approach,  $\sigma'_{vo}$  in Equation (6.48) was replaced with  $p'_o$ . It can be noticed that both networks better track the targets than the considered empirical methods. The analysis also shows that the network without  $K_o$  as the input component exhibits similar statistical features as NN(QBH|6 – 6|OR) (see also Figure F.6). A slightly worse performance of the latter can be explained by the fact that the network received a "difficult" testing set to be correlated and it is also confirmed by performance of the empirical formulas for which the same set was used (cf. Table 8.9). The same reasoning can be used to explain an improvement of statistical features of the additionally trained network NN(QBKH|6 – 6|OR). The network presents a slightly better performance than previously considered NNs. However, it seems that it is rather attributed to the received "easy" testing set than to the additional input component  $k$ . Figure 8.30(b) and 8.30(d) reveal that the NNs without information on soil permeability also cope well with "drained" patterns. In Figure 8.30(e), the  $R_p$  values predicted by NN(QBKH|6 –



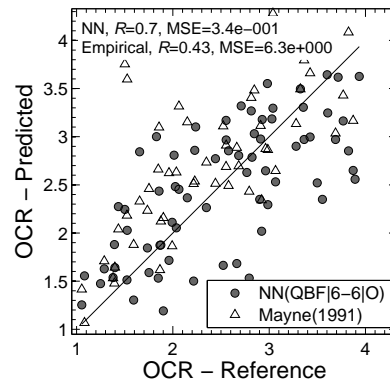
(a)



(b)

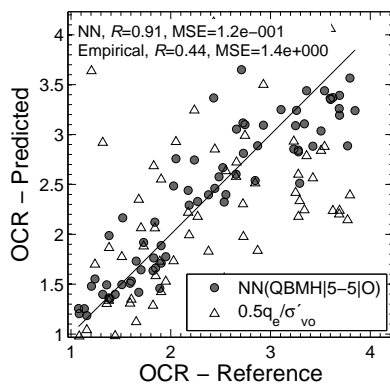


(c)

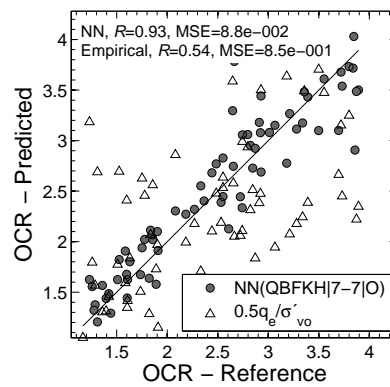


(d)

Figure 8.28: Partial drainage effect on predictions of OCR using the empirical method (empty triangles) and neural networks (solid circles).



(a)



(b)

Figure 8.29: Partial drainage effect on predictions of OCR using the empirical method (empty triangles) and neural networks (solid circles).

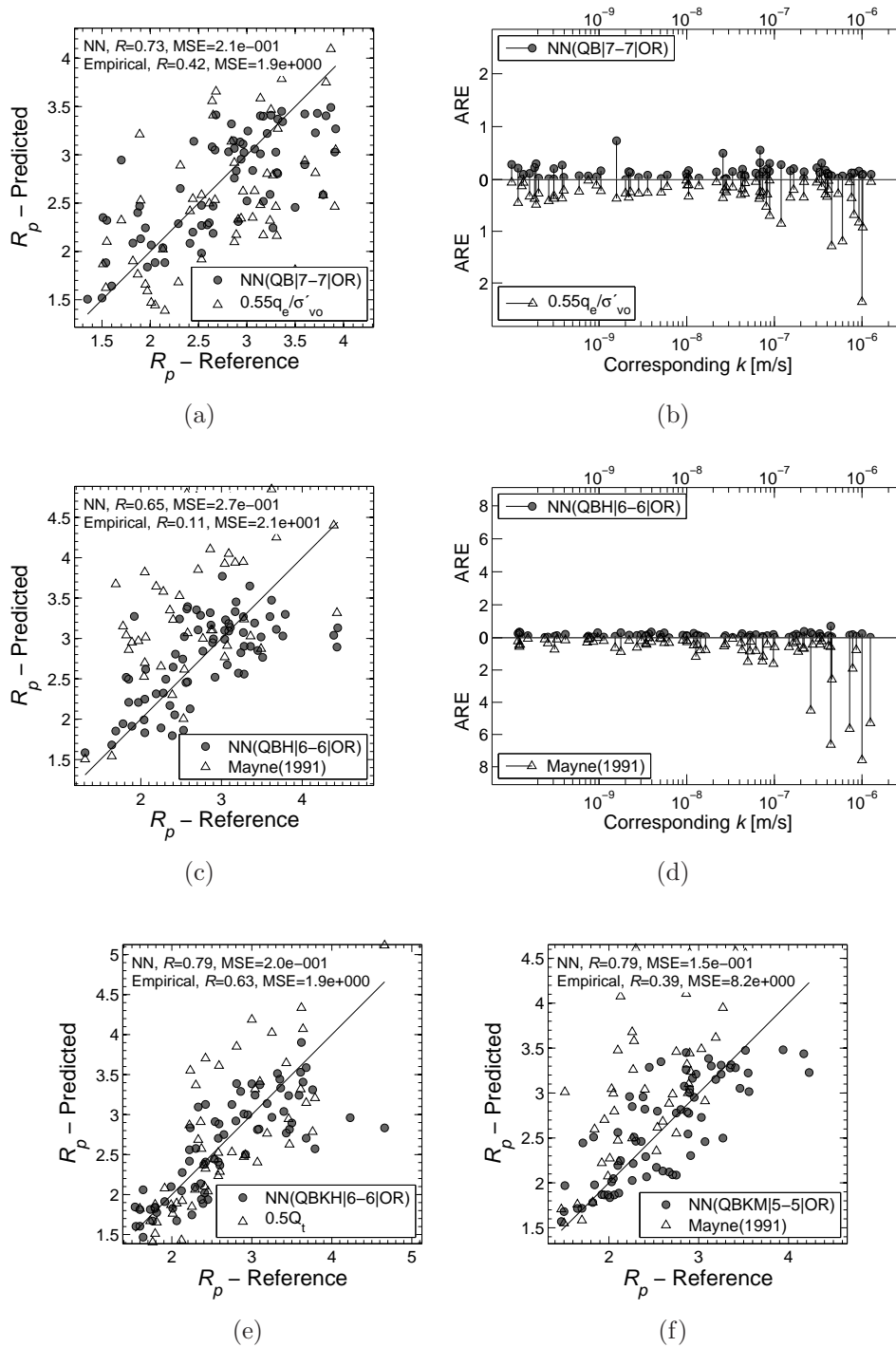


Figure 8.30: Partial drainage effect on predictions of  $R_p$  using the empirical method (empty triangles) and neural networks (solid circles).

6|OR) are compared with estimates obtained through Equation (6.45). In the case of the empirical formula, significantly better first-order estimates of  $R_p$  were obtained by tuning the empirical coefficient  $k_{\sigma t}$  to the value of 0.5<sup>4</sup>.

<sup>4</sup>Typical value of  $k_{\sigma t}$  used for the first-order estimates of OCR is usually assigned as 0.3, cf. Table 6.3.

Table 8.9: Performance the trained neural networks and the empirical approaches designed to predict OCR and  $R_p$  (statistical features obtained for testing sets containing 71 random synthetic patterns).

Method Network name	Neural network			Mayne (1991)			$0.5 \cdot q_e / \sigma'_{v_o}$			$0.3 \cdot Q_t$		
	$R$ (-)	MSE (-)	ARE <sub>m</sub> , ARE <sub>sd</sub> (%)	$R$ (-)	MSE (-)	ARE <sub>m</sub> , ARE <sub>sd</sub> (%)	$R$ (-)	MSE (-)	ARE <sub>m</sub> , ARE <sub>sd</sub> (%)	$R$ (-)	MSE (-)	ARE <sub>m</sub> , ARE <sub>sd</sub> (%)
NN(QK 6 - 6 O)	0.69	4.0e - 01	24.4	0.45	1.1e + 01	65.9	0.46	1.8e + 00	37.6	0.59	9.5e - 01	31.3
NN(QB 7 - 7 O)	0.77	2.7e - 01	19.0	0.58	3.0e + 00	46.7	0.60	6.9e - 01	25.8	0.71	9.3e - 01	30.8
NN(QBK 7 - 7 O)	0.67	3.8e - 01	20.5	0.59	8.7e + 00	61.7	0.63	1.1e + 00	28.1	0.70	8.5e - 01	29.3
NN(QBH 6 - 6 O)	0.91	1.4e - 01	11.4	0.41	9.7e + 00	65.4	0.37	2.0e + 00	36.3	0.50	1.1e + 00	33.7
NN(QBKH 6 - 6 O)	0.92	1.1e - 01	11.3	0.30	9.0e + 00	80.6	0.25	1.7e + 00	42.2	0.47	1.1e + 00	31.3
NN(QBM 6 - 6 O)	0.83	2.1e - 01	15.0	0.55	5.9e + 00	55.5	0.54	1.0e + 00	30.7	0.66	9.5e - 01	32.2
NN(QBKM 5 - 5 O)	0.85	1.9e - 01	14.6	0.51	1.4e + 00	72.7	0.58	1.6e + 00	33.8	0.70	7.6e - 01	30.6
NN(QBF 6 - 6 O)	0.70	3.4e - 01	19.9	0.43	6.3e + 00	51.1	0.40	1.8e + 00	31.9	0.52	1.2e + 00	34.3
NN(QBMH 5 - 5 O)	0.90	1.3e - 01	10.9	0.64	8.6e + 00	67.6	0.35	1.4e + 00	35.7	0.48	1.3e - 01	31.0
NN(QBFKH 7 - 7 O)	0.93	8.8e - 02	9.6	0.54	4.3e + 00	52.4	0.54	8.5e - 01	29.0	0.67	9.1e - 01	31.1
Mean				0.50	8.05	62.0	0.47	1.39	33.1	0.60	0.888	31.6
												18.8
Method Network name	Neural network			Mayne (1991)			$0.55 \cdot q_e / \sigma'_{v_o}$			$0.5 \cdot Q_t$		
	$R$ (-)	MSE (-)	ARE <sub>m</sub> , ARE <sub>sd</sub> (%)	$R$ (-)	MSE (-)	ARE <sub>m</sub> , ARE <sub>sd</sub> (%)	$R$ (-)	MSE (-)	ARE <sub>m</sub> , ARE <sub>sd</sub> (%)	$R$ (-)	MSE (-)	ARE <sub>m</sub> , ARE <sub>sd</sub> (%)
NN(QB 7 - 7 OR)*	0.72	3.6e - 01	20.4	0.27	1.6e + 01	86.1	0.42	1.9e + 00	32.1	0.55	1.5e + 00	30.3
NN(QB 7 - 7 OR)	0.73	2.1e - 01	13.8	0.27	1.6e + 01	86.1	0.42	1.9e + 00	32.1	0.55	1.5e + 00	30.3
NN(QBH 7 - 7 OR)	0.94	1.0e - 01	10.5	0.11	2.1e + 01	89.4	0.20	2.6e + 00	36.2	0.30	2.1e + 00	36.0
NN(QBH 7 - 7 OR)	0.65	2.7e - 01	14.5	0.11	2.1e + 01	89.4	0.20	2.6e + 00	36.2	0.30	2.1e + 00	36.0
NN(QBKH 6 - 6 OR)	0.93	9.5e - 02	9.6	0.50	2.2e + 01	88.4	0.56	2.4e + 00	34.3	0.63	1.9e + 00	31.6
NN(QBKH 6 - 6 OR)	0.79	2.0e - 01	11.4	0.50	2.2e + 01	88.4	0.56	2.4e + 00	34.3	0.63	1.9e + 00	31.6
NN(QBKM 5 - 5 OR)	0.82	2.1e - 01	15.5	0.39	8.2e + 00	69.1	0.45	1.5e + 00	30.7	0.57	1.3e + 00	34.0
NN(QBKM 5 - 5 OR)	0.79	1.5e - 01	11.6	0.39	8.2e + 00	69.1	0.45	1.5e + 00	30.7	0.57	1.3e + 00	34.0
Mean				0.32	16.8	83.3	0.41	2.10	33.3	0.51	1.70	32.0
												35.0

\* The regression analysis for a variable in bold.

The use of  $M$  parameter instead of  $K_o$  in the input vector yield in a similar correlation performance as for previously presented NNs (Figure 8.30(f)). In general, the presented NNs which predicts  $R_p$  exhibit the mean ARE about  $11 \div 15\%$  without any significant dispersal of data points (cf. Table 8.9).

#### 8.2.5.4 Horizontal stress

A number of NN models were investigated with regards to the estimation of the  $K_o$  variable from piezocone data. By similarity to the empirical Equation 6.53, the first designed topology includes in the input vector only the  $Q_t$  parameter. Figure 8.31(a) illustrates the regression analysis performed for this network, as well as the results derived from the empirical formula for which the empirical coefficient  $k_K$  was assumed as typical for the first-order estimation and equal to 0.1. It can be noticed that both predictions are characterized by a low degree of correlation (low  $R$  values). However, the empirical formula for the testing set exhibits higher dispersal of the data points than NN predictions. While AREs for the latter are observed up to 70% (with the mean  $ARE_m = 21\%$ ), the empirical formula gives errors of up to 110%, and  $ARE_m$  around 35% (Figure F.7). Nevertheless, the problem is poorly modelled by NN(Q|9 – 9|H) as data points are significantly rotated with reference to the center of  $K_o$  interval. Figure 8.31(b) shows that drainage conditions do not affect predictions as the error distribution remains uniform along the axis of permeability coefficient. This observation is confirmed by further analysis of two created networks NN(QBM|8 – 8|H) and NN(QBFM|8 – 8|H) which supplemented with permeability component in the input vector essentially yield the same statistical parameters, as demonstrated in Figure 8.31(c) - 8.31(f). These charts reveal a significant improvement of NN predictions as all the networks reasonable track the target values of  $K_o$ . Using supplementary input information, the mean AREs for predictions are reduced to about  $10 \div 14\%$ , as shown in Figure F.7. A summary of statistical features of the trained neural networks is provided in Table 8.10.

Table 8.10: Performance of the trained neural networks and the empirical approach designed to predict  $K_o$  (statistical features obtained for testing sets containing 71 random synthetic patterns).

Method Network name	Neural network				$0.1 \cdot Q_t$			
	$R$ (-)	MSE (-)	$ARE_m$ (%)	$ARE_{sd}$ (%)	$R$ (-)	MSE (-)	$ARE_m$ (%)	$ARE_{sd}$ (%)
NN(Q 9 – 9 H)	0.38	$3.7e - 02$	21.2	17.0	0.40	$1.1e - 01$	34.6	25.0
NN(QBM 8 – 8 H)	0.75	$1.9e - 02$	14.1	10.0	0.39	$1.0e - 01$	33.0	21.0
NN(QBKM 8 – 8 H)	0.74	$2.0e - 02$	14.2	12.0	0.37	$1.0e - 01$	35.1	24.0
NN(QBFM 8 – 8 H)	0.85	$1.1e - 02$	11.7	9.7	0.27	$1.0e - 01$	34.2	23.0
NN(QBFKM 6 – 6 H)	0.84	$1.1e - 02$	10.3	8.0	0.29	$1.2e - 01$	36.8	25.0
Mean					0.32	$1.1e - 01$	34.7	23.6



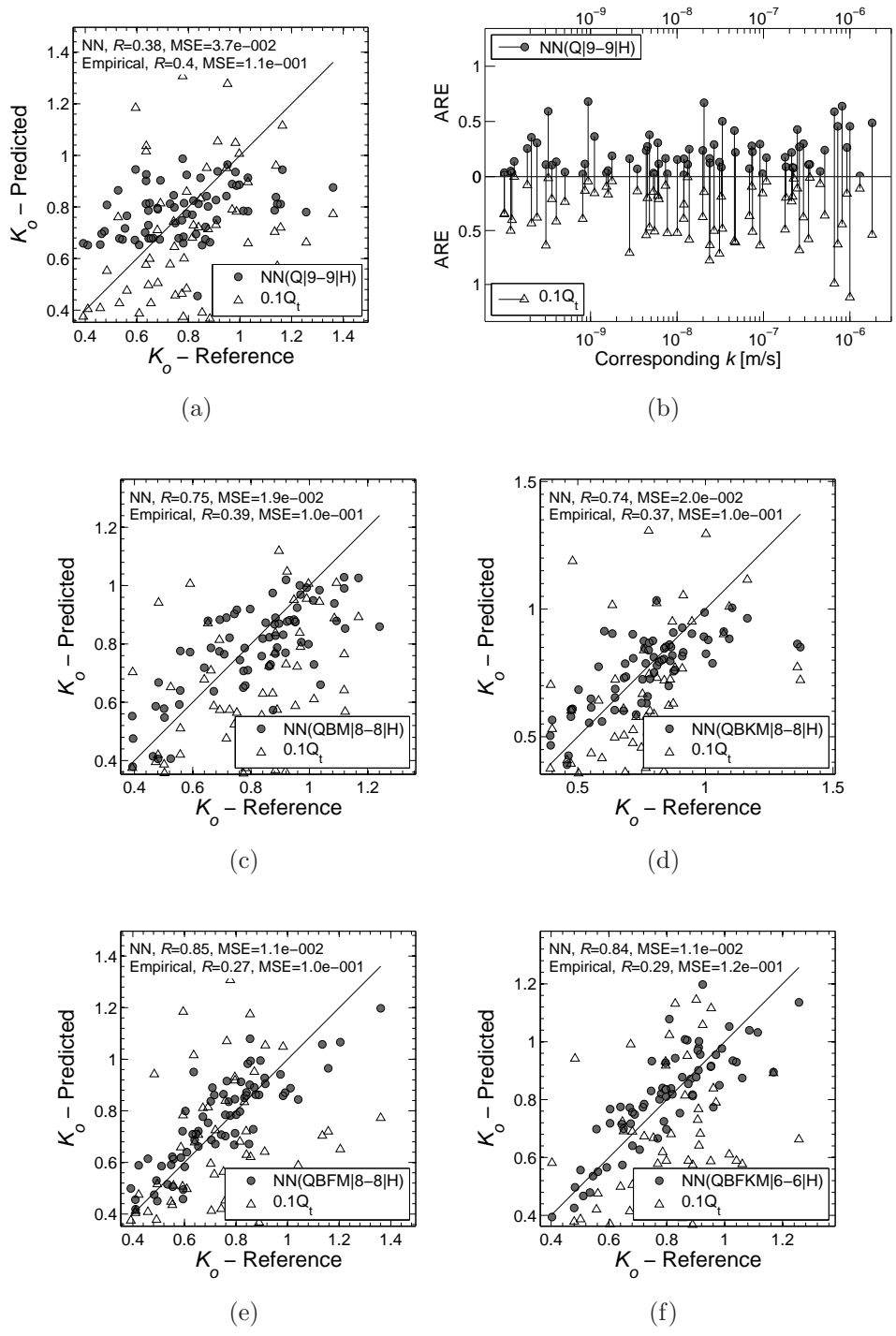


Figure 8.31: Prediction of  $K_o$  using the empirical method (Equation (6.53), empty triangles) and neural networks (solid circles).

### 8.2.5.5 Deformation characteristics

In practice, the deformation characteristic  $\lambda$  can be estimated by integration Equations (6.55) and (6.56):

$$\lambda = \frac{(1 + e_o)\sigma'_{vo}}{\alpha_n(q_t - \sigma_{vo})} = \frac{1 + e_o}{\alpha_n Q_t} \quad (8.14)$$

where  $\alpha_n$  needs to be calibrated for a specific site. The above formula is then used as a comparative method for NN predictions.

The first trained network was designed using input components equivalent to the variables included in Equation 8.14. The network presents a slightly worse correlation of the problem than the empirical formula with applied operational coefficient  $\alpha_n$  equal 2.0 for the first-order estimates, as shown in Figure 8.32(a). Predictions of NN(QV8 – 8|P) are characterized by a larger dispersal, and consequently, by larger values of  $ARE_m$  and  $ARE_{sd}$  (Figure F.8 and Table 8.11). A slight improvement of predictions can be achieved by including the remaining piezocone measurements  $B_q$  and  $F_r$  (Figure 8.32(c)). However, a few performed tests revealed that parameter  $B_q$  is not essential for the prediction of  $\lambda$ . Moreover, partial drainage has no observable influence on NN or empirical predictions, as demonstrated in Figure 8.32(b).

Further tests revealed the importance of including the parameter  $\Lambda$  in the input vector. Although the parameter does not improve data dispersal measured by  $ARE_{sd}$ , it increases the strength of correlation in terms of  $R$  (see NN(QVL|8 – 8|P) in Table 8.11). Hence, further improvement of prediction accuracy requires complementing the input vector with supplementary variables such as  $K_o$  and  $M$  (Figure 8.32(d)-8.32(e)). However, the best accuracy was obtained for the input defined as QFVLH for two different NN architectures, as summarized in Table 8.11. Figure 8.32(f) and F.8(d) present an example of the post-training analysis for NN(QFVLH|6 – 6|P) which shows superior correlation over the empirical formula. It is worth noting that although meaningful accuracy of predictions is achieved by involving three auxiliary variables which are not measured by the piezocone, none of them represents a constitutive parameter.

The following analysis explores the possibility of correlating the constitutive parameter  $\kappa$  with piezocone data. By analogy with the previous analysis, predictions derived from trained NNs are compared with results obtained through Equation (8.14). As regards the empirical formula, reasonably good correlations for considered testing sets were found by assigning  $\alpha_n$  equal to 8.0.

A preliminary analysis shows that network NN(QV6 – 6|E) with the input corresponding to the variables included in empirical formula achieves slightly weaker performance than the empirical method (Figure 8.33(a) and F.9). The analysis also shows that partial drainage does not affect NN predictions nor empirical estimates (Figure 8.33(c)). Further tests revealed that significant improvement of NN predictions can be achieved by complementing the input vector with  $F_r$  and  $K_o$ . It was recognized that these variables separately deliver amounts of information which contributes to the reduction of uncertainty of NN

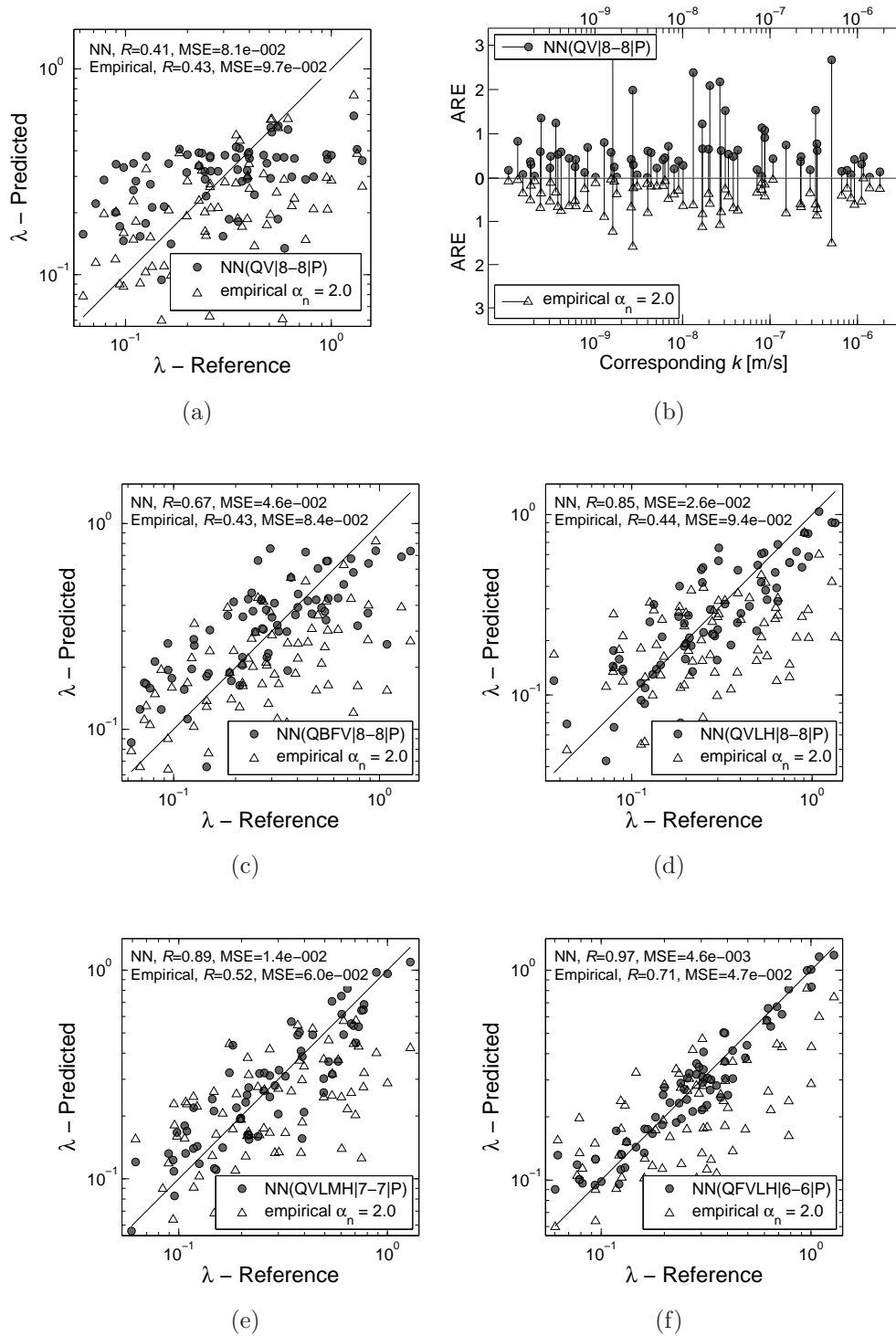


Figure 8.32: Predictions of parameter  $\lambda$  using the empirical method (empty triangles) and neural networks (solid circles).

Table 8.11: Performance of the trained neural networks and the empirical approach designed to predict  $\lambda$  and  $\kappa$  (statistical features obtained for testing sets containing 71 random synthetic patterns).

Method Network name	Neural network				Equation (8.14), $\alpha_n = 2.0$			
	$R$ (-)	MSE (-)	$ARE_m$ (%)	$ARE_{sd}$ (%)	$R$ (-)	MSE (-)	$ARE_m$ (%)	$ARE_{sd}$ (%)
NN(QV 8 – 8 P)	0.41	$8.1e - 02$	64.7	64.0	0.43	$9.7e - 02$	47.7	34.0
NN(QBFV 8 – 8 P)	0.67	$4.6e - 02$	49.6	44.0	0.43	$8.4e - 02$	45.7	30.0
NN(QVL 8 – 8 P)	0.76	$3.4e - 02$	58.6	66.0	0.45	$7.7e - 02$	56.5	61.0
NN(QVLH 8 – 8 P)	0.85	$2.6e - 02$	41.1	39.0	0.44	$9.4e - 02$	56.9	54.0
NN(QVLMH 7 – 7 P)	0.89	$1.4e - 02$	30.4	26.0	0.52	$6.0e - 02$	47.4	34.0
NN(QFVLH 6 – 6 P)	0.97	$4.6e - 03$	18.3	17.0	0.71	$4.7e - 02$	42.6	31.0
NN(QFVLH 7 – 7 P)	0.97	$4.2e - 03$	13.9	11.0	0.37	$7.2e - 02$	46.8	44.0
Mean					0.48	$7.6e - 02$	49.1	41.1
	Neural network				Equation (8.14), $\alpha_n = 8.0$			
NN(QV 6 – 6 E)	0.56	$1.2e - 03$	59.1	54.0	0.66	$9.1e - 04$	47.3	51.0
NN(QFVH 5 – 5 E)	0.97	$1.3e - 04$	14.4	11.0	0.68	$1.0e - 03$	46.5	48.0
NN(QFVH 6 – 6 E)*	0.98	$8.0e - 05$	26.4	27.0	0.66	$1.3e - 03$	121.4	150.0
NN(QVH 6 – 6 E)*	0.71	$1.1e - 03$	115.5	16.0	0.63	$1.5e - 03$	115.4	140.0

\*The network trained with the use of theoretical patterns  $I_r = 10 \div 750$ .

predictions. In effect, synergy of both variables results in excellent correlation by NN(QFVH5 – 5|E), as shown in Figure 8.33(b) and F.9. NN predictions are characterized by a significantly reduced data dispersal and a low mean value of ARE around 14%. Obviously, as soon as  $F_r$  contributes in a prediction, no reliable estimates could be expected for natural soils which exhibit the feature of sensitivity.

The above analysis showed feasibility of an accurate prediction of the constitutive parameter  $\kappa$ . However, owing to the limitations of the numerical model (cf. Section 8.2.2), an application of the developed NN is strictly limited to soft and very soft organic clays which exhibit  $I_r < 110$ . Thus, a broad application of the method should involve an extension of the synthetic data base. For the purpose of this study, a theoretical database containing "undrained" patterns was used to verify the effectiveness of predictions for a wide range of  $\kappa$ . The post-training analysis Figure 8.34 illustrates good reproduction of target values by NN(QFVH6 – 6|E). An increase of AREs can be observed for very small values of  $\kappa$ . Taking into account that the difference between the smallest and the largest value is of two log cycles, the obtained mean  $ARE_m = 26.4$  can be considered as a satisfactory result.

## 8.2.6 Knowledge extraction

The following analysis presents a feasibility of knowledge extraction from the trained NNs. For this purpose, a problem of  $R_p$  correlation with piezocone and other available input data is taken as an illustrative example. In the analysis six different combinations of input parameters were investigated by means of three various approaches, i.e. weight partitioning, "connection weights" and input perturbation (see Section 3.4). Since each NN training provides a unique NN,

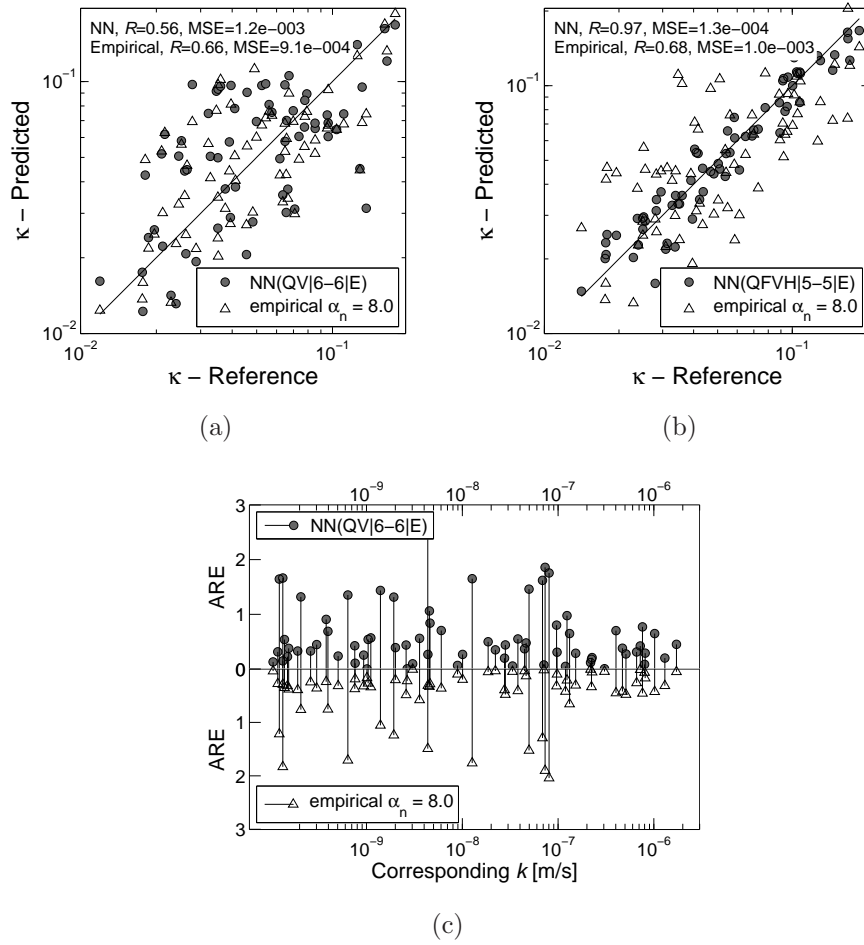


Figure 8.33: Predictions of parameter  $\kappa$  using the empirical method (empty triangles) and neural networks (solid circles).

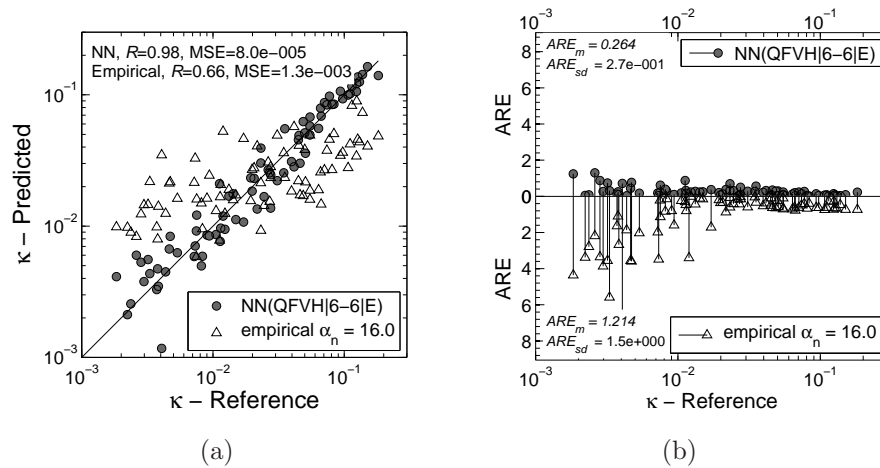


Figure 8.34: Predictions of parameter  $\kappa$  using the empirical method (empty triangles) and the neural networks (solid circles) trained with the aid of theoretical patterns ( $I_r = 10 \div 750$ ).

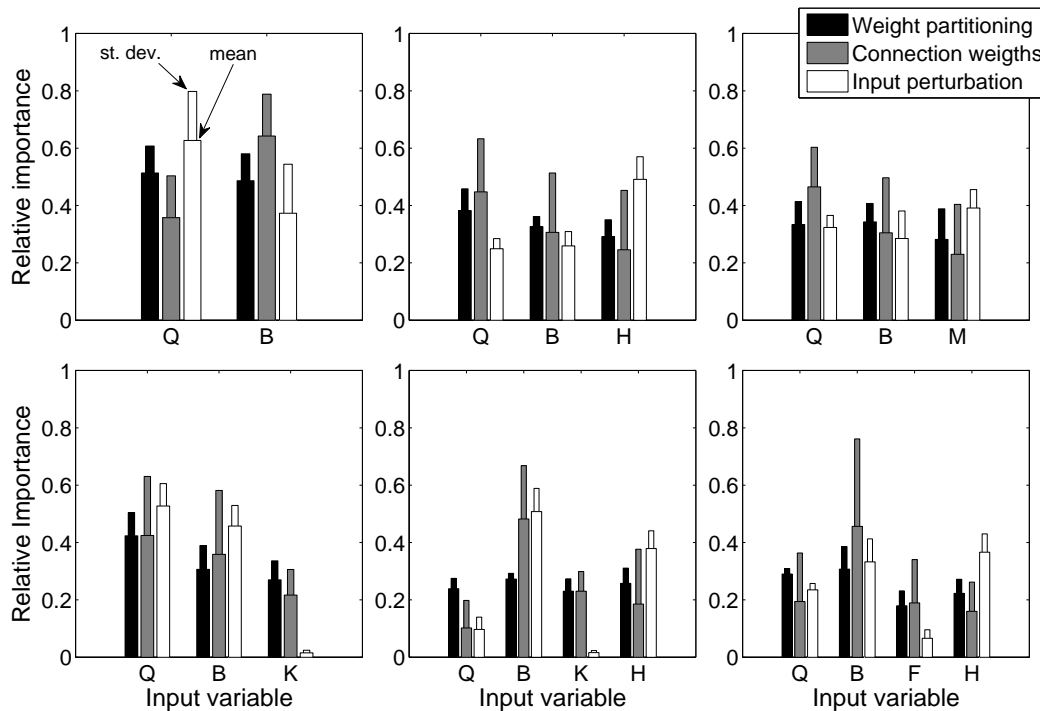


Figure 8.35: Example of knowledge extraction from different NNs designed to predict the overconsolidation ratio  $R_p$ .

five different one-layer networks for each input combination were trained<sup>5</sup>. The relative importance of particular input parameters was thus calculated as the mean value. In the case of input perturbation method, the input components of testing patterns were perturbed from 85 to 115% with regards to the reference values.

Figure 8.35 presents the results of the analysis. In general, three applied methods similarly estimate the contribution of particular inputs. It can be noticed that contribution weights of auxiliary input data such as  $K_o$  or  $M$  exhibit similar importance as the piezocone input. On the other hand, information on soil permeability contributes to a lesser extent probably because the parameters  $Q_t$  and  $B_q$  contain enough information about drainage conditions. Moreover, in the case of the input perturbation method, the small contribution of  $k$  stems from small perturbation with regards to the log cycle.

### 8.2.7 Summary

The above section related to the piezocone test presents the effectiveness of correlating constitutive parameters with cone measurements by means of the NN modeling. The NN training is based on the results derived from FE simulations with the applied constitutive law of the MCC. It has been proven that the MCC model can provide a synthetic database which exhibits a meaningful consistency

<sup>5</sup>Weight partitioning and "connection weights" algorithms are suitable to analyze one-layer networks.

with experimental trends observed in the behavior of natural soils subject to the penetration. The numerical database, which has been generated with wide intervals of constitutive parameters and different drainage conditions, provide piezocone results that correspond to the SBT of soft organic deposits, clays and silts. Some general conclusions related to the NN training with the aid of numerical database can be drawn as follows:

- NNs which contain only basic parameters derived from penetration test, i.e.  $Q_t$  and  $B_q$ , provide a similar or somewhat better accuracy of predictions than the empirical methods which employ average coefficients of correlation. A significant improvement of accuracy can be achieved by increasing the amount of information in the input vector.
- Auxiliary input components such as  $K_o$ ,  $F_r$  and  $M$ , can significantly contribute to the increase of quality of correlation and to reducing the dispersal of predictions. Meaningful accuracy of predictions can often be achieved based merely on the basic piezocone parameters complemented with state variables such as  $K_o$  or  $e_o$ . The NNs with the smallest possible number of additional parameters are recommended when applying the method to real experimental data in order to avoid "over-fitted" predictions.
- Owing to the formulation of the MCC model, predictions with the use of  $F_r$  as the input parameter, can be considered as reliable in the case of non-sensitive soils.
- The effect of partial drainage during penetration mostly affect the interpretation of  $c_u$ , OCR and  $R_p$ . In the case of parameters  $M$ ,  $\lambda$ ,  $\kappa$  or  $K_o$ , errors for NN predictions are not dependent on drainage conditions.
- In general, NN predictors correctly detect the patterns which were subject to partial consolidation during penetration. In such cases, NNs exhibit sensitivity to increasing  $Q_t$  and correspondingly decreasing  $B_q$  and provide the solutions which are free of drainage-induced errors.
- During NN training it was observed that the influence of NN topology (i.e. number of hidden neurons and number of hidden layers) was insignificant compared to the results obtained by an increasing amount of input information (i.e. number of input components). In other words, different NN topologies resulted in a very similar quality of predictions for the same input configuration.

Finally, Table 8.12 summarizes the quality of correlations obtained in this study for different parameters and for various input configurations. In this summary, the quality rating is defined in terms of the coefficient of correlation  $R$ .

Table 8.12: Perceived quality of correlations obtained in this study for different parameters and for various input configurations.

Input configuration	Identified parameter						
	$c_u$	$M$	OCR	$R_p$	$\kappa$	$\lambda$	$K_o$
Q	3						5
QK			3				
QB	2	4	2	3			
QBF*	1	3	3				
QBFH*		1					x
QBFM*							2
QBFV*						3	
QBFKH*			1				x
QBFKM*							2
QBK	2		3				
QBKH	2		1	2			x
QBKM			2	2			3
QBH	2	2	1	3			x
QBM	1	x	2				2
QBMH		x	1				x
QFVH					1		x
QFVLH						1	x
QV					4	4	
QVL						2	
QVLH						2	x
QVLMH		x				2	x

\* $F_r$  does not account for the effect of soil sensitivity.

Quality rating: | 1 High ( $R \geq 0.9$ )  
 2 High to moderate ( $0.9 > R \geq 0.75$ )  
 3 Moderate ( $0.75 > R \geq 0.6$ )  
 4 Moderate to low ( $0.6 > R \geq 0.4$ )  
 5 Low ( $R < 0.4$ )  
 Empty - not assigned or not satisfactory



# Chapter 9

## Validation of Enhanced Parameter Identification

*The man of science has learned to believe in justification,  
not by faith, but by verification.*

Thomas Huxley

This chapter presents an application of developed NN inverse models to parameter assessment from real testing measurements derived from both pressuremeter and piezocone tests. Efficiency of NN predictors is verified by performing comparative analyzes for obtained NN predictions and observable evidences collected for specific characterization sites. Experimental evidence of each site consists of parameter estimates derived from various laboratory and field tests, as well as different interpretation methods.

The chapter is divided into two main sections related to the SBPT and the CPTU test respectively. In the case of SBPT, an application of the parameter identification strategy which has been proposed in Section 2.4 is presented for SBP experimental data measured in the Fucino clay characterization site. As regards the CPTU, experimental piezocone measurements derived from a number of characterization sites are mapped onto soil properties using various NN models. The obtained parameter profiles are compared with discrete parameter estimates derived from laboratory tests, as well as other field tests. NN predictions are also compared with first-order estimates obtained through existing empirical formulas based on piezocone records. Finally, general conclusions are drawn separately with regards to analyzes presented for two considered field tests.

## 9.1 Model calibration using pressuremeter test

The following section demonstrates an application of the combined parameter identification for the field pressuremeter experimental data obtained for Fucino clay. Results of both holding and expansion tests are back-analyzed in order to derive the MCC model parameters. The quality of evaluated parameters is compared with soil properties obtained through various field and laboratory tests.

### 9.1.1 Experimental data

The investigated characterization site contains a deep clayey deposit placed in the Fucino basin in Italy. A well-documented test descriptions and field results are reported in detail by Fioravante (1988). The results of pressuremeter tests were adapted from the testing programme of 36 tests performed in two boreholes V1 and V2. The objective site was comprehensively investigated by means of other *in situ* and laboratory tests for which results are comprehensively reported by Burghignoli et al. (1991).

The investigated stratum consists of plastic clay of lacustrin origin. The deposit was subject to overconsolidation due to dessication and ground water fluctuations resulting in a light preconsolidation. It was also found that the clay was structured and possessed cemented particle bounds due to the presence of  $\text{CaCO}_3$ . The results of four cone penetration tests revealed substantial spatial homogeneity of the area under study.

Two holding tests and three expansion tests from the Fucino clay site were adopted for the purpose of this research. The tests were selected from the tests performed at depths between 9.10 and 14.0m and are presented in Table 9.1. The strain-controlled expansion tests, namely V1P5, V2P7 and V2P8, were carried out up to the cavity strain  $\epsilon_c \approx 10\%$ , with a constant rate of 1%/min. The strain and pressure holding tests, V1P6 and V2P6 respectively, were performed right after the soil yielded at the cavity expansion of about 2%. The strain

*Table 9.1:* Reference pressuremeter tests and geotechnical properties of Fucino clay (from Fioravante, 1988).

No.	Test name	Test type	Strain Rate $\dot{\epsilon}_c$ (%/min)	Depth $z$ (m)	Initial stress conditions				
					$\sigma'_{ho}$ (kPa)	$\sigma'_{vo}$ (kPa)	$u_o$ (kPa)	$K_o$	$K_{onc}$
1	V1P5	SC PET	1.00	9.10	58.21	60.10	80.07	0.97	
2	V1P6	SC PET-SHT	0.30	10.55	50.14	68.20	95.00	0.74	
3	V2P6	PC PET-PHT	$\approx 0.30$	9.50	61.14	62.30	84.00	0.98	0.65
4	V2P7	SC PET	1.00	11.00	68.70	70.40	99.00	0.98	
5	V2P8	SC PET	1.00	14.00	78.91	70.40	129.00	0.91	

SC - stress controlled, PC - pressure controlled

rate was evaluated as approximately  $0.3\%/min$  . Since the test conditions of two latter tests differ from those commonly applied and adopted in NN training presented in Section 8.1.2, the neural networks were retrained with the training patterns respecting these boundary conditions.

Table 9.2 presents a summary of mechanical geotechnical properties of the Fucino clay evaluated through various laboratory tests such as triaxial compression tests: consolidated isotropic undrained (CIUC), consolidated isotropically drained (CIDC) , as well as oedometer tests with incremental loading (IL) and constant rate of strain (CRS). The undrained shear strength was estimated through field tests such as piezocone penetration (CPTU), SBP tests and field vane tests (FVT) and in the laboratory with the triaxial unconfined undrained shear test (UU).

The CIUC and CIDC compression tests were performed on samples recovered at the depth of 9m. Since the specimens were isotropically consolidated with pressures larger than the preconsolidation stress, the soil was considered as destructured and revealed a considerable underestimation of the undrained strength ratio on average equal to  $c_u/\sigma'_{vo} = 0.350$  . As discussed by Burghignoli et al. (1991), the results of  $c_u/\sigma'_{vo}$  from field tests CPTU or in some extent FVT can be underestimated due to the destructuration caused by the probe insertion.

Table 9.2: Geotechnical properties of Fucino clay (from Fioravante, 1988; Burghignoli et al., 1991).

		Geotechnical properties (reference test)									
No.	Depth $z$ (m)	$e_o$ (-)	OCR (-) (IL/ CRS)	$k$ $\cdot 10^{-10}$ (m/s) (IL, CRS)	$M$ (-) (CIDC, CIUC)	$R_p^*$ (-)	$c_u/\sigma'_{vo}$ (FVT/ CPTU <sup>†</sup> / SBPT/ UU)	$\kappa$ (-)	$\lambda$ (-)		
1	9.10	2.04 ÷ 2.71	1.34 ÷ 1.45/ 1.49	1.83 ÷ 4.63		1.20 ÷ 1.33	0.438 0.396 0.566				
2	10.55	2.41 ÷ 3.11	1.30/ 1.50	2.39 ÷ 6.46		1.38 ÷ 1.60	0.457 0.406 0.565		0.31 (CIU)		
3	9.50	2.04 ÷ 2.71	1.45 ÷ 1.49	1.83 ÷ 4.63	1.20	1.29 ÷ 1.33	0.449 0.400 0.583 0.379	0.026 ÷ 0.091 (OEM <sup>‡</sup> )	0.452 ÷ 0.804 (OEM <sup>‡</sup> )		
4	11.00	2.41 ÷ 3.11	1.30/ 1.50	2.39 ÷ 6.46		1.16 ÷ 1.33	0.461 0.352 0.594	0.048 ÷ 0.081 (OEM <sup>§</sup> )	0.24 ÷ 0.41 (OEM <sup>§</sup> )		
5	14.00	2.15 ÷ 2.44	1.23 ÷ 1.30/ 1.18 ÷ 1.36	0.62 ÷ 3.68		1.10 ÷ 1.21	0.540 0.523 0.717				

\*  $R_p$  derived from Equation (8.4),† Cone factor  $N_{kt} = 14$ ,

‡ Cemented soil,

§ Destruered soil.

### 9.1.2 Parameter identification

In each numerical simulation, the initial state of soil was defined through the mean value of void ratio  $e_o$  at a given depth and the initial anisotropic stress conditions as shown in Table 9.1. Depending on the measured data and the type of the performed pressuremeter test, some parameters had to be predetermined and considered as optimal because of the non-uniqueness. Because of the lack of pore pressure measurements for the expansion tests, the average and constant value of  $M = 1.20$  obtained through the triaxial tests was assumed for each simulation. The initial vector of parameters was approximated using neural networks and then corrected by running the MGN algorithm to obtain a better fit between experimental and numerical data. In the case of dissipation tests, the curves were fitted using only one discrete point corresponding to 50% of the excess pore water pressure decay.

The identification of  $R_p$ ,  $\kappa$ ,  $\lambda$  and  $k$  was carried out based on the measurements of V2P6 PHT test. The NN-assigned parameters were used as the initial vector for the gradient-based optimization. Since, the model response for the predicted parameters was close to the optimal one (Figure 9.1), all the curves were effectively fitted in 4 iterations. The results of the identification are summarized in Table 9.3 where italic and bold fonts represent NN-identified and optimized parameters respectively. It is worth noting that  $\lambda$  was successfully evaluated mainly through the variation of  $\Delta\varepsilon_c$  in dissipation time and the obtained value is comparable with those derived through laboratory tests. The optimal value 0.86 is close to the upper value obtained for structured soil, probably because the holding test was initialized right after the soil yielded.

In the case of V1P6 SHT test, the identification concerned  $R_p$ ,  $\kappa$  and  $k$  while  $\lambda$  was assigned as the average value evaluated for the structured soil equal to 0.60. Despite the relatively inaccurate NN-prediction revealed by the model response (Figure 9.2), parameters were quickly corrected within 4 iterations. The inaccurate prediction was most probably occurred because the soil compressibility for an NN input was mapped through the initial part of the expansion curve (Figure 9.2(a)).

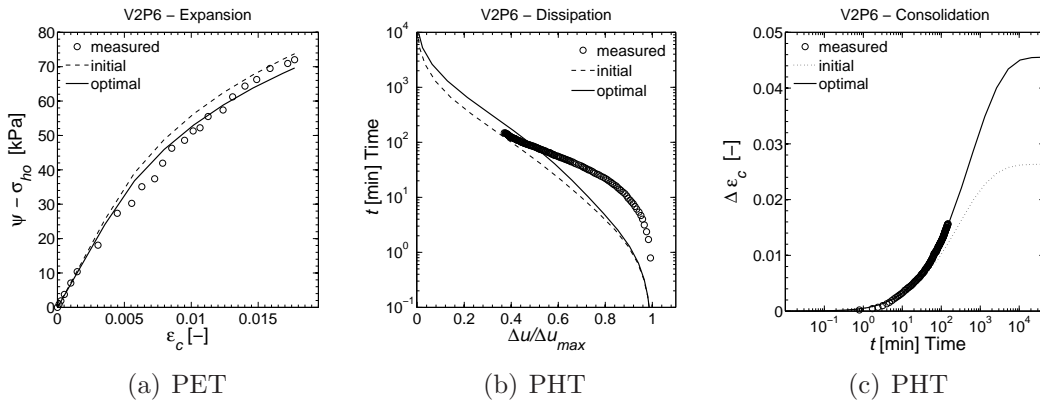


Figure 9.1: Fucino clay test V2P6: simultaneous fitting of (a) expansion test and (b-c) pressure holding test measurements.

Table 9.3: Fucino clay properties derived by means of the numerical parameter identification.

Test	Depth $z$ (m)	Parameter assignment: initially specified - User or <i>Neural Network</i> ; optimized - <b>MGN</b>						
		$e_o$ (-)	$k$ $\cdot 10^{-10}$ (m/s)	$M$ (-)	$R_p$ (-)	$c_u/\sigma'_{vo}$ (-)	$\kappa$ (-)	$\lambda$ (-)
V1P5	9.10				1.29		0.0130	
		2.40	8.42		<b>1.39</b>	<b>0.488</b>	<b>0.0177</b>	0.60
V1P6	10.55		2.69		1.29		0.0140	
		2.70	<b>8.42</b>		<b>1.40</b>	<b>0.459</b>	<b>0.0189</b>	0.60
V2P6	9.50		13.7	1.2	1.47		0.0225	0.49
		2.30	<b>16.0</b>		<b>1.40</b>	<b>0.487</b>	<b>0.0238</b>	<b>0.86</b>
V2P7	11.00				1.27		0.0159	
		2.60	16.0		<b>1.41</b>	<b>0.486</b>	<b>0.0217</b>	0.60
V2P8	14.00				1.30		0.0167	
		2.30	16.0		<b>1.58</b>	<b>0.519</b>	<b>0.0252</b>	0.60

The analysis of three remaining PETs, namely V1P5, V2P7 and V1P8, aimed to identify  $R_p$  and  $\kappa$ . The other parameters were assumed as optimally identified. The coefficients of soil permeability were assigned according to the values identified for V1P6 and V2P6, and corresponding to the boreholes. Note that for each NN-identified vector of parameters, an initial model response almost overlaps with experimental data as shown in Figure 9.3. Hence, the MGN minimization converged within 3 iterations.

### 9.1.3 Analysis of obtained results

The quantitative analysis of the numerically predicted and optimized parameters reveals a correct agreement between conventionally obtained parameters as presented in Table 9.2. Generally, the optimized values of permeability char-

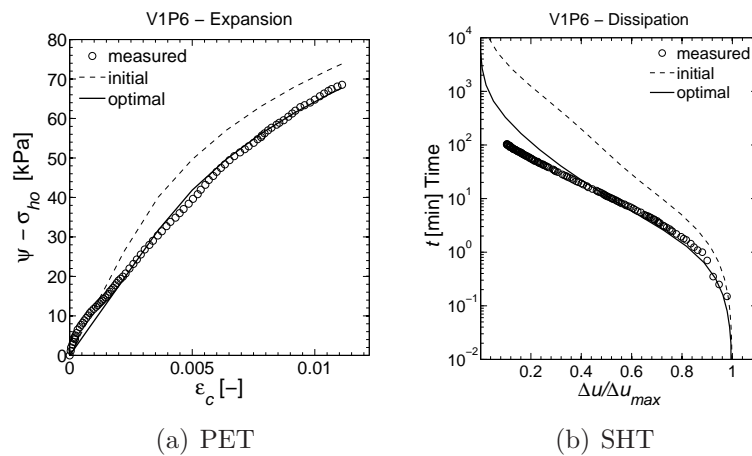


Figure 9.2: Fucino clay test V1P6: simultaneous fitting of (a) expansion test, and (b) strain holding test measurements.

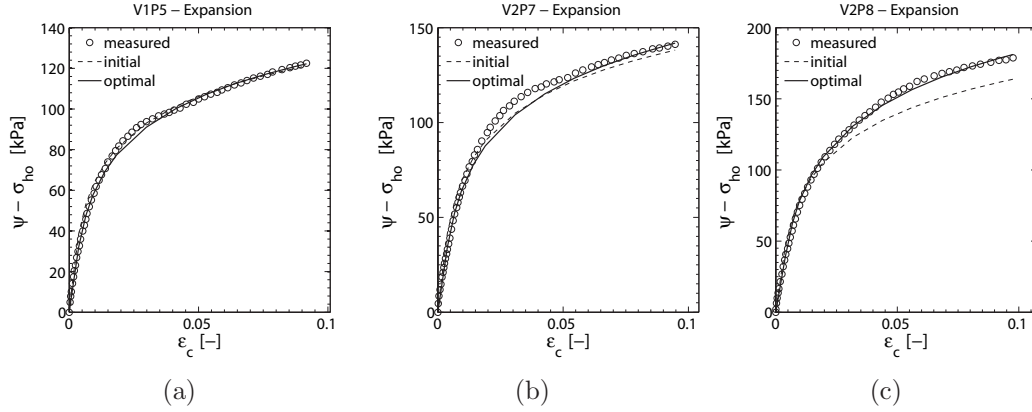


Figure 9.3: Fucino clay expansion tests fitting: (a) V1P5, (b) V2P7, (c) V2P8.

acteristics for both the SHT and the PHT, are similar to the values obtained numerically by Fioravante et al. (1994). Their parametric study shows values in the range of  $1 \div 3 \cdot 10^{-10}$  m/s for V2P6 and  $k = 10^{-9}$  m/s for V1P6. The optimized values of  $\kappa$  are generally smaller than those obtained for cemented samples by means of oedometer tests. This could be attributed to the destruction of a natural soil structure due to sampling. As discussed before, the latter may have an influence on underestimation of OCR through oedometer tests. Consequently, the optimized values of  $R_p$  may tend to be higher than those evaluated through laboratory tests. However, the comparative analysis may be less reliable because the estimates of  $R_p$  for laboratory tests were obtained through the correlation presented in Equation (8.4). The numerically optimized values of  $R_p$  may also sustain the geometry effect since all of the analyzes were carried out with the simplified numerical mesh representing a unit of pressuremeter membrane. As reported by Yu et al. (2005), the effect of geometry in lightly-consolidated soil may have an influence on the derived strength parameters resulting in the overestimation of  $c_u$  and, consequently,  $R_p$ . The geometry effect could be thus overcome by linking the MGN algorithm with a large scale model of the pressuremeter test. On the other hand, the numerically evaluated values of  $c_u/\sigma'_{vo}$  ratio show a close agreement with the values obtained through FVT. It is also considerable that the values of the undrained shear ratio obtained by Burghignoli et al. (1991) are higher than those derived numerically, which can be attributed to the assumed undrained conditions in their work.

The evaluated values of  $c_u/\sigma'_{vo}$  ratio can be also diminished owing to the strain rate effect (see Section 6.2.4, Equation (6.33)). In the case of pressuremeter test, the correction can be typically assumed around  $-10\%$ . Such a correction is however an approximative approach since it omits parameter coupling which has been considered in the simultaneous curve fitting. The use of a model that could account for the strain rate effect should be considered at the level of numerical identification.

#### 9.1.4 Summary

The effectiveness of the method has been confirmed for real experimental measurements. By applying the neural network parameter prediction for the real SBPT data, the trial-and-error guessing was avoided during the calibration of the multi-parameter constitutive model. In each identification run, the gradient-based algorithm robustly converged within 3-4 iterations only. The numerically evaluated parameters of the Fucino clay revealed considerable agreement with characteristics derived conventionally from laboratory and field tests. This confirms the correctness of the double-level parameter identification for the complex boundary value problem. Hence, such enhanced computational identification seems to be reasonable and suitable for solving inverse problems linking advanced soil models and hydro-mechanical feedback.



## 9.2 Parameter estimation using piezocone test

The following section explores the applicability of developed NN inverse models to profiling soil parameters from piezocone data. Efficiency of NN predictions is verified using soil properties measured through various laboratory and field tests. Profiling constitutive parameters for the MCC, as well as other variables is demonstrated for a number of characterization clay sites: (i) Bäckebol, (ii) Skå-Edeby, (iii) Port Huron, (iv) Amherst and (v) Bothkennar. Depending on the availability and reliability of complementary input data, different configurations of NN input vectors are analyzed for specific testing sites.

### 9.2.1 Estimation of OCR for a worldwide database

The first analysis demonstrates an application of the developed NNs to a global database of piezocone measurements in normally- and lightly overconsolidated clayey soils and corresponding OCR derived from oedometric tests. The database used in this study is extracted from a worldwide database collected by Chen and Mayne (1994) (see Appendix G.1). The data points were carefully selected so that they correspond to solution limits obtained for the generated training database.

Figure 9.4 presents a comparison of predicted values of OCR by means of two neural networks for which the input components correspond to the entry variables of two empirical approaches. The input values of permeability coefficients were approximatively assigned according to the soil type. As regards the empirical coefficients, the typical values for the first-order estimates were assumed, i.e.  $k_{\sigma t} = 0.30$  and  $k_{\sigma e} = 0.50$  (cf. Table 6.3). The results show that NNs exhibit smaller dispersal than empirical formulas. However, it can be noticed that NN(QK|6 – 6|O) presents inefficiency of predictions for OCR larger than 3. In general, the correlations by NNs achieve superior statistical features compared to empirical estimates (see Table 9.4). While empirical first-order predictions generally underestimate OCR, the neural networks reveal a tendency to overestimate OCR values. The overestimation can be due to neglecting viscous effects in the FE model formulation but a part of it can also be attributed to disturbance effects which affect results of laboratory tests.

The following analysis compare another two empirical methods with the corresponding NN models (Figure 9.5). These four models involve the  $M$  parameter as complementary input information. In the case of the formula by Mayne and Kulhawy (1982) and NN(QBMH|5 – 5|O), the input additionally requires an estimation of parameter  $K_o$ . For the purpose of this study,  $K_o$  were collected from historic data for particular characterization sites or they were estimated using the method by Sully and Campanella (1991) (see Table G.1). The results presented in Figure 9.5(a) show a fair correlation of experimental data by the NN in contrast to the formula by Mayne (1991) which, in general, strongly underestimates OCR values. The second considered network presents a similar performance to the corresponding empirical model. Both NNs exhibit relatively small magnitudes of relative errors measured in terms of the reference

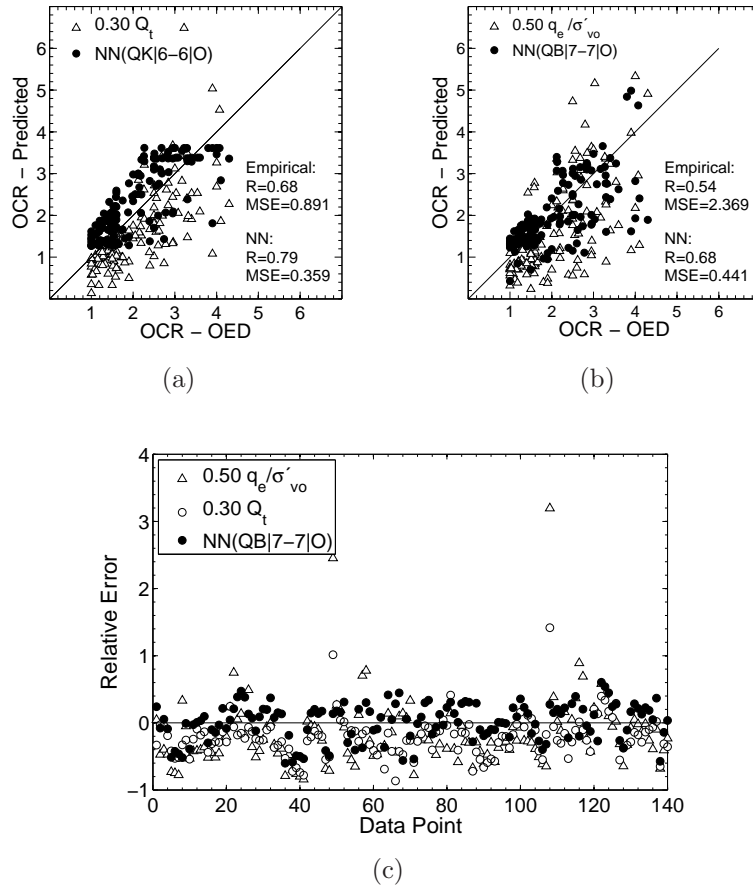


Figure 9.4: Comparison of predicted OCR for 135 piezocone data points using neural networks and the empirical formulas: (a) Equation (6.45), (b) Equation (6.46), (c) a comparison of predictions in terms of relative errors.

OCR values (see summary of statistical features in Table 9.4).

An important contribution of  $K_o$  to the quality of NN predictions was next investigated with two other NN models, as shown in Figure 9.6. An analysis of the results shows that both NN models provide a number of underestimated predictions for OCR between 2 and 3. It can be attributed to operational inefficiency of these models for real data or simply, it is a derivative of misinterpreted  $K_o$  values.

## 9.2.2 Parameter estimation for Bäckebol site, Sweden

Bäckebol testing site area is situated on the island of Hisingen in the northern part of the city of Gothenburg. The site was extensively explored by the Swedish Geotechnical Institute (SGI) in terms of the behavior of long driven piles (Larsson and Mulabdić, 1991). The clay layers in this area are about 40m deep and reveal around 60% of clay content. The upper layer consists of one-meter dry crust followed by overconsolidated gray clay down to 10m with

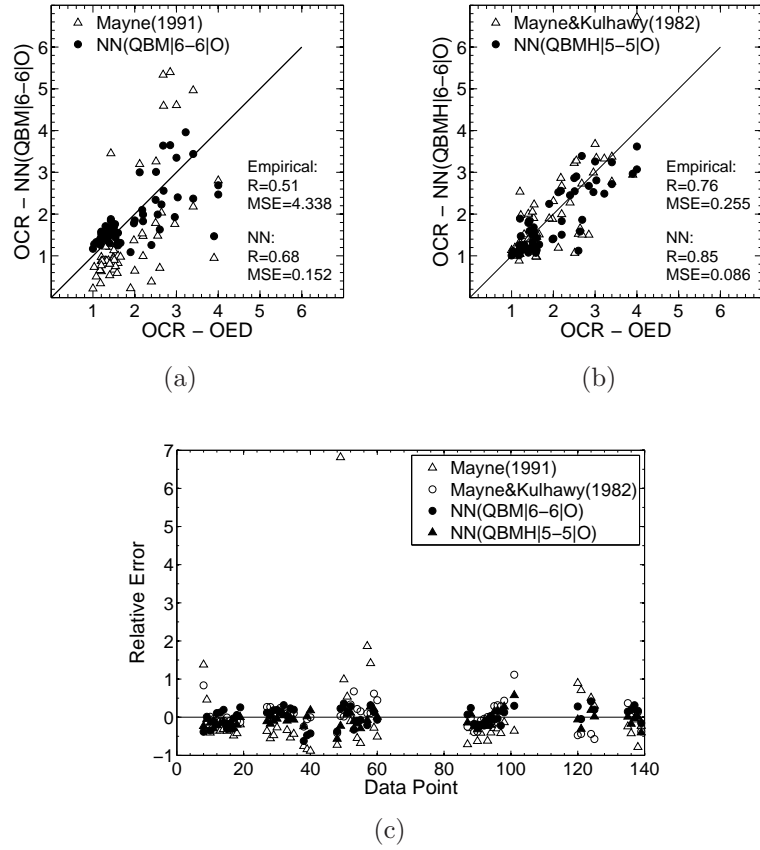
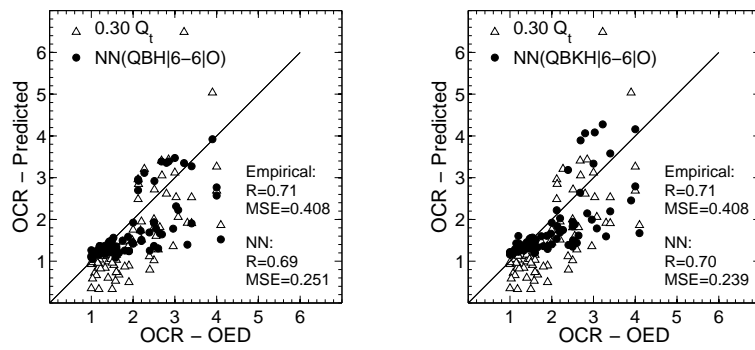


Figure 9.5: Comparison of predicted OCR for 58 piezocone data points using neural networks and empirical formulas: (a) Equation (6.48) (Mayne, 1991), (b) Equation (8.1) (Mayne and Kulhawvy, 1982), (c) comparison of predictions in terms of relative error.

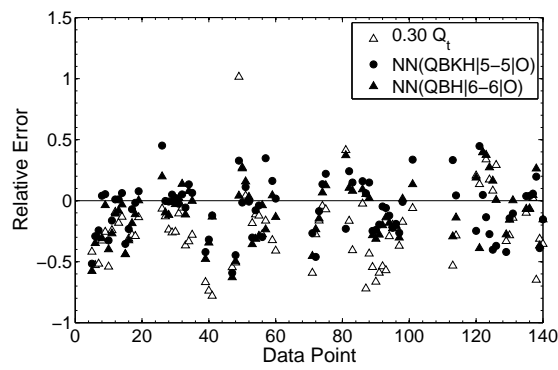
Table 9.4: Summary of OCR predictions from piezocone data for a worldwide database.

Correlating Model	Number of samples	$R$	MSE	$ARE_m$ (%)	$ARE_{sd}$ (%)
$0.3 \cdot Q_t$	141	0.68	0.891	29.6	22.1
$0.5 \cdot q_e / \sigma'_{vo}$	141	0.54	2.369	38.4	37.2
NN(QK 6 - 6 O)	141	0.79	0.359	26.5	16.2
NN(QB 7 - 7 O)	141	0.68	0.441	22.6	15.5
Mayne (1991)	58	0.51	4.338	60.3	89.4
Mayne and Kulhawvy (1982)	58	0.76	0.255	23.4	22.0
NN(QBM 6 - 6 O)	58	0.68	0.152	19.9	12.8
NN(QBMH 5 - 5 O)	58	0.85	0.086	17.0	12.4
$0.3 \cdot Q_t$	82	0.71	0.408	31.2	20.6
NN(QBH 6 - 6 O)	82	0.69	0.251	19.7	14.6
NN(QBKH 6 - 6 O)	82	0.70	0.239	18.3	14.6



(a)

(b)



(c)

Figure 9.6: Comparison of predicted OCR for 82 piezocone data points using neural networks and the empirical formula: (a-b) Equation (6.45), (c) comparison of predictions in terms of relative error.

$OCR = 1.2 \div 2.5$ . The preconsolidation pressure was determined from CRS tests and full-scale field tests. The overconsolidated layer is then followed by normally consolidated clay. The ground water level was about 0.4m below the soil surface.

The piezocone testing programme was executed down to 20m depth. Typical piezocone measurements collected from Larsson and Mulabdić (1991) were firstly smoothed and then normalized and are presented in Figure G.1 (Appendix G.2) with corresponding overburden stress profile. In general, the CPTU results are uniform and smoothing concerned only slight irregularities due to presence of shells.

The coefficient of earth pressure at rest was estimated from laboratory and field tests such as Modified Glötzl-cell and SBPT.

The investigation of undrained shear strength involved field tests FVT and DMT, and laboratory tests including TXC and DSS tests. The average friction angle derived from laboratory tests was reported as  $30^\circ$ . The soil sensitivity was measured around 17. The tests revealed a sudden increase of  $c_u$  about 10m level with a similar jump observed in the piezocone measurements.

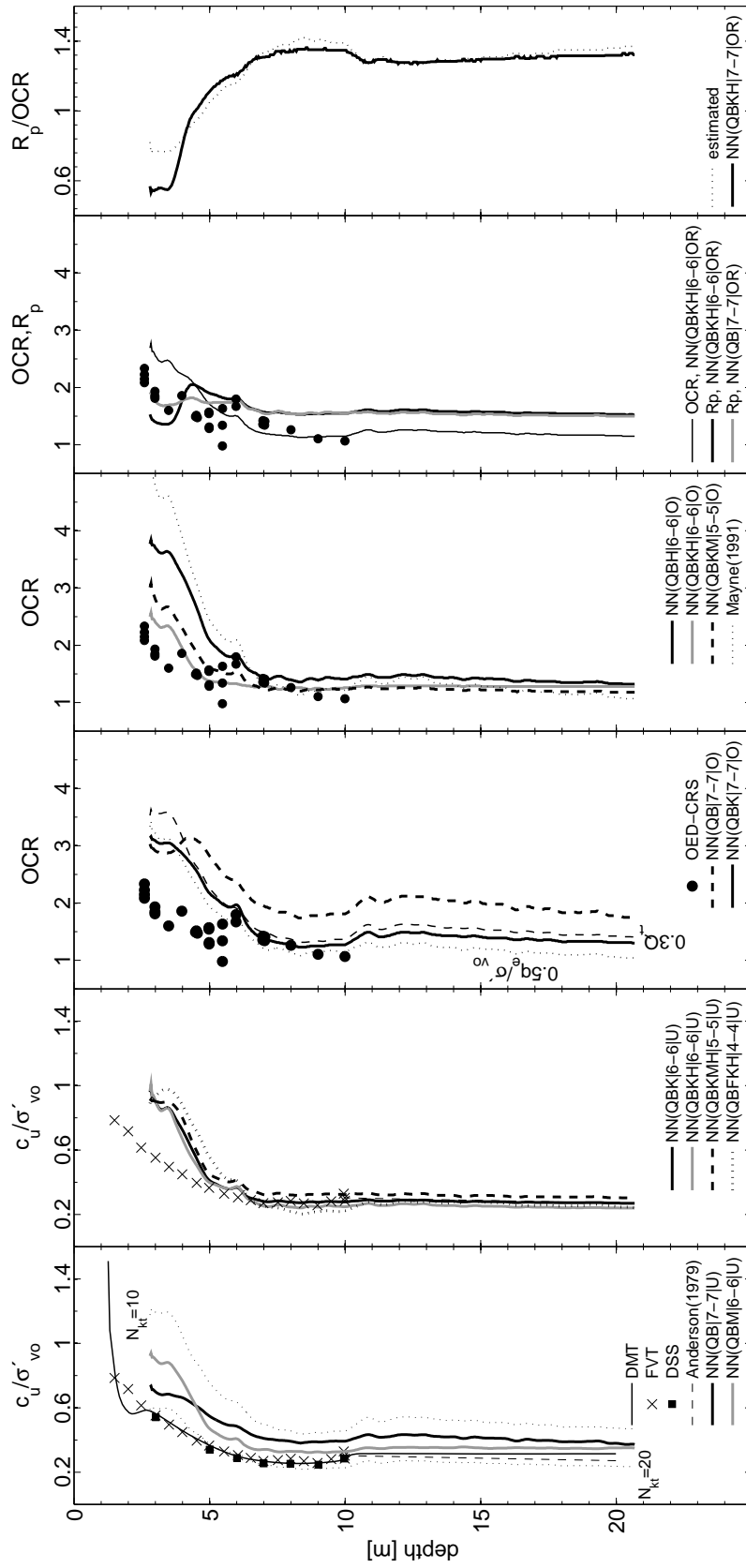


Figure 9.7: Predictions of  $c_u$ , OCR and  $R_p$  for Bäckebo site from laboratory and field tests (based on Larsson and Mulabdić, 1991) and CPTU test using empirical formulas and neural network predictors.

Figure 9.7 shows a number of NN predictions for  $c_u$ , OCR and  $R_p$ . In this analysis, supplementary input data  $M$  and  $k$  were assigned as constants and equal to 1.2 and  $10^{-9}$  m/s, respectively. A similar profile of  $c_u$  is observed below the level of 5m for all the applied networks. It can be noticed that the predictions supported with  $K_o$  and  $k$  data give a very similar profile to the results obtained by FVT and Anderson(1979). On the other hand, except for NN(QB|7 – 7|U), the NN predictions accordingly provide higher  $c_u$  than FVT or DSS from 2.5 to 5m. This difference could be attributed to the shear modes of FVT and DSS which may sometimes result in a small gradient of  $c_u/\sigma'_{vo}$  with the increasing overconsolidation ratio (cf. Jamiolkowski et al., 1985). However, the obtained lower  $c_u/\sigma'_{vo}$  profiles for FVT and DSS correspond to lower values of OCR measured by OED<sup>1</sup>. At the considered depth interval, the piezocone data predicts higher OCR than obtained in laboratory, as observed accordingly for two empirical approaches and predictions by NN(QBK|7 – 7|O). However, by supplementing the input content of the latter model, NN(QBKH|6 – 6|O) and NN(QBKM|5 – 5|O) bring closer the NN predictions to the laboratory measurements. On the other hand, the considered empirical and NN models yield similar profiles for OCR below the level of 5m with the exception of NN(QB|7 – 7|O) which considerably overestimates expected values. Following the good performance of NN(QBKH|6 – 6|O) for the Bäckebol site, the same input configuration was used to predict  $R_p$  values. As was expected for OCR < 2, the network correctly predicts the  $R_p$  values to be higher by around 30 ÷ 40% than OCR (cf. Figure 8.4). The obtained  $R_p$  profile was also controlled by NN(QB|6 – 6|OR) which provides very similar results. Furthermore the obtained profile of  $R_p$ /OCR is akin to the profile evaluated through Equation (8.4) using the values of OCR and  $K_o$  derived from empirical correlations; the correlation coefficients for Equation (6.46) and (6.53) were previously calibrated for the considered testing site.

The next analysis deals with the prediction of  $K_o$  by means of three various well-operating NN models. The obtained results are compared in Figure 9.8 with  $K_o$  profiles evaluated from other *in situ* tests and the first-order prediction by  $0.1Q_t$ . A similar shape of  $K_o$  profile can be observed for all piezocone predictions. In general, the NN predictions correspond well to the profile approximated by other tests. The empirical approach gives underestimated predictions with regards to the NN predictions. Interestingly, low values of  $F_r$  which are related to sensitive soil and which were not encompassed in the training database, do not significantly affect  $K_o$  predictions, which signifies greater importance of  $M$  for these networks (cf. Table 8.10).

An identification of the parameter  $M$  was carried out using three NNs which require  $K_o$  in the input vector. Figure 9.8 shows that two different networks with  $Q_t$ ,  $B_q$  and  $K_o$  as inputs track the average  $M$  derived from laboratory tests. Severe result inconsistencies obtained by these networks can, however, be noticed above the depth of 4.5m. It can possibly be attributed to relatively high values of  $Q_t$  (> 13) which were sparsely represented in the training popu-

---

<sup>1</sup> $c_u/\sigma'_{vo}$  and OCR can be related by the well-known relationship  $c_u/\sigma'_{vo} = S(\text{OCR})^m$ , where  $S$  is the undrained strength ratio for normally consolidated soil (OCR=1).

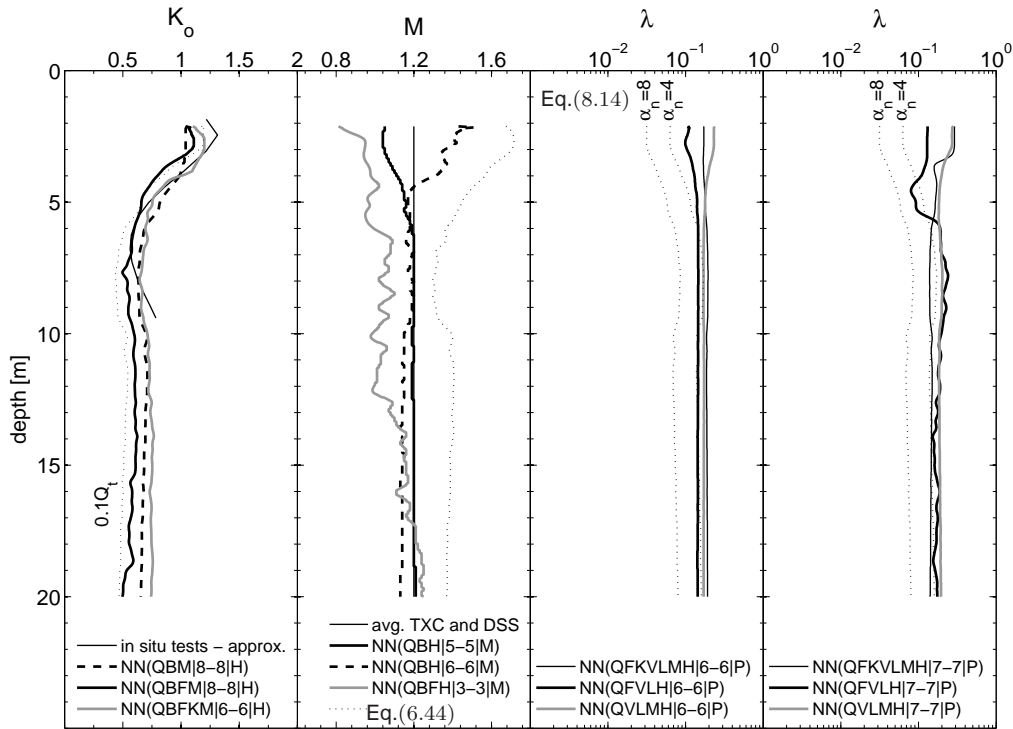


Figure 9.8: Predictions of  $K_o$ ,  $M$  and  $\lambda$  for Bäckebo site from laboratory tests and field tests using empirical formulas and neural network predictors.

lation of measurements for OCR from 1 to 3 (cf. Figure 8.19). Contrary to  $K_o$  predictions with  $F_r$  as a supplementary data, low values of  $F_r$  which were not presented to the network during training, lead to underestimated  $M$ . Finally, the empirical method given in Equation (6.44) give significantly overestimated predictions for the considered testing site.

The last two charts presented in Figure 9.8 show an attempt to predict the parameter  $\lambda$  from piezocone data. Since no reference value of  $\lambda$  derived from laboratory tests was retrieved for the Bäckebo site, the analysis investigates the consistency of results obtained for different input and NN topology configurations. In this case, predictions of the richest network regarding the amount of input information can be assumed as the reference ones. For the purpose of this analysis, the parameter  $\Lambda$  which is required for a reliable estimation of  $\lambda$  (cf. Section 8.2.5.5) was assumed as 0.75, whereas  $e_o$  was assumed equal to 2.0 along the test profile. It can be noticed that, irrespectively to provided input data, all the considered networks provide very similar  $\lambda$  profile below 4m. This profile corresponds to the results obtained through Equation (8.14) assuming the empirical coefficient  $\alpha_n = 4$ . Some differences between NN predictions and empirical estimates can, however, be observed above the depth of 4m, where NNs generally provide an opposite trend to the empirical equation. At these depths, considerable differences can also be noticed for the NNs with the same input vector. Similarly to predictions of  $M$ , this uncertainty can be attributed to relatively high values of  $Q_t$  ( $> 13$ ) which were sparsely represented in the training population of measurements.



### 9.2.3 Parameter estimation for Skå-Edeby site, Sweden

The Skå-Edeby testing area is located on Svartsjölandet lake island near Stockholm. The field was used by SGI mainly for observation of long-term settlements and a large number of *in situ* investigations (Larsson and Mulabdić, 1991). In this area, the soft clay layer of 10-15m is deposited on rock or till. The subsoil consists of the upper layer of overconsolidated, post-glacial organic clay with OCR from about 4 to 1.3 down to 4m, and underlying lightly overconsolidated varved glacial clay. The clay content between 2.5 and 10m is about 70%. The free ground water level was observed to vary seasonally from the ground surface to 1.0m below, and during the piezocone test was found as 0.8m.

The overconsolidation ratio for the layer between 4 and 10m is about 1.2, and increases to 1.3 at the level of 12m.

The undrained shear strength profile was obtained by means of testing programme including FVTs. The soil sensitivity was measured and it equals about 15. The coefficient of earth pressure was obtained through earth pressure cells. The piezocone testing programme was executed down to the firm bottom, at the depth of about 11m. Typical piezocone measurements collected from Larsson and Mulabdić (1991) were firstly smoothed and then normalized and are presented in Figure G.2 (Appendix G.2) with a corresponding overburden stress profile.

In the following analysis, the application of NNs for profiling the Skå-Edeby testing site is restricted to the piezocone data below 2.0m. High  $Q_t$  data observed above this depth were not represented in the training dataset and their interpretation could be erroneous.

The interpretation of  $c_u$  from piezocone data was investigated with four different NN models, as shown in Figure 9.9. The  $K_o$  values appearing in the inputs of two networks were interpreted from piezocone data for which empirical coefficient  $k_K = 0.11$  correlates well  $Q_t$  and measurements derived from earth pressure cells (Figure G.2). The coefficient of permeability was assumed to be equal  $10^{-9}$ m/s. Similar  $c_u$  profiles were obtained for two networks including  $k$  in the input. These profiles correspond to the profile obtained with FVT. Two other NN models predict higher values of  $c_u$  than the previous ones. It can particularly be noticed below 4.8m where high values of  $Q_t$  and  $B_q$  were recorded at the same time for lightly consolidated soil. Such combination of measurements which characterize sensitive soils exhibiting high  $I_r$  where not represented in the training population. Owing to relative importance of  $k$  on the NN output, the enforced undrained conditions for NN(QBK|6 – 6|U) and NN(QBKH|6 – 6|U) reduced predicted  $c_u/\sigma'_{vo}$ .

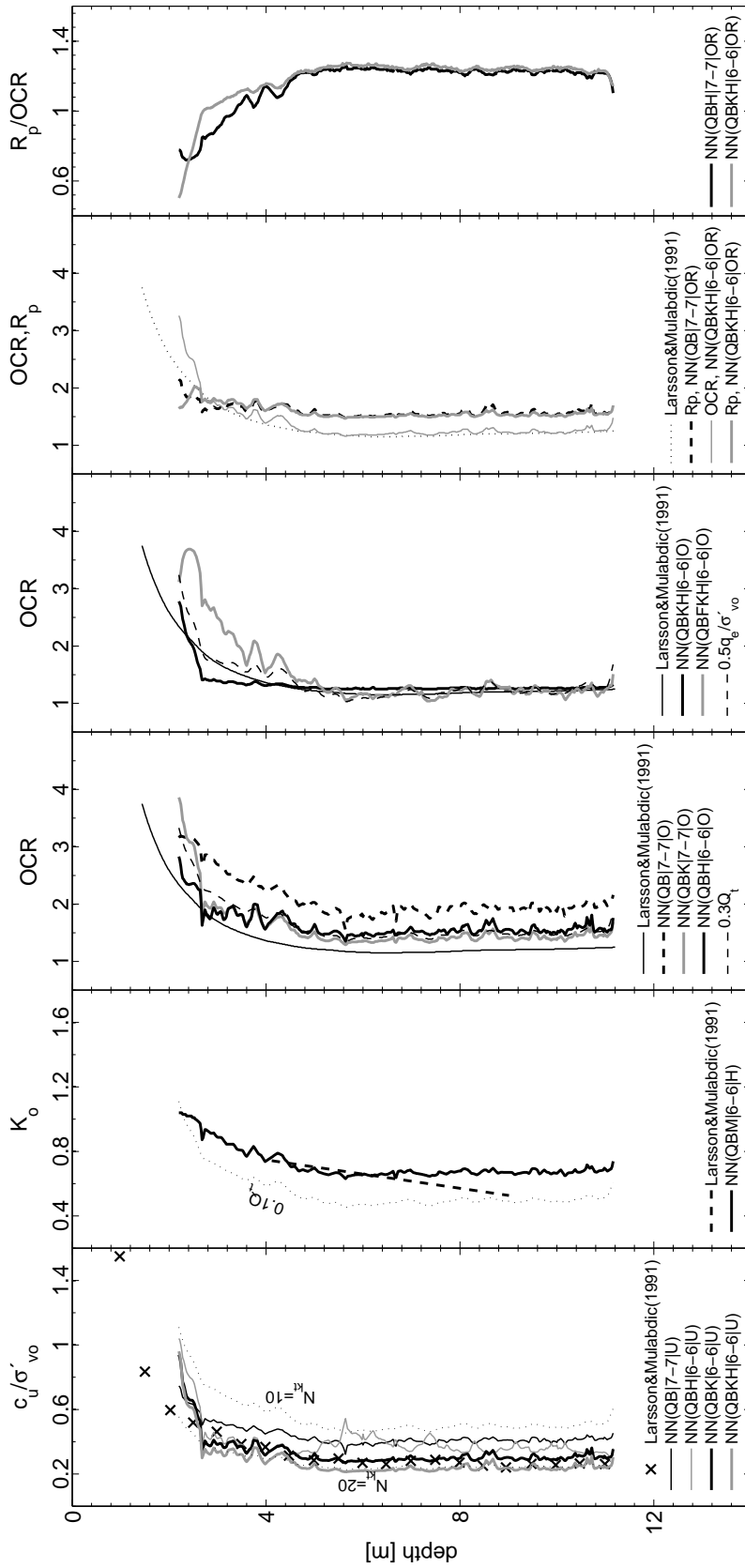


Figure 9.9: Predictions of  $c_u$ ,  $K_o$ , OCR and  $R_p$  for Skå-Edeby site from field tests using empirical formulas and neural network predictors.

Following the same reasoning, predictions of OCR without  $k$  in input generally exhibit higher values than the estimates of NNs which include this information. As shown in Figure 9.9, NN(QB|7 – 7|O) overestimates OCR, whereas NN(QBK|7 – 7|O) and NN(QBH|6 – 6|O) produce the profiles which are similar to the empirical  $0.3Q_t$ . The OCR trend reported by Larsson and Mulabdić (1991) is reproduced by NN(QBKH|6 – 6|O) and the empirical  $0.5q_e/\sigma'_{vo}$ . Low values of  $F_r$  which are characteristic to sensitive clay were next used to check the importance of this factor on NN predictions. Despite the fact that low  $F_r$  values were not represented in training population, NN(QBFKH|6 – 6|O) gives results which resemble the profile derived from  $0.5q_e/\sigma'_{vo}$ . Significant differences between these predictions can, however, be observed above the depth of 4.0m. Reliable results of QBKH input configuration prompted the author to apply NN(QBKH|6 – 6|OR) to the prediction of  $R_p$ . The obtained results reveal an almost constant profile of  $R_p$  for considered depths and similar results were also obtained with NN(QB|7 – 7|OR). As expected for low OCR, the network correctly predicts the  $R_p$  values higher by around 24% than OCR (cf. Figure 8.4). The obtained  $R_p$ /OCR profile was also controlled by NN(QBH|7 – 7|OR) which provides very similar results from about 3.6m down to the bottom of the profile.

An attempt to profiling  $K_o$  was carried out assuming  $M = 1.2$ . Figure 9.9 shows that NN(QBM|6 – 6|H) gives a similar prediction to the upper part of the profile reported by Larsson and Mulabdić (1991). First-order approximation with  $k_K = 0.10$  provides a profile which is shifted by about 0.2 with respect to the NN predictions.

#### 9.2.4 Parameter estimation for Port Huron site, USA

The testing area is located in Port Huron, Michigan. The site subsoil consists of glacial and lacustrine sediment formed during late Pleistocene (Chen and Mayne, 1994). Deep deposits from 3 to 30m below the ground surface consist of soft gray silty clays to clayey silts of low to moderate plasticity. The groundwater level was reported to be at 1.5 to 2m below the soil surface. A laboratory program executed in 1985 by a commercial laboratory consisted of one-dimensional consolidation tests on soil specimens obtained from split-barrel and thin-walled tube samples. The second site characterization took place in 1992 and included carrying out consolidation and CIUC tests by a commercial laboratory on representative specimens obtained from thin-walled tube sampler. The average value of  $M$  was reported as equal to 1.11 ( $\phi'_c = 28^\circ$ ). The testing program also included a number of CPTU and DMT soundings (for details see Chen and Mayne, 1994). The results of laboratory and field test, as well as stress history stratigraphy of site characterization are presented in parallel with piezocone data interpretations in Figure 9.10 and 9.11.

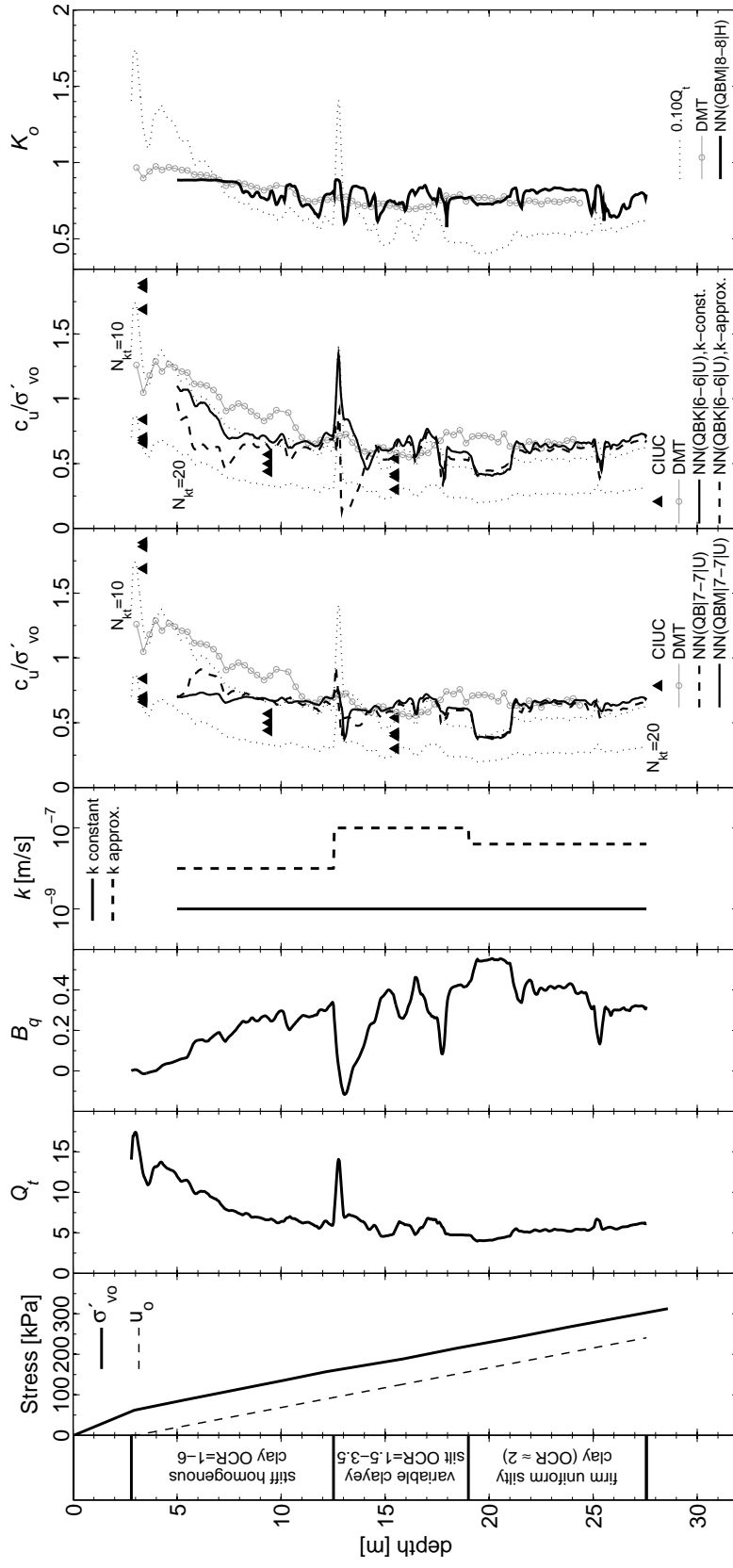


Figure 9.10: Stress soil profile, normalized smoothed results from piezocone tests at Port Huron site (based Chen and Mayne, 1994), and predictions of normalized undrained shear strength and coefficient  $K_o$ .

The prediction of soil parameters with the use of NNs were restricted to piezocone results measured from 5m below the ground surface in order to avoid uncertainty related to high  $Q_t$  values which were not densely represented in the training population. Moreover, predictions for a thin sand layer around 13m can be considered as worthless since the soil presents negative  $B_q$  and very high  $Q_t$  records.

The prediction of the normalized  $c_u$  was carried out based on mapping piezocone data by means of three different NN models, i.e. NN(QB|7 – 7|U), NN(QBM|7 – 7|U) and NN(QBK|7 – 7|U). In the analysis, two different profiles of the permeability coefficient were applied in order to investigate the influence of this factor. The first assumes "undrained" penetration ( $k = 10^{-9}$ m/s), while the second was approximatively assigned according to soil stratigraphy, as shown in Figure 9.10. Both, NN(QB|7 – 7|U) and NN(QBM|7 – 7|U) generate profiles are similar to the trend obtained for  $N_{kt} = 10$  with the exception of the layer between 5 and 6m and the thin sand layer at around 13m. In general, NNs provide higher predictions for  $c_u$  than CIUC measurements. It is difficult to unambiguously judge whether the differences stem from the quality of collected samples or unavoidable errors which can be committed by considered NNs (cf. Table 8.7). Nevertheless, NN predictions are similar to the  $c_u/\sigma'_{vo}$  values derived from DMT measurements and Marchetti's correlation (Marchetti, 1980):

$$c_u/\sigma'_{vo} = 0.22(0.5K_D)^{1.25} \quad (9.1)$$

where  $K_D$  is the horizontal stress index which is calculated based on the first dilatometer reading  $p_o$  ( $K_D = (p_o - u_o)/\sigma'_{vo}$ ).

The analysis of  $k$  factor in the case of NN(QBK|6 – 6|U) revealed no significant influence on  $c_u$  predictions below 14m from the ground surface. Some differences can, however, be observed for the layer between 5 and 9m.

Figure 9.10 also presents  $K_o$  predictions derived from CPTU and DMT. As regards DMT,  $K_o$  values were obtained using the correlation suggested by Lacasse and Lunne (1988):

$$K_o = 0.34K_D^{0.44 \div 0.64} \quad (9.2)$$

where the lower exponent value is associated with highly plastic clays. For the purpose of this analysis, the value 0.50 was adopted.

A comparison of predictions reveals similar profiles obtained through DMT measurements and NN(QBM|8 – 8|H), whereas first-order estimates using  $0.1Q_t$  achieve lower  $K_o$  values.

In the next analysis, three different configurations of input data were considered in the predictions of OCR by NNs. The results presented in Figure 9.11 reveal, in general, similar predictions using various NNs. In the case of an assumed constant, "undrained" permeability coefficient, predictions by NN(QBKM|5 – 5|O) exhibit higher OCR values below the depth of 14m than those predicted with approximated permeability. The latter predictions generally correspond to the results provided by NN(QB|7 – 7|O) and NN(QBM|6 – 6|O). It can be also noticed that below the level of 9.0m general trends generated by NNs are,

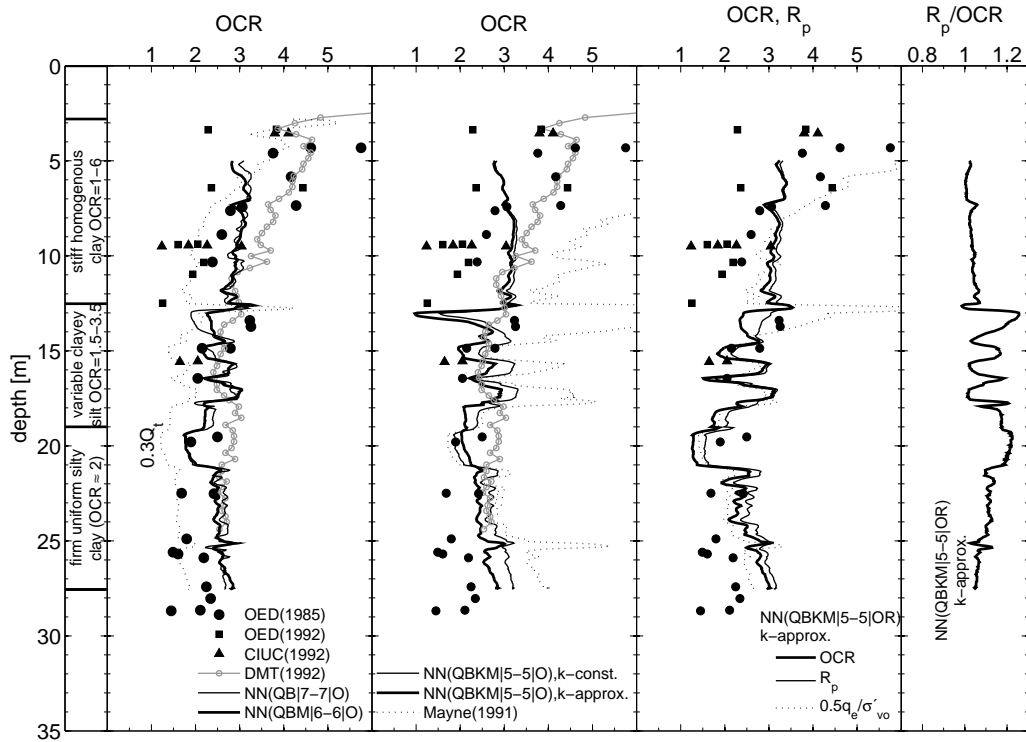


Figure 9.11: Predictions of OCR and  $R_p$  for Port Huron site from laboratory tests (from Chen and Mayne, 1994) and CPTU test using empirical formulas and neural network predictors.

in general, consistent with the profiles obtained through the empirical  $0.5q_e/\sigma'_{vo}$  and DMT.

As expected for upper layers which exhibit OCR around 3, the predicted ratio  $R_p/OCR$  is close to 1.0 (cf. Figure 8.4). In the case of lower layers, the ratio varies between 1.0 and 1.2 according to OCR which changes from 1.5 to 3.0.

The above analysis shows consistent profiling of the variable clay subsoil of the Port Huron site by all the considered NNs. In general, NNs predictions reveal similar parameter profiles to those derived from DMT correlations. Furthermore, NN predictions exhibit considerable consistency with laboratory measurements of  $c_u$  and OCR.

### 9.2.5 Parameter estimation for Amherst site, USA

The deposit of Connecticut Valley Varved Clay (CVVC) is located in Amherst, Massachusetts and is the National Geotechnical Experimentation Site of the USA. DeGroot and Lutenegro (2003) provided an extensive summary of results from field and laboratory testing carried out for this site. CVVC is lacustrine clay for which estimation of unique geotechnical properties is challenging owing to its varved nature with alternating layers of clays and silts. Individual clay layers show a clay fraction content of up to 80%, whereas silt layers have a silt fraction in excess of 80%. Therefore, the deposit exhibits a high anisotropy of material properties such as undrained shear strength which can be less in the

horizontal direction than across the varves. Likewise, because of the silt layers, hydraulic conductivities, derived from laboratory testing for the horizontal direction, vary between  $2 \cdot 10^{-9}$  and  $10^{-8}$  m/s, while across the vertical one they vary from around  $2 \cdot 10^{-10}$  to  $10^{-9}$  m/s.

The uppermost layer, down to about 3.1m, consists of low to plastic varved clay. This is underlain by deep deposits of plastic to highly plastic varved silts and clays, as delineated according to the Unified Soil Classification System (USCS). The field measurements revealed the transition from the upper crust to the soft clays below 5m from the ground surface (cf. DeGroot and Lutenegro, 2003). The average level of ground water table was measured by standpipe piezometers as around 2m below the ground surface.

A number of laboratory instruments such as triaxial cell, direct shear box and oedometer were employed to measure soil properties from high quality samples. The most reliable results for  $c_u$  was derived from DSS and CAUC tests conducted on Laval block samples. Evaluations of  $K_o$  were carried out using instrumented oedometer ring for measurement of lateral stress during IL consolidation. Estimates of preconsolidation pressure  $\sigma'_p$  were obtained based on CRS and IL consolidation tests performed on specimens obtained from a piston sampler (76mm tube) and block samples (Laval and Sherebrooke). The average values of the effective friction angle  $\phi'_c$  were reported for CIUC, CAUC and CK<sub>o</sub>UC were equal to 25°, 22° and 21°, respectively.

The field testing programme included the field vane, dilatometer and piezocone tests. Interpreted results will be provided in subsequent charts. After the source paper, the presented DMT results are correlated with clay properties through original formulas suggested by Marchetti (1980). As regards CPTU measurements, DeGroot and Lutenegro (2003) reported the average factor  $N_{kt}$  back-calculated based on DSS, CAUC and FVT tests were reported respectively equal to  $N_{kt}^{DSS} = 23$ ,  $N_{kt}^{CAUC} = 14$  and  $N_{kt}^{FVT} = 16$ . The authors also revealed a significant variability of  $k_{\sigma t}$  used in profiling OCR from  $Q_t$  data. The reported values vary between 0.25 and 0.40 with the average value equal to 0.30.

For the purpose of this study, typical piezocone measurements were firstly smoothed and then normalized. The results are presented in Figure G.3 (Appendix G.2) with corresponding overburden stress and  $K_o$  profiles. It can be noticed that typical nature of the varved clay is manifested in significant fluctuations of  $B_q$  below 5m from the ground surface.

Estimation of  $c_u$  from piezocone data by means of NNs was carried out for five different NN models, as shown in Figure 9.12. The following complementary input data were used in the analysis:

- $k$  according to the profile approximated from the horizontal coefficient of permeability evaluated from SBPT and laboratory testing (see Figure G.3),
- $M$  as constant value taken as 0.92 ( $\phi' = 22.5^\circ$ ),
- $K_o$  according to the profile estimated from laboratory testing.

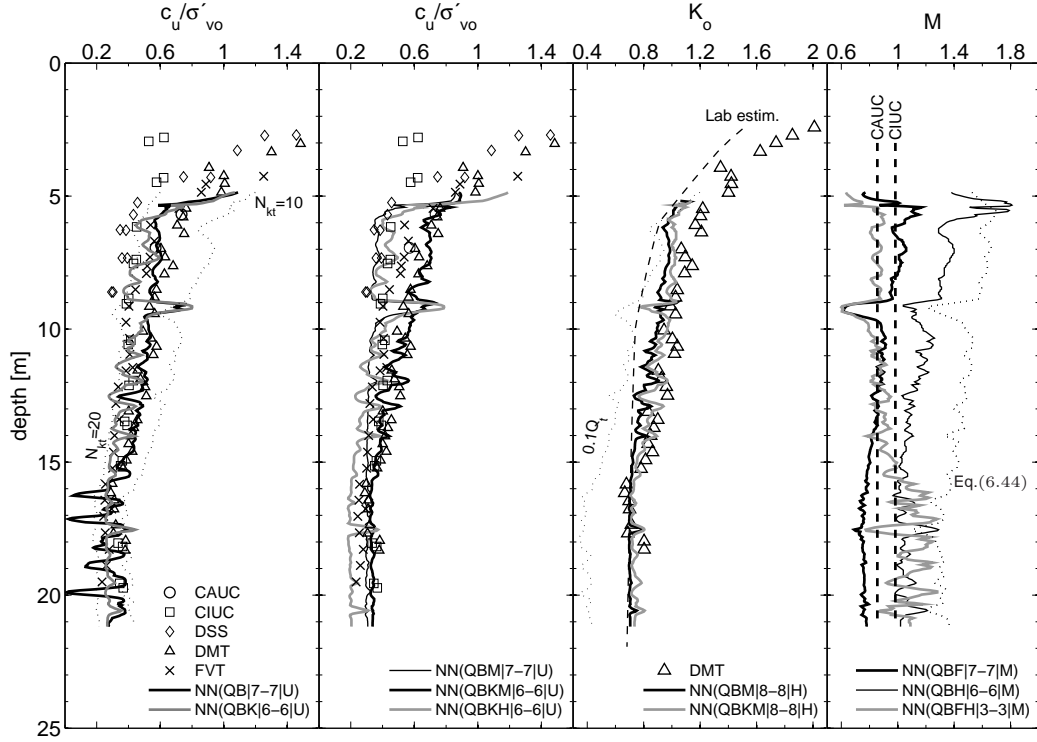


Figure 9.12: Predictions of  $c_u$ ,  $K_o$  and  $M$  for Amherst site from laboratory and field tests (from DeGroot and Lutenegeger, 2003), and CPTU test using empirical formulas and neural network predictors.

The results produced by NN(QB|7 – 7|U) generally follow the profile obtained for DMT measurements. However, much uncertainty can be expected for predictions between 15 and 20m since the oscillating  $B_q$  sometimes goes beyond magnitudes considered in the training population. Hence, the predictions for  $B_q > 0.7$  result in excessive drops of  $c_u/\sigma'_{vo}$  which can be observed around the depths of 16, 17, 19 and 20m. On the other hand, a smooth response for  $c_u$  in this region can be observed for predictions generated by NN(QBK|6 – 6|U). It can be attributed to  $k$  input contribution which decreases relative importance of  $B_q$  input. Above 15m, NN(QBK|6 – 6|U) generates predictions which are sensitive to  $B_q$  oscillations and generally fall between CIUC and FVT estimates. Further addition of  $K_o$  for NN(QBKH|6 – 6|U) slightly moves the upper part of  $c_u/\sigma'_{vo}$  profile towards DSS estimates, while the lower part seems to be underestimated. Further two tests with the imposed parameter  $M$  show a significant influence of  $k$  on NN predictions above 15m. While NN(QBM|7 – 7|U) follows the trends obtained from DSS, NN(QBKM|6 – 6|U) tracks the results of DMT. Minor differences are observed below 15m as both sets of predictions are similar and track laboratory estimates.

The above analysis showed that, although one of the input components falls out of the training set interval (here  $B_q$ ), meaningful solutions can be obtained thanks to higher relative importance of other input parameters.

Predictions of  $K_o$  were obtained by mapping piezocone data by means of two NN models, i.e. NN(QBM|8 – 8|H) and NN(QBKM|(8 – 8|U). As shown in Fig-



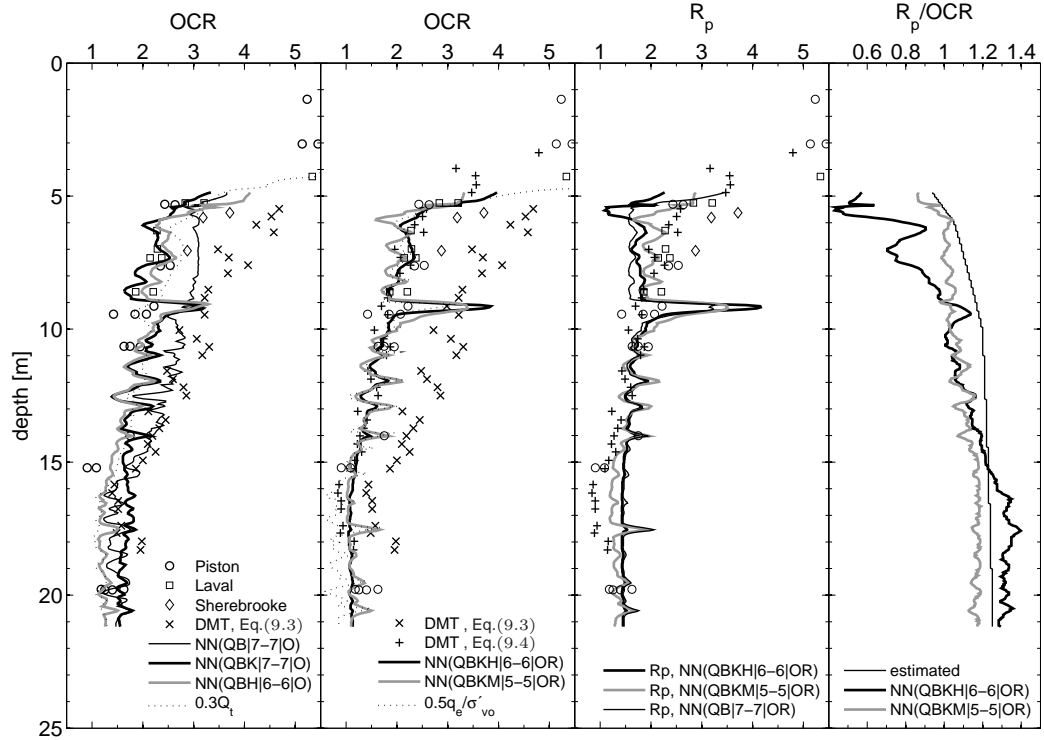


Figure 9.13: Predictions of OCR and  $R_p$  for Amherst site from laboratory tests, DMT test (from DeGroot and Lutenegeger, 2003) and CPTU test using empirical formulas and neural network predictors.

ure 9.12, both sets of NN predictions within the depth interval from 5 to 15m, fall between the profiles derived from laboratory and DMT testing. However, the original Marchetti's relationship may overestimate  $K_o$  (Lacasse and Lunne, 1988; Powell and Uglow, 1988) and Equation 9.2 could apply here. Meaningful consistency of predictions was obtained in the lower part of the  $K_o$  profile with the exception of the first-order predictions by  $0.1Q_t$  which significantly underestimates  $K_o$ .

A comparison of NN results reveals no significant influence of  $k$  on NN predictions. The observation is consistent with the results presented in Figure 8.31(b) where  $k$  does not legibly affect prediction errors.

A conceptual attempt at estimating  $M$  from piezocone data was made using three NN models. The analysis can be considered to have qualitative meaning because low  $F_r$  values which characterize the Amherst clay were not represented in the training population. As shown in 9.12, NN(QBH|6 – 6|M) and empirical Equation (6.44) significantly overestimate predictions in comparison with the average  $M$  derived from CAUC and CIUC tests. The use of supplementary  $F_r$  in the input vector attracts generated results to the triaxial measurements. It can thus be concluded that reliable  $F_r$  measurements can be an important factor which may raise confidence of  $M$  predictions from piezocone data.

Reliefs of stress history parameters were generated by means of a number of NN models. Figure 9.13 presents comparisons of OCR predictions based on OED, DMT and piezocone testing results. It can be noticed that basic input

NN(QB|(7 – 7|O) gives significantly overestimated predictions. Although they are similar to DMT interpretation, the original Marchetti’s formula:

$$\text{OCR} = (0.5K_D)^{1.56} \quad (9.3)$$

may overestimate OCR. Hence, the interpreted data points provided by DeGroot and Lutenegeger (2003) were reanalyzed with the relationship recommended by Lacasse and Lunne (1988):

$$\text{OCR} = 0.225K_D^{1.35 \div 1.67} \quad (9.4)$$

in which the lower empirical exponent applies to plastic clays, whereas the upper one to low plastic materials. The results were reanalyzed assuming the exponent coefficient equal to 1.45 which fits OED data and  $0.5q_e/\sigma'_{vo}$  interpretations. Additional information provided to NN(QBK|7 – 7|O) and NN(QBH|6 – 6|O) bring NN predictions closer to laboratory data. NN(QBH|6 – 6|O) produces a similar relief to the empirical  $0.3Q_t$  with the exception of larger fluctuations observed for NN model. Obviously, the pattern of fluctuations stems from oscillating  $B_q$  measurements and is similar to the relief computed with  $0.5q_e/\sigma'_{vo}$ . Essentially, similar OCR profiles were also obtained with NN(QBKH|6 – 6|OR) and NN(QBKM|5 – 5|OR). It is worth noting that all the considered NN models correctly react on an abrupt drop of  $B_q$  at around 9m producing increased OCRs. Interestingly, no similar peak was measured at this depth by a series of DMT tests, as verified with different  $K_D$  profiles in DeGroot and Lutenegeger (2003).

As regards predictions of  $R_p$ , three employed NN models provide essentially similar profiles with the exception of the layer from 5 to 9m. In this region, it seems that NN(QBKH|6 – 6|OR) underestimates  $R_p$ , which is also reflected in the upper part of the  $R_p/\text{OCR}$  profile produced by the NN. Meaningful consistency in predictions by NN(QBKH|6 – 6|OR) and NN(QBKM|5 – 5|OR) can be observed between 9 and 15m. In general, down to 15m, NNs provide  $R_p/\text{OCR}$  profiles which differ in shape from those estimated based on Equation (8.4)<sup>2</sup>.

The above analysis showed the efficiency of NN profiling in difficult varved subsoil. NN models revealed meaningful sensitivity to the fluctuating  $B_q$  profile which is mirrored in variable stress history profiles.

## 9.2.6 Parameter estimation for Bothkennar site, UK

The Bothkennar Clay is situated between Glasgow and Edinburgh in Scotland. This soft clay deposit was the subject of extensive cooperative site investigations carried out by British Universities. A wide range of results have been reported in the June 1992 issue of Géotechnique and other papers, particularly in the summarizing paper by (Hight and Leroueil, 2003).

It is acknowledged that the Bothkennar Clay is constituted of post-glacial deposits of clays, silts and sands. Further details about the geological setting

---

<sup>2</sup> $R_p/\text{OCR}$  was calculated with the aid of the lab-estimated  $K_o$  profile, constant value of  $M$  and  $K_{onc}$  computed as  $1 - \sin \phi'$ .

can be found in Hight et al. (1992b); Nash et al. (1992a); Hight et al. (2003). The clay beds exhibit relative uniformity which results from the post-glacial history of the region.

The hydrostatic ground water table is located between 0.5 and 1.0m below ground level. Figure G.4 (Appendix G.2) presents the *in situ* vertical total stress, the measured  $e_o$  profile and typical piezocone measurements, both collected from Nash et al. (1992a,b).

Undrained shear strength of the Bothkennar clay was measured directly in laboratory tests, whereas  $c_u$  profiles were derived from a range of field tests including FVT, DMT and SBPT (Hight et al., 2003). Figure 9.15 presents normalized  $c_u$  measured on piston, Laval and Sherbrooke samples in triaxial compression  $CK_oUC$  and in the constant volume DSS test.

Stress history of Bothkennar clay was investigated by means of laboratory and field tests. The laboratory tests included three types of one-dimensional compression tests, i.e. IL, CRS and restricted flow (RF), as described in Nash et al. (1992b). The soil is characterized by low expansibility when swelling back from pre-yield and post-yield states (Hight et al., 2003), i.e. high values of  $\Lambda$  can be expected. Typical values of  $C_c$  recalculated to  $\lambda$  are presented in Figure 9.16. Stress history profiling by field tests involved CPTU and DMT sounding. The OCR profile interpreted from DMT and provided by Hight et al. (2003) is omitted in the following comparative analysis since it essentially resembles the profile obtained from CPTU using Mayne's formula, Equation (6.48).

Low value of  $F_r$  derived from CPTU indicates the sensitive nature of Bothkennar clay. The average sensitivities with FVT were estimated as equal to around 5, whereas laboratory cone fall tests revealed soil sensitivity  $6 \div 8$  between 3 and 7m, and  $8 \div 13$  from 7 to 18m (Hight et al., 2003).

The triaxial tests on reconstituted soil samples revealed the effective friction angle  $\phi'_c = 34^\circ$  (Allman and Atkinson, 1992), which is also the lower bound of the values measured for intact samples for which the values range between  $36^\circ$  and  $45^\circ$ . The constant volume simple shear tests, direct shear box test on intact normally consolidated specimens and ring tests on remoulded soil gave  $\phi'$  respectively around  $34^\circ$ ,  $27^\circ$  and  $30^\circ \div 33^\circ$  (Hight et al., 2003).

As regards parameter profiling by means of NNs, the following complementary information about soil properties was provided to input vectors:

- $k$  according to the profile of radial permeability coefficients at in situ voids ratio evaluated from OED tests on block samples (see Hight et al., 1992b); in the assumed profile,  $k_h$  fluctuates insignificantly from  $9 \cdot 10^{-10}$  to  $2.7 \cdot 10^{-9}$ m/s,
- $M$  as constant value corresponding to lower observed bound for TXC tests, i.e. 1.33 ( $\phi' = 34^\circ$ ),
- $K_o$  according to the profile approximating measurements derived from SBPT and provided in Hight et al. (1992b) (see  $\sigma_{ho}$  in Figure G.1),
- $e_o$  according to the profile approximating laboratory measurements (see Figure G.1),

- $\Lambda$  estimated based on laboratory measurements of  $C_c$  (from Nash et al., 1992b) and SBPT-based estimations of  $\kappa$ ; in the assumed profile,  $\Lambda$  fluctuates insignificantly from 0.93 to 0.97.

A number of various NNs was used to delineate profiles of apparent preconsolidation pressure. The results presented in Figure 9.14 show that all the NNs produce very similar profiles of OCR down from 2.5m. Inconsistencies in predictions above this depth have their source in large  $Q_t$  values rarely represented in the training set. In general, NN predictions fall between the upper bound determined in IL tests and CRS measurements. The NN products are also consistent with the first-order estimates computed with the "effective" cone resistance method and the equation suggested by Mayne (1991). It is worth noting that, although some low  $F_r$  were not encompassed in the training population, NN(QBFKH|6 – 6|O) generates meaningful predictions because relative importance of particular factors is distributed over all the input variables. Meaningful consistency of NN predictions can also be observed for  $R_p$  profiles. It can be noticed that Mayne's formula with  $\sigma'_{vo}$  replaced with  $p'_o$  (cf. Equation (6.48)) gives larger estimates than NNs. The variation of  $R_p$ /OCR obtained with the empirical formula indicates an overestimation of  $R_p$  since this ratio should theoretically be obtained of about 1.2 for soil exhibiting OCR of around 2 (cf. Figure 8.4). Such values were obtained with NN predictors.

Meaningful accuracy of NN models has also been obtained for  $c_u/\sigma'_{vo}$  estimates. Figure 9.14 presents a comparison of NN predictions with various laboratory and field testing results.

Predictions of  $K_o$  were obtained by mapping piezocone data by means of two NN models, i.e. NN(QBM|8 – 8|H) and NN(QBFM|8 – 8|H). A comparison of obtained results with other field testing estimates is presented in Figure 9.16. The chart shows that NN(QBM|8 – 8|H) determines the upper bound for reasonable predictions derived from SBPT (Hight et al., 1992b), DMT measurements correlated with Equation (9.2) applying the exponent coefficient 0.55 suggested by Powell and Uglow (1988) for UK clays, and CPTU data. The empirical profiles of  $K_o$  were derived from two empirical formulas, i.e.  $0.1Q_t$  and the formula suggested for the normalized pore pressure difference (PPSV, Sully and Campanella, 1991). The analysis also shows that  $F_r$  legibly contributes to NN predictions. Its low values which are "unknown" to NN(QBFM|8 – 8|H) lead to an overestimation of  $K_o$ , and so does Marchetti's expression for DMT.

Profiling of parameter  $M$  was carried with three different NNs. Figure 9.16 presents the obtained results recalculated to  $\phi'$  as they are compared with the values derived from shear tests. Similarly to  $K_o$ , low values of  $F_r$  have unfavorable influence on the quality of NN predictions showing importance of this factor. NN(QBFH|3 – 3|H) which includes  $F_r$  in the input provide visibly underestimated  $\phi'$ . Two other NNs generate estimates between the bounds derived from DSS and TXC tests on remoulded specimens. However, it seems that there is much uncertainty in these predictions as differences between the estimates seem to be too high. On the other hand, Equation (6.44) gives a similar profile to NN(QBKH|6 – 6|M).

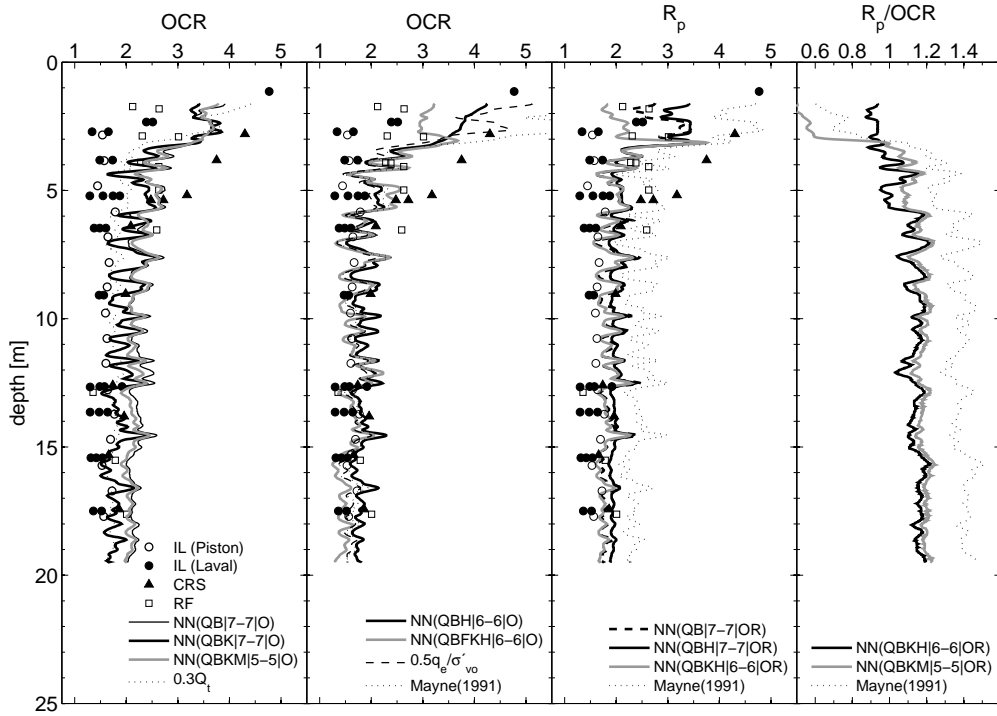


Figure 9.14: Predictions of OCR and  $R_p$  for Bothkennar site from laboratory tests (based on Nash et al., 1992b) and CPTU test using empirical formulas and neural network predictors.

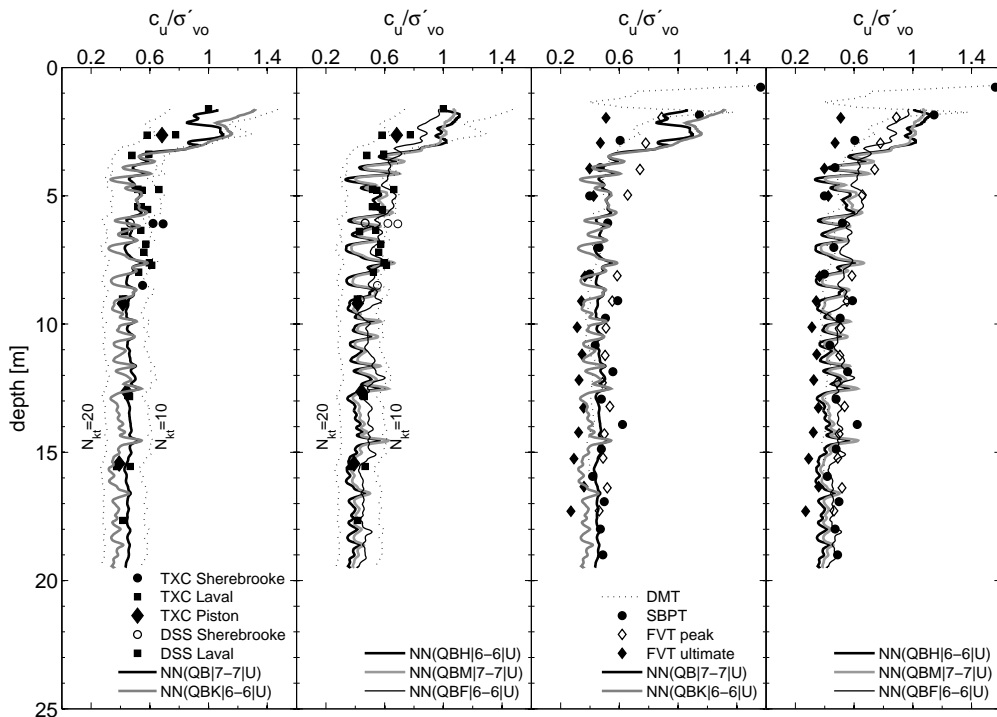


Figure 9.15: Predictions of  $c_u$  for Bothkennar site from CK<sub>o</sub>UC laboratory tests and field tests (based on Hight et al., 1992b), and CPTU test using empirical formulas and neural network predictors.

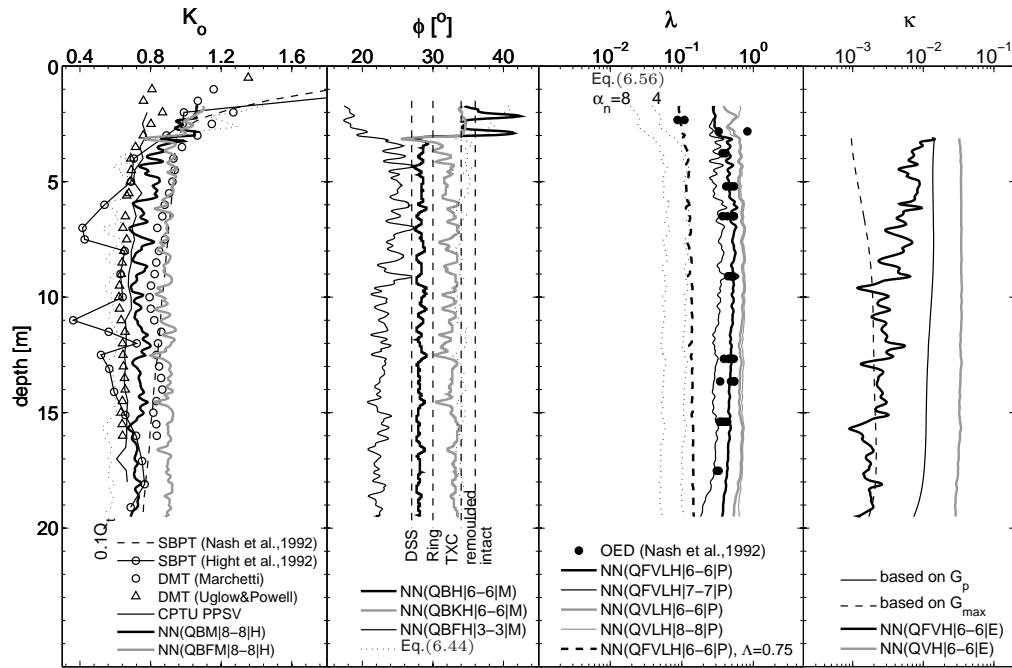


Figure 9.16: Predictions of  $K_o$ ,  $M$  and  $\lambda$  for Bothkennar site from laboratory tests and field tests (based on Hight et al., 2003; Nash et al., 1992b), and CPTU test using empirical formulas and neural network predictors.

Figure 9.16 also presents the results of profiling parameter  $\lambda$ . It can be seen that four applied NNs provide the results which are similar to  $\lambda$  values obtained through OED testing by Nash et al. (1992b). Both NNs which operate merely with  $Q_t$ ,  $e_o$ ,  $\Lambda$  and  $K_o$  slightly overestimate  $\lambda$ , while including  $F_r$  bring NN predictions closer to laboratory results. In this case, this consistency can be considered as fortunate owing to uncertainty associated with low values of  $F_r$ . The chart also shows relative importance of parameter  $\Lambda$  which assumed as 0.75, significantly moves the profile towards low values of  $\lambda$ .

An attempt at profiling parameter  $\kappa$  was carried out by means of NNs which were trained based on the training set encompassed by  $I_r = 10 \div 750$  (cf. Section 8.2.5.5). NN predictions are presented in Figure 9.16 and are compared with  $\kappa$  profiles estimated for the purpose of this study based on  $G_{\max}$  derived from SCPTU and  $G_p$  from SBPT (see Nash et al., 1992a). NN(QVH|6-6|E) reasonably predicts values of  $\kappa$  which are, however, larger than those estimated from SBPT. Similarly to the analysis presented for parameter  $\lambda$ ,  $F_r$  can affect predictions of  $\kappa$ . However, the influence of  $F_r$  on NN(QFVH|6-6|E) predictions is stronger than in the case of NN(QFVLH|6-6|P) due to a smaller number of input variables contributing to the final NN product. The strong influence of the fluctuating  $F_r$  profile (Figure G.4) is thus mirrored by an irregular relief of predicted  $\kappa$ . Predictions by NN(QFVH|6-6|E) which are close to those estimated with  $G_{\max}$ , can be considered here as fortunate.

### 9.2.7 Conclusions

The above analysis showed that the NNs trained based on a synthetic training database provide meaningful parameter predictions from piezocone data. Detailed comparative analyzes of NN predictions were performed for a number of characterization sites. In general, NNs proved to be particularly efficient in profiling parameters  $c_u$ , OCR,  $R_p$  and  $K_o$ . Predicting deformation characteristics  $\lambda$  and  $\kappa$  can also be viewed as promising. On the other hand, much uncertainty is associated with predictions of the effective strength parameter  $M$  (Table 9.5 provides a qualitative evaluation of the level of confidence for estimated characteristics obtained in this study. NNs applied together with empirical approaches may thus reduce uncertainty related to the first-order interpretation of parameters from field testing measurements.

Based on presented analyzes, some general remarks can be drawn:

- Satisfactory accuracy of  $R_p$  predictions can be achieved merely based on  $Q_t$  and  $B_q$  measurements. Such input configuration gives essentially similar results to those generated using expanded input information.
- In general, NN predictions constitute the upper bound of  $c_u$  and OCR predictions with regards to laboratory measurements. However, it is difficult to unambiguously judge whether this is a derivative of unavoidable disturbances associated with specimen sampling and field testing in undisturbed natural conditions, or a shortcoming of the FE model taken as a generator of training patterns.
- The applied NNs networks confirmed reduced ability to meaningfully approximate outputs from inputs which are rarely or not represented in the training dataset, e.g. high  $Q_t$  and  $B_q$ , or low, sensitive soil-like  $F_r$ . In the cases where  $F_r$  considerably contributes to NN predictions, NNs do not provide reliable results for sensitive clays. It was particularly visible in predictions of parameters  $K_o$  and  $M$ , for which the sleeve friction resistance can be an important factor affecting the magnitude of derived parameters. However, this drawback can be removed by considering a

Table 9.5: Perceived applicability of CPT and NN predictors for estimation initial state variables and MCC parameters in normally- and lightly overconsolidated clays.

Initial state parameters			Strength parameters		Deformation characteristics	
$K_o$	OCR	$R_p$	$c_u$	$\phi'$	$\kappa$	$\lambda$
1-2	1-3	1-2	1-2	3-5	need further validation	

Reliability rating: 1 High; 2 High to moderate;  
3 Moderate; 4 Moderate to low; 5 Low.

constitutive law for soil which accounts for structuration effects. Low relative importance of  $F_r$  in the case of NN models predicting  $c_u$  or OCR affected parameter estimates in a minor degree.

- Enforcing "undrained" penetration conditions in the case of partially drained penetration may result in higher estimates of parameters such as  $c_u$  or OCR.
- In the case of natural clays, using the NNs with specified soil permeability seems to be advantageous.



# Chapter 10

## Final Conclusions and Recommendations

### 10.1 Conclusions

The present study aimed at combining finite element modeling and the neural network (NN) technique in order to enhance parameter identification for an elasto-plastic constitutive model of soil. In practice, soil properties can be deduced from experimental measurements derived from a large number of various laboratory and field tests. Field testing makes it possible to perform soil characterization *in situ*, on a representative soil mass. By reducing soil disturbances to a minimum, field tests should enable capturing the response of virgin soil, allowing a reliable identification of parameters which may be sensitive to sampling procedures.

Self-boring pressuremeter tests (SBPT) and standard piezocone tests (CPTU) are widely used to deduce properties of clayey soils through analytical and empirical correlations between soil properties and experimental measurements. Empirical correlations usually require some tuning based on reference laboratory data because first-order estimates for typical correlation coefficients may give unreliable evaluation of soil properties. Analytical correlations are mostly based on cavity expansion methods which are restricted to either fully drained or perfectly undrained problems, so that inverse closed-form solutions for relatively simple constitutive models can be derived. In practice, however, depending on physical and consolidation properties of the soil, partially drained conditions may occur during field testing, and may lead to an erroneous estimation of clay characteristics. Therefore, the following research aimed at elaborating a generic parameter identification framework which is based on the NN technique and which can improve the reliability of soil properties derived from experimental data under complex drainage conditions.

Although the proposed strategy of parameter prediction is first adapted to the triaxial compression test, the study is focused mainly on the application of NN inverse models to the selected field tests. The research consists of four main parts related to the application of NNs to parameter identification in which:

1. A generic framework for the enhanced calibration of multi-parameter con-

stitutive models was elaborated by introducing NN predictors into the classical back analysis scheme. The strategy makes it possible to avoid potential pitfalls which are related to the gradient-based optimization, as well as to reduce the computational effort of the iterative scheme.

2. Two FE models to represent the coupled hydro-mechanical boundary value problems (BVP) of the pressuremeter and the piezocone tests were developed. Numerical simulations allowed the examination of the effect of partially drained conditions and of its impact on stress paths occurring in soil elements around the probes. As regards the piezocone test, the parametric study carried out using the FE model enabled metamodeling of the penetration problem, delineating properties of the FE model.
3. Methodology for the generation of the NN training dataset based on numerical modeling which accounts for possible partially drained conditions, is proposed.
4. Based on the pseudo-experimental data and the specified normalizing formulas, a number of NN inverse models are developed, first for the triaxial compression test, and then for the pressuremeter and the piezocone tests.

This chapter summarizes the main findings of this study and provides some recommendations for future research. For the sake of clarity, conclusions are presented according to three main fields being the subject of this dissertation: (*i*) enhanced parameter identification, (*ii*) model calibration with SBPT, and (*iii*) soil profiling with CPTU. Finally, the original contributions are summarized in a separate section.

### 10.1.1 Enhanced parameter identification

The NN method was proposed to enhance the automated numerical procedure for calibrating multi-parameter constitutive models. The potential of the two-level parameter identification method combining the standard gradient-based optimization (GBO) technique supported by the feed-forward NN algorithm was presented in detail. The efficiency of the presented strategy has been proved by means of test calibration of the Modified Cam Clay model (MCC) using experimental measurements from the benchmark triaxial drained compression test.

The application of the neural network technique to solve an inverse problem provides a quick and accurate search of the vicinity of a global minimum in the space avoiding local minima which are present on the surface of possible solutions. The close approximation of parameters preserves the minimal computational expense during the subsequent GBO (typically 2-3 iterations) and helps the user to avoid the necessity to perform time-consuming trial-and-error runs. This is a crucial feature, if the large-scale FE analyses required in the case of modeling of non-homogeneous stress state BVPs, are considered (e.g. field tests are considered during the subsequent direct searching with GBO).

Since NN inverse models are developed based on training patterns which are generated through numerical simulations, it is important to reduce the computational effort by carefully permuting FE input parameters. The number of training patterns can be decreased once reasonable constraints are imposed on the multi-dimensional space of variables.

It has been demonstrated that the pre-processed NN input vector can include a large number of discrete observational points, i.e. entire reliefs of experimental results. Applying principal component analysis (PCA) to the unprocessed input dataset results in a significant reduction of the large-dimensional input dataset with no significant loss of accuracy of evaluated parameters.

The choice of discrete points during curve fitting has a significant importance on calibrated parameters unless the constitutive model is able to precisely reproduce experimental curves. The examples presented on the triaxial compression test demonstrate that NNs possess the ability to extract meaningful information about the parameters' sensitivity from the numerical training dataset. The responses of the model with the input parameters provided by an NN revealed that an NN mapping experimental measurements, is able to properly extract soil properties.

A potential application of the NN-based technique for the parameter identification of enhanced constitutive models involves basically delivering relevant data that illustrates the physical phenomena that are considered in the model. Obviously, in the case of a calibration of more complex soil models, the parameters that can be directly estimated with the high degree of confidence can constitute a part of the NN input vector (e.g. the Poisson coefficient or the overconsolidation ratio in the presented example), whereas the parameters of non-physical meaning for a given BVP become the objects of optimization.

Using a well-designed interface, the proposed parameter identification can be adapted to any constitutive model or BVP with only few modifications. Different models, element or structural tests can be attached as modules to the fully automated pattern generator. The numerical results are used once in order to properly adjust network weights that are stored with negligible storage cost. As NNs are trained with broad intervals of parameters and a sufficient number of training patterns, they are able to map any experimental set of measurements correctly. Therefore, the trained NNs can be a part of the automated optimization module incorporated into numerical solution applications such as FE packages. This can be of particular value for multi-parameter models characterized by nontrivial parameter assessment. The use of trained NNs involves no special expertise and requires only a relevantly specified input.

### 10.1.2 Model calibration with SBPT

Literature review revealed that partial drainage which may occur in clay even for a quick pressuremeter expansion test, affects the stress-strain relationship and, in effect, the derived parameters. Therefore, a numerical model representing the BVP of two pressuremeter tests, i.e. the expansion and the holding test, was developed. The coupled hydro-mechanical FE formulation for the MCC allowed

any generated excess pore water pressure to dissipate during simulations of the expansion test and the subsequent holding tests. Numerical simulations showed that partially drained conditions may occur in a material characterized by the coefficient of permeability  $k$  larger than  $10^{-11}$  m/s.

Numerical simulations demonstrated that due to volume changes accompanying partial drainage during expansion test, the soil may locally harden near the cavity wall. This may affect parameter interpretation for both coupled pressuremeter tests. It was concluded that the use of numerical simulations is necessary during the parameter identification for complex constitutive relationships particularly in occurrence of the partial drainage. The performed sensitivity analysis confirmed coupling of deformation, strength and consolidation characteristics. The use of numerical inverse modeling was also justified by the lack of analytical solutions for the pressure holding test (PHT). It was concluded that the calibration of model characteristics should be considered as a mutual fitting of all the available experimental measurements in the same optimization run as the parameter feedback exists.

In the context of PHT, it was suggested that an evaluation of the slope of normal consolidation line,  $\lambda$ , can be performed using the variation of cavity strain radius which occurs due to increasing effective radial stress accompanying the pore pressure decay around the probe.

As the numerical model, prior to the identification of parameters, requires the initial state variables, i.e.  $e_o$  and  $\sigma'_{vo}$  ( $K_o$ ) to be specified, the influence of these variables on the identified constitutive parameters was also examined. The results revealed that the error for identified values of  $\kappa$  and  $\lambda$  may be inversely proportional to the error of input  $e_o$ , while a strong influence of  $K_o$  on  $R_p$  was observed when  $K_o$  was underestimated.

The development of NN inverse models which take into account a possible partial drainage was based on a set of synthetic test samples which were generated by the developed numerical model. Numerical measurements were obtained based on constrained random permutations of input model characteristics. In the light of *in situ* stress anisotropy, the relationship between the typical overconsolidation ratio from the one-dimensional compression test and the constitutive overconsolidation ratio for the MCC, was clarified. Thanks to the proposed normalizing formulas for all pressuremeter curves, the depth effect was removed allowing NN predictors to operate regardless of the *in situ* mean effective stress.

It has been illustrated that the characteristics of the MCC can be estimated fairly accurately by means of NNs and then corrected with a minimum computational cost related to the iterative parameter correction (max. 3-4 iterations). The effectiveness of the method was confirmed for both numerical and real experimental measurements. The example of parameter identification based on the numerical SBP measurements revealed that starting from a remote initial vector of parameters, the GBO risks either the increased computational cost or getting trapped by the local minimum. In certain cases, the latter can also lead to instabilities of an FE solver if a wrong search direction is chosen. This analysis shows that the NN-assigned parameters facilitate parameter identifica-

tion by substantially reducing the computational effort, as well as by ensuring a quick convergence of the GBO algorithm at the expected optimal vector of parameters.

By applying NN parameter prediction for real SBPT data, the trial-and-error guessing of the initial vector of parameters was avoided during the calibration of the multi-parameter constitutive model. The numerically evaluated parameters of the Fucino clay revealed considerable agreement with characteristics evaluated conventionally through laboratory and field tests. This confirmed the correctness of the double-level parameter identification for the complex boundary value problem. Hence, such enhanced computational identification seems to be suitable for solving inverse problems linking advanced soil models and the hydro-mechanical feedback.

The drawback of using NNs in this method is that considerable cost is required to produce the numerical training database. This cost is, however, borne only once because the NN is trained with a broad range of controlled parameter permutations. Thus, newly trained NNs may enrich the existing base of already trained NNs for a number of standardized test geometries and mostly used constitutive models.

### 10.1.3 Soil profiling with CPTU

The use of many complementary interpretation methods may decrease uncertainty of evaluated parameters from piezocone test data. This study demonstrated an application of NN predictors to profiling soil parameters. By similarity to the SBPT problem, a number of NN inverse models was developed based on the results derived from rigorous FE analyzes.

The FE model of piezocone penetration involved a numerical formulation for the double-phase material obeying the MCC law including the large strain theory, as well as the finite contact formulation. It has been demonstrated that a considerable computational effort related to the generation of the training database can be reduced by optimizing the mesh size and "steady-state" depth in function of soil rigidity index which determines the radius of the plastically deformed region. Different mesh sizes revealed meaningful consistency in computed measurements of  $q_t$  and  $u_2$ .

An extended parametric study including analysis of the influence of strength and stress anisotropy, rigidity index and cone roughness on two cone factors, provides new insights into the analysis of cone penetration.

Due to the failure in incorporating the arbitrary Lagrangian-Eulerian (ALE) technique into the FE model framework, an equivalent semi-numerical approach was proposed to account for frictional effects in different drainage conditions which were delineated from a number of numerical simulations. It was observed that the "rough" interface described by friction coefficients  $\mu$  larger than 0.08 lead to a severe loss of measurement accuracy observed in the finite elements passing by the cone body. The validity of the developed semi-numerical penetration model was verified in detail by means of comparisons with other theoretical solutions and parametric studies synthesized from literature, as well

as experimental evidence for both undrained and partially drained scenarios.

In accordance with centrifuge laboratory tests, numerical simulations revealed the occurrence of a partial drainage effect during the penetration for soils which exhibits values of consolidation coefficient  $c_v$  larger than  $7.14 \cdot 10^{-5} \text{m}^2/\text{s}$  roughly corresponding to the permeability coefficients larger than about  $10^{-8} \text{m}/\text{s}$ .

Unfortunately, some shortcomings of the model were caused by the inefficiency of numerical procedures. The use of the numerical model to generate synthetic database was thus limited to representing rather soft soil which exhibits the rigidity index  $I_r$  less than 110 and  $G/p'_o$  less than 70. However, an extension of model applicability for  $I_r$  larger than 110 can be carried out using the proposed theoretical solutions derived from the presented numerical simulations of the undrained scenario.

The numerical database destined for NN training which was generated with broad intervals of constitutive parameters and different drainage conditions, provided piezocone results that correspond to the soil behavior type of soft organic deposits, and non-sensitive clays and silts. It was proven that the semi-numerical model obeying the MCC law is able to provide a synthetic database which exhibits a meaningful consistency with experimental trends observed in the behavior of natural soils in terms of parameters  $Q_t$  and  $B_q$ .

Different configurations of input variables, including standard normalized piezocone metrics and other available soil characteristics were investigated in terms of the feasibility of effective NN training. Post-training regression analyzes were performed for numerical data allowing the assessment of impact of specific input variables on the accuracy of parameter estimates. Some main conclusions related to NN training with the aid of numerical database were drawn as follows:

- Consistent numerical database of piezocone measurements combined with the NN technique allows different configurations of input variables and the examination of their influence on the quality of predictions.
- NNs which contain only basic parameters derived from the penetration test, i.e.  $Q_t$  and  $B_q$ , provide a similar or somewhat better accuracy of predictions than the empirical methods which employ average coefficients of correlation. A significant improvement of accuracy can be achieved by increasing the amount of information in the input vector.
- Auxiliary input components such as  $K_o$ ,  $F_r$  and  $M$ , can significantly contribute to the increase of quality of correlation and to the reduction of the dispersal of predictions. Meaningful accuracy of predictions can often be achieved based solely on the basic piezocone parameters complemented with state variables such as  $K_o$  or  $e_o$ . The NNs with the smallest possible number of additional parameters are recommended when applying the method to real experimental data in order to avoid "over-fitted" predictions.
- Owing to the formulation of the MCC model, predictions with the use of  $F_r$  as the input parameter, can be considered as reliable in the case of

non-sensitive soils.

- The effect of partial drainage during penetration mostly affect the interpretation of  $c_u$ , OCR and  $R_p$ . In the case of parameters  $M$ ,  $\lambda$ ,  $\kappa$  or  $K_o$ , errors for NN predictions are independent on drainage conditions.
- In general, NN predictors correctly detect patterns which were subject to partial consolidation during penetration. In such cases, NNs exhibit sensitivity to increasing  $Q_t$  and correspondingly decreasing  $B_q$  and provide the solutions which are free of drainage-induced errors.
- During NN training it was observed that the influence of NN topology (i.e. number of hidden neurons and number of hidden layers) was insignificant compared to the results obtained by an increasing amount of input information (i.e. number of input components). In other words, different NN topologies resulted in a very similar quality of predictions for the same input configuration.

Finally, the developed NN models were applied to parameter profiling from field measurements for a number of characterization clay sites: Bäckebol, Skå-Edeby, Port Huron, Amherst and Bothkennar. It was demonstrated that the NNs trained based on a synthetic training database provide meaningful first-order parameter predictions from piezocone data. In general, NNs have proved to be particularly efficient in profiling parameters  $c_u$ , OCR,  $R_p$  and  $K_o$ . Predicting deformation characteristics  $\lambda$  and  $\kappa$  can also be considered promising. On the other hand, much uncertainty is associated with predictions of the effective strength parameter  $M$ . NNs applied together with empirical approaches may thus reduce uncertainty related to the first-order interpretation of parameters. The following general conclusions summarize the analysis dealing with the application of NNs to real experimental data:

- Satisfactory accuracy of  $R_p$  predictions can be achieved merely based on  $Q_t$  and  $B_q$  measurements. Such input configuration gives essentially similar results to those generated using expanded input information.
- In general, NN predictions constitute the upper bound of  $c_u$  and OCR predictions with regards to laboratory measurements. However, it is difficult to unambiguously judge whether this is a derivative of unavoidable disturbances associated with specimen sampling and field testing in undisturbed natural conditions, or a shortcoming of the semi-numerical model taken as a generator of training patterns.
- The applied NNs networks confirmed the reduced ability to meaningfully approximate outputs from inputs which are rarely or not represented in the training dataset, e.g. high  $Q_t$  and  $B_q$ , or low, sensitive soil-like  $F_r$ . In the cases where  $F_r$  considerably contributes to NN predictions, NNs do not provide reliable results for sensitive clays. It was particularly visible in predictions of parameters  $K_o$  and  $M$ , for which sleeve friction resistance can be an important factor affecting the magnitude of derived parameters. However, this drawback can be removed by considering a constitutive law for soil which accounts for structuration effects. Low relative importance

of  $F_r$  in the case of NN models predicting  $c_u$  or OCR affected parameter estimates in a minor degree.

- Enforcing "undrained" penetration conditions in the case of partially drained penetration may result in higher estimates of parameters such as  $c_u$  or OCR.
- In the case of natural clays, the use of NNs with specified soil permeability seems to be advantageous.

#### 10.1.4 Summary of original contributions

The following part summarizes the original contributions of this study:

1. A development of NN inverse models based on numerically generated populations of reference results representing *in situ* test measurements.
2. A constrained permutation of model parameters allowing the generation of a numerical population of NN training data sets (Section 8.1.1 and 8.2.1).
3. Evaluation of the slope of a normal consolidation line,  $\lambda$ , using the variation of cavity strain radius which occurs during the pressure holding test due to increasing effective radial stress accompanying the pore pressure decay around the SBP membrane (Section 6.2.3).
4. Normalization of pore pressure and cavity strain measurements from SBPT with respect to the mean effective stress, which allows removing depth effects (Section 8.1.3).
5. Prediction of the MCC parameters from SBPT measurements in complex drainage conditions with the aid of NN models.
6. A suggested framework of parallel curve-fitting accounting for hydro-mechanical coupling of SBPT measurements (Section 6.2.5).
7. An original parametric metamodeling of the CPTU test including different definitions of undrained shear strength  $c_u$  and the effect of  $R_p$ , an analysis of strength anisotropy effect on cone factors and novel formulas for the cone factor  $N_{\Delta u}$  (Section 7.2.2.1).
8. An extended numerical analysis of drainage effects for the cone penetration problem (Section 7.2.2.2) and a simplified approach for modeling the penetration problem which consists of combining an analysis of frictional effects in various drainage scenarios with measurements derived from "smooth" interface penetration (Section 7.2.2.3 and 7.2.3).
9. Parametric study of the influence of different input configurations on the quality of parameter predictions by means of NN models from the CPTU test.
10. Multi-parameter soil profiling for the MCC model using NN models and CPTU measurements in various drainage scenarios.



## 10.2 Outlook for future research

The study reveals several needs of further improvements, as well as fields of possible developments.

As regards laboratory testing, the library of NNs for the hybrid parameter identification (NN-GBO) can be expanded by further advanced constitutive models for which parameter assessment is not straightforward (e.g. models incorporating small strain stiffness or rotation of bounding surface). Such a library should also comprise inverse models designed for a variety of standardized laboratory tests.

Further development paths may consist of extending the library of numerical models representing other commonly applied field tests such as Marchetti's dilatometer or cone (push-in) pressuremeter (e.g. Yu et al., 1996), also in coarse type soils. In the case of DMT, its relevant FE modeling requires 3D discretization of the probe geometry and should also include a pre-penetration mechanism. As regards modeling of the cone pressuremeter test, a simulation of expansion should be carried out deep enough so that measurements are not affected by "immature" stress fields in overlain layers. The modeling of cone penetration can also be extended by an analysis of thinly interbedded subsoil where particular layers vary in terms of relative stiffness. Such analysis could make it possible to account for an influence of the material ahead and behind the cone (cf. Lunne et al., 1997). Hence, in order to capture correct mechanical properties, NN input could also contain measurements from over- and underlying layers.

However, an effective FE modeling of field tests requires some improvements in numerical procedures which are essential in modeling of penetration problems. Therefore, a robust formulation of the mesh adaptivity (e.g. arbitrary Lagrangian-Eulerian (ALE) technique) for coupled hydro-mechanical problems including contact elements should be incorporated in order to efficiently cope with severe mesh distortions (e.g. Nazem et al., 2008). The FE simulations of the piezocone test in two-phase materials also demand the incorporation of efficient stabilization algorithms which could cope with cone penetration into stiffer materials than those presented in this study. Obviously, other numerical methods can be used to model penetration problems such as the material point method (MPM), also known as particle-in-cell (PIC) method which is a variant of the FEM formulated in the ALE description of motion (Więckowski, 2004).

With the availability of robust mesh adaptivity, the presented model of the piezocone penetration should be reanalyzed. Furthermore, in order to improve the reliability of  $B_q$  measurements, the constitutive relationship should include a small-strain formulation which could allow excess pore water pressure to be generated yet before yielding. This is an important future when shear tests take place in undrained conditions. In the context of reproducing high  $B_q$  observed in natural sensitive and structured clays, the constitutive model should include concepts which integrate bonding and destructuration effects (Gens and Nova, 1993). These concepts could also allow a reliable incorporation of parameter  $F_r$  into the parameter identification for natural clays. Further improvements of

the penetration model may concern incorporating a viscous formulation which takes into account strain rate effects that affect cone measurements.

It could be also interesting to study the effect of partial soil saturation, also in different drainage conditions.

Regarding the SBPT model, large scale simulations accounting for the pressuremeter membrane length/diameter ratio could be considered in order to avoid geometry effects (e.g. Houlby and Carter, 1993; Yu et al., 2005). Incorporating a viscous formulation could be also advantageous in order to obtain more realistic numerical results corresponding to reference model properties.

Assuming that a constitutive model can reasonably represent real soil behavior, it could be also interesting to analyze a well monitored study case using an FE model reflecting boundary conditions of a construction. Such a study could reveal to what extent apparent parameters inferred by NNs from piezocone data and applied to an FE model fit experimental measurements during various stages of construction.

Finally, the developed methodologies, i.e. hybrid model calibration and NN-based parameter predictors, can be used to develop commercial stand-alone modules supporting the automated system identification for the existing FE packages. In this context, some improvements can be foreseen such as an increasing number of training patterns in order to ensure commercial efficiency of predictions. Considering that NN modeling is characterized by inherent non-uniqueness and so their approximations are not unique even for the same modeled problem, the use of many NN models in the context of a specific inverse problem could also be considered in order to ensure higher degree of confidence for predicted properties. Furthermore, the use of a number of NN models, also for different possible input configurations can provide a statistical evaluation of predicted parameters. Thus obtained statistical features could be then used in stochastic numerical analyzes for engineering study cases.

# References

- ABAQUS (2007). *ABAQUS theory manual, version 6.7-1*. ABAQUS, Inc. 47, 115, 116, 143
- Abu-Farsakh, M., Tumay, M., and Voyiadjis, G. (2003). A numerical parametric study of the piezocone penetration test in clays. *Int J Geomechanics*, 3(2):170–81. 92, 95, 129
- Abu-Farsakh, M., Voyiadjis, G., and Tumay, M. (1998). Numerical analysis of the miniature piezocone penetration tests (PCPT) in cohesive soils. *Int J Num Anal Meth Geomech*, 22(10):777–850. 91
- Abu-Kiefa, M. (1998). General regression neural networks for driven piles in cohesionless soils. *J Geotech Geoenv Eng ASCE*, 124(12):1177–85. 28, 30
- Agrawal, G., Chameau, J., and Bourdeau, P. (1997). Assessing the liquefaction susceptibility at a site based on information from penetration testing. In Kartam, N., Flood, I., and Garrett, J., editors, *Artificial neural networks for civil engineers: Fundamentals and applications*, pages 185–214. ASCE Expert Systems and Artificial Intelligence Committee, New York. 29
- Agrawal, G., Weeraratne, S., and Khilnani, M. (1994). Estimating clay liner and cover permeability using computational neural networks. In Khozeimeh, K., editor, *Proc. 1st Congress on Computing in Civil Engineering*, pages 115–122, Washington, D.C. ASCE. 29
- Ali, F. (1989). Generation and dissipation of excess pore pressure during pressuremeter tests. *Soils and Foundations*, 29(1):173–179. 85
- Allman, M. and Atkinson, J. (1992). Mechanical properties of reconstituted Bothkennar soil. *Géotechnique*, 42(2):289–301. 223
- Amar, S., Clarke, B., Gambin, M., and Orr, T., editors (1991). *The application of pressuremeter test results to foundation design in Europe. Part 1: Predrilled pressuremeters/self-boring pressuremeters*. Balkema, Rotterdam. 71
- Anandarajah, A. and Agarwal, D. (1991). Computer-aided calibration of soil plasticity model. *Int J Numer Anal Meth Geomech*, 15:835–856. 8, 17, 18, 21
- Anandarajah, A. and Dafalias, Y. (1986). Bounding surface plasticity. III: Application to anisotropic cohesive clays. *J Engng Mech ASCE*, 112(EM12):1292–1318. 8
- Anderson, W., Pyrah, I., and Haji-Ali, F. (1987). Rate effects in pressuremeter test in clays. *J Geotech Engng ASCE*, 113(11):1344–1358. 13
- Argyris, J., Faust, G., Szimmat, J., Warnke, E., and Willam, K. (1974). Recent development in the finite element analysis of pressure container reactor vessel. *Nuclear Engng and Design*, 28(1):42–75. 119, 120
- Baecher, G. and Christian, J. (2003). *Reliability and statistics in geotechnical engineering*. Wiley, New York. 15, 160

## References

- Baguelin, F. and Jézéquel, J. (1973). Le pressiomètre autoforeur. *Annales de l'Institut Technique du Bâtiment et des Travaux Publics*, Supplément 307-308(Série Sols et Fondations No.97):133–160. 68
- Baguelin, F., Jézéquel, J., Lemée, E., and Méhauté, A. (1972). Expansion of cylindrical probes in cohesive soils. *J Soils Mechanics and Foundation Division ASCE*, 98(SM11):1129–1142. 71, 75, 76, 83
- Baguelin, F., Jézéquel, J., and Shields, D. (1978). *The pressuremeter and foundations engineering*. Trans Tech Publications, Clausthal, Germany. 68, 71, 109
- Baligh, M. (1985). Strain path method. *J Geotech Engng ASCE*, 111(9):1108–1135. 87, 90, 95
- Baligh, M. and Levadoux, J. (1986). Consolidation after undrained piezocone penetration. II: Interpretation. *J Geotech Engng ASCE*, 112(7):727–745. 102
- Basheer, I. (2000). Selection of methodology for neural network modeling of constitutive hysteresis behavior of soils. *Computer-Aided Civil and Infrastructure Engineering*, 15(6):440–458. 28, 30
- Basheer, I. (2002). Stress-strain behavior of geomaterials in loading reversal simulated by time-delay neural networks. *J Materials in Civ Engng*, 14(3):270–273. 28
- Basheer, I., Reddi, N., and Najjar, Y. (1996). Site characterization by neuronets: an application to the landfill siting problem. *Ground Water*, 34(4):610–617. 29
- Bates, D. and Watts, D. (1988). *Nonlinear regression analysis and its applications*. John Wiley & Sons. 17
- Bathe, K., Ramm, E., and Wilson, E. (1975). Finite element formulations for large deformation dynamic analysis. *Int J Numer Meth Engng*, 9:353–386. 91
- Baziar, M. and Ghorbani, A. (2005). Evaluation of lateral spreading using artificial neural networks. *Soil Dynamics and Earthquake Engng*, 25(1):1–9. 29
- Belytschko, T., Liu, W., and Moran, B. (2000). *Nonlinear finite elements for continua and structures*. Wiley, Chichester. 48, 91
- Benoit, J. and Clough, G. (1986). Self-boring pressuremeter tests in soft clay. *J Geotech Engng ASCE*, 112(1):60–78. 72, 75, 83, 109
- Benz, T. (2007). *Small-strain stiffness of soils and its numerical consequences*. Phd, Universität Stuttgart. 8
- Bjerrum, L. (1972). Embankments on soft ground. In *Proc. Am.Soc. Civ Engs Specialty Conf. on Performance of Earth and Earth supported Structures.*, volume 2, pages 1–54, Purdue University. 13, 84
- Bolton, M. and Whittle, R. (1999). A non-linear elastic/perfectly plastic analysis for plane strain undrained expansion tests. *Géotechnique*, 49(1):133–141. 71
- Burghignoli, A., Cavallera, L., Chieppa, V., Jamiolkowski, M., Mancuso, C., Marchetti, S., Pane, V., Paoliani, P., Silvestri, F., Vinale, F., and Vittori, E. (1991). Geotechnical characterization of Fucino Clay. In *Proceedings of the 10th European Conference on Soil Mechanics and Foundation Engineering*, pages 27–40, Florence, Italy. 198, 199, 200, 203
- Burns, S. and Mayne, P. (1998). Monotonic and dilatatory pore-pressure decay during piezocone tests in clay. *Can Geotech J*, 35(6):1063–1073. 102

- Cailletaud, G. and Pilvin, P. (1994). Identification and inverse problems related to material behaviour. In Swoboda, G., editor, *Proc. Inverse Problems in Engineering Mechanics*, pages 79–86. Balkema, Rotterdam. 17
- Calvello, M. and Finno, R. (2002). Calibration of soil models by inverse analysis. In Pande and Pietruszczak, editors, *Proc. VIIIth Int Symp Numerical Models in Geomechanics NUMOG VIII*, pages 107–114, Rome. Balkema. 60, 111
- Campanella, R., Robertson, P., and Gillespie, D. (1986). Seismic cone penetration test. In Clemence, S., editor, *In Situ'86: Use of In-situ in Geotechnical Engineering*, ASCE, volume GSP6, pages 116–130, Blacksburg, VA. ASCE. 70, 100
- Cao, L., Teh, C., and Chang, M. (2001). Undrained cavity expansion in Modified Cam-clay I: Theoretical analysis. *Géotechnique*, 51(4):323–334. 8, 71, 75, 77, 78, 79, 80, 89, 98, 150
- Carter, J., Booker, J., and Yeung, S. (1986). Cavity expansion in cohesive frictional soils. *Géotechnique*, 36(3):349–353. 89
- Carter, J., Randolph, M., and Wroth, C. (1979). Stress and pore pressure changes in clay during and after the expansion of a cylindrical cavity. *Int J Numer Anal Meth in Geomech*, 3:305–322. 82
- Cekerevac, C., Girardin, S., Klubertanz, G., and Laloui, L. (2006). Calibration of an elasto-plastic constitutive model by a constrained optimisation procedure. *Computers and Geotechnics*, 33:432–443. 22
- Celk, S. and Tan, O. (2005). Determination of preconsolidation pressure with artificial neural network. *Civ Engng and Env Syst*, 22(4):217–231. 29
- Chan, W., Chow, Y., and Liu, L. (1995). Neural network: An alternative to pile driving formulas. *Computers and Geotechnics*, 17(2):135–278. 28
- Chang, C., Chang, T., Xu, Y., and To, W. (2002). Selection of training samples for model updating using neural networks. *J Sound and Vibration*, 249(5):867–883. 53
- Chang, M., Teh, C., and Cao, L. (2001). Undrained cavity expansion in Modified Cam-Clay II: Application to the interpretation of the piezocone test. *Géotechnique*, 51(4):335–350. 84, 89, 98, 99
- Chen, B. and Mayne, P. (1994). Profiling the OCR of clays by piezocone tests. Technical Report Rep. No. CEEGEO-94-1, Georgia Institute of Technology. 87, 97, 205, 215, 216, 218, 281, 282
- Chen, B. and Mayne, P. (1996). Statistical relationships between piezocone measurements and stress history of clays. *Can Geotech J*, 33:488–498. 97
- Chung, S., Randolph, M., and Schneider, J. (2006). Effect of penetration rate on penetrometer resistance in clay. *J Geotech Geoenv Engng ASCE*, 132(9):1188–1196. 104
- Cividini, A. and Gioda, G. (1988). A simplified analysis of pile penetration. In Swoboda, G., editor, *Num Meth in Geomech*, volume 2, pages 1043–1049, Innsbruck. Balkema. 91
- Cividini, A., Maier, G., and Nappi, A. (1983). Parameter estimation of a static geotechnical model using a Bayes' approach. *Int J Rock Mech Min Sci & Geomech Abstr*, 20(5):215–226. 17
- Clarke, B. (1995). *Pressuremeters in geotechnical design*. Blackie Academic & Professional, imprint Chapman & Hall, Glasgow. 76

## References

- Clarke, B., Carter, J., and Wroth, C. (1979). In situ determination of the consolidation characteristics of saturated clays. In *Proc. 7th Eur. Conf. on Soil Mechanics and Foundation Engineering*, volume 2, pages 207–211, Brighton. 69, 71, 80, 82, 109
- Clough, G., Briault, J., and Hughes, J. (1990). The development of pressuremeter testing. In *Pressuremeters, 3<sup>rd</sup> Int Symp on Pressuremeters*, pages 25–45, Oxford. Thomas Telford, London. 71
- Collins, I. and Yu, H. (1996). Undrained cavity expansion in critical state soils. *Int J Numer Anal Meth Geomech*, 20:489–516. 8, 71, 78, 89
- Cooley, R. (1993). *Regression modelling of ground-water flow. USGS-TWRI Book 3, Chapter B4*. U.S Geological Survey Techniques of Water Resources Investigations. 260
- Cooley, R. and Naff, R. (1990). *Regression modelling of ground-water flow. USGS-TWRI Book 3, Chapter B4.*, volume 3. U.S Geological Survey Techniques of Water Resources Investigations. 257, 260, 261
- Dalton, J. and Hawkins, P. (1982). Fields of stress - some measurements of the in-situ stress in a meadow in the Cambridgeshire countryside. *Ground Engineering*, 15(4):15–23. 71, 72
- Dascal, O. and Laroque, G. (1973). Caractéristique de compressibilité des argiles du complexe Nottaway-Broadback-Rupert (Baie James). *Can Geotech J*, 10(1):41–63. 53
- de Borst, R. and Vermeer, P. (1982). Finite element analysis of static penetration tests. In *2nd Eur Symp Penetration Testing*, volume 2, pages 457–462. 90
- de Borst, R. and Vermeer, P. (1984). Finite element analysis of static penetration tests. *Géotechnique*, 34(2):199–210. 90
- DeGroot, D. and Lutenecker, A. (2003). Geology and engineering properties of Connecticut Valley varved clay. In et. al, T., editor, *Characterisation and engineering properties of natural soils*, volume 1, pages 695–724, Singapore. Swets and Zeitlinger. 11, 218, 219, 220, 221, 222, 285
- DeGroot, D. and Sandven, R. (2004). General report: Laboratory and field comparisons. In de Fonseca, V. and Mayne, editors, *Proc. ISC-2 on Geotechnical and Geophysical Site Characterization*, pages 1775–1789, Porto, Portugal. Millpress, Rotterdam. 11, 67
- Demers, D. and Leroueil, S. (2002). Evaluation of preconsolidation pressure and the overconsolidation ratio from piezocone tests of clay deposits in quebec. *Can Geotech J*, 39:174–192. 8, 97, 283
- Denby, G. and Clough, G. (1980). Self-boring pressuremeter tests in clay. *J Geotech Engng ASCE*, 106(GT12):1369–1387. 71
- Diamantaras, K. and Kung, S. (1996). *Principal component neural networks: theory and applications*. Adaptive and Learning Systems for Signal Processing, Communications, and Control. Wiley, New York. 37
- Ding, W. and Shang, J. (2004). Neural networks in soil characterization. In de Fonseca, V. and Mayne, editors, *Proc. ISC-2 on Geotechnical and Geophysical Site Characterization*, pages 889–896, Porto, Portugal. Millpress, Rotterdam. 29
- Doris, J., Rizzo, D., and Dewoolkar, M. (2008). Forecasting vertical ground surface movement from shrinking/swelling soils with artificial neural networks. *Int J Num Anal Meth Geomech*, 32(10):1229–1245. 28

- Douglas, B. and Olsen, R. (1981). Soil classification using electric cone penetrometer. In *Cone Penetration Testing and Experience.*, pages 209–227, St. Louis. American Society of Civil Engineers. 70, 172
- Durgunoglu, H. and Mitchell, J. (1975). Static penetration resistance of soils. I: Analysis. In *Proc. ACSE Spec Conf on In Situ Measurements of Soil Properties*, ASCE, pages 151–171, New York. 89
- Dzwilewski, P. and Richards, A. (1974). Consolidation properties of Wilkinson basin soils. *J Geotech Engng ASCE*, GT10(100):1175–1179. 53
- Eden, W. and Law, K. (1980). Comparison of undrained shear strength results obtained by different test methods in soft clays. *Can Geotech J*, 17:369–381. 83
- Ellis, G., Yao, R., Zhao, R., and Penumadu, D. (1995). Stress-strain modeling of sands using artificial neural networks. *J Geotech Engng ASCE*, 121(5):429–435. 28, 30
- Elsworth, D. and Lee, D. (2007). Limits in determining permeability from on-the-fly uCPT sounding. *Géotechnique*, 57(8):679–685. 90, 102
- Eslami, A. and Fellenius, B. (1997). Pile capacity by direct CPT and CPTu methods applied to 102 case histories. *Can Geotech J*, 34(6):886–904. 70, 172
- Fahey, M. and Carter, J. (1986). Some effects of rate of loading and drainage on pressuremeter tests in clays. In *Proc. Specialty Geomechanics Symposium*, pages 50–55, Adelaide. 69
- Fellenius, B. and Eslami, A. (2000). Soil profile interpreted from CPTu data. In Balasubramanian, A., Bergado, D., Der-Gyey, L., Seah, T., Miura, K., Phien-wej, N., and Nutalaya, P., editors, *Int Conf "Year 2000 Geotechnics"*, volume 1, pages 163–171, Bangkok, Thailand. Asian Institute of Technology. 172
- Finnie, I. and Randolph, M. F. (1994). Punch-through and liquefaction induced failure of shallow foundations on calcareous sediments. In *Proc. Int Conf on Behaviour of Offshore Structures, BOSS'94*, pages 217–230, Boston. Pergamon. 103
- Finno, R. and Calvello, M. (2005). Supported excavations: the observational method and inverse modeling. *J Geotech Geoenv Engng ASCE*, 131(7):826–836. 17, 18, 21
- Fioravante, V. (1988). *Interpretation of self-boring tests in clay with particular reference to holding tests*. PhD thesis, Technical University of Turin. 198, 200
- Fioravante, V. (2004). General report: Enhanced characterization by combined *in situ* testing. In de Fonseca, V. and Mayne, editors, *Proc. ISC-2 on Geotechnical and Geophysical Site Characterization*, pages 1585–1596, Porto, Portugal. Millpress, Rotterdam. 12
- Fioravante, V., Jamiolkowski, M., and Lancellotta, R. (1994). An analysis of pressuremeter holding tests. *Géotechnique*, 44(2):227–238. 8, 13, 69, 82, 85, 109, 203
- Fischer, K., Sheng, D., and Abbo, A. (2007). Modeling of pile installation using contact mechanics and quadratic elements. *Computers and Geotechnics*, 34(6):449–461. 116, 123
- Flood, I. and Kartam, N. (1994a). Neural networks in civil engineering. I: principles and understanding. *J Comp Civ Engng*, 8(2):131–147. 27, 30, 36, 38, 41, 42, 54
- Flood, I. and Kartam, N. (1994b). Neural networks in civil engineering. II: systems and application. *J Comp Civ Eng*, 8(2):149–161. 9
- Fukagawa, R., Fahey, M., and Ohta, H. (1990). Effect of partial drainage on pressuremeter test in clay. *Soils and Foundations*, 30(4):134–146. 13, 85

## References

- Garson, D. (1991). Interpreting neural-network connection weights. *AI Expert*, 6(4):46–51. 42, 43
- Gens, A., Ledesma, A., and Alonso, E. (1996). Estimation of parameters in geotechnical backanalysis - II. application to a tunnel excavation problem. *Computers and Geotechnics*, 18(1):29–46. 111
- Gens, A. and Nova, R. (1993). Conceptual bases for a constitutive model for bonded soils and weak rocks. In *Proc. 1st Int Symp on Geotech of Hard Soils-Soft Rocks*, volume 1, pages 485–494, Athens. 237
- Gevrey, M., Dimopoulos, I., and Lek, S. (2003). Review and comparison of methods to study the contribution of variables in artificial neural network models. *Ecological Modelling*, 160(3):249–264. 42, 43
- Ghaboussi, J. (2001). Biologically inspired soft-computing methods in structural mechanics and engineering. *Struct Engng and Mech*, 11(5):485–502. 9, 10, 30
- Ghaboussi, J., Garrett, J., and X., W. (1991). Knowledge-based modeling of material behavior with neural networks. *J Engng Mech*, 117:132–151. 28
- Ghaboussi, J., Pecknold, D., Zhang, M., and Haj-Ali, R. (1998). Autoprogressive training of neural network constitutive models. *Int J Numer Meth Engng*, 42:105–126. 28
- Ghaboussi, J. and Sidarta, D. (1998). New nested adaptive neural networks (NANN) for constitutive modelling. *Computers and Geotechnics*, 22(1):29–52. 28, 38
- Gibson, R. and Anderson, W. (1961). In-situ measurements of soil properties with the pressuremeter. *Civ Engng Public Works Review*, 56(658):615–618. 71, 75, 80
- Gioda, G. and Sakurai, S. (1987). Back analysis procedure for the interpretation of field measurements in geomechanics. *Int J Numer Anal Meth Geomech*, 11:555–583. 15, 17, 18
- Goh, A. (1994). Seismic liquefaction potential assessed by neural networks. *J Geotech Engng ASCE*, 120(9):1467–1480. 29, 43
- Goh, A. (1995). Modeling soil correlations using neural networks. *J Comp Civ Eng ASCE*, 9(4):275. 29
- Goh, A. (1996a). Neural-network modeling of CPT seismic liquefaction data. *J Geotech Eng ASCE*, 122(1):70–73. 29
- Goh, A. (1996b). Pile driving records reanalyzed using neural networks. *J Geotech Eng ASCE*, 122(6):492–495. 28
- Goh, A. (2002). Probabilistic neural network for evaluating seismic liquefaction potential. *Can Geotech J*, 39(1):219–232. 29
- Goh, A. and Kulhawy, F. (2005). Reliability assesment of serviceability performance of braced retaining walls using a neural network approach. *Int J Numer Anal Meth in Geomech*, 29(6):627–642. 24, 28
- Goh, A., Kulhawy, F., and Chua, C. (2005). Bayesian neural network analysis of undrained side resistance of drilled shafts. *J Geotech Geoenv Engng ASCE*, 131(1):84–93. 29
- Goh, A., Wong, K., and Broms, B. (1995). Estimation of lateral wall movements in braced excavations using neural networks. *Can Geotech J*, 32(6):1059–1064. 28, 30



- Graham, J. (2006). The 2003 R.M. Hardy Lecture: Soil parameters for numerical analysis in clay. *Can Geotech J*, 43:187–209. 1, 8, 12
- Griffiths, D. (1982). Elasto-plastic analysis of deep foundations in cohesive soil. *Int J Num Anal Meth Geomech*, 6:211–218. 90
- Hagan, M., Demuth, H., and Beale, M. (1996). *Neural network design*. PWS Publishing Company, Boston, MA. 40
- Hanna, A., Morcoux, G., and Helmy, M. (2004). Efficiency of pile groups installed in cohesionless soil using artificial neural networks. *Can Geotech J*, 41(6):1241–1249. 28
- Hanna, A., Ural, D., and Saygili, G. (2007). Evaluation of liquefaction potential of soil deposits using artificial neural networks. *Int J Computer-Aided Engineering and Software*, 24(1):5–16. 30
- Hashash, Y., Jung, S., and Ghaboussi, J. (2004). Numerical implementation of a neural network based material model in finite element analysis. *Int J Numer Meth Engng*, 59:989–1005. 28
- Hashash, Y., Marulanda, C., Ghaboussi, J., and Jung, S. (2003). Systematic update of a deep excavation model using field performance data. *Computers and Geotechnics*, 30(6):477–488. 28, 30
- Haykin, S. (1999). *Neural Networks. A Comprehensive foundation*. Prentice Hall, Upper Saddle River, New Jersey, 2nd edition. 24, 27, 37, 40, 56
- Hicher, P. and Michali, A. (1996). Identifying soil parameters by means of laboratory and in situ testing. *Computers and Geotechnics*, 19(2):153–170. 111
- Hight, D., Böese, R., Butcher, A., Clayton, C., and Smith, P. (1992a). Disturbance of the Bothkennar clay prior to laboratory testing. *Géotechnique*, 42(2):199–217. 12
- Hight, D., Bond, A., and Legge, J. (1992b). Characterization of the Bothkennar clay: an overview. *Géotechnique*, 42(2):303–347. 223, 224, 225
- Hight, D. and Leroueil, S. (2003). Characterisation of soils for engineering purposes. In Tan, T., Phoon, K., Hight, D., and Leroueil, S., editors, *Characterisation and engineering properties of natural soils*, volume 1, pages 254–360, Singapore. Swets and Zeitlinger. 8, 14, 85, 97, 104, 222
- Hight, D., Paul, M., Barras, B., Powell, J., Nash, D., Smith, P., Jardine, R., and Edwards, D. (2003). The characterisation of the Bothkennar clay. In Tan, e. a., editor, *Characterisation and engineering properties of natural soils*, volume 1, pages 543–597, Singapore. Swets and Zeitlinger. 11, 223, 226
- Hill, M. (1998). *Methods and guideline for effective model calibration*. Report 98-4005, USGS, 90. U.S. Geological Survey Water-Resources Investigations, Denver, Colorado. 18, 19, 257, 260, 261
- Hornik, K., Stinchcombe, M., and White, H. (1989). Multilayer feedforward networks are universal approximators. *Neural Networks*, 2(5):359–366. 27
- Houlsby, G. (1988). Piezocone penetration test. In *Geotechnology Conference on Penetration Testing in the UK*, pages 141–146, Birmingham. 98
- Houlsby, G. (1998). Advanced analysis of field tests. In Mayne, P. and Robertson, P., editors, *1st Int Conf on Site Characterization, ISC98*, volume 1, pages 99–112, Atlanta, Georgia. Balkema. 75, 88, 94

## References

- Houlsby, G. and Carter, J. (1993). The effects of pressuremeter geometry on the results of tests in clay. *Géotechnique*, 43(4):567–576. 238
- Hu, Y. and Randolph, M. (1998). A practical numerical approach for large deformation problem in soil. *Int J Num Anal Meth Geomech*, 22(5):327–350. 92
- Huang, W., Sheng, D., Sloan, S., and Yu, H. (2004). Finite element analysis of cone penetration in cohesionless soil. *Computers and Geotechnics*, 31:517–528. 91, 115, 116, 122, 138
- Hujeux, J. (1985). Une loi de comportement pour le chargement cyclique des sols. In Davidovici, V., editor, *Génie Parasismique*, pages 287–302. E.N.P.C., Paris. 8, 45
- ISSMGE (1999). International reference test procedure for the cone penetration test (CPT) and the cone penetration test with pore pressure (CPTU). report of the (ISSMGE) technical comitee 16 on ground property charaterisation for in-situ testing. In Barends, editor, *12th European Conference on Soil Mechanics and Geotechnical Engineering*, volume 3, pages 2195–2222, Amsterdam. Balkema. 70, 135
- Jamiolkowski, M., Ladd, C., Germaine, J., and Lancellotta, R. (1985). New developments in field and laboratory testing of soils. In *Proc. 11th ICSMFE*, volume 1, pages 57–153, San Francisco. Balkema. 8, 10, 11, 12, 14, 67, 68, 70, 71, 72, 74, 87, 92, 211, 283
- Jan, J., Hung, S., Chi, S., and Chern, J. (2002). Neural network forecast model in deep excavation. *J Comp Civ Engng ASCE*, 16(1):59–65. 28
- Jardine, R. and Chow, F. (1996). *New design methods for offshore piles*, volume MTD publication 96/103. HSE Books, London. 118
- Jardine, R., Symes, M., and Burland, J. (1984). The measurement of soil stiffnes in the triaxial apparatus. *Géotechnique*, 34(3):323–340. 49
- Jefferies, M. and Davis, M. (1991). Soil classification by the cone penetration test: Discussion. *Can Geotech J*, 28(1):173–176. 172
- Juang, C., Jiang, T., and Christopher, R. (2001). Three-dimensional site characterisation: neural network approach. *Géotechnique*, 51(9):799–809. 29
- Karlsrud, K. (1999). General aspects of transportation infrastructure. In Barends, e. a., editor, *12th European Conf on Soil Mech and Geotech Engng*, volume 1, pages 17–30, Amsterdam. Balkema. 12
- Karlsrud, K., Lunne, T., Kort, D., and Strandvik, S. (2005). CPTU correlations for clays. In *Proc. 16th ICSMGE*, volume 2, pages 693–702, Osaka. Millpress. 69, 70, 96
- Kayadelen, C. (2007). Estimation of effective stress parameter of unsaturated soils by using artificial neural networks. *Int J Num Anal Meth Geomech*, 32(9):1087–1106. 29
- Keaveny, J. and Mitchell, J. (1986). Strength of fine grained soils using the piezocone. In Clemence, S., editor, *In Situ'86: Use of In-situ in Geotechnical Engineering*, ASCE, volume GSP6, pages 668–685, Blacksburg, VA. ASCE. 88, 102
- Kim, Y. (2004). Feasibility of neural network application for determination of undrained shear strength of clay from piezocone measurements. In de Fonseca, V. and Mayne, editors, *Proc. ISC-2 on Geotechnical and Geophysical Site Characterization*, pages 957–961, Porto, Portugal. Millpress, Rotterdam. 29

- Kioulos, P., Voyiadjis, G., and Tumay, M. (1988). A large strain theory and its application in the analysis of the cone penetration mechanism. *Int J Num Anal Meth Geomech*, 12:45–60. 91
- Konrad, J. and Law, K. (1987). Preconsolidation pressure from piezocone tests in marine clays. *Géotechnique*, 37(2):177–190. 282
- Koumoto, T. (1988). Ultimate bearing capacity of cones in sand. In De Ruiter, J., editor, *ISOPT-1 Penetration Testing*, volume 2, pages 809–813, Orlando. Balkema, Rotterdam. 119
- Krizek, R., Corotis, R., and El-Moursi, H. (1977). Probabilistic analysis of predicted and measured settlements. *Can Geotech J*, 14(1):17–33. 53
- Kulhawy, F. and Mayne, P. (1990). Manual on estimating soil properties for foundation design. Technical report, Electric Power Research Institute. 100, 101
- Kung, G., Hsiao, E., Schuster, M., and Juang, C. (2007). A neural network approach to estimating deflection of diaphragm walls caused by excavation in clays. *Computers and Geotechnics*, 34(5):385–396. 28
- Kurup, P. and Dudani, N. (2002). Neural networks for profiling stress history of clays from PCPT data. *J Geotech Geoenv Eng ASCE*, 128(7):569–579. 29
- Lacasse, S., Jamiolkowski, M., Lancellotta, R., and Lunne, T. (1981). In situ characteristics of two Norwegian clays. In *Proc. 10th Int Conf Soil Mech and Found Engng*, volume 2, Stockholm. 11
- Lacasse, S. and Lunne, T. (1988). Calibration of dilatometer correlations. In *Penetration Testing 88, ISOPT-1*, volume 1, pages 539–548, Orlando, Florida. 217, 221, 222
- Ladanyi, B. (1972). In-situ determination of undrained stress-strain behaviour of sensitive clays with the pressuremeter. *Can Geotech J*, 9:313–319. 71, 75, 76
- Larsson, R. and Mulabdić, M. (1991). Piezocone tests in clay. Technical Report Report No.42, Swedish Geotechnical Institute. 97, 206, 209, 210, 213, 215, 284, 285
- Ledesma, A., Gens, A., and Alonso, E. (1996a). Estimation of parameters in geotechnical backanalysis - I. maximum likelihood approach. *Computers and Geotechnics*, 18(1):1–27. 17, 111
- Ledesma, A., Gens, A., and Alonso, E. (1996b). Parameter and variance estimation in geotechnical backanalysis using prior information. *Int J Numer Anal Meth Geomech*, 20:119–141. 17, 18
- Lee, I. and Lee, J. (1996). Prediction of pile bearing capacity using artificial neural networks. *Computers and Geotechnics*, 18(3):189–200. 28
- Lee, S., Lee, S., and Kim, Y. (2003). An approach to estimate unsaturated shear strength using artificial neural network and hyperbolic formulation. *Computers and Geotechnics*, 30(6):489–503. 29
- Lefik, M. and Schrefler, B. (2003). Artificial neural network as an incremental non-linear constitutive model for a finite element code. *Comput Methods Appl Mech Engrg*, 192(31-32):3265–3283. 28, 30
- Lehane, B., Chow, F., McCabe, B., and Jardine, R. (2000). Relationships between shaft capacity of driven piles and CPT end resistance. *Proceedings of ICE Geotechnical Engineering*, 143:93–101. 118

## References

- Leroueil, S. (1988). Tenth Canadian Geotechnical Colloquium: Recent developments in consolidation of natural clays. *Can Geotech J*, 25:85–107. 13
- Leroueil, S. and Hight, D. (2003). Behaviour and properties of natural soils and soft rocks. In et. al, T., editor, *Characterisation and engineering properties of natural soils*, volume 1, pages 29–254, Singapore. Swets and Zeitlinger. 102
- Leroueil, S., Tavenas, F., and Le Bihan, J.-P. (1983a). Propriétés caractéristiques des argiles de l'est du Canada. *Can Geotech J*, 20(4):681–705. 53
- Leroueil, S., Tavenas, F., Samson, L., and Morin, P. (1983b). Preconsolidation pressure of champlain clays. part II. laboratory determination. *Can Geotech J*, 20(4):803–816. 13, 84
- Levadoux, J. and Baligh, M. (1986). Consolidation after undrained piezocone penetration. I: Prediction. *J Geotech Engng ASCE*, 112(7):707–726. 102
- Levasseur, S., Malecot, Y., Boulon, M., and Flavigny, E. (2008). Soil parameter identification using a genetic algorithm. *Int J Num Anal Meth Geomech*, 32(2):189–213. 17, 18, 21, 22
- Levasseur, S., Malecot, Y., Boulon, M., and Flavigny, E. (2009). Statistical inverse analysis based on genetic algorithm and principal component analysis: Method and developments using synthetic data. *Int J Num Anal Meth Geomech*, DOI: 10.1002/nag.776. 22
- Lu, Q., Randolph, M., Hu, Y., and Bugarski, I. (2004). A numerical study of cone penetration in clay. *Géotechnique*, 54(4):257–267. 92, 94, 95, 121
- Lunne, T. and Kleven, A. (1981). Role of CPT in North Sea foundation engineering. In Norris, G. and Holtz, R., editors, *Cone penetration testing and experience*, pages 76–107. ASCE. 94
- Lunne, T., Lacasse, S., and Rad, N. (1989). SPT, CPT, pressuremeter testing and recent developments in in situ testing. In *Proc. 7th ICSMF*, volume 4, pages 2339–403, Rio de Janeiro. Balkema, Rotterdam, 1992. 67, 170, 171, 172
- Lunne, T., Powell, J., and Robertson, P. (1995). Use of piezocone tests in non-textbook materials. In Craig, editor, *Advances in site investigation practice*, pages 438–451, London. Thomas Telford. 103
- Lunne, T., Robertson, P., and Powell, J. (1997). *Cone penetration testing in geotechnical practice*. Blackie Academic & Professional, London. 14, 15, 68, 70, 86, 88, 92, 93, 94, 96, 97, 98, 100, 101, 102, 126, 141, 142, 237
- Mair, R. and Wood, D. (1987). *Pressuremeter testing. Methods and interpretation*. Butterworths, London. 68, 71, 76
- Marchetti, S. (1980). In situ tests by flat dilatometer. *J Geotech Eng ASCE*, 106(3):299–321. 217, 219
- Markauskas, D., Kačianauskas, R., and Katzenbach, R. (2005). Simulations of piezocone penetration in saturated porous medium using the FE remeshing technique. *Found of Civ Env Engrg*, 6:103–116. 13, 92, 115, 135
- Marquardt, D. (1963). An algorithm for least-squares estimation of nonlinear parameters. *J for the Society of Industrial and Applied Mathematics*, 11(2):431–441. 18, 40, 260
- Masood, T. and Mitchell, J. (1993). Estimation of in situ lateral stresses in soils by cone-penetration test. *J Geotech Eng ASCE*, 119(10):1624–1639. 99, 282

- Masters, T. (1993). *Practical neural network recipes in C++*. Academic Press, San Diego, California. 36
- Mayne, P. (1980). Cam-clay predictions of undrained strength. *J Geotech Engng ASCE*, 106(GT11):1219–1242. 53, 150
- Mayne, P. (1988). Determining OCR in clays from laboratory strength. *J Geotech Engng ASCE*, 114(1):76–92. 167, 169
- Mayne, P. (1991). Determination of OCR in clays by piezocone tests using cavity expansion and critical state concepts. *Soils and Foundations*, 31(2):65–76. 89, 97, 98, 167, 184, 187, 205, 207, 224, 282
- Mayne, P. (2005). Versatile site characterization by seismic piezocone. In *Proc. 16th ICSMGE*, volume 2, Osaka. Millpress. 96
- Mayne, P. (2006). In-situ test calibrations for evaluating soil parameters. In Tan, Phoon, Hight, and Leroueil, editors, *Characterisation and Engineering Properties of Natural Soils*, volume 3, pages 1601–1652, Singapore. Taylor & Francis Group, London. 10, 11, 67, 68, 70, 87, 92, 97, 99, 127
- Mayne, P. (2007). Cone penetration testing. a synthesis of highway practice. Technical report, Transportation Research Board. 68, 87, 88, 92, 93, 96, 97, 150, 167
- Mayne, P. and Bachus, R. (1988). Profiling OCR in clays by piezocone soundings. In De Ruiter, J., editor, *Penetration testing, ISOPT-1*, volume 2, pages 857–864, Orlando. Balkema. 93
- Mayne, P., Barry, R. C., and DeJong, J. (2001). Manual on subsurface investigations. Technical Report Publication No. FHWA NHI-01-031, Federal Highway Administration. 88, 97, 102
- Mayne, P. and Kulhawy, F. (1982).  $K_o - OCR$  relationship in soils. *J Geotech Engng ASCE*, 108(6):851–872. 149, 150, 151, 166, 205, 207, 282
- Mayne, P. and Kulhawy, F. (1988). Independence of geostatic stress from overconsolidation in some Beaufort Sea clays: Discussion. *Can Geotech J*, 25:617–621. 282
- Mayne, P. and Rix, G. (1995). Correlations between shear wave velocity and cone tip resistance in clays. *Soils and Foundations*, 35(2):107–110. 87
- Mayoraz, F. and Vulliet, L. (2002). Neural networks for slope movement prediction. *Int J Geomechanics*, 2(2):153–173. 28
- McCulloch, W. and Pitts, W. (1943). A logical calculus of the ideas immanent in nervous activity. *Bull. Math. Biophys.*, 5:115–133. 33
- McNeilan, T. and Bugno, W. (1984). Cone penetration test results in offshore California silts. In Demars, C. a., editor, *Strength testing of marine sediments: Laboratory and in situ measurements*, volume STP883, pages 55–71, San Diego. ASTM, 1985. 103
- Medynski, M. (2003). On the global optimisation of a multivariable function. *arXiv:math.OA/0301256v1*. 261
- Meyerhof, G. (1961). The ultimate bearing capacity of wedge-shaped foundations. In *Proc. 5th Int Conf on Soil Mech and Found Engrg*, volume 2, Paris. 89

## References

- Murakami, A. and Hasegawa, T. (1988). Back analysis using Kalman filter-finite elements and optimal location of observed points. In Swoboda, G., editor, *Proc. 6<sup>th</sup> Int Conf Num Meth in Geomechanics*, pages 2051–2058, Innsbruck, Austria. Balkema, Rotterdam. 17
- Najjar, Y. and Basheer, I. (1996). Utilizing computational neural networks for evaluating the permeability of compacted clay liners. *Geotech and Geolog Engng*, 14(3):193–212. 29
- Najjar, Y., Basheer, I., and Naouss, W. (1996). On the identification of compaction characteristics by neurons. *Computers and Geotechnics*, 18(3):167–187. 29
- Najjar, Y. and Huang, C. (2007). Simulating the stress-strain behavior of Georgia kaolin via recurrent neuronet approach. *Computers and Geotechnics*, 34(5):329–422. 28
- Nakase, A. and Kamei, T. (1986). Influence of strain rate on undrained shear characteristics of  $k_o$ -consolidated cohesive soils. *Soils and Foundations*, 26(1):85–95. 13, 84
- Nardin, A., Schrefler, B., and Lefik, M. (2003). Application of artificial neural network for identification of parameters of a constitutive law for soils. In Chung, P., Hinde, C., and Ali, M., editors, *IEA/AIE*, pages 545–554. Springer. 29, 30
- Nash, D., Powell, J., and Lloyd, I. (1992a). Initial investigations of the soft clay test site at Bothkennar. *Géotechnique*, 42(2):163–181. 223, 226, 286
- Nash, D., Sills, G., and Davison, L. (1992b). One-dimensional consolidation testing of soft clay from Bothkennar. *Géotechnique*, 42(2):241–256. 223, 224, 225, 226, 286
- Nawari, N., Liang, R., and Nusairat, J. (1999). Artificial intelligence techniques for the design and analysis of deep foundations. *Electronic J Geotech Engng*, 4(<http://www.ejge.com/1996/Ppr9608/Abs9608.htm>). 29
- Nazem, M., Sheng, D., Carter, J., and Sloan, S. (2008). Arbitrary Lagrangian-Eulerian method for large-strain consolidation problems. *Int J Num Anal Meth Geomech*, 32(9):1023–1050. 92, 115, 237
- Neaupane, K. and Achet, S. (2004). Some applications of a backpropagation neural network in geo-engineering. *Environmental Geology*, 45(4):567–575. 28
- Obrzud, R., Vulliet, L., and Truty, A. (2009a). A combined neural network/gradient-based approach for the identification of constitutive model parameters using self-boring pressuremeter tests. *Int J Num Anal Meth Geomech*, 33(6):817–849. 8, 9, 30
- Obrzud, R., Vulliet, L., and Truty, A. (2009b). Optimization framework for calibration of constitutive models enhanced by neural networks. *Int J Num Anal Meth Geomech*, 33(1):71–94. 22, 29
- Olden, J. and Jackson, D. (2002). Illuminating the 'black box': a randomization approach for understanding variable contributions in artificial neural networks. *Ecological Modelling*, 154:135–150. 43
- Olden, J., Joy, M., and Death, R. (2004). An accurate comparison of methods for quantifying variable importance in artificial neural networks using simulated data. *Ecological Modelling*, 178:389–397. 42, 43
- Olsen, R. and Farr, J. (1986). Site characterization using cone penetration test. In *ASCE Speciality Conference In Situ '86: Use of In Situ Tests in Geotechnical Engineering*, pages 854–68, Blacksburg. ASCE. 172
- Ou, C. and Tang, Y. (1994). Soil parameter determination for deep excavation analysis by optimization. *J Chinese Institute of Engineers*, 17(5):671–688. 18, 262

- Pal, S., Wathugala, G., and Kundu, S. (1996). Calibration of a constitutive model using genetic algorithms. *Computers and Geotechnics*, 19(4):325–348. 22
- Palmer, A. (1972). Undrained plane strain expansion of a cylindrical cavity in clay: simple interpretation of the pressuremeter test. *Géotechnique*, 22(3):451–457. 71, 75, 76
- Penumadu, D. and Chameau, J. (1997). Strain rate effects in model pressuremeter testing. *J Geotech Geoenv Engng ASCE*, 123(11):1051–1059. 83, 84
- Penumadu, D., Skandarajah, A., and Chameau, J. (1998). Strain-rate effects in pressuremeter testing using a cuboidal shear device: experiments and modeling. *Can Geotech J*, 35:27–42. 13, 83, 84
- Penumadu, D. and Zhao, R. (1999). Triaxial compression behaviour of sand and gravel using artificial neural networks. *Computers and Geotechnics*, 24:207–230. 28
- Pichler, B., Lackner, R., and Mang, H. (2003). Back analysis of model parameters in geotechnical engineering by means of soft computing. *Int J Numer Meth Engng*, 57:1943–1978. 22, 30, 40
- Poeter, E. and Hill, M. (1998). Documentation of UCODE, a computer code for universal inverse modeling. Technical report, US Geological Survey Water-Resources Investigations Report 98-4080. 17, 149
- Powell, J. and Uglow, I. (1988). The interpretation of the marchetti dilatometer test in UK clays. In *Proc. Penetration Testing in the UK, Institution Civil Engineers*, pages 268–273, Birmingham. Thomas Telford. 221, 224
- Prapaharan, S., Chameau, J., and Holtz, R. (1989). Effect of strain rate on undrained strength derived from pressuremeter tests. *Géotechnique*, 39(4):615–624. 13, 84
- Prevost, J. and Hoeg, K. (1975). Analysis of pressuremeter in strain-softening soil. *J Geotech Engng ASCE*, 101(GT8):717–732. 71
- Prior, A. (1994). Applications of implicit and explicit finite element techniques to metal forming. *J Mater Process Technol*, 45:649–656. 115
- Rad, N. and Lunne, T. (1988). Direct correlations between piezocone test results and undrained shear strength of clay. In De Ruiter, J., editor, *ISOPT-1 Penetration Testing*, volume 2, pages 911–917, Orlando. Balkema, Rotterdam. 94
- Ramsey, N., Jardine, R., Lehane, B., and Ridley, A. (1998). A review of soil-steel interface testing with the ring shear apparatus. In Kluwer, editor, *Proc. Conf. on Offshore Site Investigation and Foundation Behaviour*, pages 237–258, London. Kluwer. 119
- Randolph, M. and Wroth, C. (1979). An analytical solution for the consolidation around a driven pile. *Int J Numer Anal Meth in Geomech*, 3(3):217–229. 80, 102
- Randolph, M. F. and Hope, S. (2004). Effect of cone velocity on cone resistance and excess pore pressures. In *Proc. Int. Symp. on Engineering Practice and Performance of Soft Deposits*, pages 147–152, Osaka, Japan. Yodagawa Kogisha Co. 104, 135
- Rangear, D., Hicher, P., and Zentar, R. (2003). Determining soil permeability from pressuremeter tests. *Int J Numer Anal Meth in Geomech*, 27:1–24. 8, 13, 85, 148
- Raphael, B. and Smith, I. (2003). A direct stochastic algorithm for global search. *Applied Math and Comp*, 146:729–758. 21

## References

- Rendon-Herrero, O. (1980). Universal compression index equation. *J Geotech Engng ASCE*, 106(GT11):1179–1200. 53
- Robertson, P. (1990). Soil classification using the cone penetration test. *Can Geotech J*, 27(1):151–158. 70, 93, 166, 172, 173
- Robertson, P., Campanella, R., Gillespie, D., and Greig, J. (1986). Use of piezometer cone data. In Clemence, S., editor, *In Situ'86: Use of In-situ in Geotechnical Engineering*, ASCE, volume GSP 6, pages 1263–80, Blacksburg, VA. American Society of Civil Engineers. 70, 126, 170, 171, 172
- Robertson, P., Sully, J., Woeller, D., Lunne, T., Powell, J., and Gillespie, D. (1992). Estimating coefficient of consolidation from piezocone tests. *Can Geotech J*, 29(4):539–550. 102
- Roscoe, K. and Burland, J. (1968). *On the generalized strain-stress behaviour of 'wet' clay*. Engineering Plasticity. Cambridge University Press, Cambridge. 45
- Rumelhart, D., Hinton, G., and Williams, R. (1986). *Learning internal representations by error propagation*, volume 1 of *Parallel distributed processing*. MIT Press, Cambridge. 39, 40
- Sakurai, S. and Takeuchi, K. (1983). Back analysis of measured displacements of tunnels. *Rock Mechanics and Rock Engineering*, 16:173–180. 15, 17
- Samarajiva, P., E.J., M., and Wathugala, W. (2005). Genetic algorithms for the calibration of constitutive models for soils. *Int J Geomechanics*, 5(3):206–217. 22
- Sandven, R., Senneset, K., and Janbu, N. (1988). Interpretation of piezocone tests in cohesive soils. In De Ruiter, J., editor, *ISOPT-1 Penetration Testing*, pages 939–953. Balkema, Rotterdam. 96, 101
- Scardi, M. and Harding, L. (1999). Developing an empirical model of phytoplankton primary production: a neural network case study. *Ecological Modelling*, 120(2-3):213–223. 43
- Schmertmann, J. (1978). Guidelines for cone penetration test, performance and design. Technical report, US Federal Highway Administration. 70, 172
- Schnaid, F. (2005). Geo-characterisation and properties of natural soils by  $\hat{A}$  in situ tests. In *16th ICSMGE*, volume 1, pages 3–45, Osaka. Millpress. 67, 84, 92, 103
- Schneider, J., Lehane, B., and Schnaid, F. (2007). Velocity effects on piezocone measurements in normally and overconsolidated clays. *Int J of Physical Modelling in Geotechnics*, 7(2):23–34. 104, 135
- Schneider, J., Randolph, M. F., Mayne, P., and Ramsey, N. (2008). Analysis of factors influencing soil classification using normalized piezocone tip resistance and pore pressure parameters. *J Geotech Geoenv Engng ASCE*, 134(11):1569–1586. 172, 173, 174
- Senneset, K., Sandven, R., and Janbu, N. (1989). The evaluation of soil parameters from piezocone tests. *Transportation Research Record*, 1235:24–37. 101
- Shahin, M., Jaksa, M., and Maier, H. (2001). Artificial neural networks applications in geotechnical engineering. *Australian Geomechanics*, 3:49–62. 30
- Shahin, M., Jaksa, M., and Maier, H. (2005). Neural network based stochastic design charts for settlement prediction. *Can Geotech J*, 42(1):110–120. 28



- Shahin, M., Jaksa, M., and Maier, H. (2008). State of the art of artificial neural networks in geotechnical engineering. *Electronic J Geotech Engng*, Special volume Bouquet 08([www.ejge.com/Bouquet08](http://www.ejge.com/Bouquet08)). 9, 30, 36, 38, 40, 41, 42
- Shahin, M., Maier, H., and Jaksa, M. (2004). Data division for developing neural networks applied to geotechnical engineering. *J of Comp Civ Engng ASCE*, 18(2):105–114. 36
- Sheahan, T., Ladd, C., and Germaine, J. (1996). Rate-dependent undrained shear behavior of saturated clay. *J Geotech Eng ASCE*, 122(2):99–108. 13
- Sheng, D., Axelsson, K., and Magnusson, O. (1997). Stress and strain fields around a penetrating cone. In Pietruszczak and Pande, editors, *Proc. 6th Int Symp on Numerical Models in Geomechanics, NUMOG-VI*, pages 456–465, Montreal. Balkema. 91, 115, 135, 140
- Sheng, D., Eigenbrod, K., and Wriggers, P. (2005). Finite element analysis of pile installation using large-slip frictional contact. *Computers and Geotechnics*, 32:17–26. 115, 165
- Sheng, D., Wriggers, P., and Sloan, S. (2006). Improved numerical algorithms for frictional contact in pile penetration analysis. *Computers and Geotechnics*, 33:341–354. 91
- Sheng, D., Wriggers, P., and Sloan, S. (2007). Application of frictional contact in geotechnical engineering. *Int J Geomechanics*, 7(3):176–185. 118
- Shin, H. S. and Pande, G. (2000). On self-learning finite element codes based on monitored response of structures. *Computers and Geotechnics*, 27:161–178. 28
- Shin, H. S. and Pande, G. (2003). Identification of elastic constants for orthotropic materials from structural test. *Computers and Geotechnics*, 30(7):571–577. 29, 30
- Sidarta, D. and Ghaboussi, J. (1998). Constitutive modeling of geomaterials from non-uniform material tests. *Computers and Geotechnics*, 22(1):53–71. 28
- Silva, M., White, D., and Bolton, M. (2006). An analytical study of the effect of penetration rate on piezocone tests in clay. *Int J Numer Anal Meth in Geomech*, 30:501–527. 90
- Silvestri, V. (1998). On determination of the stress-strain curve of the clay from the undrained plane-strain expansion of hollow cylinders: a long forgotten method. *Can Geotech J*, 35:360–363. 76
- Sivakumar, V., Doran, I., Graham, J., and Navaneethan, T. (2001). Relationship between  $k_o$  and overconsolidation ratio: a theoretical approach. *Géotechnique*, 52(3):225–230. 71, 150
- Smith, G. (1986). *Probability and statistics in civil engineering: an introduction*. Collins, London. 41
- Song, C., Voyiadjis, G., and Tumay, M. (1999). Determination of permeability of soils using the multiply piezo-element penetrometer. *Int J Num Anal Meth Geomech*, 23:1609–1629. 102
- Su, S. and Liao, H. (2002). Influence of strength anisotropy on piezocone resistance in clay. *J Geotech Eng ASCE*, 128(2):166–173. 90, 94, 95, 119, 129, 132
- Sudheer, K. (2005). Knowledge extraction from trained neural network river flow models. *J Hydrologic Engng*, 10(4):264–269. 43
- Sully, J. and Campanella, R. (1991). Effect of lateral stress on CPT penetration pore pressures. *J Geotech Eng ASCE*, 117(7):1082–1088. 8, 99, 205, 224, 281, 282

## References

- Susila, E. and Hryciw, R. (2003). Large displacement FEM modelling of the cone penetration test (CPT) in normally consolidated sand. *Int J Num Anal Meth Geomech*, 27:585–602. 91, 92, 115
- Tanaka, H. and Tanaka, M. (1999). Kay factors governing sample quality. In *Int Symp on Coastal Engng in Practice*, pages 57–82, Yokohama. 12
- Teh, C. and Houlsby, G. (1991). An analytical study of the cone penetration test. *Géotechnique*, 41(1):17–34. 92, 94, 95, 102, 127, 129
- Toll, D. (1996). Artificial intelligence applications in geotechnical engineering. *Electronic J Geotech Engng*, 1(<http://www.ejge.com/1996/Ppr9608/Abs9608.htm>). 30
- Torstensson, B. (1977). The pore pressure probe. In *Norsk Jord-Og -fjellteknisk Forbund*, pages Foredrag 34.1–34.15, Oslo, Norway. Tapir. 102
- Vaid, Y. and Campanella, R. (1977). Time-dependent behavior of undisturbed clay. *J Geotech Eng ASCE*, 103(7):693–709. 13
- Van der Berg, P. (1994). *Analysis of soil penetration*. PhD thesis, Technische Univesiteit Delft. 90, 91, 94, 95, 129
- van Eekelen, H. (1980). Isotropic yield surface in three dimensions for use in soil mechanics. *Int J Num Anal Meth Geomech*, 4:89–101. 119, 120
- Vesić, A. (1967). Ultimate loads and settlements of deep foundation in sand. In *Proc. Symp on bearing capacity and settlement of foundations.*, pages 53–68, Duke University. 89
- Vesić, A. (1972). Expansion of cavities in infinite soil mass. *J Soils Mechanics and Foundation Division ASCE*, 98(SM3):265–290. 89, 95, 121
- Vinale, F., d’Onofrio, A., Mancuso, C., and Santucci de Magistris, F. (2001). The pre-failure behavior of soils as construction materials. In *Proc. 2nd Int Symp on Pre-Pailure Deformation Characteristics of Geomaterials*, volume 2, pages 955–1007, Torino. 84
- Voyiadjis, G. and Kim, D. (2003). Finite element analysis of the piezocone test in cohesive soils using an elastoplastic-viscoplastic model and updated lagrangian formulation. *Int J Plasticity*, 19:253–280. 13, 91
- Voyiadjis, G. and Song, C. (2003). Determination of hydraulic conductivity using piezocone penetration test. *Int J Geomechanics*, 3(2):217–224. 102
- Walker, J. and Yu, H. (2006). Adaptive finite element analysis of cone penetration in clay. *Acta Geotechnica*, 1:43–57. 92, 95, 115, 122, 129
- Waszczyszyn, Z. (1998). Some new results in applications of backpropagation neural networks in structural and civil engineering. In Topping, B., editor, *Advances in Engineering Computational Technology*, pages 173–187, Edinburgh. Civil-Comp Press. 29
- Wei, L., Abu-Farsakh, M., and Tumay, M. (2005). Finite-element analysis of inclined piezocone penetration test in clays. *Int J Geomechanics*, 5(3):167–178. 91, 115
- Whittle, A. and Aubeny, C. (1991). Pore pressure fields around piezocone penetrometers installed in clay. In *Int Conf Comp Meth and Advances in Geomech*, volume 1, pages 285–90, Cairns. Balkema, Rotterdam. 124
- Whittle, A. and Kavvadas, M. (1994). Formulation of MIT-E3 constitutive model for over-consolidated clays. *J Geotech Eng ASCE*, 120(1):173–198. 8, 45, 49

- Więckowski, Z. (2004). The material point method in large strain engineering problems. *Comput Methods Appl Mech Engrg*, 193(39-41):4417–4438. 237
- Wood, D. and Wroth, C. (1977). Some laboratory experiments related to the results of pressuremeter tests. *Géotechnique*, 27(2):181–201. 68, 83, 84
- Wriggers, P. (2002). *Computational contact mechanics*. Wiley, New York. 118
- Wroth, C. (1984). The interpretation of in situ tests. *Géotechnique*, 34(4):449–489. 11, 12, 67, 83, 93, 98, 127
- Wroth, C. and Houlsby, G. (1985). Soil mechanics - property characterization and analysis procedures. In *Proc. 11th ICSMFE*, volume 1, pages 1–55, San Francisco. Balkema. 98
- Wroth, C. and Hughes, J. (1973). An instrument for the *in situ* measurements of the properties of soft clays. In *Proc. 8th ICSMFE*, volume 1, Moscow. 68
- Xiang, Z., Swoboda, G., and Cen, Z. (2003). Optimal layout of displacement measurements for parameter identification process in geomechanics. *Int J Geomechanics*, 3(2):205–216. 17, 21
- Yang, Y. and Rosenbaum, M. (2002). The artificial neural network as a tool for assessing geotechnical properties. *Geotech and Geolog Engng*, 20(2):149–168. 29
- Yang, Y. and Zhang, Q. (1997). A hierarchical analysis for rock engineering using artificial neural networks. *Rock Mechanics and Rock Engineering*, 30(4):207–222. 42, 43
- Yao, J., Teng, N., Poh, H., and Tan, C. (1998). Forecasting and analysis of marketing data using neural networks. *J Inf Sci and Engng*, 14:843–862. 43
- Yoon, J. (2007). Application of experimental design and optimization to PFC model calibration in uniaxial compression simulation. *Int J Rock Mech Min Sci*, 44(6):871–889. 8
- Yu, H. (2006). The First James K. Mitchell Lecture. in situ soil testing: from mechanics to interpretation. *Geomechanics and Geoengineering*, 1(3):165–195. 1, 11, 67
- Yu, H., Charles, M., and Khong, C. D. (2005). Analysis of pressuremeter geometry effects in clay using critical state models. *Int J Numer Anal Meth Geomech*, 29:845–859. 108, 203, 238
- Yu, H., Herrmann, L., and Boulanger, R. (2000). Analysis of steady cone penetration in clay. *J Geotech Geoenv Engng ASCE*, 126(7):594–605. 75, 94, 95, 129
- Yu, H. and Houlsby, G. (1991). Finite cavity expansion in dilatant soil: loading analysis. *Géotechnique*, 41(2):173–183. 89
- Yu, H. and Mitchell, J. (1998). Analysis of cone resistance: a review of methods. *J Geotech Geoenv Engng ASCE*, 124(2):140–9. 89, 90
- Yu, H., Schnaid, F., and Collins, I. (1996). Analysis of cone pressuremeter tests in sands. *J Geotech Engng ASCE*, 122(8):623–32. 237
- Yu, H. and Whittle, A. (1999). Combining strain path analysis and cavity expansion theory to estimate cone resistance in clay. Technical report, Unpublished Notes. 92, 95, 129
- ZACE (2003). *Z\_Soil PC 2003, User manual, Soil, Rock and Structural Mechanics in dry or partially saturated media*. ZACE Services Ltd, Software engineering, Lausanne. 47, 52, 108

## References

- Zentar, R., Hicher, P., and Moulin, G. (2001). Identification of soil parameters by inverse analysis. *Computers and Geotechnics*, 28:129–144. 18, 111
- Zhang, Z. and Tumay, M. (1999). Statistical fuzzy approach toward CPT soil classification. *J Geotech Geoenv Eng ASCE*, 125(3):179–186. 70, 172
- Zhou, Y. and Wu, X. (1994). Use of neural networks in the analysis and interpretation of site investigation data. *Computers and Geotechnics*, 16:105–122. 29
- Zhu, J.-H., Zaman, M., and Anderson, S. (1998). Modeling of soil behaviour with a recurrent neural network. *Can Geotech J*, 35(5):858–872. 28

# Appendix A

## Modified Gauss-Newton Algorithm

In this study, model calibrations have been carried out using Modified Gauss-Newton minimization algorithm (Cooley and Naff, 1990; Hill, 1998). This method is an iterative type of standard linear regression and, therefore, the use of the scaling parameter and the Marquardt parameter is necessary. For the purpose of this study, the algorithm has been coupled with the Z\_Soil v6 FEM code during the parameter optimization process in order to improve the quality of identified parameters for self-boring pressuremeter tests. In the following, the main elements of the algorithm are presented.

### Weighted least-squares objective function

The problem of calibration is defined as follows: minimize the difference between the vector of experimental measurements  $\mathbf{y}$  and the computed predictions  $\mathbf{y}'(\mathbf{b})$ . The latter is a response of the model with a given set of parameters  $\mathbf{b}$ , representing the real system. The objective function is a measure of the fit between simulated values and the observations that are being matched by the regression. The formal expression of the objective function is:

$$S(\mathbf{b}) = \frac{1}{t_1 - t_0} \int_{t_0}^{t_1} \|\mathbf{y}(t) - \mathbf{y}'(\mathbf{b}, t)\| dt \quad (\text{A.1})$$

where:

$\|\dots\|$ , is a norm in the space of the observable variables,

$(t_1 - t_0)$ , is the length of observation,

$\mathbf{b}$ , is a vector containing values of each of the NP parameters being estimated,

$\mathbf{y}(t) - \mathbf{y}'(\mathbf{b}, t)$ , represents the difference between experimental results and calculated values which is a function of  $\mathbf{b}$  and corresponds to the observations.

While measurements are taken in discrete points, then the integral can be expressed as the weighted least-squares error (Equation (A.2)) for the finite number of observations, and so  $\mathbf{y}(t)$  and  $\mathbf{y}'(\mathbf{b}, t)$  become vectors containing the ND number of measurements.

$$S(\mathbf{b}) = [\mathbf{y} - \mathbf{y}'(\mathbf{b})]^T \cdot \boldsymbol{\omega} \cdot [\mathbf{y} - \mathbf{y}'(\mathbf{b})] = \mathbf{e}^T \cdot \boldsymbol{\omega} \cdot \mathbf{e} \quad (\text{A.2})$$

where:

$\boldsymbol{\omega}$ , is a diagonal weighting matrix, introduced to transform the observable variables into dimensionless quantities, wherein the weight of every observation is taken as the inverse of its error variance,

$\mathbf{e}$ , is a vector of residuals.

## Normal Equations

The Quasi-Newton optimization procedure combines two minimization algorithms: the steepest decent method at the very beginning<sup>1</sup> is to improve initial estimates of parameters, while the modified Gauss-Newton method is to accelerate convergence of the minimization performance. Figure A.1 presents a detailed flowchart of the algorithm which is described below. As a regression is nonlinear, the values of parameters that minimize the objective function are calculated and updated in the sequence of iterations using linear equations (A.3) and (A.4). The gradient of update in each iteration is computed by solving the following system of equations:

$$(\mathbf{C}^T \mathbf{X}_r^T \boldsymbol{\omega} \mathbf{X}_r \mathbf{C} + \mathbf{I} \cdot m_r) \mathbf{C}^{-1} \cdot \mathbf{d}^r = \mathbf{C}^T \mathbf{X}_r^T \boldsymbol{\omega} (\mathbf{y} - \mathbf{y}'(\mathbf{b}^r)) \quad (\text{A.3})$$

$$\mathbf{b}^{r+1} = \rho_r \cdot \mathbf{d}^r + \mathbf{b}^r \quad (\text{A.4})$$

where:

$\mathbf{d}^r$ , is the vector which updates the parameter estimates  $\mathbf{b}^r$  and the number of its elements is equal to the number of estimated parameters,

$r$ , subscript denotes the number of consecutive iteration,

$\mathbf{X}_r$ , is a sensitivity matrix evaluated at parameter estimates  $\mathbf{b}^r$ , with elements equal:  $X_{ij} = \partial y_i / \partial b_j$ ,  $i, j = 1, \text{NP}$ , NP denotes the number of parameters, and calculated using, for instance, forward differences,

$\mathbf{X}_r^T \boldsymbol{\omega} \mathbf{X}_r$ , is a symmetric, square matrix of dimension equal to the number of parameters,

$\mathbf{C}_r$  is a diagonal scaling matrix with element  $c_{jj}$  equal to:  $c_{jj} = (X^T \cdot \boldsymbol{\omega} \cdot X)_{jj}^{-1/2}$

$\mathbf{I}$  is an identity matrix,

$m_r$ , is the Marquardt parameter,

$\rho_r$ , is a scaling parameter.

---

<sup>1</sup>Marquardt parameter is initially set to 0.

APPENDIX A. MODIFIED GAUSS-NEWTON ALGORITHM

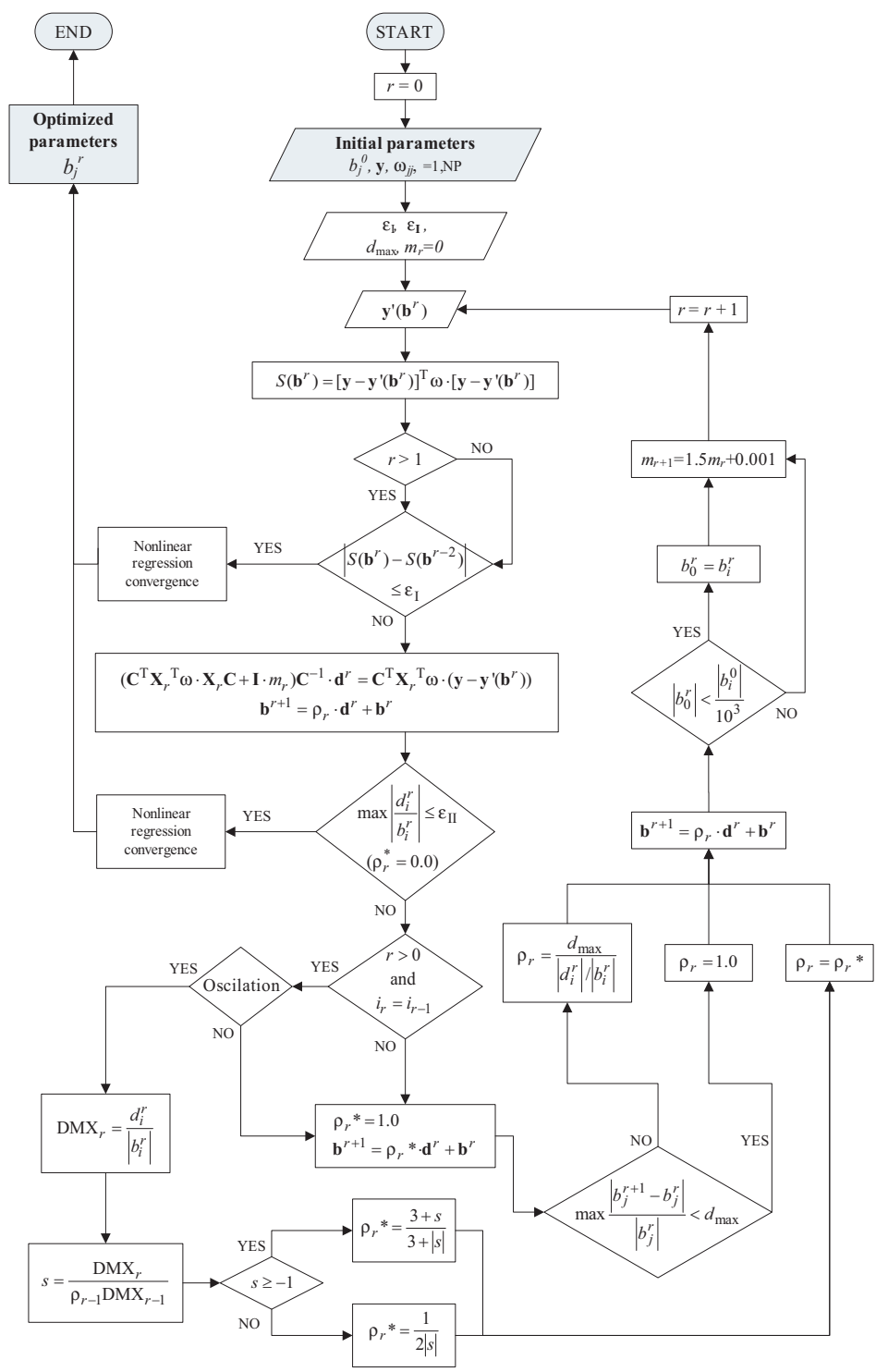


Figure A.1: Detailed flowchart of the Modified Gauss-Newton optimization algorithm.

## Marquardt parameter

The Marquardt parameter is used to accelerate the convergence of the nonlinear regression in the final stages of the iteration (Marquardt, 1963). Initially this parameter is set equal to  $m_r = 0$  and rises with each, consecutive iteration in which the vector  $\mathbf{d}^r$  defines parameter changes that are unlikely to reduce the value of the objective function (Cooley and Naff, 1990; Hill, 1998). Its new value is calculated, until the condition of the convergence is no longer met, using equation:

$$m_{r+1} = 1.5m_r + 0.001 \quad (\text{A.5})$$

## Scaling parameter

The scaling parameter is used ensure that the absolute values of fractional parameter value changes are less than user-specified value of maximal percentage change  $d_{\max}$ :

$$\max \left| \frac{b_j^{r+1} - b_j^r}{b_j^r} \right| = \max \left| \frac{d_j^r}{b_j^r} \right| < d_{\max}; j = 1, \text{NP} \quad (\text{A.6})$$

where:

$b_j^r$ , is the  $j^{\text{th}}$  element of vector  $\mathbf{b}^r$ , at estimation  $r$ ,

$b_j^{r+1}$ , is calculated from Equation (A.4) with  $\rho_r = 1.0$ .

In the case that the parameter  $b_j$  is log-transformed ( $b_j = \ln(x)$ ), the fractional change of parameter becomes  $\left[ \exp(b_j^{r+1}) - \exp(b_j^r) \right] / \exp(b_j^r) = \exp(d_j^r) - 1$ . If the largest absolute value of the NP values is bigger than  $d_{\max}$ , then  $\rho_r$  is calculated as:

$$\rho_r = \frac{d_{\max}}{|d_i^r| / |b_i^r|} \quad (\text{A.7})$$

where the  $i^{\text{th}}$  parameter is the parameter for which Equation (A.6) has the largest value; otherwise is calculated with  $\rho_r = 1.0$ . In the case of a log-transformed parameter,  $\rho_r$  is determined as:

$$\rho_r = \frac{d_{\max}}{|\exp(d_i^r) - 1|} \quad (\text{A.8})$$

however, if and  $d_{\max} < 1.0$  then  $\rho = 1.0$ . The scaling parameter is a scalar so the gradient of the vector  $d^r$  is preserved. Maximal percentage change  $d_{\max}$  is typically assigned between 1.0 and 2.0. The value 1.0 reduces excessive parameter value oscillations (Hill, 1998) whereas values less than zero do not prohibit values from changing sign because  $b_i^0$  replaces  $b_i^r$  when calculating  $\rho_r$  if  $|b_i^r| < |b_i^0| / 10^3$  as discussed below.

Moreover, the scaling parameter is introduced to avoid an oscillation that can occur when the  $i$ -th element with the smallest  $\rho_r$  in iteration  $r$  is defined by the opposite directions of  $d_i$  (Cooley, 1993). Thus, if the following condition is not satisfied:

$$\begin{cases} r > 0 \\ i_r = i_{r-1} \\ -0.7 \leq \frac{d_i^{r-1}}{d_i^r} \leq -1.3 \end{cases} \quad (\text{A.9})$$



## APPENDIX A. MODIFIED GAUSS-NEWTON ALGORITHM

oscillations are minimized using the scaling parameter which is calculated according Cooley and Naff (1990); Hill (1998) as follows:

$$\text{DMX}_r = \frac{d_i^r}{|b_i^r|} \quad (\text{A.10})$$

Then, if the following condition is executed  $r > 0$  and  $j_r = j_{r-1}$ , where  $j_r$  is the parameter with the smallest  $\rho_r$  in iteration  $r$ , the parameter  $s$  is calculated from:

$$s = \frac{\text{DMX}_r}{\rho_{r-1} \cdot \text{DMX}_{r-1}} \quad (\text{A.11})$$

And depending on the value of  $s$ , a preliminary scaling parameter  $\rho_r^*$  is calculated.

$$\rho_r^* = \begin{cases} \frac{3+s}{3+|s|} & \text{if } s \geq -1 \\ \frac{1}{2|s|} & \text{if } s < -1 \end{cases} \quad (\text{A.12})$$

When the scaling parameter is finally established, the updates for the parameters are assigned according the Equation (A.4). Sometimes, it is useful to improve parameters increasing when they are calculated near zero,  $|b_i^r| < |b_i^0|/10^3$ , by substituting  $b_i^0$  in the place of  $b_i^r$ .

## Convergence criteria

The performance of the optimization algorithm is terminated when one of two convergence conditions is achieved:

1. The weighted least-squares objective function  $S(\mathbf{b})$  changes less than user-defined amount  $\varepsilon_{\text{II}} = \Delta S(\mathbf{b})_{\text{min}}$  for three sequential iterations.
2. The largest and absolute change of the parameter is less than the percentage of the value of the parameter at the previous iteration. It is suggested that the optimization is well done with the percentage value no larger than 1% ( $\varepsilon_{\text{II}} \leq 0.01$ ).

## Efficiency and convergence test of algorithm

Numerical methods of optimization are standardly tested on benchmark problems. The efficiency, stability and convergence of algorithms can be verified by special mathematical functions for which the minimization should be effectively achieved (Medynski, 2003). The convergence and stability of the implemented Gauss-Newton algorithm was performed on four functions with known vectors containing arguments for which these functions reach the minimum. The following test functions were used to check the algorithm:

1. Rosenbrock's function - the minimum of the function is reached at the point  $x^* = (1, 1)$  and  $f(x^*) = (0)$ ; initial vector  $x^0 = (-1.2, 1.0)$ ,

$$f(x_1, x_2) = 100(x_2 - x_1^2)^2 + (1 - x_1)^2 \quad (\text{A.13})$$

## Appendix A

2. Fletcher - Powell's function - the minimum of the function is reached at the point  $x^* = (1, 0, 0)$  and  $f(x^*) = (0)$ ; initial vector  $x^0 = (-1, 0, 0)$ ,

$$f(x_1, x_2) = 100 \left\{ [x_3 - 5\theta(x_1, x_2)]^2 + \left[ \sqrt{x_1^2 + x_2^2} - 1 \right]^2 \right\} + x_3^2 \quad (\text{A.14a})$$

$$\theta(x_1, x_2) = \begin{cases} \frac{1}{\pi} \arctan\left(\frac{x_2}{x_1}\right) & \text{if } x_1 > 0 \\ 1 + \frac{1}{\pi} \arctan\left(\frac{x_2}{x_1}\right) & \text{if } x_1 < 0 \end{cases} \quad (\text{A.14b})$$

3. Powell's function - the minimum of the function is reached at the point  $x^* = (0, 0, 0, 0)$  and  $f(x^*) = (0)$ ; initial vector  $x^0 = (3, -1, 0, 1)$ ,

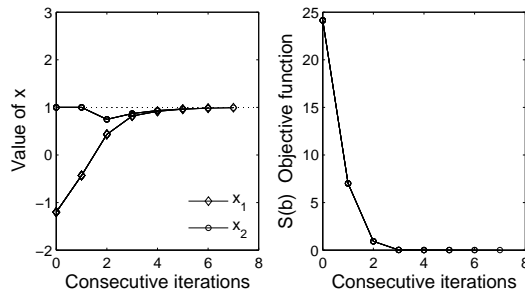
$$f(x_1, x_2, x_3, x_4) = (x_1 + 10x_2)^2 + 5(x_3 - x_4)^2 + (x_2 - 2x_3)^4 + 10(x_1 - x_4)^4 \quad (\text{A.15})$$

4. Wood's function the minimum of the function is reached at the point  $x^* = (1, 1, 1, 1)$  and  $f(x^*) = (0)$ ; initial vector  $x^0 = (0.2, -1.2, 4, -3)$ ,

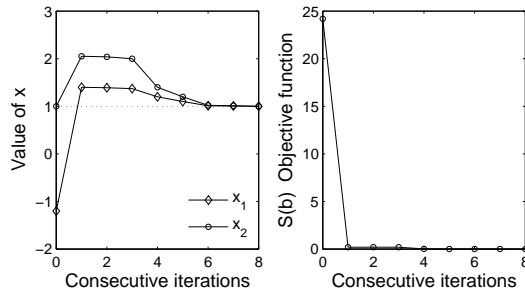
$$f(x_1, x_2, x_3, x_4) = 100(x_2 - x_1^2)^2 + (1 - x_1)^2 + 90(x_4 - x_3^2)^2 + (1 - x_3)^2 + 10.1 \{ (x_2 - 1)^2 + (x_4 - 1)^2 \} + 19.8(x_2 - 1)(x_4 - 1) \quad (\text{A.16})$$

In order to check the efficiency of the optimization code, the results from first three verification tests are compared with the results from tests performed by Ou and Tang (1994). In their work two algorithms were employed: the conjugate method of Fletcher and Reeves to find the direction of the minimum value, and Powell's quadratic interpolation method to determine the optimum scaling parameter. Figures A.2, A.3, A.4 and A.5 present the comparisons of optimization records for four functions using the Modified Gauss-Newton algorithm and the conjugate algorithm. It can be seen that the Modified Gauss-Newton and the conjugate method algorithm converge in the analogous number of iterations for Rosenbrock's and Powell's function, whereas in the case of the Fletcher-Powell's function the first algorithm is six times faster. An additional test on the Wood's function with some local minimums confirms the stability of the algorithm. On the basis of the above benchmark tests, the effectiveness and convergence of the implemented Modified Gauss-Newton optimization code have been verified.

APPENDIX A. MODIFIED GAUSS-NEWTON ALGORITHM

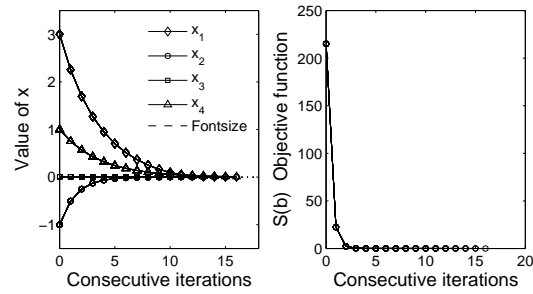


(a) Modified Gauss-Newton

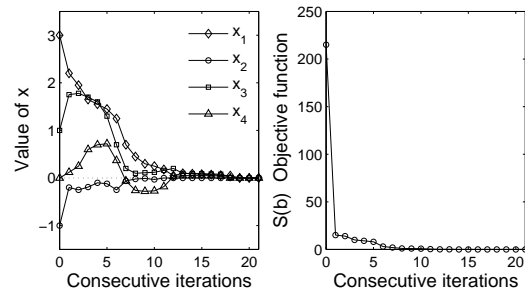


(b) Conjugate algorithm

Figure A.2: Minimization of the Rosenbrock's function.



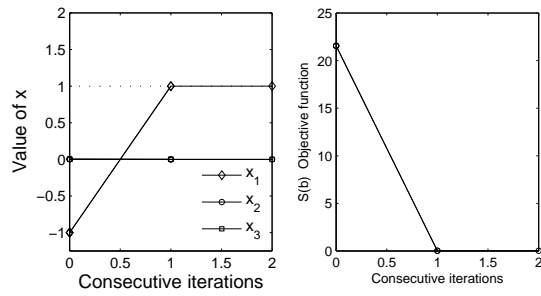
(a) Modified Gauss-Newton



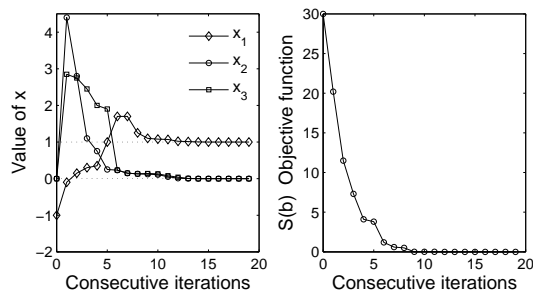
(b) Conjugate algorithm

Figure A.3: Minimization of the Powell's function.

Appendix A



(a) Modified Gauss-Newton



(b) Conjugate algorithm

Figure A.4: Minimization of the Fletcher-Powell's function.

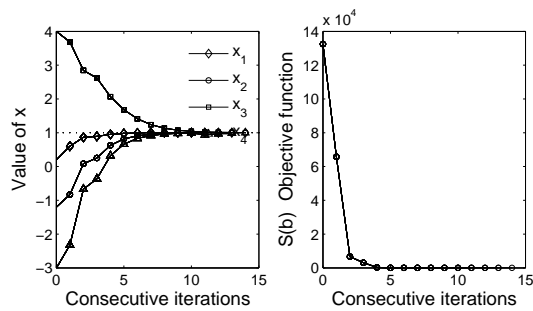


Figure A.5: Minimization of the Wood's function by the Modified Gauss-Newton algorithm.

# Appendix B

## Material Data for Numerical Simulations

Table B.1: Reference parameters for numerical model of SBPT used for parametric study in Section 7.1.1.

Parameter	Symbol	Value
Poisson's ratio	$\nu$	0.32
Slope of primary consolidation	$\lambda$	0.1
Slope of secondary consolidation	$\kappa$	0.05
Preconsolidation pressure	$p_{co}$	200 kPa
Slope of critical state line	$M$	1.0
Coefficient of earth pressure 'at rest'	$K_o$	1.0
Overconsolidation ratio	$R_p$	2.0
Initial void ratio	$e_o$	1.0
Degree of saturation	$S$	1.0
Fluid bulk modulus	$K_f$	2.2 GPa
Unit weight of water	$\gamma_f$	10 kN/m <sup>3</sup>
Cavity strain rate	$\dot{\epsilon}_c$	1.0 %/min

Table B.2: Reference model parameters ( $I_r = 25$ ) adopted in the analysis of the cone penetration model in Section 7.2.2.

Parameter	Symbol	Value
Poisson's ratio	$\nu$	0.3
Initial voids ratio	$e_o$	1.0
Coefficient of earth pressure 'at rest'	$K_o$	1.0* kPa
Initial effective vertical stress	$\sigma'_{vo}$	100* kPa
Initial total vertical stress	$\sigma_{vo}$	100* kPa
Initial mean effective stress	$p'_o$	100 kPa
Slope of unloading-reloading curve	$\kappa$	0.1**
Plastic strain ratio	$\Lambda$	0.75
Overconsolidation ratio	$R_p$	1.5**
Slope of critical state line	$M$	1.0
Strength anisotropy ratio ( $= M_e/M_c$ )	$k_a$	0.78
Soil unit weight	$\gamma$	0.0 kN/m <sup>3</sup>
Fluid bulk modulus	$K_f$	2.2e6 kPa
Unit weight of water	$\gamma_f$	10 kN/m <sup>3</sup>

\* adjustable to various initial stress anisotropy parameters  $\Delta$

\*\* adjustable to various rigidity index  $I_r$



# Appendix C

## $R_p$ versus OCR in the MCC

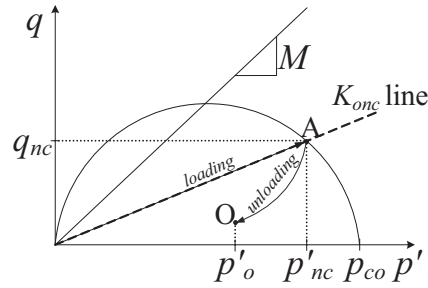


Figure C.1: Definition of initial preconsolidation pressure  $p_{co}$  and overconsolidation ratio  $R_p$  in terms of the mean effective stress.

In the MCC, the overconsolidation ratio is defined as  $R_p = p_{co}/p'_o$ . The relationship between  $R_p$  and OCR can be established using expression for the plastic surface of the MCC (Figure C.1). The virgin loading during formation of the deposit expands the yield surface due to the plastic straining and reaches the point A. This point corresponds to the maximum vertical effective pressure acting on the soil,  $\sigma'_{vnc}$  so the effective stress at this point can be derived in the following form:

$$p'_{nc} = \frac{1}{3}\sigma'_{vnc}(1 + 2K_{onc}) \quad \text{and} \quad q_{nc} = \sigma'_{vnc}(1 - K_{onc}) \quad (C.1)$$

By introducing  $p'_{nc}$  and  $q_{nc}$  into the equation of the yield surface (Equation (4.1)):

$$\frac{\sigma'^2_{vnc}(1 - K_{onc})^2}{\frac{1}{3}\sigma'_{vo}(1 + 2K_o)} - M^2\frac{1}{3}\sigma'_{vnc}(1 + 2K_{onc})(R_p - \frac{p'_{nc}}{p'_o}) = 0 \quad (C.2)$$

and defining  $\text{OCR} = \sigma'_{vnc}/\sigma'_{vo}$ :

$$\frac{9\text{OCR}(1 - K_{onc})^2}{M^2(1 + 2K_o)(1 + 2K_{onc})} - \left(R_p - \frac{p'_{nc}}{p'_o}\right) = 0 \quad (C.3)$$

the relationship between  $R_p$  and OCR can be written as:

$$R_p = \text{OCR} \frac{9(1 - K_{onc})^2 + M^2(1 + 2K_{onc})^2}{M^2(1 + 2K_o)(1 + 2K_{onc})} \quad (C.4)$$





# Appendix D

## Pattern Generation for CPTU

The scheme presents an algorithm for generation of parameter permutations used in numerical generation of training patterns for CPTU test (see Section 8.2.2). Parameter intervals are provided in Table 8.5.

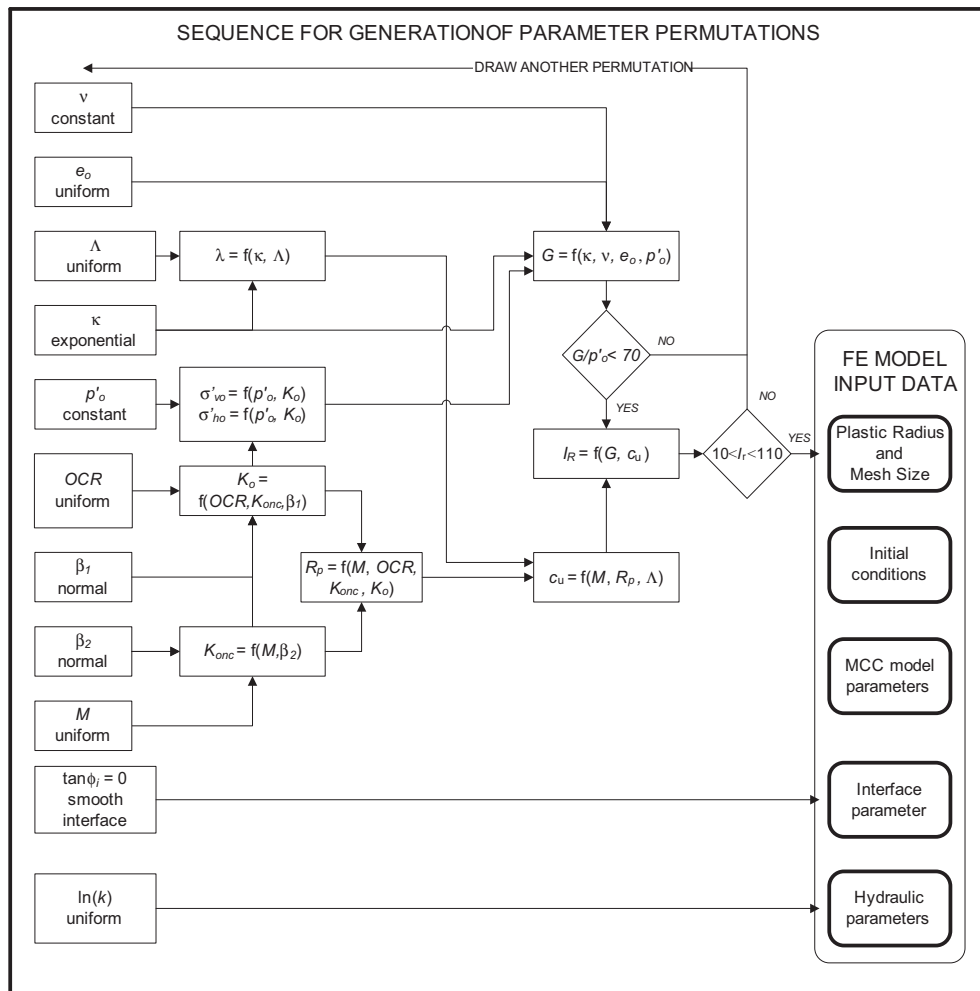


Figure D.1: Algorithm for generation of parameter permutations used in training pattern generation.



# Appendix E

## GUI for CPTU Data

This appendix demonstrates a graphical user interface (GUI) designed for parameter prediction from CPTU data according to the flowchart presented in Figure 8.16. Two modules simplify the process of input data treatment, selection of a suitable neural network, its activation, as well as a dynamic upgrade of existing database of trained NNs.

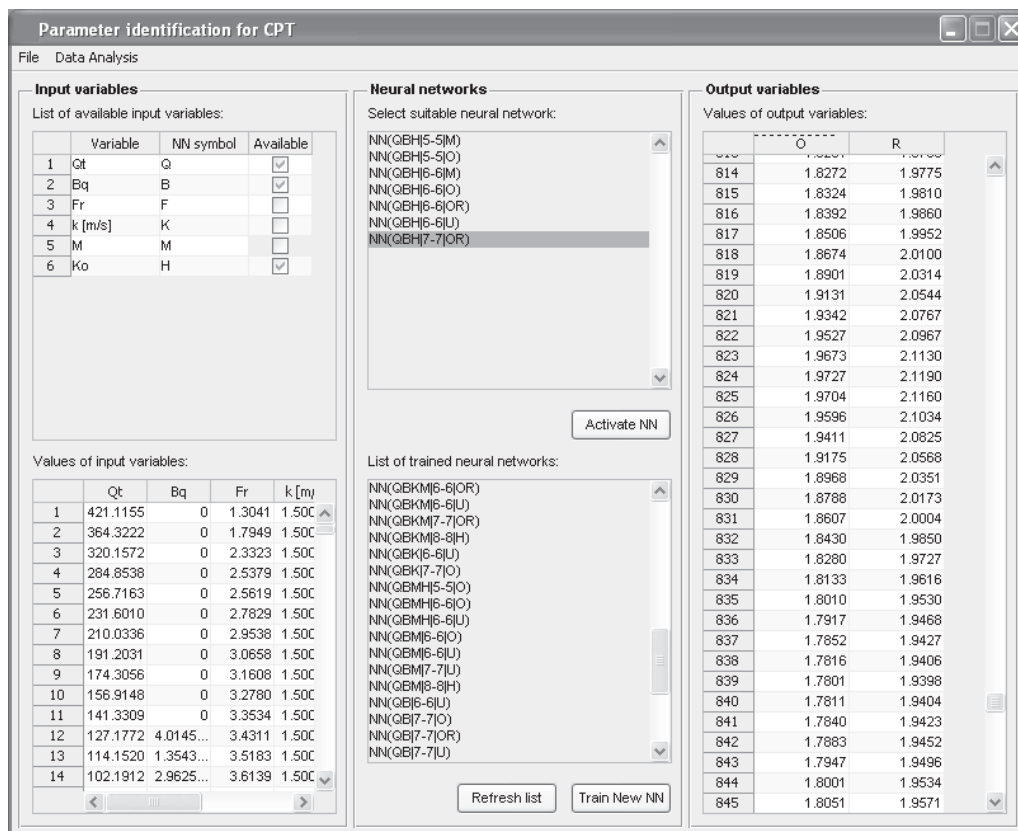


Figure E.1: Graphical user interface for treatment of available CPTU input data, selecting neural networks and activating a suitable neural network.

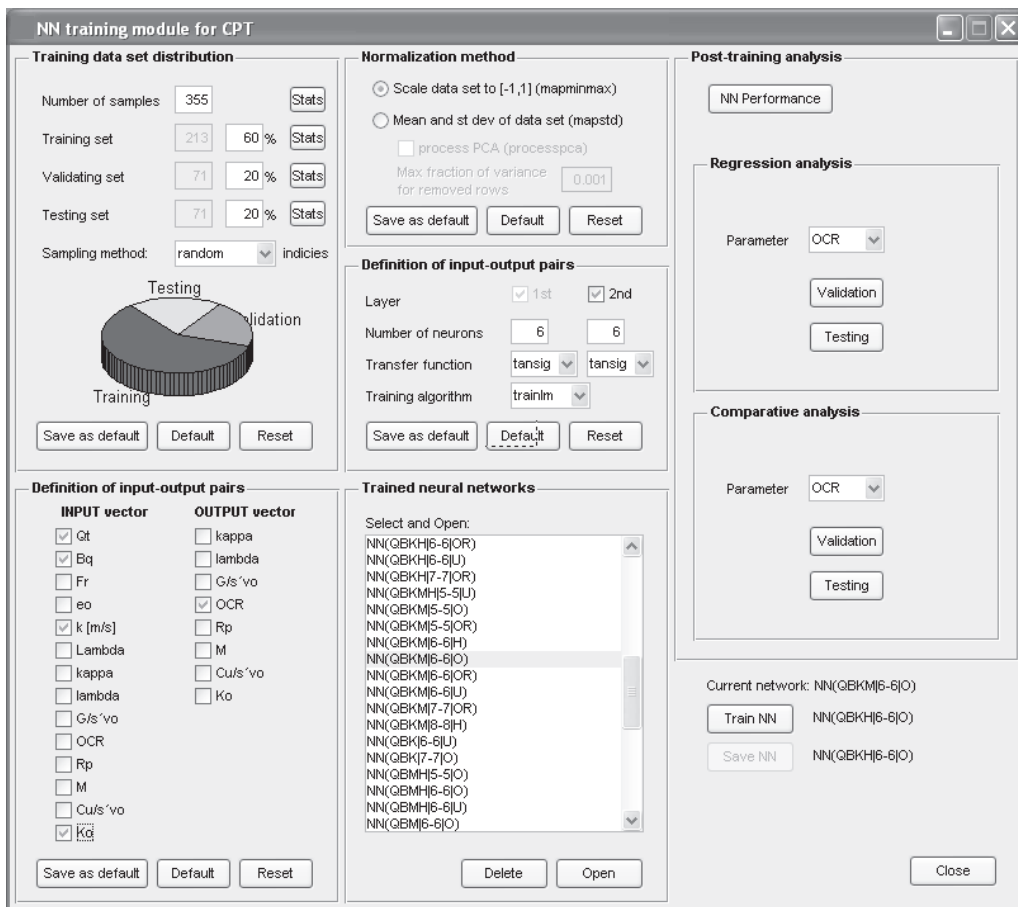


Figure E.2: Graphical user interface for NN training based on collected CPTU data and other available information.

# Appendix F

## NN Training for CPTU Data

The appendix provides supplementary results of post-training analyzes presented in Section 8.2.5.

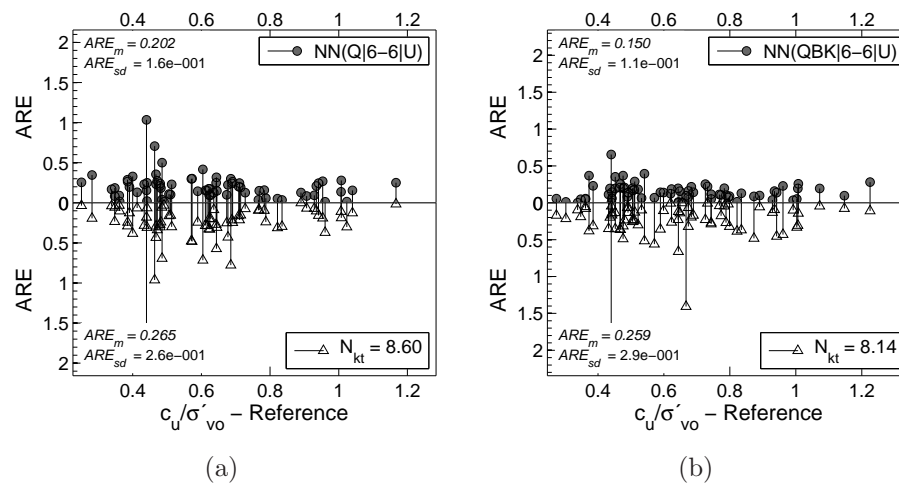


Figure F.1: Comparison of predictions and absolute relative errors for  $c_u$  derived from the empirical method and the neural networks. Post-training analysis for 71 numerical patterns previously unknown to the trained neural network.

## Appendix F

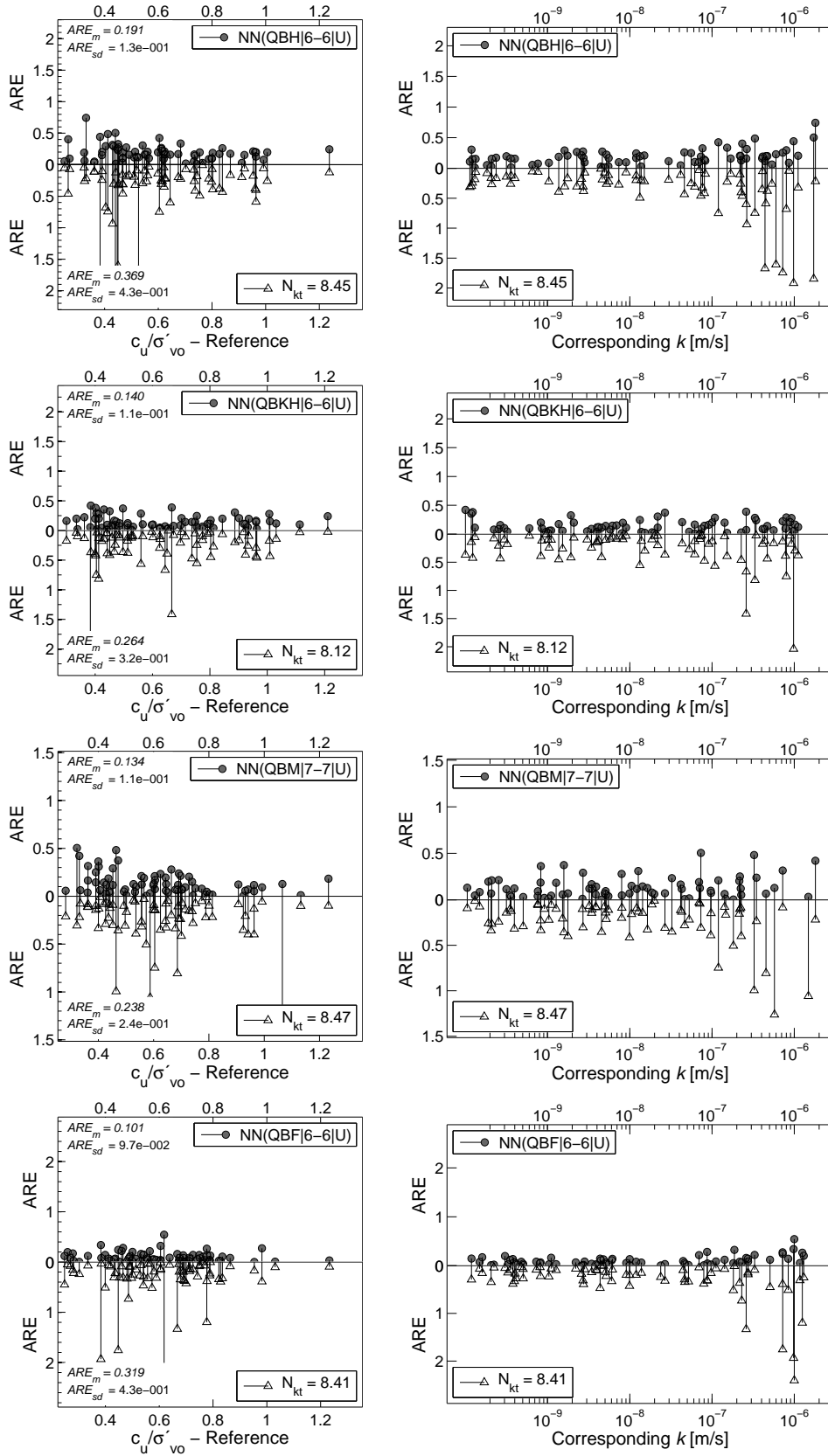


Figure F.2: Comparison of predictions and absolute relative errors for  $c_u$  derived from the empirical method and the neural networks. Post-training analysis for 71 numerical patterns previously unknown to the trained neural network.

APPENDIX F. NN TRAINING FOR CPTU DATA

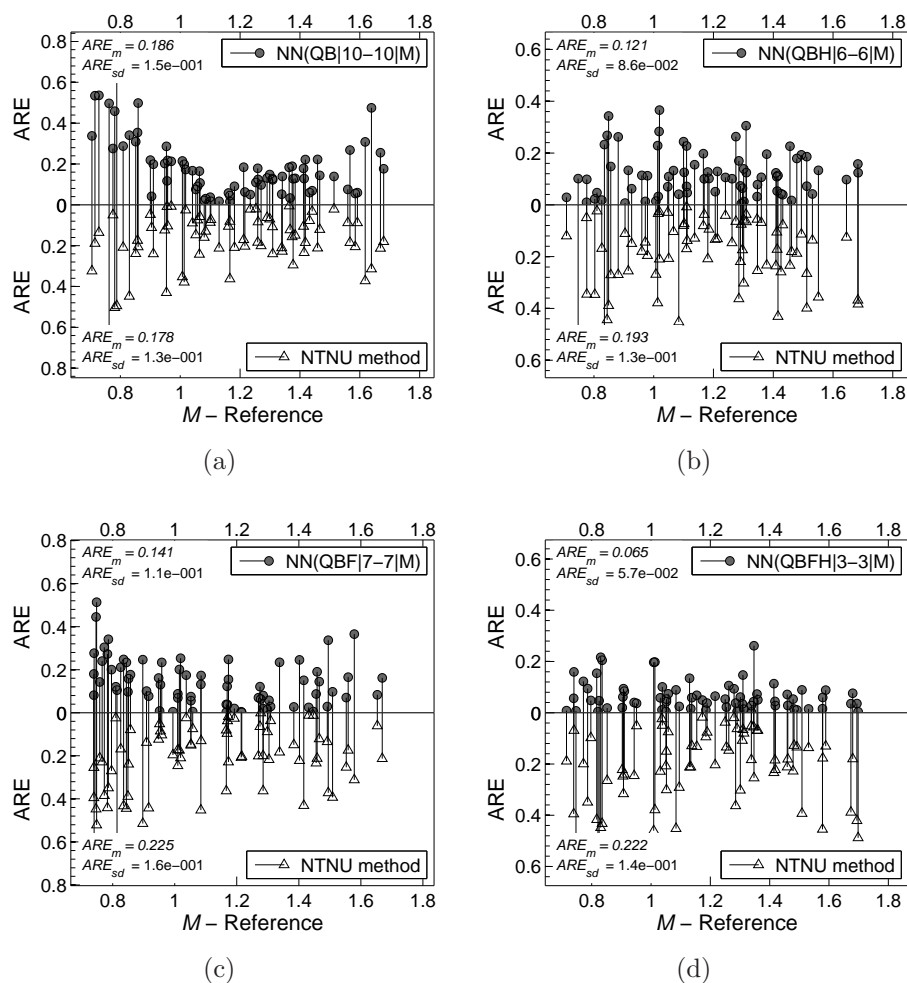


Figure F.3: Comparison of predictions and absolute relative errors for parameter  $M$  derived from the NTNU method (Equation (6.44)) and neural networks. Post-training analysis for 71 numerical patterns previously unknown to the trained neural network.

Appendix F

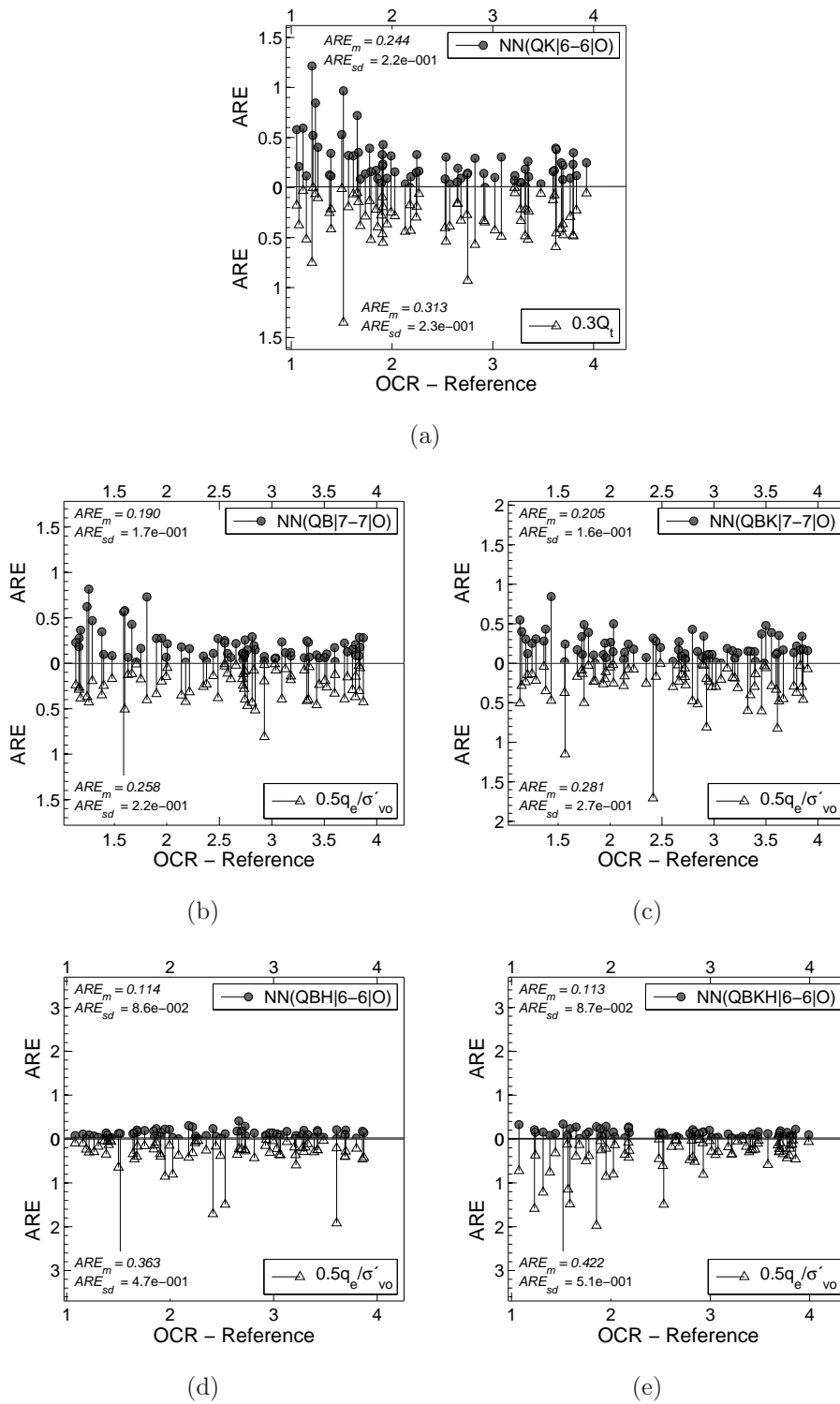


Figure F.4: Comparison of predictions and absolute relative errors for parameter OCR derived from the empirical methods and neural networks. Post-training analysis for 71 numerical patterns previously unknown to the trained neural network.



APPENDIX F. NN TRAINING FOR CPTU DATA

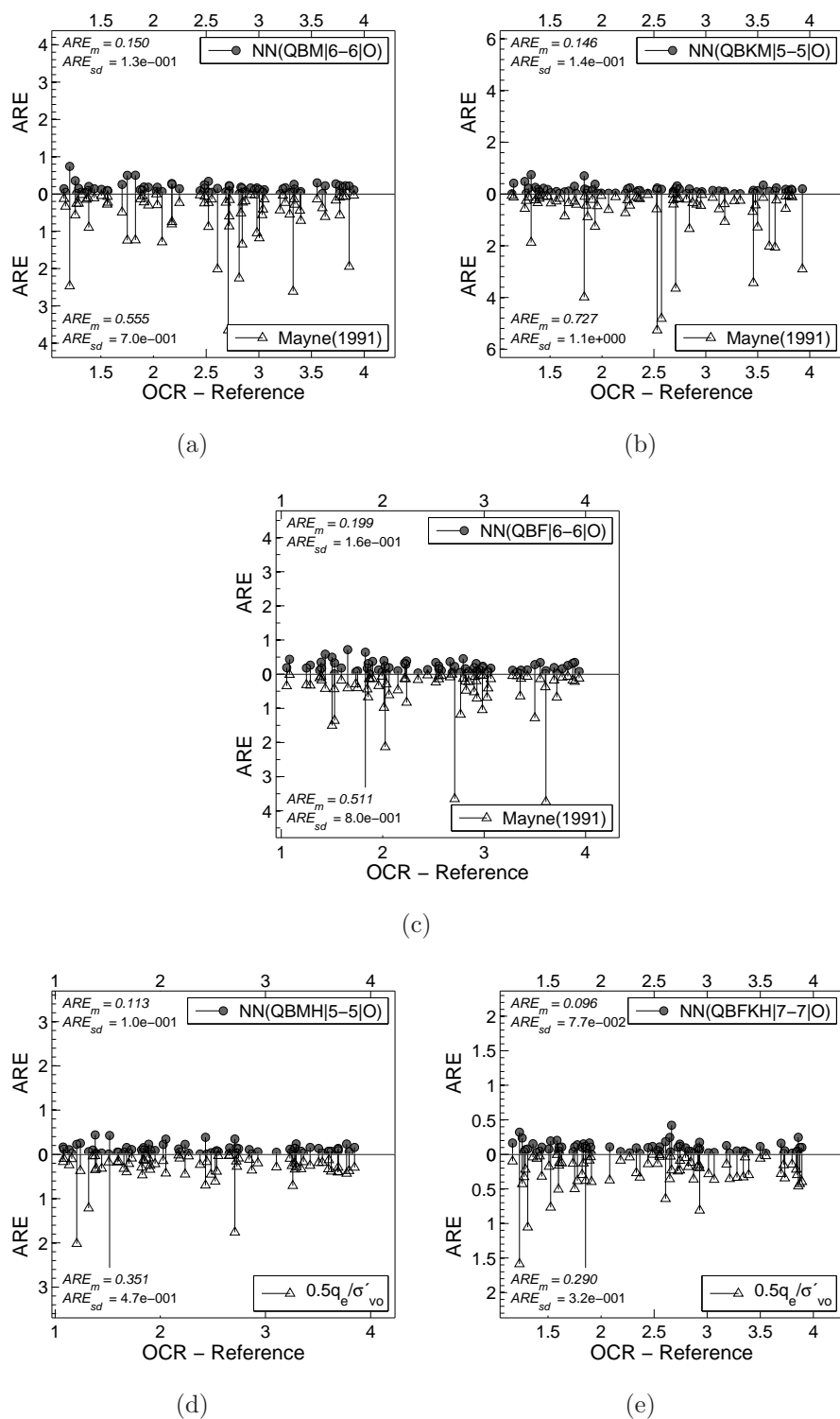


Figure F.5: Comparison of predictions and absolute relative errors for parameter OCR derived from the empirical methods and neural networks. Post-training analysis for 71 numerical patterns previously unknown to the trained neural network.

Appendix F

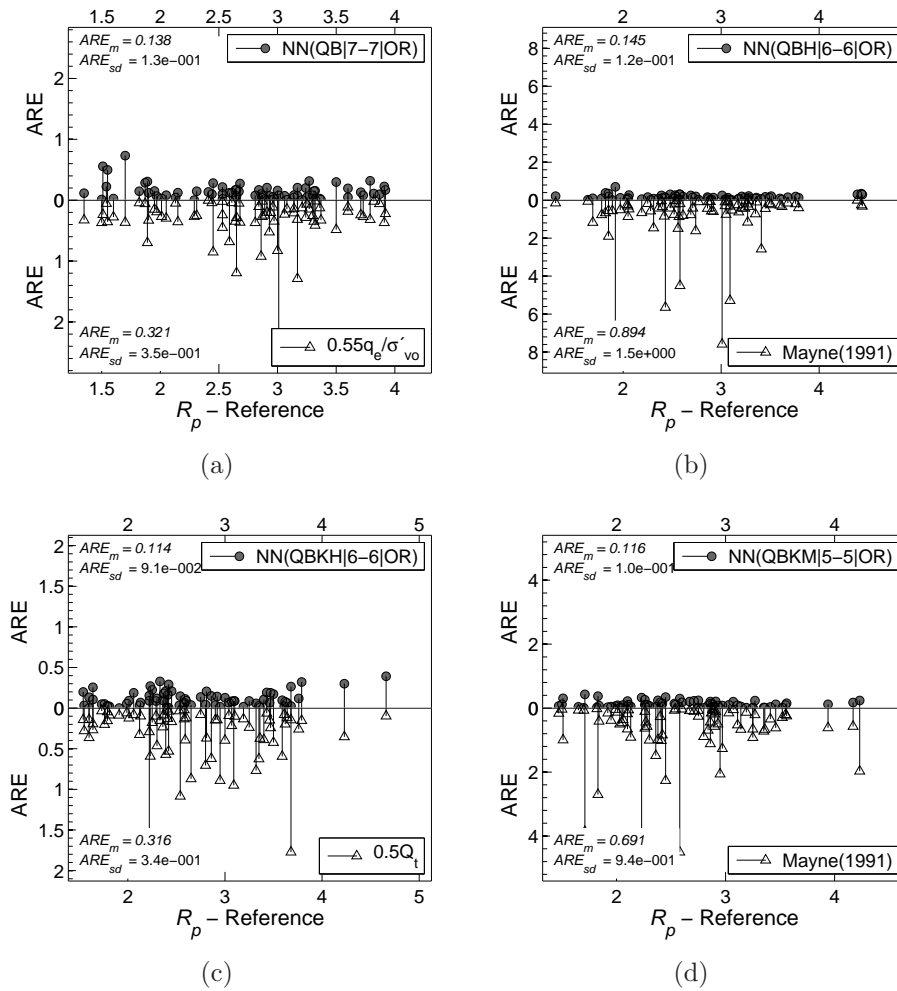


Figure F.6: Comparison of predictions and absolute relative errors for parameter  $R_p$  derived from the empirical methods and neural networks. Post-training analysis for 71 numerical patterns previously unknown to the trained neural network.

APPENDIX F. NN TRAINING FOR CPTU DATA

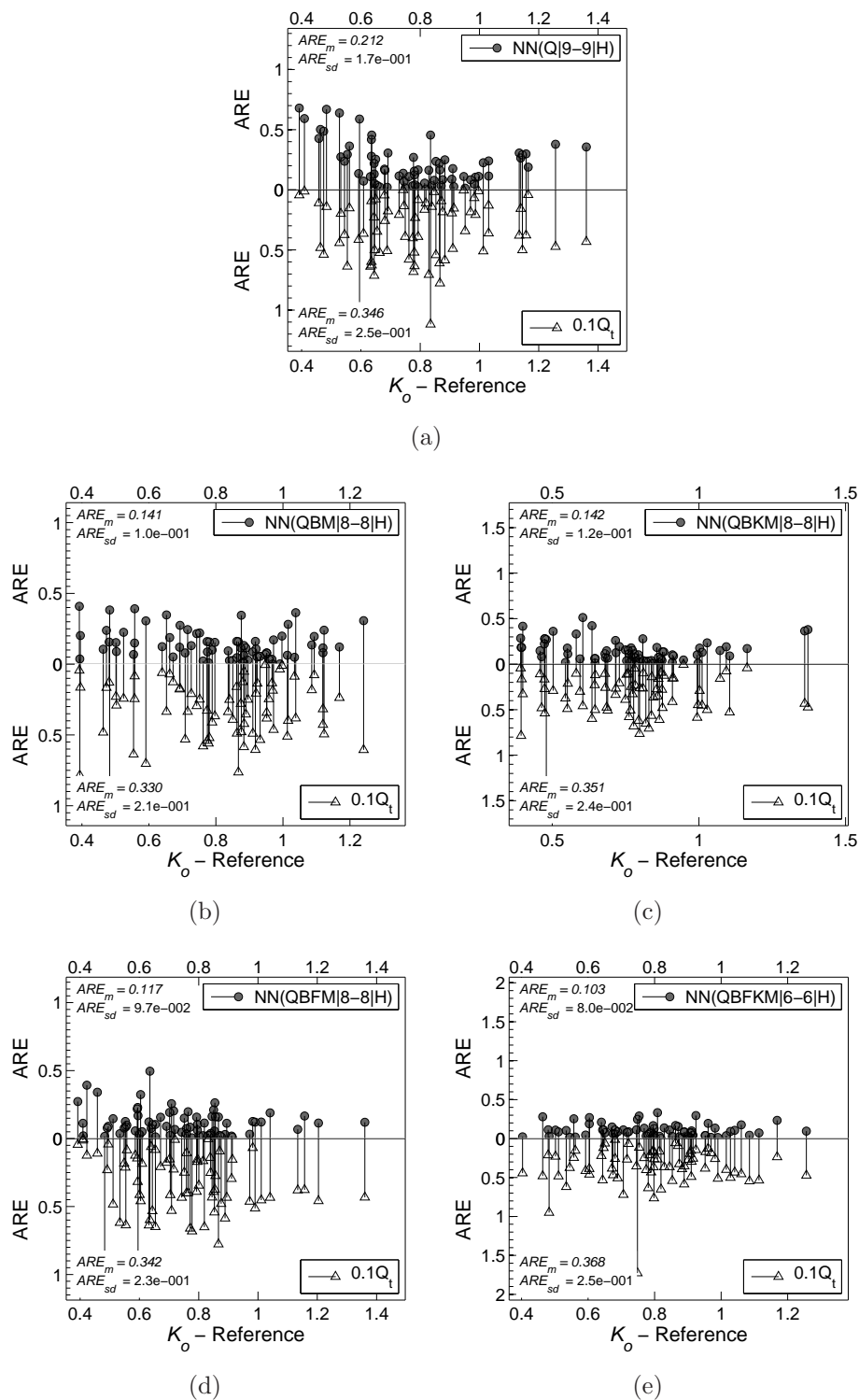


Figure F.7: Comparison of predictions and absolute relative errors for parameter  $K_o$  derived from the empirical method (Equation (6.53)) and neural networks. Post-training analysis for 71 numerical patterns previously unknown to the trained neural network.

Appendix F

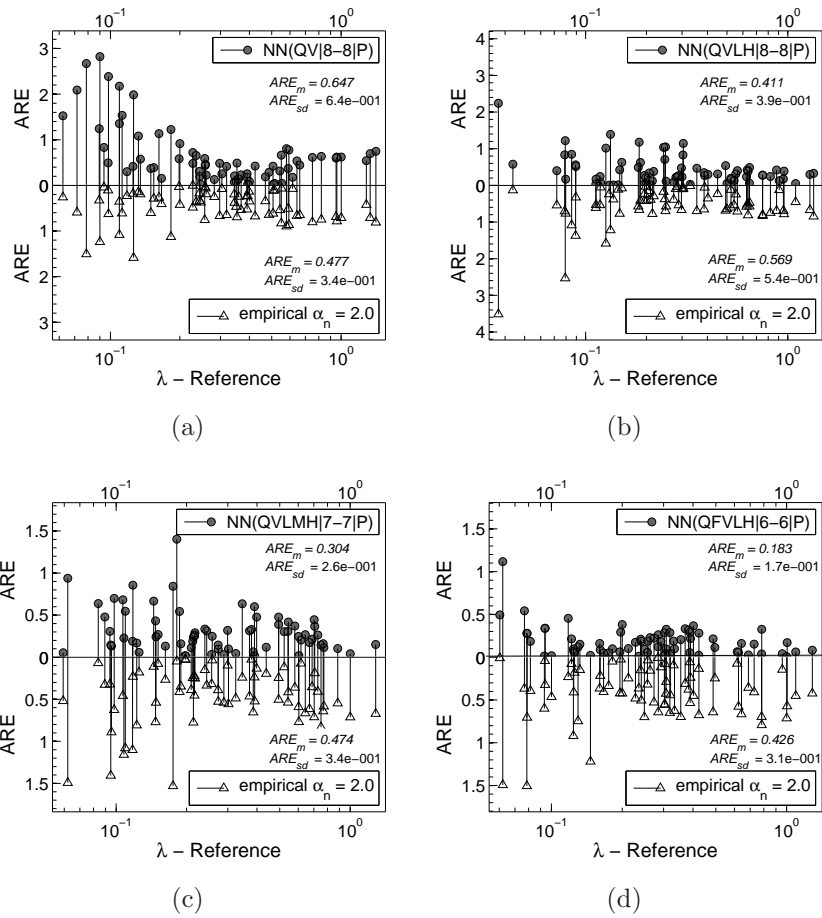


Figure F.8: Comparison of predictions and absolute relative errors for parameter  $\lambda$  derived from the empirical method and neural networks. Post-training analysis for 71 numerical patterns previously unknown to the trained neural network.

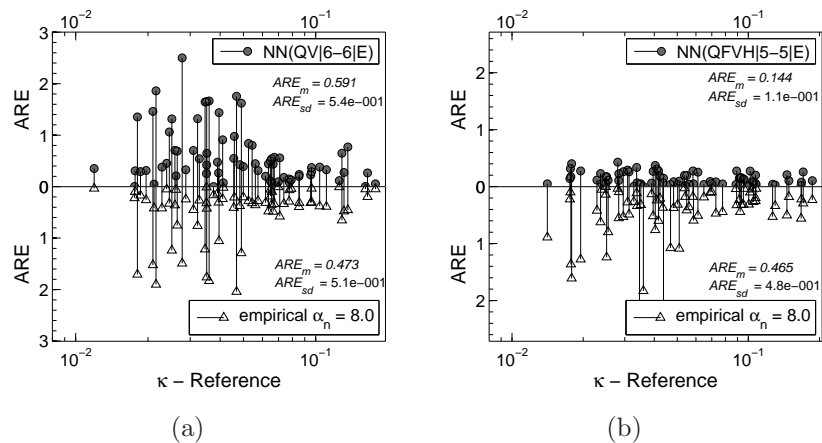


Figure F.9: Comparison of predictions and absolute relative errors for parameter  $\kappa$  derived from the empirical method and neural networks. Post-training analysis for 71 numerical patterns previously unknown to the trained neural network.

# Appendix G

## Material Data

### G.1 Database of discrete piezocone results from clay sites

This appendix provides results from piezocone tests in normally- and lightly overconsolidated clays used in 8.2 to perform regression analysis for trained neural networks. The results for 49 characterization sites were selected from the extensive database compiled in Chen and Mayne (1994). Each of 141 data points which corresponds to a given testing depth, contains the values of overconsolidation ratio obtained by oedometer tests ( $OCR = \sigma'_c/\sigma'_{vo}$ ) and the piezocone measurements: corrected cone tip resistance  $q_t$  and the pore pressure measured behind the tip  $u_2$ <sup>1</sup>. The database also provides the values of the *in situ* total and effective vertical stresses,  $\sigma_{vo}$  and  $\sigma'_{vo}$  which are necessary to normalize cone measurements. Additional information for tested soils was compiled by the author from available sources. This data includes the values of slope of critical state line  $M$  obtained through the laboratory tests and estimations of  $K_o$ . Some of  $M$  values were directly found in Chen and Mayne (1994), others in the source publications (refer to the footnotes). As regards  $K_o$ , the estimates were collected from either reference sources or estimated through current interpretation methods (refer to the footnotes).

---

<sup>1</sup>Chen and Mayne (1994) provided also measurements of  $u_1$  which were used in certain cases to estimate  $K_o$  by means of formula  $K_o = 0.11(u_1 - u_2)/\sigma'_{vo} + 0.5$  (Sully and Campanella, 1991).

## Appendix G

Table G.1: Database of piezocone results from clay sites extracted from Chen and Mayne (1994).

Soil Site	Clay Type	Data Point	OCR OED	$\sigma_{vo}$ (kPa)	$\sigma'_{vo}$ (kPa)	$q_t$ (kPa)	$u_2$ (kPa)	$M$ (-)	$K_o$ (-)
Alex Fraser Bridge	silt	1	1.38	740	362	1855	810		
Arnprior	intact	2	1.60	180	80	594	459		
Arnprior	intact	3	1.60	252	112	824	608		
Arnprior	intact	4	1.60	324	144	946	702		
Bakklandet	intact	5	3.30	91.8	82	616	470		0.58 <sup>4</sup>
Bakklandet	intact	6	1.90	326.5	199	920	728		0.55 <sup>4</sup>
Bakklandet	intact	7	1.80	406	238	1096	905		0.55 <sup>4</sup>
Baton Rouge	fissured	8	4.00	524.5	290	3123	31	1.13	1.35 <sup>4</sup>
Baton Rouge	fissured	9	3.40	620.5	336	3453	1281	1.13	0.85 <sup>4</sup>
Boston Blue Clay	intact	10	2.96	214.7	102.8	680	394	1.06 <sup>2</sup>	0.90 <sup>3</sup>
Boston Blue Clay	intact	11	1.98	304.7	141.7	1013	688	1.06	0.73 <sup>3</sup>
Boston Blue Clay	intact	12	1.48	352.6	162.5	1080	798	1.06	0.63 <sup>3</sup>
Boston Blue Clay	intact	13	1.37	521.2	235.5	1401	1013	1.06	0.60 <sup>3</sup>
Boston Blue Clay	intact	14	1.29	521.9	235.8	1401	1013	1.06	0.59 <sup>3</sup>
Boston Blue Clay 2	intact	15	3.40	233	104	895	554	1.06	0.95 <sup>3</sup>
Boston Blue Clay 2	intact	16	2.20	320	150	1078	714	1.06	0.75 <sup>3</sup>
Boston Blue Clay 2	intact	17	1.60	372	173	1036	767	1.06	0.65 <sup>3</sup>
Boston Blue Clay 2	intact	18	1.40	425	196	1074	774	1.06	0.61 <sup>3</sup>
Boston Blue Clay 2	intact	19	1.20	476	217	1226	844	1.06	0.56 <sup>3</sup>
Bothkennar	intact	20	3.54	41.4	30	295	127		
Charles City County	intact	21	2.95	383.2	203.2	2873	1394		
Colebrook Road	intact	22	1.59	94	52	353	64		
Colebrook Road	intact	23	1.19	212	117	592	299		
Colebrook Road	intact	24	1.10	268	120	640	340		
Colebrook Road	intact	25	1.00	326	145	698	461		
Cowden	fissured	26	2.80	387	227	2366	472		0.95 <sup>4</sup>
Drammen	silty clay	27	1.50	122	65	405	280	1.23 <sup>2</sup>	0.68 <sup>3,4</sup>
Drammen	silty clay	28	1.50	157	80	462	345	1.23	0.68 <sup>3,6</sup>
Drammen	silty clay	29	1.20	229	113	563	405	1.23	0.56 <sup>3,5</sup>
Drammen	silty clay	30	1.20	178	91	521	303	1.23	0.56 <sup>3,5</sup>
Drammen 2	silty clay	31	1.53	140	73	473	263	1.23	0.68 <sup>3,3</sup>
Drammen 2	silty clay	32	1.48	105	58	384	197	1.23	0.68 <sup>3,3</sup>
Drammen 2	silty clay	33	1.33	208	102	494	310	1.23	0.60 <sup>5</sup>
Drammen 2	silty clay	34	1.08	288	143	631	463	1.23	0.54 <sup>5</sup>
Drammen 2	silty clay	35	1.17	320	155	755	531	1.23	0.56 <sup>5</sup>
Eberg	intact	36	2.78	55	40	230	183		
Eberg	intact	37	2.19	87	52	319	200		
Emmerstad	quick clay	38	3.90	107	73	370	200		
Emmerstad	quick clay	39	2.40	163	108	450	325	1.61	0.62 <sup>6</sup>
Emmerstad	quick clay	40	1.90	221	144	460	350	1.61	0.55 <sup>6</sup>
Emmerstad	quick clay	41	1.50	278	179	475	390		0.54 <sup>6</sup>
Emmerstad 2	quick clay	42	3.29	69.3	35	350	115		
Emmerstad 2	quick clay	43	2.84	93.6	45	430	185		
Emmerstad 2	quick clay	44	2.50	120.7	52	500	255		
Fort Road	intact	45	1.60	260	126.6	814	448		
Fort Road	intact	46	1.28	420	185.5	1050	700		
Glava	intact silt	47	4.10	200	105	852	581		
Glava	intact silt	48	2.60	333	168	1050	799	1.19	0.62 <sup>4</sup>
Gloucester	aged NC leda	49	3.22	21	21	475	8	1.11 <sup>6</sup>	0.93 <sup>5</sup>
Gloucester	aged NC leda	50	2.68	74	39	517	254	1.11	0.85 <sup>5</sup>
Grangemouth	soft alluv.	51	3.00	32	32	365	136	1.42 <sup>7</sup>	0.90 <sup>4</sup>
Grangemouth	soft alluv.	52	1.43	112	63	417	249	1.42	0.62 <sup>4</sup>
Haga 2	marine	53	4.00	88	88	1045	662	1.21	1.29 <sup>8</sup>
Haga 2	marine	54	2.20	118	118	885	654	1.21	0.82 <sup>8</sup>
Haga 2	marine	55	2.00	135	135	924	735	1.21	0.76 <sup>8</sup>
Halsen	silt	56	2.00	190	100	673	225		0.67 <sup>8</sup>
Hamilton AFB	buy mud	57	3.03	39.5	36.8	350	-30	1.20	0.91 <sup>9</sup>
Hamilton AFB	buy mud	58	1.43	88.5	52.5	310	43	1.20	
Hamilton AFB	buy mud	59	1.22	159.5	75.5	367	233	1.20	0.70 <sup>9</sup>
Hamilton AFB	buy mud	60	1.54	221.1	95.4	510	360	1.20	0.75 <sup>9</sup>
Inchinnan	intact	61	1.52	133	84	355	219		
Inchinnan	intact	62	1.27	171	102	445	283		
Keelung River	intact	63	2.74	135	63	314	86		
Keelung River	intact	64	1.43	211	98	607	288		
Keelung River	intact	65	1.72	213	99	540	247		
Kobe City 1	intact	66	1.00	94	42	113	66		
Kobe City 1	intact	67	1.00	161	72	299	141		
Kringalik Plateau	fissured	68	4.30	531	126	1485	248		

<sup>2</sup>Mayne and Kulhawy (1982)

<sup>3</sup>Mayne and Kulhawy (1988)

<sup>4</sup>Estimated using Sully and Campanella (1991) formula

<sup>5</sup>Estimated using  $K_o = 0.515OCR^{0.508}$  (Mayne and Kulhawy, 1988)

<sup>6</sup>Konrad and Law (1987)

<sup>7</sup>Mayne (1991)

<sup>8</sup>Estimated using  $K_o = 0.44OCR^{0.77}$  (Mayne and Kulhawy, 1988)

<sup>9</sup>Masood and Mitchell (1993)

APPENDIX G. MATERIAL DATA

Table G.1 – Continued

Soil Site	Clay Type	Data Point	OCR OED	$\sigma_{vo}$ (kPa)	$\sigma'_{vo}$ (kPa)	$q_t$ (kPa)	$u_2$ (kPa)	$M$ (-)	$K_o$ (-)
Kringalik Plateau	fiured	69	2.70	686	206	2054	857		
Kringalik Plateau	fiured	70	2.50	813	271	2483	679		
Lierstranda	intact	71	2.50	90	60	294	227		0.83 <sup>9</sup>
Lierstranda	intact	72	2.50	163	93	724	367		0.46 <sup>9</sup>
Lierstranda	intact	73	1.75	236	126	851	524		0.72 <sup>9</sup>
Lierstranda	intact	74	1.10	318	158	872	605		0.51 <sup>9</sup>
Lierstranda	intact	75	1.00	391	191	982	699		0.49 <sup>9</sup>
Louiseville	aged NC leda	76	3.32	32.3	26	204	60		
Louiseville	aged NC leda	77	1.90	180	90	671	492		
Louiseville	aged NC leda	78	1.60	324	154	1047	712		
Lower 232nd ST.	clay silt	79	3.27	86.5	36.5	502	254		
Lower 232nd ST.	clay silt	80	1.00	352	147	824	643		
Munkedal	intact	81	2.27	78	46	570	331		0.62 <sup>4</sup>
Munkedal	intact	82	1.15	311	161	826	598		0.64 <sup>4</sup>
Munkedal	intact	83	1.12	384	259	958	716		0.54 <sup>4</sup>
Museum Park	intact	84	1.30	327	147	875	509		
Museum Park	intact	85	1.00	381	171	862	618		
Museum Park	intact	86	1.00	436	196	1073	796		
Norco	intact	87	1.18	162.5	84	255	190	1.04	0.53 <sup>4</sup>
Norco	intact	88	1.03	238.7	119	470	296	1.11	0.53 <sup>4</sup>
Norco	intact	89	1.60	530.7	256	1153	680	1.10	0.53 <sup>4</sup>
Norco	intact	90	1.58	623.6	295	1145	784	1.10	0.53 <sup>4</sup>
Norkfolk Road	intact	91	1.66	97	69	253	132	1.05	0.67 <sup>5</sup>
Norkfolk Road	intact	92	1.60	162	102	413	182	1.10	0.65 <sup>5</sup>
Norkfolk Road	intact	93	1.40	444	244	933	647	1.15	0.61 <sup>5</sup>
Norrkoping	intact	94	1.51	185	80	470	318	1.29	0.59 <sup>4</sup>
North Sea GC	marine	95	2.50	68	34	295	175	1.46	0.82 <sup>5</sup>
North Sea GC	marine	96	2.18	114	57	444	265	1.46	0.77 <sup>5</sup>
North Sea GC	marine	97	2.55	148	74	544	318	1.46	0.83 <sup>5</sup>
North Sea S	intact	98	1.40	922	410	2502	1427	1.46	0.62 <sup>4</sup>
NRCC	leda	99	2.84	160	72	827	526		
NRCC	leda	100	2.26	208	90	993	614		
ONsoy 2	marine	101	1.20	404	164	1020	730	1.37	0.74 <sup>9</sup>
Ottawa STP	leda	102	4.07	114	77	1276	821		
Ottawa STP	leda	103	3.29	212.5	124	1660	1083		
Ottawa STP	leda	104	3.17	297.7	164	1843	1205		
Pontida	intact	105	3.60	142.5	80.7	705	420		
Pontida	intact	106	2.95	256.5	135.8	859	550		
Pontida	intact	107	2.95	389.5	200.2	2018	1600		
Port Huron	intact	108	3.80	33	28	890	-3		
Port Huron	intact	109	2.56	170	112.7	1077	278		
Port Huron	intact	110	2.15	287.2	170.1	1188	444		
Port Huron	intact	111	2.40	433.8	241.9	1779	754		
Port Huron	intact	112	2.27	527.5	287.9	2365	846		
Porto Tolle	intact	113	2.39	231.2	118.4	672	227		0.69 <sup>10</sup>
Porto Tolle	intact	114	1.47	426.7	210.3	1163	515		0.45 <sup>10</sup>
Porto Tolle	intact	115	1.26	490	240	1387	560		10
Prince George Coun	intact	116	2.50	91.5	72	700	19		
Prince George Coun	intact	117	1.58	176	111	700	107		
Singapore	intact	118	2.05	306	131	969	562		
Singapore	intact	119	1.75	506	231	1276	812		
St. Alban	leda	120	2.85	22.9	14.6	190	88	1.16 <sup>12</sup>	0.63 <sup>3,4</sup>
St. Alban	leda	121	2.69	25.3	15.4	182	87	1.16	0.63 <sup>3,4</sup>
St. Alban	leda	122	2.12	48	23.1	276	121	1.16	0.55 <sup>3,4</sup>
St. Alban	leda	123	2.13	60.8	27.4	321	155		0.54 <sup>3,4</sup>
St. Alban	leda	124	2.12	92.1	37.9	406	229	1.16	0.556 <sup>3,4</sup>
St. Alban	leda	125	2.51	111.1	44.3	512	302	1.16	0.53 <sup>3,4</sup>
Strong Pit	clay silt	126	3.90	122	122	2170	1200		0.95 <sup>4</sup>
Tiller	intact	127	3.30	126	81	524	158		
Tiller	intact	128	2.62	316	171	1246	928		
Tokyo	intact	129	3.08	51	51	401	189		0.70 <sup>3</sup>
Tokyo	intact	130	1.88	119	99	563	218		0.55 <sup>3</sup>
Tokyo	intact	131	1.50	255	155	921	434		0.47 <sup>3</sup>
Tongji	intact	132	1.50	298	140	873	461		
Tongji	intact	133	1.50	320	152	861	466		
Tongji	intact	134	1.50	333	155	1002	544		
Troll East, Area 2	intact	135	1.50	127.3	48.8	347	239	1.24	0.70 <sup>4</sup>
Troll East, Area 2	intact	136	1.40	206.7	79.1	552	417	1.24	0.61 <sup>4</sup>
Troll East, Area 2	intact	137	1.30	323	126.8	884	587	1.24	0.60 <sup>4</sup>
Upper 232nd St.	silty NC	138	1.00	144	94	254	194	1.30	0.50 <sup>4</sup>
Valoya	intact	139	2.64	380	215	1679	1007	1.07	0.69 <sup>4</sup>
Vancouver	intact	140	1.60	348	178	960	522		0.61 <sup>4</sup>
Vancouver	intact	141	1.50	441	221	1150	675		0.61 <sup>3</sup>

<sup>10</sup>Jamiolkowski et al. (1985)

<sup>12</sup>Demers and Leroueil (2002)

## G.2 Database of continuous CPTU results from clay sites

This appendix provides profiles of continuous piezocone data from Bäckebol, Skå-Edeby, Amhrest and Bothkennar sites. The charts include stress profiles of soils, as well as the smoothed and normalized cone measurements  $Q_t$ ,  $B_q$  and  $F_r$ . The procedure of smoothing was performed on raw measurements of  $q_t$ ,  $u_2$  and  $f_s$  respectively.

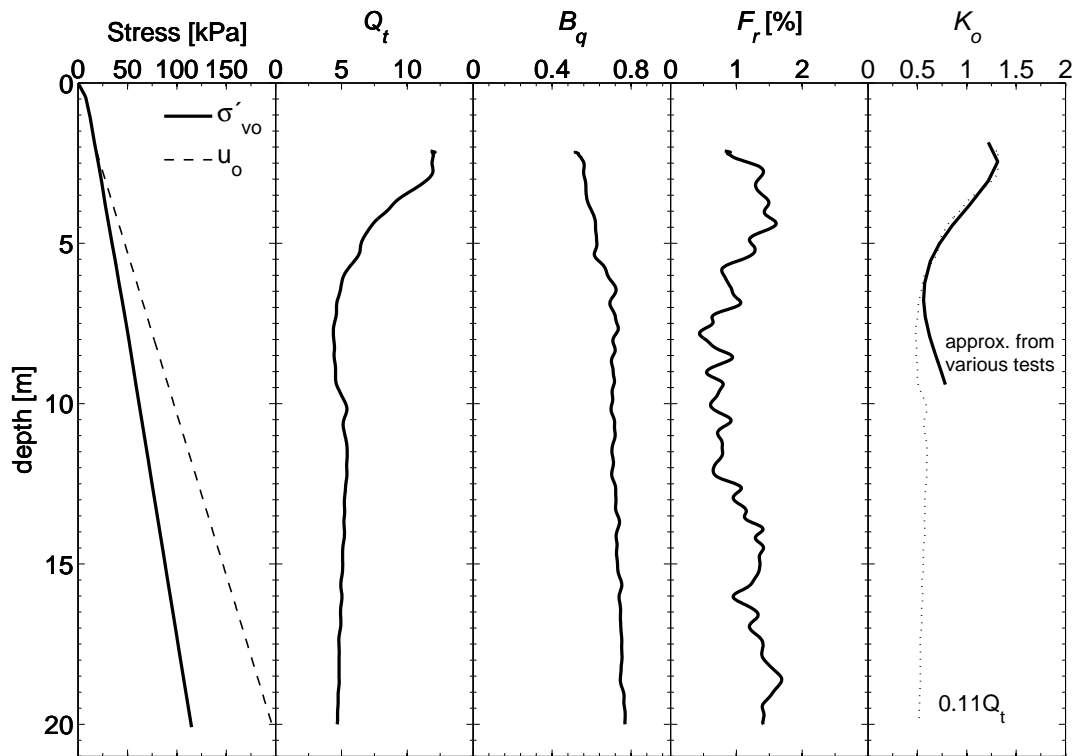


Figure G.1: Stress soil profile and normalized smoothed results from piezocone tests at Bäckebol site (based on Larsson and Mulabdić, 1991).



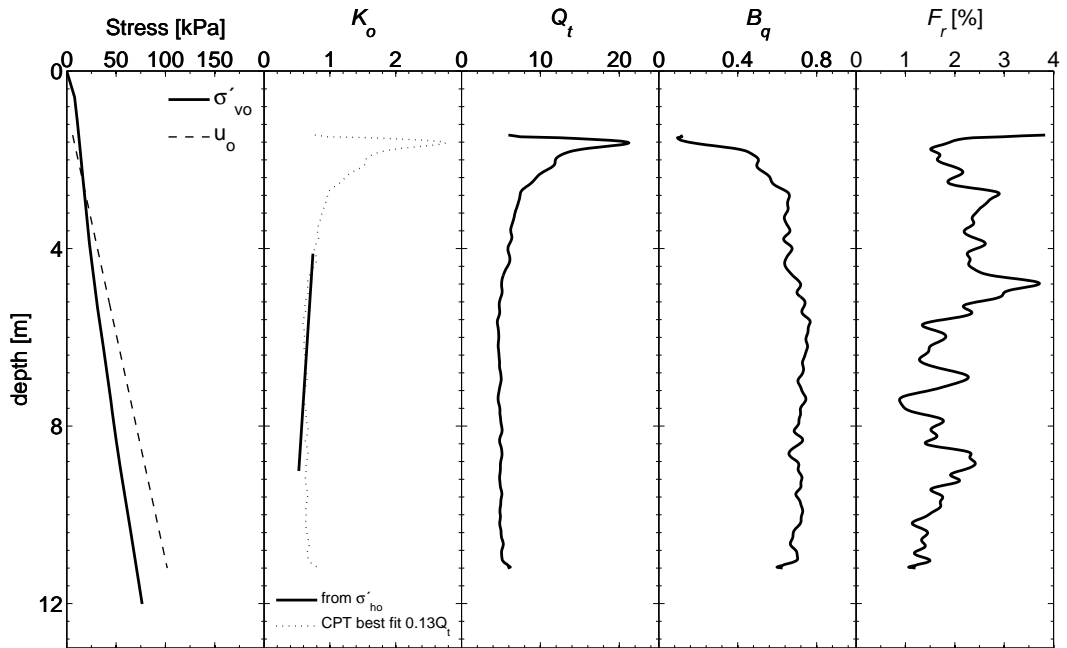


Figure G.2: Stress soil profile and normalized smoothed results from piezocone tests at Skå-Edeby site (based on Larsson and Mulabdić, 1991).

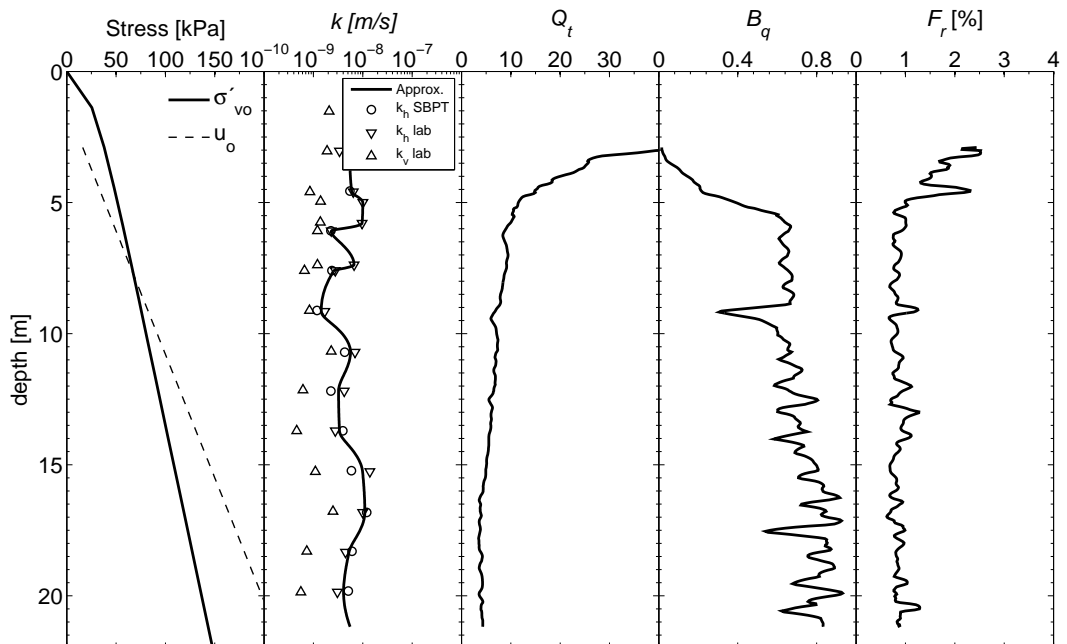


Figure G.3: Stress soil profile and normalized smoothed results from piezocone tests at Amhrest site (based on DeGroot and Lutenegeger, 2003).

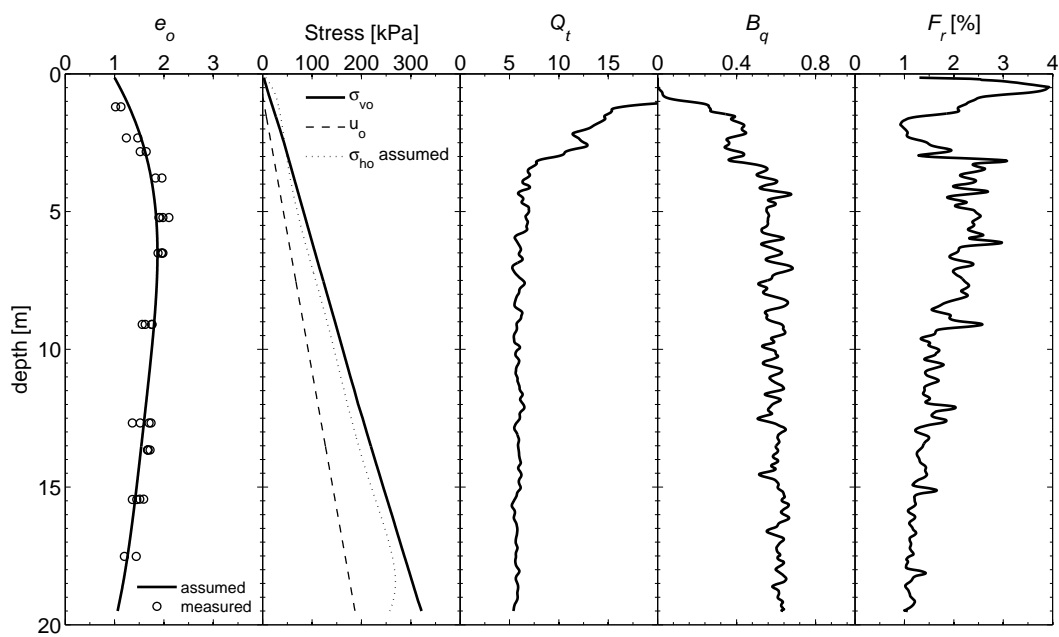


Figure G.4: Profiles of voids ratio, *in situ* stress and normalized smoothed results from piezocone tests at Bothkennar site (based on Nash et al., 1992a,b).

# CURRICULUM VITAE

## Rafał Filip Obrzud

ul. Armii Krajowej 87/17  
30-150 Cracow, Poland  
rafal.obrzud@gmail.com

### Personal

Born on January 25, 1977 in Kraków (Cracow), Poland.

Polish Citizen.

### Education

1996–2001, M.Sc. Civil Engineering, Cracow University of Technology (PK), Poland, Specialization: Buildings and Engineering Constructions.

1992–1996, VII Secondary School in Cracow (Poland), Class orientation: Physics and Mathematics.

1984–1992, 145<sup>th</sup> Primary School in Cracow (Poland).

### Employment

Since 2006, Soil Mechanics Laboratory, École Polytechnique Fédérale de Lausanne (EPFL), Switzerland.

2001–2005, Teaching Assistant, Institute of Geotechnics, Cracow University of Technology (PK), Poland.

2001–2005, Junior Engineer, AB-Projekt, Cracow, Poland.

### Publications

#### Journal Articles

A combined neural network/gradient-based approach for the identification of constitutive model parameters using self-boring pressuremeter tests. Obrzud RF, Vulliet L, Truty A, *Int J Num Anal Meth Geomech*, 2009, 33(6):817-849.

Optimization framework for calibration of constitutive models enhanced by neural networks. Obrzud RF, Vulliet L, Truty A, *Int J Num Anal Meth Geomech*, 2009, 33(1):71-94.

## Proceedings

Constitutive model calibration supported by neural networks. Obrzud R, Truty A, Vulliet L, II Polish Conference on Computer Methods in Geotechnics and Geological Engineering, Poznań-Rydzyzna, November 23-25, 2007, (*in press*).

Sztywność gruntów w zakresie małych odkształceń (*in Polish*, Soils stiffness in small strains). Truty A, Konior T, Obrzud R, XVII Sci Conf "Metody Komputerowe w Projektowaniu i Analizie Konstrukcji Hydrotechnicznych", Korbiewów, 7-10 March, pp.117-126, 2005.

Load capacity analysis of the multi-layered subsoil. Gaszynski J, Obrzud R, *in Proc.: New methods in geotechnical engineering*, Bratislava, June 23-24, pp.217-222, 2003.

## Abstracts/Conference Presentations

Application of neural networks to parameter identification for soil from *in situ* tests (*in Polish*), Truty A, Obrzud RF, Vulliet L. XX Sci Conf "Metody Komputerowe w Projektowaniu i Analizie Konstrukcji Hydrotechnicznych", Korbiewów, 3-6 March, 2008.

Identification of model parameters supported by artificial intelligence, Obrzud RF, Vulliet L, Truty A. ALERT Geomaterials Workshop, Session 2: Inverse and Stochastic Modelling, Aussois, France, 8-10 October 2007.